ADVANCES IN THE DEVELOPMENT OF ARTIFICIAL METALLOENZYMES

EDITED BY: Tatjana N. Parac-Vogt, Andrea Erxleben, Gerhard Schenk and Rajeev Prabhakar
PUBLISHED IN: Frontiers in Chemistry

About Frontiers

Frontiers is more than just an open-access publisher of scholarly articles: it is a pioneering approach to the world of academia, radically improving the way scholarly research is managed. The grand vision of Frontiers is a world where all people have an equal opportunity to seek, share and generate knowledge. Frontiers provides immediate and permanent online open access to all its publications, but this alone is not enough to realize our grand goals.

Frontiers Journal Series

The Frontiers Journal Series is a multi-tier and interdisciplinary set of open-access, online journals, promising a paradigm shift from the current review, selection and dissemination processes in academic publishing. All Frontiers journals are driven by researchers for researchers; therefore, they constitute a service to the scholarly community. At the same time, the Frontiers Journal Series operates on a revolutionary invention, the tiered publishing system, initially addressing specific communities of scholars, and gradually climbing up to broader public understanding, thus serving the interests of the lay society, too.

Dedication to Quality

Each Frontiers article is a landmark of the highest quality, thanks to genuinely collaborative interactions between authors and review editors, who include some of the world's best academicians. Research must be certified by peers before entering a stream of knowledge that may eventually reach the public - and shape society; therefore, Frontiers only applies the most rigorous and unbiased reviews.
Frontiers revolutionizes research publishing by freely delivering the most outstanding research, evaluated with no bias from both the academic and social point of view. By applying the most advanced information technologies, Frontiers is catapulting scholarly publishing into a new generation.

What are Frontiers Research Topics?

Frontiers Research Topics are very popular trademarks of the Frontiers Journals Series: they are collections of at least ten articles, all centered on a particular subject. With their unique mix of varied contributions from Original Research to Review Articles, Frontiers Research Topics unify the most influential researchers, the latest key findings and historical advances in a hot research area! Find out more on how to host your own Frontiers Research Topic or contribute to one as an author by contacting the Frontiers Editorial Office: researchtopics@frontiersin.org

ADVANCES IN THE DEVELOPMENT OF ARTIFICIAL METALLOENZYMES

Topic Editors:
Tatjana N. Parac-Vogt, KU Leuven, Belgium
Andrea Erxleben, National University of Ireland, Ireland
Gerhard Schenk, The University of Queensland, Australia
Rajeev Prabhakar, University of Miami, USA
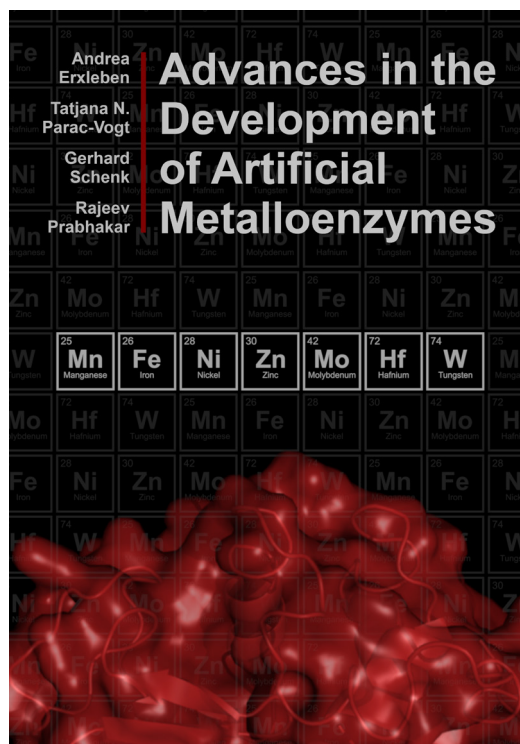
Advances in the development of artificial metalloenzymes.
Image: Laurens Vandebroek.

Reactions catalyzed by metalloenzymes have great potential for applications in the biotechnology and pharmaceutical industries. While only a few of these enzymes have yet been used in such applications, in the last few decades numerous efficient, selective, environmentally friendly and economical synthetic analogues have been described, including supramolecular, polymeric, nanoparticulate and low-molecular-weight organometallic complexes, and metal organic frameworks. In this Research Topic, we present a collection of original research and review articles that show significant recent advances made in the rational design of such artificial metalloenzymes.

Table of Contents

Editorial: Advances in the Development of Artificial Metalloenzymes

Tatjana N. Parac-Vogt[1], Andrea Erxleben[2], Gerhard Schenk[3] and Rajeev Prabhakar[4]*

[1] *Department of Chemistry, KU Leuven, Leuven, Belgium,* [2] *School of Chemistry, National University of Ireland, Galway, Ireland,* [3] *School of Chemistry and Molecular Biosciences, The University of Queensland, St. Lucia, QLD, Australia,*
[4] *Department of Chemistry, University of Miami, Coral Gables, FL, United States*

Editorial on the Research Topic

Advances in the Development of Artificial Metalloenzymes

A wide range of chemical reactions such as hydrolyses, oxidations/reductions, isomerizations, and ligations are catalyzed by metalloenzymes. Many of these reactions have great potential for applications in the biotechnology and pharmaceutical industries. However, only a few of these enzymes have yet been used in such applications, frequently with some shortcomings (e.g., low stability, non-optimal substrate specificity, and high production costs). Therefore, in the last few decades intensive efforts have been made for the design of efficient, selective, environmentally friendly, and economical synthetic analogs of metalloenzymes, also called artificial metalloenzymes. As a result, multiple types of such analogs have been developed, including supramolecular, polymeric, nanoparticulate and low-molecular-weight organometallic complexes, and metal organic frameworks. In this Research Topic, we present a collection of original research and review articles that show significant recent advances made in the rational design of artificial metalloenzymes.

Metal complexes have been commonly used for the hydrolysis of extremely stable peptide and phosphoester bonds. Anyushin et al. demonstrated that Hf(IV)-substituted Wells-Dawson polyoxometalate (POM), $K_{16}[Hf(\alpha_2-P_2W_{17}O_{61})_2]$ (Hf1-WD2) can act as an efficient and site-selective artificial protease by hydrolyzing ovalbumin (OVA). They proposed that the positively charged patches on the surface of OVA were critical for its activity rather than its overall charge. Crans et al. showed that a Wells-Dawson POM cluster $[P_2W_{18}O_{62}]^{6-}$ interacts with the ribosome through the W=O sites of the POM and stabilize its structure. This complex will help crystallographers to address the phase problem and improve a high-resolution X-ray structure of the ribosome. Horn et al. synthesized and characterized binuclear analogs of Ni-containing phosphoesterase enzymes [Ni complex of 1,3-bis(bis(pyridin-2-ylmethyl)amino)propan-2 ol]. An outstanding question concerning the mechanism of dimetallic phosphoesterases is the identity of the nucleophile (bridging or terminal water). They showed that this complex utilizes a terminal water molecule, rather than a bridging one, as a nucleophile. Hu et al. employed Density Functional Theory (DFT) calculations to investigate the phosphatase activities of six di- and tetravalent metal-cyclen (M-C) complexes (Zn-C, Cu-C, Co-C, Ce-C, Zr-C, and Ti-C). They showed that activities of these complexes can be rationally predicted using the metal-ligand and metal-nucleophile bond lengths, strain of the cyclen ring, atomic charges, and coordination number of the metal ion as parameters. Despite the remarkable success of metal complexes in unraveling the mechanisms of hydrolytic reactions, this approach has not been without challenges. Erxleben reviewed the current mechanistic understanding that has been gained from these molecules as well as the limitations

of this strategy. The importance of the often overlooked regeneration of these hydrolyzing agents was also highlighted. In another review on this topic, Williams and Grant discussed the progress in hydrolysis of lipids by a wide range of di- and tetravalent metal ion centers. In particular, the roles of conditions such as temperature and pH in their activities were explored.

In addition to hydrolysis, metal complexes have been successfully employed to study oxidation and decarboxylation reactions. Leone et al. designed an Mn-containing artificial enzyme belonging to the mimochrome VI (MC6) family with peroxygenase activity. Quite interestingly, it served as a bridge between native proteins and small-molecule catalysts. Das et al. synthesized and characterized a new Fe-oxo cluster with a sulfur containing ligand for alkene oxidation. This cluster catalyzed the reaction partially through a metal-centered process in tandem with free radical oxidation by reactive oxygen species. On the other hand, Costa et al. reported the synthesis and characterization of an unusual binuclear mixed-valent Mn-Mn compound with dual catalase and superoxide dismutase activities. The often elusive intermediates in both reactions were also identified. Ahmadi et al. designed a Mo^{IV} mono-oxido bis-dithiolene complex, $[MoO(mohdt)_2]^{2-}$ (mohdt = 1-methoxy-1-oxo-4-hydroxy-but-2-ene-2,3-bis-thiolate) as a model for molybdenum oxidoreductase enzymes to catalyze an oxygen atom transfer reaction. This aliphatic ligand-containing complex was shown to exhibit an activity comparable to that of its counterparts that contain aromatic dithiolene ligands. Sheng et al. employed combined theoretical and experimental techniques to study the mechanism of C-C bond cleavage by the metal-dependent iso-orotate decarboxylase (IDCase). They also predicted the identity of the relevant metal ion (Mn or Zn) and the substrate specificity of IDCase. Finally, Singh reviewed the enormous potential of nanozymes in biomedical applications.

The advantages and disadvantages of nanozymes over natural, as well as artificial enzymes were discussed.

The rational design of efficient artificial metalloenzymes has been widely acknowledged as one of the holy grails in chemistry. However, in the last few decades impressive advancements have been made in the design and synthesis of molecules to mimic both structural and functional aspects of natural metalloenzymes. Since the existing synthetic analogs of enzymes are still quite inferior in terms of rate, selectivity and turnover, we believe that it will continue to be an exceedingly important area of research.

AUTHOR CONTRIBUTIONS

All authors listed have made a substantial, direct and intellectual contribution to the work, and approved it for publication.

FUNDING

Selective Hydrolysis of Ovalbumin Promoted by Hf(IV)-Substituted Wells-Dawson-Type Polyoxometalate

Alexander V. Anyushin[1†], Annelies Sap[1], Thomas Quanten[1], Paul Proost[2] and Tatjana N. Parac-Vogt[1*]

[1] *Laboratory of Bio-Inorganic Chemistry, Department of Chemistry, KU Leuven, Leuven, Belgium,* [2] *Laboratory of Molecular Immunology, Department of Microbiology and Immunology, KU Leuven, Leuven, Belgium*

The reactivity and selectivity of Wells-Dawson type polyoxometalate (POM), $K_{16}[Hf(\alpha_2\text{-}P_2W_{17}O_{61})_2]\cdot19H_2O$ (Hf1-WD2), have been examined with respect to the hydrolysis of ovalbumin (OVA), a storage protein consisting of 385 amino acids. The exact cleavage sites have been determined by Edman degradation experiments, which indicated that Hf1-WD2 POM selectively cleaved OVA at eight peptide bonds: Phe13-Asp14, Arg85-Asp86, Asn95-Asp96, Ala139-Asp140, Ser148-Trp149, Ala361-Asp362, Asp362-His363, and Pro364-Phe365. A combination of spectroscopic methods including ^{31}P NMR, Circular Dichroism (CD), and Tryptophan (Trp) fluorescence spectroscopy were employed to gain better understanding of the observed selective cleavage and the underlying hydrolytic mechanism. ^{31}P NMR spectra have shown that signals corresponding to Hf1-WD2 gradually broaden upon addition of OVA and completely disappear when the POM-protein molar ratio becomes 1:1, indicating formation of a large POM/protein complex. CD demonstrated that interactions of Hf1-WD2 with OVA in the solution do not result in protein unfolding or denaturation even upon adding an excess of POM. Trp fluorescence spectroscopy measurements revealed that the interaction of Hf1-WD2 with OVA ($K_q = 1.1 \times 10^5$ M^{-1}) is both quantitatively and qualitatively slightly weaker than the interaction of isostructural Zr-containing Wells-Dawson POM (Zr1-WD2) with human serum albumin (HAS) ($K_q = 5.1 \times 10^5$ M^{-1}).

Keywords: polyoxometalates, ovalbumin, hafnium, Wells-Dawson, protein, hydrolysis

INTRODUCTION

Polyoxometalates (POMs) are a diverse class of metal-oxygen clusters with a wide range of tunable parameters such as their size, polarity, charge density, solubility and acid-strength (Pope, 1983; Long et al., 2010). Their easily modifiable properties (Sullivan et al., 2018) make them highly applicable in various research domains such as modern catalysis (Lv et al., 2012; Wang and Yang, 2015; Huang et al., 2018; Martin-Sabi et al., 2018; Yu et al., 2018), green energy production and storage (Chen et al., 2017, 2018), material science (Bijelic and Rompel, 2015; Sun et al., 2015; Boyd et al., 2017; Vilà-Nadal and Cronin, 2017; Zhan et al., 2017; Luo et al., 2018), bio-mimics design (Kulikov et al., 2017), and medicine (Bijelic et al., 2018a,b). Currently nearly 80% of all patents concerning POMs are related to catalysis, reflecting their importance as catalysts in various applications (Wang and Yang, 2015; Weinstock et al., 2018). The interest in developing

POMs as catalysts is to a large extent related to their rich structural chemistry which allows fine-tuning of their reactivity and other chemical properties such as redox potentials and acidity. The majority of POM-based catalysis has been focused on Brønsted catalyzed reactions and oxidations (Zhou et al., 2014). However, the use of POMs as catalysts in Lewis acid catalyzed reactions has recently also gained in importance. Lewis acid active POMs are typically obtained by incorporating highly charged metal cations into the lacunar site in a POM structure. At the same time, the coordination number of the imbedded metal cation should remain large in order to assure its interaction with the substrate. Due to their large coordination number, which is typically eight, Zr(IV) and Hf(IV) have been shown to be the most suitable choice for creating a Lewis acid active POM. Incorporation of Zr(IV) and Hf(IV) into POMs has led to catalysts that have been active in a wide range of different reactions such as the Mukaiyama aldol and Mannich-type additions (Boglio et al., 2007). The high Lewis acidity of Zr(IV)-POMs makes them also interesting as catalysts for the hydrolysis of the extremely stable phosphoester and peptide bonds, which are found in DNA and proteins, respectively. Our previous work has shown that Zr(IV) substituted Wells-Dawson $[[Zr(\alpha_2\text{-}P_2W_{17}O_{61})_2]^{16-}$, Zr1-WD2 (Vanhaecht et al., 2013), and $[Zr_4(\alpha_2\text{-}P_2W_{16}O_{59})_2(\mu_3\text{-}O)_2(OH)_2(H_2O)_4]^{14-}$ POMs (Luong et al., 2016a), as well as Keggin POMs $[(Et_2NH_2)_8[\{\alpha\text{-}PW_{11}O_{39}Zr(\mu\text{-}OH)(H_2O)\}_2]$ and $(Et_2NH_2)_{10}[(\alpha\text{-}PW_{11}O_{39})_2Zr]$ (Luong et al., 2014, 2015a,b, 2016b, 2017)], efficiently catalyze the cleavage of phosphoester bonds in nucleic acids as model substrates (Vanhaecht et al., 2013; Luong et al., 2014, 2015a,b, 2016a,b,c; Kandasamy et al., 2016). Also the selective cleavage of double-stranded DNA has been demonstrated (Luong et al., 2017). Interestingly, even though Zr(IV) and Hf(IV) have similar chemical properties and show a very similar coordination chemistry, the Hf(IV)-substituted Wells-Dawson POM showed a slightly higher reaction rate in the hydrolysis of phosphodiester bonds compared to the Zr(IV)-substituted Wells-Dawson POM (Zr1-WD2) (Vanhaecht et al., 2012). These POMs also exhibited hydrolyzing activity for a wide range of dipeptides (Absillis and Parac-Vogt, 2012; Ly et al., 2013a,b, 2016; Vanhaecht et al., 2013) oligopeptides (Absillis and Parac-Vogt, 2012; Vanhaecht et al., 2013; Ly et al., 2015b, 2016) and proteins (Stroobants et al., 2013, 2014a,b; Ly et al., 2015a; Sap et al., 2015a). Due to their negative charge POMs can specifically interact with positive regions of protein surfaces via electrostatic forces (Guangjin et al., 2007; Zhang et al., 2007, 2008; Zheng et al., 2009; Goovaerts et al., 2013), resulting in selective hydrolysis of peptide bonds located in the positive patches of proteins (Stroobants et al., 2014a). So far, several proteins such as hen egg white lysozyme (HEWL) (Sap et al., 2015b), human insulin β-chain (Sap et al., 2015a), human serum albumin (HSA) (Stroobants et al., 2014a,b), horse heart myoglobin (HHM) (Ly and Parac-Vogt, 2017), and cytochrome c (Cyt c) (Sap et al., 2016; Quanten et al., 2018) have been selectively hydrolyzed by Zr(IV)-substituted POMs (Stroobants et al., 2014a,b). Although these studies demonstrate the potential of Lewis acidic POMs to selectively hydrolyze peptide bonds in proteins, considering the very large variety

FIGURE 1 | Combined polyhedral/ball-and-stick representation of $[Hf(\alpha_2\text{-}P_2W_{17}O_{61})_2]^{16-}$ in $K_{16}[Hf(\alpha_2\text{-}P_2W_{17}O_{61})_2]\cdot19H_2O$. WO_6 octahedrons are shown in olive green, PO_4 tetrahedrons are shown in orange, and the Hf(IV) center is represented as a red sphere.
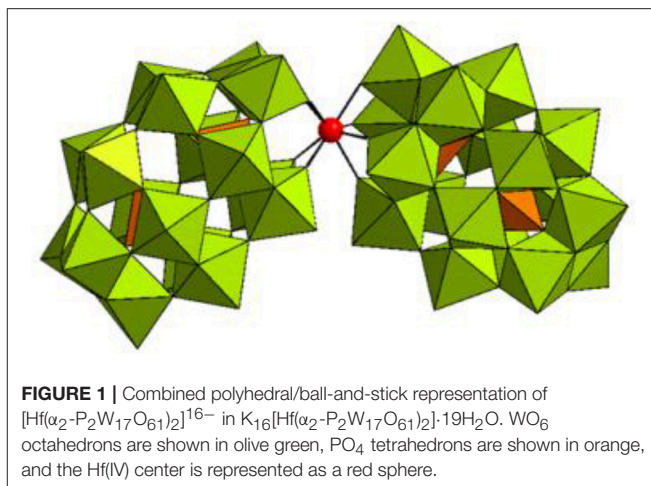
of the possible structures and sizes of the proteins, further research is needed in order to understand the influence of these structural effects on the selectivity and efficiency of peptide bond hydrolysis. Specifically, the ability of highly negatively charged POMs to hydrolyze proteins with low pI and overall negative charge needs further investigation. Furthermore, except for one recent example (Vandebroek et al., 2018), nearly all the hydrolysis experiments have been performed with Zr-substituted POMs, while the protease activity of Hf-substituted POMs on proteins remains virtually unexplored. In this study, the reactivity of the Lewis acidic Hf(IV)-substituted Wells-Dawson POM, $K_{16}[Hf(\alpha_2\text{-}P_2W_{17}O_{61})_2]\cdot19H_2O$ (Hf1-WD2, see **Figure 1**), was investigated toward the hydrolysis of a relatively large phosphorylated glycoprotein, ovalbumin (OVA). It is the most abundant protein in egg white, consisting of 385 amino acid residues and has a total molecular mass of 44.3 kDa. The secondary structural elements of OVA consist primarily of β-strands and α-helices. Moreover, ovalbumin (OVA) has a pI of 4.54 which means that at physiological pH, it has a net charge of −14, which might hinder the efficient binding to the Hf-POM catalyst. The interaction between OVA and Hf-POM has been investigated with a range of spectroscopic techniques in order to gain insight into the factors that influence the protein hydrolysis.

RESULTS AND DISCUSSION

Reactivity of Hf1-WD2 in the Hydrolysis of OVA

In this study, a solution of OVA was incubated with Hf1-WD2 at 60°C in phosphate buffer (10.0 mM, pH 7.4). Aliquots of the reaction mixtures containing OVA (0.02 mM) and POM (2.0 mM) were taken at time intervals up to 7 days after mixing and were analyzed using sodium dodecyl sulfate polyacrylamide gel electrophoresis (SDS-PAGE) (see **Figure 2**). No precipitation was observed during the course of the reaction. New bands with a lower MW appeared on the SDS-PAGE gel after incubation for ∼2 days at 60°C, indicating that hydrolysis of OVA had
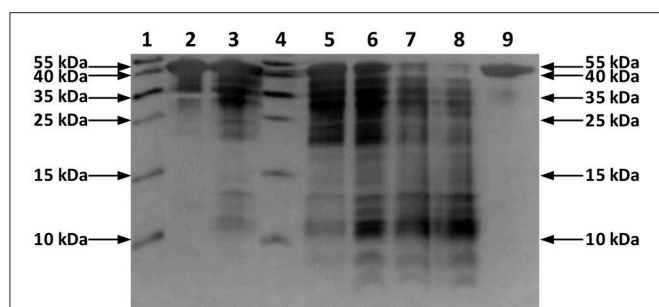
FIGURE 2 | Silver-stained SDS-PAGE gel of OVA in the presence of the Hf1-WD2 POM. OVA (0.02 mM) was incubated with 100 equivalents of Hf1-WD2 at 60°C for up to 7 days in phosphate buffer (10.0 mM, pH 7.4). Lanes 1–9 from left to right: protein ladder, OVA and POM immediately after mixing, after 1 day, protein ladder, after 2, 4, 6, 7 days, and OVA only after 7 days.
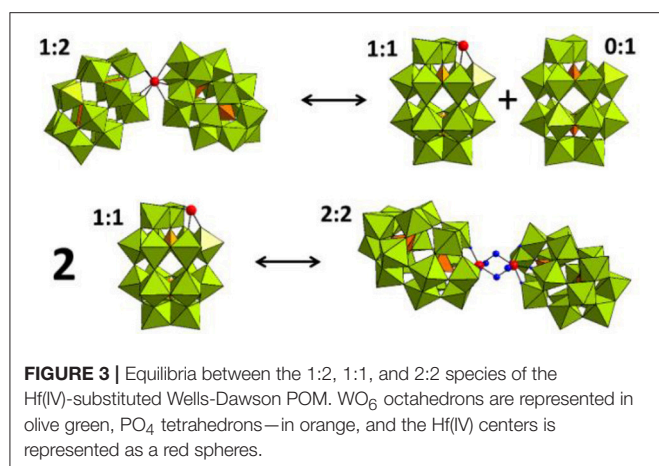
FIGURE 3 | Equilibria between the 1:2, 1:1, and 2:2 species of the Hf(IV)-substituted Wells-Dawson POM. WO_6 octahedrons are represented in olive green, PO_4 tetrahedrons—in orange, and the Hf(IV) centers is represented as a red spheres.
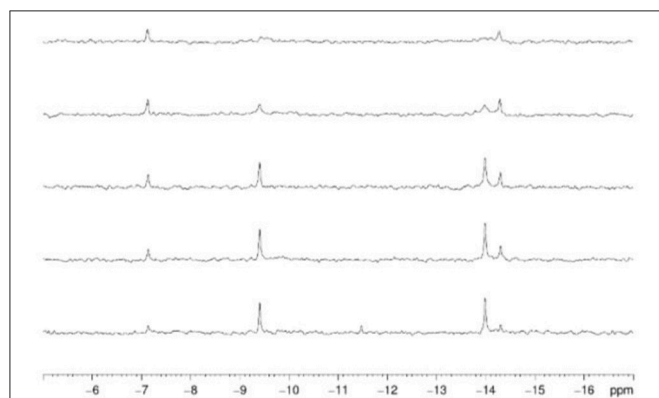
FIGURE 4 | ^{31}P NMR spectra of Hf1-WD2 (2.0 mM) with increasing concentrations of ovalbumin in phosphate buffer (10.0 mM, pH 7.4, 10 % D_2O) after mixing. From bottom to top: 0.0, 0.2 mM (10:1), 0.4 mM (5:1), 1.0 mM (2:1), 2.0 mM (1:1) of ovalbumin was added.

taken place in the presence of Hf1-WD2. To prove that Hf1-WD2 was indeed responsible for promoting hydrolysis of OVA, several control experiments were performed. In a first control

experiment, OVA was incubated in the absence of POM up to 7 days at 60°C (**Figure 2** right lane). Under these conditions, only the parent OVA protein was observed on the SDS-PAGE gel and there was no sign of hydrolysis. In a second control experiment, OVA was incubated for 7 days at 60°C with the α_2-Wells-Dawson POM, which is similar to Hf1-WD2 except for the absence of the embedded Hf(IV) ion, but again no hydrolysis was observed. In a third control experiment, OVA was incubated with $HfCl_2O \cdot 8H_2O$ salt for 7 days at 60°C. Under these conditions, only a minimal hydrolysis of OVA was observed, however also precipitation was observed in the reaction mixture (data not shown). All these tests clearly show that the Hf(IV) ion is a necessary component to induce hydrolysis, while the POM ligand serves as a stabilizing agent for Hf(IV) that prevents formation of insoluble gels in aqueous solution. To test whether Hf1-WD2 would be hydrolytically active toward OVA under both physiological temperature and pH, the temperature was lowered to 37°C, however very little hydrolysis was observed at pH 7.4 after 7 days. To evaluate the possible influence of the pH of the solution on the reactivity profile, the hydrolytic reaction was also followed in acetate buffer (10.0 mM, pH 4.4) and Tris-HCl buffer (10.0 mM, pH 9.0). Although one would expect that lowering the pH to pH 4.4 would result in improved interaction with Hf1-WD2 as the acidic environment increases the amount of positive charges on the OVA surface, interestingly only slight protein hydrolysis was observed. Similarly, no hydrolysis was revealed after incubation at 60°C and pH 9.0 for up to 6 days. The absence of hydrolysis might be due to the presence of precipitation which was observed under both these pH conditions and which probably resulted in the loss of Hf1-WD2 catalyst (see **Figure S1**). In addition, the presence of different buffers might also contribute to the observed changes in the reactivity, similarly to the recently reported inhibition and activation effect of buffers on the catalytic activity of Zr-POMs (Collins-Wildman et al., 2018).

POM Speciation and Interaction Study

^{31}P NMR spectroscopy was used to gain insight into the equilibria between the different POM catalyst species present in solution. In solution, Hf1-WD2 undergoes different equilibria which are highly influenced by factors such as concentration, pH, temperature and incubation time (see **Figure 3**). As can be deduced from **Figure 4**, Hf1-WD2 is presented as the 1–2 dimeric species in the absence of OVA, as indicated by the two peaks at −9.4 and −14.0 ppm (Kato et al., 2006). However, the additional appearance of two small signals at approximately −7.15 and −14.3 ppm indicate that the α_2-Wells-Dawson species is also present in solution. The formation of the α_2-Wells-Dawson POM appears to be induced by the phosphate buffer as these peaks are absent in D_2O solutions that do not contain phosphate buffer (see **Figure S2**). In the presence of increasing concentrations of OVA, the signals corresponding to the α_2-Wells-Dawson POM remain present (see **Figure 4**). However, the signals corresponding to the 1–2 dimeric species of Hf1-WD2 gradually broaden and completely disappear when the POM-protein molar ratio becomes 1:1. This fact is in a good relationship with the previously described mechanism of
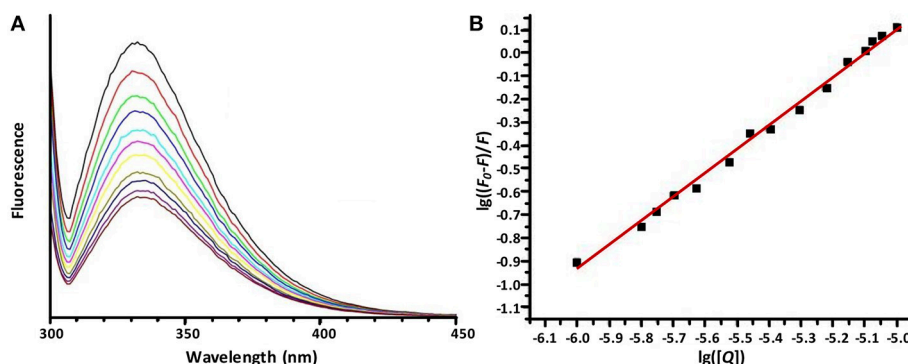
FIGURE 5 | The emission spectra of OVA (10.0 μM) in sodium phosphate buffer (10 mM, pH 7.4) in the presence of increasing concentrations of Hf1-WD2. **(A)** demonstrates dependence of the emission fluorescence spectra (from top to bottom) from the concentration of Hf1-WD2, which was increased stepwise from 0 to 10 μM. All spectra were recorded from 300 to 420 nm while the sample was excited at 295 nm. The spectra are dominated by the Trp fluorescence with a maximum at around 337 nm. **(B)** displays the plot of the Stern-Volmer equation (with $R^2 = 0.976$) that represents the quenched maximum fluorescence ($lg((F-F_0)/F)$) in function of the logarithm of the concentration of the quencher ($lg[Q]$). From the plot, K_q and n were calculated to be 1.1×10^5 M^{-1} and 0.85, respectively.

docking of the WD POM species on the surface of the proteins (Vandebroek et al., 2018). According to that knowledge, the broadening of the ^{31}P NMR signals of Hf1-WD2 was observed because of the docking of the 1–2 dimeric species in the positive patch on the surface of OVA and the consecutive dynamic equilibria between the Hf1-WD2 dimer and the products of dissociation.

As the coordination sphere of Hf(IV) is fully saturated, it is unlikely that the dimeric 1:2 POM shown in the ^{31}P NMR spectra is a catalytically active species. In contrast to the dimeric species, the 1–1 monomer does have free coordination sites available for binding to the protein substrate. It is therefore likely that a fast equilibrium takes place in solution in which the 1:2 dimeric species interconverts with the 1:1 monomeric species. In a recent study, we have shown that even though the dimeric Hf1-WD2 was mixed with HEWL, only the 1:1 monomeric species of the Hf(IV)-substituted Wells-Dawson POM was observed in a non-covalent complex with HEWL (Vandebroek et al., 2018). The single crystal X-ray structure of the non-covalent complex suggests that the monomeric POM species indeed can be formed in solutions containing a protein and the dimeric Hf1-WD2, and that it is the likely active catalytic species in protein hydrolysis experiments. ^{31}P NMR measurements were also performed to investigate the stability and speciation of Hf1-WD2 in the presence of OVA throughout the hydrolytic reaction. As shown in **Figure S3**, Hf1-WD2 is stable in the presence of OVA during incubation for 7 days at 60°C and presents as the dimeric species.

Interaction Between OVA and Hf1-WD2

Circular dichroism (CD) measurements show the presence of α-helical structure elements in OVA which are characterized by two minima at 208 nm and 222 nm. Titration experiments show that the α-helical structure is preserved upon addition of increasing concentrations of Hf1-WD2 (see **Figure S4**), suggesting that the interaction with the POM does not result in protein unfolding or denaturation.

The interaction between OVA and Hf1-WD2 was further studied using tryptophan (Trp) fluorescence quenching. OVA contains three tryptophan (Trp) and ten tyrosine (Tyr) residues, however despite the presence of ten Tyr residues, its emission spectrum is dominated by Trp fluorescence (see **Figure 5**), since Trp absorbs at higher wavelengths where Tyr no longer absorbs (above 290 nm). Moreover, any energy absorbed by Tyr residues is often efficiently transferred to the Trp residues in the same protein (Lakowicz, 2007). Therefore, using excitation light at 295 nm avoids any detectable emission of the Tyr residues. Trp fluorescence is widely used as a tool to monitor changes in the local protein environment and to study protein-POM interactions (Goovaerts et al., 2015a,b; Ly and Parac-Vogt, 2017).

As **Figure 5** shows, the Trp fluorescence of OVA is quenched by the addition of Hf1-WD2, indicating that binding took place. This quenching can be fitted to the derived Stern-Volmer equation (**1**) (Hungerford et al., 2010):

$$lg\left(\frac{(F_0 - F)}{F}\right) = lgK_q + n \cdot lg([Q]) \qquad (1)$$

Herein F_0 represents the unquenched fluorescence, F the quenched fluorescence, $[Q]$ the concentration of the quencher, K_q the quenching constant and n the number of bound quenching molecules to the protein. According to equation (**1**), the calculated values of $K_q(M^{-1})$ and n are $(1.1\pm0.3) \times 10^5$ and 0.85 ± 0.04 ($R^2 = 0.976$), respectively, for the interaction between OVA and Hf1-WD2 (see **Table 1**).

This K_q value is in the same range of magnitude as the K_q which was found for the binding between Zr1-WD2 and HSA [$K_q(M^{-1}) = 5.1 \times 10^5$] (Goovaerts et al., 2015b). The slightly stronger interaction observed in the case of HSA might be due to the larger size of HSA (585 amino acids and 66.5 kDa compared to 385 amino acids and 44.3 kDa for OVA), which is noticeable by the smaller number of POMs that OVA can accommodate (0.85 for OVA compared to 1.5 for HSA). The second factor is the higher pI of HSA than OVA (5.2 and 4.5, respectively) leading to

TABLE 1 | Calculated values of the quenching constants (K_q), their corresponding number of bound molecules (n), the percentage of hydrolyzed OVA and HSA (Stroobants et al., 2014a) after 48 h incubation at pH 7.4 and 60°C for different POM-protein complexes.

Protein	POM	K_q (M^{-1})	n	Hydrolysis (%) after 48 h
OVA	Hf1-WD2	1.1×10^5	0.85	~50 (This study)
HSA	Zr1-WD2	5.1×10^5	1.52	~75 (Stroobants et al., 2014a)

a less negative total surface charge of HSA (about-12) compared to OVA (about-14) at the experimental pH (7.4). Nevertheless, the positively charged patch on the OVA surface presents even at pH = 7.4 and defines the selectivity of docking of the POM species on the surface of the protein. The size of the positive patch on the surface of OVA is 1.3×1.0 nm, that correlates quite well with the size of the monomeric POM species (1.2×1.0 nm) and significantly smaller than the size of the dimeric species (about 3.0×1.4 nm). The single Trp residue in HSA is located inside a highly positive cleft which can nicely accommodate a Zr1-WD2, which is not the case for Trp residues found in OVA. While two of the three Trp residues in OVA are accessible for a solvent and are located near a positively charged surface area (see **Figure 6**), the third Trp residue (Trp185) is not solvent accessible, but it is in close proximity to the surface of the protein. Considering that the peak position and profile do not change as more POM is added, it is reasonable to assume that all Trp residues are affected by the binding of the POM (Lakowicz, 2007). One of the likely binding sites is close to Trp149 as this residue is located in an easily accessible and wide surface area. While binding close to Trp268 cannot be excluded, interaction around this residue is less likely as this residue is surrounded by negatively charged regions.

Selectivity of Hydrolysis

To identify the exact cleavage sites in OVA induced by Hf1-WD2, the protein fragments from the SDS-PAGE gel were first transferred to a polyvinylidene fluoride (PVDF) membrane which was then Coomassie-stained. Thereafter, Edman degradation was performed on the Coomassie-stained protein fragments which demonstrated that Hf1-WD2 POM selectively hydrolyzed OVA at Phe13-Asp14, Arg85-Asp86, Asn95-Asp96, Ala139-Asp140, Ser148-Trp149, Ala361-Asp362, Asp362-His363, and Pro364-Phe365 bonds (see **Figures S5, S6, Table S1**).

All hydrolyzed peptide bonds in OVA are located in the positively charged surface regions of the protein to which the negatively charged Wells-Dawson POM can easily dock prior to hydrolysis. Moreover, all observed cleavage sites always contained Asp, either as part of the hydrolyzed peptide bond (Asp-X or X-Asp, see **Figures S5, S6**) or in the close proximity to the hydrolyzed peptide bond. Interestingly, there are nine X-Asp bonds present in OVA which are not hydrolyzed by Hf1-WD2, which can most likely be attributed to these sites being sterically inaccessible.

The affinity of Hf1-WD2 to hydrolyze peptide bonds in the vicinity of Asp residues is consistent with the previous studies involving Zr-POM catalysts. For example, it was shown that three out of the four hydrolyzed peptide bonds in HSA were at X-Asp or X-Glu (Stroobants et al., 2014a). Similarly, HHM was exclusively hydrolyzed at Asp-X peptide bonds by different Zr(IV)-POMs (Ly et al., 2015a). Furthermore, two out of three hydrolysis sites in Cyt c hydrolyzed by Zr(IV)-substituted Keggin POMs were also cleaved at Asp-X peptide bonds (Sap et al., 2016), and a recent study has shown that Hf1-WD2 hydrolyzed HEWL at nine sites, all of which were Asp-X or X-Asp (Vandebroek et al., 2018). In all cases, the hydrolyzed peptide bonds were situated close to a positively charged patch of the protein to which the negatively charged POM can dock. The selectivity of POMs toward peptide bonds in the proximity of an Asp residue is not yet fully understood and is currently being investigated with the help of theoretical methods. It is however plausible that the carboxylate group found in the side chain of Asp can assist hydrolysis either via direct intramolecular nucleophilic attack on the carbonyl carbon, or via accepting protons from water molecules which then act as effective nucleophiles. In either cases the interaction between the Lewis acid metal ion [Zr(IV), Hf(IV)] and the carbonyl oxygen of the peptide bond is essential as it polarizes carbonyl bonds and makes carbon atoms more susceptible for nucleophilic attack (Ly et al., 2015c; Mihaylov et al., 2016).

CONCLUSIONS

In this study, the Hf(IV)-substituted Wells-Dawson POM, $K_{16}[Hf(\alpha_2\text{-}P_2W_{17}O_{61})_2]$ (Hf1-WD2) was shown to act as an efficient and site-selective artificial protease for the hydrolysis of OVA. In accordance to previously studied proteins, the hydrolysis preferentially occurs in the vicinity of Asp residues located in positively charged patches of proteins. A combination of POM-protein electrostatic interactions and Asp side chain assisted nucleophilic attack on the carbon atom of the peptide bond are likely at the origin of the observed selectivity. The Hf(IV) and Zr(IV) substituted Wells-Dawson POMs seem to show similar selectivity in hydrolysis experiments, which can be attributed to their similar structures and a similar Lewis acidic behavior of these two metal ions. Interestingly, the highly negatively charged Hf1-WD2 was able to hydrolyze OVA protein which has a relatively low pI of 4.54 and an overall negative charge of −14 under physiological pH. This suggests that for the hydrolysis to occur the overall charge of the protein is not the limiting factor as long as the protein contains the positively charged patches which are accessible for interaction with the POM catalyst.

EXPERIMENTAL

Materials

Albumin from chicken egg white lyophilized powder (ovalbumin, OVA), deuteriumoxide (D_2O), N,N,N′,N′-tetramethylethylenediamine (TEMED), and disodium phosphate (Na_2HPO_4) were bought from Sigma-Aldrich. Hafnium oxychloride octahydrate ($HfOCl_2 \cdot 8H_2O$) and diethyl ether (Et_2O) were purchased from ChemLab. Aqueous hydrochloric acid (HCl, 37%), acetic acid (CH_3COOH), sodium
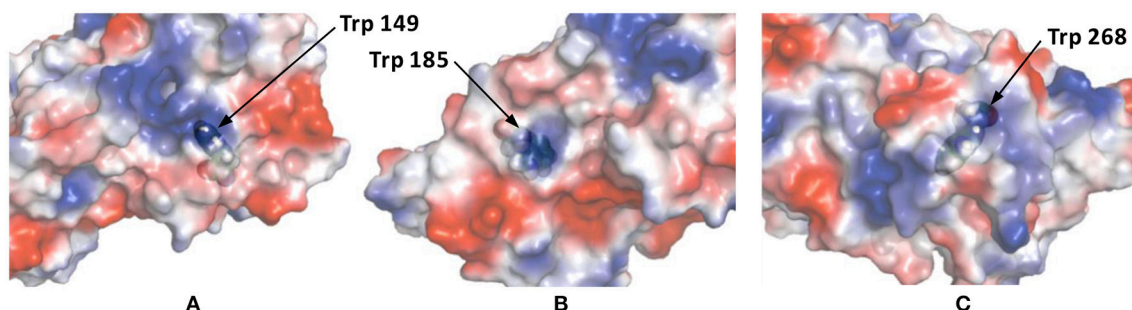
FIGURE 6 | The surface charge of OVA as rendered by PyMol's Vacuum Electrostatics. Red, white and blue stand for negative, neutral and positive surface charges, respectively. **(A)** displays Trp residue 149 and is solvent accessible through a positive surface patch. **(B)** shows Trp residue 185, which is not solvent accessible, but is still in close proximity of a positive patch. The final Trp residue, 268, is shown in **(C)**. This solvent accessible Trp residue is located in a small, positive surface patch.

acetate (CH_3COONa), and potassium hydrogen carbonate ($NaHCO_3$) were obtained from Acros Organics. Methanol and monosodiumphosphate (NaH_2PO_4) were purchased from VWR. Ethanol, aqueous orthophosphoric acid (H_3PO_4, 85%), and protein ladders were acquired from Thermo Fisher Scientific. Potassium chloride (KCl), tris(hydroxymethyl)aminomethane (TRIS), and acrylamide:bisacrylamide (29:1) solution (30%) were procured from AppliChem. All compounds were purchased in the highest available purity and were used without further purification. α-/β-$K_6P_2W_{18}O_{62}\cdot14/19H_2O$ (Contant et al., 1990), α_2-$K_{10}P_2W_{17}O_{61}\cdot20H_2O$ (Contant et al., 1990), and $K_{16}[Hf(\alpha_2$-$P_2W_{17}O_{61})_2]\cdot19H_2O$ (Kato et al., 2006) were synthesized according to the reported literature procedures.

Methods

Hydrolysis Study
Solutions containing OVA (0.02 mM) and $K_{16}[Hf(\alpha_2$-$P_2W_{17}O_{61})_2]\cdot19H_2O$ (2.0 mM) were prepared in phosphate buffer (10 mM, pH 7.4), acetate buffer (10 mM, pH 4.4), or Tris-HCl buffer (10 mM, pH 9.0) Samples were incubated at 60 or 37°C and aliquots were taken at different time increments and analyzed by SDS-PAGE.

Electrophoresis
SDS-PAGE was performed on a 16% (wt./vol.) polyacrylamide resolving gel (Tris-HCl buffer, 1.5 M, pH 8.8) and a 4% (wt./vol.) polyacrylamide stacking gel (Tris-HCl, 0.5 M, pH 6.8). Each sample (15 μL) was mixed with sample buffer (5 μL) and heated to 95°C for 5 min. A volume of 10 μL of the resulting solution was loaded onto the gel. A PageRuler prestained protein ladder (10–170 kDa) was used as a molecular mass standard. An OmniPAGE electrophoretic cell was used with an EV243 power supply (both produced by Consort). Two SDS-PAGE gels were run at the same time in a Tris-Glycine-SDS running buffer with the maximum voltage set to 200 V, a constant current set to 70 mA, and the maximum power set to 50 W. The total running time was ~1.5 h. SDS-PAGE gels were visualized with silver staining or coomassie staining and an image of each gel was taken using a GelDoc EZ Imager (BioRad).

Edman Degradation
SDS-PAGE-separated proteins were blotted onto a PVDF membrane (using a BioRad Trans-Blot Turbo RTA Transfer Kit) and stained with Coomassie blue. The bands were cut from the stained membrane, destained in methanol, rinsed with ultrapure water, and then subjected to automated NH_2-terminal amino acid sequence analysis (Procise 491 cLC protein sequencer, Applied Biosystems, Foster City, CA) based on the Edman degradation reaction (Loos et al., 2009).

^{31}P NMR Spectroscopy
All ^{31}P NMR spectra were recorded on a Bruker Avance 400 (161.98 MHz) spectrometer. As an external standard, 25% H_3PO_4 in D_2O in a sealed capillary was used. Upon mixing: Solutions containing $K_{16}[Hf(\alpha_2$-$P_2W_{17}O_{61})_2]\cdot19H_2O$ (2.0 mM) and increasing concentrations of OVA (0, 0.2, 0.4, 1.0, and 2.0 mM) were prepared in phosphate buffer (10.0 mM, pH 7.4, 10% D_2O) and measured directly after mixing. During the reaction: A solution containing $K_{16}[Hf(\alpha_2$-$P_2W_{17}O_{61})_2]\cdot19H_2O$ (2.0 mM) and OVA (0.4 mM) was prepared in phosphate buffer (10.0 mM, pH 7.4, 10% D_2O) and was measured after mixing and after incubation for 7 d at 60°C.

Circular Dichroism Spectroscopy
Solutions containing OVA (5.0 μM) and $K_{16}[Hf(\alpha_2$-$P_2W_{17}O_{61})_2]\cdot19H_2O$ (Hf1-WD2) (0 to 25 μM) were prepared in phosphate buffer (10.0 mM, pH 7.4). CD measurements were performed using a JASCO-1500 directly after preparation of the samples. The samples were analyzed in quartz cells with a path length of 1.0 mm. Scans were recorded in the far-UV wavelength region (185–260 nm) where peptide bond absorption takes place. All CD spectra were corrected for the background effect by subtracting the spectrum of the respective buffer solution from the spectrum of the protein.

Fluorescence Spectroscopy
Steady state fluorescence was measured on an Edinburgh Instruments FS900 spectrofluorimeter, using quartz cuvettes

with a 10.0 mm optical path length. Tryptophan fluorescence spectra of buffered 10.0 μM protein solutions (pH 7.4, 10.0 mM sodium phosphate buffer), were recorded at ambient temperature ranging from 300 to 450 nm, with a maximum at ∼330 nm. The samples were excited at 295 nm to avoid excitation of the tyrosine residues. Each emission spectrum was recorded in threefold and averaged to take any random error into account. The concentration of the POMs was increased from 0 to 10.0 μM in 1.0 μM steps.

AUTHOR CONTRIBUTIONS

ACKNOWLEDGMENTS

SUPPLEMENTARY MATERIAL

The Supplementary Material for this article can be found online at: https://www.frontiersin.org/articles/10.3389/fchem.2018.00614/full#supplementary-material

REFERENCES

Absillis, G., and Parac-Vogt, T. N. (2012). Peptide bond hydrolysis catalyzed by the Wells-Dawson $Zr(\alpha_2-P_2W_{17}O_{61})_2$ polyoxometalate. *Inorg. Chem.* 51, 9902–9910. doi: 10.1021/ic301364n

Bijelic, A., Aureliano, M., and Rompel, A. (2018a). The antibacterial activity of polyoxometalates: structures, antibiotic effects and future perspectives. *Chem. Commun.* 54, 1153–1169. doi: 10.1039/c7cc07549a

Bijelic, A., Aureliano, M., and Rompel, A. (2018b). Polyoxometalates as potential next-generation metallodrugs in the combat against cancer. *Angew. Chem. Int. Ed.* 57, 2–22. doi: 10.1002/anie.201803868

Bijelic, A., and Rompel, A. (2015). The use of polyoxometalates in protein crystallography - an attempt to widen a well-known bottleneck. *Coord. Chem. Rev.* 299, 22–38. doi: 10.1016/j.ccr.2015.03.018

Boglio, C., Micoine, K., Remy, P., Hasenknopf, B., Thorimbert, S., Lacote, E., et al. (2007). Increased Lewis acidity in hafnium-substituted polyoxotungstates. *Chem. Eur. J.* 13, 5426–5432. doi: 10.1002/chem.200700010

Boyd, T., Mitchell, S. G., Gabb, D., Long, D.-L., Song, Y.-F., and Cronin, L. (2017). POMzites: a family of zeolitic polyoxometalate frameworks from a minimal building block library. *J. Am. Chem. Soc.* 139, 5930–5938. doi: 10.1021/jacs.7b01807

Chen, J.-J., Symes, M. D., and Cronin, L. (2018). Highly reduced and protonated aqueous solutions of $[P_2W_{18}O_{62}]^{6-}$ for on-demand hydrogen generation and energy storage. *Nat. Chem.* 10, 1042–1047. doi: 10.1038/s41557-018-0109-5

Chen, J.-J., Ye, J.-C., Zhang, X.-G., Symes, M. D., Fan, S.-C., Long, D.-L., et al. (2017). Design and performance of rechargeable sodium ion batteries, and symmetrical Li-ion batteries with supercapacitor-like power density based upon polyoxovanadates. *Adv. Energy Mater.* 8:1701021. doi: 10.1002/aenm.201701021

Collins-Wildman, D. L., Kim, M., Sullivan, K. P., Plonka, A. M., Frenkel, A. I., Musaev, D. G., et al. (2018). Buffer-induced acceleration and inhibition in polyoxometalate-catalyzed organophosphorus ester hydrolysis. *ACS Catal.* 8, 7068–7076. doi: 10.1021/acscatal.8b00394

Contant, R., Klemperer, W. G., and Yaghi, O. (1990). "Chapter 3: early transition metal polyoxoanions 18. Potassium Octadecatungstodiphosphates(V) and related lacunary compounds," in *Inorganic Syntheses,* Vol. 27, ed A. P. Ginsberg (New York, NY: JohnWiley & Sons), 104–107.

Goovaerts, V., Stroobants, K., Absillis, G., and Parac-Vogt, T. N. (2013). Molecular interactions between serum albumin proteins and Keggin type polyoxometalates studied using luminescence spectroscopy. *Phys. Chem. Chem. Phys.* 15, 18378–18387. doi: 10.1039/c3cp52848k

Goovaerts, V., Stroobants, K., Absillis, G., and Parac-Vogt, T. N. (2015a). Eu(III) luminescence and tryptophan fluorescence spectroscopy as a tool for understanding interactions between hen egg white lysozyme and metal-substituted Keggin type polyoxometalates. *J. Inorg. Biochem.* 102, 72–80. doi: 10.1016/j.jinorgbio.2015.03.015

Goovaerts, V., Stroobants, K., Absillis, G., and Parac-Vogt, T. N. (2015b). Understanding the regioselective hydrolysis of human serum albumin by Zr(IV)-substituted polyoxotungstates using tryptophan fluorescence spectroscopy. *Inorganics* 3, 230–245. doi: 10.3390/inorganics3020230

Guangjin, Z., Keita, B., Craescu, C. T., Miron, S., de Oliveira, P., and Nadjo, L. (2007). Polyoxometalate binding to human serum albumin: a thermodynamic and spectroscopic approach. *J. Phys. Chem. B* 111, 11253–11259. doi: 10.1021/jp072947u

Huang, Y., Hu, J., Xu, H., Bian, W., Ge, J., Zang, D., et al. (2018). Fine tuning electronic structure of catalysts through atomic engineering for enhanced hydrogen evolution. *Adv. Energy Mater.* 8:1800789. doi: 10.1002/aenm.201800789

Hungerford, G., Hussain, F., Patzke, G. R., and Green, M. (2010). The photophysics of europium and terbium polyoxometalates and their interaction with serum albumin: a time-resolved luminescence study. *Phys. Chem. Chem. Phys.* 12, 7266–7275. doi: 10.1039/b925547h

Kandasamy, B., Vanhaecht, S., Nkala, F. M., Beelen, T., Bassil, B. S., Parac-Vogt, T. N., et al. (2016). Gallium(III)-containing, sandwich-type heteropolytungstates: synthesis, solution characterization, and hydrolytic studies toward phosphoester and phosphoanhydride bond cleavage. *Inorg. Chem.* 55, 9204–9211. doi: 10.1021/acs.inorgchem.6b01030

Kato, C. N., Shinohara, A., Hayashi, K., and Nomiya, K. (2006). Syntheses and X-ray crystal structures of zirconium(IV) and hafnium(IV) complexes containing monovacant Wells–Dawson and Keggin polyoxotungstates. *Inorg. Chem.* 45, 8108–8119. doi: 10.1021/ic060656e

Kulikov, V., Johnson, N. A. B., Surman, A. J., Hutin, M., Kelly, S. M., Hezwani, M., et al. (2017). Spontaneous assembly of an organic–inorganic nucleic acid Z-DNA double-helix structure. *Angew. Chem. Int. Ed.* 56, 1141–1145. doi: 10.1002/anie.201606658

Lakowicz, J. R. (2007). *Principles of Fluorescence Spectroscopy.* New York, NY: Springer.

Long, D.-L., Tsunashima, R., and Cronin, L. (2010). Polyoxometalates: building blocks for functional nanoscale systems. *Angew. Chem. Int. Ed.* 49, 1736–17588. doi: 10.1002/anie.200902483

Loos, T., Mortier, A., and Proost, P. (2009). "Chemokines, part B," in *Methods in Enzymology*, Vol. 461, eds T. M. Handel, and D. J. Hamel (Oxford: Academic Press, Elsevier), 3–29.

Luo, J., Chen, K., Yin, P., Li, T., Wan, G., Zhang, J., et al. (2018). Effect of cation–π interaction on macroionic self-assembly. *Angew. Chem. Int. Ed.* 57, 4067–4072. doi: 10.1002/anie.201800409

Luong, T. K., Absillis, G., Shestakova, P., and Parac-Vogt, T. N. (2014). Solution speciation of the dinuclear Zr[IV]-substituted keggin polyoxometalate [{α-PW₁₁O₃₉Zr(μ-OH)(H₂O)}₂]⁸⁻ and its reactivity towards DNAmodel phosphodiester hydrolysis. *Eur. J. Inorg. Chem.* 2014, 5276–5284. doi: 10.1002/ejic.201402735

Luong, T. K., Absillis, G., Shestakova, P., and Parac-Vogt, T. N. (2015a). Hydrolysis of the RNA model substrate catalyzed by a binuclear Zr[IV]-substituted Keggin polyoxometalate. *Dalton Trans.* 44, 15690–15696. doi: 10.1039/c5dt02077h

Luong, T. K., Govaerts, I., Robben, J., Shestakova, P., and Parac-Vogt, T. N. (2017). Polyoxometalates as artificial nucleases: hydrolytic cleavage of DNA promoted by a highly negatively charged Zr(IV)-substituted Keggin polyanion. *Chem. Commun.* 53, 617–620. doi: 10.1039/c6cc08555e

Luong, T. K., Shestakova, P., Mihaylov, T. T., Absillis, G., Pierloot, K., and Parac-Vogt, T. N. (2015b). Multinuclear diffusion NMR spectroscopy and DFT modeling: a powerful combination for unraveling the mechanism of phosphoester bond hydrolysis catalyzed by metal-substituted polyoxometalates. *Chem. Eur. J.* 21, 4428–4439. doi: 10.1002/chem.201405810

Luong, T. K. N., Mihaylov, T. T., Absillis, G., Shestakova, P., Pierloot, K., and Parac-Vogt, T. N. (2016c). Phosphate ester bond hydrolysis promoted by lanthanide-substituted keggin-type polyoxometalates studied by a combined experimental and density functional theory approach. *Inorg. Chem.* 55, 9898–9911. doi: 10.1021/acs.inorgchem.6b01802

Luong, T. K. N., Shestakova, P., Absillis, G., and Parac-Vogt, T. N. (2016b). Detailed mechanism of phosphoanhydride bond hydrolysis promoted by a binuclear zr(iv)-substituted keggin polyoxometalate elucidated by a combination of ³¹P, ³¹P DOSY, and ³¹P EXSY NMR spectroscopy. *Inorg. Chem.* 55, 4864–4873. doi: 10.1021/acs.inorgchem.6b00385

Luong, T. K. N., Shestakova, P., and Parac-Vogt, T. N. (2016a). Kinetic studies of phosphoester hydrolysis promoted by a dimeric tetrazirconium(IV) Wells–Dawson polyoxometalate. *Dalton Trans.* 45, 12174–12180. doi: 10.1039/c6dt02211a

Lv, H., Geletii, Y. V., Zhao, C., Vickers, J. W., Zhu, G., Luo, Z., et al. (2012). Polyoxometalate water oxidation catalysts and the production of green fuel. *Chem. Soc. Rev.* 41, 7572–7589. doi: 10.1039/c2cs35292c

Ly, H. G. L., and Parac-Vogt, T. N. (2017). Spectroscopic study of the interaction between horse heart myoglobin and zirconium(IV)-substituted polyoxometalates as artificial proteases. *ChemPhysChem.* 18, 2451–2458. doi: 10.1002/cphc.201700680

Ly, H. G. T., Absillis, G., Bajpe, S. R., Martens, J. A., and Parac-Vogt, T. N. (2013a). Hydrolysis of dipeptides catalyzed by a zirconium(IV)-substituted lindqvist type polyoxometalate. *Eur. J. Inorg. Chem.* 2013, 4601–4611. doi: 10.1002/ejic.201300270

Ly, H. G. T., Absillis, G., Janssens, R., Proost, P., and Parac-Vogt, T. N. (2015a). Highly amino acid selective hydrolysis of myoglobin at aspartate residues as promoted by zirconium(IV)-substituted polyoxometalates. *Angew. Chem., Int. Ed.* 54, 7391–7394. doi: 10.1002/ange.201502006

Ly, H. G. T., Absillis, G., and Parac-Vogt, T. N. (2013b). Amide bond hydrolysis in peptides and cyclic peptides catalyzed by a dimeric Zr(IV)-substituted Keggin type polyoxometalate. *Dalton Trans.* 42, 10929–10938. doi: 10.1039/c3dt50705j

Ly, H. G. T., Absillis, G., and Parac-Vogt, T. N. (2015b). Comparative study of the reactivity of zirconium(IV)-substituted polyoxometalates towards the hydrolysis of oligopeptides. *Eur. J. Inorg. Chem.* 2015, 2206–2215. doi: 10.1002/ejic.201500161

Ly, H. G. T., Absillis, G., and Parac-Vogt, T. N. (2016). Influence of the amino acid side chain on peptide bond hydrolysis catalyzed by a dimeric Zr(IV)-substituted Keggin type polyoxometalate *New J. Chem.* 40, 976–984. doi: 10.1039/c5nj00561b

Ly, H. G. T., Mihaylov, T., Absillis, G., Pierloot, K., and Parac-Vogt, T. N. (2015c). Reactivity of dimeric tetrazirconium(IV) Wells-Dawson polyoxometalate toward dipeptide hydrolysis studied by a combined experimental and density functional theory approach. *Inorg. Chem.* 54, 11477–11492. doi: 10.1021/acs.inorgchem.5b02122

Martin-Sabi, M., Soriano-López, J., Winter, R. S., Chen, J.-J., Vilà-Nadal, L., Long, D.-L., et al. (2018). Redox tuning the Weakley-type polyoxometalate archetype for the oxygen evolution reaction. *Nat. Catal.* 1, 208–213. doi: 10.1038/s41929-018-0037-1

Mihaylov, T. T., Ly, H. G. T., Pierloot, K., and Parac-Vogt, T. N. (2016). Molecular insight from DFT computations and kinetic measurements into the steric factors influencing peptide bond hydrolysis catalyzed by a dimeric Zr(IV)-substituted Keggin type polyoxometalate. *Inorg. Chem.* 55, 9316–9328. doi: 10.1021/acs.inorgchem.6b01461

Pope, M. T. (1983). *Heteropoly and Isopoly Oxometalates*. Berlin: Springer-Verlag.

Quanten, T., De Mayaer, T., Shestakova, P., and Parac-Vogt, T. N. (2018). Selectivity and reactivity of Zr[IV] and Ce[IV] substituted Keggin type polyoxometalates toward cytochrome c in surfactant solutions. *Front. Chem.* 6:372. doi: 10.3389/fchem.2018.00372

Sap, A., Absillis, G., and Parac-Vogt, T. N. (2015a). Selective hydrolysis of oxidized insulin chain B by a Zr(IV)-substitutedWells-Dawson polyoxometalate. *Dalton Trans.* 44, 1539–1548. doi: 10.1039/C4DT01477D

Sap, A., de Zitter, E., van Meervelt, L., and Parac-Vogt, T. N. (2015b). Structural characterization of the complex between hen egg-white lysozyme and Zr[IV]-substituted Keggin polyoxometalate as artificial protease. *Chem. Eur. J.* 21, 11692–11695. doi: 10.1002/chem.201501998

Sap, A., Van Tichelen, L., Mortier, A., Proost, P., and Parac-Vogt, T. N. (2016). Tuning the selectivity and reactivity of metal-substituted polyoxometalates as artificial proteases by varying the nature of the embedded lewis acid metal ion. *Eur. J. Inorg. Chem.* 2016, 5098–5105. doi: 10.1002/ejic.201601098

Stroobants, K., Absillis, G., Moelants, E., Proost, P., and Parac-Vogt, T. N. (2014a). Regioselective hydrolysis of human serum albumin by Zr[IV] substituted polyoxotungstates at the interface of positively charged protein surface patches and negatively charged amino acid residues. *Chem. Eur. J.* 20, 3894–3897. doi: 10.1002/chem.201303622

Stroobants, K., Goovaerts, V., Absillis, G., Bruylants, G., Moelants, E., Proost, P., et al. (2014b). Molecular origin of the hydrolytic activity and fixed regioselectivity of a Zr[IV]-substituted polyoxotungstate as artificial protease. *Chem. Eur. J.* 20, 9567–9577. doi: 10.1002/chem.201402683

Stroobants, K., Moelants, E., Ly, H. G., Proost, P., Bartik, K., and Parac-Vogt, T. N. (2013). Polyoxometalates as a novel class of artificial proteases: selective hydrolysis of lysozyme under physiological pH and temperature promoted by a cerium(IV) Keggin-type polyoxometalate. *Chem. Eur. J.* 19, 2848–2858. doi: 10.1002/chem.201203020

Sullivan, K. P., Yin, Q., Collins-Wildman, D. L., Tao, M., Geletii, Y. V., Musaev, D. G., et al. (2018). Multi-tasking POM systems. *Front. Chem.* 6:365. doi: 10.3389/fchem.2018.00365

Sun, H., Gao, N., Ren, J., and Qu, X. (2015). Polyoxometalate-based rewritable paper. *Chem. Mater.* 27, 7573–7576. doi: 10.1021/acs.chemmater.5b03711

Vandebroek, L., De Zitter, E., Ly, H. G. T., Conic, D., Mihaylov, T., Sap, A., et al. (2018). Protein-assisted formation and stabilization of catalytically active polyoxometalate species. *Chem. Eur. J.* 24, 10099–10108. doi: 10.1002/chem.201802052

Vanhaecht, S., Absillis, G., and Parac-Vogt, T. N. (2012). Hydrolysis of DNA model substrates catalyzed by metal-substituted Wells-Dawson polyoxometalates. *Dalton Trans.* 41, 10028–10034. doi: 10.1039/c2dt30588g

Vanhaecht, S., Absillis, G., and Parac-Vogt, T. N. (2013). Amino acid side chain induced selectivity in the hydrolysis of peptides catalyzed by a Zr(IV)-substituted Wells-Dawson type polyoxometalate. *Dalton Trans.* 42, 15437–15446. doi: 10.1039/c3dt51893k

Vilà-Nadal, L., and Cronin, L. (2017). Design and synthesis of polyoxometalate-framework materials from cluster precursors. *Nat. Rev. Mat.* 2:17054. doi: 10.1038/natrevmats.2017.54

Wang, S. S., and Yang, G. Y. (2015). Recent advances in polyoxometalate-catalyzed reactions. *Chem. Rev.* 115, 4893–4962. doi: 10.1021/cr500390v

Weinstock, I. A., Schreiber, R. E., and Neumann, R. (2018). Dioxygen in polyoxometalate mediated reactions. *Chem. Rev.* 118, 2680–2717. doi: 10.1021/acs.chemrev.7b00444

Yu, H., Wang, J., Zhai, Y., Zhang, M., Ru, S., Han, S., et al. (2018). Visible-light-driven photocatalytic oxidation of organic chlorides using air and an inorganic-ligand supported nickel-catalyst without photosensitizers. *ChemCatChem.* 10, 1–7. doi: 10.1002/cctc.201800629

Zhan, C., Cameron, J. M., Gabb, D., Boyd, T., Winter, R. S., Vilà-Nadal, L., et al. (2017). A metamorphic inorganic framework that can be switched between eight single-crystalline states. *Nat. Commun.* 8:14185. doi: 10.1038/ncomms14185

Zhang, G., Keita, B., Brochon, J.-C., de Oliveira, P., Nadjo, L., Craescu, C. T., et al. (2007). Polyoxometalate binding to human serum albumin:

molecular interaction and energy transfer between human serum albumin and polyoxometalates. *J. Phys. Chem. B* 111, 1809–1814. doi: 10.1021/jp063758z

Zhang, G., Keita, B., Craescu, C. T., Miron, S., de Oliveira, P., and Nadjo, L. (2008). Molecular interactions between Wells–Dawson type polyoxometalates and human serum albumin. *Biomacromolecules* 9, 812–817. doi: 10.1021/bm701120j

Zheng, L., Ma, Y., Zhang, G., Yao, J., Bassil, B. S., Kortz, U., et al. (2009). Molecular interaction between a gadolinium–polyoxometalate and humanserum albumin. *Eur. J. Inorg. Chem.* 5189–5193. doi: 10.1002/ejic.200900610

Zhou, Y., Chen, G., Long, Z., and Wang, J. (2014). Recent advances in polyoxometalate-based heterogeneous catalytic materials for liquid-phase organic transformations. *RSC Adv.* 4, 42092–42113. doi: 10.1039/c4ra05175k

Exploring Wells-Dawson Clusters Associated With the Small Ribosomal Subunit

Debbie C. Crans[1]*, Irma Sánchez-Lombardo[1,2] and Craig C. McLauchlan[3]*

[1] Department Chemistry and the Cell and Molecular Biology Program, Colorado State University, Fort Collins, CO, United States, [2] División Académica de Ciencias Básicas, Universidad Juárez Autónoma de Tabasco, Cunduacán, Mexico, [3] Department of Chemistry, Illinois State University, Normal, IL, United States

The polyoxometalate $P_2W_{18}O_{62}^{6-}$, the Wells-Dawson cluster, stabilized the ribosome sufficiently for the crystallographers to solve the phase problem and improve the structural resolution. In the following we characterize the interaction of the Wells-Dawson cluster with the ribosome small subunit. There are 14 different $P_2W_{18}O_{62}^{6-}$ clusters interacting with the ribosome, and the types of interactions range from one simple residue interaction to complex association of multiple sites including backbone interactions with a Wells-Dawson cluster. Although well-documented that bridging oxygen atoms are the main basic sites on other polyoxometalate interaction with most proteins reported, the W=O groups are the main sites of the Wells-Dawson cluster interacting with the ribosome. Furthermore, the peptide chain backbone on the ribosome host constitutes the main sites that associate with the Wells-Dawson cluster. In this work we investigate the potential of one representative pair of closely-located Wells-Dawson clusters being a genuine Double Wells-Dawson cluster. We found that the Double Wells-Dawson structure on the ribosome is geometrically sound and in line with other Double Wells-Dawson clusters previously observed in the solid state and solution. This information suggests that the Double Wells-Dawson structure on the ribosome is real and contribute to characterization of this particular structure of the ribosome.

Keywords: ribosome, polyoxotungstate, Dawson cluster, H-bonding, protein oxometalate interactions, double Dawson cluster

INTRODUCTION

Polyoxomoetalates (POMs; Wu, 1920; Dawson, 1953; Pope, 1976; Acerete et al., 1979b) have been used for many applications including being a selective and effective inhibitor of enzymes (Stephan et al., 2013), such as ecto-nucleotide pyrophosphatases/phosphodiesterases (NPPs; Lee et al., 2015), and as an artificial proteases (Stroobants et al., 2013), as nanocages for heteroanions (Zheng et al., 2015), and effective in catalysis (Wang and Yang, 2015). POMs have also been found to facilitate X-ray structure analysis of proteins and have been used for solving the structure of proteins such as the small subunit of the ribosome (Janell et al., 2001; Bashan and Yonath, 2008; Yonath, 2009). Proteins are synthesized in an organelle referred to as the ribosome, located in the endosomal reticulum. The large ribosomal subunit contains over 50 different proteins but consists primarily of RNA (over 60%). Understanding the structure for this RNA-protein complex became a goal for many biologists, biochemists, and bioinorganic scientists, considering the importance of this

RNA-protein complex for cellular growth. Scientists from several groups were working on solving the X-ray structure for the ribosome, and the successes of three groups in solving the structures of the bacterial small subunit (30S), large subunit (50S), and complete ribosome (70S) structures led to the 2009 Nobel prize to Venkatraman Ramakrishnan (Wimberly et al., 2000), Thomas A. Steitz (Ban et al., 1998), and Ada Yonath (Thygesen et al., 1996; Tocilj et al., 1999). Because of the formidable challenge, the process is still ongoing aiming to determine the structures of ribosomes from different organisms as well as from cells under pressure, so that details can be observed which were not previously accessible. The ribosomal structure has been refined through incremental progress over the past decade by small improvements to overall structure (**Figure 1**). That is, the co-ordinates are fine-tuned by solving many crystals of interacting species, such as antibiotics, and phasing agents, including the polyoxometalates (POMs) such as the polyoxotungstates shown in red in **Figure 1**. Over the series of structures of ribosomal small subunit from the extremophile *Thermus thermophilus* (T30S) by Yonath et al. (Thygesen et al., 1996; Tocilj et al., 1999; Weinstein et al., 1999; Schluenzen et al., 2000; Janell et al., 2001; Auerbach-Nevo et al., 2005; Bashan and Yonath, 2008; Yonath, 2009) the Wells-Dawson cluster, $P_2W_{18}O_{62}^{6-}$ (P_2W_{18}), (**Figure 2**) was used extensively. This approach was accompanied by studies with complementary techniques such as electron cryomicroscopy (Cryo-EM) to yield additional details (Winkler et al., 2017; Brown and Shao, 2018). Combined, such approaches have been used resulting in datasets that reveal improved details and allow for better insights into how the polyoxotungstates are stabilizing the protein (Yonath, unpublished data). This manuscript concerns the specific interactions of the most successful POM used in the early crystallographic studies with the small ribosomal unit, P_2W_{18}.

POM clusters, and heavy metals in general, have been especially important for use in X-ray crystallography by stabilizing the POM-protein complexes and several excellent reviews are available on this topic (Dauter, 2005; Dahms et al., 2013; Bijelic and Rompel, 2015). The interactions between POMs and proteins are also of interest in several other contexts considering the reports of specific protein labeling (Kluger and Alagic, 2004), as well as applications of POMs for treatment of various diseases (Hill et al., 1990; Rhule et al., 1998; Stroobants et al., 2013; Leon et al., 2014; Arefian et al., 2017; Bijelic et al., 2018, 2019). The stabilizing interactions between a range of different POMs with proteins continues to be a topic of interest to the scientific community (Bijelic and Rompel, 2015), because of the rising number of structures being reported containing different classes of POMs and other oxometalates (Bijelic and Rompel, 2015, 2017). For example, reorganization of the peptide structure for the tyrosinase (Mauracher et al., 2014) shows that stabilizing interactions are important and may be a general phenomenon and a useful tool for crystallographers with challenging systems (Zhang et al., 2007; Bošnjaković-Pavlović et al., 2011; Dahms et al., 2013; Bijelic and Rompel, 2015, 2017). The advantage of POMs is the presence of heavy atoms to allow for phasing and anomalous dispersion (Weinstein et al.,

1999; Rudenko et al., 2003; Dauter, 2005; Blazevic et al., 2015), but another second advantage is that the anionic nature of POMs, as Rompel and co-workers noted, "could act as a 'glue' to connect these otherwise electrostatically repulsive surfaces" (Zhang et al., 2008; Mauracher et al., 2014), a fact which has also been observed for the Ribosome T30S as well (Auerbach-Nevo et al., 2005; Bashan and Yonath, 2008; Yonath, 2009). The fact is that several POMs are included in the kits currently commercially available to life scientists to assist protein crystallization illustrate the effectiveness of these systems (e.g., Jena Biosciences, 2019). Although the improvement in quality of solved protein structures through the use of POMs in co-crystallization has been profound, it is striking that the major success with the ribosomal subunit remained fleeting until the Wells-Dawson POM was employed (*vide infra*), particularly because these POMs have not been used in studies with other proteins.

The Wells-Dawson POM cluster structure shown in **Figure 2** was found to be the most effective stabilizing cluster used to begin to solve the phasing problem for the ribosome by the Yonath group (Tocilj et al., 1999). The P_2W_{18} cluster has long been known to have two unique tungsten sites (Acerete et al., 1979b), namely the belt and the cap (**Figure 2B**), and was one of the first species ever studied using ^{183}W NMR spectroscopy owing to its stability and well-defined structure (Acerete et al., 1979a). The cluster ideally possesses D_{3h} symmetry (Contant and Thouvenot, 1993; Vilà-Nadal et al., 2012), although there is little energetic difference between other symmetry options such as D_{3d} (Vilà-Nadal et al., 2012). There are eight different oxygen sites in the cluster, some exhibiting differences based on symmetry and some on chemistry (see **Figure 2A**; Dawson, 1953; Janik et al., 2003; Poblet et al., 2003). Interestingly, this POM has not been reported in any other *deposited* protein-POM structures besides the T30S Ribosome. Based on its structure one can thus anticipate that this oxometalate is particularly useful for different systems because the variety of possible sites on the P_2W_{18} clusters are likely to interact differently with the protein surface and allow more types of interactions than, for example, the flat Anderson-Evans structure type (e.g., $TeW_6O_{24}^{n-}$). The question of whether this POM exhibited similar stabilizing effects of other POMs in general is therefore of particular interest to the scientific community and there is a need to be able to examine the protein-oxometalate interactions in various published structures (Bijelic and Rompel, 2015, 2017). However, scientists working on the large protein structures have sometimes used the concept of "form factor," so that the electron density in these large oxometalates are averaged, and only one central spot of the POM molecules are reported in the newer structures (or no evidence for POM was reported; Ban et al., 1998, 1999). *For an inorganic chemist interested in the interactions of the POM with the protein or those that wanted to use this complementary for design of future systems such an approach is very limiting. Specifically, one cannot always simply download the protein structural files and examine the interactions between the oxometalate from the newer X-ray structures because the coordinates deposited are often simplified using form factors leading to incomplete descriptions of the details of the interactions between the oxometalate and the protein.*
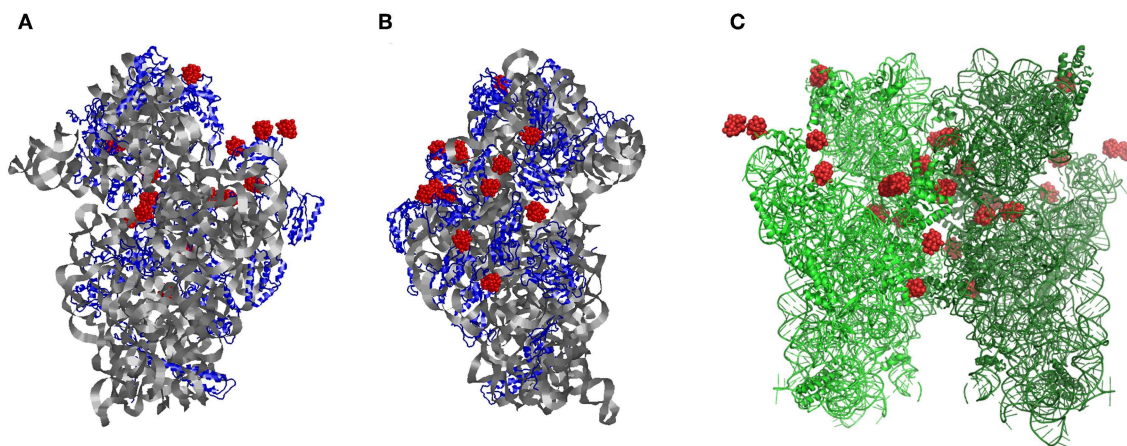
FIGURE 1 | The structure of the small ribosomal subunit from *Thermus thermophilus* (T30S) from the **(A)** front and **(B)** side, respectively. **(C)** Symmetry-generated dimeric form of two ribosomal small subunit structure within their crystals showing each of the P_2W_{18} sites (red). Modified with permission from Bashan and Yonath (2008).
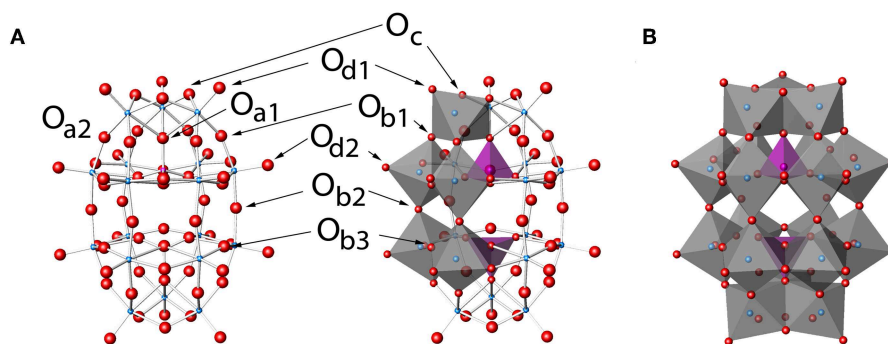
FIGURE 2 | P_2W_{18}, $P_2W_{18}O_{62}^{6-}$ in **(A)** ball-and-stick and **(B)** polyhedral representations. Labels in **(A)** show the eight unique types of oxygen atoms and follow a modification to the naming conventions of Keggin clusters (Janik et al., 2003). Darker and lighter polyhedra in **(B)** represent the cap and belt types of tungsten sites, respectively. The Wells-Dawson structure by Kato et al. (2013) with refcode RIBFUF is the structure with the lowest R_1 value reported (Kato et al., 2013) and is used in this work as a reference Wells-Dawson structure.

Examining the interactions of the metal complexes with proteins is interesting but has several issues, as detailed in previous works (Janell et al., 2001; Crans et al., 2014; McLauchlan et al., 2015; Sanchez Lombardo et al., 2015). Briefly, issues relating to resolution (Weinstein et al., 1999; Rudenko et al., 2003; Dauter, 2005; Blazevic et al., 2015), phasing (Thygesen et al., 1996; Pioletti et al., 2001), and degradation (including photoreduction) (Rich et al., 1998; George et al., 2012) all become of critical importance. Protein X-ray crystallography is thus very different than small molecule crystallography because the protein structure diffraction data are often collected across numerous crystals rather than a single crystal more typical of a small molecule, although techniques have been developed to alleviate this issue in certain cases (Janell et al., 2001; Heras and Martin, 2005). Seeking improvements in the structure, interacting species, such as antibiotics, and phasing agents, including the polyoxotungstates were used to improve the overall structure (*vide infra*). Because the focus of the investigating researchers is on the main structure of the proteins, not the interacting species, it is often the case that the non-protein metal clusters are not even shown or deposited (e.g., Ban et al., 1999). This simplification is in contrast to the inclusion/treatment of the antibiotic species' coordinates, usually because they are deemed potentially more relevant (Pioletti et al., 2001). The lack of deposited coordinates for the metal clusters, then, makes studying protein-metal interactions a challenge in those cases.

The Wells-Dawson polyoxometalate, $P_2W_{18}O_{62}^{6-}$ (P_2W_{18}), provided the heavy metal electron density critical to one of the approaches to managing the phase problem for solving the structure of the small ribosomal subunit (Brodersen et al., 2003; Dauter, 2005; Barrier et al., 2009). Since first described by Perutz with hemoglobin (Green et al., 1954), heavy atom derivatization has been employed for many years in solving structures and is well-reviewed as a technique in the literature (Garman and Murray, 2003; Dauter, 2005). In practice, ribosomal protein crystals may be soaked with P_2W_{18} solutions and large amounts

of the P_2W_{18} remain in the crystal even after washing, helping with diffraction and phasing (Janell et al., 2001). In addition, the Yonath group reported that the P_2W_{18} POM served to anchor the protein conformation and stabilize the ribosomal proteins in their preparations, although other groups did not observe similar stabilization of the ribosome in their preparations (Wimberly et al., 2000; Clemons et al., 2001). The stabilization led to superior diffraction patterns and to the improved resolution X-ray structure solved by Bashan and Yonath (2008). Incremental progress in resolution was obtained from above 4 to 3.3 Å and below (Thygesen et al., 1996; Tocilj et al., 1999; Weinstein et al., 1999; Schluenzen et al., 2000; Auerbach-Nevo et al., 2005; Bashan and Yonath, 2008; Yonath, 2009). This structure was a vast improvement compared to the low resolution structures investigated earlier with no P_2W_{18}. In addition to providing the increased electron density the P_2W_{18} caused some significant structural organization in the ribosomal protein subunit S2, (Pioletti et al., 2001; Auerbach-Nevo et al., 2005) which in this unit cell is situated proximal to the crystallographic 2 axis. Because use of P_2W_{18} allowed improvement in the resolution of the T30S structure in a way not seen using other POMs [even though those POMs are successfully employed in other protein structures (Bijelic and Rompel, 2015)] this led us to examine the nature of the P_2W_{18} interactions with the biological portions of the structure. In some of the recent ribosome structures, however, the deposited protein structures contain the spherically averaged form-factor (labeled PW) and are represented as a point charge near the protein, as is often employed when non-symmetric heavy metal agents with not-necessarily-specific interactions with the protein are used in this way (Thygesen et al., 1996; Yonath, unpublished data). Therefore, all the detail in the interaction of the POM with the protein is lost, and not accessible to the bioinorganic chemist or other crystallographers wanting to use these types of systems for future crystallization of new proteins.

In the following we use data-mining studies to explore specifically how the Wells-Dawson cluster and a possible Double Wells-Dawson cluster interact with the ribosomal protein. To carry out this analysis we introduce a systematic approach that can be employed while investigating the POM-protein structures deposited in the Protein Data Bank (PDB; Berman et al., 2000). Some of these protein structures include the spherically averaged form-factor ("PW") and no longer contain the detailed electron density for POM near the protein (Schluenzen et al., 2000). Using the structure of one crystallographically-characterized Wells-Dawson molecule we can complete the model for any incomplete P_2W_{18} POM-structures on the protein by overlaying a selected Wells-Dawson model structures. As a result, we will be able to examine the structures of the reported POM-ribosome complexes, in which the POM-unit was not reported intact in the PDB. We specifically investigate using data mining whether two closely located P_2W_{18} POMs, "Double Wells-Dawson," associated with the ribosome is likely real. These studies provide information on the interaction of the Well-Dawson structure with a protein, and illustrate a strategy to investigate these types of protein structures in which spherically averaged form-factors are used to indicate the location of a POM.

EXPERIMENTAL

Files of Ribosomes From Protein Data Bank (PDB)

The structure of the small ribosomal unit has been solved in pieces with incremental progress in a series of works (Thygesen et al., 1996; Tocilj et al., 1999; Weinstein et al., 1999; Pioletti et al., 2001; Auerbach-Nevo et al., 2005; Bashan and Yonath, 2008; Yonath, 2009), culminating in the report of the T30S structure reported in 2000 (Schluenzen et al., 2000) and deposited in the Protein Data Bank (PDB) (Berman et al., 2000) with PDB code 1FKA (resolution 3.3 Å). This original publication (Schluenzen et al., 2000) modeled the electron density of a $P_2W_{18}O_{62}^{6-}$ unit at the center of mass of the cluster labeled WO2 as the "spherically averaged form-factor" with the label "PW" (Schluenzen et al., 2000). Subsequent work included further inclusion of the clusters in more detail (Pioletti et al., 2001). The original authors used the Crystallography & NMR System (CNS, Brünger et al., 1998) for their refinements. The Protein Data Bank (PDB) defines Wells-Dawson as "WO2" and all WO2-containing structures were examined and the coordinates downloaded (**Table S1**). We concentrated our efforts on the best resolution structure for the Ribosome T30S from the PDB, PDB code 1I94 (**Figure 3**; Pioletti et al., 2001). In examining the interactions of the POMs with T30S, the locations of the POMs must first be established before the adjacent protein residues are identified.

Selection of Model Wells-Dawson Structure

An analysis of the Cambridge Crystal Structure Database (CSD, November 2017) (Allen, 2002) affords 146 hits with the composition "$P_2W_{18}O_{62}$" as part of a single molecule. The structure of a hydrated lithium salt by Kato et al. (2013) with refcode RIBFUF is the Dawson complex with the lowest R_1 value (Kato et al., 2013), which is taken to correspond to the best model fit in the literature. We used the anion in this Wells-Dawson-containing structure as the archetypical cluster for examination.

Completing POM Structures Associated With the Ribosome

For structures containing the Wells-Dawson clusters missing atoms or those X-ray structures in which averaged form-factors (PW) are used (Schluenzen et al., 2000), it is not trivial to access the details in the structural interaction of the Wells-Dawson-ribosome complex. That is, oxygen atoms and in some cases W-atoms can be missing and not provide a complete description of the P_2W_{18} cluster.

When the averaged form-factors are used by the crystallographers there are no details regarding the interaction of the Wells-Dawson cluster associated with the ribosome. However, given the well-defined nature of Wells-Dawson clusters, it seemed reasonable that an overlaid ideal structure could be identified based on known structures and that such constructs would suggest where the missing atoms should be and provide the interactions of the entire cluster with the protein or RNA portions of the ribosome. This is particularly important because the missing oxygen atoms generally are at the surface

FIGURE 3 | Crystals of the small ribosomal subunits (T30S) were soaked for a few minutes in solutions containing small amounts of the Wells-Dawson tungstate complex (P_2W_{18}, PW_{18} by the authors, WO2 in the PDB). The structure of the complex of the ribosomal subunits with the cluster (PDB Ref code 1I94) is shown. The P_2W_{18} residues that are described in detail in this manuscript are P_2W_{18} numbers 1,014 and 1,006 for the discrete clusters and 1,001 and 1,004 for the Double Wells-Dawson cluster (Pioletti et al., 2001).

of the POM and thus likely to engage in H-bonding with the ribosome. This is not possible when a point sphere is used, but it can be minimized when at least a portion of the cluster is present.

RESULTS

Most publications mentioning the P_2W_{18} clusters in the T30S structures mention seven P_2W_{18} sites (e.g., Janell et al., 2001), and there are only seven unique WO2 sites in 1FKA (Schluenzen et al., 2000), however, there appear to be 14 crystallographically-unique locations in 1I94, each half-occupied by a cluster. Experiments showed that more tungsten was present in the crystals than accounted for in the X-ray diffraction studies (Janell et al., 2001), but the choice of 50% occupancy is a reasonable one in the absence of any compelling data to the contrary. It is not surprising that the clusters may not have similar crystallographic occupancy over the entire clusters (Tocilj et al., 1999), and although it could reflect lacunary structures associated with the protein, it could also simply be a statistical averaging. This occupancy is of particular importance in examining the P_2W_{18} clusters in the T30S structure because, although most of the clusters on the ribosome are spread out over the surface of the minor ribosomal subunit, three pairs of clusters are particularly close together. In 1I94, eight of the Wells-Dawson cluster sites appear discrete, that is there is no other P_2W_{18} cluster within 10

Å, but six of the clusters appear to be in pairs, much closer to one another. The three pairs of clusters reside at closest interactions of 2.365, 4.364, and 6.297 Å, respectively.

Three Discrete Wells-Dawson Structures: 1,014, 1,006, and 1,576

The large and stable nature of the clusters made them useful for phasing and even if an entire cluster was not visible in the electron density map, the X-ray crystallographers rationalized that although the resolution of the ribosomal structure is not sufficient to identify all of the clusters atoms, they could take advantage of the well-known structure of the Wells-Dawson cluster and focus the model so that details about the structure "of interest," namely the ribosome RNA-protein complex, can be extracted. In some structures (e.g., PDB ID 1I94) the clusters are more complete than in others and the deposited coordinates may not even contain any details about the P_2W_{18}, i.e., PDB ID 1FKA. In examining the ribosome structures containing P_2W_{18}, the number of P_2W_{18} sites is not identical across all five of the deposited T30S structures. In PDB ID 1I96, for instance, several of the P_2W_{18} clusters found in the others of the series (i.e., 1I94, 1I95, and 1I97) are missing (**Figure S1**).

Cluster 1,014 is off on the periphery of the ribosome surface (**Figures 3**, **4**). This P_2W_{18} interacts strongly with many interactions with one Lys residue through the W-atoms on the belt of the P_2W_{18}. The location of this Wells-Dawson on the tip of the ribosome unit may seem surprising; this POM, though, serves a key role to organize the different protein units in the crystal (interactions not shown), and interacts with proteins in adjacent unit cells. In the case of cluster 1,006, a very different mode of interaction is observed and close interactions with many peptide parts including strands in the peptide chains G (x 2) and K (x 2 alpha helices) (**Figure 4**). This cluster has the entire peptide backbone chain wrapped around it showing interaction with the backbone of a number of amino-acids. The peptides involved in this interaction with cluster 1,006 include Ala, Arg, Ala, Tyr, Ala, Tyr, Arg, and Trp.

In this article our focus is on the protein interactions with many of the P_2W_{18} clusters in 1I94, however, considering the high RNA content, there are also some interactions of some P_2W_{18} clusters with the RNA as well. For example, cluster 1,576 is one such cluster that interacts with RNA (**Figure 4C**). Portions of this cluster also interact with a Gln side chain, but there are also interactions between the terminal oxo units and phosphate backbones, ribose oxygen, and oxygen and nitrogen from uracil. Given the prevalence of RNA in the ribosomal subunit and the fact that the interacting RNA units each come from different RNA strands in this case, cluster-RNA interactions certainly help play a part in the stability of these crystals. Further analysis and investigation of such interactions are warranted, but they are not our primary focus here.

Completing the Wells-Dawson Structures

In some data sets, including some still unpublished, the complete P_2W_{18} clusters are not present or are only partially found in the electron density difference maps. We had originally considered modeling such a system but instead focused on the publicly
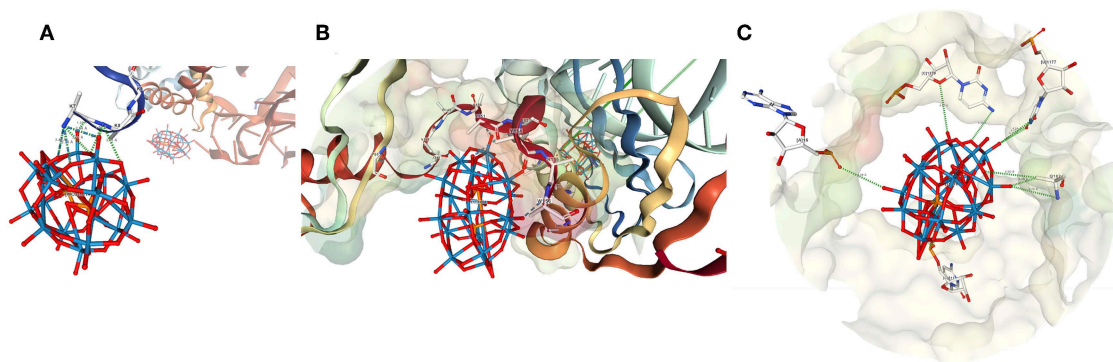
FIGURE 4 | The structure of POMs number **(A)** 1,014 **(B)** 1,006, and **(C)** 1,576 from 1I94. Numbering as shown in **Figure 3** (Pioletti et al., 2001).

available data sets as a starting point. It is impossible to model the spherical point used in 1FKA, but a partially complete P_2W_{18} cluster would have been possible. An idealized P_2W_{18} unit (*vide infra*) was placed using the structural overlay feature of *Mercury* (Macrae et al., 2008) and the "define cluster feature" of Crystal Maker allowing us to approximate the missing oxygen-atoms in the $P_2W_{18}O_{62}^{6-}$ (**Figures 2**, **3**) for those protein structures where P_2W_{18} is not fully found.

This structure was used to measure the distances of each amino acid or backbone atom to the oxygen-atoms on the surface of the P_2W_{18} unit. When present, experimentally-located oxygen atoms were used. Typically, the differences in distances between experimentally-located oxygens vs. idealized oxygens were on the order of 0.010 Å. We anticipate that in 5 years or less, it may even be possible to use a routine program to provide these types of overlays and, therefore, interactions.

Possible Structures for Double Wells-Dawson Structures

Hypothetically, one can construct several potential Double Dawson structures based on common motifs of POM chemistry (**Figure 5**; Dawson, 1953; Zhao et al., 2008; Barrier et al., 2009): the two Dawson POM structures being connected through a joint oxygen atom on a corner (corner-shared, **Figure 5A**) or on an edge (edge-shared, **Figure 5B**) or the two Dawson units can be connected through H-bonding (**Figure 5C**) or some other linker (**Figure 5D**). With two chemically distinct tungsten sites, further complexities arise with H-bonding even, with belt-to-belt, belt-to-cap, and cap-to-cap possibilities. In the 1I94 structure, the shortest distances between the clusters 1,001 and 1,004 themselves is about 2.365 and 2.367 Å, respectively. These distances are much too long to allow consideration of an edge-shared, or even corner-shared type arrangement, even if the geometries were more reasonably oriented. These distances *are* of a length typical of a H-bond (Crans et al., 1994; Tocilj et al., 1999; Barrier et al., 2009; Bijelic and Rompel, 2015; Winkler et al., 2017). Such considerations suggest that if the clusters on the ribosome are Double Wells-Dawson Clusters, that they would be like that shown in **Figure 5C** and shown for the Double Cluster on the ribosome in **Figure 3** (Dawson, 1953; Zhao et al.,

2008; Barrier et al., 2009). Importantly, the part of the cluster in which the connection between the clusters is made is that of the cap on each cluster, which is the position of the interactions of clusters that has been observed for the Wells-Dawson Double Clusters in the literature (**Figures 2**, **5**; reference codes JETSOR, PUPJUG, PUPJOA, and FUVXAW as well as the Wells-Dawson complex) as detailed below (Dawson, 1953; Zhao et al., 2008; Barrier et al., 2009). With this interaction of the two P_2W_{18} clusters in mind, we may now consider the interactions with the rest of the T30S structure.

Interactions of a Possible Double Wells-Dawson Structure (1,001···1,004) and Protein Moieties in the Small Ribosomal Subunit Structure

The interactions of Clusters 1,001 and 1,004 with the ribosome structure shown in **Figure 6** were identified and the distances measured and listed in **Table 1**. Interactions of <5 Å are considered significant with POMs in proteins (Crans et al., 1994; Felts et al., 2006; Steens et al., 2010; Goovaerts et al., 2013; Bijelic and Rompel, 2015, 2017; Arefian et al., 2017; Winkler et al., 2017), and shorter interactions (between 1.8 and 3.6 Å) can be considered possible for hydrogen bond interactions (Crans et al., 1994). The POM anions contains three different oxygen-atom sites that the protein can interact with. Which oxygen atoms associate most with the protein and the distances associated will define the stability of the complex formed between the ribosome and the POM.

As seen from **Table 1**, **Figure 6**, and **Figure S2**, some of the amino acids are interacting with several parts of the POM including both the bridging and W=O oxygen atoms. **Table 1** shows that the Wells-Dawson clusters are mainly interacting with the peptide backbone of neutral amino acids (Ala, Gln, Glu, Ile) and with the side chains of neutral amino acids (Asn, Thr) and backbone and side chains of positively charged amino acids (Lys and Arg). In Cluster 1,001, there is an unrealistically short interaction with the oxo of Asn37 and then 27 more modest interactions with side chains and the protein backbone, with the closest being an oxo from the cluster interacting with the nitrogen
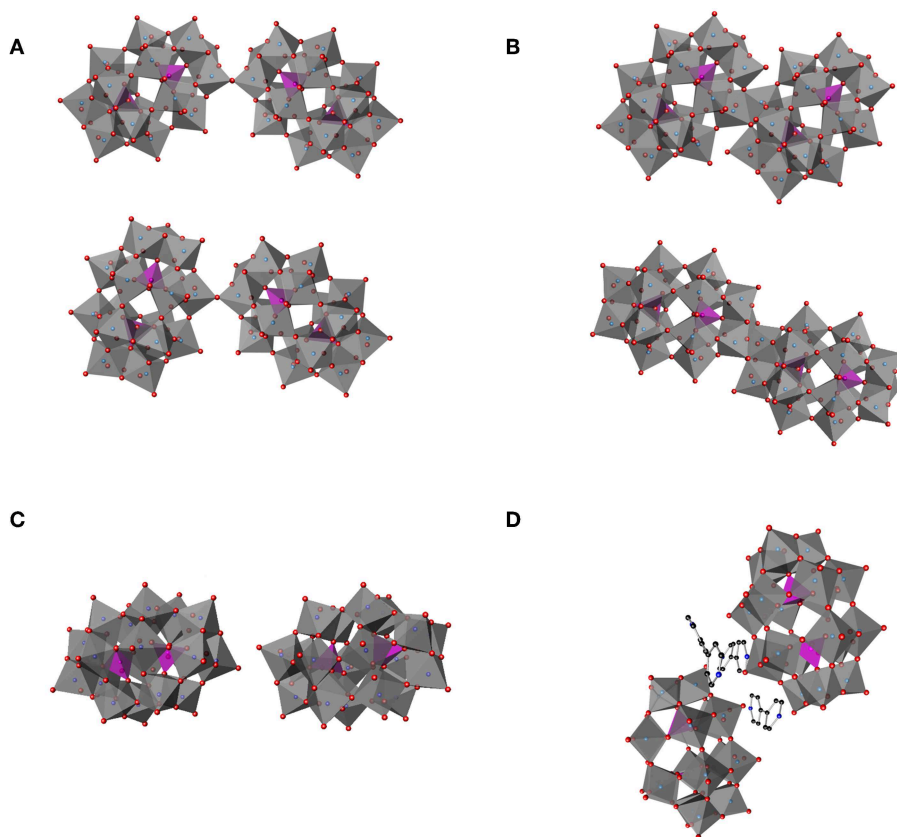
FIGURE 5 | Schematic illustration of several hypothetical double Dawson clusters. **(A)** Double Dawson structures may be connected through a joint oxygen atom on a corner, corner-shared $(P_2W_{18}O_{61})_2O$, in a cap-to-cap (top) or belt-to-cap (bottom). **(B)** Two structural possibilities where the Double Dawson structure are connected through the edge, edge-shared $(P_2W_{18}O_{60})_2O_2$, with belt-to-belt (top) and cap-to-cap (bottom). Two full P_2W_{18} Dawson units can be interacting through **(C)** H-bonding (2:2 isomer) [from YEFRAF (Liu et al., 2014)] or **(D)** through some other linker such as 4,4'-bipyridine from Zhao et al. (2008).
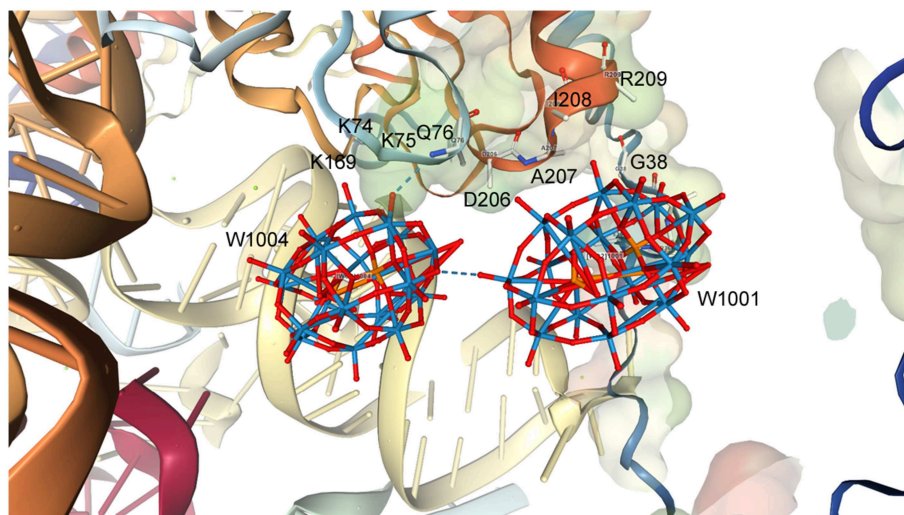
FIGURE 6 | The structure of a representative Double Wells-Dawson cluster consisting of clusters 1,001 **(Right)** and 1,004 **(Left)** from 1I94.

Cluster	Residue	Distance, Å	Interaction
1,001	Glu B 35	4.33	backbone N$\cdots$ O-W$_2$
1,001	Glu B 35	4.53	backbone N$\cdots$O=W
1,001	Arg B 36	3.38	O$\cdots$O-W$_2$
		3.49	
		4.35	
		4.53	
1,001	Arg B 36	3.49	O$\cdots$O=W
		4.55	
1,001	Asn B 37	4.18	backbone N$\cdots$ O-W$_2$
		4.46	
1,001	Asn B 37	4.27	O$\cdots$O=W
1,001	Asn B 37	1.44	O$\cdots$O-W$_2$
		3.54	
		3.82	
		3.95	
1,001	Gly B 38	3.40	backbone N$\cdots$O=W
		4.35	
1,001	Gly B 38	4.16	backbone N$\cdots$ O-W$_2$
		4.97	
1,001	Ala B 207	3.61	backbone N$\cdots$O=W
		4.16	
1,001	Ala B 207	4.62	backbone N$\cdots$ O-W$_2$
		4.90	
1,001	Ile B 208	3.01	backbone N$\cdots$O=W
		4.10	
1,001	Ile B 208	4.14	backbone N$\cdots$ O-W$_2$
		4.52	
1,001	Arg B 209	3.67	backbone N$\cdots$O=W
1,001	Arg B 209	4.80	backbone N$\cdots$ O-W$_2$
1,004	Thr B 73	4.26	O$\cdots$O=W
1,004	Lys B 74	4.09	backbone N$\cdots$O=W
1,004	Lys B 75	2.09	backbone N$\cdots$O=W
		4.90	
1,004	Lys B 75	3.92	backbone N$\cdots$ O-W$_2$
		4.39	
		4.43	
		4.93	
1,004	Gln B 76	2.96	backbone N$\cdots$O=W
1,004	Gln B 76	4.01	backbone N$\cdots$ O-W$_2$
		4.86	
1,004	Lys B 169	4.87	O$\cdots$O=W

atom in the backbone of Ile208. The closest interactions with Cluster 1,001 therefore come from two regions of the ribosome with amino acids 35–38 and from amino acids 207–209, forming a region of protein and POM closely associated with each other, as described previously, in a nest. For Cluster 1,004, though, there are fewer interactions than with Cluster 1,001, and most are with the nitrogen atoms on the protein backbone. The two closest interactions are between a single W=O unit and both the Lys75 and Gln76 backbone. The part of the protein that associates with the POM can be several parts of the peptide both on the backbone and on the side chains. The backbone interacting with

the POM includes both C=O as well as the amide nitrogen-atom of the ribosomal subunit. In the case of both clusters, there are numerous other interactions with side chains, but all are longer than 5.0 Å. Owing to the nature of the deposited data, only interaction information with the backbone with the Wells-Dawson clusters is available. Ideally, one would prefer to have both the cluster *and* the side chain positional information.

Precedent for Double Wells-Dawson Structures in the Solid State

A search of the Cambridge Crystal Structure Database (CSD, November 2017 update) (Allen, 2002) for crystallographically-reported Double Clusters was conducted. A general summary of the data in the CSD is presented. Using ConQuest (Bruno et al., 2002) as a searching tool, 3,752 structures containing W, P, and O all in the same molecule, 3,111 clusters in CSD contain a W—O—W unit, and 2,804 structures contain W—O—W—O—W were identified. Within those data, 952 clusters contain both W/P/O and W—O—W—O—W. If one examines all six coordinate W(=O)O$_5$ functionalities in the CSD database, there are a total of 20,405 such sites which have an average W=O length of 1.711 Å (range of 1.077–2.435, with a median of 1.710 Å). The W—O average of *all* data is 2.0024 Å with a minimum of 1.077 and maximum distance of 3.612 Å, respectively. Further analysis of the tungsten coordination geometry within the group of 952 clusters mentioned above of W/P/O and W—O—W—O—W-containing clusters yield 630 compounds which have these coordination geometrical parameters and gives six coordinate W(=O)O$_5$ units with an average W=O distance of 1.703 Å (with a range of 1.571–1.808 Å). The W—O average of *all* these data in the subset is 2.00099 Å with a minimum of 1.697 and a maximum W—O distance of 2.518 Å.

Of principal interest to this work was the W-systems within the Wells-Dawson cluster itself, not just general WO$_6$ systems. In a P$_2$W$_{18}$O$_{62}$ targeted search, there are 146 hits, 105 of which have coordination geometric parameters such as angles and distances. This leaves a total of 1,069 sites described as six coordinate W(=O)O$_5$ in these Wells-Dawson structures. These structures have an average W=O distance of 1.703 Å (range of 1.571–1.808 Å), which is a more narrow range than the distance noted in the more general search described above. The W—O average of *all* Wells-Dawson structure data gives an average bond length of 2.001419 Å with with a minimum distance of 1.697 and a maximum distance of 2.518 Å. This is a more limited range of compounds. Because the authors based the atomic positions of the W atoms in the ribosome structure largely by using the average positions in a typical Wells-Dawson structure, the Wells-Dawson structures described in the deposited protein structures fall within these parameters.

DISCUSSION

The importance of POMs and their interactions with proteins has been established in the preceding sections. Here we will focus on the Wells-Dawson POM and the structure of the small ribosomal subunit and the possibility of a Double Wells-Dawson cluster

forming on the small subunit of the ribosome. The use of POMs for structure solution continues for the ribosome structure as well, including the recent elucidation of an *E coli* model (Noeske et al., 2015).

Double Wells-Dawson Clusters

In the following sections we discuss two Wells-Dawson clusters (Clusters 1,001 and 1,004, **Figure 6**), that are very close together leading us to refer to them as the "Double Wells-Dawson" structure on the ribosome. We are investigating the interactions of each of the two clusters with the protein and each other, as well as investigating precedent for Double Wells-Dawson clusters reported in the literature. Because these P_2W_{18} clusters on the ribosome are only half occupied crystallographically, it is not clear from this structure alone if this Double Wells-Dawson structure is real or if the half-occupancy in model results from *on average* (over the course of all of the atoms in the entire crystal structure) half of one of the two Wells-Dawson sites are occupied (and the other may or may not be) and *on average* half of the other Wells-Dawson sites are occupied over the course of the entire structure. Such statistical electronic distribution in this case allows for a distribution of occupancies that means there could be (a) a double cluster, (b) one or the other site occupied, or (c) neither site occupied in any given site over the entire crystal. If all these possibilities were equally favorable statistically, 25% of the time there will be a Double Wells-Dawson cluster associated with the protein and no Wells-Dawson associated with the protein, and 50% of the time there would be one of the two structures associated with the protein. However, the possibility of the Double Wells-Dawson forming requires that the structure has the proper geometry, which is what has been considered above in this manuscript. To properly evaluate these possibilities one must be able to investigate the dimensions of the system and the coordinates of the entire P_2W_{18} must be available.

Precedent for Double Wells-Dawson Structures

In order to consider how the Wells-Dawson clusters interact in the ribosomal subunit precedent for isolated and reported P_2W_{18} structures are investigated. Analysis of the parameters for known species in the solid-state and solution will allow us to determine if the Double Wells-Dawson structure associated with the protein in the small ribosomal subunit has a geometrically reasonable structure. Will the observed structure be similar to the description of the Dawson Wells-Cluster shown in **Figure 2A**, originally identified by Dawson in his 1953 description of the structure (Dawson, 1953) or similar to any of the Double Wells-Dawson structures that have been reported in the solid state or in solution since then? Such a comparison will allow us to evaluate the possibility whether the Double Wells-Dawson structure observed on the ribosome could be real. If our analysis shows that the structure has precedent between POMs in the solid-state, including the P_2W_{18} Wells-Dawson cluster, then it is more likely that the Double Wells-Dawson Cluster on the ribosomal subunit may actually be a real. However, in addition to investigating the geometry of the cluster, we are also interested in the occupancy of the clusters associated with the ribosome.

Although the P_2W_{18} units remain in the crystals even after several rinses (Janell et al., 2001), the fact remains that soaking of multiple crystals used to solve the X-ray structures means the possibility exists of varying cluster occupancy in any given crystal, which is then averaged in the final structure. Often the occupancy of the POMs on the ribosome varies and this impacts the observed properties of the complex. That is, half occupancy of each site of a dimer is consistent with the possibility that only one site or the other may be occupied in any given unit. Electron density is important to how the cluster associates with the protein, and impacts the occupancy as well. Furthermore, the occupancy is particularly sensitive in cases where the cluster itself sits on a symmetry axis (Mauracher et al., 2014).

Precedent for Double Wells-Dawson Structures in the Solid State

Solid-state interactions between polyoxometalates are investigated by X-ray crystallography by characterizing the intermolecular interactions which include H-bonding, stacking, and other van der Waals interactions. These interactions have been used for designing templating effects in metal-organic-framework structures (Ban et al., 1999). In **Figure 5** four different possible classes of dimeric structures are shown. In examining the 105 structures emerged in the CSD "$P_2W_{18}O_{62}$" search, four structures that can been described as a "double cluster" were identified by containing two crystallographically unique clusters in close proximity, i.e., refcodes JETSOR, PUPJUG, PUPJOA, and FUVXAW (*vide infra*) (Gong et al., 2006; Barrier et al., 2009; Yang et al., 2010). Although these reported structures also suffer from relatively large reliability (R_1) indices in their models, the resolution is much higher for these solid-state structures than in proteins and allows a glimpse of possible examples. One of the four Double Wells-Dawsons identified, refcode JETSOR (CCDC #257590), contains very close interaction between neighboring clusters, the terminal oxo units (O_{d1}-O_{d1}) are only 1.054 Å apart. For reference, a distance of 1.054 Å is near an C—H or O—H bond or could be considered as a peroxo bond by coordination chemists (Gong et al., 2006). Because no precedent for a Wells-Dawson-peroxo type coordination has been reported [although a peroxodecavanadate compound has been reported (Klištincová et al., 2009)], the Double Wells-Dawson structures described here are not within the common bond lengths either, and we have not attempted to analyze this cluster further. Combined these data do provide a framework for evaluation regarding the possibility that the Double Wells-Dawson-ribosome complex is a real dimer.

The remaining three clusters identified all consist of organic bridging structures of hydrogen-bonded networks including a counterion interaction. Interactions directly between the clusters themselves are between oxo-oxo, oxo-bridged, and bridged-bridged oxygens atoms. In the structure with refcode PUPJUG (CCDC #743675, Yang et al., 2010), there are numerous interactions, but the shortest include one terminal W=O bond on the belt (O_{d2}). This oxygen interacts with a triangular face of W=O on the other cluster (O_{d1}, O_{d1}, and O_{d2}) with distances ranging from 2.818 to 3.641 Å. In addition, the interactions of

that same W=O bond with the bridging oxygens on the face (O_{b1}, O_{b1}, and O_{b3}) occur at distances of 2.978, 3.317, and 3.470 Å. Other, longer terminal-bridging ($O_d \cdots O_b$ in both directions) interactions exist in this complex, with the longest interactions being the $O_b \cdots O_b$ bridging-bridging interactions. One method for describing the relationship in space between the two clusters is through the angle between the horizontal mirror planes of the clusters, defined as mean planes of the center six oxygen atoms for each. In this case, that angle is 41.16°. In the double cluster of T30S, for instance, that angle is 47.96°, indicating that the axes in the T30S are slightly less parallel but that the general structure is similar.

In the structure with refcode PUPJOA, (CCDC #743674, Yang et al., 2010) there are three 4,4-bipyridine molecules directly between the clusters and, therefore fewer direct interactions. Two belt oxo units (O_{d2}) of one cluster interact with one belt (O_{d2}) and one cap (O_{d1}) of the other. There is a 43.78° angle between horizontal mirrors. Structure refcode FUVXAW (CCDC #701467, Zhao et al., 2008) also has 4,4-bipyridine between the clusters, but only two. Two belt oxo units of one cluster (O_{d2}) interact with one belt (O_{d2}) and one cap (O_{d1}) of the other. The clusters have a 41.47° angle between the horizontal mirrors. There are limited interactions, all quite long: terminal O_{d1} to O_{d2} of 3.000 Å and O_{d2} to O_{d2} of 3.579 Å, several terminal to bridging oxygens in both directions, ranging from 4.401 to 5.76 Å. None of these clusters are consistent with the corner- or edge-sharing POM models proposed in **Figures 5A,B**, but rather each is more consistent with a 2:2 or H-bond shown in **Figures 5C,D**.

In summary, it is noticeable that the observed interactions with the ribosome involves the oxo groups on the Wells-Dawson structures in contrast to the protein decavanadate ($V_{10}O_{28}^{q-}$) and Keggin (general form $XMo_{12}O_{40}^{q-}$) structures where the interactions often involve the bridged oxygen atoms, but akin to the Anderson-Evans ($TeW_6O_{24}^{6-}$) cluster, which also involves the terminal oxo atoms (Blazevic et al., 2015; Bijelic and Rompel, 2017). In the case of the Double Wells-Dawson structures of the types shown in **Figure 6C** the oxo groups are often paired with another oxo group bridged by, for example, H_2O, H_3O^+, R_2NH, or $R_2NH_2^+$ molecules, the latter illustrated in **Figure 5C**. Although the very first and original X-ray structure by Dawson lacks the detail to show H-bonding interactions categorized in **Figure 5C** (Dawson, 1953), the original structure has beautiful hydrogen bond interactions with a small cation bridging two clusters in a manner that qualify as a "Double Wells-Dawson" in the manner we are describing in this work.

Of the 105 Wells-Dawson-cluster-containing structures in the CSD, several examples of short cluster-cluster interactions with symmetry equivalent clusters are known. Exemplary structures include compounds with structure codes COSVIR (CCDC #1003304, Chen et al., 2014) and RIBFUF (CCDC #933195, Kato et al., 2013), which show belt-to-belt interactions of the oxo units, whereas GUHNIH CCDC #718729, (Kurashina et al., 2009) and YEFRAF (CCDC #653498, Liu et al., 2014) show cap-to-cap interactions. Specifically, COSVIR has short interactions of 2.662 Å between belt oxo units on adjacent clusters (O_{d2}) along with several longer interactions (3.116 and

3.213 Å) and interactions between the oxo unit (O_{d2}) and a bridging oxygen (O_{b1} or O_{b2}) on the neighboring cluster (3.013 and 3.323 Å). Hydrogen bonding with a likely water molecule between a belt oxo (O_{d2}) and a cap oxo (O_{d1}; 2.968 and 2.869 Å O-H···O, respectively) is also present. RIBFUF has many interactions between the symmetry-equivalent clusters, but a 2.868 Å $O_{d1} \cdots O_{d1}$ interaction is the shortest. The short cluster-cluster interactions in the T30S Ribosome structures is better described as cap-to-cap, and GUHNIH and YEFRAF are examples of structures of that type. As shown above, in 1I94 (Pioletti et al., 2001) the double cluster unit appears to have a cap oxo unit in one cluster (O_{d1} in 1,001) in close contact with a bridging oxo as well as two cap oxo units on the adjacent cluster (O_c and O_{d1}, respectively in 1,004). In YEFRAF, the O_{d1} oxo unit is 2.716 Å from the other symmetry-generated oxo unit and 2.968 and 3.218 Å from O_c bridging atoms in the adjacent symmetrically-equivalent cluster. In GUHNIH, there are many more interactions between the two symmetry-equivalent clusters; oxo-oxo ($O_{d1} \cdots O_{d1}$) distances are 3.577 to 4.204 Å; unique distances between the oxo units and the adjacent-cluster bridging oxygen atoms (O_c) are 2.794–3.626 Å; whereas the unique bridging-oxygen to bridging-oxygen distances are 3.073–4.127 Å. The YEFRAF structure is furthermore stabilized by hydrogen bonding through four dimethylammonium cations between the caps of the clusters. These symmetry-generated Double Wells-Dawson clusters, then, also have inter-cluster distances that appear in line with the Double Wells-Dawson clusters seen in the ribosomal structures.

Precedent for Double Wells-Dawson Structures in Solution

In addition to forming dimers that are characterized by X-ray crystallography, information is available on the structural evolution in polyoxometalates in solution. There are no specific examples reported of P_2W_{18} clusters dimerizing/polymerizing in solution, but derivatives and lacunary species of these and other POMs have been examined, often leading to compounds with interesting properties. For example, the Zr(IV)–containing polyoxometalates derivatives that are found to effectively cleave proteins near aspartate residues (Absillis and Parac-Vogt, 2012; Ly et al., 2013; Stroobants et al., 2013; Vanhaecht et al., 2013). Both experimental studies and theoretical studies are available in some cases documenting the dimerization of polyoxometalates and formation of different isomers (Gong et al., 2006; Zhao et al., 2008; Barrier et al., 2009; Kurashina et al., 2009; Yang et al., 2010; Liu et al., 2014), e.g., the mechanistic study of peptide bond hydrolysis by the Wells-Dawson cluster (Absillis and Parac-Vogt, 2012). Dimerization of Lindqvist and Keggin Clusters through M-μ-O-M junctions have been investigated using DFT methods (Lopez et al., 2006), but it should be noted that W is not commonly engaged in these processes and dimer formation is more common for metal ions such as Nb, Ti, Cr, Fe, and Zr (Gong et al., 2006; Zhao et al., 2008; Barrier et al., 2009; Kurashina et al., 2009; Yang et al., 2010; Liu et al., 2014). Some of these clusters form through interaction with coordination complexes such as a peptide complex which can

then react by replacement of the ligand to form a dimer (Lopez et al., 2006). Such dimers have been characterized by X-ray crystallography, and importantly information is available on the reactivity and structural changes of these polyoxometalates in solution.

Another common method of dimerization is through coordination of organometallic ligands which can react to form larger structures (Nomiya et al., 2001). Most of the organometallic complexes are covalently bound to three of the bridging oxygen atoms in a cap of the cluster unit documenting the need for the complex coordination (Edlund et al., 1988; Pohl et al., 1995; Nagata et al., 1997; Nomiya et al., 2007). The Wells-Dawson clusters and derivatives are very versatile and are known to form dimeric/polymeric structures with strong covalent bonds and interactions as hydrogen bond ones. These strategies have been used effectively for synthesis of larger structures, and in some of these derivatives the organometallic unit persists; in others the unit has been replaced. Indeed, ligands have been found to affect reactivity showing that the *cap* region of the Wells-Dawson reacts first (Poblet et al., 2003). The presence of water has even been reported to change the selectivity of the catalysts on solid heteropolyacids (Micek-Ilnicka, 2009) documenting that water molecules and potential protonation can have a dramatic effect on the reactivity and catalysis of the Wells-Dawson cluster. Wells-Dawson clusters and the protonation states have been shown to be very important in catalysis (Wang and Yang, 2015).

Because the POM cluster contains central (O_a), terminal (O_d), edge-sharing (O_c), and corner-sharing (O_b) oxygen atoms (**Figure 2**), there is a potential to protonate different oxygen atoms and the literature is divided on which oxygen is most basic (Lopez et al., 2002; Poblet et al., 2003). DFT calculations on $X_2M_{18}O_{62}^{q-}$ clusters (Vilà-Nadal et al., 2012) report that the edge-sharing oxygen (O_c) atoms are the preferred proton location sites but the stabilization is <10 kJ mol^{-1} from the other possible sites (Janik et al., 2009). These studies also report that the first unoccupied molecular orbital (LUMO) of the Wells-Dawson is delocalized over the equatorial/belt region, whereas the first virtual orbital located on the *cap* region has been computed to be 0.85 eV higher in energy (Absillis and Parac-Vogt, 2012; Vilà-Nadal et al., 2012). Since ligands and the environment of the cluster are known to impact the stability of POMs, such effects are likely to be important for the observed preferential structures.

The effects of ligands, pH, and environments may reconcile the seemingly contradictory and inconclusive literature with regard to protonation of POMs (Howarth and Jarrold, 1978; Ozeki et al., 1994; Minato et al., 2014; Lopez, 2017). Studies on decavanadate ($V_{10}O_{28}^{q-}$) and Keggin anions (general form $XMo_{12}O_{40}^{q-}$) show that the bridging oxygen atoms (O_c and O_b) are the most basic sites (Roman et al., 1995; Lopez, 2017; Zhang et al., 2017), however, this is not what is observed in the Double Wells-Dawson structure (Rocchiccioli-Deltcheff et al., 1983; Minato et al., 2014; Lopez, 2017), where the terminal oxygen-atoms (O_d) are the functionalities associating with the ribosomal protein. It is known that ligands can affect the site of protonation and probably yield a very different set

of HOMO-LUMO orbitals (Lopez et al., 2002; Zhang et al., 2017). The fact that conclusions from studies based on FT-IR spectroscopy (Rocchiccioli-Deltcheff et al., 1983), ^{17}O NMR spectroscopy, and various NMR spectroscopic methods may not directly confirm the theoretical predictions is also important because the DFT calculations generally focus on properties of compounds in the gas phase (Rocchiccioli-Deltcheff et al., 1983; Lopez et al., 2002; Poblet et al., 2003; Li et al., 2006; Leng et al., 2009; Vilà-Nadal et al., 2012; Minato et al., 2014; Wu et al., 2015). Therefore, the stability order may vary as observed when comparing results from gas phase calculations with experimental solution experiments (Lopez et al., 2002; Poblet et al., 2003; Lopez, 2017).

We therefore conclude that combining these observations supports the potential for coordinating oxygen sites could associate with the ribosomal subunit and that possible complexes could be sufficiently close in energy allowing for protein-POM complexes. Consequently, observation of a Wells-Dawson cluster associating with the ribosome can be assisted by protonation, hydrogen-bonding, or metal ion complexation. In solution the oxo-groups are generally protonated following the μ-O atoms, and this stabilization may explain why so many of Wells-Dawson clusters associate with the protein through the oxo groups.

Evaluating if the Double Wells-Dawson on the Ribosome Is Real

Given the literature precedents for Double Wells-Dawson clusters, we now re-examine the Double Wells-Dawson cluster in the ribosomal subunit structure, specifically 1I94. The interactions that we have identified from the point of stabilizing the protein with more short distances to Cluster 1,001 suggest that this cluster is the most stabilizing cluster in the Double Dawson cluster. However, when considering that Cluster B is supporting the same amino acids 74–76 in both clusters, the two clusters do seem to both stabilize the ribosome structure and thus support the possibility that the Double Wells-Dawson cluster is a real dimer. As Bashan and Yonath had noted previously (Bashan and Yonath, 2008), the Wells-Dawson and Double Wells-Dawson clusters supported a rearrangement of the protein subunit that not only stabilize this conformation of the protein structure but also allows crystallization. In the Wells-Dawson-containing ribosome-X-ray structure for PDB ID 1I94 there are eight interactions <2.0 Å, and one is as close as 1.33 Å. In all these systems the interactions are otherwise chemically reasonable and the structures have normal distances with electrostatically favorable structural arrangements. However, the low occupancies in the model system presented for the highlighted clusters do allow the possibilities that each Wells-Dawson cluster in the Double Wells-Dawson cluster are not present in both sites at the same time, but the geometry and coordination environments allow for both clusters to be present.

The distances and angles between Clusters 1,001 and 1,004 in the double Double Wells-Dawson are also consistent with a real interaction (that is a normal bond/interaction) between Wells-Dawson clusters found in the solid state in the CSD. Distances

are consistent with the known structures containing the Wells-Dawson cluster and are consistent with a cap-to-cap interaction of the two clusters. Solution data in conjunction with theoretical data also support the existence of Double Clusters of the type that is observed on the ribosome. The structures outlined in **Figure 5** show the range of Double Clusters that can form. The cluster formed on the small ribosomal subunit appear to be one that is supported through H-bonding and illustrated in **Figure 5C**. The discussion of protonation and basic sites on the Wells-Dawson cluster in solution is strongly influenced by what is observed on the smaller clusters that have been more extensively investigated such as the decavanadate, Anderson-Evans, and Keggin structures. In the case of the Wells-Dawson cluster the most basic oxygen-atoms are less clear as well as the effect of environment on cluster formation. Therefore, the information in the literature would suggest that the structure formed on the ribosome would not necessarily be the isomer or conformation expected to form in solution. The observation that the Double Cluster consists of interactions through mainly the W=O units and less so the bridging oxygen atoms from the point of view of the POM and from backbone interactions from the point of view of the protein is not what would have been anticipated. However, POMs have been shown to be sensitive to their environment and that ligands can favor a behavior different than that generally observed. It is therefore possible that the presence of the protein does change the stability order of which oxygen atom is most basic and thus explains the observed form of the Double Wells-Dawson structure (2:2 isomer). As seen in **Figure 6**, Cluster 1,004 is interacting with Cluster 1,001 through a W=O unit and Cluster 1,001 is interacting through a W=O and a bridged oxygen atom.

Potential Applications of Wells-Dawson-Ribosome Clusters

The presence of the POM on the ribosome has been shown to impact the structure of the ribosome and helps the organization of it within the crystals, thus leading to higher resolution diffraction and to a refinement of the crystal structure (Thygesen et al., 1996; Tocilj et al., 1999; Weinstein et al., 1999; Schluenzen et al., 2000; Auerbach-Nevo et al., 2005; Bashan and Yonath, 2008; Yonath, 2009). Highly stable and symmetric clusters are desirable for phasing [see for example (Blazevic and Rompel, 2016)], but multi-metal clusters for crystallization are often unpredictable because the interactions typically occur between high symmetry clusters and low symmetry proteins (Thygesen et al., 1996; Tocilj et al., 1999). There is also a tendency for the clusters to bind along crystallographic symmetry axes (see Ladenstein et al., 1987; Thygesen et al., 1996; Rudenko et al., 2003; Dahms et al., 2013).

The T30S ribosomal subunit structure reported previously has 28 sites for Wells-Dawson polyoxotungstates per dimeric unit (Tocilj et al., 1999; Weinstein et al., 1999; Pioletti et al., 2001; Bashan and Yonath, 2008), each of which are half-occupied (**Figure 1C**). In later ribosome structures the location of these polyoxometalates in the structure deposited in the Protein Data Bank (PDB) (Berman et al., 2000; Schluenzen et al., 2000) database (both 1FKA and 1I94) were simplified from the point

of view of the protein. However, these coordinates do not always include the detailed Wells-Dawson structural information and thus lose information with regard to the protein-oxometalate interactions. Because of the symmetry of the space group in which the ribosome crystallizes ($P4_12_12$), 14 of these sites are unique as described subsequently.

One of the more surprising results in the studies is that the shortest bond lengths and interactions are with the nitrogen-backbone residues rather than side chains, although much side chain information is not detailed in the deposited data. Most interactions are also with the terminal oxo units (O_d) on the Dawson clusters, not the bridging oxygen atoms (O_b or O_c), which is surprising given that the most basic sites and hydrogen bonding acceptor is more likely the bridging oxygen-atoms (*vide supra*; Lopez et al., 2002; Poblet et al., 2003; Janik et al., 2009). In general, these interactions are therefore not what one would have expected both from the point of view of the POMs and from the point of view of the protein. Further analysis of a more complete data set is desirable.

The fact that the Wells-Dawson-ribosome interface was made up not by one single part of the protein, but that amino acids came from different parts of the peptide show that the protein is folding and packing in the presence of the POM (**Figure 4C**). Similar reorganization of the peptide structure has also been reported for the tyrosinase enzyme (Mauracher et al., 2014) and demonstrates that these types of interactions are important not only for the interactions with the ribosomal protein but in a more general sense as well (Tocilj et al., 1999). The ability of POMs, and specifically P_2W_{18}, to template interactions with surrounding peptide ligands result in stable POM-protein complexes that can facilitate protein crystallization.

CONCLUSIONS

In this manuscript, we have characterized the molecular details of the Wells-Dawson Clusters (P_2W_{18}) associated with the ribosome as well as one Double Wells-Dawson cluster using data mining. We have examined the interactions of the P_2W_{18} with the small ribosomal subunit, including the interactions of a pair of two Wells-Dawson structures close together. It was found that the stabilization of the ribosome appears to be mainly through interactions of the peptide backbone with the W=O groups in the P_2W_{18} clusters and by the side chains of positively charged amino acids Lys and Arg. By examining the reported examples of Double Clusters we found that the Double Cluster on the ribosome has a structure consistent with the reports in the literature of Double Wells-Dawson clusters in the solid state and in solution. However, it appears that the isomers formed in aqueous solution are different than the form we observe on the ribosomal subunit in a less polar environment. We conclude that the data obtained are consistent with the Double Cluster formed on the ribosome being structurally possible and a real structure. These results and current data sets do not preclude the possibility that some of the structures have partial occupation of each of the two separate sites.

DATA AVAILABILITY

All datasets generated for this study are included in the manuscript and/or the **Supplementary Files** or are available through the PDB /CSD.

AUTHOR CONTRIBUTIONS

DC and CM wrote on the manuscript and worked on the project in a collaborative manner, although the expertise tended to divide the contributions in the areas of the biology and data interpretation (for DC) and crystallography (for CM). IS-L carried out the literature search for the solution chemistry of Wells-Dawson complexes.

ACKNOWLEDGMENTS

SUPPLEMENTARY MATERIAL

The Supplementary Material for this article can be found online at: https://www.frontiersin.org/articles/10.3389/fchem.2019.00462/full#supplementary-material

REFERENCES

Absillis, G., and Parac-Vogt, T. N. (2012). Peptide bond hydrolysis catalyzed by the wells-Dawson $Zr(\alpha_2-P_2W_{17}O_{61})_2$ polyoxometalate. *Inorg. Chem.* 51, 9902–9910. doi: 10.1021/ic301364n

Acerete, R., Hammer, C. F., and Baker, L. C. W. (1979a). Direct tungsten-183 nuclear magnetic resonance: a powerful new structural tool for heteropoly- and isopolytungstate chemistry. *J. Amer. Chem. Soc.* 101, 267–269. doi: 10.1021/ja00495a070

Acerete, R., Harmalker, S., Hammer, C. F., Pope, M. T., and Baker, L. C. W. (1979b). Concerning isomerisms and interconversions of 2: 18 and 2: 17 heteropoly complexes and their derivatives. *J. Chem. Soc. Chem. Comm.* 777–779. doi: 10.1039/c39790000777

Allen, F. H. (2002). The Cambridge structural database: a quarter of a million crystal structures and rising. *Acta Crystallogr. Sect. B Struct. Crystallogr. Cryst. Chem.* 58, 380–388. doi: 10.1107/S010876810203890

Arefian, M., Mirzaei, M., Eshtiagh-Hosseini, H., and Frontera, A. (2017). A survey of the different roles of polyoxometalates in their interaction with amino acids, peptides and proteins. *Dalton Trans.* 46, 6812–6829. doi: 10.1039/C7DT00894E

Auerbach-Nevo, T., Zarivach, R., Peretz, M., and Yonath, A. (2005). Reproducible growth of well diffracting ribosomal crystals. *Acta Crystallogr. Sect. D* 61, 713–719. doi: 10.1107/S0907444905006311

Ban, N., Freeborn, B., Nissen, P., Penczek, P., Grassucci, R. A., Sweet, R., et al. (1998). A 9 Å resolution X-ray crystallographic map of the large ribosomal subunit. *Cell* 93, 1105–1115. doi: 10.1016/S0092-8674(00)81455-5

Ban, N., Nissen, P., Hansen, J., Capel, M., Moore, P. B., and Steitz, T. A. (1999). Placement of protein and RNA structures into a 5 Å-resolution map of the 50S ribosomal subunit. *Nature* 400, 841–847. doi: 10.1038/23641

Barrier, N., Fontaine, B., Pierrefixe, S., Gautier, R., and Gougeon, P. (2009). Synthesis, crystal and electronic structures, and physical properties of the novel compounds $LaR_4Mo_{36}O_{52}$ (R = Dy, Er, Yb, and Y) containing infinite chains of trans-edge-shared Mo_6 octahedra and Mo_2 Pairs and rectangular Mo_4 clusters with triple Mo-Mo bonds. *Inorg. Chem.* 48, 3848–3856. doi: 10.1021/ic801942d

Bashan, A., and Yonath, A. (2008). The linkage between ribosomal crystallography, metal ions, heteropolytungstates, and functional flexibility. *J. Mol. Struct.* 890, 289–294. doi: 10.1016/j.molstruc.2008.03.043

Berman, H. M., Westbrook, J., Feng, Z., Gilliland, G., Bhat, T. N., Weissig, H., et al. (2000). The protein data bank. *Nucleic Acids Res.* 28, 235–242. doi: 10.1093/nar/28.1.235

Bijelic, A., Aureliano, M., and Rompel, A. (2018). The antibacterial activity of polyoxometalates: structures, antibiotic effects and future perspectives. *Chem. Commun.* 54, 1153–1169. doi: 10.1039/C7CC07549A

Bijelic, A., Aureliano, M., and Rompel, A. (2019). Polyoxometalates as potential next-generation metallodrugs in the combat against cancer. *Angew. Chem. Int. Ed.* 58, 2980–9299. doi: 10.1002/anie.201803868

Bijelic, A., and Rompel, A. (2015). The use of polyoxometalates in protein crystallography – An attempt to widen a well-known bottleneck. *Coord. Chem. Rev.* 299, 22–38. doi: 10.1016/j.ccr.2015.03.018

Bijelic, A., and Rompel, A. (2017). Ten good reasons for the use of the tellurium-centered Anderson–Evans polyoxotungstate in protein crystallography. *Acc. Chem. Res.* 50, 1441–1448. doi: 10.1021/acs.accounts.7b00109

Blazevic, A., Al-Sayed, E., Roller, A., Giester, G., and Rompel, A. (2015). Tris-functionalized hybrid anderson polyoxometalates: synthesis, characterization, hydrolytic stability and inversion of protein surface charge. *Chem. Eur. J.* 21, 4762–4771. doi: 10.1002/chem.201405644

Blazevic, A., and Rompel, A. (2016). The Anderson–Evans polyoxometalate: from inorganic building blocks via hybrid organic–inorganic structures to tomorrows "Bio-POM." *Coord. Chem. Rev.* 307, 42–64. doi: 10.1016/j.ccr.2015.07.001

Bošnjaković-Pavlović, N., Prévost, J., and Spasojević-De Biré, A. (2011). Crystallographic statistical study of decavanadate anion based-structures: toward a prediction of noncovalent interactions. *Cryst. Growth Des.* 11, 3778–3789. doi: 10.1021/cg200236d

Brodersen, D. E., Clemons W. M Jr., Carter, B. T., Wimberly, B. T., and Ramakrishnan, V. (2003). Phasing the 30S ribosomal subunit structure. *Acta Crystallogr. Sect. D Biol. Crystallogr.* D59, 2044–2050. doi: 10.1107/S0907444903017669

Brown, A., and Shao, S. (2018). Ribosomes and cryo-EM: a duet. *Curr. Opin. Struct. Biol.* 52, 1–7. doi: 10.1016/j.sbi.2018.07.001

Brünger, A. T., Adams, P. D., Clore, G. M., DeLano, W. L., Gros, P., Grosse-Kunstleve, R. W., et al. (1998). Crystallography & NMR system: a new software suite for macromolecular structure determination. *Acta Crystallogr. Sect. D* 54, 905–921. doi: 10.1107/S0907444998003254

Bruno, I. J., Cole, J. C., Edgington, P. R., Kessler, M., Macrae, C. F., Mccabe, P., et al. (2002). New software for searching the Cambridge structural database and visualizing crystal structures. *Acta Crystallogr. Sect. B* 58, 389–397. doi: 10.1107/S0108768102003324

Chen, W.-H., Zhang, Z.-S., Hu, Z.-B., and Mi, J.-X. (2014). The first hybrid Wells-Dawson-type polytungstate monosupported by Cd-coordination complex via di-bridging O-atom. *Jiegou Huaxue* 33, 1550–1559. doi: 10.5517/cc12p0nf

Clemons, W. M., Brodersen, D. E., Mccutcheon, J. P., May, J. L. C., Carter, A. P., Morgan-Warren, R. J., et al. (2001). Crystal structure of the 30 S ribosomal subunit from *Thermus thermophilus*: purification, crystallization, and structure determination. *J. Mol. Biol.* 310, 827–843. doi: 10.1006/jmbi.2001.4778

Contant, R., and Thouvenot, R. (1993). A reinvestigation of isomerism in the Dawson structure: syntheses and [183]W NMR structural characterization of three new polyoxotungstates $[X_2W_{18}O_{62}]^{6-}$ (X = PV, AsV). *Inorg. Chim. Acta* 212, 41–50. doi: 10.1016/S0020-1693(00)92306-5

Crans, D. C., Mahroof-Tahir, M., Anderson, O. P., and Miller, M. M. (1994). X-ray structure of $(NH_4)_6(Gly-Gly)_2V_{10}O_{28}\bullet H_2O$: model studies of polyoxometalate-protein interactions. *Inorg. Chem.* 33, 5586–5590. doi: 10.1021/ic00102a036

Crans, D. C., Tarlton, M. L., and Mclauchlan, C. C. (2014). Trigonal bipyramidal or square pyramidal coordination geometry? Investigating the most potent geometry for vanadium phosphatase inhibitors. *Eur. J. Inorg. Chem.* 2014, 4450–4468. doi: 10.1002/ejic.201402306

Dahms, S. O., Kuester, M., Streb, C., Roth, C., Strater, N., and Than, M. E. (2013). Localization and orientation of heavy-atom cluster compounds in protein crystals using molecular replacement. *Acta Crystallogr. Sect. D* 69, 284–297. doi: 10.1107/S0907444912046008

Dauter, Z. (2005). Use of polynuclear metal clusters in protein crystallography. *Comp. Rend. Chim.* 8, 1808–1814. doi: 10.1016/j.crci.2005.02.032

Dawson, B. (1953). The structure of the 9(18)-heteropoly anion in potassium 9(18)-tungstophosphate, $K_6(P_2W_{18}O_{62}).14H_2O$. *Acta Crystallogr.* 6, 113–126. doi: 10.1107/S0365110X53000466

Edlund, D. J., Saxton, R. J., Lyon, D. K., and Finke, R. G. (1988). Trisubstituted heteropolytungstates as soluble metal-oxide analogs.4. The synthesis and characterization of organic solvent-soluble $(Bu_4N)_{12}H_4P_4W_{30}Nb_6O_{123}$ and $(Bu_4N)_9P_2W_{15}Nb_3O_{62}$ and solution specroscopic and other evidence for the supported organometallic derivatives $(Bu_4N)_7(C_5Me_5)Rh \cdot P_2W_{15}Nb_3O_{62}$ and $(Bu_4N)_7(C_6H_6)Ru \cdot P_2W_{15}Nb_3O_{62}$. *Organometallics* 7, 1692–1704. doi: 10.1021/om00098a003

Felts, R. L., Reilly, T. J., and Tanner, J. J. (2006). Structure of *Francisella tularensis* acid phosphatase A (AcpA). *J. Biol. Chem.* 281, 30289–30298. doi: 10.1074/jbc.M606391200

Garman, E., and Murray, J. M. (2003). Heavy-atom derivatization *Acta Crytallogr. Sect. D* D59, 1903–1913. doi: 10.1107/S0907444903012794

George, G. N., Pickering, I. J., Pushie, J., Nienaber, K., Hackett, M. J., Ascone, I., et al. (2012). X-ray-induced photo-chemistry and X-ray absorption spectroscopy of biological samples. *J. Synchrotron Rad.* 19, 875–886. doi: 10.1107/S090904951203943X

Gong, Y., Li, Y.-G., Li, H., Wang, Y.-H., and Hu, C.-W. (2006). Synthesis, characterization and properties of two novel complexes based on 2-aminopyridine and polyoxometalates. *Chin. J. Chem.* 24, 1148–1153. doi: 10.1002/cjoc.200690216

Goovaerts, V., Stroobants, K., Absillis, G., and Parac-Vogt, T. N. (2013). Molecular interactions between serum albumin proteins and Keggin type polyoxometalates studied using luminescence spectroscopy. *Phys. Chem. Chem. Phys.* 15, 18378–18387. doi: 10.1039/c3cp52848k

Green, D. W., Ingram, V. M., and Perutz, M. F. (1954). The structure of haemoglobin - IV. Sign determination by the isomorphous replacement method. *Proc. R. Soc. Lond. Ser. A Math. Phys. Sci.* 225, 287–307. doi: 10.1098/rspa.1954.0203

Heras, B., and Martin, J. L. (2005). Post-crystallization treatments for improving diffraction quality of protein crystals. *Acta Crystallogr. Sect. D Biol. Crystallogr.* D61, 1173–1180. doi: 10.1107/S0907444905019451

Hill, C. L., Hartnup, M., Faraj, M., Weeks, M., Prosser-Mccartha, C. M., Brown, R. B. Jr., et al. (1990). "Polyoxometalates as inorganic anti-HIV-1 compounds," in *Structure-Activity Relationships,* eds R. B. Diasio and J.-P. Sommandosi (New York, NY: Pergamon Press), 33–41. doi: 10.1177/0956320295006 00206

Howarth, O. W., and Jarrold, M. (1978). Protonation of decavanadate(6-) ion: aVanadium-51 nuclear magnetic-resonance study. *J. Chem. Soc. Dalton Trans.* 503–506. doi: 10.1039/DT9780000503

Janell, D., Tocilj, A., Kolln, I., Schlünzen, F., Glühmann, M., Hansen, H., et al. (2001). "Ribosomal crystallography and heteropolytungstates," in *Polyoxometalate Chemistry From Topology via Self-Assembly to Applications,* eds M. T. Pope and A. Müller (Dordrecht: Kluwer Academic Publishers), 391–415.

Janik, M. J., Campbell, K. A., Bardin, B. B., Davis, R. J., and Neurock, M. (2003). A computational and experimental study of anhydrous phosphotungstic acid and its interaction with water molecules. *Appl. Cat. A Gen.* 256, 51–68. doi: 10.1016/S0926-860X(03) 00388-0

Janik, M. J., Macht, J., Iglesia, E., and Neurock, M. (2009). Correlating acid properties and catalytic function: a first-principles analysis of alcohol

dehydration pathways on polyoxometalates. *J. Phys. Chem. C* 113, 1872–1885. doi: 10.1021/jp8078748

Jena Biosciences (2019). *Jena Biosciences*. Available online at: https://www.jenabioscience.com/crystallography/phasing/phasing-kits/jbs-tungsten-cluster-derivatization-kits (accessed April 17, 2019).

Kato, C., Nishihara, S., Tsunashima, R., Tatewaki, Y., Okada, S., Ren, X.-M., et al. (2013). Quick and selective synthesis of $Li_6[\alpha-P_2W_{18}O_{62}]\cdot28H_2O$ soluble in various organic solvents. *Dalton Trans.* 42, 11363–11366. doi: 10.1039/c3dt51120k

Klištincová, L., Rakovsky, E., and Schwendt, P. (2009). Decavanadate ion as bridging ligand. Synthesis and crystal structure of $(NH_4)_2[Cu_2(NH_3CH_2CH_2COO)_4(V_{10}O_{28})]\cdot10H_2O$. *Inorg. Chem. Commun.* 11, 1140–1142. doi: 10.1016/j.inoche.2008.06.020

Kluger, R., and Alagic, A. (2004). Chemical cross-linking and protein–protein interactions—a review with illustrative protocols. *Bioorg. Chem.* 32, 451–472. doi: 10.1016/j.bioorg.2004.08.002

Kurashina, T., Aoki, S., Hirasawa, R., Hasegawa, T., Kasahara, Y., Yoshida, S., et al. (2009). Cyclic oligomer of oxide clusters through a siloxane bond. Synthesis and structure of reaction products of α_2-mono-lacunary Dawson polyoxometalate with tetrachlorosilane and tetraethoxysilane. *Dalton Trans.* 28, 5542–5550. doi: 10.1039/b902904d

Ladenstein, R., Bacher, A., and Huber, R. (1987). Some observations of a correlation between the symmetry of large heavy-atom complexes and their binding sites on proteins. *J. Mol. Biol.* 195, 751–753. doi: 10.1016/0022-2836(87)90196-3

Lee, S.-Y., Fiene, A., Li, W., Hanck, T., Brylev, K. A., Fedorov, V. E., et al. (2015). Polyoxometalates—Potent and selective ecto-nucleotidase inhibitors. *Biochem. Pharmacol.* 93, 171–181. doi: 10.1016/j.bcp.2014.11.002

Leng, Y., Wang, J., Zhu, D., Ren, X., Ge, H., and Lei Shen, L. (2009). Heteropolyanion-based ionic liquids: reaction-induced self-separation catalysts for esterification. *Angew. Chem. Int. Ed.* 48, 168–171. doi: 10.1002/anie.200803567

Leon, I. E., Porro, V., Astrada, S., Egusquiza, M. G., Cabello, C. I., Bollati-Fogolin, M., et al. (2014). Polyoxometalates as antitumor agents: bioactivity of a new polyoxometalate with copper on a human osteosarcoma model. *Chem. Biol. Interact.* 222, 87–96. doi: 10.1016/j.cbi.2014.10.012

Li, Z., Zhang, Q., Liu, H., Hea, P., Xua, X., and Li, J. (2006). Organic–inorganic composites based on room temperature ionic liquid and 12-phosphotungstic acid salt with high assistant catalysis and proton conductivity. *J. Power Sour.* 158, 103–109. doi: 10.1016/j.jpowsour.2005.09.028

Liu, Y.-J., Sun, N., Ying, J., Tian, A.-X., and Zhang, Y.-P. (2014). Synthesis and crystal structure of two Dawson-type supramolecular compounds modified by $[Ln_2(HINC)_4]^{6+}$ (Ln=Ce, Eu) dimer. *Fenzi Kexue Xuebao* 30:324. doi: 10.13563/j.cnki.jmolsci.2014.04.011

Lopez, X. (2017). Effect of protonation, composition, and isomerism on the redox properties and electron (de)localization of classical polyoxometalates. *Phys. Sci. Rev.* 2:11. doi: 10.1515/psr-2017-0137

Lopez, X., Bo, C., and Poblet, J. M. (2002). Electronic properties of polyoxometalates: electron and proton affinity of mixed-addenda Keggin and Wells-Dawson anions. *J. Amer. Chem. Soc.* 124, 12574–12582. doi: 10.1021/ja020407z

Lopez, X., Weinstock, I. A., Bo, C., Sarasa, J. P., and Poblet, J. M. (2006). Structural evolution in polyoxometalates: a DFT study of dimerization processes in Lindqvist and Keggin cluster anions. *Inorg. Chem.* 45, 6467–6473. doi: 10.1021/ic060112c

Ly, H. G. T., Absillis, G., and Parac-Vogt, T. N. (2013). Amide bond hydrolysis in peptides and cyclic peptides catalyzed by a dimeric Zr(IV)-substituted Keggin type polyoxometalate. *Dalton Trans.* 42, 10929–10938. doi: 10.1039/c3dt50705j

Macrae, C. F., Bruno, I. J., Chisholm, J. A., Edgington, P. R., Mccabe, P., Pidcock, E., et al. (2008). Mercury CSD 2.0 - new features for the visualization and investigation of crystal structures. *J. Appl. Crystallogr.* 41, 466–470. doi: 10.1107/S0021889807067908

Mauracher, S. G., Molitor, C., Al-Oweini, R., Kortz, U., and Rompel, A. (2014). Latent and active *ab*PPO4 mushroom tyrosinase cocrystallized with hexatungstotellurate(VI) in a single crystal. *Acta Crystallogr. Sect. D* 70, 2301–2315. doi: 10.1107/S1399004714013777

McLauchlan, C. C., Peters, B. J., Willsky, G. R., and Crans, D. C. (2015). Vanadium-phosphatase complexes: Phosphatase inhibitors favor the trignonal

bipyramidal transition state geometries. *Coord. Chem. Rev.* 301–302, 163–199. doi: 10.1016/j.ccr.2014.12.012

Micek-Ilnicka, A. (2009). The role of water in the catalysis on solid heteropolyacids. *J. Mol. Cat. A Chem.* 308, 1–14. doi: 10.1016/j.molcata.2009.04.003

Minato, T., Suzuki, K., Kamata, K., and Mizuno, N. (2014). Synthesis of α-dawson-type silicotungstate $[\alpha\text{-}Si_2W_{18}O_{62}]^{8-}$ and protonation and deprotonation inside the aperture through intramolecular hydrogen bonds. *Chem. Eur. J.* 20, 5946–5952. doi: 10.1002/chem.201400390

Nagata, T., Pohl, M., Weiner, H., and Finke, R. G. (1997). Polyoxoanion-supported organometallic complexes: carbonyls of Rhenium(I), Iridium(I), and Rhodium(I) that are soluble analogs of solid-oxide-supported $M(CO)_n^+$ and that exhibit novel $M(CO)_n^+$ mobility. *Inorg. Chem.* 36, 1366–1377. doi: 10.1021/ic960910a

Noeske, J., Wasserman, M. R., Terry, D. S., Altman, R. B., Blanchard, S. C., and Cate, J. H. D. (2015). High-resolution structure of the *Escherichia coli* ribosome. *Nat. Struct. Mol. Biol.* 22, 336–341. doi: 10.1038/nsmb.2994

Nomiya, K., Kasahara, Y., Sado, Y., and Shinohara, A. (2007). Synthesis, isolation and spectroscopic characterization of Dawson polyoxotungstate-supported, organometallic complex, $[\{(C_6H_6)Ru\}P_2W_{15}V_3O_{62}]^{7-}$: The two positional isomers. *Inorg. Chim. Acta* 360, 2313–2320. doi: 10.1016/j.ica.2006.11.014

Nomiya, K., Torii, H., Nomura, K., and Sato, Y. (2001). Synthesis and characterization of a monoruthenium(III)-substituted Dawson polyoxotungstate derived by Br_2 oxidation of the 1: 2 complex of ruthenium(II) and $[\alpha_2\text{-}P_2W_{17}O_{61}]^{10-}$. The reactivity of cis- $RuCl_2(DMSO)_4$ as a ruthenium source. *J. Chem. Soc. Dalton Trans.* 2001, 1506–1512. doi: 10.1039/b009483h

Ozeki, T., Yamase, T., Naruke, H., and Sasaki, Y. (1994). X-ray structural characterization of the protonation sites in the dihydrogenhexaniobate anion *Bull. Chem. Soc. Jpn.* 67, 3249–3253. doi: 10.1246/bcsj.67.3249

Pioletti, M., Schlünzen, F., Harms, J., Zarivach, R., Glühmann, M., Avila, H., et al. (2001). Crystal structures of complexes of the small ribosomal subunit with tetracycline, edeine and IF3. *EMBO J.* 20, 1829–1839. doi: 10.1093/emboj/20.8.1829

Poblet, J. M., Lopez, X., and Bo, C. (2003). *Ab initio* and DFT modelling of complex materials: towards the understanding of electronic and magnetic properties of polyoxometalates. *Chem. Soc. Rev.* 32, 297–308. doi: 10.1039/B109928K

Pohl, M., Lin, Y., Weakley, T. J. R., Nomiya, K., Kaneko, M., Weiner, H., et al. (1995). Trisubstituted heteropolytungstates as soluble metal-oxide analogs—isolation and characterization of $[(C_5Me_5)Rh\cdot P_2W_{15}Nb_3O_{62}]^{7-}$ and $[(C_6H_6)Rh\cdot P_2W_{15}Nb_3O_{62}]^{7-}$, including the first crystal-structure of a Dawson-type polyoxoanions-supported organometallic complex. *Inorg. Chem.* 34, 767–777. doi: 10.1021/ic00108a005

Pope, M. T. (1976). Structural isomers of 1:12 and 2:18 heteropoly anions. Novel and unexpected chirality. *Inorg. Chem.* 15, 2008–2010. doi: 10.1021/ic50162a063

Rhule, J. T., Hill, C. L., Judd, D. A., and Schinazi, R. F. (1998). Polyoxometalates in medicine. *Chem. Rev.* 98, 327–358. doi: 10.1021/cr960396q

Rich, A. M., Armstrong, R. S., Ellis, P. J., Freeman, H. C., and Lay, P. A. (1998). Determination of iron-ligand bond lengths in horse heart met- and deoxymyoglobin using multiple-scattering XAFS analyses. *Inorg. Chem.* 37, 5743–5753. doi: 10.1021/ic9714549

Rocchiccioli-Deltcheff, C., Fournier, M., Franck, R., and Thouvenot, R. (1983). Vibrational investigations of polyoxometalates. 2. Evidence for anion-anion interactions in Molybdenum(VI) and Tungsten(VI) compounds related to the keggin structure. *Inorg. Chem.* 22, 207–216. doi: 10.1021/ic00144a006

Roman, P., Aranzabe, A., Luque, A., Gutierrezzorrilla, J. M., and Martinezripoll, M. (1995). Effects of protonation in decavanadates—crystal-structure of tetrakis (N-hexylamonium dihydrogendecavanadates(V)). *J. Chem. Soc. Dalton Trans.* 1995, 2225–2231. doi: 10.1039/DT9950002225

Rudenko, G., Henry, L., Vonrhein, C., Bricogne, G., and Deisenhofer, J. (2003). 'MAD'ly phasing the extracellular domain of the LDL receptor: a medium-sized protein, large tungsten clusters and multiple non-isomorphous crystals. *Acta Crystallogr. Sect. D* 59, 1978–1986. doi: 10.1107/S0907444903021383

Sanchez Lombardo, I. A., Santiago; McLauchlan, C. C., and Crans, D. C. (2015). Evaluating transition state structures of vanadium–phosphatase protein complexes using shape analysis. *J. Inorg. Biochem.* 147, 153–164. doi: 10.1016/j.jinorgbio.2015.04.005

Schluenzen, F., Tocilj, A., Zarivach, R., Harms, J., Gluehmann, M., Janell, D., et al. (2000). Structure of functionally activated small ribosomal subunit at 3.3 Å resolution. *Cell* 102, 615–623. doi: 10.1016/S0092-8674(00)00084-2

Steens, N., Ramadan, A. M., Absillis, G., and Parac-Vogt, T. N. (2010). Hydrolytic cleavage of DNA-model substrates promoted by polyoxovanadates. *Dalton Trans.* 39, 585–592. doi: 10.1039/B913471A

Stephan, H., Kubeil, M., Emmerling, F., and Müller, C. E. (2013). Polyoxometalates as Versatile Enzyme Inhibitors. *Eur. J. Inorg. Chem.* 2013, 1585–1594. doi: 10.1002/ejic.201201224

Stroobants, K., Moelants, E., Ly, H. G. T., Proost, P., Bartik, K., and Parac-Vogt, T. N. (2013). Polyoxometalates as a novel class of artificial proteases: selective hydrolysis of lysozyme under physiological pH and temperature promoted by a Cerium(IV) Keggin-type polyoxometalate. *Chem. Eur. J.* 19, 2848–2858. doi: 10.1002/chem.201203020

Thygesen, J., Weinstein, S., Franceschi, F., and Yonath, A. (1996). The suitability of multi-metal clusters for phasing in crystallography of large macromolecular assemblies. *Structure* 4, 513–518. doi: 10.1016/S0969-2126(96)00057-3

Tocilj, A., Schlünzen, F., Janell, D., Glühmann, M., Hansen, H. A. S., Harms, J., et al. (1999). The small ribosomal subunit from *Thermus thermophilus* at 4.5 Å resolution: pattern fittings and the identification of a functional site. *Proc. Nat. Acad. Sci. U.S.A.* 96, 14252–14257. doi: 10.1073/pnas.96.25.14252

Vanhaecht, S., Absillis, G., and Parac-Vogt, T. N. (2013). Amino acid side chain induced selectivity in the hydrolysis of peptides catalyzed by a Zr(IV)-substituted Wells-Dawson type polyoxometalate. *Dalton Trans.* 42, 15437–15446. doi: 10.1039/c3dt51893k

Vilà-Nadal, L., Romo, S., López, X., and Poblet, J. M. (2012). "Structural and Electronic Features of Wells-Dawson Polyoxometalates," in *Complexity in Chemistry and Beyond: Interplay Theory and Experiment,* eds C. L. Hill and D. G. Musaev (Dordrecht: Springer), 171–183. doi: 10.1007/978-94-007-5548-2_10

Wang, S.-S., and Yang, G.-Y. (2015). Recent advances in polyoxometalate-catalyzed reactions. *Chem. Rev.* 115, 4893–4962. doi: 10.1021/cr500390v

Weinstein, S., Jahn, W., Glotz, C., Schlünzen, F., Levin, I., Janell, D., et al. (1999). Metal compounds as tools for the construction and the interpretation of medium-resolution maps of ribosomal particles. *J. Struct. Biol.* 127, 141–151. doi: 10.1006/jsbi.1999.4135

Wimberly, B. T., Brodersen, D. E., Clemons, W. M., Morgan-Warren, R. J., Carter, A. P., Vonrhein, C., et al. (2000). Structure of the 30S ribosomal subunit. *Nature* 407, 327–339. doi: 10.1038/35030006

Winkler, P. A., Huang, Y., Sun, W., Du, J., and Lu, W. (2017). Electron cryo-microscopy structure of a human TRPM4 channel. *Nature* 552, 200–204. doi: 10.1038/nature24674

Wu, H. (1920). Contribution to the chemistry of phosphomolybdic acids, phosphotungstic acids, and allied substances *J. Biol. Chem.* 43, 189–220.

Wu, X., Huang, T., Xie, Z., Zhao, R., Wu, Q., and Yan, W. (2015). Facile fabrication of self-assembly polyoxometalate-type hybrid material through supermolecular interactions. *Mat. Lett.* 154, 156–159. doi: 10.1016/j.matlet.2015.04.083

Yang, H., Lin, X., Xu, B., You, Y., Cao, M., Gao, S., et al. (2010). Syntheses, structures, and properties of a series of supramolecular hybrids based on Keggin or Wells–Dawson polyoxometalates and 4,4'-bipyridines. *J. Mol. Struct.* 966, 33–38. doi: 10.1016/j.molstruc.2009.11.062

Yonath, A. (2009). Large facilities and the evolving ribosome, the cellular machine for genetic-code translation. *J. R. Soc. Interface* 6, S575–S585. doi: 10.1098/rsif.2009.0167.focus

Zhang, F. Q., Gao, J. P., Yan, L. K., Guan, W., Yao, R. X., and Zhang, X. M. (2017). Unveiling the relative stability and proton binding of non-classical Wells-Dawson isomers of $[(NaF_6)W_{18}O_{54}(OH)_2]^{7-}$ and $[(SbO_6)W_{18}O_{54}(OH)_2]^{9-}$: a DFT study. *Dalton Trans.* 46, 16145–16158. doi: 10.1039/C7DT03200E

Zhang, G., Keita, B., Brochon, J.-C., De Oliveira, P., Nadjo, L., Craescu, C. T., et al. (2007). Molecular interaction and energy transfer between human serum albumin and polyoxometalates. *J. Phys. Chem. B* 111, 1809–1814. doi: 10.1021/jp063758z

Zhang, G., Keita, B., Craescu, C. T., Miron, S., De Oliveira, P., and Nadjo, L. (2008). Molecular interactions between Wells–Dawson type polyoxometalates and human serum albumin. *Biomacromolecules* 9, 812–817. doi: 10.1021/bm701120j

Zhao, J. W., Chen, L.-J., and Wang, J.-P. (2008). Double cluster compounds. *Huaxue Yanjiu* 19:14. doi: 10.5517/ccrjxz4

Zheng, Q., Vilà-Nadal, L., Busche, C., Mathieson, J. S., Long, D.-L., and Cronin, L. (2015). Following the reaction of heteroanions inside a $\{W_{18}O_{56}\}$ polyoxometalate nanocage by NMR spectroscopy and mass spectrometry. *Angew. Chem. Int. Ed.* 54, 7895–7899. doi: 10.1002/anie.2015 02295

Conflict of Interest Statement: The authors declare that the research was conducted in the absence of any commercial or financial relationships that could be construed as a potential conflict of interest.

Synthesis, Magnetic Properties, and Catalytic Properties of a Nickel(II)-Dependent Biomimetic of Metallohydrolases

Adolfo Horn Jr. [1*], Daniel Englert [2,3], Asha E. Roberts [2], Peter Comba [2], Gerhard Schenk [3†], Elizabeth H. Krenske [3] and Lawrence R. Gahan [3*]

[1] Laboratório de Ciências Químicas, Universidade Estadual do Norte Fluminense Darcy Ribeiro, Campos dos Goytacazes, Brazil, [2] Anorganisch-Chemisches Institut and Interdisciplinary Center of Scientific Computing, Universität Heidelberg, Heidelberg, Germany, [3] School of Chemistry and Molecular Biosciences, The University of Queensland, Brisbane, QLD, Australia

A dinickel(II) complex of the ligand 1,3-bis(bis(pyridin-2-ylmethyl)amino)propan-2-ol (HL1) has been prepared and characterized to generate a functional model for nickel(II) phosphoesterase enzymes. The complex, $[Ni_2(L1)(\mu\text{-}OAc)(H_2O)_2](ClO_4)_2 \cdot H_2O$, was characterized by microanalysis, X-ray crystallography, UV-visible, and IR absorption spectroscopy and solid state magnetic susceptibility measurements. Susceptibility studies show that the complex is antiferromagnetically coupled with the best fit parameters $J = -27.4$ cm^{-1}, $g = 2.29$, $D = 28.4$ cm^{-1}, comparable to corresponding values measured for the analogous dicobalt(II) complex $[Co_2(L1)(\mu\text{-}OAc)](ClO_4)_2 \cdot 0.5\,H_2O$ ($J = -14.9$ cm^{-1} and $g = 2.16$). Catalytic measurements with the diNi(II) complex using the substrate bis(2,4-dinitrophenyl)phosphate (BDNPP) demonstrated activity toward hydrolysis of the phosphoester substrate with $K_m \sim 10$ mM, and $k_{cat} \sim 0.025$ s^{-1}. The combination of structural and catalytic studies suggests that the likely mechanism involves a nucleophilic attack on the substrate by a terminal nucleophilic hydroxido moiety.

Keywords: nickel, phosphoesterase, magnetism, DFT, kinetics, mechanism

INTRODUCTION

Our understanding of the bioinorganic significance of nickel can be traced to the discovery that the specific activity of the soluble jack bean urease, after partial EDTA-promoted inactivation, was a linear function of the nickel content, consistent with the presence of two nickel(II) ions per subunit of the pure enzyme (Dixon et al., 1980; Blakeley et al., 1982; Blakeley and Zerner, 1984). Previous to this discovery the importance of metal ions in general for the activity of urease was known, although the specific requirement for Ni(II) ions was not (Jacoby, 1933; Shaw, 1954; Shaw and Raval, 1961; Spears et al., 1977). Subsequently it was recognized that nickel is also required for the enzymatic activity of carbon monoxide dehydrogenase, (Ensign et al., 1989, 1990; Shin and Lindahl, 1992; Gencic and Grahame, 2003) and plays an important role in other bioinorganic systems, (Ashwini, 2006) including [NiFe]-hydrogenase (Przybyla et al., 1992; Sargent, 2016; Vaissier and Van, 2017) and a nickel dependent superoxide dismutase (Barondeau et al., 2004). In contrast to other bioinorganic systems Ni(II) complexes have received less attention. A limited number of studies have focussed on di-Ni(II) model complexes for urease (Meyer, 2009) and FeNi complexes

for hydrogenases (Vaissier and Van, 2017), and Neves and colleagues have developed several Ni(II) models for phosphatases, in particular purple acid phosphatases (PAPs) (Greatti et al., 2008; Piovezan et al., 2012; Xavier and Neves, 2016). PAPs present an ideal system to study biomimetics, in parts because of the wealth of sequence (Flanagan et al., 2006), structural and functional data available (Schenk et al., 2013), but also because these enzymes occur in homo- and hetero-bimetallic form in nature, using a range of metal ions (Fe, Zn, Mn; Mitić et al., 2009, 2010). Furthermore, the Fe(III)Ni(II) form of PAP is catalytically active, one of the few known metallohydrolases that can accommodate Ni(II) and maintain functionality (Schenk et al., 2008). This flexibility of PAPs with respect to their use of metal ions may be a reflection of their dual function as a phosphatase and peroxidase; indeed, in its di-Fe(III) form PAP is easily and reversibly reduced to the heterovalent Fe(III)Fe(II) form (redox potential ~340 mV), a process that allows the enzyme to act as a Fenton catalyst (Sibille et al., 1987; Bernhardt et al., 2004).

The metal ion composition of PAP may also influence its reaction mechanism; in particular, the identity of the hydrolysis-initiating nucleophile may be affected by the identity of the metal ions (Mitić et al., 2010; Selleck et al., 2017). Here, we selected ligand 1,3-bis(bis(pyridin-2-ylmethyl)amino)propan-2-ol (**Figure 1**) to probe the possibility that a di-Ni(II) biomimetic may promote phosphatase activity. This ligand, previously used to generate a di-Mn(II) system (Suzuki et al., 1989; Sato et al., 1992), offers an opportunity to investigate the hydrolytic mechanism as it offers a limited number of possible pathways for the nucleophile.

EXPERIMENTAL SECTION

General Methods

Chemicals were purchased from Sigma-Aldrich, Merck, ABCR, Acros or Alfa Aeser and used without further purification. Reactions requiring the exclusion of moisture and/or oxygen were carried out under nitrogen atmosphere using standard Schlenk techniques. TLC was performed on TLC Silica gel 60 F_{254} TLC plates purchased from Merck and visualization of the spots was carried out by fluorescence quenching with 254 nm UV light. Purification of raw products by column chromatography were performed using silica gel (grade 9385, 60 Å, 230–400 mesh size) purchased from Sigma-Aldrich. NMR spectra were recorded with a Bruker Avance III 300 system at 300 K. Chemical shifts (δ) are given in ppm and coupling constants (J) in Hz. ^{1}H and ^{13}C spectra were referenced to the protio impurity or the ^{13}C signal of the deuterated solvent. Abbreviations used for observed multiplicities are d for doublet, dd for doublet of doublets, td for triplet of doublets and m for multiplet. IR spectra were measured with a Perkin Elmer Frontier FT-IR spectrometer, transmittance data are given in wave number $\tilde{\nu}$ (cm^{-1}). Abbreviations used for observed intensities are w for weak, m for medium and s for strong. UV-Vis absorption spectra were recorded with an Agilent Technologies Cary 60 UV-Vis spectrophotometer. Elemental analyses were performed by the elemental microanalysis service at the School of Chemistry & Molecular Biosciences of the

FIGURE 1 | (A) 1,3-bis(bis(pyridin-2-ylmethyl)amino)propan-2-ol (HL1); **(B)** N,N,N',N'-tetrakis[(6-methyl-2-pyridyl)methyl]-1,3-diaminopropan-2-ol (Me4tpdpH).
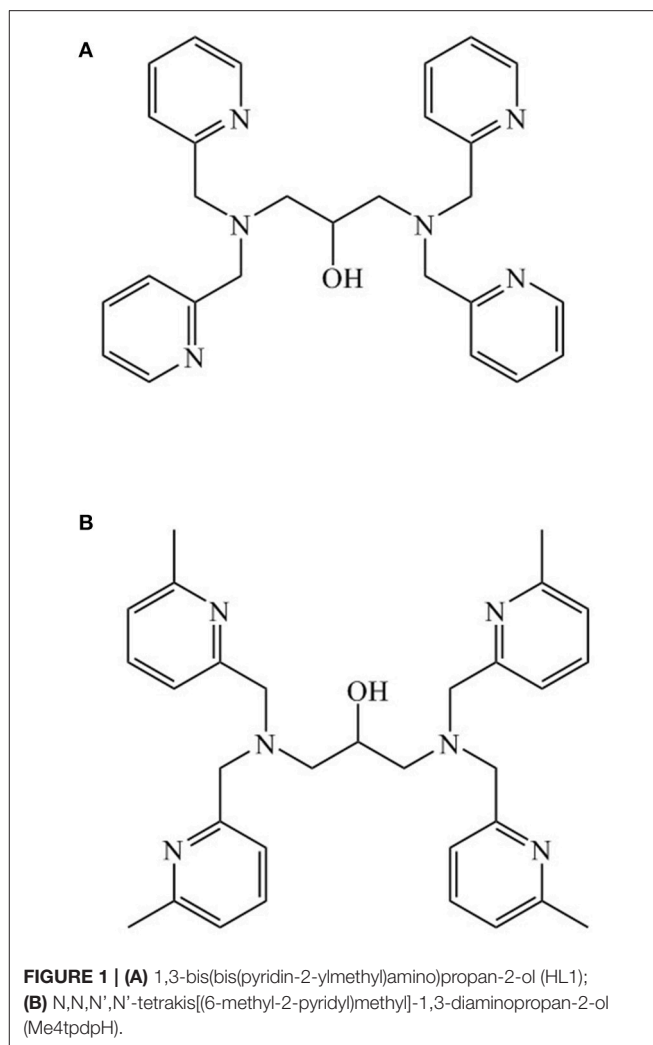
University of Queensland. The synthesis of the cobalt(II) complex, [Co$_2$(L1)(μ-OAc)](ClO$_4$)$_2$·0.5 H$_2$O, is described in the **Supplementary Material**.

Hydrolysis Studies

Kinetic studies were conducted using a Varian Cary50 Bio UV/Visible spectrophotometer with a Peltier temperature controller (25°C) and 10-mm quartz cuvettes, and employing bis-(2,4-dinitrophenol)phosphate (BDNPP) as substrate. Assays were measured in a solvent system composed of 50:50 acetonitrile:buffer. An aqueous multicomponent buffer was employed made up of 50 mM 2-(N-morpholino)ethanesulfonic acid (MES), 4-(2-hydroxyethyl)-1-piperazineethanesulfonic acid (HEPES), 2-(N-cyclohexylamino)ethane sulfonic acid (CHES) and N-cyclohexyl-3-aminopropanesulfonic acid (CAPS), with ionic strength controlled with LiClO$_4$ (250 mM). The pH values reported for the buffers are those of the aqueous component (Kaminskaia et al., 2000). The initial-rate method was employed and assays were measured such that the initial linear portion of the data was used for analysis. Product formation was determined by monitoring the formation of 2,4-dinitrophenolate; the

extinction coefficient of this product at 400 nm varies from 7,180 at pH 4.5, 10,080 at pH 5.0; 11,400 at pH 5.5 to 12,000 at 6.0 and 12,100 at pH 6.5–11 (Smith et al., 2007). Assays to evaluate the pH dependence of the reaction contained 40 µM complex and 5 mM BDNPP; to evaluate the effect of [substrate], 0.5 mM complex was mixed with 1–11.5 mM BDNPP. Catalytic rates could be measured reliably up to pH 11.0 and were fit to the simplest possible model to describe the pH dependence of the observed catalytic rates (Kantacha et al., 2011). The model invokes one relevant protonation equilibrium and is described by an equation of the form

$$y(x) = \frac{a}{1 + \frac{x}{b}}$$

Here, a and b represent fitting parameters (i.e., V_{max} and K_a, respectively), while x is the variable ([H^+] in this case) for a function of y (representing the measurable catalytic rate v). At very high [H^+] (low pH; x/b>>0) the denominator is >>V_{max} and hence the rate is approximating 0. At very low [H^+] (high pH; x/b~0) the denominator approximates 1 and hence the rate approaches V_{max}. The fitting parameter b, representing the relevant acid dissociation constant K_a, is thus the [H^+] where the rate v reaches half of its maximum value V_{max}.

The catalytic rates were measured as a function of substrate concentration. Experimental limitations (imposed by the solubility of the substrate) prevented accurate measurements above 6 mM. The data displayed hyperbolic behavior but saturation was not achieved. Consequently, the data were analyzed with a combination of non-linear regression and double-reciprocal linear fits, using the Michaelis-Menten equation

$$v_0 = \frac{V_{max}\,[S]}{K_m + [S]},$$

where V_0 is the initial rate, V_{max} is the maximum rate, K_M is the Michaelis constant, and [S] is the substrate concentration.

Susceptibility Measurements

The magnetic data were collected using an MPMS-XL 5T (Quantum Design) SQUID magnetometer. Fixed powder samples were prepared by pressing the powder into PTFE tape to prevent field-induced reorientation. Data were corrected for contributions of the sample holders and, using Pascal's constants (Bain and Berry, 2008), for the diamagnetic contributions of the samples. Effective magnetic moments were calculated using the relationship $\mu_{eff} = 2.828(\chi_M T)^{1/2}$.

Crystallographic Measurements

Crystallographic data for the complex were collected at 190(2) K using an Oxford Diffraction Gemini Ultra dual source (Mo and Cu) CCD diffractometer with Mo ($\lambda_{K\alpha} = 0.71073$ Å) radiation. The structure was solved by direct methods (SIR-92) and refined by full matrix least squares methods (SHELXL 97) based on F^2 (Sheldrick, 1997), accessed through the WINGX 1.70.01 crystallographic collective package (Farrugia, 1999). Hydrogen atoms were fixed geometrically and not refined. X-ray data

of the published structure was deposited with the Cambridge Crystallographic Data Centre, CCDC 1844565.

Computational Details

Geometry optimizations of the cations of [Ni$_2$(L1)(µ-OAc)(H$_2$O)$_2$](ClO$_4$)$_2$·H$_2$O and [Co$_2$(L1)(µ-OAc)](ClO$_4$)$_2$·0.5H$_2$O were undertaken with the Gaussian 09 set of programs (Frisch et al., 2013) starting from the X-ray structural data. The B3LYP functional (Becke, 1993), Noodleman's broken symmetry, (Noodleman et al., 1988) the TZV basis set (Schaefer et al., 1992). Orca 2.6.04 (Neese, 2012) was used for the magnetic coupling constant calculation essentially as described previously (Comba et al., 2009).

Synthesis

1,3-Bis(Bis(Pyridin-2-ylmethyl)Amino)Propan-2-ol (HL1)

2-(Chloromethyl)pyridine hydrochloride (4.00 eq, 6.01 g, 36.62 mmol) was dissolved in 3 mL distilled water and 15 mL of an aqueous 5 M NaOH solution was added while stirring. 1,3-diaminopropan-2-ol (1.00 eq, 825 mg, 9.15 mmol), 15 mL of 5 M NaOH solution and tetraoctylammonium bromide (0.02 eq, 100 mg, 183 µmol) were then added. The resulting red mixture was stirred at room temperature overnight. The reaction mixture was transferred into a separatory funnel with 40 mL chloroform, 40 mL of brine, the aqueous phase was extracted twice with 10 mL chloroform, and the combined organic layers washed with 50 mL water. The separated organic layer was dried over magnesium sulfate, filtered and concentrated under reduced pressure. The crude product was purified using a MeOH-equilibrated silica column (Merck) according to the manufacturer's instructions. After removal of the solvent under reduced pressure the product was obtained as orange oil (88%, 3.66 g, 8.05 mmol). ^{1}H NMR (300 MHz, CDCl$_3$): δ 8.49–8.45 (4H, m), 7.54 (4H, td, $J = 11.5$ Hz, $J = 1.8$ Hz), 7.37–7.31 (4H, m), 7.12–7.05 (4H, m), 4.03–3.92 (1H, m), 3.89 (4H, d, $^2J = 14.7$ Hz), 3.84 (4H, d, $^2J = 14.7$ Hz), 2.69 (2H, dd, $^2J = 13.3$ Hz, $^3J = 4.1$ Hz), 2.59 (2H, dd, $^2J = 13.3$ Hz, $^3J = 7.8$ Hz) ppm. ^{13}C NMR (75 MHz, CDCl$_3$): δ 159.3, 149.0, 136.5, 123.2, 122.1, 67.2, 60.8, 59.1 ppm.

[Ni$_2$(L1)(µ-OAc)(H$_2$O)$_2$](ClO$_4$)$_2$·H$_2$O

Nickel(II) acetate tetrahydrate (2.00 eq, 109.5 mg, 440 µmol) was dissolved in 6 mL MeOH. Lithium perchlorate trihydrate (4.00 eq, 153.4 mg, 880 µmol) and 4 mL of a methanol solution of 1,3-bis(bis(pyridin-2-ylmethyl)amino)propan-2-ol (HL1) (1.00 eq, 100.0 mg, 220 mmol) were added and the reaction mixture stirred under reflux for 1 h. Upon cooling to room temperature, the solvent was removed under reduced pressure and the resulting product was recrystallized in a water/acetone mixture resulting in blue crystals (46%, 89.6 mg). IR: $\tilde{v} = 3489$ (w), 3221 (w), 2801 (w), 1651 (m), 1606 (s), 1548 (s), 1482 (m), 1445 (s), 1427 (s), 1287 (m), 1161 (m), 1070 (s), 1056 (s), 1037 (s), 1023 (s), 990 (m), 928 (m), 886 (m), 760 (s), 620 (s) cm^{-1}. UV/vis λ_{max} (ε), 950 nm (57 M^{-1}cm^{-1}), 590 nm (43 M^{-1}cm^{-1}). Calc. for C$_{29}$H$_{38}$Cl$_2$N$_6$Ni$_2$O$_{14}$: C, 39.45; H, 4.34; N, 9.52 %. Found: C, 39.49; H, 4.13; N, 9.37%.

RESULTS AND DISCUSSION

Syntheses

The ligand 1,3-bis(bis(pyridin-2-ylmethyl)amino)propan-2-ol (HL1) was prepared by a modification of previously described procedures (Suzuki et al., 1989; Sato et al., 1992). The nomenclature HL1 indicates that the ligand is protonated at the hydroxido moiety and on formation of the complex the ligand is deprotonated and coordinates as the monoanion $L1^-$. We have reported previously a diZn(II) complex with $L1^-$ as a functional model for zinc(II) phosphoesterase enzymes (Mendes et al., 2016).

In this work the dinuclear nickel complex $[Ni_2(L1)(\mu-OAc)(H_2O)_2](ClO_4)_2 \cdot H_2O$ was synthesized from a reaction of HL1 with two equivalents of nickel(II) acetate in methanol

TABLE 1 | Crystallographic data for $[Ni_2(L1)(\mu-OAc)(H_2O)_2](ClO_4)_2 \cdot H_2O$.

Complex	$[Ni_2(L1)(\mu-OAc)(H_2O)_2](ClO_4)_2 \cdot H_2O$
Empirical formula	$C_{29}H_{36}Cl_2N_6Ni_2O_{13}$
Formula weight	864.96
Wavelength (Å)	0.71073 (Mo K$_\alpha$)
Crystal system	Monoclinic
Space group	C 2/c
a (Å)	12.7975(10)
b (Å)	21.0734(13)
c (Å)	13.8612(8)
α (°)	90
β (°)	105.169(7)
γ (°)	90
Vol (Å^3)	3,607.9(4)
Z	4
μ (mm^{-1})	1.263
$F(000)$	1,784
ρ (Mg/m^3)	1.592
Reflns col.	8510
Ind. Reflns (R_{int})	3,178(0.0533)
θ range (°)	3.48 to 25.00
GOOF on F^2	1.042
final R indices [I>2σ(I)]	R1 = 0.0523, wR2 = 0.1171
R indices (all data)	R1 = 0.0733, wR2 = 0.1312

TABLE 2 | Selected bond lengths (Å) and angles (°) for $[Ni_2(L1)(\mu-OAc)(H_2O)_2](ClO_4)_2 \cdot H_2O$.

N(1)-Ni(1) 2.078(3)	N(2)-Ni(1) 2.110(4)	N(3)-Ni(1) 2.080(4)
O(1)-Ni(1) 1.990(2)	O(2)-Ni(1) 2.058(3)	O(3)-Ni(1) 2.132(3)
Ni(1)-O(1)-Ni(1) 131.6(2)	O(1)-Ni(1)-O2 93.57(13)	O(1)-Ni(1)-N(1) 96.25(10)
O(2)-Ni(1)-N(1) 97.99(13)	O(1)-Ni(1)-N(3) 92.40(10)	O(2)-Ni(1)-N(3) 99.49(13)
N(1)-Ni(1)-N(3) 159.95(14)	O(1)-Ni(1)-N(2) 83.55(14)	O(2)-Ni(1)-N(2) 176.71(13)
N(1)-Ni(1)-N(2) 80.79(14)	N(3)-Ni(1)-N(2) 82.26(14)	O(1)-Ni(1)-O(3) 176.18(12)
O(2)-Ni(1)-O(3) 89.54(12)	N(1)-Ni(1)-O(3) 85.50(13)	N(3)-Ni(1)-O(3) 84.89(12)
N(2)-Ni(1)-O(3) 93.40(13)		

solution in the presence of LiClO$_4$. The nickel complex was obtained as bright blue crystals after recrystallization in a water/acetone mixture.

A complex with the same ligand and formulated as $[Ni_2(L1)(\mu-OAc)_2](PF_6) \cdot MeOH$ has been reported previously (Moffat et al., 2014). In that case the synthesis involved the reaction of the ligand HL1, nickel(II) acetate in methanol, in the presence of triethylamine and NaPF$_6$ under reflux. On standing at $-18°C$ the pink crystals which initially formed were removed, the mother liquor collected and concentrated under vacuum and upon slow diffusion of diethylether on standing the deep blue crystals of $[Ni_2(L1)(\mu-OAc)_2](PF_6) \cdot MeOH$ were collected and structurally characterized (Moffat et al., 2014). In addition, the Ni(II) complex of a similar ligand N,N,N',N'-tetrakis((6-methyl-2-pyridyl)methyl)-1,3-diaminopropan-2-ol (Me$_4$tpdpH), prepared by reaction of nickel(II) acetate, NaClO$_4$ with Me$_4$tpdpH in methanol at room temperature, and crystallized from a methanol/diethyl ether solution as light green crystals, has also been reported. The complex was formulated as $[Ni_2(Me_4tpdp)(\mu-OAc)(ClO_4)(CH_3OH)](ClO_4)$ (Yamaguchi et al., 1997, 2001). The synthesis and characterization of the cobalt complex $[Co_2(L1)(\mu-OAc)](ClO_4)_2$ has been reported previously (Siluvai and Murthy, 2009).

Spectroscopy

The infrared spectrum of $[Ni_2(L1)(\mu-OAc)(H_2O)_2](ClO_4)_2$ displayed bands attributed to the asymmetric and the symmetric acetate stretch ($v_{as} = 1,548$ cm^{-1}, $v_s = 1,445$ cm^{-1}), indicating the presence of a bridging acetate anion (Deacon and Phillips, 1980). Furthermore, characteristic bands at 1,606 cm^{-1} and 1,576 cm^{-1} were assigned to $v_{C=N}$ and $v_{C=C}$ of the pyridyl groups of the ligand, and those 1,070 cm^{-1} to the perchlorate counter ion.
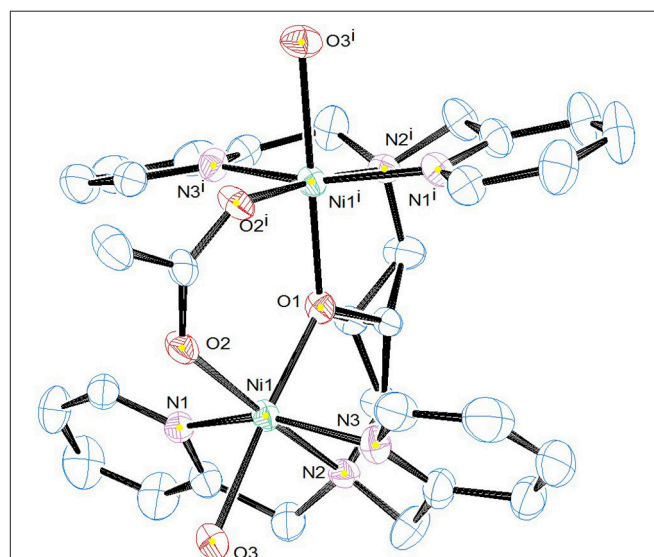

FIGURE 2 | ORTEP plot of the cation $[Ni_2(L1)(\mu-OAc)(H_2O)_2]^{2+}$. Counter ions and hydrogen atoms have been omitted for clarity (25% ellipsoid probability in ORTEP plot).

The electronic spectrum of $[Ni_2(L1)(\mu\text{-}OAc)(H_2O)_2](ClO_4)_2$ was measured in acetonitrile. For octahedrally coordinated Ni(II) ions there are three spin allowed d-d transitions from the $^3A_{2g}$ ground state to the higher excited triplet states $^3T_{2g}$, $^3T_{1g}$, and $^3T_{1g}$ (P). Spectral bands with maxima at 950 and 590 nm were assigned to the $^3A_{2g} \rightarrow {}^3T_{2g}$ and $^3A_{2g} \rightarrow {}^3T_{1g}$ transitions, respectively. The $^3A_{2g} \rightarrow {}^3T_{1g}$ (P) transition is probably hidden under the intense band of the pyridyl groups with a maximum at 255 nm; a small shoulder around 400 nm could arise from this spin-allowed transition. A shoulder around 800 nm is assigned to the spin-forbidden d-d $^3A_{2g} \rightarrow {}^1E_{1g}$ transition. The Racah parameter B and the ligand field splitting energy Dq of the d^8 Ni(II) system were determined using the bands of the $^3A_{2g} \rightarrow {}^3T_{2g}$ and $^3A_{2g} \rightarrow {}^3T_{1g}$ transitions and determined to be 877 and 1,053 cm^{-1}, respectively.

X-Ray Crystal Structure

Selected crystallographic data for $[Ni_2(L1)(\mu\text{-}OAc)(H_2O)_2](ClO_4)_2 \cdot H_2O$ are shown in **Table 1** and selected bond lengths and angles are displayed in **Table 2**. An ORTEP plot is shown in **Figure 2**. The structure is composed of the ligand mono-anion, two metal(II) ions and a bridging acetate with the Ni(II) structure containing two coordinated aqua ligands completing the hexacoordinate coordination sphere. The charge is balanced by perchlorate ions. In the diNi(II) complex there is disorder around the carbon atom of the bridging hydroxide. The coordination symmetry around each Ni(II) site for $[Ni_2(L1)(\mu\text{-}OAc)(H_2O)_2](ClO_4)_2 \cdot H_2O$ is octahedral and the donor set of both nickel atoms is N_3O_3, which is composed of a tertiary amino-N atom (Ni(1)-N(2): 2.110(4) Å), two pyridyl-N atoms (Ni(1)-N(1): 2.078(3) Å; Ni(1)-N(3): 2.080(4) Å), a bridging alkoxo-O atom (Ni(1)-O(1): 1.990(2) Å), an μ-acetato O atom (Ni(1)-O(2): 2.058(3) Å) and an O atom of a coordinating water molecule (Ni(1)-O(3): 2.132(3) Å). The bridging angle Ni-O(1)-Ni is 131.6° and the two nickel atoms are separated by a distance of 3.63 Å. The C(8) atom is disordered between two different positions.

For the previously reported complex $[Ni_2(L1)(\mu\text{-}OAc)_2](PF_6)\cdot MeOH$, the two Ni(II) octahedral sites are composed of two μ-acetate ligands, the three N donors of the L1 ligand, and the μ-O of the ligand (**Figure 3**, top; Moffat et al., 2014). The differences in the two diNi(II) structures of L1$^-$ involve the absence of the second bridging acetate ligand and the presence of the two terminal water molecules in $[Ni_2(L1)(\mu\text{-}OAc)(H_2O)_2](ClO_4)_2 \cdot H_2O$, as well as the presence of the ClO$_4$ $^-$ anions. Furthermore, the coordinating groups present in the ligand arms show a meridional coordination mode, which induces the coordination of the water molecules in positions *anti* to each other.

The X-ray crystal structure of $[Ni_2(Me_4tpdp)(\mu\text{-}OAc)(ClO_4)(CH_3OH)](ClO_4)$ has been reported (**Figure 3**, bottom; Yamaguchi et al., 1997, 2001). The structure shows that both Ni(II) sites are six coordinate, the two metal ions separated by 3.62 Å and bridged by the ligand μ-O alkoxide and μ-acetato ligands. The sixth coordination site of one Ni(II) is made up of the O from a perchlorato ligand, whilst for the other metal ion a CH$_3$OH ligand completes the sixth coordination
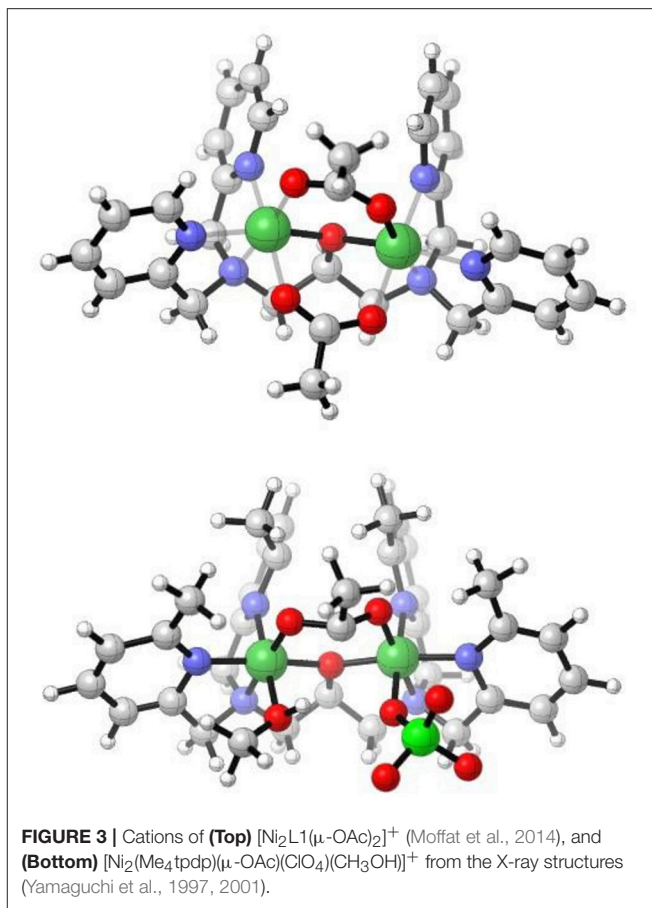
FIGURE 3 | Cations of **(Top)** $[Ni_2L1(\mu\text{-}OAc)_2]^+$ (Moffat et al., 2014), and **(Bottom)** $[Ni_2(Me_4tpdp)(\mu\text{-}OAc)(ClO_4)(CH_3OH)]^+$ from the X-ray structures (Yamaguchi et al., 1997, 2001).

(Yamaguchi et al., 1997, 2001). Whereas for the complex $[Ni_2(L1)(\mu\text{-}OAc)(H_2O)_2](ClO_4)_2 \cdot H_2O$ the coordinated aqua ligands are *trans* to the μ-alkoxo-O atom, effectively bisecting the two pyridyl rings of the ligand, this arrangement is not observed in the structure of the analogous $[Ni_2(Me_4tpdp)(\mu\text{-}OAc)(ClO_4)(CH_3OH)](ClO_4)$ complex. Here, the methanol and perchlorato ligands are located *cis* to the μ-alkoxo-O atom (Yamaguchi et al., 1997), and presumably replaced by aqua ligands in solution, an important consideration in subsequent hydrolytic studies (Yamaguchi et al., 2001).

The X-ray crystal structure of $[Co_2(L1)(\mu\text{-}OAc)](ClO_4)_2$ has been reported (Siluvai and Murthy, 2009). The structure shows a pseudo C$_2$-axis of symmetry with the μ-acetate ligand bridging the two Co(II) ions in a symmetric μ-1,3 mode. The two Co(II) sites display slightly distorted trigonal bipyramidal geometry with τ_{av}, the index of trigonality, equal to 0.93; a τ value of unity would perfect trigonal bipyramidal geometry (Addison et al., 1984; Siluvai and Murthy, 2009).

Magnetic Susceptibility

The magnetic susceptibility of the diNi(II) and diCo(II) complexes was measured over the temperature range 300 to 7 K in an applied field of 500 G. The χ_M vs. T, and $\chi_M T$ vs. T plots are presented in **Figure 4** for $[Ni_2(L1)(\mu\text{-}OAc)(H_2O)_2](ClO_4)_2 \cdot H_2O$

FIGURE 4 | χ_M vs. T, and χ_MT vs. T (insert) plots for $[Ni_2(L1)(\mu\text{-OAc})(H_2O)_2](ClO_4)_2 \cdot H_2O$.

FIGURE 5 | χ_M vs. T, and χ_MT vs. T (insert) plots for $[Co_2(L1)(\mu\text{-OAc})](ClO_4)_2 \cdot 0.5H_2O$.

FIGURE 6 | (A) pH dependence profile, and **(B)** Michaelis-Menten plot for the hydrolysis of BDNPP catalyzed by $[Ni_2(L1)(\mu\text{-OAc})(H_2O)_2](ClO_4)_2 \cdot H_2O$.
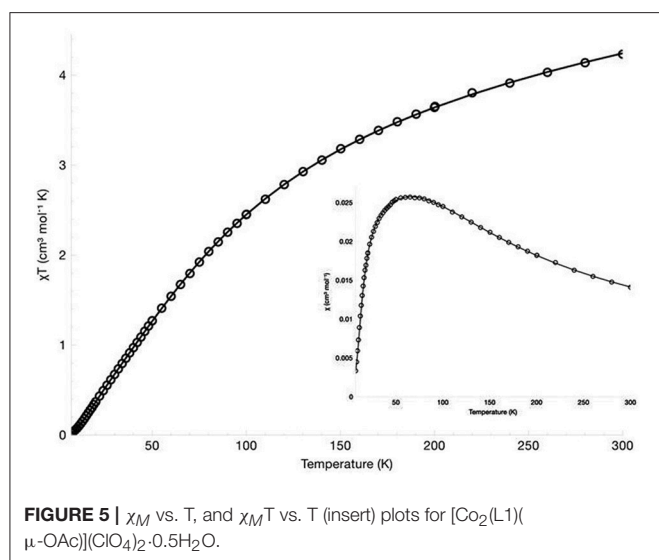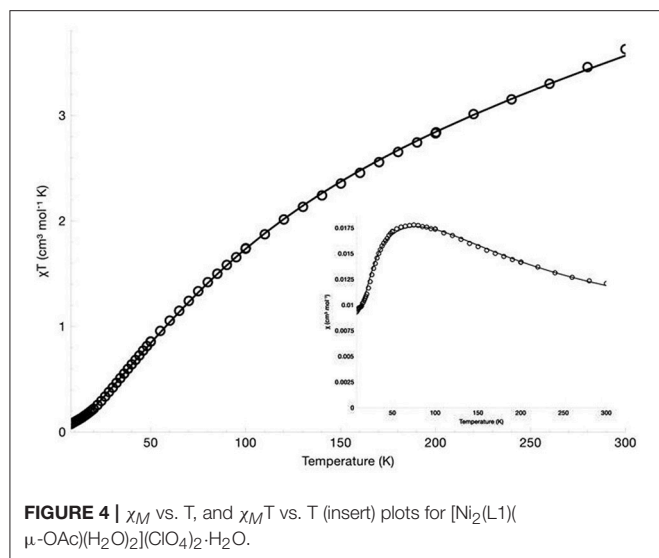
and **Figure 5** for $[Co_2(L1)(\mu\text{-OAc})](ClO_4)_2 \cdot 0.5H_2O$. For both complexes the susceptibility data were fitted using the program PHI (Chilton et al., 2013) with the isotropic exchange Hamiltonian $\hat{H} = -2J\hat{S}_1 \cdot \hat{S}_2$.

For $[Ni_2(L1)(\mu\text{-OAc})(H_2O)_2](ClO_4)_2 \cdot H_2O$ the χ_MT vs. T plot indicates antiferromagnetic coupling between the two Ni(II) centers, with χ_MT gradually decreasing from 3.63 cm^3 K mol^{-1} (μ_{eff} = 5.39 μ_B) at 300 K to 0.075 cm^3 K mol^{-1} (μ_{eff} = 0.77 μ_B) at 8 K. The room temperature value of χ_MT is larger than the spin-only value for two non-interacting high-spin nickel(II) ions (χ_MT = 2.00 cm^3 K mol^{-1}, μ_{SO} = 4.00 μ_B, g = 2.00, S = 1). While no orbital angular momentum is expected for the $^3A_{2g}$ ground state of the octahedral d^8 centers, it is expected for the excited $^3T_{2g}$ and $^3T_{1g}$ states. The theoretical χ_MT value with orbital angular momentum included is 4.99 cm^3 K mol^{-1} (μ_{SL} = 6.32 μ_B, L = 3), which suggests some orbital contributions are present in this case. The best fit gave parameters
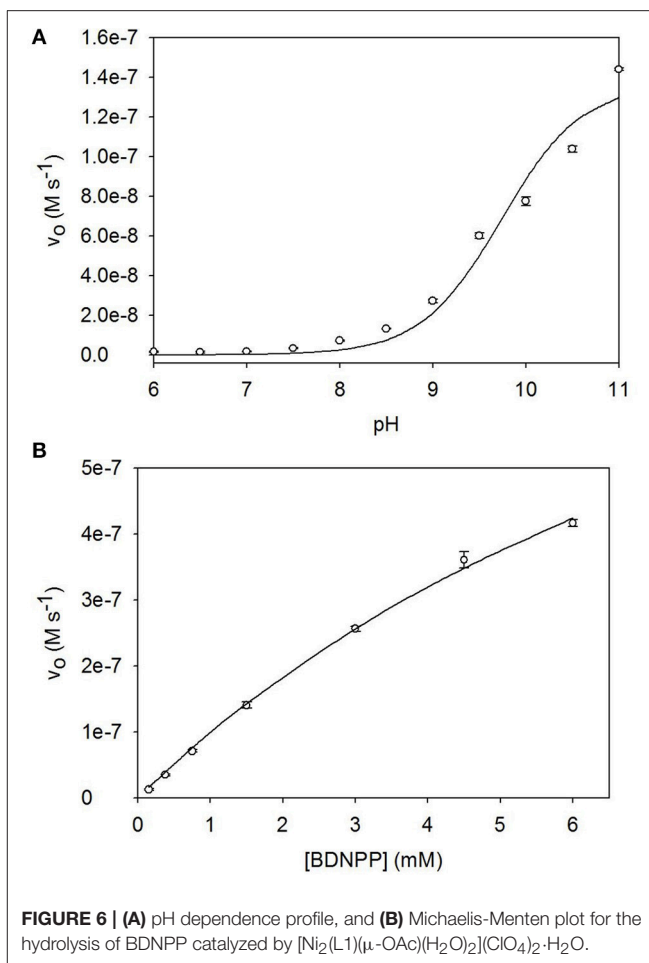
$J = -27.4$ cm^{-1}, $g = 2.29$, $D = 28.4$ cm^{-1} and $\chi_{TIP} = 4.75 \times 10^{-9}$ m^3 mol^{-1}. The inclusion of neither a rhombic zero-field splitting (ZFS) parameter E nor an intermolecular magnetic exchange parameter zJ led to an improvement of the fit and were thus omitted.

For $[Co_2(L1)(\mu\text{-OAc})](ClO_4)_2 \cdot 0.5H_2O$ the magnetic moment has been reported as 4.09 μ_B/Co(II), measured in d$_3$-acetonitrile at room temperature (Siluvai and Murthy, 2009). In the study reported herein, the variable temperature magnetic susceptibility of the complex was measured from 300–7 K. The χ_MT value at 300 K is 4.23 cm^3 K mol^{-1} (μ_{eff} = 5.82 μ_B), which is within the range of similar binuclear cobalt(II) complexes (Zeng et al., 2004; Tian et al., 2007, 2008; Massoud et al., 2008; Jung et al., 2009; Daumann et al., 2013a; Khandar et al., 2015; Li et al., 2015; Alam et al., 2016). The value is higher than the expected spin-only value for two non-interacting high-spin cobalt(II) ions (3.74 cm^3 K mol^{-1}, μ_{SO} = 5.47 μ_B, g = 2.00, S = 3/2) but significantly lower than expected with the inclusion of orbital angular momentum (6.76 cm^3 K mol^{-1}, μ_{SL} = 7.35 μ_B, L = 3), suggesting only very minor orbital contributions. The value of χ_MT shows a gradual decrease with decreasing temperature and reaches 0.025 cm^3 K mol^{-1} at 7 K, indicative of antiferromagnetic coupling between the two centers. The best fit to the data gave parameters $J = -14.9$

cm^{-1}, $g = 2.16$ and TIP $= 2.22 \times 10^{-9}$ m^3 mol^{-1}. The inclusion of intermolecular magnetic exchange zJ was found to have little effect on the fit and, therefore, was not included. The fitted g value is larger than the free ion g value ($g_e = 2.00$) and is explained by second-order effects. While the $^4A_2'$ ground state arising from the trigonal bipyramidal coordination of a d^7 ion has no orbital angular momentum, admixture of the excited $^4E''$ state with the orbital angular momentum introduces second-order orbital momentum, resulting in a larger g value and magnetic moment (Hempel and Miller, 1981; Hossain and Sakiyama, 2002; Bai et al., 2005).

A computational study was undertaken employing the B3LYP functional, Noodleman's broken symmetry, the TZV basis set and the Orca set of programs (Noodleman et al., 1988; Schaefer et al., 1992; Becke, 1993; Neese, 2012; Frisch et al., 2013) in order to calculate the magnitude of the coupling in both complexes (Comba et al., 2009). The calculations were performed based on the X-ray structural parameters for the respective complexes. For the [Ni$_2$(L1)(μ-OAc)(H$_2$O)$_2$](ClO$_4$)$_2$·H$_2$O complex the computed value of $2J$ was similar to the experimentally determined value (-26.4 cm^{-1} compared with -27.4 cm^{-1}, respectively). For [Co$_2$(L1)(μ-OAc)](ClO$_4$)$_2$·0.5H$_2$O the difference in the calculated and experimental values was greater (-20.1 cm^{-1} compared with -14.9 cm^{-1}, respectively).

Attempts have been made to correlate structural parameters with the strength of coupling for both diNi(II) and diCo(II) complexes (Nanda et al., 1994a,b,c; Schultz et al., 1997; Johansson et al., 2008; Tomkowicz et al., 2012; Daumann et al., 2013b). In the case of diNi(II) complexes, an initial study reported a linear correlation between the magnitude and sign of J with the Ni-O-Ni angle for five diNi(II) complexes of the macrocyclic ligand 1^5,9^5-dimethyl-3,7,11,15-tetraaza-1,9(1,3)-dibenzenacyclohexadecaphane-1^2,9^2-diol, with aqua, thiocyanate, methanol, imidazole, and pyridine ligands completing the coordination sphere (Nanda et al., 1994c). The authors proposed that at an Ni-O-Ni angle of 97° a cross over from antiferro- to ferro-magnetic coupling occurred (Nanda et al., 1994c). The study was subsequently expanded to include examples of other diNi(II) complexes with phenoxido-bridged ligands and it was concluded that, with the availability of more structural data, a more definitive correlation between J and the Ni-O-Ni angle could be expected (Nanda et al., 1994a,b). In line with the previous analysis of the relationship between J and Ni-X bonds lengths it was suggested that, in hexacoordinate complexes, the antiferromagnetic coupling was amplified with an increase in bond lengths of one of the axial bonds (Nanda et al., 1994a). Further, the studies suggested that a significant increase in the magnitude of -J occurred in the situation where a tetragonally elongated hexacoordinate complex transformed to a five-coordinate square pyramidal complex (Nanda et al., 1994a). Subsequently, a series of studies reported and expanded on the correlations between the sign and magnitude of J and both the Ni-O-Ni and Ni-X bond lengths (Allen et al., 1978; Wages et al., 1993; Halcrow and Christou, 1994; Adams et al., 2001; Bu et al., 2001; Mochizuki et al., 2004; Prushan et al., 2007; Greatti et al., 2008; Pawlak et al., 2008; Mandal et al., 2009; Chattopadhyay

FIGURE 7 | After loss of the μ-acetato ligands in the complex [Ni$_2$(L1)(μ-OAc)(H$_2$O)$_2$] $^{2+}$ these structures represent **(A)** μ-1,3 coordination of BDNPP$^-$ to the two Ni(II) sites with two aqua ligands positioned *trans* to the μ-alkoxo moiety; and **(B)** monodentate coordination of BDNPP- with a OH/H$_2$O ligand occupying the vacant site on the second Ni(II) and poised as the intramolecular terminal nucleophile. Structures generated from DFT calculations.

et al., 2010; Ren et al., 2011; Biswas et al., 2012, 2017; Botana et al., 2014; Mahapatra et al., 2016; Massoud et al., 2016; Sanyal et al.,

**TABLE 3 |** Michaelis Menten kinetic data of dinuclear Ni(II) complexes that mimic metallophosphatases.

Ligand[a]	Complex	Substrate	Solvent	k_{cat} (s^{-1})	K_m (mM L^{-1})	References
2-[(4,7-diisopropyl-1,4,7-triazonan-1-yl)methyl]-4-methyl-6-[(pyridine-2-ylmethylamino)methyl]phenol (HL) (**1**)	[Ni$_2$(L)(μ-OAc)$_2$(OH$_2$)](BPh$_4$).H$_2$O	BDNPP	Acetonitrile/ aqueous buffer	0.013 (pH 9)	3.44	Xavier and Neves, 2016
2,6-bis[bis(2-pyridylmethyl)aminomethyl]-4-chlorophenol (HL^{ClO}) (**2**)	[Ni$_2$(L^{ClO})(μ-OAc)$_2$](PF$_6$).3H$_2$O	BDNPP	Acetonitrile/ aqueous buffer	2.80 × 10^{-3} (pH 7) 0.065 (pH 10.5)	0.21 (pH 7) 2.18 (pH 10.5)	Massoud et al., 2016
2-[(N-benzyl-N-2-pyridylmethylamine)]-4-methyl-6-[N-(2-pyridylmethyl)aminomethyl)])-4-methyl-6-formylphenol) (H$_2$BPPAMFF) (**3**)	[Ni$_2$(HBPPAMFF)(μ-OAc)$_2$(H$_2$O)](BPh$_4$)	BDNPP	Acetonitrile/ aqueous buffer	0.054 (pH 9)	1.57	Piovezan et al., 2012
2-[N-(2-(pyridyl-2-yl)ethyl)(1-methylimidazol-2-yl)aminomethyl]-4-methyl-6-[N-(2-(imidazol-4-yl)ethyl)aminomethyl]phenol (HL2) (**4**)	[Ni$_2$(L2)(μ-OAc)$_2$(CH$_3$CN)](BPh$_4$)	BDNPP	Acetonitrile/ aqueous buffer	0.034 (pH 9)	1.19	Greatti et al., 2008
2-[N-bis-(2-pyridylmethyl)aminomethyl]-4-methyl-6-[N-(2-pyridylmethyl)aminomethyl] phenol (HL$_A$1) (**5**)	[Ni$_2$(L$_A$1)(μ-OAc)$_2$(H$_2$O)]ClO$_4$.H$_2$O	BDNPP	Acetonitrile/ aqueous buffer	0.386 (pH 9)	5.67	Greatti et al., 2004, 2008
1,3-bis(bis(pyridin-2-ylmethyl)amino)propan-2-ol (HL^1) (**6**)	[Ni$_2$L^1(μ-OAc)(H$_2$O)$_2$](ClO$_4$)$_2$·H$_2$O	BDNPP	Acetonitrile/ aqueous buffer	∼0.025 (pH 11)	10	This work
N-4-methyl-homopiperazine-N'-[N-(2-pyridylmethyl)-N-2-(2-pyridylethylamine)-1,3-diaminopropan-2-ol (HL) (**7**)	[Ni$_2$(L)(OH)]$^{2+}$	BNPP	Aqueous buffer	7.4 × 10^{-5} (pH 8.4)	6.95	Wu and Wang, 2014
2-[[(2-piperidylmethyl)amino]methyl]-4-bromo-6-[(1-methylhomopiperazine-4-yl)methyl]phenol (HL) (**8**)	[Ni$_2$(L)(OH)]$^{2+}$	BNPP	Ethanol/ aqueous buffer	1.49 × 10^{-4} (pH 8.3)	7.25	Ren et al., 2011
N,N,N',N'-tetrakis[(6-methyl-2-pyridyl)methyl]-1,3-diaminopropan-2-ol (Me$_4$tpdpH) (**9**)	[Ni$_2$(Me$_4$tpdp)(μ-OAc)$_2$(H$_2$O)] (ClO$_4$)	BNP	Acetonitrile/ aqueous buffer	k_{BNP} = 3.4 × 10^{-2} M^{-1} s^{-1}		Yamaguchi et al., 2001

[a]The numbers refer to the ligands shown in **Scheme 1**.

2016; Xavier and Neves, 2016). As the number of studies, and hence the number of examples of diNi(II) complexes with various bridging ligand types, has increased the relationship between J and a structural parameter (Ni-O-Ni angle; Ni-X distance) has been described in terms of both linear, albeit with considerable scatter (Mahapatra et al., 2016), and polynomial functions (Bu et al., 2001). Clearly, the relationship is dependent on a set of parameters and even on the type of bridging ligands (Krupskaya et al., 2010; Botana et al., 2014). The sign and magnitude of J (-27.4 cm^{-1}) for [Ni$_2$(L1)(μ-OAc)(H$_2$O)$_2$](ClO$_4$)$_2$·H$_2$O are consistent with the Ni^{II}-μO-Ni^{II} angle of 131.6(2)° (**Table S1** and **Figure S1**) (Nanda et al., 1994c; Mochizuki et al., 2004; Biswas et al., 2012, 2017; Massoud et al., 2016).

The relationship between the structural parameters and the magnitude of the observed magnetic coupling for dicobalt(II) complexes has been reviewed (Arora et al., 2012, p. 703; Tomkowicz et al., 2012; Daumann et al., 2013a). It was concluded that for complexes with a μ-O$_{bridge}$/bis(μ$_2$-RCOO-κ^{2}O:O') core, the variations in magnitude of J could be related to the type of μ-O$_{bridge}$, the Co-O$_{bridge}$-Co angle and the type of R-group (Tomkowicz et al., 2012). Further, it was proposed

that the strength of the coupling varied according to bridge type (μ-O^{2-} >μ-OH$^-$ >μ-H$_2$O) (Schultz et al., 1997), and that Co(II)-O-Co(II) bond angles around 96° in some examples resulted in ferromagnetic coupling via orthogonal magnetic orbitals (Tudor et al., 2008; Fabelo et al., 2009; Tomkowicz et al., 2012), and it was also suggested that bis(μ$_2$-syn,syn-CH$_3$COO-κ^{2}O:O') bond angles were important (Arora et al., 2012). Extremely weak antiferro- or ferro-magnetic coupling was proposed for diCo(II) complexes with the μ-O$_{(phenoxido)}$;bis(μ$_2$-OAc-κ^{2}O:O') bridge, although exceptions occurred (Arora et al., 2012; Daumann et al., 2013a). Complexes with the μ-H$_2$O;bis(μ$_2$-RCOO-κ^{2}O:O') core appear to promote weak antiferromagnetic coupling, although stronger than that seen with the μ-O$_{(phenoxido)}$ analog; the bis(μ$_2$-RCOO-κ^{2}O:O');μ$_2$-O;κ^{2}O,O'-CH$_3$COO core appeared to promote ferromagnetic coupling (Daumann et al., 2013a). The relationship between Co(II)-X bond distances and the magnitude and sign of J was extremely weak, and both the Co(II)·Co(II) distance and extent of distortion around the Co(II) center seemingly having little bearing on the coupling (Daumann et al., 2013a). Of the structural parameters considered in this analysis, the

SCHEME 1 | The ligands listed in **Table 3**.
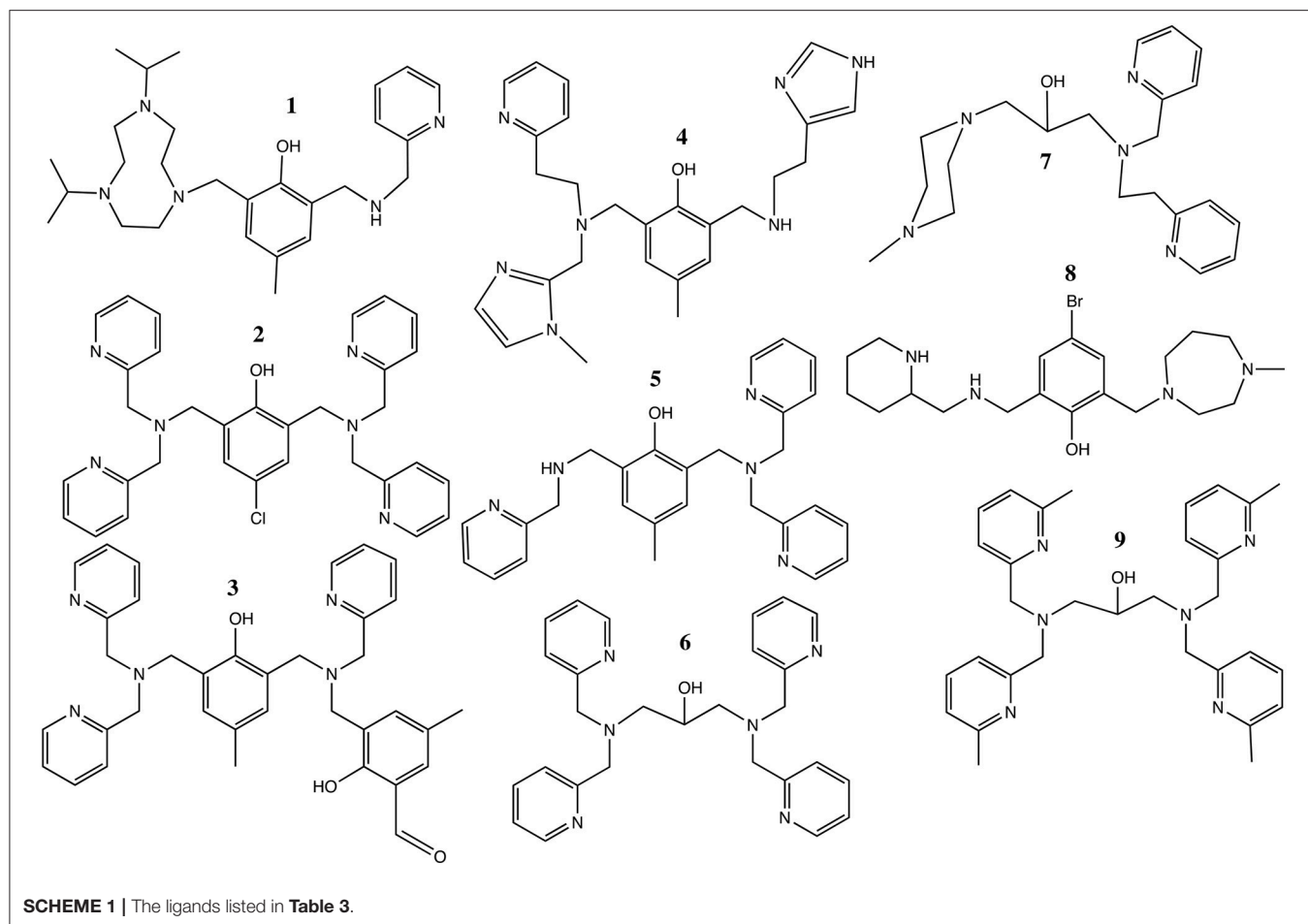
Co(II)-X-Co(II) bridge angles appear to have some influence on the sign and magnitude of J (Daumann et al., 2013a), in agreement with earlier studies, but none of the structural relationships appears to be particularly strong (**Table S2** and **Figure S2**; Johansson et al., 2008; Tudor et al., 2008; Fabelo et al., 2009; Tomkowicz et al., 2012).

Phosphoesterase Activity

The pH dependence of BDNPP hydrolysis by $[Ni_2(L1)(\mu\text{-}OAc)(H_2O)_2](ClO_4)_2 \cdot H_2O$ was analyzed between pH 4.75 and pH 11.0; the rate enhances sharply at pH values ≥ 9.0, reaching a maximum at pH ≥ 11.0. Data were fit as described in the Experimental section and resulted in an estimate of the pK_a value (9.7 ± 0.1) of the catalytically relevant protonation equilibrium (**Figure 6A**). Since the measurements of the catalytic rates as a function of [S] did not reach full saturation obtained catalytic parameters need to be viewed with some caution. A combination of non-linear and linear regression analyses indicate that plausible values for V_{max} and K_m are around 6–7×10^{-5} M.min^{-1} and 10 mM, respectively (**Figure 6B**). For the following comparison of the catalytic efficiencies of a number of Ni-dependent biomimetics we will use the rate of hydrolysis of 6 mM [S] by 40 μM $[Ni_2(L1)(OAc)(H_2O)_2](ClO_4)_2 \cdot H_2O$, i.e., 2.50×10^{-5} M.min^{-1}. This rate corresponds to a k_{cat} of ~ 0.01 s^{-1}.

Several previous studies focused on the phosphatase-like activity of di-Ni(II) complexes (**Table 3** and **Scheme 1**; Yamaguchi et al., 1997, 2001; Yamane et al., 1997, 2001; Parimala and Kandaswamy, 2003; Jikido et al., 2005; Greatti et al., 2008; Ren et al., 2011; Piovezan et al., 2012; Wu and Wang, 2014; Massoud et al., 2016; Xavier and Neves, 2016). In a number of cases the experimental conditions in terms of solvent (acetonitrile/aqueous buffer) and substrate (BDNPP) were similar to those employed in the present work, although the pH at which the k_{cat} and K_m values were determined did vary, making direct comparisons difficult (Greatti et al., 2004, 2008; Piovezan et al., 2012; Massoud et al., 2016; Xavier and Neves, 2016). The nucleophilic agent in these reactions has been proposed as either a terminal (Yamaguchi et al., 2001; Vichard and Kaden, 2002; Parimala and Kandaswamy, 2003; Jikido et al., 2005; Greatti et al., 2008; Massoud et al., 2016; Sanyal et al., 2016) or a bridging (Ren et al., 2011; Piovezan et al., 2012; Wu and Wang, 2014) hydroxido moiety.

Of the examples listed in **Table 3**, the complex with the ligand 2-[N-bis-(2-pyridylmethyl)aminomethyl]-4-methyl-6-[N-(2-pyridylmethyl)aminomethyl]phenol, $[Ni_2(L_A1)(\mu\text{-}OAc)_2(H_2O)]ClO_4 \cdot H_2O$, was the most effective and efficient catalyst for the hydrolysis of BDNPP with $k_{cat} = 0.386$ s^{-1} at pH 9 (Greatti et al., 2008). The rate enhancement was rationalized
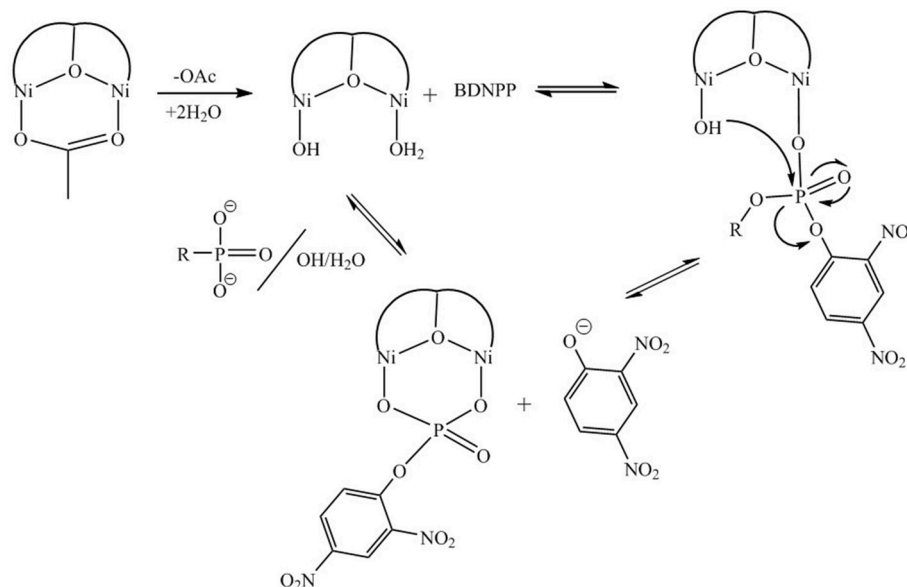
FIGURE 8 | Proposed mechanism of reaction between [Ni$_2$(L1)(μ-OAc)(H$_2$O)$_2$]$^{2+}$ and BDNPP$^-$ adapted from (Vichard and Kaden, 2004). The proposed mechanism resembles that of the lower pH mechanism proposed by Massoud et al. (2016).

in terms of the fact that in solution at pH 9.00, the active species [Ni$_2$(L$_A$1)(H$_2$O)$_2$(μ-OH)]$^{2+}$ made up approximately 85% of the complexes present in solution (Greatti et al., 2008). The proposed mechanism for the reaction involved initial loss of the bridging acetate ligands and coordination of BDNPP after replacement of one aqua ligand (Greatti et al., 2008). The substrate is thus proposed to coordinate in a monodentate manner and orient *cis* to a terminal Ni-OH moiety, the latter promoting a nucleophilic attack on the phosphorus atom with release of the nitrophenolate anion and formation of a bridging DNP molecule. A subsequent intramolecular nucleophilic attack by a μ-OH moiety on the μ-DNP was proposed to result in loss of a second nitrophenolate anion and formation of coordinated phosphate anion which was subsequently replaced by H$_2$O/OH$^-$ to complete the cycle (Greatti et al., 2008). In the case of the complex [Ni$_2$(Me$_4$tpdp)(μ-OAc)$_2$(H$_2$O)](ClO$_4$), a mechanism was proposed whereby the substrate, bis(4-nitrophenyl)phosphate (BNP) was coordinated in a μ-1,3 manner to the diNi(II) complex, after loss of the acetate ligands, with subsequent nucleophilic attack by a terminal Ni-OH moiety at the phosphorus center (Yamaguchi et al., 2001). In that case the reaction is facilitated by the fact that the relevant hydroxido ligand is arranged *cis*, and thus adjacent, to the substrate (Yamaguchi et al., 2001). A variation of the above mechanisms was proposed for [Ni$_2$(L^{Cl}O)(μ-OAc)$_2$](PF$_6$).3H$_2$O by Massoud et al.; in the initial phase of the catalytic cycle one of two metal-bridging acetate groups is displaced and the substrate BDNPP binds to one of the Ni(II). Subsequently, dependent on pH, the attack of a terminal hydroxide that either resides on the same (high pH) or the opposite (low pH) metal as the substrate attacks the phosphorus moiety, leading to the DNPP product being coordinated either bidentately to one metal or to both metals, respectively (Massoud et al., 2016).

For [Ni$_2$(L1)(μ-OAc)(H$_2$O)$_2$](ClO$_4$)$_2$.H$_2$O both Ni(II) sites are six-coordinate. Loss of the μ-acetato ligand is thus a prerequisite for catalytic activity as it generates vacant positions for the substrate to bind (**Figure 7A**). However, according to the crystal structure (**Figure 2**) none of the available aqua/hydroxido ligands are positioned suitably to act as nucleophiles for the reaction. We thus propose that the release of the μ-acetato group enables the monodentate coordination of the substrate to one of the Ni(II) ions and a water molecule (with a pK_a of ~9.7) to the other metal ion (**Figure 7B**). The subsequent attack by the deprotonated water ligand on the phosphorus moiety of the substrate triggers catalysis (**Figure 8**). Insofar, the model resembles that of the lower pH mechanism proposed by Massoud et al. (2016). In the latter complex the presence of two metal-bridging acetate groups provides the basis for an enhanced mechanistic flexibility (i.e., low and high pH pathways), where the nucleophile can be either bound to the same or the opposite metal ion as the substrate.

The phosphatase-like activity of the analogous [Co$_2$L1(μ-OAc)](ClO$_4$)$_2$·0.5.H$_2$O could not be investigated under corresponding experimental conditions since the initially red colored solution turned yellow after the addition of the aqueous buffer solution. The absorbance of the mixture at 400 nm increased upon standing, making any attempt to measure the formation of the dinitrophenolate anion difficult. The change of color of the solution may be explained by the oxidation of cobalt(II) ions (Suzuki et al., 1990).

CONCLUSIONS

The dinickel(II) and dicobalt(II) complexes of 1,3-bis(bis(pyridin-2-ylmethyl)amino)propan-2-ol have been

prepared and some of their properties were compared. Magnetic susceptibility studies confirmed that the two metal ions in both complexes are antiferromagnetically coupled and computational studies verified the experimental magnetic coupling constants. Attempted correlation of the relationship between structural parameters, particularly the M-O-M angles, with the strength of the magnetic coupling were only partially successful. Kinetic analysis with the activated substrate BDNPP suggested that for the diNi(II) complex a terminal water is the nucleophile with a kinetically relevant pK_a of 9.7 ± 0.1 and a k_{cat} value as high as 0.025 s^{-1} (**Table 3**). The complex is thus at the higher end of the range for catalytic efficiency for similar diNi(II) complexes with this substrate (the corresponding diCo(II) complex was found to oxidize readily in the buffer solution). Thus, although no suitable nucleophile (OH$^-$) is present in the original molecule the replacement of the two acetate bridges by water and/or substrate molecules (**Figure 8**) may not be rate-limiting. The complex is proposed to employ a similar mechanism as proposed for a series of analogous model systems for enzymes such as PAPs (Smith et al., 2009; Comba et al., 2012a,b; Bernhardt et al., 2015; Roberts et al., 2015; Bosch et al., 2016). The majority of complexes listed in **Table 3** attain optimal catalytic efficiency under alkaline conditions (>pH 9.0), somewhat higher than the pH optimum of the di-Ni(II) enzyme urease (pH 7.4). This difference may be due to the fact that the majority of model systems use a terminally bound nucleophile to initiate the hydrolytic reaction, whereas urease employs a metal ion-bridging hydroxide (Zambelli et al., 2011). Nonetheless, it is apparent that the complexes listed in **Table 3** represent suitable functional models for biological catalysts such as ureases and PAPs.

AUTHOR CONTRIBUTIONS

AH designed the project and supervised the synthetic chemistry and hydrolytic experiments, contributed to the writing of the manuscript. DE undertook the syntheses of the ligand and the metal complex and undertook the spectroscopic characterization. AR undertook the magnetochemical study and analyzed the results. PC in association with AR supervised the magnetochemical study and data analysis. GS contributed to the design of the project, supplied the funding for the work, and contributed to the writing of the manuscript. EK contributed to the writing of the DFT section of the manuscript and assisted with DFT calculations. LG undertook the X-ray structure analysis, contributed to the analysis of the kinetic data, undertook the DFT studies, and contributed to the writing of the manuscript.

ACKNOWLEDGMENTS

SUPPLEMENTARY MATERIAL

The Supplementary Material for this article can be found online at: https://www.frontiersin.org/articles/10.3389/fchem. 2018.00441/full#supplementary-material

REFERENCES

Adams, H., Bradshaw, D., and Fenton, D., E. (2001). Dinuclear nickel(II) and zinc(II) complexes of 2,6-[N,N'-bis(2-hydroxyphenylmethyl)-N,N'-bis(2-pyridylmethyl)aminomethyl]-4-methyl-phenol. *Supramol. Chem*. 13, 513–519. doi: 10.1080/10610270108028297

Addison, A. W., Rao, T. N., Reedijk, J., Van Rijn, J., and Verschoor, G. C. (1984). Synthesis, structure, and spectroscopic properties of copper(II) compounds containing nitrogen-sulfur donor ligands: the crystal and molecular structure of aqua[1,7-bis(N-methylbenzimidazol-2'-yl)-2,6-dithiaheptane]copper(II) perchlorate. *J. Chem. Soc. Dalton Trans*. 1349–1356. doi: 10.1039/DT9840001349

Alam, R., Pal, K., Shaw, B. K., Dolai, M., Pal, N., and Ali, M. (2016). Synthesis, structure, catalytic and magnetic properties of a pyrazole based five coordinated di-nuclear cobalt(II) complex. *Polyhedron* 106, 84–91. doi: 10.1016/j.poly.2015.12.062

Allen, K. G., Stewart, J. A., Johnson, P. E., and Wettlaufer, D. G. (1978). Identification of the ionic groups of papain by pH/rate profile analysis. *Eur. J. Biochem*. 87, 575–582. doi: 10.1111/j.1432-1033.1978.tb12409.x

Arora, H., Barman, S. K., Lloret, F., and Mukherjee, R. (2012). Isostructural dinuclear phenoxo/acetato bridged mangnaese(II), cobalt(II) and zinc(II) complexes with labile sites: kinetics of transesterification of 2-hydroxypropyl-p-nitrophenylphosphate. *Inorg. Chem*. 51, 5539–5553. doi: 10.1021/ic201971t

Ashwini, K. (2006). Importance of elements in daily life. *J. Teach. Res. Chem*. 13, 86–89.

Bai, S.-Q., Gao, E.-Q., He, Z., Fang, C.-J., and Yan, C.-H. (2005). Crystal structures and magnetic behavior of three new azido-bridged dinuclear cobalt(II) and copper(II) complexes. *New J. Chem*. 29, 935–941. doi: 10.1039/b418239a

Bain, G. A., and Berry, J. F. (2008). Diamagnetic corrections and Pascal's constants. *J. Chem. Educ*. 85, 532–536. doi: 10.1021/ed085p532

Barondeau, D. P., Kassmann, C. J., Bruns, C. K., Tainer, J. A., and Getzoff, E. D. (2004). Nickel superoxide dismutase structure and mechanism. *Biochemistry* 43, 8038–8047. doi: 10.1021/bi0496081

Becke, A. D. (1993). Density-functional thermochemistry. III. the role of exact exchange. *J. Chem. Phys*. 98, 5648–5652. doi: 10.1063/1.464913

Bernhardt, P. V., Bosch, S., Comba, P., Gahan, L. R., Hanson, G. R., Wadepohl, H., et al. (2015). An approach to more accurate model systems for purple acid phosphatases (PAPs). *Inorg. Chem*. 54, 7249–7263. doi: 10.1021/acs.inorgchem.5b00628

Bernhardt, P. V., Schenk, G., and Wilson, G. J. (2004). Direct electrochemistry of porcine purple acid phosphatase (Uteroferrin). *Biochemistry* 43: 10387–10392. doi: 10.1021/bi0490338

Biswas, A., Das, L. K., Drew, M. G., Aromí, G., Gamez, P., and Ghosh, A. (2012). Synthesis, crystal structures, magnetic properties and catecholase activity of

double phenoxido-bridged penta-coordinated dinuclear nickel(II) complexes derived from reduced schiff-base ligands: mechanistic inference of catecholase activity. *Inorg. Chem.* 51, 7993–8001. doi: 10.1021/ic202748m

Biswas, A., Drew, M. G. B., Gomez-Garcia, C. J., and Ghosh, A. (2017). Formation of a dinuclear and a trinuclear Ni(II) complex on slight variation of experimental conditions: Structural analysis and magnetic properties. *Polyhedron* 121, 80–87. doi: 10.1016/j.poly.2016.09.050

Blakeley, R. L., Treston, A., Andrews, R. K., and Zerner, B. (1982). Nickel(II)-promoted ethanolysis and hydrolysis of N-(2-pyridylmethyl)urea. a model for urease. *J. Am. Chem. Soc.* 104, 612–614. doi: 10.1021/ja00366a040

Blakeley, R. L., and Zerner, B. (1984). Jack bean urease: the first nickel enzyme. *J. Mol. Catal.* 23, 263–292. doi: 10.1016/0304-5102(84)80014-0

Bosch, S., Comba, P., Gahan, L. R., and Schenk, G. (2016). *Asymmetric mono- and dinuclear GaIII and ZnII complexes as models for purple acid phosphatases. J. Inorg. Biochem.* 162, 343–355. doi: 10.1016/j.jinorgbio.2015.12.028

Botana, L., Ruiz, J., Mota, A. J., Rodriguez-Dieguez, A., Seco, J. M., Colacio, E., et al. (2014). Anion controlled structural and magnetic diversity in unusual mixed-bridged polynuclear NiII complexes with a versatile bis(2-methoxy phenol)diamine hexadentate ligand. an experimental and theoretical magneto-structural study. *Dalton Trans.* 43, 13509–13524. doi: 10.1039/C4DT01253D

Bu, X.-H., Du, M., Zhang, L., Liao, D.-Z., Tang, J.-K., Shionoya, R.-M., et al. (2001). Novel nickel(II) complexes with diazamesocyclic ligands functionalized by additional phenol donor pendant(s): synthesis, characterization, crystal structures and magnetic properties. *J. Chem. Soc. Dalton Trans.* 593–598. doi: 10.1039/b008297j

Chattopadhyay, T., Mukherjee, M., Mondal, A., Maiti, P., Banerjee, A., Banu, K., et al. (2010). A unique nickel system having versatile catalytic activity of biological significance. *Inorg. Chem.* 49, 3121–3129. doi: 10.1021/ic901546t

Chilton, N. F., Anderson, R. P., Turner, L. D., Soncini, A., and Murray, K. S. (2013). PHI: a powerful new program for the analysis of anisotropic monomeric and exchange-coupled polynuclear d- and f-block complexes. *J. Comput. Chem.* 34, 1164–1175. doi: 10.1002/jcc.23234

Comba, P., Gahan, L. R., Hanson, G. R., Mereacre, V., Noble, C. J., Powell, A. K., et al. (2012a). Monoesterase activity of a purple acid phosphatase mimic with a cyclam platform. *Chem. Eur. J.* 18, 1700–1710. doi: 10.1002/chem.201100229

Comba, P., Gahan, L. R., Mereacre, V., Hanson, G. R., Powell, A. K., Schenk, G., et al. (2012b). Spectroscopic characterization of the active FeIIIFeIII and FeIIIFeII forms of a purple acid phosphatase model system. *Inorg. Chem.* 51, 12195–12209. doi: 10.1021/ic301347t

Comba, P., Hausberg, S., and Martin, B. (2009). Calculation of exchange coupling constants of transition metal complexes with DFT. *J. Phys. Chem. A* 113, 6751–6755. doi: 10.1021/jp900752p

Daumann, L. J., Comba, P., Larrabee, J. A., Schenk, G., Stranger, R., Gahan, L. R. et al. (2013a). Synthesis, magnetic properties, and phosphoesterase activity of dinuclear cobalt(II) complexes. *Inorg. Chem.* 52, 2029–2043. doi: 10.1021/ic302418x

Daumann, L. J., Larrabee, J. A., Comba, P., Schenk, G., and Gahan, L. R. (2013b). Dinuclear cobalt(II) complexes as metallo-β-lactamase mimics. *Eur. J. Inorg. Chem.* 3082–3089. doi: 10.1002/ejic.201300280

Deacon, G. B., and Phillips, R. J. (1980). Relationships between the carbon-oxygen stretching frequencies of carboxylato complexes and the type of carboxylate coordination. *Coord. Chem. Rev.* 33, 227–250. doi: 10.1016/S0010-8545(00)80455-5

Dixon, N. E., Gazzola, C., Asher, C. J., Lee, D. S., Blakeley, R. L., and Zerner, B. (1980). Jack been urease (EC 3.5.1.5). II. the relationship between nickel, enzymatic activity, and the "abnormal" ultraviolet spectrum. the nickel content of jack beans. *Can. J. Biochem.* 58, 474–480. doi: 10.1139/o80-063

Ensign, S. A., Bonam, D., and Ludden, P. W. (1989). Nickel is required for the transfer of electrons from carbon monoxide to the iron-sulfur center(s) of carbon monoxide dehydrogenase from Rhodospirillum rubrum. *Biochemistry* 28, 4968–4973. doi: 10.1021/bi00438a010

Ensign, S. A., Campbell, M. J., and Ludden, P. W. (1990). Activation of the nickel-deficient carbon monoxide dehydrogenase from *Rhodospirillum rubrum*: kinetic characterization and reductant requirement. *Biochemistry* 29, 2162–2168. doi: 10.1021/bi00460a029

Fabelo, O., Cañadillas-Delgado, L., Pasán, J., Delgado, F. S., Lloret, F., Ruiz-Perez, C., et al. (2009). Study of the influence of the bridge on the magnetic coupling in cobalt(II) complexes. *Inorg. Chem.* 48, 11342–11351. doi: 10.1021/ic901843r

Farrugia, L. J. (1999). WinGX suite for small-molecule single-crystal crystallography. *J. Appl. Crystallogr.* 32, 837–838. doi: 10.1107/S0021889899006020

Flanagan, J. U., Cassady, A. I., Schenk, G., Guddat, L. W., and Hume, D. A. (2006). Identification and molecular modelling of a novel, plant-like, human purple acid phosphatase. *Gene* 377, 12–20. doi: 10.1016/j.gene.2006.02.031

Frisch, M. J., Trucks, G. W., Schlegel, H. B., Scuseria, G. E., Robb, M. A., Fox, D. J., et al. (2013). *Gaussian 09, Revision D.01.* Wallingford CT: Gaussian, Inc.

Gencic, S., and Grahame, D. A. (2003). Nickel in subunit beta of the acetyl-CoA decarbonylase/synthase multienzyme complex in methanogens. catalytic properties and evidence for a binuclear Ni-Ni site. *J. Biol. Chem.* 278, 6101–6110. doi: 10.1074/jbc.M210484200

Greatti, A., Scarpellini, M., Peralta, R. A., Casellato, A., Bortoluzzi, A. J., Xavier, F. R., et al. (2008). Synthesis, structure, and physicochemical properties of dinuclear NiII complexes as highly efficient functional models of phosphohydrolases. *Inorg. Chem.* 47, 1107–1119. doi: 10.1021/ic702132t

Greatti, A. M., Aires de Brito, Bortoluzzi, A. J., and Ceccato, A. S. (2004). Synthesis, characterization and structure of a new dinickel(II) complex as model for urease. *J. Mol. Struct.* 688, 185–190. doi: 10.1016/j.molstruc.2003.10.008

Halcrow, M. A., and Christou, G. (1994). Biomimetic chemistry of nickel. *Chem. Rev.* 94, 2421–2481. doi: 10.1021/cr00032a008

Hempel, J. C., and Miller, M. E. (1981). Ground state properties of trigonal prismatic and trigonal bipyramidal d1,9, d2,8, d3,7, and d5 systems: effects of trigonal distortion. *J. Chem. Phys.* 75, 2959–2970. doi: 10.1063/1.442387

Hossain, M. J., and Sakiyama, H. (2002). Two typical cases of magnetism for dinuclear high-spin cobalt(II) complexes in trigonal-bipyramidal fields. *Inorg. Chim. Acta* 338, 255–259. doi: 10.1016/S0020-1693(02)01053-8

Jacoby, M. (1933). The action of metals on enzymes. *Biochem. Z* 259, 211–222.

Jikido, R., Shiraishi, H., Matsufuji, K., Ohba, M., Furutachi, H., Suzuki, M., et al. (2005). Mass spectrometric and spectroscopic studies on hydrolysis of phosphoesters by bis(μ-acetato)-μ-phenolato dinuclear metal(II) complexes (metal = Mn, Co, Ni, and Zn). *Bull. Chem. Soc. Jpn.* 78, 1795–1803. doi: 10.1246/bcsj.78.1795

Johansson, F. B., Bond, A. D., Nielsen, U. G., Moubaraki, B., Murray, K., S., McKenzie, C. J. et al. (2008). Dicobalt II-II, II-III, and III-III complexes as spectroscopic models for dicobalt enzyme active sites. *Inorg. Chem.* 47, 5079–5092. doi: 10.1021/ic7020534

Jung, M., Sharma, A., Hinderberger, D., Braun, S., Schatzschneider, U., and Rentschler, E. (2009). Nitronyl nitroxide radicals linked to exchange-coupled metal dimers - studies using X-ray crystallography, magnetic susceptibility measurements, EPR spectroscopy, and DFT calculations. *Eur. J. Inorg. Chem.* 1495–1502. doi: 10.1002/ejic.200801248

Kaminskaia, N. V., Spingler, B., and Lippard, S., J. (2000). Hydrolysis of β-lactam antibiotics catalyzed by dinuclear zinc(II) complexes: functional mimics of metallo-β-lactamases. *J. Am. Chem. Soc.* 122, 6411–6422. doi: 10.1021/ja993704l

Kantacha, A., Buchholz, R., Smith, S. J., Schenk, G., and Gahan, L. R. (2011). Phosphate ester cleavage promoted by a tetrameric iron(III) complex. *J. Biol. Inorg. Chem.* 16, 25–32. doi: 10.1007/s00775-010-0696-0

Khandar, A. A., Kirschbaum, K., Abedi, M., Mock, K., Tracy, G., Spasojevic, V., et al. (2015). Synthesis, characterization and crystal structures of mono and dinuclear macrocyclic cobalt(II) complexes with a new tetraaza m-xylyl-based macrocyclic ligand. *New J. Chem.* 39, 2822–2831. doi: 10.1039/C4NJ01608D

Krupskaya, Y., Alfonsov, A., Parameswaran, A., Kataev, V., Klingeler, R., Steinfeld, G., et al. (2010). Interplay of magnetic exchange interactions and Ni-S-Ni bond angles in polynuclear nickel(II) complexes. *ChemPhysChem* 11, 1961–1970. doi: 10.1002/cphc.200900935

Li, J.-L., Jiang, L., Wang, B.-W., Tian, J.-L., Gu, W., Yan, P., et al. (2015). Bio-relevant cobalt(II) complexes with compartmental polyquinoline ligand: synthesis, crystal structures and biological activities. *J. Inorg. Biochem.* 145, 19–29. doi: 10.1016/j.jinorgbio.2014.11.003

Mahapatra, P., Ghosh, S., Giri, S., and Ghosh, A. (2016). The unusual intermediate species in the formation of Ni(II) complexes of unsymmetrical Schiff bases by Elder's method: structural, electrochemical and magnetic

characterizations. *Polyhedron* 117, 427–436. doi: 10.1016/j.poly.2016.06.020

Mandal, S., Balamurugan, V., Lloret, F., and Mukherjee, R. (2009). Syntheses, X-ray structures, and physicochemical properties of phenoxo-bridged dinuclear nickel(II) complexes: kinetics of transesterification of 2-hydroxypropyl-p-nitrophenyl phosphate. *Inorg. Chem.* 48, 7544–7556. doi: 10.1021/ic8018937

Massoud, S. S., Broussard, K. T., Mautner, F. A., Vicente, R., Saha, M. K., and Bernal, I. (2008). Five-coordinate cobalt(II) complexes of tris(2-pyridylmethyl)amine (TPA): synthesis, structural and magnetic characterization of a terephthalato-bridged dinuclear cobalt(II) complex. *Inorg. Chim. Acta* 361, 123–131. doi: 10.1016/j.ica.2007.06.021

Massoud, S. S., Ledet, C. C., Junk, T., Bosch, S., Comba, P., Mautner, F. A., et al. (2016). Dinuclear metal(II)-acetato complexes based on bicompartmental 4-chlorophenolate: syntheses, structures, magnetic properties, DNA interactions and phosphodiester hydrolysis. *Dalton Trans.* 45, 12933–12950. doi: 10.1039/C6DT02596J

Mendes, L. L., Englert, D., Fernandes, C., Gahan, L. R., Schenk, G., and Horn, A. (2016). Metallohydrolase biomimetics with catalytic and structural flexibility. *Dalton Trans.* 45, 18510–18521. doi: 10.1039/C6DT03200A

Meyer, F. (2009). Synthetic models for the urease active site. *Prog. Inorg. Chem.* 56, 487–542. doi: 10.1002/9780470440124.ch6

Mitić, N., Hadler, K. S., Gahan, L. R., Hengge, A. C., and Schenk, G. (2010). The divalent metal ion in the active site of uteroferrin modulates substrate binding and catalysis. *J. Am. Chem. Soc.* 132, 7049–7054. doi: 10.1021/ja910583y

Mitić, N., Noble, C. J., Gahan, L. R., Hanson, G. R., and Schenk, G. (2009). Metal ion mutagenesis – conversion of a purple acid phosphatase from sweet potato to a neutral phosphatase with the formation of an unprecedented catalytically competent Mn^{II}Mn^{II} active site. *J. Am. Chem. Soc.* 131, 8173–8179. doi: 10.1021/ja900797u

Mochizuki, K., Hasegawa, A., and Weyhermuller, T. (2004). Synthesis, structures, and magnetic properties of dicopper(II) and dinickel(II) complexes with a new bis(macrocycle), 7,7'-(2-hydroxypropane-1,3-diyl)bis{3,7,11,17-tetraazabicyclo[11.3.1]- heptadeca-1(17),13,15-triene}. *Inorg. Chim. Acta* 357, 3245–3250. doi: 10.1016/j.ica.2004.01.047

Moffat, C. D., Weiss, D. J., Shivalingam, A., White, A. J., Salaün, P., and Vilar, R. (2014). Molecular recognition and scavenging of arsenate from aqueous solution using dimetallic receptors. *Chem. Eur. J.* 20, 17168–17177. doi: 10.1002/chem.201404723

Nanda, K. K., Das, R., Thompson, L., K., Venkatsubramanian, K., Paul, P., and Nag, K. (1994b). Magneto-structural correlations in macrocyclic dinickel(II) complexes: tuning of spin exchange by varying stereochemistry and auxiliary ligands. *Inorg. Chem.* 33, 1188–1193. doi: 10.1021/ic00084a036

Nanda, K. K., Das, R., Thompson, L. K., Venkatsubramanian, K., and Nag, K. (1994a). Combined Effect of phenoxy and carboxylate bridges on magnetic properties of a series of macrocyclic dinickel(II) complexes. *Inorg. Chem.* 33, 5934–5939. doi: 10.1021/ic00103a048

Nanda, K. K., Thompson, L., K., Bridson, J., N., and Nag, K. (1994c). Linear dependence of spin exchange coupling constant on bridge angle in phenoxy-bridged dinickel(II) complexes. *J. Chem. Soc. Chem. Commun.* 1337–1338. doi: 10.1039/c39940001337

Neese, F. (2012). The ORCA program system. wiley Interdiscip. *Rev. Comput. Mol. Sci.* 2, 73–78. doi: 10.1002/wcms.81

Noodleman, L., Case, D. A., and Aizman, A. (1988). Broken symmetry analysis of spin coupling in iron-sulfur clusters. *J. Am. Chem. Soc.* 110, 1001–1005. doi: 10.1021/ja00212a003

Parimala, S., and Kandaswamy, M. (2003). Mononuclear, dinuclear nickel(II) and heterodinuclear Zn(II)Ni(II) complexes as models for the active site of phosphatase. *Inorg. Chem. Commun.* 6, 1252–1254. doi: 10.1016/S1387-7003(03)00243-0

Pawlak, P. L., Malkhasian, A. Y. S., Sjlivic, B., Tiza, M. J., Kucera, B. E., Chavez, F. A., et al. (2008). Synthesis, structure, and magnetic properties of a new binuclear Ni(II) complex supported by 1,4,8-triazacyclounodecane. *Inorg. Chem. Commun.* 11, 1023–1026. doi: 10.1016/j.inoche.2008.05.014

Piovezan, C., Silva, J. M. R., Neves, A., Bortoluzzi, A. J., Haase, W., Rossi, L. M., et al. (2012). Design of a dinuclear nickel(II) bioinspired hydrolase to bind covalently to silica surfaces: synthesis, magnetism, and reactivity studies. *Inorg. Chem.* 51, 6104–6115. doi: 10.1021/ic300018t

Prushan, M. J., Tomezsko, D. M., Lofland, S., Zeller, M., and Hunter, A. D. (2007). A nickel(II) di-μ2-phenolato bridged dinuclear complex: weak antiferromagnetic interactions in nickel(II) dimers. *Inorg. Chim. Acta* 360, 2245–2254. doi: 10.1016/j.ica.2006.11.008

Przybyla, A. E., Robbins, J., Menon, N., and Peck, H. D. Jr (1992). Structure-function relationships among the nickel-containing hydrogenases. *FEMS Microbiol. Rev.* 8, 109–135. doi: 10.1111/j.1574-6968.1992.tb04960.x

Ren, Y.-W., Lu, J.-X., Cai, B.-W., Shi, D.-B., Jiang, H.-F., Chen, J., et al. (2011). A novel asymmetric di-Ni(II) system as a highly efficient functional model for phosphodiesterase: synthesis, structures, physicochemical properties and catalytic kinetics. *Dalton Trans.* 40, 1372–1381. doi: 10.1039/C0DT01194K

Roberts, A. E., Schenk, G., and Gahan, L. R. (2015). A heterodinuclear Fe^{III}Zn^{II} complex as a mimic for purple acid phosphatase with site-specific Zn^{II} binding. *Eur. J. Inorg. Chem.* 2015, 3076–3086. doi: 10.1002/ejic.201500351

Sanyal, R., Zhang, X., Chakraborty, P., Giri, S., Chattopadhyay, S. K., Das, D. et al. (2016). Role of solvent in the phosphatase activity of a dinuclear nickel(II) complex of a Schiff base ligand: mechanistic interpretation by DFT studies. *New J. Chem.* 40, 7388–7398. doi: 10.1039/C6NJ01043A

Sargent, F. (2016). The Model [NiFe]-hydrogenases of *escherichia coli. Adv. Microb. Physiol.* 68, 433–507. doi: 10.1016/bs.ampbs.2016.02.008

Sato, M., Mori, Y., and Iida, T. (1992). Convenient synthesis of N,N,N',N'-tetrakis(2-pyridylmethyl)-α,ω-alkanediamines using a phase-transfer catalyst. *Synthesis* 539–540. doi: 10.1055/s-1992-26157

Schaefer, A., Horn, H., and Ahlrichs, R. (1992). Fully optimized contracted Gaussian basis sets for atoms lithium to krypton. *J. Chem. Phys.* 97, 2571–2577. doi: 10.1063/1.463096

Schenk, G., Mitić, N., Hanson, G. R., and Comba, P. (2013). Purple acid phosphatase: a journey into the function and mechanism of a colourful enzyme. *Coord. Chem. Rev.* 257, 473–482. doi: 10.1016/j.ccr.2012.03.020

Schenk, G., Peralta, R. A., Batista, S. C., Bortoluzzi, A. J., Szpoganicz, B., Neves, A., et al. (2008). Probing the role of the divalent metal ion in uteroferrin using metal ion replacement and a comparison to isostructural biomimetics. *J. Biol. Inorg. Chem.* 13, 139–155. doi: 10.1007/s00775-007-0305-z

Schultz, B. E., Ye, B.-H., Li, X.-Y., and Chan, S. I. (1997). Electronic paramagnetic resonance and magnetic properties of model complexes for binuclear active sites in hydrolase enzymes. *Inorg. Chem.* 36, 2617–2622. doi: 10.1021/ic960988r

Selleck, C., Clayton, D., Gahan, L. R., Mitić, N., McGeary, R. P., Schenk, G., et al. (2017). Visualization of the reaction trajectory and transition state in a hydrolytic reaction catalyzed by a metalloenzyme. *Chem. Eur. J.* 23, 4778–4781. doi: 10.1002/chem.201700866

Shaw, W. H. R. (1954). Inhibition of urease by various metal ions. *J. Am. Chem. Soc.* 76, 2160–2163. doi: 10.1021/ja01637a034

Shaw, W. H. R., and Raval, D. N. (1961). The inhibition of urease by metal ions at pH 8.9. *J. Am. Chem. Soc.* 83, 3184–3187. doi: 10.1021/ja01476a004

Sheldrick, G. M. (1997). *SHELXL97: Program for the Refinement of Crystal Structures*. Germany, University of Gottingen.

Shin, W., and Lindahl, P. A. (1992). Discovery of a labile nickel ion required for CO/acetyl-CoA exchange activity in the NiFe complex of carbon monoxide dehydrogenase from Clostridium thermoaceticum. *J. Am. Chem. Soc.* 114, 9718–9719. doi: 10.1021/ja00050a094

Sibille, J. C., Doi, K., and Aisen, P. (1987). Hydroxyl radical formation and iron-binding proteins. stimulation by the purple acid phosphatases. *J. Biol. Chem.* 262, 59–62.

Siluvai, G. S., and Murthy, N. N. (2009). X-ray structure and spectroscopic characterization of divalent dinuclear cobalt complexes containing carboxylate- and phosphodiester- auxiliary bridges. *Inorg. Chim. Acta* 362, 3119–3126. doi: 10.1016/j.ica.2009.02.010

Smith, S. J., Casellato, A., Hadler, K. S., Mitić, N., Riley, M. J., Gahan, L. R., et al. (2007). The reaction mechanism of the Ga(III)Zn(II) derivative of uteroferrin and corresponding biomimetics. *J. Biol. Inorg. Chem.* 12, 1207–1220. doi: 10.1007/s00775-007-0286-y

Smith, S. J., Riley, M. J., Noble, C. J., Hanson, G. R., Stranger, R., Gahan, L. R., et al. (2009). Structural and catalytic characterization of a heterovalent Mn(II)Mn(III) complex that mimics purple acid phosphatases. *Inorg. Chem.* 48, 10036–10048. doi: 10.1021/ic9005086

Spears, J. W., Smith, C. J., and Hatfield, E. E. (1977). Rumen bacterial urease requirement for nickel. *J. Dairy Sci.* 60, 1073–1076. doi: 10.3168/jds.S0022-0302(77)83990-8

Suzuki, M., Sugisawa, T., Senda, H., Oshio, H., and Uehara, A. (1989). Synthesis and characterization of a novel tetranuclear manganese(II,III,III,II) mixed valence complex. *Chem. Lett.* 1091–1094. doi: 10.1246/cl.1989.1091

Suzuki, M., Sugisawa, T., and Uehara, A. (1990). Dinuclear cobalt(II) complexes containing 1,3-(or 1,5-)bis[bis-(2-pyridylmethyl)amino]-2-propanolato (or−3-pentanolato): preparation and reaction with molecular oxygen. *Bull. Chem. Soc. Jpn.* 63, 1115–1120. doi: 10.1246/bcsj.63.1115

Tian, J.-L., Feng, L., Gu, W., Xu, G.-J., Yan, S.-P., Cheng, D.-P., et al. (2007). Synthesis, crystal structure, magnetic property and nuclease activity of a new binuclear cobalt(II) complex. *J. Inorg. Biochem.* 101, 196–202. doi: 10.1016/j.jinorgbio.2006.08.009

Tian, J.-L., Gu, W., Yan, S.-P., Liao, D.-Z., and Jiang, Z.-H. (2008). Synthesis, structures and magnetic properties of two binuclear cobalt(II) complexes bridged by bis(p-nitrophenyl) phosphate or diphenylphosphinate ion. *Z. Anorgan. Allgem. Chem.* 634, 1775–1779. doi: 10.1002/zaac.200800130

Tomkowicz, Z., Ostrovsky, S., Foro, S., Calvo-Perez, V., and Haase, W. (2012). Magnetooptical and structural investigations of five dimeric cobalt(II) complexes mimicking metalloenzyme active sites. *Inorg. Chem.* 51, 6046–6055. doi: 10.1021/ic202529p

Tudor, V., Marin, G., Lloret, F., Kravtsov, V. C., Simonov, Y. A., Andruh, M., et al. (2008). New alkoxo-bridged mixed-valence cobalt clusters: synthesis, crystal structures and magnetic properties. *Inorg. Chim. Acta* 361, 3446–3452. doi: 10.1016/j.ica.2008.03.007

Vaissier, V., and Van, V. T. (2017). Quantum chemical approaches to [NiFe] hydrogenase. *Essays Biochem* 61, 293–303. doi: 10.1042/EBC20160079

Vichard, C., and Kaden, T. A. (2002). Phosphate and phosphonate ester hydrolysis promoted by dinuclear metal complexes. *Inorg. Chim. Acta* 337, 173–180. doi: 10.1016/S0020-1693(02)00997-0

Vichard, C., and Kaden, T. A. (2004). Phosphate diester hydrolysis in biological relevant compounds by dinuclear metal complexes. *Inorg. Chim. Acta* 357, 2285–2293. doi: 10.1016/j.ica.2003.12.041

Wages, H. E., Taft, K. L., and Lippard, S. J. (1993). Tris(acetato)bis(N,N,N′,N′-tetramethylethylenediamine)(urea)dinickel(1+) triflate and [Ni(OAc)(urea)2(tmen)](OTf), model complexes for the enzyme urease. *Inorg. Chem.* 32, 4985–4987. doi: 10.1021/ic00075a001

Wu, A.-Z., and Wang, T. (2014). Synthesis, crystal structures and phosphodiesterase activities of alkoxide-bridged asymmetric dinuclear nickel(II) complexes. *Trans. Met. Chem.* 39, 205–211. doi: 10.1007/s11243-013-9791-8

Xavier, F. R., and Neves, A. (2016). Synthesis, physicochemical properties and *in vitro* catalytic activity of a dinuclear nickel(II) complex with a N5O-hexadentate ligand: a functional model for phosphohydrolases. *Polyhedron* 109, 59–66. doi: 10.1016/j.poly.2016.02.013

Yamaguchi, K., Akagi, F., Fujinami, S., Suzuki, M., Shionoya, M., and Suzuki, S. (2001). Hydrolysis of phosphodiester with hydroxo- or carboxylate-bridged dinuclear Ni(II) and Cu(II) complexes. *J. Chem. Soc. Chem. Commun.* 375–376. doi: 10.1039/b008994j

Yamaguchi, K., Koshino, S., Akagi, F., Suzuki, M., Uehara, A., and Suzuki, S. (1997). Structures and catalytic activities of carboxylate-bridged dinickel(II) complexes as models for the metal center of urease. *J. Am. Chem. Soc.* 119, 5752–5753. doi: 10.1021/ja963982+

Yamane, H., Hosokawa, Y., Nakao, Y., Matsumoto, K., Takamizawa, S., Mori, W., et al. (1997). Dinuclear nickel(II) complexes as models for the active site of urease. *J. Inorg. Biochem.* 67:186. doi: 10.1016/S0162-0134(97)80063-3

Yamane, H., Nakao, Y., Kawabe, S., Xie, Y., Kanehisa, N., Kai, Y., et al. (2001). Synthesis, structures and characterization of the dinuclear nickel(II) complexes containing N,N,N′,N′-tetrakis[(1-ethyl-2-benzimidazolyl)methyl]-2-hydroxy-1,3-diaminopropane and their urea complexes relevant to the urease active site. *Bull. Chem. Soc. Jpn.* 74, 2107–2112. doi: 10.1246/bcsj.74.2107

Zambelli, B., Musiani, F., Benini, S., and Ciurli, S. (2011). Chemistry of Ni²⁺ in Urease: Sensing, Trafficking, and Catalysis. *Acc. Chem. Res.* 44, 520–530. doi: 10.1021/ar200041k

Zeng, M.-H., Gao, S., and Chen, X.-M. (2004). A novel 3D coordination polymer containing pentacoordinate cobalt(II) dimers with antiferromagnetic ordering. *Inorg. Chem. Commun.* 7, 864–867. doi: 10.1016/j.inoche.2004.05.008

Effects of the Metal Ion on the Mechanism of Phosphodiester Hydrolysis Catalyzed by Metal-Cyclen Complexes

Qiaoyu Hu, Vindi M. Jayasinghe-Arachchige, Joshua Zuchniarz and Rajeev Prabhakar*

Department of Chemistry, University of Miami, Coral Gables, FL, United States

In this study, mechanisms of phosphodiester hydrolysis catalyzed by six di- and tetravalent metal-cyclen (**M-C**) complexes (**Zn-C, Cu-C, Co-C, Ce-C, Zr-C** and **Ti-C**) have been investigated using DFT calculations. The activities of these complexes were studied using three distinct mechanisms: (1) direct attack (**DA**), (2) catalyst-assisted (**CA**), and (3) water-assisted (**WA**). All divalent metal complexes (**Zn-C, Cu-C** and **Co-C**) coordinated to the BNPP substrate in a monodentate fashion and activated its scissile phosphoester bond. However, all tetravalent metal complexes (**Ce-C, Zr-C,** and **Ti-C**) interacted with BNPP in a bidentate manner and strengthened this bond. The **DA** mechanism was energetically the most feasible for all divalent **M-C** complexes, while the **WA** mechanism was favored by the tetravalent complexes, except **Ce-C**. The divalent complexes were found to be more reactive than their tetravalent counterparts. **Zn-C** catalyzed the hydrolysis with the lowest barrier among all **M-C** complexes, while **Ti-C** was the most reactive tetravalent complex. The activities of **Ce-C** and **Zr-C,** except **Ti-C**, were improved with an increase in the coordination number of the metal ion. The structural and mechanistic information provided in this study will be very helpful in the development of more efficient metal complexes for this critical reaction.

Keywords: phosphodiester hydrolysis, metal-cyclen complexes, di- and tetravalent metal ions, reaction mechanisms, density functional theory (DFT)

INTRODUCTION

The phosphoester bond $[(O=)(RO)(RO)(P-O-R)]$ is ubiquitous in a wide range of biomolecules such as proteins, nucleic acids, and lipids (Oivanen et al., 1998; Cleland and Hengge, 2006; Neidle, 2008; Kamerlin and Warshel, 2009). For instance, this bond constitutes the backbones of DNA and RNA by connecting the adjacent nucleotides (Sharp, 1985; Robinson et al., 1995; Mikkola et al., 2001; Chandra et al., 2009). It is also present in organophosphorus compounds (OPs) that have been utilized as pesticides and chemical nerve agents (Dubois, 1971; Jeyaratnam, 1990; The, 1998). Thus, the selective hydrolysis of this bond is required in numerous biological and biotechnological applications. In biology, this process has been implicated in DNA repair, post-translational modification of proteins and energy metabolism (Eichler and Lehman, 1977; Sancar and Sancar, 1988; Kia-Ki and Martinage, 1992; Mol et al., 2000). In biotechnology, it is involved in gene sequencing, therapeutics, and bioremediation of pesticides and nerve agents (Gewirtz et al., 1998; Eid et al., 2009; Corda et al., 2014). In nature, three types of phosphoester bonds exist:

mono-, di-, and triester (Hadler et al., 2008; Kirby and Nome, 2015). Among them, the phosphodiester bond $[(O=)(O^-)(RO)(P-O-R)]$ is exceptionally stable with a half-life of approximately 3×10^7 years at room temperature and a neutral pH (Williams and Wyman, 2001). To hydrolyze this bond at biologically relevant rates, $\sim 10^{16}$ times rate-acceleration, nature has devised highly specialized metalloenzymes known as nucleases and phosphoesterases (Wilcox, 1996; Cowan, 1998; Weston, 2005; Fang et al., 2007). Although these enzymes exhibit remarkable activities, they suffer from several limitations such as undesirable selectivity, difficulties in extraction or synthesis, high cost and narrow functional temperature, and pH range (Kövári and Krämer, 1996; Cowan, 2001; Mancin et al., 2012). Therefore, in the last couple of decades, intensive efforts have been made to design small metal complexes as synthetic analogs of natural enzymes for phosphoester hydrolysis (Burstyn and Deal, 1993; Hegg and Burstyn, 1998; Komiyama and Sumaoka, 1998; Blaskó and Bruice, 1999; Williams et al., 1999; Sreedhara and Cowan, 2001; Deck et al., 2002; Mitić et al., 2006; Niittymaki and Lonnberg, 2006; Bonomi et al., 2008; Krauser et al., 2010; Mancin et al., 2012; Daver et al., 2016; Sullivan et al., 2018). These analogs can offer multiple advantages over natural enzymes in terms of cost, size, and functionality (Weston, 2005; Yoji et al., 2006). To advance this goal, among others, several chemically distinct polyazamacrocyclic ligands were synthesized through the Stetter-Richman-Atkins method (Richman and Atkins, 1974; Weisman and Reed, 1996). In particular, 1,4,7,10-tetraazacyclododecane (cyclen, **C**) and its derivatives containing mononuclear metal complexes have been utilized for phosphodiester and peptide hydrolysis (**Figure 1A**) (Koike et al., 1994; Shionoya et al., 1994; Hettich and Schneider, 1997; Chae et al., 2005; Fang et al., 2007; Junghun et al., 2007; Subat et al., 2008; Zhang et al., 2014, 2016b). In most studies of phosphodiester hydrolysis, the bis(4-nitrophenyl) phosphate (BNPP) molecule has been used as a model of DNA (**Figure 1A**). Koike and Kimura (1991) investigated BNPP hydrolysis by the Zn(II)-cyclen (**Zn-C**) complex and reported the pseudo-first order rate constant of 2.8×10^{-9} s^{-1} at 35°C and pH 7. This complex provided a 46-fold rate acceleration compared to the background reaction. The Co(III)-cyclen based complexes (cyclen attached to polystyrene or methyl benzoate) also hydrolyzed the phosphodiester bond of DNA and RNA efficiently (Jeung et al., 2001; Delehanty et al., 2005). The polystyrene complex decreased the half-life of supercoiled DNA to 40 min at 4°C, while the one with methyl benzoate promoted the hydrolysis of $\sim$96% of mRNA population within 24 h at 25°C. Furthermore, a Cu(II)-cyclen analog with two pyridine subunits was shown to degrade supercoiled DNA with $k_{cat} = 2.31 \times 10^{-3}$ min^{-1} under physiological conditions (Li et al., 2007).

Additionally, several tri- and tetravalent lanthanides (Eu, La, Zr, and Ce) containing complexes have been reported to hydrolyze the phosphoester bond (Rammo et al., 1996; Baykal et al., 1999; Franklin, 2001; Gómez-Tagle and Yatsimirsky, 2001; Luedtke and Schepartz, 2005). Fanning et al. (2006) synthesized several cyclen based trivalent Eu(III) and La(III) complexes that hydrolyzed 2-hydroxypropyl 4-nitrophenyl phosphate (HPNP, an RNA model compound) within the physiological pH range.

FIGURE 1 | (A) Structures of a metal-cyclen (**M-C**) complex (side-view and top-view) and the BNPP substrate. **(B)** Different conformations of a **M-C** complex.
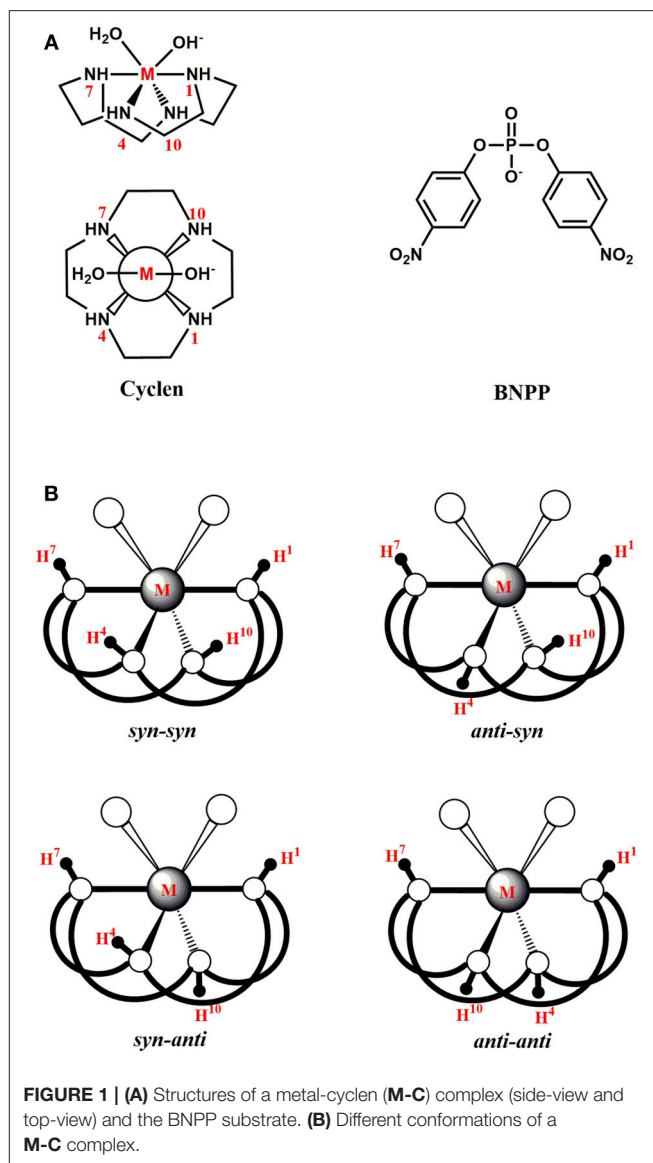
Furthermore, tetravalent Ce(IV) in an aqueous solution provided 10^{11} times rate-acceleration over the background reaction and 20–1000 times over the trivalent lanthanides for DNA hydrolysis (Komiyama et al., 1999). However, the exact nature of the active complexes in this reaction was not known. Nonetheless, based on the X-ray absorption fine structure data, remarkable activity of the Ce complex was proposed to be promoted by a weak covalent interaction between Ce(IV) and the phosphate group of the substrate (Hidemi et al., 1999).

In the proposed mechanism of phosphoester hydrolysis, the metal ion has been suggested to play the following key roles: (1) Lewis acid activation of the substrate, (2) creation of a nucleophile, and (3) generation of a good leaving group of the substrate (Chin, 1991; Bashkin and Jenkins, 1994; Fothergill et al., 1995; Williams et al., 1999; Das et al., 2013). Additionally, it stabilizes the transition states and intermediates by neutralizing their negative charges. To accomplish these functions, a metal ion

should possess high Lewis acidity, strong nucleophilicity, redox stability, borderline hardness and low ligand field stabilization energy (Wilkinson et al., 1987; Hegg and Burstyn, 1998). However, an increase in its Lewis acidity causes a decrease in the nucleophilicity and these two effects require the right balance for the optimum reactivity (Koike and Kimura, 1991; Kimura et al., 1995; Bonfá et al., 2003; Coleman et al., 2010).

The metal-cyclen (**M-C**) complex can exist in equilibrium between several diastereoisomers (*sys-syn*, *anti-syn*, *syn-anti*, and *anti-anti*) associated with the orientation of protons (H^4 or H^{10}) on the nitrogen atoms of the cyclen macrocycle (**Figure 1B**; Hay and Norman, 1997). The H^4 or H^{10} atoms face the substrate in the *syn* conformation, while they are located on the opposite side of the substrate in the *anti* conformation. The NMR data showed that *syn-anti* conformation of [Co(cyclen)Cl$_2$]$^+$ was more stable than other conformations (Sosa and Tobe, 1985). The X-ray structure of [Co(cyclen)(NO$_2$)$_2$]$^+$ exhibited that this complex also existed in the *syn-anti* conformation (Iitaka et al., 1974). Additionally, the X-ray structures of both [Co(cyclen)(NH$_3$)$_2$]$^{3+}$ and [Co(cyclen)(diamine)]$^{3+}$ (diamine = H$_2$N(CH$_2$)$_2$NH$_2$, H$_2$N(CH$_2$)$_3$NH$_2$) complexes were crystallized in the *syn-anti* conformation (Clarkson et al., 2000). However, the exact conformation of a **M-C** complex has been proposed to depend on the nature of the metal ion (Zhang et al., 2014).

The experimentally proposed mechanism, termed direct attack (**DA**), utilized by metal complexes for the phosphodiester hydrolysis is shown in **Figure 2A** (Hendry and Sargeson, 1989; Komiyama et al., 1999; Mancin and Tecilla, 2007). In the initial form of the **M-C** complex (**R$_i$**), the metal ion is coordinated to the cyclen macrocycle, a hydroxyl ion and a water molecule (Kim et al., 2009). The protonation states of the hydroxyl ion and water molecule were based on the measured pK_a values of the **Co-C** complex (pK_{a1} = 5.66 and pK_{a2} = 8.14) (Kim et al., 2009). According to this mechanism, from **R$_i$**, substitution of the metal-bound water molecule by the substrate creates an active complex (**R**). In the next step, a nucleophilic attack by the metal-bound hydroxyl group on the phosphorus center generates a five-membered phosphorane intermediate (**I$_D$**). In the final step, the P-OR bond *trans* to the nucleophile is cleaved to form the final product (**P**).

Recently, based on DFT calculations, another mechanism called catalyst-assisted (**CA**) was proposed for the **Cu-C** complex (**Figure 2A**; Zhang et al., 2016b). According to this mechanism, the metal-bound hydroxide functions as a base and abstracts a proton from the nitrogen atom (N^1) of the cyclen to generate a water molecule (**I1$_C$**). In the next step, the N^1 atom acts as a base and accepts the previously donated proton. The hydroxide nucleophile created in this process attacks the electrophilic phosphorus atom of BNPP to form an intermediate (**I2$_C$**). From **I2$_C$**, the cleavage of the P-O bond can occur spontaneously and the charged leaving group (RO$^-$) coordinates to the metal ion in the product (**P**).

Additionally, BNPP hydrolysis could occur through a third mechanism, termed a water assisted (**WA**) mechanism (**Figure 2B**; Dal Peraro et al., 2004; Jayasinghe-Arachchige et al., 2019). According to this mechanism, an external water molecule is employed for the nucleophilic attack and/or leaving group

departure. After the formation of the reactant (**R$_W$**), the metal-bound hydroxide functions as a base and abstracts a proton from a solvent water molecule to generate a free nucleophile (-OH). This hydroxyl nucleophile concomitantly attacks the BNPP substrate. Depending on the nature of the metal ion (di- or tetravalent), this mechanism could also occur in a stepwise manner after this step. In this pathway, the metal-bound water molecule assists the cleavage of the phosphoester bond and creates a neutral leaving group (ROH).

Quite clearly, the metal-bound hydroxyl group play different roles in these mechanisms: (1) nucleophile only (**DA** mechanism), (2) both base and nucleophile (**CA** mechanism), and (3) base only (**WA** mechanism). The rate of this reaction is likely to depend on the stability of the rate-limiting transition state, which is connected with the Lewis acidity of the metal ion and the geometry of the metal-BNPP complex.

Despite the availability of a wealth of experimental and theoretical information, several unresolved issues concerning the exact mechanism, structures and roles of the metal ion still remain. For example, the conformation of the substrate bound **M-C** complexes (*sys-syn*, *anti-syn*, *syn-anti*, and *anti-anti*) for different metals (di- and tetravalent) is not known experimentally. The structures (transition states and short-lived intermediates) and energetics of the reaction mechanism for a specific metal ion are also not available. We have addressed all these important issues for a variety of **M-C** complexes using two sets of metal ions, divalent [Zn(II), Cu(II), and Co(II)] and tetravalent [Ce(IV), Zr(IV), and Ti(IV)], for BNPP hydrolysis through all three (**DA**, **CA**, and **WA**) mechanisms. The available experimental and theoretical information has been fully integrated in these calculations. These results will provide intricate details of the metal assisted phosphodiester hydrolysis and pave the way for the design of the next generation of synthetic metallohydrolases to catalyze this critical reaction.

COMPUTATIONAL DETAILS

Method

All Density Functional Theory (DFT) calculations were performed using the Gaussian 09 program package (Frisch et al., 2009). The geometry optimizations of reactants, transition states, intermediates and products were conducted using the B3LYP functional (Becke, 1988, 1993) without any constraints. Mixed basis sets were utilized for the structure optimization and frequency analysis. In particular, the Stuttgart relativistic effective core potential (ECP) basis set (RSC97) (Lee et al., 1988; Dolg et al., 1989) was applied for the metal ions. This is a double zeta basis set that uses 28 core electrons ([Ar]+3d) for the second-row transition metals and the lanthanides and 10 core electrons ([Ne]) for the first row transition metals. The 6-311G(d,p) basis set was used for the O, N and P atoms, while 6-31G was used for C and H atoms (Ditchfield et al., 1971). The final energies of the optimized structures were further improved by performing single point calculations using a bigger triple zeta quality 6-311+G(d,p) basis set for P, O, N, C and H atoms and RSC97 for metal ions. Hessians were calculated at the same level of theory as the optimizations to confirm the nature of the stationary
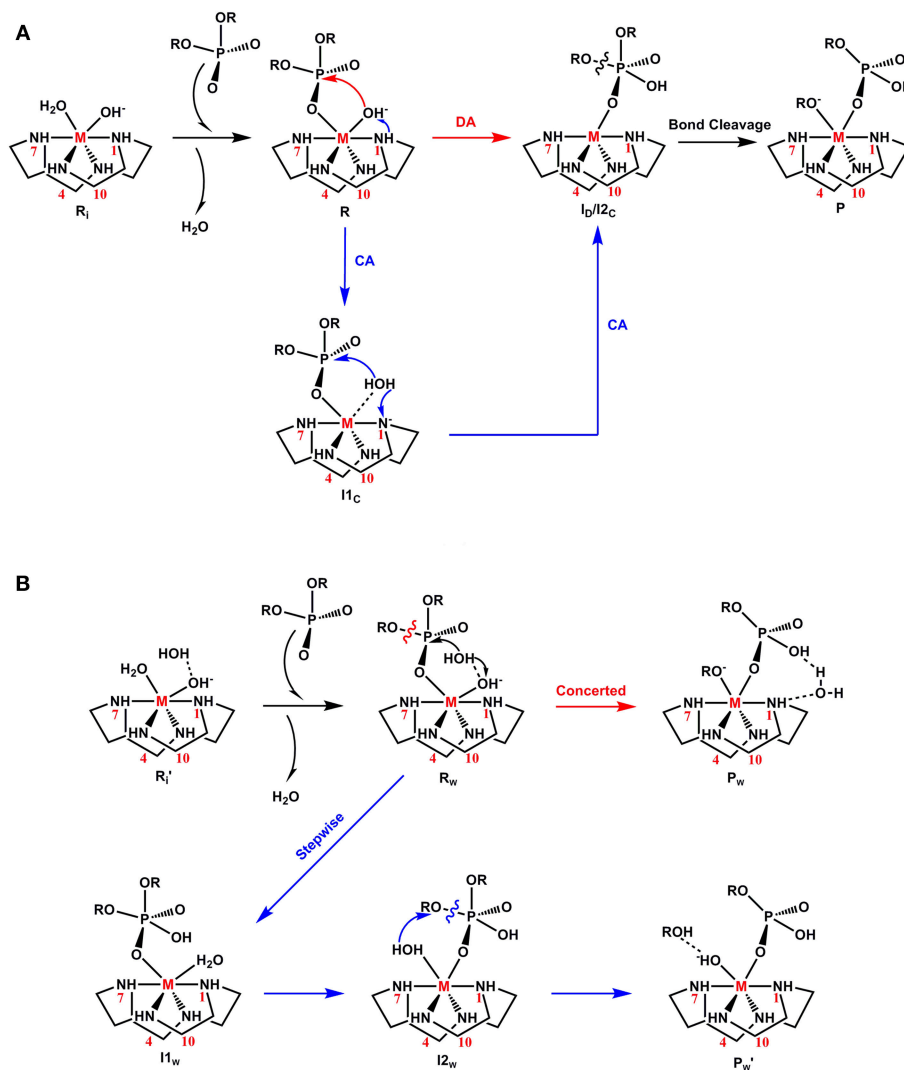
FIGURE 2 | Proposed mechanisms for phosphoester hydrolysis: **(A)** Direct-attack (**DA**) and Catalyst-assisted (**CA**) and **(B)** Water-assisted (**WA**).

points along the reaction coordinates. The transition states were confirmed to have only one negative eigenvalue corresponding to the reaction coordinates. The intrinsic reaction coordinate (IRC) approach (Ischtwan and Collins, 1988) that connects a transition state to the corresponding minima was utilized. The natural atomic charge for each atom was calculated by natural bond orbital (NBO) analysis using the NBO version 3 (Foster and Weinhold, 1980; Reed and Weinhold, 1983). Solvent effects for water (dielectric constant = 78.39) were calculated utilizing the polarizable continuum model (PCM) using the integral equation formalism variant (IEFPCM), which is a default self-consistent reaction field (SCRF) method (Cancès et al., 1997). The B3LYP energies were compared with the energies calculated using the M06L (Zhao and Truhlar, 2006), MPW1PW91 (Adamo and Barone, 1998) and PBE1PBE (Perdew et al., 1996) functionals. All energy barriers using these functionals were within 2.7–3.6 kcal/mol and provided similar potential energy surfaces (PES).

The final energies computed at the B3LYP/6-311+G(d,p) level including zero-point vibrational (unscaled), thermal (298.15 K, 1 atm), entropy corrections (298.15 K) and solvent effects were used to discuss the activities of all **M-C** complexes. The measured k_{cat} values were converted into activation energy using the Arrhenius equation (k = Ae$^{-Ea/RT}$, where A is the pre-exponential factor, Ea is the activation energy, R is the gas constant and T is the temperature). It is noteworthy that calculations were performed at room temperature (25°C), while some k_{cat} values were measured at a higher temperature. Due to the temperature dependence of the pre-exponential constant in the Arrhenius equation, it was not possible to accurately estimate the measured barrier at 25°C.

Models

In the calculations, the metal ion was coordinated to the 1,4,7,10-tetraazacyclododecane (cyclen) ligand, a hydroxyl ion and water

molecules (Chin et al., 1989; Kim et al., 2009). The number of water molecules was determined by the chemical nature of the metal ion and the underlying mechanism. The overall charge for the **Zn-C**, **Cu-C**, and **Co-C** complexes was 0, while for **Ce-C**, **Zr-C**, and **Ti-C** the charge was +2. **Cu-C** and **Co-C** existed in the doublet spin state, while all the other **M-C** complexes existed in the singlet spin state. BNPP was used as the model of DNA because it contains two nitrophenyl groups which are similar to the deoxyribose rings of DNA.

RESULTS AND DISCUSSION

The activities of all six **M-C** complexes (**Zn-C**, **Cu-C**, **Co-C**, **Ce-C**, **Zr-C**, and **Ti-C**) were investigated using three different mechanisms: (1) direct attack (**DA**), (2) catalyst-assisted (**CA**), and (3) water-assisted (**WA**), **Figure 2**. Their energetics were compared using the metal-ligand, metal-nucleophile and P-O bond lengths, strain of the cyclen ring, atomic charges and coordination number of metal ions as parameters. The Lewis acidity and nucleophilicity of the metal ions can be qualitatively characterized by the metal-substrate and metal-nucleophile bond lengths (Bertini et al., 1990; Coleman et al., 2010). In this section, the **DA, CA** and **WA** mechanisms were first discussed for the divalent metal complexes [**Zn-C**, **Cu-C**, and **Co-C**] followed by for the tetravalent complexes [**Ce-C**, **Zr-C** and **Ti-C**].

The starting point of all these mechanisms was the BNPP substrate bound structure of the **M-C** complexes. The *syn-syn* conformation was found to be the energetically most stable for all six metals (**Figure 1B**). The other conformations were 1.8–27.9 kcal/mol higher in energy. The relative stability of the *syn-syn* structure could be due to its lower strain computed as the sum of the N^1-M-N^7 and N^4-M-N^{10} angles (**Figure 1**). This conformation possessed the largest angle (204.22–255.99°),

and least strain, in comparison to the other three conformers. Additionally, the H^4 and H^{10} atoms of the cyclen formed hydrogen bonds with the phosphate group of BNPP to provide extra stabilization to this conformation.

Phosphodiester Hydrolysis by Divalent Metal-Cyclen (M-C) Complexes

The divalent Zn, Cu, and Co ions are known to form stable complexes with a common coordination number of six for the phosphodiester and peptide hydrolysis (Holm et al., 1996; Berreau, 2006; Jang and Suh, 2008; Chei et al., 2011). Therefore, the BNPP substrate could only be singly coordinated to these metal ions (P-O-M mode), and the remaining coordination sites were occupied by four nitrogen atoms (N^1, N^4, N^7, and N^{10}) of the cyclen ligand and one hydroxyl group. In this section, for the sake of clarity, all three mechanisms for **Zn-C** were discussed in detail followed by comparisons with the **Cu-C** and **Co-C** complexes.

Direct Attack (DA) Mechanism

In the reactant (**R_{Zn}** in **Figure 3**) of **Zn-C**, one phosphoryl oxygen (O^1) atom of BNPP was bound to the Zn(II) ion, while the other one (O^2) interacted with the -$N^{10}H$ group of the cyclen through a hydrogen bond. This metal-substrate coordination elongated the scissile P-O^4 bond of BNPP by 0.04 Å in comparison to this bond in its free form (P-O^4 = 1.64 Å in **Figure 3**). In **R_{Zn}**, the Lewis acidity of the Zn ion played a key role in the activation of the P-O^4 bond. The interaction between the *p* orbital of the oxygen atom with the *d* orbital of the Zn atom promoted this activation (**Figure S1**). In the first step, the Zn-bound -O^HH^H nucleophile directly attacked the electrophilic P atom of the substrate to generate a five-membered trigonal bipyramidal phosphorane
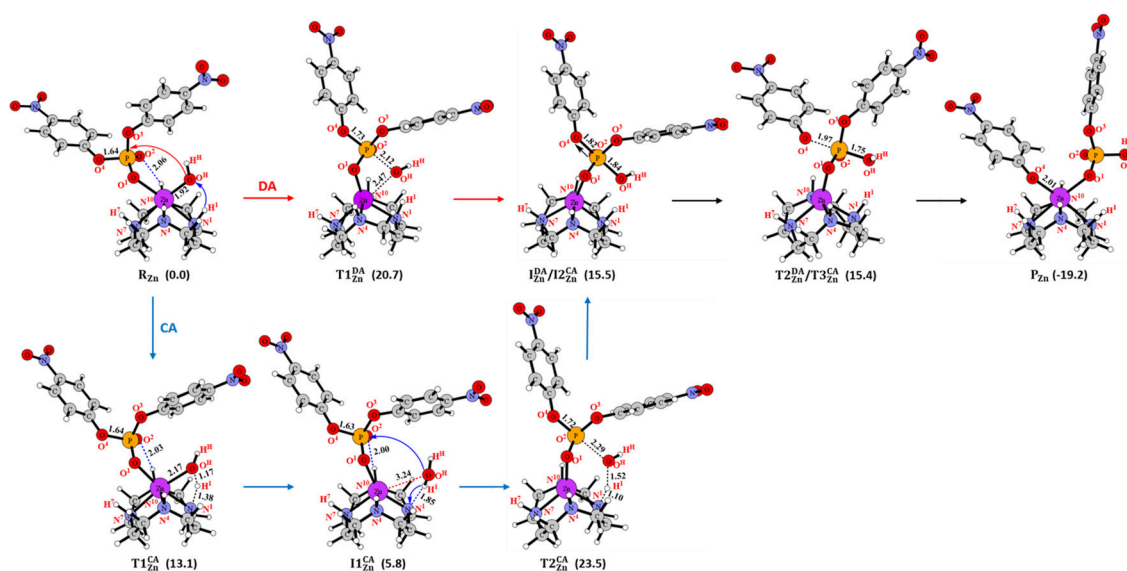

FIGURE 3 | Structures (in Å) and energies (in kcal/mol) in the *DA* and *CA* mechanisms for **Zn-C**.

intermediate (I_{Zn}^{DA}). This process occurred with a barrier of 20.7 kcal/mol and in the optimized transition state ($T1_{Zn}^{DA}$) the Zn-$O^H H^H$ and P-O^4 bonds, *trans* to the nucleophile, became substantially longer by 0.55 and 0.09 Å, respectively (**Figure 3** and **Table S1**). I_{Zn}^{DA} was endergonic by 15.5 kcal/mol from R_{Zn} and the P-O^4 bond was significantly activated but not completely broken in this intermediate (P-O^4 = 1.82 Å). However, this bond was cleaved in the next step and the nitrophenolate (-$OC_6H_4NO_2$) group was released. In the transition state ($T2_{Zn}^{DA}$) for this process, the P-O^4 bond was significantly elongated to 1.97 Å (**Figure 3**). The negatively charged nitrophenolate group generated in this process was coordinated to the Zn ion in the product (P_{Zn}). P_{Zn} was computed to be exergonic by 19.2 kcal/mol from R_{Zn}. The overall barrier (20.7 kcal/mol) for this mechanism was somewhat underestimated in comparison to the measured barrier of 29.3 kcal/mol (computed from the k_{cat} value using the Arrhenius equation) for BNPP hydrolysis by **Zn-C** (Koike and Kimura, 1991).

The overall energetics of this mechanism for **Cu-C** and **Co-C** were quite comparable to that of **Zn-C** (**Figures S2, S3**). However, the barrier (22.0 and 23.4 kcal/mol) and endergonicity (17.7 and 17.2 kcal/mol) of the rate-limiting first step were slightly higher for **Cu-C** and **Co-C**, respectively, in comparison to **Zn-C**. This difference could be due to the greater strength of the Zn-bound nucleophile in R_{Zn} i.e., longer Zn-O^H distance and higher charge on the O^H atom (**Tables S1, S2**).

These results suggested that both Lewis acidity and nucleophilicity of the metal center controlled the energetics of this mechanism. **Zn-C** was found to be slightly more reactive than the **Cu-C** and **Co-C** complexes.

Catalyst-Assisted (CA) Mechanism

The catalyst-assisted (*CA*) mechanism (**Figure 3**; Zhang et al., 2016b) started with the same reactant (R_{Zn}) as the *DA* mechanism. In the first step, the Zn-bound hydroxyl group of R_{Zn} functioned as a base and abstracted the H^1 proton from the cyclen ring to form a water molecule ($O^H H^H H^1$). This process occurred with a barrier of 13.1 kcal/mol and the Zn-O^H bond was extended by 0.25 Å in the optimized transition state ($T1_{Zn}^{CA}$) in comparison to the corresponding distance in R_{Zn}. The intermediate ($I1_{Zn}^{CA}$) formed in this process was 5.8 kcal/mol endergonic from R_{Zn} (**Figure 3**). In $I1_{Zn}^{CA}$, the water molecule was not coordinated to the Zn ion and associated with the N^1 atom of the cyclen ligand through a hydrogen bond. The strain of the cyclen ring and the acidity of the -$N^1 H^1$ group controlled the energetics of this step. The sum of the N^1-M-N^7 and N^4-M-N^{10} angles (238.6° in R_{Zn}) was increased by 15.3° in $T1_{Zn}^{CA}$ (253.9°) i.e., less strain in $T1_{Zn}^{CA}$. However, a high charge (−0.77e) on the N^1 atom of the cyclen ligand also lowered the acidity of the H^1 atom. From $I1_{Zn}^{CA}$, the cyclen ligand directly participated in the mechanism by creating a nucleophile and regenerating the ligand through activation of the previously generated water molecule ($O^H H^H H^1$ in **Figure 3**). In this step, the N^1 atom of the ligand abstracted the H^1 proton concomitantly with the attack of the -$O^H H^H$ nucleophile to the electrophilic P atom of BNPP. This concerted process, through transition state ($T2_{Zn}^{CA}$), led to the creation of the phosphorane intermediate ($I2_{Zn}^{CA}$) that was

endergonic by 15.5 kcal/mol (**Figure 3**). From R_{Zn}, this step occurred with a barrier of 23.5 kcal/mol and found to be the rate-limiting step of the *CA* mechanism. At $I2_{Zn}^{CA}$, both *DA* and *CA* mechanisms merged and led to the generation of the common product (P_{Zn} in **Figure 3**).

The structures of the reactants for **Cu-C** and **Co-C** (R_{Cu} and R_{Co}, respectively) were quite similar to R_{Zn} (**Figures S2, S3**). However, the barrier of the first step for **Cu-C** and **Co-C** was lowered by 1.4 and 4.4 kcal/mol, respectively, in comparison to the barrier for **Zn-C**. Additionally, the phosphorane intermediate for these systems was found to be more stable by 4.8 and 4.3 kcal/mol, respectively (**Figures S2, S3**). These energy differences were likely to be caused by lower strain of the cyclen ring i.e., 238.6°, 245.0°, and 256.0° For R_{Zn}, R_{Cu}, and R_{Co}, respectively. Additionally, a lower charge on the N^1 atom increased the acidity of the -$N^1 H^1$ group of **Cu-C** and **Co-C** and made this process energetically more favorable (**Table S2**). The computed barrier of the next rate-determining step for **Cu-C** and **Co-C** (24.3 and 24.6 kcal/mol, respectively) was slightly higher than the barrier for **Zn-C** (23.5 kcal/mol). Here, due to the higher basicity of the N^1 atom in **Zn-C**, the proton transfer occurred with a lower barrier.

These results suggested that the *CA* mechanism was energetically less favorable than the *DA* mechanism for all divalent metals. Due to the direct involvement of the cyclen ligand, the strain of the cyclen ring and acidity of the $N^1 H^1$ group determined the energetics of the *CA* mechanism. Similar to the *DA* mechanism, **Zn-C** was more reactive than **Cu-C** and **Co-C**.

Water-Assisted (WA) Mechanism

The major difference between the *DA* and *WA* mechanisms is that in the latter, the metal-bound hydroxide played the role of a base and created a nucleophile through activation of an external water molecule (**Figure 2B**). In the reactant (R_{Zn}^{WA}) of **Zn-C**, the Zn-bound hydroxyl group (-$O^H H^H$) interacted with an external water molecule ($HO^w H^w$) through a hydrogen bond (**Figure 4A**). This interaction elongated the Zn-$O^H H^H$ bond by 0.05 Å in comparison to R_{Zn}. From R_{Zn}^{WA}, the Zn-bound hydroxyl (-$O^H H^H$) abstracted the H^w proton of the external water molecule and generated the free -$O^w H$ nucleophile that concomitantly attacked the BNPP substrate and cleaved the P-O^4 bond. This concerted process occurred through transition state (T_{Zn}^{WA}) with a barrier of 20.9 kcal/mol (**Figure 4A** and **Table 1**). In the product (P_{Zn}^{WA}), the negatively charged -$OC_6H_4NO_2$ group created by the nucleophilic attack coordinated to the Zn ion with the release of the water molecule ($H^w O^H H^H$). P_{Zn}^{WA} was 13.9 kcal/mol exergonic from R_{Zn}^{WA}. The strength of the hydroxyl nucleophile generated from an external water was weaker than that of a metal-bound nucleophile. However, quite surprisingly, the barrier for the *WA* mechanism (20.9 kcal/mol) was quite comparable to the one computed for the *DA* mechanism (20.7 kcal/mol). That could be due to the extra stability of the five-membered transition state (T_{Zn}^{WA}) formed in the former, in comparison to the four-membered transition state ($T1_{Zn}^{DA}$) created in the latter. For **Cu-C** and **Co-C** the barrier for the *WA* mechanism was also slightly higher by 2.2 and 1.0 kcal/mol, respectively, than for the *DA* mechanism (**Figures 4B,C**). However, the barrier for the *WA* mechanism for **Cu-C** and **Co-C** was 3.3 and 3.5 kcal/mol,
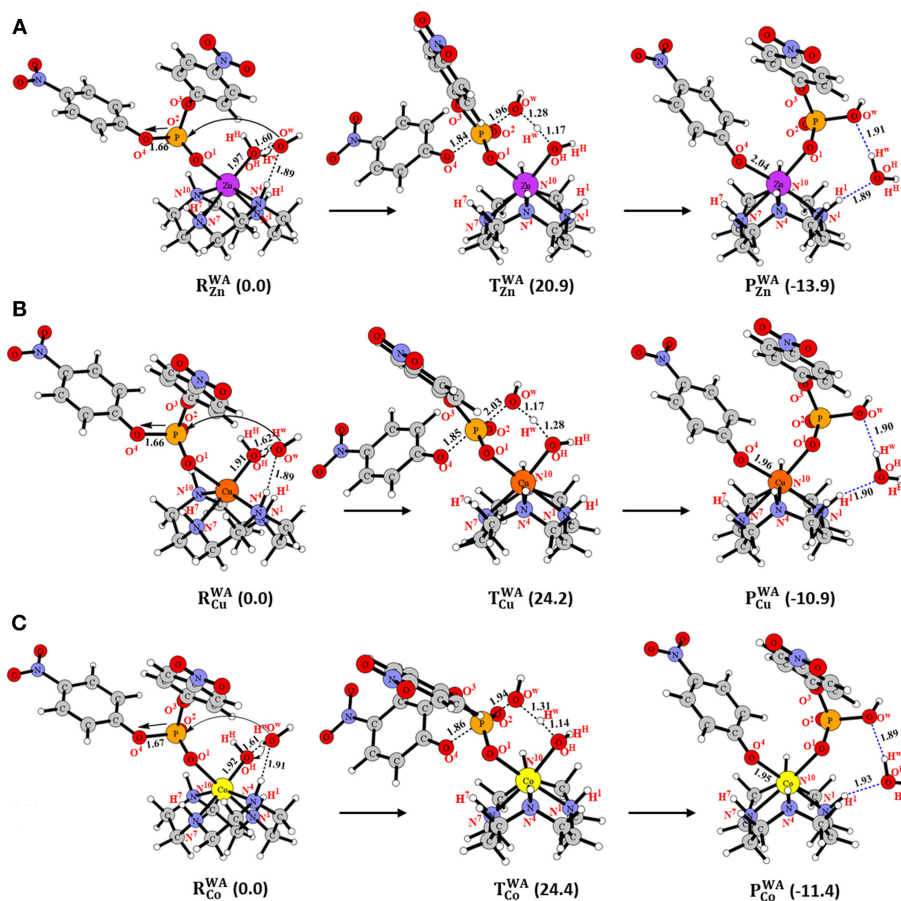
FIGURE 4 | Structures (in Å) and energies (in kcal/mol) in the **WA** mechanism for **(A) Zn-C**, **(B) Cu-C** and **(C) Co-C**.

respectively higher than the barrier for **Zn-C** i.e., 24.2 and 24.4 kcal/mol, respectively (**Figure 4**). This difference was likely to be due to the stronger basicity of the Zn-$O^H H^H$ group among all three complexes. It was caused by the longer M-O^H distance and higher charge on the O^H atom in **Zn-C** (**Tables S1, S2**). Additionally, in contrast to the singlet spin state of Zn in **Zn-C**, both Cu and Co existed in the doublet spin state in **Cu-C** and **Co-C**. That might also be the reason for the similar energetics of **Cu-C** and **Co-C**.

According to these results, the basicity of the M-O^H group influenced the energetics of the **WA** mechanism. Additionally, energetics of all three mechanisms (**DA**, **CA,** and **WA**) were quite comparable for all divalent metal complexes. Furthermore, **Zn-C** was found to be more reactive than **Cu-C** and **Co-C** for all three mechanisms.

Phosphodiester Hydrolysis by Tetravalent Metal-Cyclen (M-C) Complexes

The tetravalent metals (Ce, Zr, and Ti) form complexes with higher coordination numbers 6–12, than the divalent metals (Zn, Cu, and Co) with coordination numbers 5–6. Among tetravalent metals, Ce can form complexes with coordination numbers 7–12,

while Zr and Ti with 6–8 (Komiyama et al., 1999; Bonomi et al., 2010). Here, due to the difference in their coordination number, all three **DA**, **CA,** and **WA** mechanisms are first discussed for **Ce-C**, followed by for **Zr-C** and **Ti-C**.

Direct Attack (DA) Mechanism for the Ce-C Complex

The activity of **Ce-C** was studied using three different coordination numbers (7–9). Due to the steric hindrance, complexes with higher coordination numbers (10–12) could not be optimized. In the reactant (**R_{Ce}**) with coordination number 7, BNPP was coordinated to the Ce ion through the O^1 and O^2 atoms in the bidentate form. In contrast, BNPP binding to the divalent metals occurred in the monodentate fashion. As a result, the scissile P-O^4 bond became stronger by 0.03 Å in **Ce-C** (**Figure S5**). In **R_{Ce}**, all metal-ligand distances (**Table S3**) were significantly longer than those in the reactant of **Zn-C** (**Table S1**). The excellent hydrolytic activity of the Ce ion in aqueous solution was reported to be due to the hybridization of the 4f orbitals of Ce with the 2p orbitals of the coordinated oxygen atoms of the substrate (Komiyama, 2016). However, Ce can form complexes with different coordination numbers in the solution, and the actual active complex in the previous study was not known. Here, substrate-bound mononuclear **Ce-C** complex

was not found to activate the P-O^4 bond (**Figure S4**). The direct nucleophilic attack of the metal-bound hydroxide (-O^{H}H^H) to BNPP occurred with a barrier of 39.1 kcal/mol (**Figure S5**), which was almost twice the barrier computed for **Zn-C**. The reason for this significantly higher barrier was the change of **Ce-C** from a hepta-coordinated (coordination number 7) **R$_{Ce}$** to an unfavorable hexa-coordinated (coordination number 6) **T1$_{Ce}^{DA}$**. From **I$_{Ce}^{DA}$**, the P-O^4 bond was completely broken with a small barrier of 2.1 kcal/mol and the separated nitrophenolate (-OC$_6$H$_4$NO$_2$) and phosphate [-(O)$_2$P(OC$_6$H$_4$NO$_2$)OH] groups were coordinated to the Ce(IV) ion in the product (**P$_{Ce}$** in **Figure S5**).

This mechanism was further studied by including extra water as a ligand (coordination number of Ce = 8). It was also suggested in our previous study (Zhang et al., 2017) that an increased coordination number of the metal ion enhanced the peptidase activity of the Zr(IV) azacrown ether complex [Zr-(NO$_2$)(OH^H)(H$_2$O)$_n$]. In the reactant (**R'$_{Ce}$**) with coordination number 8 (**Figure S6**), the additional Ce-bound water formed a hydrogen bond with BNPP. From **R'$_{Ce}$**, the barrier for the nucleophilic attack in the rate-determining first step was lowered slightly by 1.4 kcal/mol i.e., 37.7 kcal/mol from **R'$_{Ce}$**. The inclusion of the second water molecule (coordination number of Ce = 9) further lowered the barrier for this step by 1.5 kcal/mol i.e., 36.2 kcal/mol from the reactant (**R"$_{Ce}$** in **Figure S7**). This slight reduction of barrier upon increasing the coordination number of Ce (7–9) could be caused by a slight increase in the metal-nucleophile (Ce-O^H) distance and a decrease in the charge on the Ce atom (**Tables S3, S4**). This indicates the provision of a stronger nucleophile in the complexes with a higher coordination number.

These results suggested that, in comparison to the divalent metals, the lower activity of all **Ce-C** complexes with different coordination numbers (7–9) was caused by the strengthening of the scissile phosphoester bond and weaker nucleophilicity of the hydroxyl nucleophile. However, the reactivity of the **Ce-C** complex was slightly enhanced with an increase in the coordination number (7–9) of the Ce ion.

Catalyst-Assisted (CA) Mechanism for the Ce-C Complex

In this mechanism, from **R$_{Ce}$**, an abstraction of the H^1 proton of the cyclen ring by the Ce-bound hydroxyl (-O^{H}H^H) took place with a barrier of 26.9 kcal/mol (**Figure S5**). Similar to the **DA** mechanism, the barrier for this process was 13.8 kcal/mol higher than the barrier for **Zn-C** (**Figure 3**). The metal-nucleophile (Ce-O^H) distance was significantly elongated from 2.04 Å to 2.33 and 2.50 Å in the transition state (**T1$_{Ce}^{CA}$**) and the intermediate (**I1$_{Ce}^{CA}$**), respectively, in comparison to **R$_{Ce}$**. In the next step, the reverse transfer of the H^1 proton from the Ce-bound water molecule (H^{H}O^{H}H^1) to the N^1 atom of the cyclen and simultaneous nucleophilic attack of the hydroxide (-O^{H}H^H) to BNPP generated a phosphorane intermediate (**I2$_{Ce}^{CA}$**). This synchronous process occurred in the rate-limiting step with a barrier of 46.8 kcal/mol and **I2$_{Ce}^{CA}$** was endergonic by 35.5 kcal/mol from **R$_{Ce}$**. After its formation, the product (**P$_{Ce}$**) was generated through the cleavage of the P-O^4 bond (**Figure S5**).

The inclusion of an additional water molecule to this complex increased the coordination number of Ce to 8 and lowered the barrier for the rate-limiting step by 2.3 kcal/mol i.e., 44.5 kcal/mol from the corresponding reactant (**R'$_{Ce}$** in **Figure S6**). The inclusion of the second water molecule (coordination number of Ce = 9) further lowered the barrier only by 0.5 kcal/mol i.e., 44.0 kcal/mol from the reactant (**R"$_{Ce}$** in **Figure S7**). This lowering of the barrier could be attributed to an increase in the Ce-O^{H}H^H (nucleophile) distance (**Table S3**) and a reduction in charge of the Ce atom (**Table S4**).

Similar to divalent metal-complexes, the **CA** mechanism was found to be energetically less favorable than the **DA** mechanism and the energetics of this mechanism improved slightly with an increase in the coordination number of Ce.

Water-Assisted (WA) Mechanism for the Ce-C Complex

The reactant (**R$_{Ce}^{WA}$**) of the **WA** mechanism was similar to **R$_{Ce}$**, except for an external water molecule that was hydrogen bonded to the Ce-bound hydroxyl (-O^{H}H^H) and BNPP (**Figure S8**). In the first step the nucleophile (-O^{1w}H), generated through the abstraction of a proton (H^{1w}) by the Ce-O^{H}H^H group simultaneously attacked BNPP. This process took place with a barrier of 43.5 kcal/mol and led to the creation of the

TABLE 1 | Computed energy barrier in the rate-limiting step for all **M-C** complexes.

Complex	Coordination number	Mechanism	Barrier (kcal/mol)
Zn-C	6	DA	20.7
		CA	23.5
		WA	20.9
Cu-C	6	DA	22.0
		CA	24.3
		WA	24.2
Co-C	6	DA	23.4
		CA	24.6
		WA	24.4
Ce-C	7	DA	39.1
Ce-C (+1w)	8	DA	37.7
Ce-C (+2w)	9	DA	36.2
Ce-C	7	CA	46.8
Ce-C (+1w)	8	CA	44.5
Ce-C (+2w)	9	CA	44.0
Ce-C	7	WA	44.3
Ce-C (+1w)	8	WA	41.5
Ce-C (+2w)	9	WA	37.0
Zr-C	7	DA	42.7
Zr-C (+1w)	8	DA	40.3
Zr-C	7	WA	37.0
Zr-C (+1w)	8	WA	36.2
Ti-C	7	DA	39.0
Ti-C (+1w)	8	DA	48.0
Ti-C	7	WA	32.7
Ti-C (+1w)	8	WA	34.1

phosphorane intermediate (I_{Ce}^{WA}). In I_{Ce}^{WA}, the scissile P-O^4 bond was substantially activated to 1.81 Å but not completely broken. In the next step, this bond was cleaved with a small barrier of 2.2 kcal/mol i.e., 44.3 kcal/mol from R_{Ce}^{WA}. The nitrophenolate group bound product (P_{Ce}^{WA}) was computed to be exergonic by 4.7 kcal/mol from R_{Ce}^{WA}.

As observed previously, the inclusion of an additional water molecule (coordination number of Ce = 8) lowered the barrier for the rate-limiting second step by 2.8 kcal/mol i.e., 41.5 kcal/mol from the corresponding reactant (R'^{WA}_{Ce}, **Figure S9**). The addition of the second water molecule (coordination number of Ce = 9) further lowered this barrier by 4.5 kcal/mol i.e., 37.0 kcal/mol from the reactant (R''^{WA}_{Ce} in **Figure S10**). This lowering in the barrier (44.3 > 41.5 > 37.0 kcal/mol) with an increase in the coordination number of Ce was due to the following factors. R''^{WA}_{Ce} possessed the longest Ce-O^H distance (2.05 Å) followed by R'^{WA}_{Ce} (1.99 Å) and R_{Ce}^{WA} (1.98 Å), **Table S3**. Additionally, the charge on the Ce atom followed the order R_{Ce}^{WA} > R'^{WA}_{Ce} > R''^{WA}_{Ce} (**Table S4**). These differences indicated that the basicity of the metal-bound hydroxide in R''^{WA}_{Ce} was greater than its basicity in R'^{WA}_{Ce} and R_{Ce}^{WA}.

The reactivity of **Ce-C** was enhanced with an increase in the coordination number (7-9) of the Ce atom. The *CA* mechanism was substantially less favorable, and the *WA* and *DA* mechanisms were quiet comparable for **Ce-C**. Based on these results, the *CA* mechanism was not explored for **Zr-C** and **Ti-C** in the next section.

Direct Attack (DA) Mechanism for the Zr-C and Ti-C Complexes

Zr and Ti have been reported to prefer different coordination numbers i.e., 8 and 7, respectively (Luong et al., 2016; Zhang et al., 2016a; Assi et al., 2017). In the reactant (R_{Zr}) with coordination number 8, an external water molecule was directly coordinated to the Zr ion (**Figure S11**). In comparison to R'_{Ce} (the reactant of **Ce-C** with the same coordination number), all metal-ligand distances, except P-O^4, were substantially shorter in R_{Zr} (**Tables S3, S5**). From R_{Zr}, the Zr bound -O^{H}H^H nucleophile attacked BNPP with a barrier of 40.3 kcal/mol, which was 2.6 kcal/mol higher than the one (37.7 kcal/mol) computed for **Ce-C**. A weaker nucleophile (shorter Zr-O^H distance by 0.05 Å) and increase in the charge of Zr (by 0.15e) raised the barrier for this step. The intermediate (I_{Zr}^{DA}) formed in this step was endergonic by 28.3 kcal/mol from R_{Zr}. However, the P-O^4 bond in I_{Zr}^{DA} was substantially stronger (by 0.12 Å) than in the **Ce-C** case (**Figures S11, S6**). Due to the extra stability of this bond, unlike the mechanism for **Ce-C**, a complete cleavage of this bond required the assistance of metal-bound water in the next step. From I_{Zr}^{DA}, the Zr-bound water donated a proton to the O^4 atom and cleaved the P-O^4 bond. The splitting of this bond occurred with a barrier of 8.8 kcal/mol from I_{Zr}^{DA} i.e., 37.1 kcal/mol from R_{Zr} (**Figure S11**). In the product (P_{Zr}^{DA}), the neutral nitrophenol group was hydrogen bonded to the Zr-hydroxyl moiety and it was exergonic by 9.9 kcal/mol. The removal of a water ligand from this complex (coordination number of Zr = 7) raised the barrier for the rate-limiting first step by 2.4 kcal/mol (**Figure S12**).

Since Ti prefers coordination number 7, the geometry of the reactant (R_{Ti}) of **Ti-C** was different from the reactant of **Zr-C**. In R_{Ti} (**Figure S13**), an external water molecule, instead of directly coordinating to the metal ion, was bridged through hydrogen bonding between the cyclen ring and BNPP. All metal-ligand distances in R_{Ti} were substantially shorter than the corresponding distances in R_{Zr} (**Table S5**), while the P-O^4 bond distance (P-O^4 = 1.57 Å) remained unchanged. From R_{Ti}, the nucleophilic attack took place with a barrier of 39.0 kcal/mol. This barrier was slightly (1.3 kcal/mol) lower than the one computed for **Zr-C**. The intermediate (I_{Ti}^{DA}) formed in this step was endergonic by 24.9 kcal/mol from R_{Ti}. The cleavage of the P-O^4 bond using the Ti-bound water molecule took place with a barrier of 11.5 kcal/mol from I_{Ti}^{DA} i.e., 36.4 kcal/mol from R_{Ti} (**Figure S13**). The product (P_{Ti}^{DA}) in which the neutral nitrophenol group was associated with the metal-bound hydroxyl through hydrogen bonding was exergonic by 10.7 kcal/mol. The inclusion of a water ligand to this complex (coordination number of Ti = 8) raised the barrier for the rate-limiting step by 9.0 kcal/mol i.e., 48.0 kcal/mol from the corresponding reactant (**Figure S14**).

Zr-C and **Ti-C** showed higher activity with different coordination numbers i.e., 8 and 7 for Zr and Ti, respectively. They also required assistance of an external water, unlike **Ce-C**, for the complete cleavage of the P-O bond. However, both **Zr-C** (coordination number = 8) and **Ti-C** (coordination number = 7) were found to be less active than **Ce-C** (with coordination number 9) for the *DA* mechanism (**Table 1**).

Water-Assisted (WA) Mechanism for the Zr-C and Ti-C Complexes

In the reactant (R_{Zr}^{WA}) of **Zr-C**, an external water molecule was hydrogen bonded between the Zr-O^{H}H^H and BNPP (**Figure S15**). In this mechanism, the Zr-bound hydroxyl functioned as a base and created a hydroxyl (-O^{1w}H^{1w}) nucleophile from the external water molecule that concomitantly attacked the electrophilic P atom of BNPP. This synchronous step took place with a barrier of 28.8 kcal/mol (**Figure S15**). The barrier for this step was significantly (6.0 kcal/mol) lower than the barrier for **Ce-C**. The intermediate ($I1_{Zr}^{WA}$) formed in this step was 22.3 kcal/mol endergonic from R_{Zr}^{WA}. As observed for the previous *DA* mechanism, the scissile P-O^4 bond in $I1_{Zr}^{WA}$ was activated but still quite strong (1.62 Å) i.e., 0.13 Å stronger than for **Ce-C**. The complete cleavage of this bond also needed the assistance of a metal-bound water molecule in the next step. The $I1_{Zr}^{WA}$ intermediate reoriented itself and created another 3.0 kcal/mol endergonic intermediate ($I2_{Zr}^{WA}$) in which the water molecule was located in a position to protonate the O^4 atom of BNPP. From $I2_{Zr}^{WA}$, this water molecule donated its proton and cleaved the P-O^4 bond with a barrier of 10.9 kcal/mol. The final product (P_{Zr}^{WA}) was 33.6 kcal/mol exergonic from R_{Zr}^{WA} (**Figure S15**). The removal of a water molecule in this complex (coordination number of Zr = 7) slightly raised the rate-limiting barrier by 0.8 kcal/mol (**Figure S16**).

The reactant (R_{Ti}^{WA}) of **Ti-C** (for coordination number of Ti = 7) was structurally similar to R_{Zr}^{WA} (**Figure S17**). However, all metal-ligand distances in the former were shorter than the
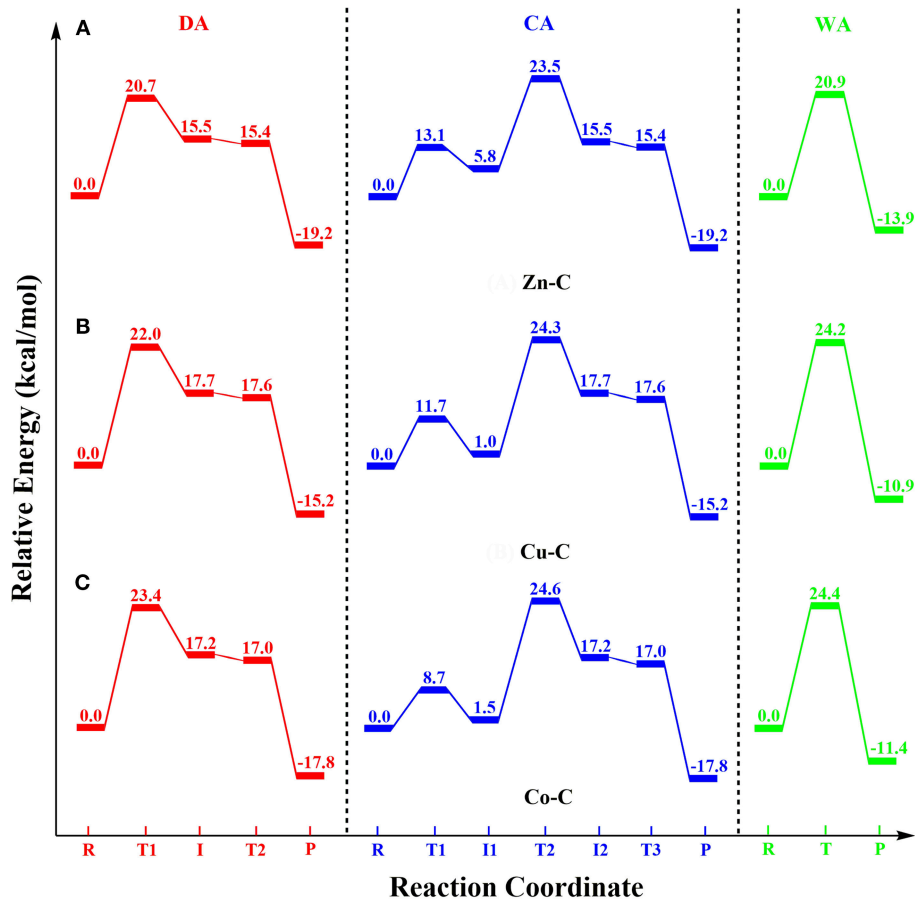
FIGURE 5 | Potential energy surface diagrams for the divalent **M-C** complexes: **(A) Zn-C**, **(B) Cu-C** and **(C) Co-C**.

corresponding distances in the latter (**Table S5**). From R_{Ti}^{WA}, proton abstraction from the external water molecule occurred with a barrier of 32.7 kcal/mol (**Figure S17**). The barrier in this nucleophilic attack step was 3.9 kcal/mol higher than the one computed for **Zr-C**. As discussed previously, this increase was due to a shorter M-O^H bond distance (by 0.19 Å) and lower charge on the O^H atom (by 0.22e) in R_{Ti}^{WA} (**Tables S5, S6**). However, the phosphorane intermediate ($I1_{Ti}^{WA}$) in this step was 7.2 kcal/mol more favorable than in the **Zr-C** case. i.e., 15.1 kcal/mol endergonic from R_{Ti}^{WA}. The presence of a stronger hydrogen bond provided extra stability to this complex. Similar to **Zr-C**, the newly formed Ti-bound water molecule in $I1_{Ti}^{WA}$ reoriented itself between the cyclen ring and BNPP to create another intermediate $I2_{Ti}^{WA}$. This intermediate was 5.7 kcal/mol higher in energy than $I1_{Ti}^{WA}$. From $I2_{Ti}^{WA}$, the transfer of the H^{1w} proton to the O^4 atom led to the splitting of the P-O^4 bond. This process took place with a barrier of 11.5 kcal/mol from $I2_{Ti}^{WA}$. In the product (P_{Ti}^{WA}), the released nitrophenol group was hydrogen bonded to the metal-bound hydroxyl and it was 14.8 kcal/mol exergonic from R_{Ti}^{WA}. The addition of a water molecule in this complex (coordination number of Ti = 8) slightly increased the barrier in the rate-limiting step by 1.4 kcal/mol (**Figure S18**).

These results suggest that the *WA* mechanism was energetically more favorable than the *DA* mechanism for both **Zr-C** and **Ti-C**. Among these two complexes, **Ti-C** was found to be more reactive than **Zr-C**.

CONCLUSIONS

In this DFT study, phosphodiester hydrolysis by metal-cyclen (**M-C**) complexes using both divalent [Zn(II), Cu(II) and Co(II)] and tetravalent [Ce(IV), Zr(IV), and Ti(IV)] metals were investigated. The reactivities of all six **M-C** complexes (**Zn-C, Cu-C, Co-C, Ce-C, Zr-C** and **Ti-C**) for BNPP hydrolysis were studied using three different mechanisms: (1) direct attack (*DA*), (2) catalyst-assisted (*CA*), and (3) water-assisted (*WA*). Their energetics were compared using the metal-ligand, metal-nucleophile and P-O bond lengths, strain of the cyclen ring, atomic charges and coordination number of metal ions as parameters. The potential energy surface diagrams (PES) of all these mechanisms for the divalent and tetravalent complexes are shown in **Figures 5**, **6**, respectively.

For all divalent metal complexes (**Zn-C, Cu-C,** and **Co-C**), the binding of the BNPP substrate in the monodentate fashion
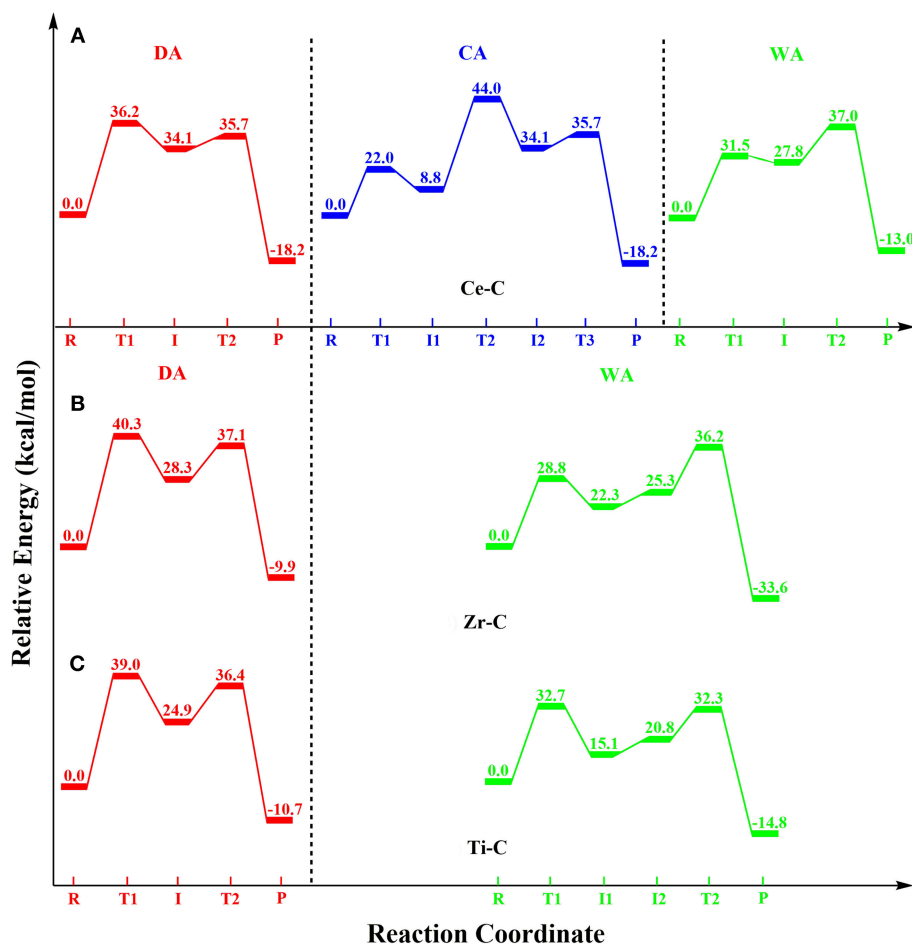
FIGURE 6 | Potential energy surface diagrams for the tetravalent **M-C** complexes: **(A) Ce-C** (coordination number = 9), **(B) Zr-C** (coordination number = 8), and **(C) Ti-C** (coordination number = 7).

activated its scissile phosphoester bond (P-O^4) by ∼0.04 Å. Their energetics were controlled by distinct chemical factors: nucleophilicity of the metal center in the *DA* mechanism; basicity of the N^1 atom of the cyclen ring in the *CA* mechanism; and basicity of the metal bound hydroxyl group in the *WA* mechanism. The *DA* mechanism was found to be energetically most favorable for all these complexes. Among the divalent complexes, **Zn-C** was more reactive than **Cu-C** and **Co-C** for all three mechanisms (**Figure 5**, **Table 1**).

On the other hand, the binding of BNPP to the tetravalent metal complexes (**Ce-C**, **Zr-C,** and **Ti-C**) in the bidentate manner strengthened its P-O^4 bond by ∼0.03 Å. The computed barriers for these complexes were substantially higher than the barriers for their divalent counterparts for all three mechanisms (**Table 1**). Unlike the *DA* mechanism for divalent **M-C** complexes, the *WA* mechanism was energetically most favorable for **Zr-C** and **Ti-C**. On the other hand, energetics of both *DA* and *WA* mechanisms were comparable for **Ce-C**. The activities of **Ce-C** and **Zr-C** improved with an increase in the coordination number (7-9) of the metal ion for all three mechanisms, while **Ti-C** exhibited

the opposite trend (**Table 1**). In comparison to **Ce-C**, both **Zr-C** and **Ti-C** required additional assistance for the complete cleavage of the P-O^4 bond. **Ce-C** exhibited the highest activity with a coordination number of Ce = 9, **Zr-C** with a coordination number of Zr = 8 and **Ti-C** with a coordination number of Ti = 7. However, among all tetravalent complexes, **Ti-C** was found to be the most reactive (barrier = 32.7 kcal/mol using the *WA* mechanism) followed by **Ce-C** and **Zr-C** (**Figure 6**, **Table 1**).

These results have provided detailed structural, mechanistic and kinetic information regarding the activities of a wide range of **M-C** complexes. They will pave the way for the design of efficient synthetic metallohydrolases for applications in biology, biotechnology and medicine.

AUTHOR CONTRIBUTIONS

QH performed most of the DFT calculations and analyzed them. He also wrote the first draft of the manuscript and made figures and tables. VJ-A performed some DFT

calculations and analyzed them. She also helped with the writing of the draft. JZ started the project and performed initial DFT calculations. RP designed and supervised the project. He also analyzed the results and edited the manuscript.

FUNDING

ACKNOWLEDGMENTS

SUPPLEMENTARY MATERIAL

The Supplementary Material for this article can be found online at: https://www.frontiersin.org/articles/10.3389/fchem.2019.00195/full#supplementary-material

REFERENCES

Adamo, C., and Barone, V. (1998). Exchange functionals with improved long-range behavior and adiabatic connection methods without adjustable parameters: the mPW and mPW1PW models. *J. Chem. Phys.* 108, 664–675. doi: 10.1063/1.475428

Assi, H., Mouchaham, G., Steunou, N., Devic, T., and Serre, C. (2017). Titanium coordination compounds: from discrete metal complexes to metal–organic frameworks. *Chem. Soc. Rev.* 46, 3431–3452. doi: 10.1039/C7CS00001D

Bashkin, J. K., and Jenkins, L. A. (1994). The role of metals in the hydrolytic cleavage of DNA and RNA. *Comments Inorg. Chem.* 16, 77–93. doi: 10.1080/02603599408035852

Baykal, U., Akkaya, M. S., and Akkaya, E. U. (1999). A novel lanthanide complex with remarkable phosphodiester transesterification activity and DNA-conjugatable functionality. *J. Incl. Phenom. Macrocycl. Chem.* 35, 311–315. doi: 10.1023/A:1008111418731

Becke, A. D. (1988). Density-functional exchange-energy approximation with correct asymptotic behavior. *Phys .Rev. A Gen. Phys.* 38, 3098–3100. doi: 10.1103/PhysRevA.38.3098

Becke, A. D. (1993). Density-functional thermochemistry. III. The role of exact exchange. *J. Chem. Phys.* 98, 5648–5652. doi: 10.1063/1.464913

Berreau, L. M. (2006). "Kinetic and mechanistic studies of the reactivity of Zn–OHn (n=1 or 2) species in small molecule analogs of zinc-containing metalloenzymes," in *Advances in Physical Organic Chemistry,* ed J. P. Richard (Cambridge, MA: Academic Press), 79–181.

Bertini, I., Luchinat, C., Rosi, M., Sgamellotti, A., and Tarantelli, F. (1990). pKa of zinc-bound water and nucleophilicity of hydroxo-containing species. Ab initio calculations on models for zinc enzymes. *Inorg. Chem.* 29, 1460–1463. doi: 10.1021/ic00333a004

Blaskó, A., and Bruice, T. C. (1999). Recent studies of nucleophilic, general-acid, and metal ion catalysis of phosphate diester hydrolysis. *Acc. Chem. Res.* 32, 475–484. doi: 10.1021/ar980060y

Bonfá, L., Gatos, M., Mancin, F., Tecilla, P., and Tonellato, U. (2003). The ligand effect on the hydrolytic reactivity of Zn(II) complexes toward phosphate diesters. *Inorg. Chem.* 42, 3943–3949. doi: 10.1021/ic034139x

Bonomi, R., Scrimin, P., and Mancin, F. (2010). Phosphate diesters cleavage mediated by Ce(IV) complexes self-assembled on gold nanoparticles. *Org. Biomol. Chem.* 8, 2622–2626. doi: 10.1039/b926916a

Bonomi, R., Selvestrel, F., Lombardo, V., Sissi, C., Polizzi, S., Mancin, F., et al. (2008). Phosphate Diester and DNA hydrolysis by a multivalent, nanoparticle-based catalyst. *J. Am. Chem. Soc.* 130, 15744–15745. doi: 10.1021/ja801794t

Burstyn, J. N., and Deal, K. A. (1993). Selective catalytic hydrolysis of a simple phosphodiester by a macrocyclic copper(II) complex. *Inorg. Chem.* 32, 3585–3586. doi: 10.1021/ic00069a005

Cancès, E., Mennucci, B., and Tomasi, J. (1997). A new integral equation formalism for the polarizable continuum model: theoretical background and applications to isotropic and anisotropic dielectrics. *J. Chem. Phys.* 107, 3032–3041. doi: 10.1063/1.474659

Chae, P. S., Kim, M.-S., Jeung, C.-S., Lee, S. D., Park, H., Lee, S., et al. (2005). Peptide-cleaving catalyst selective for peptide deformylase. *J. Am. Chem. Soc.* 127, 2396–2397. doi: 10.1021/ja044043h

Chandra, M., Sachdeva, A., and Silverman, S. K. (2009). DNA-catalyzed sequence-specific hydrolysis of DNA. *Nat. Chem. Biol.* 5, 718–720. doi: 10.1038/nchembio.201

Chei, W. S., Ju, H., and Suh, J. (2011). New chelating ligands for Co(III)-based peptide-cleaving catalysts selective for pathogenic proteins of amyloidoses. *J. Biol. Inorg. Chem.* 16, 511–519. doi: 10.1007/s00775-010-0750-y

Chin, J. (1991). Developing artificial hydrolytic metalloenzymes by a unified mechanistic approach. *Acc. Chem. Res.* 24, 145–152. doi: 10.1021/ar00005a004

Chin, J., Banaszczyk, M., Jubian, V., and Zou, X. (1989). Cobalt(III) complex-promoted hydrolysis of phosphate diesters: comparison in reactivity of rigid cis-diaquo(tetraaza)cobalt(III) complexes. *J. Am. Chem. Soc.* 111, 186–190. doi: 10.1021/ja00183a029

Clarkson, A. J., Buckingham, D. A., Rogers, A. J., Blackman, A. G., and Clark, C. R. (2000). Kinetic origin of the chelate effect. Base hydrolysis, H-exchange reactivity, and structures of syn,anti-[Co(cyclen)(NH3)2]3+ and syn,anti-[Co(cyclen)(diamine)]3+ Ions (diamine = H2N(CH2)2NH2, H2N(CH2)3NH2). *Inorg. Chem.* 39, 4769–4775. doi: 10.1021/ic000325g

Cleland, W. W., and Hengge, A. C. (2006). Enzymatic mechanisms of phosphate and sulfate transfer. *Chem. Rev.* 106, 3252–3278. doi: 10.1021/cr050287o

Coleman, F., Hynes, M. J., and Erxleben, A. (2010). Ga(III) complexes as models for the M(III) site of purple acid phosphatase: ligand effects on the hydrolytic reactivity toward bis(2,4-dinitrophenyl) phosphate. *Inorg. Chem.* 49, 6725–6733. doi: 10.1021/ic100722w

Corda, D., Mosca, M. G., Ohshima, N., Grauso, L., Yanaka, N., and Mariggi,ò, S. (2014). The emerging physiological roles of the glycerophosphodiesterase family. *FEBS J.* 281, 998–1016. doi: 10.1111/febs.12699

Cowan, J. A. (1998). Metal activation of enzymes in nucleic acid biochemistry. *Chem. Rev.* 98, 1067–1088. doi: 10.1021/cr960436q

Cowan, J. A. (2001). Chemical nucleases. *Curr. Opin. Chem. Biol.* 5, 634–642. doi: 10.1016/S1367-5931(01)00259-9

Dal Peraro, M., Llarrull, L. I., Rothlisberger, U., Vila, A. J., and Carloni, P. (2004). Water-assisted reaction mechanism of monozinc β-lactamases. *J. Am. Chem. Soc.* 126, 12661–12668. doi: 10.1021/ja048071b

Das, P., Chandar, N. B., Chourey, S., Agarwalla, H., Ganguly, B., and Das, A. (2013). Role of metal ion in specific recognition of pyrophosphate ion under physiological conditions and hydrolysis of the phosphoester linkage by alkaline phosphatase. *Inorg. Chem.* 52, 11034–11041. doi: 10.1021/ic401243h

Daver, H., Das, B., Nordlander, E., and Himo, F. (2016). Theoretical study of phosphodiester hydrolysis and transesterification catalyzed by an unsymmetric biomimetic dizinc complex. *Inorg. Chem.* 55, 1872–1882. doi: 10.1021/acs.inorgchem.5b02733

Deck, K. M., Tseng, T. A., and Burstyn, J. N. (2002). Triisopropyltriazacyclononane Copper(II): an efficient phosphodiester hydrolysis catalyst and DNA cleavage agent. *Inorg. Chem.* 41, 669–677. doi: 10.1021/ic0107025

Delehanty, J. B., Stuart, T. C., Knight, D. A., Goldman, E. R., Thach, D. C., Bongard, J. E., et al. (2005). RNA hydrolysis and inhibition of translation by a Co(III)–cyclen complex. *RNA* 11, 831–836. doi: 10.1261/rna.7156805

Ditchfield, R., Hehre, W. J., and Pople, J. A. (1971). Self-consistent molecular-orbital methods. IX. An Extended Gaussian-Type Basis for Molecular-Orbital Studies of Organic Molecules. *J. Chem. Phys.* 54, 724–728. doi: 10.1063/1.1674902

Dolg, M., Stoll, H., and Preuss, H. (1989). Energy-adjusted ab initio pseudopotentials for the rare earth elements. *J. Chem. Phys.* 90, 1730–1734. doi: 10.1063/1.456066

Dubois, K. P. (1971). The toxicity of organophosphorus compounds to mammals. *Bull. World Health Organ.* 44, 231–240.

Eichler, D. C., and Lehman, I. R. (1977). On the role of ATP in phosphodiester bond hydrolysis catalyzed by the recBC deoxyribonuclease of Escherichia coli. *J. Biol. Chem.* 252, 499–503.

Eid, J., Fehr, A., Gray, J., Luong, K., Lyle, J., Otto, G., et al. (2009). Real-time DNA sequencing from single polymerase molecules. *Science* 323, 133–138. doi: 10.1126/science.1162986

Fang, Y.-G., Zhang, J., Chen, S.-Y., Jiang, N., Lin, H.-H., Zhang, Y., et al. (2007). Chiral multinuclear macrocyclic polyamine complexes: synthesis, characterization and their interaction with plasmid DNA. *Biorg. Med. Chem.* 15, 696–701. doi: 10.1016/j.bmc.2006.10.057

Fanning, A.-M., Plush, S. E., and Gunnlaugsson, T. (2006). Tuning the properties of cyclen based lanthanide complexes for phosphodiester hydrolysis; the role of basic cofactors. *Chem. Commun.* 36, 3791–3793. doi: 10.1039/B609923H

Foster, J. P., and Weinhold, F. (1980). Natural hybrid orbitals. *J. Am. Chem. Soc.* 102, 7211–7218. doi: 10.1021/ja00544a007

Fothergill, M., Goodman, M. F., Petruska, J., and Warshel, A. (1995). Structure-energy analysis of the role of metal ions in phosphodiester bond hydrolysis by DNA polymerase I. *J. Am. Chem. Soc.* 117, 11619–11627. doi: 10.1021/ja00151a001

Franklin, S. J. (2001). Lanthanide-mediated DNA hydrolysis. *Curr. Opin. Chem. Biol.* 5, 201–208. doi: 10.1016/S1367-5931(00)00191-5

Frisch, M. J., Trucks, G. W., Schlegel, H. B., Scuseria, G. E., Robb, M. A., Cheeseman, J. R., et al. (2009). *Gaussian 09*. Wallingford CT: Gaussian, Inc.

Gewirtz, A. M., Sokol, D. L., and Ratajczak, M. Z. (1998). Nucleic acid therapeutics: state of the art and future prospects. *Blood* 92, 712–736.

Gómez-Tagle, P., and Yatsimirsky, A. K. (2001). Phosphodiester hydrolysis by lanthanide complexes of bis-tris propane. *Inorg. Chem.* 40, 3786–3796. doi: 10.1021/ic0010205

Hadler, K. S., Tanifum, E. A., Yip, S. H.-C., Mitić, N., Guddat, L. W., Jackson, C. J., et al. (2008). Substrate-promoted formation of a catalytically competent binuclear center and regulation of reactivity in a glycerophosphodiesterase from enterobacter aerogenes. *J. Am. Chem. Soc.* 130, 14129–14138. doi: 10.1021/ja803346w

Hay, R. W., and Norman, P. R. (1997). The kinetics and mechanism of aquation and base hydrolysis of the cis-[Co(cyclen)Cl2]+ cation (cyclen=1,4,7,10-tetraazacyclododecane). *Transition Met. Chem.* 22, 248–253. doi: 10.1023/A:1018460307204

Hegg, E. L., and Burstyn, J. N. (1998). Toward the development of metal-based synthetic nucleases and peptidases: a rationale and progress report in applying the principles of coordination chemistry. *Coord. Chem. Rev.* 173, 133–165. doi: 10.1016/S0010-8545(98)00157-X

Hendry, P., and Sargeson, A. M. (1989). Metal ion promoted phosphate ester hydrolysis. Intramolecular attack of coordinated hydroxide ion. *J. Am. Chem. Soc.* 111, 2521–2527. doi: 10.1021/ja00189a025

Hettich, R., and Schneider, H.-J. (1997). Cobalt(III) polyamine complexes as catalysts for the hydrolysis of phosphate esters and of DNA. A measurable 10 million-fold rate increase1. *J. Am. Chem. Soc.* 119, 5638–5647. doi: 10.1021/ja964319o

Hidemi, M., Masahiko, I., and Koji, M. (1999). Extended x-ray absorption fine structure study on the cerium(IV)-induced DNA hydrolysis: implication to the roles of 4f orbitals in the catalysis. *Appl. Phys. Lett.* 74, 460–462. doi: 10.1063/1.123036

Holm, R. H., Kennepohl, P., and Solomon, E. I. (1996). Structural and functional aspects of metal sites in biology. *Chem. Rev.* 96, 2239–2314. doi: 10.1021/cr9500390

Iitaka, Y., Shina, M., and Kimura, E. (1974). Crystal structure of dinitro(1,4,7,10-tetraazacyclododecane)cobalt(III) chloride. *Inorg. Chem.* 13, 2886–2891. doi: 10.1021/ic50142a023

Ischtwan, J., and Collins, M. A. (1988). Determination of the intrinsic reaction coordinate: comparison of gradient and local quadratic approximation methods. *J. Chem. Phys.* 89, 2881–2885. doi: 10.1063/1.454992

Jang, S. W., and Suh, J. (2008). Proteolytic activity of Cu(II) complex of 1-Oxa-4,7,10-triazacyclododecane. *Org. Lett.* 10, 481–484. doi: 10.1021/ol702860h

Jayasinghe-Arachchige, V. M., Hu, Q., Sharma, G., Paul, T. J., Lundberg, M., Quinonero, D., et al. (2019). Hydrolysis of chemically distinct sites of human serum albumin by polyoxometalate: a hybrid QM/MM (ONIOM) study. *J. Comput. Chem.* 40, 51–61. doi: 10.1002/jcc.25528

Jeung, C. S., Kim, C. H., Min, K., Suh, S. W., and Suh, J. (2001). Hydrolysis of plasmid DNA catalyzed by Co(III) complex of cyclen attached to polystyrene. *Bioorg. Med. Chem. Lett.* 11, 2401–2404. doi: 10.1016/S0960-894X(01)00439-5

Jeyaratnam, J. (1990). Acute pesticide poisoning: a major global health problem. *World. Health. Stat. Q.* 43, 139–144.

Junghun, S., Ho, Y. S., Gyum, K. M., Keunhong, J., Young, A. J., Myoung-Soon, K., et al. (2007). Cleavage agents for soluble oligomers of amyloid β peptides. *Angew. Chem. Int. Ed.* 46, 7064–7067. doi: 10.1002/anie.200702399

Kamerlin, S. C. L., and Warshel, A. (2009). On the energetics of ATP hydrolysis in solution. *J. Phys. Chem. B* 113, 15692–15698. doi: 10.1021/jp907223t

Kia-Ki, H., and Martinage, A. (1992). Post-translational chemical modification(S) of proteins. *Int. J. Biochem.* 24, 19–28. doi: 10.1016/0020-711X(92)90225-P

Kim, H. M., Jang, B., Cheon, Y. E., Suh, M. P., and Suh, J. (2009). Proteolytic activity of Co(III) complex of 1-oxa-4,7,10-triazacyclododecane: a new catalytic center for peptide-cleavage agents. *J. Biol. Inorg. Chem.* 14, 151–157. doi: 10.1007/s00775-008-0434-z

Kimura, E., Kodama, Y., Koike, T., and Shiro, M. (1995). Phosphodiester hydrolysis by a New Zinc(II) macrocyclic tetraamine complex with an alcohol pendant: elucidation of the roles of Ser-102 and Zinc(II) in Alkaline Phosphatase. *J. Am. Chem. Soc.* 117, 8304–8311. doi: 10.1021/ja00137a002

Kirby, A. J., and Nome, F. (2015). Fundamentals of phosphate transfer. *Acc. Chem. Res.* 48, 1806–1814. doi: 10.1021/acs.accounts.5b00072

Koike, T., and Kimura, E. (1991). Roles of zinc(II) ion in phosphatases. A model study with zinc(II)-macrocyclic polyamine complexes. *J. Am. Chem. Soc.* 113, 8935–8941. doi: 10.1021/ja00023a048

Koike, T., Takamura, M., and Kimura, E. (1994). Role of Zinc(II) in .beta.-Lactamase II: a model study with a Zinc(II)-macrocyclic tetraamine (1,4,7,10-Tetraazacyclododecane, Cyclen) Complex. *J. Am. Chem. Soc.* 116, 8443–8449. doi: 10.1021/ja00098a002

Komiyama, M. (2016). Design of highly active Ce(IV) catalysts for DNA hydrolysis and their applications. *Chem. Lett.* 45, 1347–1355. doi: 10.1246/cl.160786

Komiyama, M., and Sumaoka, J. (1998). Progress towards synthetic enzymes for phosphoester hydrolysis. *Curr. Opin. Chem. Biol.* 2, 751–757. doi: 10.1016/S1367-5931(98)80113-0

Komiyama, M., Takeda, N., and Shigekawa, H. (1999). Hydrolysis of DNA and RNA by lanthanide ions: mechanistic studies leading to new applications. *Chem. Commun.* 1443–1451. doi: 10.1039/A901621J

Kövári, E., and Krämer, R. (1996). Rapid phosphodiester hydrolysis by an ammonium-functionalized Copper(II) complex. A model for the cooperativity of metal ions and NH-acidic groups in phosphoryl transfer enzymes. *J. Am. Chem. Soc.* 118, 12704–12709. doi: 10.1021/ja962806y

Krauser, J. A., Joshi, A. L., and Kady, I. O. (2010). Metal complexes of modified cyclen as catalysts for hydrolytic restriction of plasmid DNA. *J. Inorg. Biochem.* 104, 877–884. doi: 10.1016/j.jinorgbio.2010.04.007

Lee, C., Yang, W., and Parr, R. G. (1988). Development of the Colle-Salvetti correlation-energy formula into a functional of the electron density. *Phys. Rev. B* 37, 785–789. doi: 10.1103/PhysRevB.37.785

Li, Y., Lu, X.-M., Sheng, X., Lu, G.-Y., Shao, Y., and Xu, Q. (2007). DNA cleavage promoted by Cu2+ complex of cyclen containing pyridine subunit. *J. Incl. Phenom. Macrocycl. Chem.* 59, 91–98. doi: 10.1007/s10847-007-9299-y

Luedtke, N. W., and Schepartz, A. (2005). Lanthanide-mediated phosphoester hydrolysis and phosphate elimination from phosphopeptides. *Chem. Commun.* 43, 5426–5428. doi: 10.1039/B510123A

Luong, T. K. N., Mihaylov, T. T., Absillis, G., Shestakova, P., Pierloot, K., and Parac-Vogt, T. N. (2016). Phosphate ester bond hydrolysis promoted by lanthanide-substituted keggin-type polyoxometalates studied by a combined experimental and density functional theory approach. *Inorg. Chem.* 55, 9898–9911. doi: 10.1021/acs.inorgchem.6b01802

Mancin, F., Scrimin, P., and Tecilla, P. (2012). Progress in artificial metallonucleases. *Chem. Commun.* 48, 5545–5559. doi: 10.1039/C2CC3 0952A

Mancin, F., and Tecilla, P. (2007). Zinc(ii) complexes as hydrolytic catalysts of phosphate diester cleavage: from model substrates to nucleic acids. *New J. Chem.* 31, 800–817. doi: 10.1039/B703556J

Mikkola, S., Kaukinen, U., and Lönnberg, H. (2001). The effect of secondary structure on cleavage of the phosphodiester bonds of RNA. *Cell Biochem. Biophys.* 34, 95–119. doi: 10.1385/cbb:34:1:95

Mitić, N., Smith, S. J., Neves, A., Guddat, L. W., Gahan, L. R., and Schenk, G. (2006). The catalytic mechanisms of binuclear metallohydrolases. *Chem. Rev.* 106, 3338–3363. doi: 10.1021/cr050318f

Mol, C. D., Izumi, T., Mitra, S., and Tainer, J. A. (2000). DNA-bound structures and mutants reveal abasic DNA binding by APE1 DNA repair and coordination. *Nature* 403, 451–456. doi: 10.1038/35000249

Neidle, S. (2008). "The building-blocks of DNA and RNA," in *Principles of Nucleic Acid Structure,* ed S. Neidle. (New York, NY: Academic Press), 20–37.

Niittymaki, T., and Lonnberg, H. (2006). Artificial ribonucleases. *Org. Biomol. Chem.* 4, 15–25. doi: 10.1039/b509022a

Oivanen, M., Kuusela, S., and Lönnberg, H. (1998). Kinetics and mechanisms for the cleavage and isomerization of the phosphodiester bonds of RNA by brønsted acids and bases. *Chem. Rev.* 98, 961–990. doi: 10.1021/cr960425x

Perdew, J. P., Burke, K., and Ernzerhof, M. (1996). Generalized gradient approximation made simple. *Phys. Rev. Lett.* 77, 3865–3868. doi: 10.1103/PhysRevLett.77.3865

Rammo, J., Hettich, R., Roigk, A., and Schneider, H.-J. (1996). Catalysis of DNA cleavage by lanthanide complexes with nucleophilic or intercalating ligands and their kinetic characterization. *Chem. Commun.* 105–107. doi: 10.1039/CC9960000105

Reed, A. E., and Weinhold, F. (1983). Natural bond orbital analysis of near-Hartree–Fock water dimer. *J. Chem. Phys.* 78, 4066–4073. doi: 10.1063/1.445134

Richman, J. E., and Atkins, T. J. (1974). Nitrogen analogs of crown ethers. *J. Am. Chem. Soc.* 96, 2268–2270. doi: 10.1021/ja00814a056

Robinson, H., Jung, K.-E., Switzer, C., and Wang, A. H. J. (1995). DNA with 2'-5' phosphodiester bonds forms a duplex structure in the A-type conformation. *J. Am. Chem. Soc.* 117, 837–838. doi: 10.1021/ja00107a036

Sancar, A., and Sancar, G. B. (1988). DNA repair enzymes. *Annu. Rev. Biochem* 57, 29–67. doi: 10.1146/annurev.bi.57.070188.000333

Sharp, P. A. (1985). On the origin of RNA splicing and introns. *Cell* 42, 397–400. doi: 10.1016/0092-8674(85)90092-3

Shionoya, M., Ikeda, T., Kimura, E., and Shiro, M. (1994). Novel "Multipoint" molecular recognition of nucleobases by a New Zinc(II) complex of acridine-pendant cyclen (Cyclen = 1,4,7,10-Tetraazacyclododecane). *J. Am. Chem. Soc.* 116, 3848–3859. doi: 10.1021/ja00088a021

Sosa, M. E., and Tobe, M. L. (1985). Proton exchange and base hydrolysis of syn,anti-cis-dichloro(1,4,7,10-tetra-azacyclododecane)cobalt(III) cations. *J. Chem. Soc. Dalton Trans.* 475–477. doi: 10.1039/DT9850000475

Sreedhara, A., and Cowan, J. A. (2001). Catalytic hydrolysis of DNA by metal ions and complexes. *J. Biol. Inorg. Chem.* 6, 337–347. doi: 10.1007/s007750100209

Subat, M., Woinaroschy, K., Gerstl, C., Sarkar, B., Kaim, W., and Konig, B. (2008). 1,4,7,10-tetraazacyclododecane metal complexes as potent promoters of phosphodiester hydrolysis under physiological conditions. *Inorg. Chem.* 47, 4661–4668. doi: 10.1021/ic702413q

Sullivan, K. P., Yin, Q., Collins-Wildman, D. L., Tao, M., Geletii, Y. V., Musaev, D. G., et al. (2018). Multi-tasking POM Systems. *Front Chem.* 6:365. doi: 10.3389/fchem.2018.00365

The, L. (1998). Organophosphorus compounds: good, bad, and difficult. *Lancet* 352:499. doi: 10.1016/S0140-6736(98)21033-6

Weisman, G. R., and Reed, D. P. (1996). A new synthesis of cyclen (1,4,7,10-Tetraazacyclododecane). *J. Org. Chem.* 61, 5186–5187. doi: 10.1021/jo9606665

Weston, J. (2005). Mode of Action of Bi- and trinuclear zinc hydrolases and their synthetic analogues. *Chem. Rev.* 105, 2151–2174. doi: 10.1021/cr020057z

Wilcox, D. E. (1996). Binuclear metallohydrolases. *Chem. Rev.* 96, 2435–2458. doi: 10.1021/cr950043b

Wilkinson, G., Gillard, R. D., and Mccleverty, J. A. (1987). *Comprehensive Coordination Chemistry: The Synthesis, Reactions, Properties & Applications of Coordination Compounds.* Oxford: Pergamon Press.

Williams, N. H., Takasaki, B., Wall, M., and Chin, J. (1999). Structure and nuclease activity of simple dinuclear metal complexes: quantitative dissection of the role of metal ions. *Acc. Chem. Res.* 32, 485–493. doi: 10.1021/ar9500877

Williams, N. H., and Wyman, P. (2001). Base catalysed phosphate diester hydrolysis. *Chem. Commun.* 1268–1269. doi: 10.1039/B103317B

Yoji, Y., Akihiko, U., Akira, W., Hiroyuki, A., and Makoto, K. (2006). Chemical-reaction-based site-selective DNA cutter for PCR-free gene manipulation. *Chem. Bio. Chem.* 7, 673–677. doi: doi: 10.1002/cbic.200500402

Zhang, G., Liu, C., Long, D.-L., Cronin, L., Tung, C.-H., and Wang, Y. (2016a). Water-soluble pentagonal-prismatic titanium-oxo clusters. *J. Am. Chem. Soc.* 138, 11097–11100. doi: 10.1021/jacs.6b06290

Zhang, T., Sharma, G., Paul, T. J., Hoffmann, Z., and Prabhakar, R. (2017). Effects of ligand environment in Zr(IV) assisted peptide hydrolysis. *J. Chem. Inf. Model.* 57, 1079–1088. doi: 10.1021/acs.jcim.6b00781

Zhang, T., Zhu, X., and Prabhakar, R. (2014). Peptide hydrolysis by metal-cyclen complexes and their analogues: insights from theoretical studies. *Organometallics* 33, 1925–1935. doi: 10.1021/om400903r

Zhang, X., Liu, X., Phillips, D. L., and Zhao, C. (2016b). Mechanistic insights into the factors that influence the DNA nuclease activity of mononuclear facial copper complexes containing hetero-substituted cyclens. *ACS Catal.* 6, 248–257. doi: 10.1021/acscatal.5b01735

Zhao, Y., and Truhlar, D. G. (2006). A new local density functional for main-group thermochemistry, transition metal bonding, thermochemical kinetics, and noncovalent interactions. *J. Chem. Phys.* 125:194101. doi: 10.1063/1.2370993

Check for
updates

Mechanistic Studies of Homo- and Heterodinuclear Zinc Phosphoesterase Mimics: What Has Been Learned?

Andrea Erxleben*

School of Chemistry, National University of Ireland Galway, Galway, Ireland

Phosphoesterases hydrolyze the phosphorus oxygen bond of phosphomono-, di- or triesters and are involved in various important biological processes. Carboxylate and/or hydroxido-bridged dizinc(II) sites are a widespread structural motif in this enzyme class. Much effort has been invested to unravel the mechanistic features that provide the enormous rate accelerations observed for enzymatic phosphate ester hydrolysis and much has been learned by using simple low-molecular-weight model systems for the biological dizinc(II) sites. This review summarizes the knowledge and mechanistic understanding of phosphoesterases that has been gained from biomimetic dizinc(II) complexes, showing the power as well as the limitations of model studies.

Keywords: zinc, hydrolysis (esters), phosphatase, biomimicry, catalysis

INTRODUCTION

The hydrolytic cleavage of phosphate esters is an important biochemical reaction in living systems, playing a fundamental role in energy metabolism (Berg et al., 2010), DNA repair (Cowan, 1998), RNA splicing (Kuimelis and McLaughlin, 1998), and signaling (Berg et al., 2010). It is relevant to the breaking down of bone material by osteoclasts (bone resorbing cells) in mammals and to the absorption and mobilization of phosphorus in plants (Cashikar et al., 1997; Oddie et al., 2000; Cleland and Hengge, 2006; Mitić et al., 2006; Schenk et al., 2013; Daumann et al., 2014). In certain bacteria phosphotriesterases have evolved that can hydrolyze organophosphates including insecticides and chemical warfare agents (Donarski et al., 1989; Dumas et al., 1990).

Under physiological conditions, phosphate esters are highly resistant toward hydrolysis (Cleland and Hengge, 2006). The half-life of a phosphodiester bond in the backbone of DNA has been estimated to be on the order of hundreds to thousands of millions of years (Williams et al., 1999; Schroeder et al., 2006). Yet DNAses can cleave DNA within seconds to minutes (Cowan, 1998). The majority of enzymes that catalyze phosphate ester hydrolysis contain two or more metal ions in their active site. Zn^{2+}, which is a strong Lewis acid, labile and not redox active, is ideally suited for biological hydrolysis reactions. The use of metal complexes that mimic the structure and function of a metalloenzyme is a well-established approach in bioinorganic chemistry to develop highly effective catalysts modeled after nature and to gain a molecular level understanding of the enzymatic mechanism. In the late 1970s and 1980s pioneering work by the groups of Sargeson (Anderson et al., 1977; Jones et al., 1983; Hendry and Sargeson, 1989), Breslow (Gellman et al., 1986; Breslow et al., 1989), and Chin (Chin, 1991) among others gave the first insight into the role of the metal ion(s) in the mechanisms of phosphoester hydrolysis by metallohydrolases.

Using phosphate esters with good leaving groups and kinetically inert mononuclear Co(III) complexes, metal-catalyzed hydrolysis reactions were shown to proceed through the following mechanisms: (i) Lewis acid activation, in which the metal polarizes the P-O bond and activates the phosphorus for nucleophilic attack (**Figure 1A**); (ii) metal hydroxide activation, in which the metal generates (metal-bound) hydroxide to act as an efficient nucleophile at pH 7 or as a general base (**Figures 1B,C**); (iii) stabilization of the leaving group (**Figure 1D**); and (iv) combinations of (i), (ii), and (iii). Mechanistic information was obtained through detailed kinetic studies including the measurement of rate-pH profiles and kinetic isotope effects. The rate accelerations achieved by the different activation modes could be quantified (Williams et al., 1999). Kimura and coworkers used macrocyclic dinuclear Zn(II) complexes to study the relationship between the number and type of donor atoms and the catalytic efficiency (Koike and Kimura, 1991). Later, the work was extended to dinuclear complexes that model the cooperativity of the metal ions in bimetallic hydrolases and to metal complexes, with pendant functional groups to mimic secondary interactions between the substrate and amino acid side chains in the active site of metalloenzymes (Young and Chin, 1995; Kimura, 2000; Daumann et al., 2014). A lot of what has been learned through the early studies has informed the rational design of highly efficient catalysts, often with non-biological metals such as lanthanides (Franklin, 2001; Liu and Wang, 2009). Metal complex-based hydrolysis catalysts have been discussed in several excellent review articles (Franklin, 2001; Mancin and Tecilla, 2007; Liu and Wang, 2009; Desbouis et al., 2012; Yu and Cowan, 2018).

The increasing role of computational chemistry has led to a renewed interest in mechanistic questions and a significant number of theoretical and combined theoretical and experimental studies have been published that investigated the mechanistic pathways in detail. This review intends to give a concise account of the contribution of experimental and computational studies of dinuclear biomimetic zinc(II) complexes to our current understanding of the mechanistic details of enzymatic phosphate ester hydrolysis with a focus on the recent literature.

PHOSPHOMONOESTER HYDROLYSIS

The half-life for the spontaneous hydrolysis of dianionic phosphomonoesters, $ROP(O)_3^{2-}$,

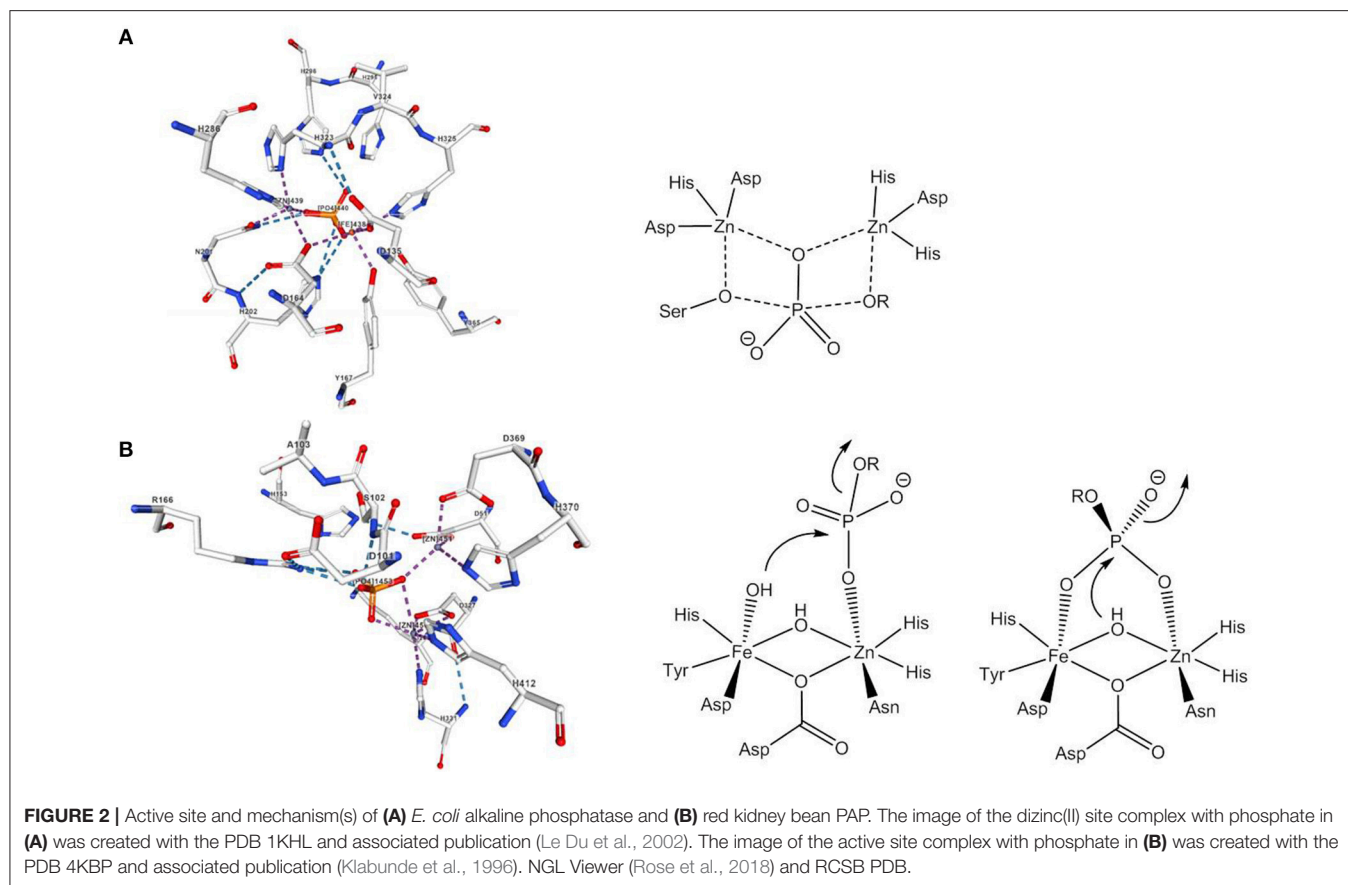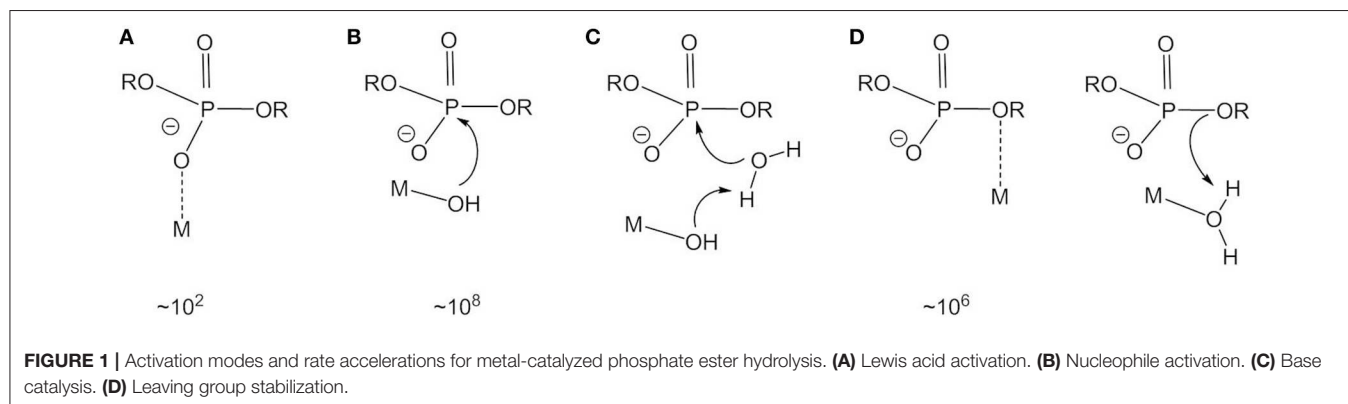$$ROP(O)_3^{2-} + H_2O \rightarrow HPO_4^{2-} + ROH$$
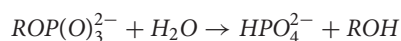
is on the order of 10^{12} years at ambient temperature (Lad et al., 2002). In principle the reaction can proceed through different mechanisms; a dissociative mechanism involving a PO_3^- intermediate ($D_N + A_N$), an associative mechanism with a five-coordinate phosphorane intermediate ($A_N + D_N$) or a concerted mechanism (A_ND_N) with an associative or dissociative transition state depending on the synchronicity of bond formation and departure of the leaving group.

In nature, the hydrolysis of phosphomonoesters is catalyzed by phosphomonoesterases such as alkaline phosphatase, purple acid phosphatase or inositol monophosphatase. The active site of alkaline phosphatase from *E. coli* contains two Zn^{2+} ions and a Mg^{2+} ion (Le Du et al., 2002). One of the phosphoryl oxygens is coordinated by the two Zn^{2+} ions, which also bind the nucleophile, a deprotonated serine, and the leaving group, respectively (**Figure 2A**). Experimental and theoretical data agree with a dissociative mechanism (Zalatan et al., 2007; López-Canut et al., 2009). Probably the best studied phosphomonoesterases are purple acid phosphatases (PAPs). PAPs are non-specific hydrolases that cleave a variety of phosphate esters and anhydrides at acidic pH. They contain a heterodinuclear Fe(III)-M(II) site and their characteristic purple color is due to a tyrosinate-to-Fe(III) ligand-to-metal charge transfer at about 560 nm (Mitić et al., 2006). The active site of red kidney bean PAP in which the divalent metal ion is Zn(II) (Sträter et al., 1995) is shown in **Figure 2B**. Although the sequence homology between PAPs from different sources is low, the seven amino acids that constitute the primary coordination sphere of the Fe(III)-M(II) core are conserved in all PAPs. The mechanism proposed by Klabunde et al. involves the monodentate coordination of the phosphate ester to the divalent metal ion followed by nucleophilic attack by Fe(III)-bound hydroxide (Klabunde et al., 1996). The strong Lewis acidity of Fe(III) allows the formation of Fe(III)-OH at acidic pH. For sweet potato PAP an alternative mechanism with bridging phosphate ester coordination and nucleophilic attack by a μ-(hydr)oxide was suggested (Schenk et al., 2005). Ga(III) can replace Fe(III) in the active site and studies indicated that PAPs can switch between the two mechanisms depending on the metal ion composition/availability/solubility, the second coordination sphere, the actual substrate, and the pH value ("one enzyme–two mechanisms" hypothesis; Mitić et al., 2006; Smith et al., 2007). While a bridging oxide would be an efficient nucleophile, the nucleophilicity of a hydroxide that is tightly bound to two metals should be rather low. It was therefore suggested that the bridging hydroxide in hydrolytic enzymes shifts to a (*pseudo*-)terminal position on binding of the substrate (Bennett and Holz, 1997; Wang et al., 1999). Computational evidence for such a μ-OH shift was seen in model systems for phosphodiesterases and will be discussed in the next section.

In contrast to the large number of studies on the catalysis of phosphodiester hydrolysis, the cleavage mechanism of phosphomonoesters by biomimetic zinc(II) complexes is little investigated (Anbu et al., 2012; Zhang et al., 2014a,c; Sanyal et al., 2015). In recent years, various studies have been aimed at elucidating the role of the heterodimetallic Fe(III)-Zn(II) site in PAP. However, the substrate employed is generally the phosphodiester bis (2,4-dinitrophenyl) phosphate (BDNPP), a widely used model for the phosphodiester linkages in DNA. Heterodinuclear Fe(III)-Zn(II) biomimetics that mostly do not show monophosphatase activity will therefore be discussed in the section on phosphodiester hydrolysis.

Phosphomonoester hydrolysis by dizinc(II) complexes is usually studied using 4-nitrophenyl phosphate as an ester with a good leaving group (NPP, **Figure 3**). The mechanism of the hydrolysis of the NPP^{2-} dianion is generally believed

FIGURE 1 | Activation modes and rate accelerations for metal-catalyzed phosphate ester hydrolysis. **(A)** Lewis acid activation. **(B)** Nucleophile activation. **(C)** Base catalysis. **(D)** Leaving group stabilization.

FIGURE 2 | Active site and mechanism(s) of **(A)** *E. coli* alkaline phosphatase and **(B)** red kidney bean PAP. The image of the dizinc(II) site complex with phosphate in **(A)** was created with the PDB 1KHL and associated publication (Le Du et al., 2002). The image of the active site complex with phosphate in **(B)** was created with the PDB 4KBP and associated publication (Klabunde et al., 1996). NGL Viewer (Rose et al., 2018) and RCSB PDB.

to be concerted with a loose transition state, while for phosphomonoester monoanions a dissociative mechanism involving metaphosphate as the intermediate has not been ruled out (Cleland and Hengge, 2006; Klähn et al., 2006; Kamerlin and Wilkie, 2007; Zhang et al., 2014a,c; Sanyal et al., 2015). The dianion is less reactive than the monoanion due to the higher negative charge of the transition state.

Kandaswamy and coworkers synthesized dizinc(II) complexes with a series of dinucleating, oxyimine-based macrocyclic ligands (Anbu et al., 2012, **Figure 3**). The dizinc complex of the symmetric ligand H_2L1^a that had the shortest

Zn(II)···Zn(II) distance and the least distorted geometry hydrolyzed monoanionic NPP[−] with a higher k_{cat} value than did the analogous complexes of unsymmetric H_2L1^{b-f}. The reaction kinetics showed a change in the reaction order at higher complex concentrations. Zhao and coworkers carried out DFT calculations to investigate the reaction mechanism (Zhang et al., 2014a,c). Different competitive catalytic mechanisms were found, depending on the concentration of the complex. At high concentrations two dinuclear entities form a hydroxido-bridged dimer that binds NPP[−] to give the catalyst-substrate complex. Substrate coordination to two dizinc(II) entities

FIGURE 3 | Substrate (NPP) and ligands in dinuclear Zn(II) complexes used to study phosphomonoester hydrolysis.
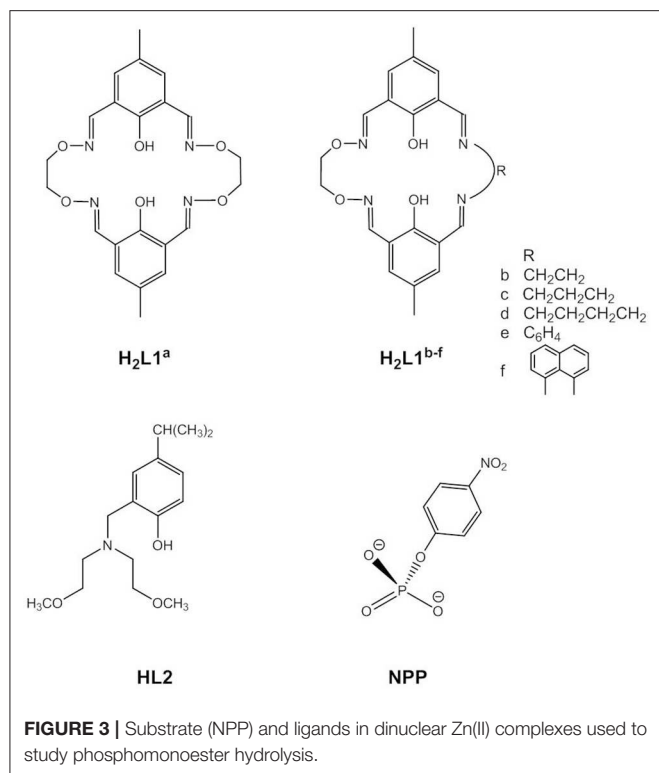
is also favored in the medium concentration range. More relevant to the enzymatic reaction, at low concentrations NPP$^-$ binds in a monodentate fashion to the catalytic species trans-[Zn$_2$**L1**^{a}(H$_2$O)(OH)]$^+$ followed by nucleophilic attack by Zn-OH to give a distorted trigonal bipyramidal phosphorane transition state (**Figure 4**). Substrate binding is stabilized by hydrogen bonding between the P-OH proton and Zn-OH. Cleavage of the P-O bond to the leaving group and protonation of the leaving group oxygen occur concurrently. In the case of unsymmetrical trans-[Zn$_2$**L1**^{f}(H$_2$O)(OH)]$^+$ hydrogen bonding between Zn-OH and P=O and between P-OH and Zn-OH exists in the catalyst-substrate complex (Zhang et al., 2014c). Again, the theoretical calculations indicated a concerted mechanism involving simultaneous bond formation to the nucleophile and breaking of the bond to the leaving group in the transition state. The P-OH proton forms a H-bond with the leaving group oxygen in the transition state and proton transfer and P-O bond cleavage are simultaneous. Modeling of a transition state with one phosphoryl atom coordinated to both Zn(II) centers of Zn**L1**^{f} and one Zn(II) additionally binding to the leaving group oxygen demonstrated that metal-induced leaving group activation is less favorable than proton transfer-assisted leaving group departure. In the calculated mechanisms NPP$^-$ binds to the Zn(II) in the imine site, while the Zn(II) in the oxyimine site provides the nucleophile. The authors argued that the more electronegative oxygen atoms next to the imine nitrogens strengthen the Zn-N bonds and weaken the bond to the nucleophile. However, the X-ray structure of [Zn$_2$**L1**^{c}(H$_2$O)$_2$](ClO$_4$)$_2$·3H$_2$O revealed no significant differences in the Zn-N and Zn-OH$_2$ bond lengths between both binding sites. Furthermore, other studies

led to the opposite conclusion that electron-withdrawing substituents result in a stronger M-OH bond and thus decrease the nucleophilicity of metal-bound hydroxide by increasing the Lewis acidity of the metal ion (Coleman et al., 2010).

In the 2:2 complexes [Zn$_2$**L2**$_2$X$_2$] (X = Cl, Br, I) two Zn(II)**L2** entities are linked through two phenoxide bridges. X-ray analysis revealed the expected trans orientation of the two halides and Zn(II)···Zn(II) distances around 3.1 Å, i.e., close to the metal-metal distance in zinc hydrolases (Sanyal et al., 2015). The phosphatase activity toward NPP^{2-} was studied in aqueous DMF, although it is not clear if the dinuclear structure is retained in solution. Theoretical calculations were described in the same paper and suggested that the D-cis form of the dinuclear complex is slightly more catalytically favorable than the D-trans form. In contrast to the macrocyclic complexes, a concerted reaction mechanism involving bidentate coordination of the phosphomonoester to both Zn(II) was found to be most favorable. One of the phenoxide bridges is replaced with a hydroxide so that Zn retains the more stable five-coordinate geometry. This bridging hydroxide serves as the nucleophile as proposed for sweet potato PAP (**Figure 2B**).

PHOSPHODIESTER HYDROLYSIS

Hydrolysis of DNA Model Substrates

It is assumed that the uncatalyzed hydrolysis of phosphodiesters proceeds via a concerted mechanism with a loose transition state (Hengge, 2002). An example for a Zn(II) containing phosphodiesterase is P1 nuclease that cleaves single-stranded RNA and DNA into mononucleotides. P1 nuclease has a trimetallic active site; Zn3 binds to the phosphodiester group, while a hydroxide that bridges Zn1 and Zn2 at a distance of 3.2 Å is believed to act as the nucleophile (Volbeda et al., 1991; **Figure 5**).

Many phosphodiesterase mimics have been designed with bridging acetate ligands and it is generally assumed that these are substituted by terminal and/or bridging hydroxide ligands in aqueous solution. It has also been shown that phosphodiesters can readily replace carboxylate ligands in dizinc(II) complexes (Daumann et al., 2013). The most popular models for the phosphodiester linkages in DNA are bis(2,4-dinitrophenyl) phosphate, BDNPP, and bis(4-nitrophenyl) phosphate, BNPP, (**Figure 6**) that are usually converted to 2,4-dinitrophenyl phosphate and 4-nitrophenyl phosphate without further hydrolysis of the respective monoester taking place.

Based on kinetic data, X-ray analysis of the complex cocrystallized with a phosphodiester and binding studies, the following mechanisms have been assigned to dinuclear zinc(II) catalysts; (i) monodentate coordination of the phosphodiester to one Zn(II) and nucleophilic attack by OH bound to the other Zn(II) (Bazzicalupi et al., 2004; Jarenmark et al., 2010; Pathak et al., 2018) or to the same Zn(II) (Massoud et al., 2016); (ii) nucleophilic attack by Zn-OH on the bridging substrate (Bazzicalupi et al., 1997, 2004; Daumann et al., 2012, 2013; Brown et al., 2016) and (iii) nucleophilic attack of the bridging substrate by a bridging hydroxide (Das et al., 2014, 2018; Montagner et al., 2014; Daver et al., 2016). As discussed above, a shift of μ-OH to a

FIGURE 4 | Catalytic species and proposed mechanism for NPP$^-$ hydrolysis by the dizinc(II) complex of **H$_2$L1**^{a}.

FIGURE 5 | (A) Active site of nuclease from Aspergillus oryzae with a coordinated phosphate. **(B)** Mechanism of phosphodiester hydrolysis catalyzed by P1 nuclease. The image in **(A)** was created with the PDB 5FBA and associated publication (Koval et al., 2016). NGL Viewer (Rose et al., 2018) and RCSB PDB.

terminal position in mechanism (iii) would render the attacking hydroxide a better nucleophile. Das et al. carried out DFT calculations on the hydrolysis of BDNPP by the unsymmetric dinuclear Zn(II) complex [Zn$_2$**L3**(μ-OH)]$^+$ (**Figure 7**) which indicated that in the first step the phosphodiester binds to

Zn1 in the N_3O_2 site followed by a concerted step with a transition state in which μ-OH is shifted toward Zn1 and the substrate adopts a bridging coordination mode (Das et al., 2014). DFT studies on the dizinc(II) complex of an analogous N_5O_2 ligand containing two 1-methylimidazole moieties (Das

FIGURE 6 | Chemical structures of the DNA models BDNPP and BNPP.
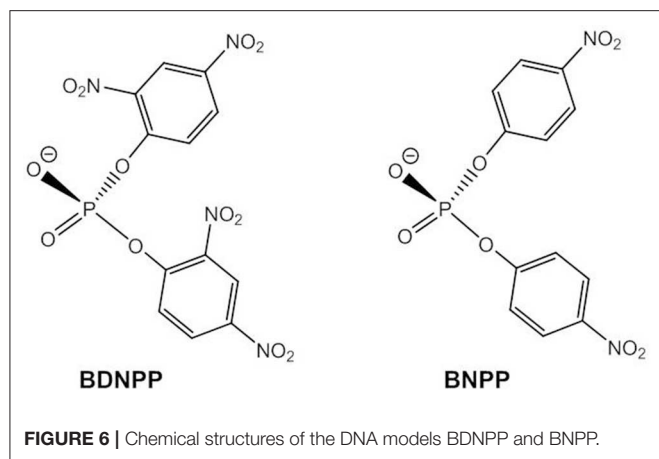
et al., 2018) and on the related unsymmetric dizinc(II) complex $[Zn_2L4(\mu\text{-}OH)(OH)]$ found the same mechanism (Daver et al., 2016). By contrast, DFT calculations of the hydrolysis of BNPP by trans-$[Zn_2(L1^a)(H_2O)(OH)]^+$ suggested a stepwise mechanism involving nucleophilic attack by a terminally Zn-bound hydroxide and formation of the phosphorane intermediate as the rate-determining step (Zhang et al., 2014b). In the calculated mechanism bridging substrate binding also takes place in a stepwise manner with the phosphodiester binding initially via one phosphoryl oxygen to one Zn(II), followed by the formation of a second coordination bond between the nucleophile-binding Zn(II) and the other phosphoryl oxygen. This pathway appears to be favored over a concerted mechanism and over bridging OH acting as the nucleophile. It was noted that the macrocyclic ligand provides a rigid coordination sphere for the dizinc(II) site and imposes a relatively fixed Zn(II)···Zn(II) distance of 3.047 Å, close to the distance between the two phosphoryl oxygens in a phosphodiester (ca. 2.7 Å), which of course should affect the preferred mechanistic pathway.

The ability to provide a (metal-bound) hydroxide at physiological pH value is obviously a key feature of metallophosphatases—or in fact of any hydrolytic metalloenzyme. Binding to two Zn^{2+} ions in dinuclear model systems can decrease the pK_a of the Zn-bound water to below 8; however, as discussed above, a bridging coordination mode of the hydroxide is detrimental to its nucleophilicity. Meyer and coworkers developed a class of highly preorganized pyrazolate-based dizinc(II) complexes that allowed the systematic variation of the Zn(II)···Zn(II) distance (Bauer-Siebenlist et al., 2005; Meyer, 2006). By choosing the appropriate side arms, a large Zn(II)···Zn(II) separation could be enforced that accommodated a Zn-(H)O···HO(H)-Zn motif in which a Zn-bound hydroxide is held by strong hydrogen bonding in an intramolecular O_2H_3 bridge (**Figure 8**). It was shown that the formation of the Zn-(H)O···HO(H)-Zn unit brings about a similar decrease in the pK_a of $Zn\text{-}OH_2$ to around the physiological pH as does the formation of the tightly bridged Zn-(μ-OH_2)-Zn motif.

Another question addressed in model studies concerns the role of Zn-alkoxide. In some metallohydrolases, alcohol moieties are involved in the enzymatic mechanism (Weston, 2005). An

example is alkaline phosphatase, whose two Zn^{2+} ions bind a phosphate ester in a bridging mode which is then nucleophilically attacked by a serine alcoholate. In the next step the P-O bond of the phosphorylated serine intermediate is cleaved following nucleophilic attack by a Zn-bound hydroxide. Alkaline phosphatase catalyzes the hydrolysis of phosphomonoesters under basic conditions. However, model studies were carried out with BDNPP and are therefore discussed in this section. For mononuclear Zn(II) complexes it has been shown that a coordinated alcohol is a better nucleophile than a coordinated water (Koike et al., 1995; Xia et al., 2003; Livieri et al., 2004). On this basis, Chen et al. proposed a mechanism involving nucleophilic attack by a Zn-bound alcoholate for the reaction of $[Zn_2HL5]^{2+}$, with BNPP giving a "transition complex" with the transesterification product covalently attached to the catalyst (Chen et al., 2005). However, the regeneration of the active site remained an open question. Daumann et al. studied the reaction in a $H_2^{16}O/H_2^{18}O/$acetonitrile mixture (Daumann et al., 2012). The observation that ^{18}O was incorporated into the hydrolysis product demonstrated the participation of a Zn-OH nucleophile and a reaction pathway analogous to that of alkaline phosphatase seems possible (**Figure 9A**). The dinucleating macrocycle **HL6** containing an alcohol pendant was designed by Bazzicalupi et al. to model alkaline phosphatase (Bazzicalupi et al., 1999). The dizinc(II) complex contains a Zn-OR and a Zn-OH function and on the basis of ^{31}P NMR data and the characterization of the isolated BNPP cleavage product sequential nucelophilic attack by Zn-OR and Zn-OH was proposed (**Figure 9B**). The complex proved to have a higher reactivity than the parent complex lacking the pendant alcohol group, consistent with Zn-OR presenting the better nucleophile. In contrast to the proposed mechanism for $[Zn_2HL5]^{2+}$, the P-O bond to 4-nitrophenolate is cleaved in the second step which is more in line with its better leaving group property compared to that of the ligand side arm. In other reported model complexes a Zn-bound alcohol group may also adopt the role of an acid catalyst and protonate the leaving group oxygen (Yashiro and Kawahara, 2004).

A DFT study of the cleavage of BDNPP by $[Zn_2H_4L7(OH_{(2)})]^{2+/3+}$ revealed a 10.6 kcal mol^{-1} higher energy barrier for alkoxide-mediated attack than for hydroxide-mediated attack (Brown et al., 2016). Liu et al. observed a 93:7 ratio of hydrolysis to ethanolysis product of methyl-(2-chlorophenyl) phosphate in the presence of $[Zn_2L8]^{4+}$ when the reaction was carried out in ethanol containing 3.8 vol% water (Liu et al., 2008a). A detailed analysis taking into account the ionization constant of water in ethanol and the kinetics of the reaction demonstrated that the catalytically active species is $[Zn_2L8(\mu\text{-}OH)]^{3+}$ and confirmed the large selectivity for activating water as a nucleophile over ethanol. It is also noteworthy that this dizinc(II) complex provides an extremely high rate acceleration of 17 orders of magnitude over the background reaction in 96.2:3.8 ethanol/water (v/v) which is in the same order as the acceleration rates observed for highly efficient enzymatic phosphodiester hydrolysis. The contribution of a synergistic medium effect to this enormous rate enhancement will be discussed in the next section. The catalysis of the methanolysis of a series of methyl aryl phosphate
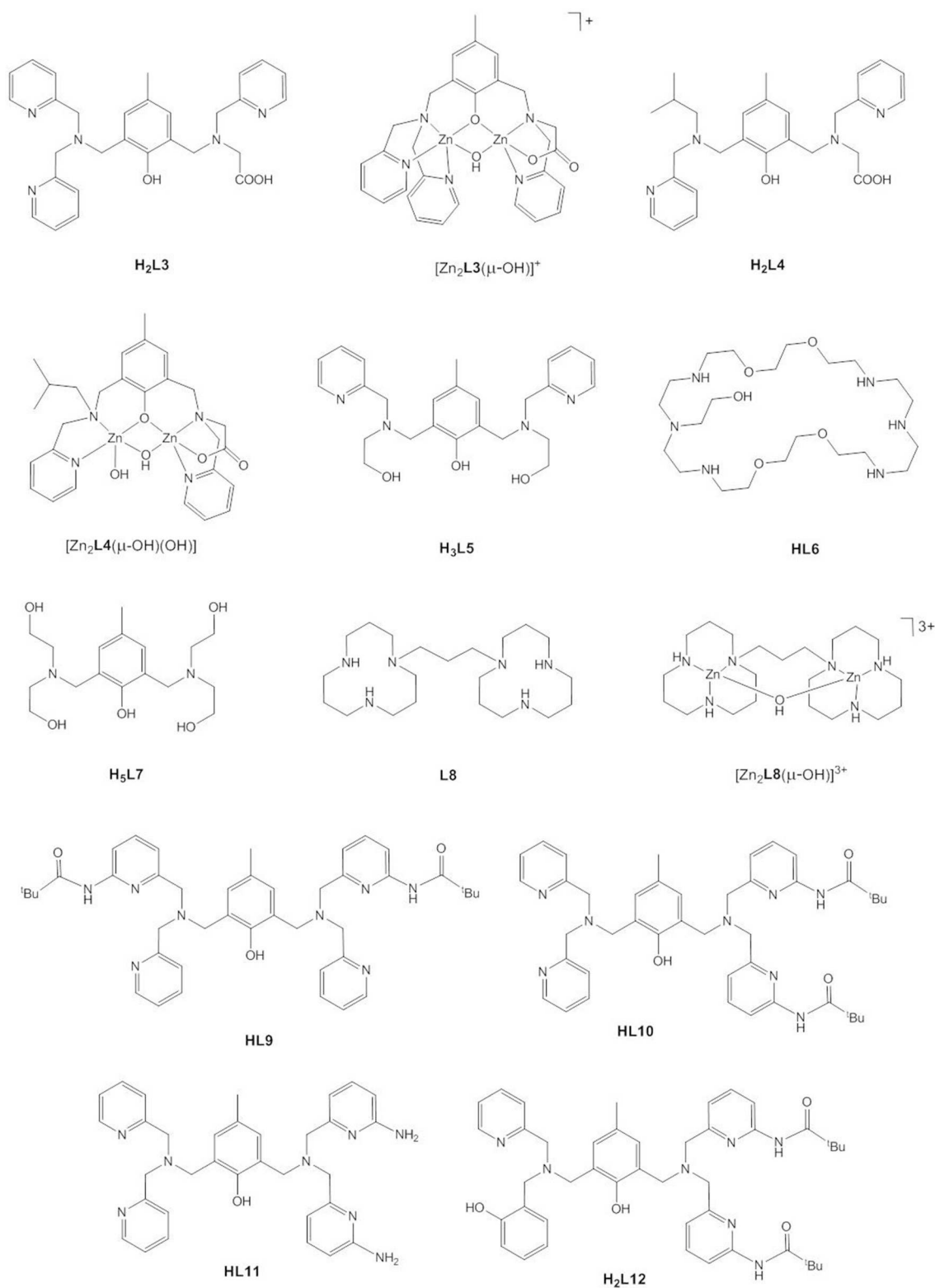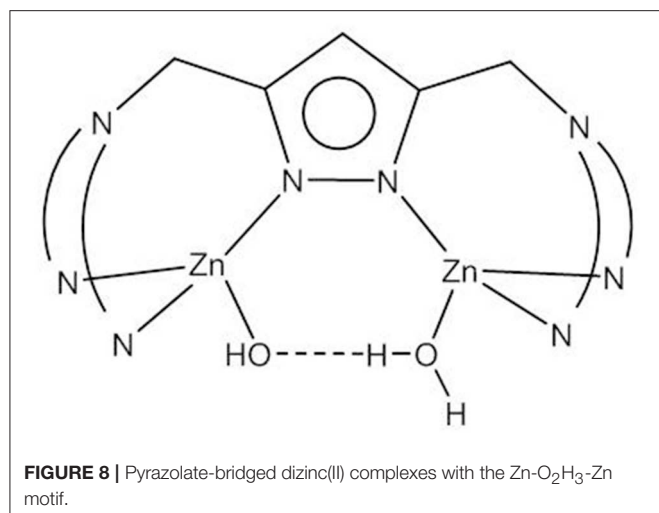
FIGURE 7 | Chemical structures of ligands **H₂L3 – H₂L12** and the dinuclear Zn(II) complexes [Zn₂**L3**(μ-OH)]⁺, [Zn₂**L4**(μ-OH)(OH)], and [Zn₂**L8**(μ-OH)]³⁺.

FIGURE 8 | Pyrazolate-bridged dizinc(II) complexes with the Zn-O$_2$H$_3$-Zn motif.

diesters in methanol by the same complex was investigated and the kinetic data were found to be consistent with a two-step mechanism with rate-limiting formation of the phosphorane intermediate following nucleophilic attack of the bridging substrate by a monocoordinate Zn-methoxide (Neverov et al., 2008). Maxwell et al. reported DFT calculations on the $[Zn_2\mathbf{L8}(\mu\text{-}OCH_3)]^{3+}$-mediated cleavage of 4-nitrophenyl methyl phosphate which gave three viable mechanisms with comparable energy barriers (Maxwell et al., 2013). In all three mechanisms the methoxide dissociates from one Zn(II) and nucleophilic attack on the bridging substrate and expulsion of the leaving group are concerted. The mechanisms differ in whether μ-OCH$_3$ acts as the nucleophile or as a general base by deprotonating an external CH$_3$OH and in whether leaving group departure is assisted by direct metal-binding or via a metal-bound solvent molecule.

Bosch et al. investigated the role of the second coordination sphere and the influence of hydrogen bonding on substrate binding and catalytic activity (Bosch et al., 2014). The presence of amino and pivaloylamide substituents in ortho position to the pyridine nitrogen in **HL9**–**H$_2$L12** led to lower Michaelis-Menten constants and thus higher catalytic efficiencies for hydrolysing BDNPP compared to the unsubstituted complexes. The orientation of the substituents (symmetric substitution in **HL9** vs. unsymmetric substitution in **HL10**) had a crucial influence on the shape of the rate-pH profile (sigmoidal vs. bell-shaped), the kinetic pK$_a$ value, the turnover number, and the maximum reaction rate. The authors also studied the effect of product inhibition and found that at high pH, the dizinc(II) complex of **HL9** formed a less stable product-catalyst complex than [**Zn$_2$L11**], resulting in higher catalytic activity for the former.

For some of the active site mimics that hydrolyzed a DNA model substrate, the DNase activity was also evaluated using plasmid DNA. While there are examples for DNA cleavage activity (Peralta et al., 2010; Anbu et al., 2012; Montagner et al., 2014; Silva et al., 2017; Camargo et al., 2018), it is apparent that factors that are not important for simple phosphodiesters

affect the hydrolysis of macromolecular DNA. Binding to a phosphodiester group in DNA can be sterically hindered by a bulky organic ligand (Massoud et al., 2016). On the other hand, metal complexes can show binding preferences for certain nucleotide sequences or structural motifs due to specific ligand-DNA interactions (Camargo et al., 2018). Thus, model studies as those described in this section should not be seen predominantly as a predictive tool for developing efficient DNA cleavage agents, but as a means of studying the role of a dizinc(II) entity in the hydrolysis of the extremely stable phosphodiester linkages that form the backbone of DNA.

Cleavage of RNA Dinucleotides and RNA Model Substrates

Examples for biological RNA cleavage by a dimetallic site are ribozyme reactions (Steitz and Steitz, 1993) and HIV reverse transcriptase (Davies et al., 1991). RNA is more easily cleaved than DNA due to the 2′-OH group of the ribose ring which can act as an internal nucleophile. As shown in **Figure 10,** intramolecular attack on the phosphorus leads to the formation of a 2′,3′-cyclophosphate. Thus, RNA is not cleaved by hydrolysis but through transesterification. Whether this reaction proceeds by a stepwise mechanism via a pentacoordinated phosphorane intermediate or by a concerted mechanism via a pentacoordinated transition state has been debated. Evidence is now in favor of a two-step process in the case of the base-catalyzed reaction (Perreault and Anslyn, 1997; Oivanen et al., 1998; Lönnberg et al., 2004). At physiological pH the pentacoordinate phosphorane is monoanionic and relatively stable so that it can undergo pseudorotation. As a consequence, migration of the phosphodiester group to the 2′-position of the ribose ring can compete with RNA cleavage (**Figure 10**). In line with the principle of microscopic reversibility the leaving group has to depart from an axial position as the nucleophile attacks at an axial position. Under alkaline conditions the dianionic phosphorane is too short-lived and pseudorotation to an intermediate with the 3′-oxygen and a negatively charged oxygen in the axial positions is too energetically unfavorable for 3′ → 2′ isomerization to occur. Experimental and computational data suggest that the reaction switches to a concerted pathway involving a dianionic pentacoordinate transition state, when the transesterification to the cyclophosphate is catalyzed by metal ions (Bunn et al., 2007; Humphry et al., 2008; Tsang et al., 2009; Edwards et al., 2010). Isomerization is not possible in this case.

2-Hydroxypropyl-p-nitrophenyl phosphate (HPNP, **Figure 10**) is a popular model for the phosphodiester linkages in RNA. The enhanced catalytic activity of various dinuclear zinc(II) complexes relative to their mononuclear analogs is usually attributable to double Lewis acid activation of HPNP adopting a bridging coordination mode. Like the catalysis of the hydrolysis of DNA models, HPNP transesterification is often more efficiently catalyzed by dizinc(II) complexes with unsymmetric ligands that have more available coordination sites to bind the substrate and water/hydroxide for base catalysis (Carlsson et al., 2004; Jarenmark et al., 2008). As the 2′-OH group is an internal, thus more efficient nucleophile, Zn-OH does not
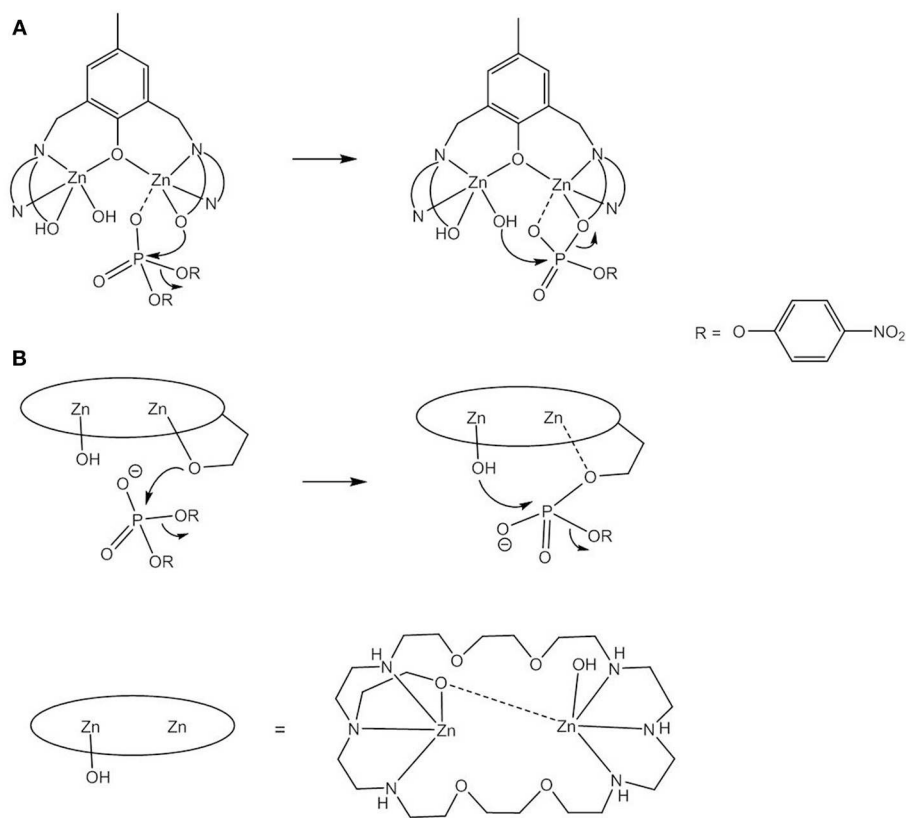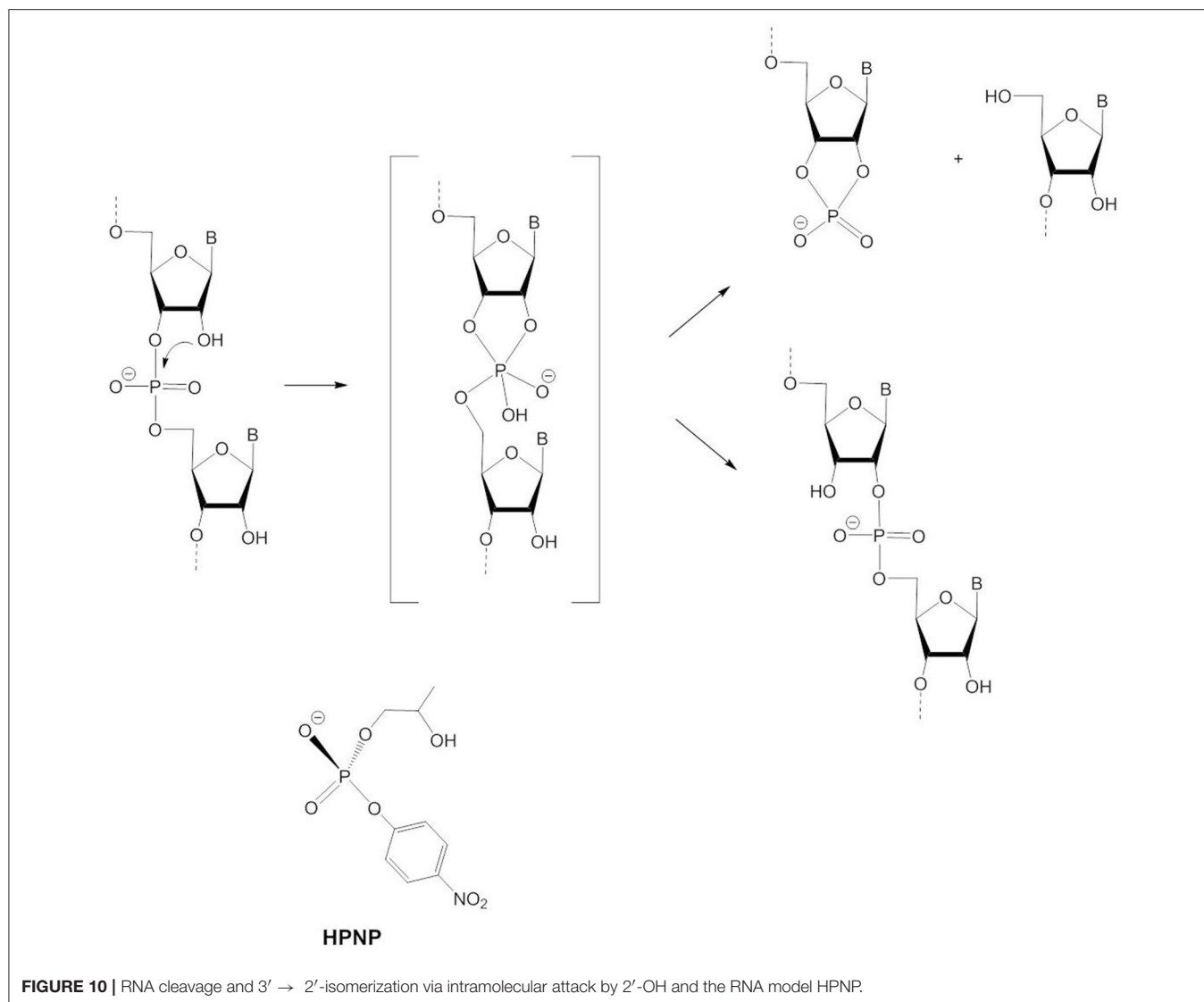
FIGURE 9 | Sequential involvement of a Zn-OR and Zn-OH nucleophile in the cleavage of BNPP by $[Zn_2HL5]^{2+}$ **(A)** and $[Zn_2L6(OH)]^{2+}$ **(B)**.

participate in the reaction mechanism as a nucleophile but serves as a base catalyst. Depending on the model complex and the solvent system, different conclusions were reached regarding the question of whether Zn-OH acts as a general or a specific base catalyst. In general base catalysis, deprotonation of the 2′-OH group by Zn-OH occurs concurrently with nucleophilic attack, while in specific base catalysis the 2'-oxyanion is formed in a pre-equilibrium step prior to rate-determining substrate cleavage.

The dinuclear Zn(II) complex of **L8** is one of the most efficient RNA/HPNP cleavage catalysts reported to date. In methanol, in the presence of one equivalent CH_3O^- $[Zn_2L8]^{4+}$ gives a 10^8-fold rate acceleration of the cleavage of HPNP over the methoxide-catalyzed reaction (Neverov et al., 2006). Tsang et al. carried out a kinetic analysis of the transesterification of different 2-hydroxypropyl-aryl and alkyl esters by $[Zn_2L8(OCH_3)]^{3+}$ and found that the reaction proceeds through a transition state in which the departure of the leaving group has progressed to 45% (Tsang et al., 2009). A DFT study by Maxwell et al. revealed three plausible, competing mechanisms, all involving bridging substrate coordination (Maxwell et al., 2013): (i) direct nucleophilic attack by the metal-bound HPNP alkoxide concurrent with the cleavage of the leaving group bond— the departure of the leaving group is assisted by a terminally bound methanol acting as an H bond donor; (ii) rate-limiting

nucleophilic attack through a general base mechanism leading to a phosphorane intermediate—subsequent bond cleavage is assisted by metal binding and (iii) nucleophilic attack through a general base mechanism and leaving group departure occurring in concert—the expulsion of the leaving group is assisted by hydrogen bonding with a terminally coordinated methanol. While experimental data were reported for the $[Zn_2L8(OCH_3)]^{3+}$-promoted transesterification of HPNP and 2-hydroxypropyl-phenyl phosphate that are consistent with both a concerted and a stepwise mechanism, it has been argued that a stepwise pathway may be more likely because a strong electrostatic interaction between the highly charged dizinc(II) site and the putative dianionic phosphorane should stabilize the intermediate and the transition state leading to it (Bunn et al., 2007). Energetics calculations indicated that the transition state of the catalyzed reaction is stabilized by about −21 to −23 kcal mol^{-1} relative to the transition state of the methoxide reaction. The charge of a phosphodiester increases from −1 to −2 when the catalyst-substrate complex proceeds to the transition state. It has been predicted that the coordination of two metal ions to a phosphate ester monoanion has the same effect as neutralizing it. It is believed that substrate binding to $[Zn_2L8(OCH_3)]^{3+}$ in alcoholic medium takes place in two steps (Bunn et al., 2007); The substrate binds initially as a monodentate ligand to one Zn^{2+} ion and then rearranges to the catalytically

FIGURE 10 | RNA cleavage and 3′ → 2′-isomerization via intramolecular attack by 2′-OH and the RNA model HPNP.

active species with a bridging coordination mode allowing double Lewis acid activation. For substrates with a good leaving group such as 4-nitrophenolate this rearrangement is rate-determining and the following steps of the transesterification reaction are fast. In the case of substrates with a poor leaving group complete equilibrium binding of the substrate occurs and the rate determining step is a chemical one that depends on the pK_a value of the leaving group. Nucleophilic attack is rate-determining when the pK_a of the leaving group is lower than that of the nucleophile. When the leaving group pK_a is greater, fission of the leaving group bond becomes rate-limiting. The change of the rate-determining step from formation to breakdown of the phosphorane intermediate manifests itself as a break in the Brønsted plot (plot of $\log k_{cat}$ vs. leaving group pK_a) at the point where the effective pK_a of the leaving group and the nucleophile are the same. For the transesterification in ethanol in the presence of $[Zn_2\mathbf{L8}(OC_2H_5)]^{3+}$, general-base catalyzed deprotonation of the 2′-OH group by Zn-OC$_2$H$_5$ was proposed. Specific-base

catalysis by an external ethoxide could be excluded, because the cleavage rate in ethanol exceeded the diffusion limit (Liu et al., 2008b). Support for concerted nucleophilic attack and loss of the leaving group comes from a study of the reaction of $[Zn_2\mathbf{L8}(OR)]^{3+}$ with a stable phosphonate analog of HPNP (Edwards et al., 2010). If the slow cleavage of 2-hydroxypropyl phenyl phosphonate were to proceed via a five-coordinate phosphorane intermediate, isomerization to 1-hydroxypropyl phenyl phosphonate should be observed, which was not the case.

In contrast to the general-base catalyzed cleavage of HPNP by $[Zn_2\mathbf{L8}(OC_2H_5)]^{3+}$ in ethanol, experimental data for the related dizinc(II) complex $[Zn_2\mathbf{L13}(OH_2)]^{3+}$ (**Figure 11**) have been interpreted in terms of both general and specific base catalysis. Concerted nucleophilic attack and leaving group loss with specific-base catalysis in aqueous solution is now favored (Iranzo et al., 2003b; Yang et al., 2005; Humphry et al., 2008). Likewise, two conflicting computational studies were reported that came to different conclusions. DFT calculations that were most consistent
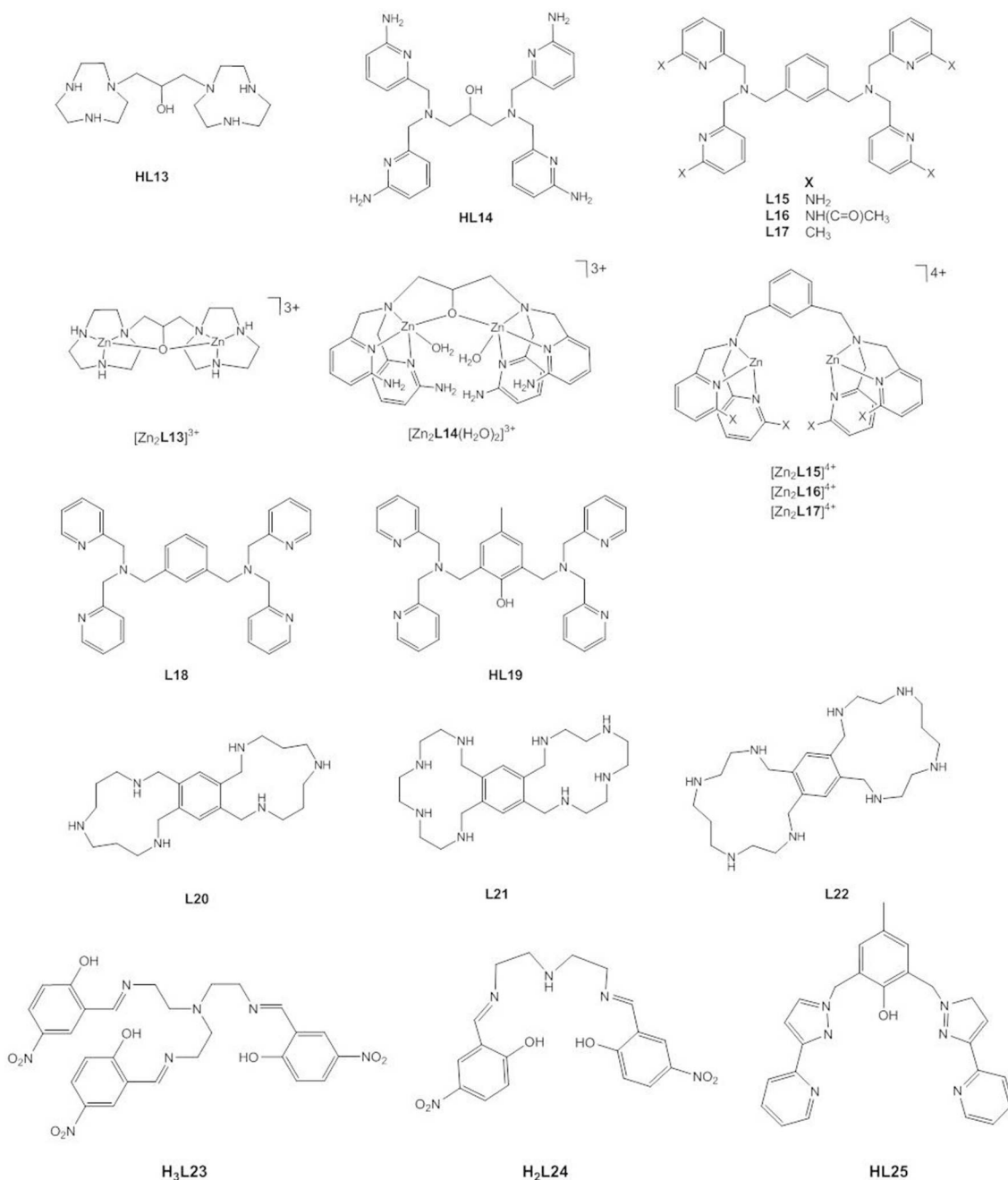
FIGURE 11 | Chemical structures of ligands **HL13–HL25** and the dinuclear Zn(II) complexes [Zn$_2$**L13**]$^{3+}$, [Zn$_2$**L14**(H$_2$O)$_2$]$^{3+}$, [Zn$_2$**L15**]$^{4+}$, [Zn$_2$**L16**]$^{4+}$ and [Zn$_2$**L17**]$^{4+}$.

with the experimental data found the substrate to bind via the two phosphoryl oxygens in a bridging mode and via the nucleophilic 2′-OH group. The pre-equilibrium step involving the activation of the 2′-OH group through specific-base catalysis by Zn-OH is followed by the concerted nucleophilic attack and cleavage of the leaving group bond (Gao et al., 2011). Similar to the mechanism (i) in the DFT study of [Zn$_2$**L8**]$^{4+}$, [Zn$_2$**L13**]$^{3+}$ alters the loose transition state of the uncatalyzed reaction to a more associative

or tight one. The second theoretical study published earlier found the same substrate binding mode but proposed a two-step pathway with general base catalysis (Fan and Gao, 2010). It was pointed out that the large rate accelerations of the cleavage of RNA models provided by [Zn$_2$**L13**]$^{3+}$ were due to the dominant role of electrostatics in stabilizing the dianionic transition state (Iranzo et al., 2003b; Yang et al., 2005, 2007). The densely charged core of two close packed Zn^{2+} ions binds the transition state

with high affinity, leading to a transition state stabilization that is ca. 50% of that estimated for the corresponding enzymatic reaction. Kinetic analysis revealed 2.1 kcal mol^{-1} of greater stabilization of the transition state for the cleavage of uridylyl(3′ → 5′)uridine (UpU) compared to the transition state for the cleavage of uridine-3′-4-nitrophenyl phosphate (UpPNP) which demonstrates that the transition state stabilization of the

developing negative charge on the leaving group oxygen of UpU is stronger than the stabilizing interaction between the catalyst and the C-2′ oxyanion nucleophile at the rate-determining transition state of UpPNP cleavage (O'Donoghue et al., 2006).

Mikkola, Williams and coworkers studied the hydrolysis of HPNP, UpU, and uridine-3′-alkyl phosphates by $[Zn_2L14(H_2O)_2]^{3+}$ and observed that the complex not

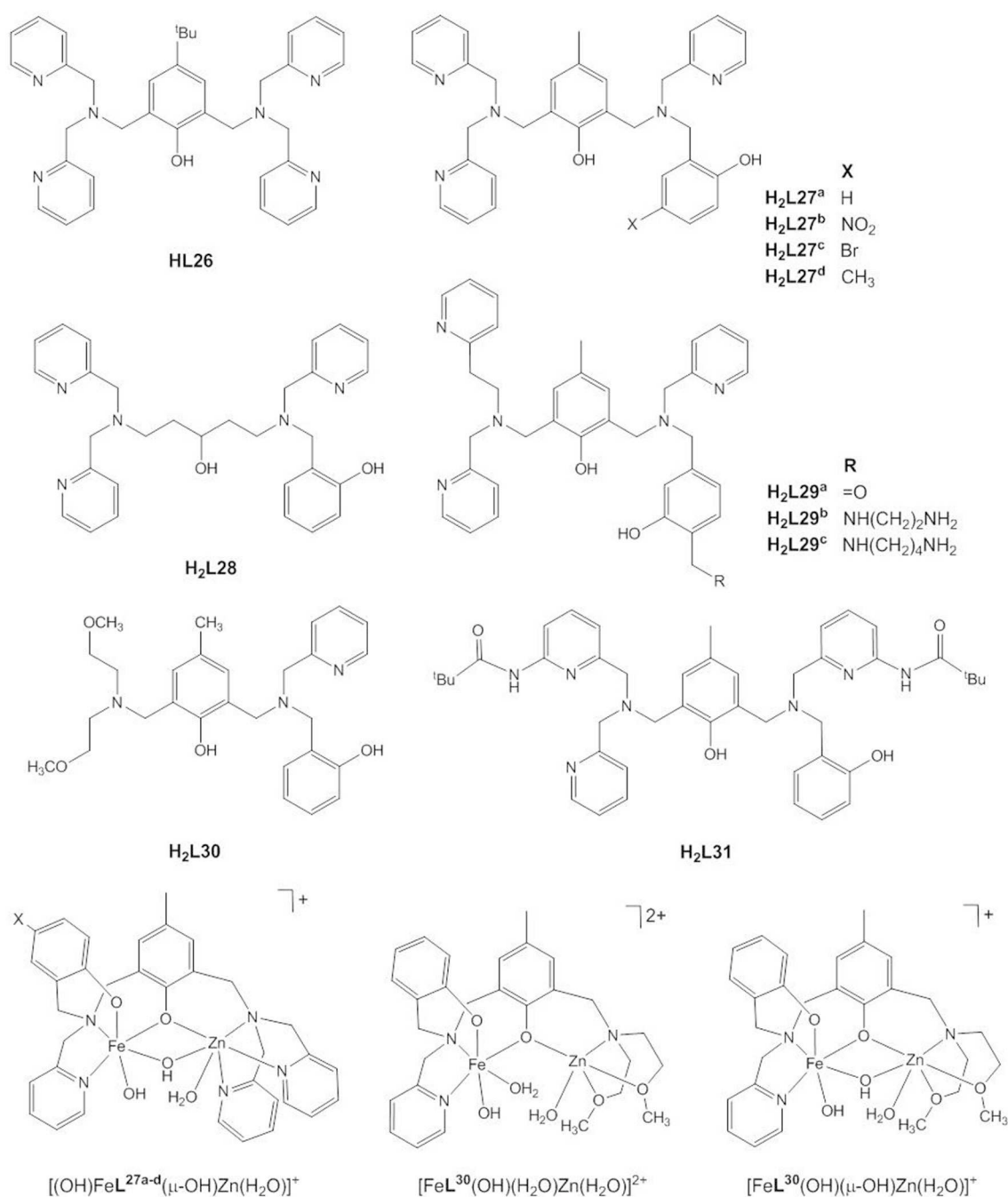**FIGURE 12 |** Chemical structures of ligands **HL26** - **H₂L31** and the catalytically active species [(OH)Fe**L27**$^{a-d}$(μ-OH)Zn(H₂O)]$^{+}$, [Fe**L30**(OH)(H₂O)Zn(H₂O)]$^{2+}$, and [Fe**L30**(OH)(μ-OH)Zn(H₂O)]$^{+}$.

only provides an enormous 10^6-fold rate acceleration of the cleavage reaction in aqueous solution, but also catalyzes the isomerization to the corresponding uridine-2′-alkyl phosphates (Feng et al., 2006; Linjalahti et al., 2008; Korhonen et al., 2012). This means that the dizinc(II) entity stabilizes the phosphorane intermediate sufficiently to allow pseudorotation, and is clear evidence for a stepwise mechanism. It was proposed that the expulsion of the leaving group is the rate-determining step and is general-acid catalyzed. Cocrystallization of the zinc(II) complex with 4-nitrophenyl phosphate confirmed that the phosphoryl oxygen atoms of the bridging phosphate ester are in hydrogen bonding distance of the four amino substituents. By serving as second-sphere H-bond donors, the amino groups contribute to the stabilization of the dianionic phosphorane and provide a further 10^3-fold rate enhancement of the cleavage of HPNP compared to the unsubstituted complex due to tighter binding of the substrate to the catalyst and to the transition state. Again, it becomes clear that charge neutralization by an electrophilic catalyst plays a dominant role. The dinuclear complex stabilizes the phosphorane to the same extent as complete neutralization of one negative charge and to an extent that enables $3′ \rightarrow 2′$ isomerization. The isomerization is catalyzed less efficiently than the cleavage reaction. While binding to the zinc(II) complex stabilizes the phosphorane, it restrains its conformational change required for isomerization to occur.

Interestingly, Mohamed and Brown found that the dizinc(II) complexes of **L15**, **L16**, and **L17**—having amino, acetamido and methyl substituents, respectively—gave similar increases in k_{cat} for the cleavage of HPNP in methanol (Mohamed and Brown, 2010). The kinetic data were interpreted to suggest that hydrogen bonding effects are important for catalysis, but less so for substrate binding. The key conclusion, however, was that the creation of a hydrophobic pocket by the methyl substituents is just as effective as hydrogen bonding. By contrast, methylation of the coordinating nitrogens in **L8** reduces the catalytic efficiency and the synergism between the two Zn^{2+}

ions, most likely due to steric effects that impair substrate binding (Song et al., 2012).

Besides introducing substituents, the linker between the two triaza macrocycles in **L8** was varied (Liu et al., 2009; Guo et al., 2011). When more rigid aromatic linkers were employed, the synergistic effect of the two metals varied between 5- and 700-fold (Guo et al., 2011). Replacing the propylene linker in **L8** with a butylene linker led to an increase in the activation energy ΔG_{cat} of around 1–1.6 kcal mol^{-1}, which was attributed to a less tightly bound substrate-catalyst complex at the transition state (Liu et al., 2009). The presence of the 2-propoxy linker in $[Zn_2\textbf{L13}]^{3+}$ leads to a 37,000-fold decrease in the catalytic activity toward HPNP in methanol compared to $[Zn_2\textbf{L8}(OCH_3)]^{3+}$ (Mohamed et al., 2009). Possible reasons for this include the reduction in Lewis acidity of the Zn^{2+} ions, the higher coordination number of the Zn^{2+} ions, decreased stabilization of the negative charge development in the transition state and the loss of conformational flexibility (Mohamed et al., 2009; Maxwell et al., 2013). DFT calculations showed that the $Zn(II)\cdots Zn(II)$ distance in $[Zn_2\textbf{L8}(OCH_3)]^{3+}$ expands from ca. 3.6 Å to over 5 Å in the intermediates and transition states (Maxwell et al., 2013). Likewise, the dinuclear Zn(II) complex of **L18** is more active in methanol than the analogous complex of **HL19** (Mohamed et al., 2009). Energetics calculations showed a greater stabilization of 3.7 kcal mol^{-1} of the transition state by the former compared to the latter. Interestingly, the situation seems to be different in aqueous solution. In water, the bridging linker is believed to be crucial to achieve cooperativity between the metal ions (Iranzo et al., 2003a; Morrow, 2008). There is no doubt about the importance of medium effects. While the zinc(II) complex of **HL13** is an efficient catalyst in aqueous solution, in ethanol it accelerates the transesterification of HPNP by an impressive 12 orders of magnitude relative to the background reaction at the same $^s_s pH$ (Bunn et al., 2007). It has been proposed that the reduced polarity of the solvent results in desolvation of the ionic components and a better solvation and stabilization of the charge-dispersed transition state (Bunn et al., 2007; Korhonen et al., 2012). The effect of a lower dielectric constant on the binding of ions of opposite charge will increase the catalyst-substrate binding constant. Energetics calculations gave a $\Delta G^{\neq}_{stab}$ of −21 kcal mol^{-1} for the $[Zn_2\textbf{L8}]^{4+}$-mediated cleavage of HPNP in methanol which is close to the $\Delta G^{\neq}_{stab}$ expected for highly efficient phosphodiesterase enzymes (Bunn et al., 2007).

For $[Zn_2\textbf{L19}(\mu\text{-OH})]^{2+}$, a medium effect on the reaction pathway was also described (Selmeczi et al., 2007). DFT calculations indicated that the hydroxypropyl arm of the bridging HPNP is oriented at the hydrogen bonding distance to the μ-OH group. This H-bond facilitates the deprotonation of the attacking nucleophile by the hydroxido bridge. In aqueous solution, a further proton transfer to an external hydroxide takes place, while in a non-aqueous medium (DMSO), the protonated μ-OH$_2$ shifts to a terminal position. In both cases DFT calculations agreed with the concurrent deprotonation of 2′-OH and P-O bond formation, leading to a pentacoordinate phosphorane which, however, appears to be not as viable in the non-aqueous
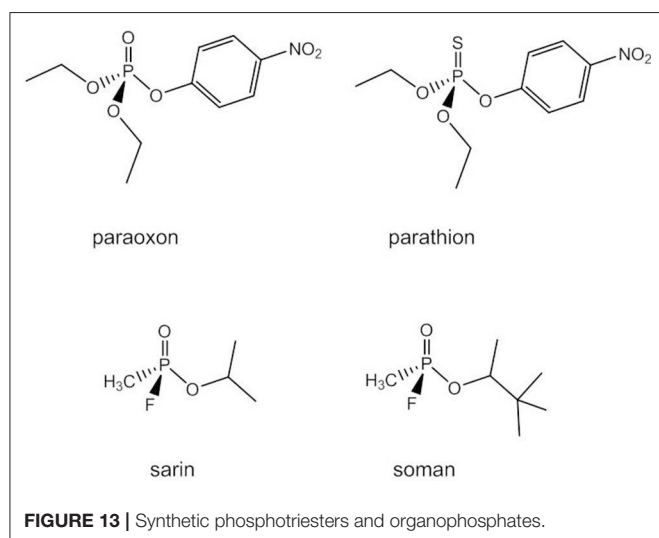

FIGURE 13 | Synthetic phosphotriesters and organophosphates.

medium. In DMSO, the μ_2-$\kappa^1 O$:$\kappa^1 O'$-bridging coordination mode of the cyclophosphate product is in equilibrium with the cyclophosphate forming a monoatomic bridge. This "phosphate shift" was not observed in aqueous solution.

Bim et al. studied dinuclear Zn(II) complexes with the conformationally constrained bis-polyazamacrocycles **L20 – L22** (Bím et al., 2016). Only [Zn$_2$**L20**]$^{2+}$ showed catalytic activity in aqueous buffer. Kinetic data and DFT calculations were consistent with two mechanistic scenarios with similar energy barriers and with the substrate coordinating via the two phosphoryl oxygens to both Zn and via the deprotonated 2-hydroxy group to one Zn (Zn1). In mechanism (1) nucleophilic attack and dissociation of the leaving group take place in two steps. In (2) an additional water molecule binds to Zn2 and the mechanism becomes a one-step process. By contrast, DFT calculations for the unsymmetric complex [Zn$_2$**L4**(μ-OH)(OH)] clearly favor a concerted associative mechanism for HPNP transesterification (Daver et al., 2016). While the deprotonation of the 2-OH nucleophile in a pre-equilibrium step was proposed on the basis of experimental data (Jarenmark et al., 2010), the DFT calculations indicated a significantly lower energy barrier for a general-base mechanism in which the deprotonation of the bridging HPNP by Zn-OH and nucleophilic attack occur concomitantly.

Three-metal cooperativity was recently reported for the trinuclear complex [Zn$_3$(**L23**)$_2$(H$_2$O)$_4$]·H$_2$O·2DMF (Joshi et al., 2018). It was suggested that the cooperative action of the three metals comprising double Lewis acid activation of the bridging HPNP and base catalysis by the third Zn^{2+} ion is assisted by the cup-shaped cavity of the complex. The trinuclear complex gives a ca. 4-fold higher k_{cat} value than the analogous dinuclear complex [Zn$_2$(**L24**)$_2$(H$_2$O)$_2$](ClO$_4$)$_2$, for which monodentate substrate coordination to Zn1 and base catalysis by Zn2-OH were proposed.

As discussed in a previous section, there are conflicting data in the literature on the correlation between the catalytic activity of phosphoesterase models and the Lewis acidity of the metal ion(s). Arora et al. compared the rate acceleration of HPNP transesterification provided by [Zn$_2$**L25**(H$_2$O)$_x$(OH)$_y$]$^{n+}$ and the analogous Co(II) and Mn(II) complexes and found a linear correlation of the rate constant k_2 with the Z_{eff}/r value of the metal ion (Arora et al., 2012). Thus, Lewis acid activation of the phosphorus is more important than activation of the nucleophile in this case. It may be relevant that the nucleophile is an internal one that is *per se* more efficient than the external one for general phosphate ester substrates.

As is evident from the above, in the majority of studies the model substrate HPNP was used. Some caution must be exercised when applying conclusions drawn from these analyses to RNA. It has been pointed out in the literature that the 2-OH group in HPNP is more flexible than the ribose 2′-OH and also has a higher pK$_a$ value (Korhonen et al., 2012). Hydrophobic and π-stacking interactions between the linker moiety or heteroaromatic binding site of a dinuclear ligand and the 4-nitrophenyl group have been demonstrated to enhance substrate binding and to increase the catalytic activity (Bazzicalupi et al., 2004). Leivers and Breslow showed that this can incorrectly suggest cooperativity between two metal centers (Leivers and Breslow, 2001). Furthermore, the literature shows that the rate-determining step depends on the nature of the leaving group, when the reaction proceeds through the A$_N$+D$_N$ mechanism (vide supra). Mikkola and coworkers published a comprehensive analysis of the dizinc(II) complex-mediated cleavage of uridine-3′-aryl and uridine-3′-alkyl phosphates. The observed cooperativity of the two metals in dinuclear catalysts changes with the acidity of the leaving group of the substrate. In the case of alkyl groups, the cooperativity decreases with decreasing acidity, whereas in the case of aryl
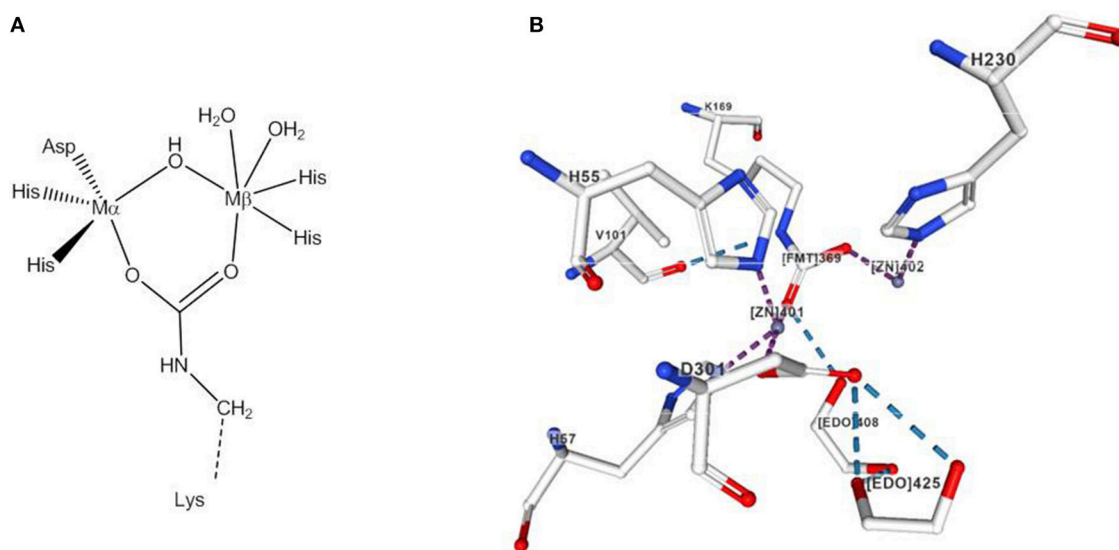

FIGURE 14 | (A) Active site of OpdA and OPH. **(B)** View of the active site region of the X-ray structure of phosphotriesterase isolated from *Pseudomonas diminuta* created with the PDB 1HZY and associated publication (Benning et al., 2001). NGL Viewer (Rose et al., 2018) and RCSB PDB.

phosphates the cooperativity increases with decreasing acidity—i.e., as nucleophilic attack becomes more rate-determining. They concluded that there is no universal mechanism for the transesterification of RNA and its analogs that covers all substrate-catalyst combinations (Korhonen et al., 2013).

Phosphodiester Hydrolysis Catalyzed by Heterodinuclear Fe(III)Zn(II) Complexes

Following earlier work by Borovik and Que and by Wieghardt and coworkers who synthesized heterodinuclear, carboxylate-/hydroxide-bridged Fe(III)/M(II) complexes to model iron-oxido proteins (Borovik et al., 1988; Hotzelmann et al., 1992), a number of biomimetic studies were targeted specifically at the mechanism of the heterodinuclear Fe(III)Zn(II) site of plant PAPs. Pathak et al. reported the Fe(III)Zn(II) complex of the symmetric ligand **HL26** (Pathak et al., 2018), but usually unsymmetric ligands with the two binding sites differing in the number and/or nature of the donor atoms are employed to stabilize the heterodimetallic site (**Figure 12**). **H₂L27**[a] was specifically designed to provide a hard N_2O_4 site for the trivalent Fe(III), and a softer N_3O_3 site for the divalent Zn(II) in the presence of additional bridging carboxylate or hydroxido ligands and to model the terminal tyrosinate ligand in PAP (Lanznaster et al., 2002; Neves et al., 2007). Single crystal structures of both the acetate- and hydroxido-bridged complexes, [Fe(III)Zn(II)**L27**[a](μ-CH₃COO₂)₂]ClO₄ and [(H₂O)Fe(III)Zn(II)**L27**[a](μ-OH)](ClO₄)₂, could be obtained showing that the M(III)···M(II) distance decreases from 3.490(9) to 3.040(1) Å when the carboxylate ligands are replaced with a μ-OH ligand. The Fe(III)···Zn(II) distance in the latter is slightly shorter but comparable to that of 3.20 Å in red kidney bean PAP (Klabunde et al., 1996).

While in the majority of the Fe(III)Zn(II) complexes of **HL26**–**H₂L31** the metals are bridged by two acetates in the solid state, in solution dissociation of the acetate ligands leads to [(H₂O)Fe**L**(μ-OH₂)Zn(H₂O)]$^{n+}$, [(H₂O)Fe**L**(μ-OH)Zn(H₂O)]$^{(n-1)+}$, [(OH)Fe**L**(μ-OH)Zn(H₂O)]$^{(n-2)+}$, and [(OH)Fe**L**(μ-OH)Zn(OH)]$^{(n-3)+}$ species, depending on the pH value (Lanznaster et al., 2002; Neves et al., 2007; Peralta et al., 2010; Piovezan et al., 2010; Jarenmark et al., 2011; Roberts et al., 2015; Pathak et al., 2017). Rate-pH profiles and potentiometric titration data indicate that [(OH)Fe**L**(μ-OH)Zn(H₂O)]$^{n+}$, which is present in weakly acidic solution is the catalytically active species. In all cases the kinetic data are consistent with the mechanism of PAP proposed by Klabunde et al. (**Figure 2B**, Klabunde et al., 1996). The phosphodiester replaces the Zn-bound water in a monodentate binding mode while Fe(III)-OH acts as the nucleophile.

The effect of substituents in para position to the terminally-bound phenolate oxygen in **H₂L27**[a−d] confirms the role of Fe(III) as the provider of the nucleophile. Electron-withdrawing groups (NO₂, Br) lead to a decrease in the hydrolysis rate, while electron-donating groups (CH₃) enhance the phosphodiesterase activity (Peralta et al., 2010). The higher the electron-donating property of the ligand, the lower the Lewis acidity of the metal ion is and the weaker the M-OH interaction is. When there is less pull of the electron density by the metal, the metal-bound hydroxide presents a stronger nucleophile. The observation that the analogous Ga(III)Zn(II) complex of **H₂L27**[a] hydrolyses BDNPP more efficiently than does the Fe(III)Zn(II) complex is also in line with nucleophilic attack by M(III)-OH (Smith et al., 2007). The authors of the study attributed the higher catalytic activity of the Ga(III)Zn(II) complex to the importance of the higher lability of Ga(III) compared to Fe(III) when product release is the rate-determining step. However, the difference in the pKₐ value of Ga(III)-OH₂ (pKₐ = 5.59) and Fe(III) (pKₐ = 4.86) may also suggest that Ga(III) provides a stronger nucleophile.

Ferreira et al. carried out DFT calculations on the reaction mechanism of the hydrolysis of dimethyl phosphate by the closely related complex [(OH)Fe**L28**(μ-OH)Zn]$^+$ (Ferreira et al., 2008). The optimized structure of the substrate-catalyst complex showed that substrate binding is stabilized by a H-bond between Fe-OH and a phosphoryl oxygen with a Gibbs free energy variation of −55.1 kcal mol⁻¹. The hydrolysis reaction proceeds by a two-step associative mechanism. The first, rate-determining step involves the nucleophilic attack of Fe-OH at the Zn-bound phosphodiester resulting in the pentacoordinate phosphorane intermediate. The movement of the OH group toward the phosphorus and P-O bond formation is accompanied by a fast proton transfer from OH to the phosphoryl oxygen. In the second step, the simultaneous proton transfer from P-OH to the leaving group oxygen and breaking of the leaving group bond lead to the release of CH₃OH.

H₂L29[a], **H₂L29**[b], and **H₂L29**[c] were synthesized to model secondary interactions between the phosphate ester substrate and positively charged amino acid residues in the active site of PAP (Silva et al., 2017). The presence of the side chains in **H₂L29**[b] and **H₂L29**[c] led to a decrease in the pKₐ value of Fe(III)-OH₂ by 0.6 and 0.8 pH units compared to the parent complex and to a shift of the redox potential of Fe(III) to less negative values. This was rationalized by hydrogen bonding between the ammonium group of the side chain and the bridging hydroxide as observed in the optimized solid-state structures of [Fe**L29**[b](OH)(μ-OH)Zn(H₂O)](ClO₄)₂ and [Fe**L29**[c](OH)(μ-OH)Zn(H₂O)](ClO₄)₂. The higher k_{cat} and lower K_m values of [Fe**L29**[b](OH)(μ-OH)Zn(H₂O)](ClO₄)₂ and [Fe**L29**[c](OH)(μ-OH)Zn(H₂O)](ClO₄)₂ compared to [Fe**L29**[a](OH)(μ-OH)Zn(H₂O)](ClO₄)₂ reflect the enhanced binding affinity of the substrate for the side-chain bearing complexes. The changes in K_m were found to correlate with the proximity of the side chain to the phosphate group in the optimized structures of the catalyst-substrate complexes. Camargo et al. attached one and two pyrene moieties via a diamine spacer to the ortho position of the phenol ring in **H₂L27**[a] (Camargo et al., 2018). They suggested that the 6-fold increase in K_{ass} for BDNPP was due to H-bond formation and hydrophobic interactions between pyrene and 4-nitrophenol. The determination of the activation parameters for BDNPP hydrolysis revealed a decrease of $\Delta H^{\neq}$ by ca 10 kJ mol⁻¹ with respect to the corresponding complex having a carbonyl group as a substituent, and this was attributed to hydrogen bonding and the stabilization of the negatively charged transition state. However, this favorable enthalpic contribution was offset by a

less favorable $\Delta S^{\neq}$, probably due to a higher degree of structural organization in the transition state.

The unsymmetric ligand H_2L30 provides an N_2O_2 and an NO_3 site. The speciation plot and rate-pH profile suggest that its Fe(III)Zn(II) complex mimics the mechanistic flexibility of PAP (Roberts et al., 2015). At a low pH, $[FeL30(OH)(H_2O)Zn(H_2O)]^{2+}$ is the active species and the terminally bound OH acts as the nucleophile. At higher pH, the bridging OH of $[FeL30(OH)(\mu-OH)Zn(H_2O)]^{+}$ becomes the nucleophile. $[FeL30(OH)(\mu-OH)Zn(H_2O)]^{+}$ is the better catalyst. Jarenmark et al. synthesized $[FeZnL4(\mu-CH_3COO)_2(CH_3OH)]PF_6$ to model the distinct donor atoms as well as the different coordination numbers of Fe(III) and Zn(II) in PAP (Jarenmark et al., 2011). The complex hydrolyzes BDNPP and also shows some activity toward HPNP. At high pH the complex converts to an inactive μ-oxido-bridged dimer of heterodinuclear dimers.

$HL9$, $HL10$, and H_2L31 contain sterically demanding pivaloyl-amide substituents. A detailed kinetic analysis of the hydrolysis of BDNPP by the respective heterodinuclear Ga(III)Zn(II), homodinuclear Zn(II)$_2$, mononuclear Zn(II), and Ga(III) complexes gave insight into the influence of the secondary coordination sphere, the effect of the properties of the binding site and the role of the heterodinuclear site (Bosch et al., 2016). Hydrogen bonding capacity shifts the pH optimum to higher pH values. The presence of H-bond donating substituents also leads to higher hydrolysis rates and higher catalytic efficiencies, especially when the two H-bond donors are located proximal to the Zn(II) site. The Ga(III)Zn(II) complex of $HL9$ hydrolyses BDNPP faster and with larger turnover numbers than the corresponding $HL10$ complex. However, the introduction of the H-bond donating substituents decreases the substrate affinity, which may be a steric effect. A comparison of $HL9$ and H_2L31 showed that the pH optimum shifts to lower pH values when the binding site becomes more electron-rich. The catalytic activity of the heterodinuclear complex of $HL10$ is greater than the sum of the activities of the mononuclear Zn(II) and Ga(III) complexes confirming the cooperativity of the metals in the dimetallic site. The Ga(III)Zn(II) complex of $HL9$ hydrolyzes BDNPP about 20 times faster at pH 7 than the dizinc(II) complex. Interestingly, K_m is three times higher for the Ga(III)Zn(II) complex. A weaker substrate affinity of the heterodinuclear complex compared to the corresponding homodinuclear Zn(II)$_2$ complex was also seen for $[Fe(III)Zn(II)L26(\mu-CH_3COO)_2]^{2+}$ (Pathak et al., 2018). It appears that the electronic effect of the heterodimetallic site on substrate and/or nucleophile activation is more important than the formation of the catalyst/substrate complex.

Hydrolysis of Phosphotriesters and Organophosphates

Due to their neutral charge phosphotriesters are more easily hydrolyzed at pH 7 than phosphodi- and -monoesters. The mechanism of the uncatalyzed reaction is believed to be associative with both a two-step addition-elimination and a concerted pathway being possible. Phosphotriesters do not occur naturally. Synthetic organophosphate triesters

have been widely used as pesticides and insecticides (e.g., paraoxon, parathion, **Figure 13**). In mammals, they cause nerve and organ failure due to their ability to inhibit acetylcholinesterase and some highly toxic organophosphorus compounds such as sarin and soman are employed as chemical warfare agents (Raushel, 2002). Bacterial phosphotriesterases can degrade phosphotriesters and their analogs into less toxic diesters and have probably evolved in response to the intense application of synthetic organophosphates in agriculture (Donarski et al., 1989; Dumas et al., 1990).

Two of the best-studied phosphotriesterases are the Zn-containing organophosphate degrading enzymes from *Agrobacterium radiobacter* (OpdA) and organophosphate hydrolase from *Pseudomonas diminuta* (OPH). Glycerophosphodiesterase from *Enterobacter aerogenes* (GpdQ) is also known to hydrolyze organophosphate triesters. OpdA and OPH share a high sequence and structure homology
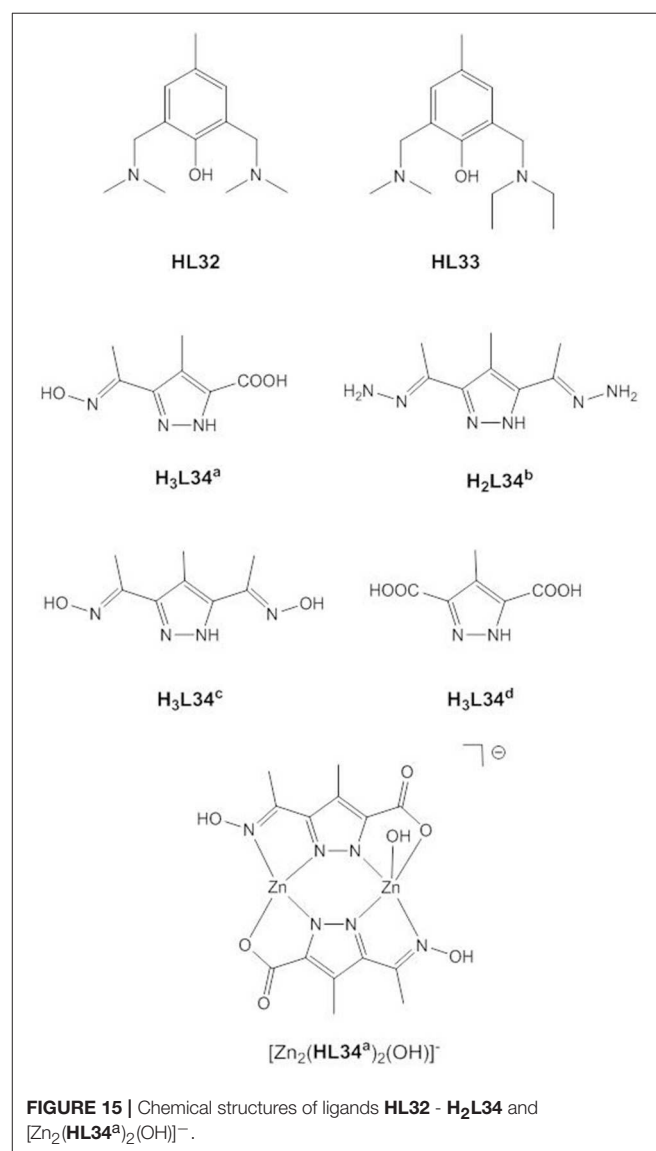

FIGURE 15 | Chemical structures of ligands **HL32** - H_2L34 and $[Zn_2(HL34^a)_2(OH)]^{-}$.

(Yang et al., 2003). In their active site two Zn^{2+} ions, referred to as α- and β-site are bridged by a carboxylated lysine side chain and a hydroxide/water (Benning et al., 2001; **Figure 14**). Small-molecule models of OpdA have been previously reviewed (Daumann et al., 2014).

The mechanism of enzymatic phosphotriester hydrolysis was investigated in theoretical studies that indicated an associative pathway involving binding of the phosphoryl oxygen to the β-site and nucleophilic attack by the bridging hydroxide (Ely et al., 2010, 2011). On substrate coordination, the μ-OH bond to the β-site weakens and the bridging hydroxide shifts to a *pseudo*-terminal position. However, like PAPs, phosphotriesterases appear to exhibit mechanistic flexibility. Experimental and theoretical studies showed that in the case of the Co(II) form of OpdA under alkaline conditions, the μ-OH group shifts to the β-site following substrate binding and a hydroxide or water from the environment coordinates terminally to the α-site to act as the reaction-initiating nucleophile (Ely et al., 2010, 2011). There is also evidence that the rate-determining step varies with the nature of the leaving group. For leaving groups with a $pK_a > 7$, P-O bond cleavage seems to be rate-determining (Ely et al., 2010). Based on kinetic and crystallographic data and computational modeling of the Fe(II)Zn(II) form of OpdA Jackson et al. proposed that the bridging hydroxide serves as a base and deprotonates a water molecule terminally coordinated to the α-site (Jackson et al., 2008). However, such a mechanism appears unlikely for the dizinc(II) form of OPH (Kim et al., 2008).

To address the need for effective bioremediators to decontaminate organophosphate-containing water and soil, biomimetic zinc(II) sites have been assembled into metal-organic frameworks or onto graphene oxide, and promising catalysts are described in the recent literature (Jacques et al., 2008; Ma et al., 2017; Xia et al., 2017). However, detailed mechanistic studies using model complexes and phosphotriesters are rarely reported and most of our current mechanistic understanding of dizinc(II) phosphotriesterases stems from theoretical studies such as those described above. In contrast to the polymer and metal organic framework-based active catalysts, little success has been achieved so far in the development of low-molecular-weight dizinc(II) phosphotriesterase mimics. Only modest phosphotriesterase activity was observed for the small number of dinuclear zinc(II) complexes investigated (**Figure 15**). The low activities of $[Zn_2L32(μ-CH_3COO)(CH_3COO)_2(H_2O)]$ (Tamilselvi and Mugesh, 2010) and $[Zn_2L33(μ-CH_3COO)(CH_3COO)_2(H_2O)]$ (Umayal and Mugesh, 2011) toward 4-nitrophenyl diphenyl phosphate was attributed to inhibition by the phosphodiester hydrolysis product that binds in a bridging mode to the dizinc(II) site. Two of the few examples of dizinc(II) complexes with phosphotriesterase activity were reported by Guo et al. (Guo et al., 2015). $[Zn_2L5]^+$ and $[Zn_2L7]^-$ hydrolyze sarin at 303 K with k_{cat}/K_m values of 0.051 and 0.11 s^{-1} M^{-1}, respectively. DFT calculations confirmed a stepwise associative mechanism with a pentacoordinate phosphoryl intermediate. One of the Zn1-bound alkoxides serves as a general base and deprotonates an incoming water nucleophile which attacks the phosphorus of the Zn2-coordinated substrate. In the catalyst-substrate complex the incoming water molecule

hydrogen bonds to Zn-OR and to another alkoxide that bridges Zn1 and Zn2. P-O_w bond formation and proton transfer from the water molecule to the terminal alkoxide occur simultaneously. The higher catalytic activity of $[Zn_2L7]^-$ was attributed to the higher basicity of the alkoxide groups in **L7** compared to **L5**.

Penkova et al. investigated the hydrolysis of paraoxon by a series of dinuclear pyrazolate complexes (Penkova et al., 2009). The Zn(II)···Zn(II) distances in $[Zn_2(\mathbf{HL34^a})_2(pyridine)_2]$, $[Zn_2(\mathbf{HL34^b})_2(CH_3COO)_2]$, $[Zn_2(\mathbf{H_2L34^c})_2(NO_3)_2]$ and $(imH)_2[Zn_2(\mathbf{L34^d})_2(H_2O)_4]$ (imH = imidazolium) range from 3.75 to 4.115 Å, i.e., are longer than those in phenoxide-bridged enzyme models and close to the metal-metal distance in alkaline phosphatase (4.0 Å, Stec et al., 2000). Based on the kinetic data and speciation in solution it was proposed that the phosphotriester binds monodentally to one Zn(II) of $[Zn_2(\mathbf{HL34^a})_2(OH)]^-$, while the other Zn(II) provides a metal-bound hydroxide as the nucleophile. $[Zn_2(\mathbf{L34^d})_2(H_2O)_4]^{2-}$ gave a two-fold lower rate acceleration compared to $[Zn_2(\mathbf{L34^a})_2(OH)]^-$, which was attributed to the lack of Zn-OH. The relatively small difference in activity between $[Zn_2(\mathbf{L34^a})_2(OH)]^-$ and $[Zn_2(\mathbf{L34^d})_2(H_2O)_4]^{2-}$ led the authors to the conclusion that Lewis activation is more important for efficient catalysis than metal hydroxide activation. Although the rate constants for the uncatalyzed cleavage of paraoxon and the RNA model HPNP are comparable, the pyrazolate complexes cleave HPNP with a second order rate constant that is about one order of magnitude larger than that for the hydrolysis of paraoxon. This was rationalized with the bridging coordination of the phosphodiester to the dizinc(II) site allowing for double Lewis acid activation.

CONCLUDING REMARKS

It is hoped that this review has shown that the metal catalysis of what appears to be a rather simple chemical reaction has been and continues to be a challenging research question. Model studies using dinuclear zinc(II) complexes have given insight into the possible roles of the Zn^{2+} ions in the dimetallic active sites of phosphatases, the potential effects of metal-substrate interaction on transition state stabilization and the contribution of the different interaction modes to the lowering of the overall energy barrier. In this regard small-molecule biomimetics have proven to be extremely powerful tools. Less has been learned from small-molecule phosphatase models on the actual mechanistic pathway of the natural enzymes, e.g., distinguishing between a monodentate substrate coordination/terminal Zn-OH nucleophile mechanism and a bridging substrate coordination/μ-OH nucleophile mechanism for a specific phosphoesterase and this is not the aim of model studies. There is no universal mechanism for the catalysis of phosphate esters by dinuclear dizinc(II) phosphoesterases. Even when a particular phosphoesterase is considered, there is accumulating evidence that phosphoesterases with a low substrate specificity hydrolyze different substrates by distinct mechanisms.

Small-molecule enzyme models have inherent limitations. They lack the pre-organization of enzymatic sites and the surrounding protein matrix that supports the correct substrate orientation and provides a hydrophobic environment. While the latter has been modeled by non-aqueous media and model systems are increasingly designed to take secondary interactions into account by introducing substituents with hydrogen bonding functionality, it is still (and probably will always be) impossible to mimic the complexity of natural enzymes. Studies in non-aqueous solvents showed a clear effect of the medium on the catalytic activity, but an effect on the mechanism (e.g., A_ND_N vs. A_N+D_N) must also be considered. Most experimental studies using small-molecule phosphatase models rely on kinetic data, which highlights the inherent difficulty that the data can support different, kinetically equivalent mechanisms. The use of 4-nitrophenyl esters as DNA and RNA models has been criticized in the literature (Menger and Ladika, 1987) and a few caveats have been pointed out in this review. On the other hand, systematic studies with different phosphate esters have shown changes in the mechanism and the rate-determining step,

when the leaving group was changed and thus contributed to a better fundamental understanding of metal-catalyzed phosphate ester hydrolysis.

In contrast to the large amount of data that has been collected on the cleavage of phosphate esters at biomimetic dizinc(II) sites, little attention has been paid to the regeneration of the catalyst. After hydrolysis of the phosphotri-, di- or monoester, the resulting diester, monoester or ortho phosphate will be coordinated in a bridging mode and will bind more strongly to the catalyst as the anionic charge has increased. Ejection of the hydrolysis product would require nucleophilic attack of water on the metal(s). Obviously, the regeneration of the dizinc(II) site is important for catalytic turnover and there is a clear need for future work in this direction.

AUTHOR CONTRIBUTIONS

The author confirms being the sole contributor of this work and has approved it for publication.

REFERENCES

Anbu, S., Kamalraj, S., Varghese, B., Muthumary, J., and Kandaswamy, M. (2012). A series of oxyimine-based macrocyclic dinuclear zinc(II) complexes enhances phosphate ester hydrolysis, DNA binding, DNA hydrolysis, and lactate dehydrogenase inhibition and induces apoptosis. *Inorg. Chem.* 51, 5580–5592. doi: 10.1021/ic202451e

Anderson, B., Milburn, R. M., Harrowfield, J. M., Robertson, G. B., and Sargeson, A. M. (1977). Cobalt(III)-promoted hydrolysis of a phosphate ester. *J. Am. Chem. Soc.* 99, 2652–2661. doi: 10.1021/ja00450a042

Arora, H., Barman, S. K., Lloret, F., and Mukherjee, R. (2012). Isostructural dinuclear phenoxo-/acetato-bridged manganese(II), cobalt(II), and zinc(II) complexes with labile sites: kinetics of transesterification of 2-hydroxypropyl-p-nitrophenylphosphate. *Inorg. Chem.* 51, 5539–5553. doi: 10.1021/ic201971t

Bauer-Siebenlist, B., Meyer, F., Farkas, E., Vidovic, D., and Dechert, S. (2005). Effect of Zn· · ·Zn separation on the hydrolytic activity of model dizinc phosphodiesterases. *Chem. Eur. J.* 11, 4349–4360. doi: 10.1002/chem.200400932

Bazzicalupi, C., Bencini, A., Berni, E., Bianchi, A., Fedi, V., Fusi, V., et al. (1999). Carboxy and diphosphate ester hydrolysis by a dizinc complex with a new alcohol-pendant macrocycle. *Inorg. Chem.* 38, 4115–4122. doi: 10.1021/ic9902929

Bazzicalupi, C., Bencini, A., Berni, E., Bianchi, A., Fornasari, P., Giorgi, C., et al. (2004). Zn(II) coordination to polyamine macrocycles containing dipyridine units. New insights into the activity of dinuclear Zn(II) complexes in phosphate ester hydrolysis. *Inorg. Chem.* 43, 6255–6265. doi: 10.1021/ic049754v

Bazzicalupi, C., Bencini, A., Bianchi, A., Fusi, V., Giorgi, C., Paoletti, P., et al. (1997). Carboxy and phosphate esters cleavage with mono- and dinuclear zinc(II) macrocyclic complexes in aqueous solution. Crystal structure of $[Zn_2L1(\mu-PP)_2(MeOH)_2](ClO_4)_2$ (L1 = [30]aneN$_6$O$_4$, PP- = diphenyl phosphate). *Inorg. Chem.* 36, 2784–2790. doi: 10.1021/ic961521j

Bennett, B., and Holz, R. C. (1997). EPR Studies on the mono- and dicobalt(II)-substituted forms of the aminopeptidase from aeromonas proteolytica. Insight into the catalytic mechanism of dinuclear hydrolases. *J. Am. Chem. Soc.* 119, 1923–1933. doi: 10.1021/ja963021v

Benning, M. M., Shim, H., Raushel, F. M., and Holden, H. M. (2001). High resolution X-ray structures of different metal-substituted forms of phosphotriesterase from pseudomonas diminuta. *Biochemistry* 40, 2712–2722. doi: 10.1021/bi002661e

Berg, J. M., Tymoczko, J. L., and Stryer, L. (2010). *Biochemistry. 7th edn.* New York, NY: W. H. Freeman and Co.

Bím, D., Svobodová, E., Eigner, V., Rulíšek, L., and Hodačová, J. (2016). Copper(II) and zinc(II) complexes of conformationally constrained polyazamacrocycles as efficient catalysts for RNA model substrate cleavage in aqueous solution at physiological pH. *Chem. Eur. J.* 22, 10426–10437. doi: 10.1002/chem.201601175

Borovik, A. S., Que, L. Jr., Papaefthymiou, V., Muenck, E., Taylor, L. F., and Anderson, O. P. (1988). Heterobimetallic complexes with (μ-phenoxo)bis(μ-carboxylato) cores. *J. Am. Chem. Soc.* 110, 1986–1988. doi: 10.1021/ja00214a065

Bosch, S., Comba, P., Gahan, L. R., and Schenk, G. (2014). Dinuclear zinc(II) complexes with hydrogen bond donors as structural and functional phosphatase models. *Inorg. Chem.* 53, 9036–9051. doi: 10.1021/ic5009945

Bosch, S., Comba, P., Gahan, L. R., and Schenk, G. (2016). Asymmetric mono- and dinuclear Ga^{III} and Zn^{II} complexes as models for purple acid phosphatases. *J. Inorg. Biochem.* 162, 343–355. doi: 10.1016/j.jinorgbio.2015.12.028

Breslow, R., Huang, D. L., and Anslyn, E. (1989). On the mechanism of action of ribonucleases: dinucleotide cleavage catalyzed by imidazole and zinc(2+). *Proc. Natl. Acad. Sci. U.S.A.* 86, 1746–1750. doi: 10.1073/pnas.86.6.1746

Brown, J. J., Gahan, L. R., Schöffler, A., Krenske, E. H., and Schenk, G. (2016). Investigation of the identity of the nucleophile initiating the hydrolysis of phosphate esters catalyzed by dinuclear mimics of metallohydrolases. *J. Inorg. Biochem.* 162, 356–365. doi: 10.1016/j.jinorgbio.2016.02.008

Bunn, S. E., Liu, C. T., Lu, Z. L., Neverov, A. A., and Brown, R. S. (2007). The dinuclear Zn(II) complex catalyzed cyclization of a series of 2-hydroxypropyl aryl phosphate RNA models: progressive change in mechanism from rate-limiting P–O bond cleavage to substrate binding. *J. Am. Chem. Soc.* 129, 16238–16248. doi: 10.1021/ja076847d

Camargo, T. P., Neves, A., Peralta, R. A., Chaves, C., Maia, E. C. P., Lizarazo-Jaimes, E. H., et al. (2018). Second-sphere effects in dinuclear Fe^{III}Zn^{II} hydrolase biomimetics: tuning binding and reactivity properties. *Inorg. Chem.* 57, 187–203. doi: 10.1021/acs.inorgchem.7b02384

Carlsson, H., Haukka, M., and Nordlander, E. (2004). Structural and functional models of the active site of zinc phosphotriesterase. *Inorg. Chem.* 43, 5681–5687. doi: 10.1021/ic0354522

Cashikar, A. G., Kumaresan, R., and Rao, N. M. (1997). Biochemical characterization and subcellular localization of the red kidney bean purple acid phosphatase. *Plant Physiol.* 114, 907–915. doi: 10.1104/pp.114.3.907

Chen, J., Wang, X., Zhu, Y., Lin, J., Yang, X., Li, Y., et al. (2005). An asymmetric dizinc phosphodiesterase model with phenolate and carboxylate bridges. *Inorg. Chem.* 44, 3422–3430. doi: 10.1021/ic048654m

Chin, J. (1991). Developing artificial hydrolytic metalloenzymes by a unified mechanistic approach. *Acc. Chem. Res.* 24, 145–152. doi: 10.1021/ar00005a004

Cleland, W. W., and Hengge, A. C. (2006). Enzymatic mechanisms of phosphate and sulfate transfer. *Chem. Rev.* 106, 3252–3278. doi: 10.1021/cr050287o

Coleman, F., Hynes, M. J., and Erxleben, A. (2010). Ga(III) complexes as models for the M(III) site of purple acid phosphatase: ligand effects on the hydrolytic reactivity toward bis(2,4-dinitrophenyl)phosphate. *Inorg. Chem.* 49, 6725–6733. doi: 10.1021/ic100722w

Cowan, J. A. (1998). Metal activation of enzymes in nucleic acid biochemistry. *Chem. Rev.* 98, 1067–1087. doi: 10.1021/cr960436q

Das, B., Daver, H., Pyrkosz-Bulska, M., Gumienna-Kontecka, E., Himo, F., and Nordlander, E. (2018). An unsymmetric ligand with a N_5O_2 donor set and its corresponding dizinc complex: a structural and functional phosphoesterase model. *Eur. J. Inorg. Chem.* 4004–4013. doi: 10.1002/ejic.201701416

Das, B., Daver, H., Pyrkosz-Bulska, M., Persch, E., Barman, S. K., Mukherjee, R., et al. (2014). A dinuclear zinc(II) complex of a new unsymmetric ligand with an N_5O_2 donor set; A structural and functional model for the active site of zinc phosphoesterases. *J. Inorg. Biochem.* 132, 6–17. doi: 10.1016/j.jinorgbio.2013.08.001

Daumann, L. J., Dalle, K. E., Schenk, G., McGeary, R. P., Bernhardt, P. V., Ollis, D. L., et al. (2012). The role of Zn–OR and Zn–OH nucleophiles and the influence of para-substituents in the reactions of binuclear phosphatase mimetics. *Dalton Trans.* 41, 1695–1708. doi: 10.1039/C1DT11187F

Daumann, L. J., Marty, L., Schenk, G., and Gahan, L. R. (2013). Asymmetric zinc(II) complexes as functional and structural models for phosphoesterases. *Dalton Trans.* 42, 9574–9584. doi: 10.1039/C3DT50514F

Daumann, L. J., Schenk, G., Ollis, D. L., and Gahan, L. R. (2014). Spectroscopic and mechanistic studies of dinuclear metallohydrolases and their biomimetic complexes. *Dalton Trans.* 43, 910–928. doi: 10.1039/c3dt52287c

Daver, H., Das, B., Nordlander, E., and Himo, F. (2016). Theoretical study of phosphodiester hydrolysis and transesterification catalyzed by an unsymmetric biomimetic dizinc complex. *Inorg. Chem.* 55, 1872–1882. doi: 10.1021/acs.inorgchem.5b02733

Davies, J. F., Hostomska, Z., Hostomsky, Z., Jordan, S. R., and Matthews, D. A. (1991). Crystal structure of the ribonuclease H domain of HIV-1 reverse transcriptase. *Science* 252, 88–95. doi: 10.1126/science.1707186

Desbouis, D., Troitsky, I. P., Belousoff, M. J., Spiccia, L., and Graham, B. (2012). Copper(II), zinc(II) and nickel(II) complexes as nuclease mimetics. *Coord. Chem. Rev.* 256, 897–937. doi: 10.1016/j.ccr.2011.12.005

Donarski, W. J., Dumas, D. P., Heitmeyer, D. P., Lewis, V. E., and Raushel, F. M. (1989). Structure-activity relationships in the hydrolysis of substrates by the phosphotriesterase from *Pseudomonas diminuta*. *Biochemistry* 28, 4650–4655. doi: 10.1021/bi00437a021

Dumas, D. P., Durst, H. D., Landis, W. G., Raushel, F. M., and Wild, J. R. (1990). Purification and properties of the phosphotriesterase for *Pseudomonas diminuta*. *Arch. Biochem. Biophys.* 277, 155–159. doi: 10.1016/0003-9861(90)90564-F

Edwards, D. R., Tsang, W.-Y., Neverov, A. A., and Brown, R. S. (2010). On the question of stepwise vs. concerted cleavage of RNA models promoted by a synthetic dinuclear Zn(II) complex in methanol: implementation of a noncleavable phosphonate probe. *Org. Biomol. Chem.* 8, 822–827. doi: 10.1039/B918310H

Ely, F., Hadler, K. S., Gahan, L. R., Guddat, L. W., Ollis, D. L., and Schenk, G. (2010). The organophosphate-degrading enzyme from *Agrobacterium radiobacter* displays mechanistic flexibility for catalysis. *Biochem. J.* 432, 565–573. doi: 10.1042/BJ201054

Ely, F., Hadler, K. S., Mitić, N., Gahan, L. R., Ollis, D. L., Plugis, N. M., et al. (2011). Electronic and geometric structures of the organophosphate-degrading enzyme from *Agrobacterium radiobacter* (OpdA). *J. Biol. Inorg. Chem.* 16, 777–787. doi: 10.1007/s00775-011-0779-6

Fan, Y.-B., and Gao, Y.-Q. (2010). Cooperativity between metals, ligands and solvent: a DFT study on the mechanism of a dizinc complex-mediated phosphodiester cleavage. *Acta Phys. Chim. Sin.* 26, 1034–1042. doi: 10.3866/PKU.WHXB20100447

Feng, G., Natale, D., Prabaharan, R., Mareque-Rivas, J. C., and Williams, N. H. (2006). Efficient phosphodiester binding and cleavage by a Zn^{II} complex combining hydrogen-bonding interactions and double Lewis acid activation. *Angew. Chem. Int. Ed.* 45, 7056–7059. doi: 10.1002/anie.200602532

Ferreira, D. E. C., De Almeida, W. B., Neves, A., and Rocha, W. R. (2008). Theoretical investigation of the reaction mechanism for the phosphate diester hydrolysis using an asymmetric dinuclear metal complex as a biomimetic model of the purple acid phosphatase enzyme. *Phys. Chem. Chem. Phys.* 10, 7039–7046. doi: 10.1039/b809189g

Franklin, S. J. (2001). Lanthanide-mediated DNA hydrolysis. *Curr. Opin. Chem. Biol.* 5, 201–208. doi: 10.1016/S1367-5931(00)00191-5

Gao, H., Ke, Z., DeYonker, N. J., Wang, J., Xu, H., Mao, Z.-W., et al. (2011). Dinuclear Zn(II) complex catalyzed phosphodiester cleavage proceeds via a concerted mechanism: a density functional theory study. *J. Am. Chem. Soc.* 133, 2904–2915. doi: 10.1021/ja106456u

Gellman, S. H., Petter, R., and Breslow, R. (1986). Catalytic hydrolysis of a phosphate triester by tetracoordinated zinc complexes. *J. Am. Chem. Soc.* 108, 2388–2394. doi: 10.1021/ja00269a041

Guo, N., Zhong, J.-Y., Chen, S.-L., Liu, J.-Q., Min, Q., and Shi, R.-X. (2015). Experimental and theoretical studies of hydrolysis of nerve agent sarin by binuclear zinc biomimetic catalysts. *Chem. Phys.* 457, 70–77. doi: 10.1016/j.chemphys.2015.05.011

Guo, Z.-F., Yan, H., Lia, Z.-F., and Lu, Z.-L. (2011). Synthesis of mono- and di-[12]aneN$_3$ ligands and study on the catalytic cleavage of RNA model 2-hydroxypropyl-p-nitrophenyl phosphate with their metal complexes. *Org. Biomol. Chem.* 9, 6788–6796. doi: 10.1039/C1OB05942D

Hendry, P., and Sargeson, A. M. (1989). Metal ion promoted phosphate ester hydrolysis. *Intramolecular attack of coordinated hydroxide ion. J. Am. Chem. Soc.* 111, 2521–2527. doi: 10.1021/ja00189a025

Hengge, A. C. (2002). Isotope effects in the study of phosphoryl and sulfuryl transfer reactions. *Acc. Chem. Res.* 35, 105–112. doi: 10.1021/ar000143q

Hotzelmann, R., Wieghardt, K., Ensling, J., Romstedt, H., Guetlich, P., Bill, E., et al. (1992). Synthesis, crystal structures, Moessbauer, susceptibility, and EPR studies of a series of spin exchange coupled complexes containing the (μ-oxo)bis(μ-acetato)rutheniummetal core and its hydroxo-bridged analog (metal = vanadium, chromium, manganese, iron, cobalt). *J. Am. Chem. Soc.* 114, 9470–9483. doi: 10.1021/ja00050a028

Humphry, T., Iyer, S., Iranzo, O., Morrow, J. R., Richard, J. P., Paneth, P., et al. (2008). Altered transition state for the reaction of an RNA model catalyzed by a dinuclear Zinc(II) catalyst. *J. Am. Chem. Soc.* 130, 17858–17866. doi: 10.1021/ja8059864

Iranzo, O., Elmer, T., Richard, J. P., and Morrow, J. R. (2003a). Cooperativity between metal ions in the cleavage of phosphate diesters and RNA by dinuclear Zn(II) catalysts. *Inorg. Chem.* 42, 7737–7746. doi: 10.1021/ic030131b

Iranzo, O., Kovalevsky, A. Y., Morrow, J. R., and Richard, J. P. (2003b). Physical and kinetic analysis of the cooperative role of metal ions in catalysis of phosphodiester cleavage by a dinuclear Zn(II) complex. *J. Am. Chem. Soc.* 125, 1988–1993. doi: 10.1021/ja027728v

Jackson, C. J., Foo, J. L., Kim, H. K., Carr, P. D., Liu, J. W., Salem, G., et al. (2008). In crystallo capture of a Michaelis complex and product-binding modes of a bacterial phosphotriesterase. *J. Mol. Biol.* 375, 1189–1196. doi: 10.1016/j.jmb.2007.10.061

Jacques, B., Dro, C., Bellemin-Laponnaz, S., Wadepohl, H., and Gade, L. H. (2008). Self-assembly of a cyclic Zn_4O_4 tetramer by aerobic oxidation of a bisoxazoline: a molecular "nest" for nucleophilic OH^-. *Angew. Chem. Int. Ed.* 47, 4546–4550. doi: 10.1002/anie.200800870

Jarenmark, M., Csapó, E., Singh, J., Wöckel, S., Farkas, E., Meyer, F., et al. (2010). Unsymmetrical dizinc complexes as models for the active sites of phosphohydrolases. *Dalton Trans.* 39, 8183–8194. doi: 10.1039/B925563J

Jarenmark, M., Haukka, M., Demeshko, S., Tuczek, F., Zuppiroli, L., Meyer, F., et al. (2011). Synthesis, characterization, and reactivity studies of heterodinuclear complexes modeling active sites in purple acid phosphatases. *Inorg. Chem.* 50, 3866–3887. doi: 10.1021/ic1020324

Jarenmark, M., Kappen, S., Haukka, M., and Nordlander, E. (2008). Symmetrical and unsymmetrical dizinc complexes as models for the active sites of hydrolytic enzymes. *Dalton Trans.* 28, 993–996. doi: 10.1039/B713664A

Jones, D. R., Lindoy, L. F., and Sargeson, A. M. (1983). Hydrolysis of phosphate esters bound to cobalt(III). Kinetics and mechanism of intramolecular attack of hydroxide on coordinated 4-nitrophenyl phosphate. *J. Am. Chem. Soc.* 105, 7327–7336. doi: 10.1021/ja00363a021

Joshi, P., Hussain, N., Ali, S. R., Rishu, and Bhardwaj, V. K. (2018). Enhanced activity of trinuclear Zn(II) complexes towards phosphate ester bond cleavage

by introducing three-metal cooperativity. *New J. Chem.* 42, 2204–2215. doi: 10.1039/C7NJ03759G

Kamerlin, S. C. L., and Wilkie, J. (2007). The role of metal ions in phosphate ester hydrolysis. *J. Org. Biomol. Chem.* 5, 2098–2108. doi: 10.1039/B701274H

Kim, J., Tsai, P. C., Chen, S. L., Himo, F., Almo, S. C., and Raushel, F. M. (2008). Structure of diethyl phosphate bound to the binuclear metal center of phosphotriesterase. *Biochemistry* 47, 9497–9504. doi: 10.1021/bi800971v

Kimura, E. (2000). Dimetallic hydrolases and their models. *Curr. Opin. Chem. Biol.* 4, 207–213. doi: 10.1016/S1367-5931(99)00076-9

Klabunde, T., Sträter, N., Fröhlich, R., Witzel, H., and Krebs, B. (1996). Mechanism of Fe(III) – Zn(II) purple acid phosphatase based on crystal structures. *J. Mol. Biol.* 259, 737–748. doi: 10.1006/jmbi.1996.0354

Klähn, M., Rosta, E., and Warshel, A. (2006). On the mechanism of hydrolysis of phosphate monoesters dianions in solutions and proteins. *J. Am. Chem. Soc.* 128, 15310–15323. doi: 10.1021/ja065470t

Koike, T., Kajitani, S., Nakamura, I., Kimura, E., and Shiro, M. (1995). The catalytic carboxyester hydrolysis by a new zinc(II) complex with an alcohol-pendant cyclen (1-(2-hydroxyethyl)-1,4,7,10-tetraazacyclododecane): a novel model for indirect activation of the serine nucleophile by zinc(II) in zinc enzymes. *J. Am. Chem. Soc.* 117, 1210–1219. doi: 10.1021/ja00109a004

Koike, T., and Kimura, E. (1991). Roles of zinc(II) ion in phosphatases. A model study with zinc(II)-macrocyclic polyamine complexes. *J. Am. Chem. Soc.* 113, 8935–8941. doi: 10.1021/ja00023a048

Korhonen, H., Koivusalo, T., Toivola, S., and Mikkola, S. (2013). There is no universal mechanism for the cleavage of RNA model compounds in the presence of metal ion catalysts. *Org. Biomol. Chem.* 11, 8324–8339. doi: 10.1039/C3OB41554F

Korhonen, H., Mikkola, S., and Williams, N. H. (2012). The mechanism of cleavage and isomerisation of RNA promoted by an efficient dinuclear Zn^{2+} complex. *Chem. Eur. J.* 18, 659–670. doi: 10.1002/chem.201100721

Koval, T., Østergaard, L. H., Lehmbeck, J., Nørgaard, A., Lipovová, P., Dušková, J., et al. (2016). Structural and catalytic properties of S1 nuclease from *Aspergillus oryzae* responsible for substrate recognition, cleavage, non-specificity, and inhibition. *PLoS ONE* 11:e0168832. doi: 10.1371/journal.pone.0168832

Kuimelis, R. G., and McLaughlin, L. W. (1998). Mechanisms of ribozyme-mediated RNA cleavage. *Chem. Rev.* 98, 1027–1044. doi: 10.1021/cr960426p

Lad, C., Williams, N. H., and Wolfenden, R. (2002). The rate of hydrolysis of phosphomonoester dianions and the exceptional catalytic proficiencies of protein and inositol phosphatases. *Proc. Natl. Acad. Sci. U.S.A.* 100, 5607–5610. doi: 10.1073/pnas.0631607100

Lanznaster, M., Neves, A., Bortoluzzi, A. J., Szpoganicz, B., and Schwingel, E. (2002). New $Fe^{III}Zn^{II}$ complex containing a single terminal $Fe-O_{phenolate}$ bond as a structural and functional model for the active site of red kidney bean purple acid phosphatase. *Inorg. Chem.* 41, 5641–5643. doi: 10.1021/ic025892d

Le Du, M. H., Lamoure, C., Muller, B. H., Bulgakov, O. V., Lajeunesse, E., Menez, A., et al. (2002). Artificial evolution of an enzyme active site: structural studies of three highly active mutants of *Escherichia coli* alkaline phosphatase. *J. Mol. Biol.* 316, 941–953. doi: 10.1006/jmbi.2001.5384

Leivers, M., and Breslow, R. (2001). Concerning two-metal cooperativity in model phosphate hydrolysis. *Bioorg. Chem.* 29, 345–356. doi: 10.1006/bioo.2001.1221

Linjalahti, H., Feng, G., Mareque-Rivas, J. C., Mikkola, S., and Williams, N. H. (2008). Cleavage and isomerization of UpU promoted by dinuclear metal ion complexes. *J. Am. Chem. Soc.* 130, 4232–4233. doi: 10.1021/ja711347w

Liu, C., and Wang, L. (2009). DNA hydrolytic cleavage catalyzed by synthetic multinuclear metallonucleases. *Dalton Trans.* 2, 227–239. doi: 10.1039/B811616D

Liu, C. T., Melnychuk, S. A., Liu, C., Neverov, A. A., and Brown, R. S. (2009). Cleavage of models for RNA mediated by a diZn(II) complex of bis[1,4-N_1,N_1'. Cleavage of models for RNA mediated by a diZn(II) complex o*Can. J. Chem.* 87, 640–649. doi: 10.1139/V09-026

Liu, C. T., Neverov, A. A., and Brown, R. S. (2008a). Enzyme-like acceleration for the hydrolysis of a DNA model promoted by a dinuclear Zn(II) catalyst in dilute aqueous ethanol. *J. Am. Chem. Soc.* 130, 13870–13872. doi: 10.1021/ja805801j

Liu, C. T., Neverov, A. A., and Brown, R. S. (2008b). Biomimetic cleavage of RNA models promoted by a dinuclear Zn(II) complex in ethanol. Greater than 30

kcal/mol stabilization of the transition state for cleavage of a phosphate diester. *J. Am. Chem. Soc.* 130, 16711–16720. doi: 10.1021/ja806462x

Livieri, M., Mancin, F., Tonellato, U., and Chin, J. (2004). Multiple functional group cooperation in phosphate diester cleavage promoted by Zn(II) complexes. *Chem. Comm.* 40, 2862–2863. doi: 10.1039/B412111B

Lönnberg, H., Strömberg, R., and Williams, A. (2004). Compelling evidence for a stepwise mechanism of the alkaline cyclisation of uridine 3omplexesthan 30 kcal*Org. Biomol. Chem.* 2, 2165–2167. doi: 10.1039/B406926A

López-Canut, V., Martí, S., Bertrán, J., Moliner, V., and Tuñón, I. (2009). Theoretical modeling of the reaction mechanism of phosphate monoester hydrolysis in alkaline phosphatase. *J. Phys. Chem. B.* 113, 7816–7824. doi: 10.1021/jp901444g

Ma, X., Zhang, L., Xia, M., Li, S., Zhang, X., and Zhang, Y. (2017). Mimicking the active sites of organophosphorus hydrolase on the backbone of graphene oxide to destroy nerve agent simulants. *ACS Appl. Mater. Interfaces* 9, 21089–21093. doi: 10.1021/acsami.7b07770

Mancin, F., and Tecilla, P. (2007). Zinc(II) complexes as hydrolytic catalysts of phosphate diester cleavage: from model substrates to nucleic acids. *New J. Chem.* 31, 800–817. doi: 10.1039/b703556j

Massoud, S. S., Ledet, C. C., Junk, T., Bosch, S., Comba, P., Herchel, R., et al. (2016). Dinuclear metal(II)-acetato complexes based on bicompartmental 4-chlorophenolate: syntheses, structures, magnetic properties, DNA interactions and phosphodiester hydrolysis. *Dalton Trans.* 45, 12933–12950. doi: 10.1039/C6DT02596J

Maxwell, C. I., Mosey, N. I., and Brown, R. S. (2013). DFT computational study of the methanolytic cleavage of DNA and RNA phosphodiester models promoted by the dinuclear Zn(II) complex of 1,3-bis(1,5,9-triazacyclododec-1-yl)propane. *J. Am. Chem. Soc.* 135, 17209–17222. doi: 10.1021/ja4088264

Menger, F. M., and Ladika, M. (1987). Origin of rate accelerations in an enzyme model: the p-nitrophenyl ester syndrome. *J. Am. Chem. Soc.* 109, 3145–3146. doi: 10.1021/ja00244a047

Meyer, F. (2006). Clues to dimetallohydrolase mechanisms from studies on pyrazolate-based bioinspired dizinc complexes – Experimental evidence for a functional $Zn-O_2H_3-Zn$ motif. *Eur. J. Inorg. Chem.* 3789–3800. doi: 10.1002/ejic.200600590

Mitić, N., Smith, S. J., Neves, A., Guddat, L. W., Gahan, L. R., and Schenk, G. (2006). The catalytic mechanisms of binuclear metallohydrolases. *Chem. Rev.* 106, 3338–3363. doi: 10.1021/cr050318f

Mohamed, M. F., and Brown, R. S. (2010). Cleavage of an RNA model catalyzed by dinuclear Zn(II) complexes containing rate-accelerating pendants. Comparison of the catalytic benefits of H-bonding and hydrophobic substituents. *J. Org. Chem.* 75, 8471–8477. doi: 10.1021/jo1017316

Mohamed, M. F., Neverov, A. A., and Brown, R. S. (2009). Investigation of the effect of oxy bridging groups in dinuclear Zn(II) complexes that catalyze the cleavage of a simple phosphate diester RNA analogue. *Inorg. Chem.* 48, 11425–11433. doi: 10.1021/ic9015965

Montagner, D., Gandin, V., Marzano, C., and Erxleben, A. (2014). Phosphate diester cleavage, DNA interaction and cytotoxic activity of a bimetallic bis(1,4,7-triazacyclonane) zinc complex. *Eur. J. Inorg. Chem.* 25, 4084–4092. doi: 10.1002/ejic.201402319

Morrow, J. R. (2008). Speed limits for artificial ribonucleases. *Comments Inorg. Chem.* 29, 169–188. doi: 10.1080/02603590802551801

Neverov, A. A., Liu, C. T., Bunn, S. E., Edwards, D., White, C. J., Melnychuk, S. A., et al. (2008). A simple DNase model system comprising a dinuclear Zn(II) complex in methanol accelerates the cleavage of a series of methyl aryl phosphate diesters by 10^{11}-10^{13}. *J. Am. Chem. Soc.* 130, 6639–6649. doi: 10.1021/ja8006963

Neverov, A. A., Lu, Z.-L., Maxwell, C. I., Mohamed, M. F., White, C. J., Tsang, J. S. W., et al. (2006). Combination of a dinuclear Zn^{2+} complex and a medium effect exerts a 10^{12}-fold rate enhancement of cleavage of an RNA and DNA model system. *J. Am. Chem. Soc.* 128, 16398–16405. doi: 10.1021/ja0651714

Neves, A., Lanznaster, M., Bortoluzzi, A. J., Peralta, R. A., Casellato, A., Castellano, E. E., et al. (2007). An unprecedented $Fe^{III}(\mu\text{-}OH)Zn^{II}$ complex that mimics the structural and functional properties of purple acid phosphatases. *J. Am. Chem. Soc.* 129, 7486–7487. doi: 10.1021/ja10.1021/ic025892d071184l

Oddie, G. W., Schenk, G., Angel, N. Z., Walsh, N., Guddat, L. W., de Jersey, J., et al. (2000). Structure, function, and regulation of tartrate-resistant acid phosphatase. *Bone* 27, 575–584. doi: 10.1016/S8756-3282(00)00368-9

O'Donoghue, A., Pyun, S. Y., Yang, M.-Y., Morrow, J. R., and Richard, J. P. (2006). Substrate specificity of an active dinuclear Zn(II) catalyst for cleavage of RNA analogues and a dinucleoside. *J. Am. Chem. Soc.* 128, 1615–1621. doi: 10.1021/ja056167f

Oivanen, M., Kuusela, S., and Lönnberg, H. (1998). Kinetics and mechanisms for the cleavage and isomerization of the phosphodiester bonds of RNA by Brønsted acids and bases. *Chem. Rev.* 98, 961–990. doi: 10.1021/cr960425x

Pathak, C., Gupta, S. K., Gangwar, M. K., Prakasham, A. P., and Ghosh, P. (2017). Modeling the active site of the purple acid phosphatase enzyme with hetero-dinuclear mixed valence M(II)–Fe(III) [M = Zn, Ni, Co, and Cu] complexes supported over a [N₆O] unsymmetrical ligand. *ACS Omega* 2, 4737–4750. doi: 10.1021/acsomega.7b00671

Pathak, C., Kumar, D., Gangwar, M. K., Mhatre, D., Roisnel, T., and Ghosh, P. (2018). Heterodinuclear Zn(II)-Fe(III) and homodinuclear M(II)-M(II) [M = Zn and Ni] complexes of a bicompartmental [N₆O] ligand as synthetic mimics of the hydrolase family of enzymes. *J. Inorg. Biochem.* 185, 30–42. doi: 10.1016/j.jinorgbio.2018.04.018

Penkova, L. V., Maciag, A., Rybak-Akimova, E. V., Haukka, M., Pavlenko, V. A., Iskenderov, T. S., et al. (2009). Efficient catalytic phosphate ester cleavage by binuclear zinc(II) pyrazolate complexes as functional models of metallophosphatases. *Inorg. Chem.* 48, 6960–6971. doi: 10.1021/ic900520j

Peralta, R. A., Bortoluzzi, A. J., de Souza, B., Jovito, R., Xavier, F. R., Couto, R. A. A., et al. (2010). Electronic structure and spectro-structural correlations of Fe^III^Zn^II^ biomimetics for purple acid phosphatases: relevance to DNA cleavage and cytotoxic activity. *Inorg. Chem.* 49, 11421–11438. doi: 10.1021/ic101433t

Perreault, D. M., and Anslyn, E. V. (1997). Unifying the current data on the mechanism of cleavage–transesterification of RNA. *Angew. Chem. Int. Ed.* 36, 432–450. doi: 10.1002/anie.199704321

Piovezan, C., Jovito, R., Bortoluzzi, A. J., Terenzi, H., Fischer, F. L., Severino, P. C., et al. (2010). Heterodinuclear Fe^III^Zn^II^-bioinspired complex supported on 3-aminopropyl silica. Efficient hydrolysis of phosphate diester bonds. *Inorg. Chem.* 49, 2580–2582. doi: 10.1021/ic902489j

Raushel, F. M. (2002). Bacterial detoxification of organophosphate nerve agents. *Curr. Opin. Microbiol.* 5, 288–295. doi: 10.1016/S1369-5274(02)00314-4

Roberts, A. E., Schenk, G., and Gahan, L. R. (2015). A heterodinuclear Fe^III^Zn^II^ complex as a mimic for purple acid phosphatase with site-specific Zn^II^ binding. *Eur. J. Inorg. Chem.* 3076–3086. doi: 10.1002/ejic.201500351

Rose, A. S., Bradley, A. R, Valasatava, Y., Duarte, J. M, Prlic, A., and Rose, P. W. (2018). NGL viewer: web-based molecular graphics for large complexes. *Bioinformatics* 34, 3755–3758. doi: 10.1093/bioinformatics/bty419

Sanyal, R., Zhang, X., Kundu, P., Chattopadhyay, T., Zhao, C., Mautner, F. A., et al. (2015). Mechanistic implications in the phosphatase activity of Mannich-based dinuclear zinc complexes with theoretical modeling. *Inorg. Chem.* 54, 2315–2324. doi: 10.1021/ic502937a

Schenk, G., Gahan, L. R., Carrington, L. E., Mitić, N., Valizadeh, M., Hamilton, S. E., et al. (2005). Phosphate forms an unusual tripodal complex with the Fe–Mn center of sweet potato purple acid phosphatase. *Proc. Natl. Acad. Sci. U.S.A.* 11, 273–278. doi: 10.1073/pnas.0407239102

Schenk, G., Mitic, N., Hanson, G. R., and Comba, P. (2013). Purple acid phosphatase: a journey into the function and mechanism of a colorful enzyme. *Coord. Chem. Rev.* 257, 473–482. doi: 10.1016/j.ccr.2012.03.020

Schroeder, G. K., Lad, C., Wyman, P., Williams, N. H., and Wolfenden, R. (2006). The time required for water attack at the phosphorus atom of simple phosphodiesters and of DNA. *Proc. Natl. Acad. Sci. U.S.A.* 103, 4052–4055. doi: 10.1073/pnas.0510879103

Selmeczi, K., Michel, C., Milet, A., Gautier-Luneau, I., Philouze, C., Pierre, J.-L., et al. (2007). Structural, kinetic, and theoretical studies on models of the zinc-containing phosphodiesterase active center: medium-dependent reaction mechanisms. *Chem. Eur. J.* 13, 9093–9106. doi: 10.1002/chem.200700104

Silva, G. A., Amorim, A. L., Souza, B., Gabriel, P., Terenzi, H., Nordlander, E., et al. (2017). Synthesis and characterization of Fe^III^(μ-OH)Zn^II^ complexes: effects of a second coordination sphere and increase in the chelate ring size on the hydrolysis of a phosphate diester and DNA. *Dalton Trans.* 46, 11380–11394. doi: 10.1039/C7DT02035J

Smith, S. J., Casellato, A., Hadler, K. S., Mitić, N., Riley, M. J., Bortoluzzi, A. J., et al. (2007). The reaction mechanism of the Ga(III)Zn(II) derivative of

uteroferrin and corresponding biomimetics. *J. Biol. Inorg. Chem.* 12, 1207–1220. doi: 10.1007/s00775-007-0286-y

Song, Y., Zan, J., Yan, H., Lu, Z.-L., and Wang, R. (2012). Steric effects on the catalytic activities of zinc(II) complexes containing [12]aneN₃ ligating units in the cleavage of the RNA and DNA model phosphates. *Org. Biomol. Chem.* 10, 7714–7720. doi: 10.1039/C2OB25624J

Stec, B., Holtz, K. M., and Kantrowitz, E. R. (2000). A revised mechanism for the alkaline phosphatase reaction involving three metal ions. *J. Mol. Biol.* 299, 1303–1311. doi: 10.1006/jmbi.2000.3799

Steitz, T. A., and Steitz, J. A. (1993). A general two-metal-ion mechanism for catalytic RNA. *Proc. Natl. Acad. Sci. U.S.A.* 90, 6498–6502. doi: 10.1073/pnas.90.14.6498

Sträter, N., Klabunde, T., Tucker, P., Witzel, H., and Krebs, B. (1995). Crystal structure of a purple acid phosphatase containing a dinuclear Fe(III)-Zn(II) active site. *Science* 268, 1489–1492. doi: 10.1126/science.7770774.

Tamilselvi, A., and Mugesh, G. (2010). Hydrolysis of organophosphate esters: phosphotriesterase activity of metallo-β-lactamase and its functional mimics. *Chem. Eur. J.* 16, 8878–8886. doi: 10.1002/chem.201000282

Tsang, W. Y., Edwards, D. R., Melnychuk, S. A., Liu, C. T., Liu, C., Neverov, A. A., et al. (2009). Dinuclear Zn(II) complex promotes cleavage and isomerization of 2-hydroxypropyl alkyl phosphates by a common cyclic phosphate intermediate. *J. Am. Chem. Soc.* 131, 4159–4166. doi: 10.1021/ja900525t

Umayal, M., and Mugesh, G. (2011). Metallo-β-lactamase and phosphotriesterase activities of some zinc(II) complexes. *Inorg. Chim. Acta* 372, 353–361. doi: 10.1016/j.ica.2011.03.064

Volbeda, A., Lahm, A., Sakiyama, F., and Suck, D. (1991). Crystal structure of *Penicillium citrinum* P1 nuclease at 2.8 A resolution. *EMBO J.* 10, 1607–1618.

Wang, X., Ho, R. Y. N., Whiting, A. K., and Que, L. Jr. (1999). Spectroscopic characterization of a ternary phosphatase–substrate–fluoride complex. Mechanistic implications for dinuclear hydrolases. *J. Am. Chem. Soc.* 121, 9235–9236. doi: 10.1021/ja990732v

Weston, J. (2005). Mode of action of bi- and trinuclear zinc hydrolases and their synthetic analogues. *Chem. Rev.* 105, 2151–2174. doi: 10.1021/cr020057z

Williams, N. H., Takasaki, B., Wall, M., and Chin, J. (1999). Structure and nuclease activity of simple dinuclear metal complexes: quantitative dissection of the role of metal ions. *Acc. Chem. Res.* 32, 485–493. doi: 10.1021/AR9500877

Xia, J., Shi, Y.-,b., Zhang, Y., Miao, Q., and Tang, W.-X. (2003). Deprotonation of zinc(II)–water and zinc(II)–alcohol and nucleophilicity of the resultant zinc(II) hydroxide and zinc(II) alkoxide in double-functionalized complexes: theoretical studies on models for hydrolytic zinc enzymes. *Inorg. Chem.* 42, 70–77. doi: 10.1021/ic020040z

Xia, M., Zhuo, C., Ma, X., Zhang, X., Sun, H., Zhai, Q., et al. (2017). Assembly of the active center of organophosphorus hydrolase in metal–organic frameworks via rational combination of functional ligands. *Chem. Comm.* 53, 11302–11305. doi: 10.1039/C7CC06270B

Yang, H., Carr, P. D., McLoughlin, S. Y., Liu, J. W., Horne, I., Qiu, X., et al. (2003). Evolution of an organophosphate-degrading enzyme: a comparison of natural and direct evolution. *Protein Eng. Des. Sel.* 16, 135–145. doi: 10.1093/proeng/gzg013

Yang, M.-Y., Iranzo, O., Richard, J. P., and Morrow, J. R. (2005). Solvent deuterium isotope effects on phosphodiester cleavage catalyzed by an extraordinarily active Zn(II) complex. *J. Am. Chem. Soc.* 127, 1064–1065. doi: 10.1021/ja044617i

Yang, M.-Y., Morrow, J. R., and Richard, J. P. (2007). A transition state analog for phosphate diester cleavage catalyzed by a small enzyme-like metal ion complex. *Bioorg. Chem.* 35, 366–374. doi: 10.1016/j.bioorg.2007.02.003

Yashiro, M., and Kawahara, R. (2004). Molecular design of an acid–base cooperative catalyst for RNA cleavage based on a dizinc complex. *J. Biol. Inorg. Chem.* 9, 914–921. doi: 10.1007/s00775-004-0596-2

Young, M. J., and Chin, J. (1995). Dinuclear copper(II) complex that hydrolyzes RNA. *J. Am. Chem. Soc.* 117, 10577–10578. doi: 10.1021/ja00147a022

Yu, Z., and Cowan, J. A. (2018). Metal complexes promoting catalytic cleavage of nucleic acids - biochemical tools and therapeutics. *Curr. Opin. Chem. Biol.* 43, 37–42. doi: 10.1016/j.cbpa.2017.10.029

Zalatan, J. G., Catrina, I., Mitchell, R., Grzyska, P. K., O'Brien, P. J., Herschlag, D., et al. (2007). Kinetic isotope effects for alkaline phosphatase reactions: implications for the role of active-site metal ions in catalysis. *J. Am. Chem. Soc.* 129, 9789–9798. doi: 10.1021/ja072196+

Zhang, X., Xu, X., Xu, H., Zhang, X., Phillips, D. L., and Zhao, C. (2014a). Mechanistic investigation into the cleavage of a phosphomonoester mediated by a symmetrical oxyimine-based macrocyclic zinc(II) complex. *ChemPhysChem* 15, 1887–1898. doi: 10.1002/cphc.201301216

Zhang, X., Zheng, X., Phillips, D. L., and Zhao, C. (2014b). Mechanistic investigation of the cleavage of phosphodiester catalyzed by a symmetrical oxyimine-based macrocyclic dinuclear zinc complex: a DFT study. *Dalton Trans.* 43, 16289–16299. doi: 10.1039/c4dt01491j

Zhang, X., Zhu, Y., Zheng, X., Phillips, D. L., and Zhao, C. (2014c). Mechanistic investigation on the cleavage of phosphate monoester catalyzed by unsymmetrical macrocyclic dinuclear complexes: the selection of metal centers and the intrinsic flexibility of the ligand. *Inorg. Chem.* 53, 3354–3361. doi: 10.1021/ic402717x

Conflict of Interest Statement: The author declares that the research was conducted in the absence of any commercial or financial relationships that could be construed as a potential conflict of interest.

Metal-Assisted Hydrolysis Reactions Involving Lipids: A Review

Dominique E. Williams[1] and Kathryn B. Grant[2]*

[1] Department of Chemistry, University of Richmond, Richmond, VA, United States, [2] Department of Chemistry, Georgia State University, Atlanta, GA, United States

This report covers major advances in the use of metal ions and complexes to hydrolyze ester and phosphate ester lipid bonds. These metal-based Lewis acids have been investigated as catalysts to isolate fatty acids from biological sources, as probes to study phospholipid bilayer properties, as tools to examine signal transduction pathways, and as lead compounds toward the discovery of therapeutic agents. Metal ions that accelerate phosphate ester hydrolysis under mild conditions of temperature and pH may have the potential to mimic phospholipase activity in biochemical applications.

Keywords: cleavage, fatty acids, liposomes, phospholipase mimics, triglycerides

INTRODUCTION

Metal ions and complexes that hydrolyze biological molecules have become increasingly important to the fields of chemistry and biology (Grant and Kassai, 2006; Mancin et al., 2012, 2016; Wezynfeld et al., 2016; Yu et al., 2016). The majority of the studies in this area have focused on the reversible addition of water across ribo- and deoxyribonucleic acid phosphodiester bonds and peptide and protein amide bonds. Hydrolytically active metal ion centers such as Ce(IV), Co(II), Co(III), Cu(II), Fe(III), Ln(III), Ni(II), Mo(IV), Pd(II), Zn(II), and Zr(IV) have been considered for a number of diverse applications, e.g., as probes to study protein function and solution structure, as enzyme models that examine metallo-hydrolase activity, and as hydrolytic agents in nucleic acid and protein engineering experiments. Although metal-assisted hydrolysis of lipids remains relatively unexplored, it is undoubtedly of equal importance. Lipids play central roles in biological systems as energy-storage molecules and as chemical messengers in cell signaling (Wenk, 2010). As the major components of the biological membranes that surround all cells and organelles, phospholipids are of particular significance to almost all known life forms (**Figure 1A**).

ISOLATION AND RECYCLING OF FATTY ACIDS FROM BIOLOGICAL SOURCES

Fatty acids (**Figure 1B**) are key building blocks of complex lipid molecules including phospholipids, triglycerides, and sterol esters. Lipids containing 2-hydroxy fatty acid units (**Figure 1C**) are found in wool wax, microorganisms, as well as in the animal central nervous system, skin, and kidney (Kishimoto and Radin, 1963). In phospholipid bilayers, the $2'$-OH group of 2-hydroxy lipids forms hydrogen bonds that strengthen membrane structure (Hama, 2010).

In one of the earliest reports appearing on metal-assisted lipid hydrolysis, Wernette and co-workers isolated free 2-hydroxy fatty acids by using $Cu(NO_3)_2$ to hydrolyze 2-hydroxy fatty acid methyl esters (50°C in water or methanol-water, 3 to 6 h) (Boyer et al., 1979). Methyl ester cleavage was proposed to occur via the formation of a bis complex containing a central copper(II) ion and two 2-hydroxy fatty acid ligands (**Figure 1D**). Interaction of the metal ion center of
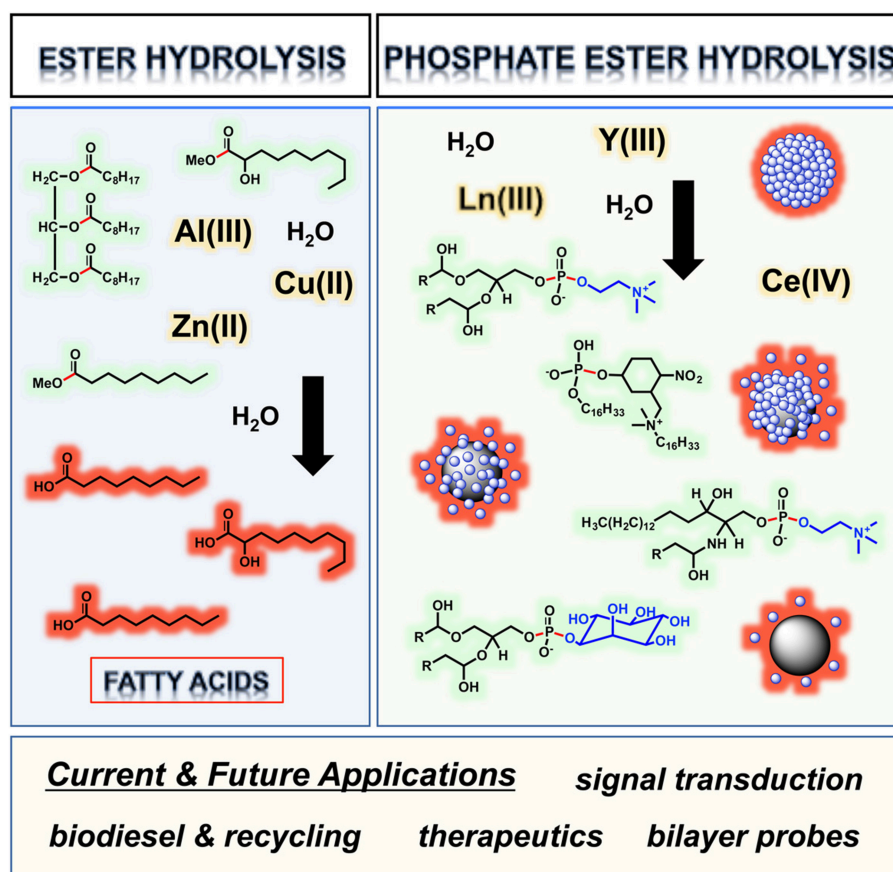
GRAPHICAL ABSTRACT | Metal ion centers hydrolyzing ester bonds in lipids and the phosphate ester bonds of phospholipid liposomes, with scissile linkages and polar head groups respectively highlighted in red and blue.

the complex with the methyl ester carbonyl oxygen atom of each fatty acid unit activated the corresponding carbonyl carbon toward nucleophilic attack by water (or hydroxide), leading to the production of two equiv. of methanol and a Cu(2-hydroxy acid)$_2$ precipitate. Subsequent EDTA treatment released the 2-hydroxy fatty acid ligands in 80–82% yield (Entry 1 in **Table S1**, Supplementary Material). Wernette suggested that it should be possible to employ Cu(II) ions to hydrolyze complex lipids present in biological extracts, allowing for naturally occurring 2-hydroxy fatty acids to be isolated readily.

Free fatty acid building blocks have also been generated by using metal ions to hydrolyze triglycerides (**Figure 1E**). In addition to their importance as key components of biological lipids, fatty acids are of considerable commercial interest as a raw material in the manufacture of detergents, soaps, lubricants, plasticizers, and biodiesel, a fuel consisting of mono alkyl esters prepared using fatty acids from vegetable oil and animal fat (Knothe, 2010). Recycling of fatty acids from *waste oils* has led to important new, environmentally friendly processes for biodiesel production (Hajjari et al., 2017). Toward these ends, Ratnasamy et al. reacted the solid Fe(II)-Zn(II) double-metal cyanine catalyst K$_4$Zn$_4$[Fe(CN)$_6$]$_3$•H$_2$O (Fe-Zn DMC) with vegetable oils and animal fats in batch reactors (Satyarthi et al., 2011). DMC

catalysts have zeolite-like cage structures and are traditionally used in the manufacture of polyether polyols (Almora-Barrios et al., 2015). Compared to the 14% hydrolysis yield obtained in the absence of catalyst, Ratnasamy et al. used Fe-Zn DMC to convert triglycerides in the starting material to free fatty acids with a yield of 72% and a turnover number of 25 (190°C in water, 8 h; Entry 2 in **Table S1**). Tetrahedrally coordinated Zn(II) Lewis acid centers within the catalyst were proposed to activate acyl ester bonds in the triglycerides toward nucleophilic attack by water.

As an innovative approach to biodiesel production, Ismadji et al. utilized synthetic *Cu(II)-laden wastewater* to hydrolyze acylglycerides in waste cooking oil (Ong et al., 2016, 2017). The authors viewed the proposed method as a process that would not only furnish free fatty acid, but one that would remediate wastewater toxicity and conserve the large amounts of water consumed in traditional oil splitting. Using an aqueous solution of CuSO$_4$ and waste cooking oil from a local restaurant, a total of 83.0% of the acylglycerides in the oil was hydrolyzed to fatty acids (77.6% yield, 225°C, 8 h; Entry 3 in **Table S1**) (Ong et al., 2016). While these values were only slightly lower in reactions run with copper-free water (75.7% acylglyceride conversion, 69.6% fatty acid yield), 51.8% of the copper(II) in the wastewater was
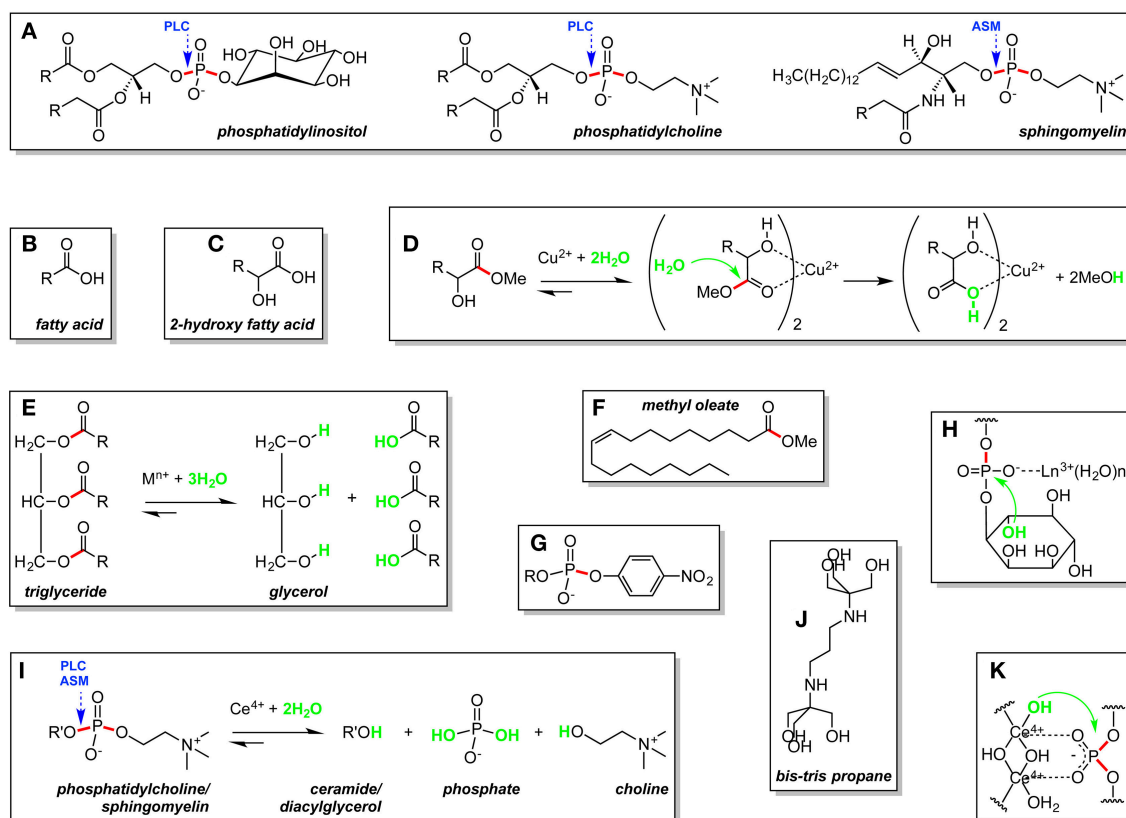
FIGURE 1 | Lipid **(A–G)** and ligand **(J)** structures, metal-assisted lipid hydrolysis reactions **(D,E,I)**, and metal-assisted lipid hydrolysis mechanisms **(D,H,K)** described in the manuscript. R, hydrocarbon chain; R', diacylglycerol for phosphatidylcholine and ceramide for sphingomyelin; M, metal; n+, charge. Scissile ester bonds are in red. Nucleophiles are in green. Bond hydrolyzed by phospholipase C (PLC) and acid sphingomyelinase (ASM) are identified with blue arrows.

successfully removed by the hydrolyzed oil phase of the reaction. Cumulative copper(II) detoxification was increased from 51.8 to 85.2% when the same sample of wastewater was utilized to treat a second batch of cooking oil (77.6% acylglyceride conversion, 72.2% fatty acid yield).

While the global production and consumption of biodiesel have expanded, there are concerns that the oxygen atoms present in biodiesel lipids adversely affect stability, energy density, and other fuel properties (Knothe, 2010). Triglycerides from vegetable oils and animal fats have therefore been subjected to direct hydrodeoxygenation reactions to generate oxygen-free, hydrocarbon-based renewable (green) diesel fuels (Knothe, 2010). Coumans and Hensen recently studied the interactions between the heterogeneous sulfided green diesel catalyst NiMo/γ-Al$_2$O$_3$ and the "model triglyceride" methyl oleate (**Figure 1F**) (Coumans and Hensen, 2017). The NiMo/γ-Al$_2$O$_3$ catalyst was prepared by grinding and sieving a porous γ-alumina (γ-Al$_2$O$_3$) solid support pre-treated with Ni(NO$_3$)$_2$•6H$_2$O and (NH$_4$)$_6$Mo$_7$O$_{24}$•7H$_2$O. Reactions between methyl oleate and the catalyst were conducted in a single-pass micro flow reactor under trickle flow conditions (260°C in tetralin, 60 bar, ∼2 h; Entry 4 in **Table S1**). Near-complete conversion of methyl oleate to C17 and C18 hydrocarbons was observed. Based on the distribution of reaction intermediates and

products, Coumans and Hensen proposed a reaction pathway in which hydrolysis of methyl oleate to fatty acid intermediates was catalyzed by coordinately unsaturated Al(III) centers of high Lewis acid strength located on the γ-alumina surface (Wischert et al., 2014). Direct hydrodeoxygenation of the fatty acids by the Ni(II)/Mo(VI) metal sulfide phase of the catalyst then gave rise to C18 hydrocarbons, while H$_2$S-assisted decarbonylation (or decarboxylation) yielded C17 hydrocarbons.

SYNTHETIC LIPID ANALOGS: ANALYSIS OF BILAYER PERMEABILITY AND DYNAMICS

Metal ions and complexes that hydrolyze lipids under non-denaturing conditions of temperature and pH have been used to investigate the properties of phospholipid bilayers under physiological conditions (Mancin et al., 2016). In these studies, Moss et al. modeled bilayers by incorporating double-chain synthetic lipid analogs containing *p-nitrophenol activated* phosphate ester bonds into unilamellar liposomes (**Figure 2**). While *p*-nitrophenol is an excellent colorimetric tool, integrating this chromophore into a synthetic phospholipid (**Figure 1G**) increases the susceptibility of scissile bonds toward hydrolysis.
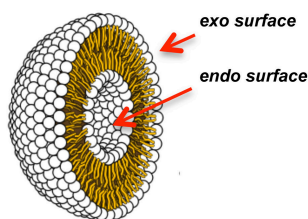
FIGURE 2 | Cross-section through a unilamellar liposome.

The liposomes were reacted under mild conditions upon the addition of the lanthanide metal ions Eu(III), Lu(III), Tb(III), Tm(III), and/or Yb(III) to the external bulk solution (25–27°C and pH 7.0–7.3; Entries 5 and 6 in **Table S1**) (Moss et al., 1995; Scrimin et al., 1998, 2000). Reactions were monitored via colorimetric detection of the *p*-nitrophenolate anion that was released upon metal-assisted hydrolysis (**Figure S1**). Relevant information relating to transverse lipid diffusion (flip-flop) rates was then revealed. At temperatures below the phase transition temperature (T_c) of the liposome, hydrolysis of the *p*-nitrophenol activated phosphate ester lipid bonds occurred only at the exoliposomal bilayer surface facing the bulk solution, independent of the charge, positive or negative, of the bilayer lipids (**Figure 2**). This confirmed that free ions are generally unable to permeate across biological membranes. Above the T_c however, rapid transverse diffusion of the synthetic lipids from the interior endo surface to the exo surface of the liposomes gave rise to additional metal-assisted cleavage. The hydrolytically active lanthanides were also used to manipulate bilayer properties. For example, Moss et al. showed that the permeability barrier of liposomes could be overcome by utilizing lipophilic amine ligands to coordinate to metal ions and then transport them by transverse diffusion from the outer to the inner membrane leaflet (Scrimin et al., 1998). When Ln(III) ions were employed to hydrolyze one of the two aliphatic chains of *p*-nitrophenol activated exo surface lipids (**Figure S2**), the rapid exposure of the endoliposomal surface to metal ions triggered an escalation in cleavage accompanied by the release of fluorescent reporter molecules stored within the liposomes' interior (Scrimin et al., 2000).

METAL IONS AS PHOSPHOLIPASE MIMICS

In addition to synthetically activated phosphate esters, lanthanide ions can hydrolyze unactivated phosphate ester bonds in naturally occurring phospholipids. As strong Lewis acids equipped with high charge densities, high coordination numbers, and rapid ligand exchange rates, the lanthanides are ideally suited as oxophilic, hydrolytic agents (Franklin, 2001). Consistent with the electrostatic nature of lanthanide-ligand interactions, these metal ion centers are drawn to negatively charged oxygen atoms in phospholipid phosphate ester bonds (Hauser and Phillips, 1976). When hydrolysis of unactivated phospholipids occurs at physiological temperature and pH, the lanthanide ions have the potential to mimic phospholipase activity.

Phospholipases are enzymes that hydrolyze ester or phosphate ester bonds. They can be either cytoplasmic or lysosomal in origin. An important example of a cytoplasmic phospholipase is phosphatidylinositol-specific phospholipase C (PLC), which converts the phosphoglyceride phosphatidylinositol (PI; **Figure 1A**) to diacylglycerol and phosphorylated inositol, important secondary messengers in signal transduction (**Figure S3**) (Cocco et al., 2015). The lysosome is a cellular organelle that contains acid hydrolases that hydrolytically breakdown macromolecules into their original, monomeric building blocks (Appelqvist et al., 2013). Unlike cytoplasmic enzymes, acid hydrolase activity is typically optimal at lysosomal pH ($\sim$ pH 4.8) and significantly lower at cytoplasmic pH ($\sim$ 7.2). Examples of acid hydrolases that engage in phosphate ester bond hydrolysis include: (i) acid sphingomyelinase (ASM) (Jenkins et al., 2009), which acts on the sphingolipid sphingomyelin (SM) to release ceramide and (ii) lysosomal phospholipase C (Matsuzawa and Hostetler, 1980), that hydrolyzes phosphoglycerides such as phosphatidylcholine (PC) and phosphatidylinositol to form diacylglycerol (**Figure 1A**).

Cytoplasmic Phospholipase Mimics: Tools to Study Signal Transduction

The first phospholipase mimics were discovered by the research groups of Komiyama and Liu, who used Ce(III), Eu(III), La(III), Tb(III), Tm(III), and Y(III) metal ion salts under near-physiological conditions (30–37°C, pH 7.5–8.5; Entries 7 and 8 in **Table S1**) to hydrolyze naturally occurring, unactivated phosphatidylinositol (**Figure 1A**) in liposomes (Matsumura and Komiyama, 1994) and intact erythrocyte membranes (Liu et al., 2001). The rare earth ions "mimicked" the activity of cytoplasmic phosphatidylinositol-specific phospholipase C by converting the phosphatidylinositol to diacylglycerol and phosphorylated inositol (**Figure S3**). The two most active metal ions were Y(III) in PI liposomes (32% yield, 30°C and pH 8.0, 24 h) and La(III) in PI-laden erythrocyte membranes. In contrast, hydrolysis was not observed when PC liposomes were treated with Y(III). Komiyama thus proposed a hydrolytic mechanism in which a rare earth ion binds to a negatively charged phosphate oxygen atom of PI, activating the phosphorous atom toward nucleophilic attack by the 2-hydroxy group specific to inositol (**Figure 1H**). The results of these investigations suggested that it should be possible to use hydrolytically active rare earth metal ions as "cytoplasmic phospholipase mimics" to study signal transduction pathways, e.g., via the generation of diacylglycerol and phosphorylated inositol in phospholipase deficient cell lines and animal models (Li et al., 2000).

Mimicking Lysosomal Phospholipase: A Potential Therapeutic Application for Cerium(IV)

Williams, Grant et al. have focused on phosphatidylcholine (**Figure 1A**) and sphingomyelin (**Figure 1A**) (Kassai et al., 2011; Cepeda et al., 2012), which make up approximately 50% of

the phospholipid content of eukaryotic bilayer membranes. The authors utilized unactivated liposomes to model biological membranes and phosphate-specific colorimetric detection based on malachite green to quantitate hydrolysis. When PC and SM liposomes were treated with metal ion salts of Ce(IV), Zr(IV), Hf(IV), Co(II), Cu(II), Eu(III), La(III), Ni(II), Pd(II), Y(III), Yb(III), and Zn(II) at 60°C (20 h), cerium(IV) displayed overwhelmingly superior levels of phosphodiester cleavage, releasing inorganic phosphate in appreciable yields at lysosomal pH (∼4.8; PC 41%, SM 22%) and in low yields under near neutral conditions (∼pH 7.2; PC 13%, SM 5%; Entries 9 and 10 in **Table S1**; **Figure 1I**). Two major factors where proposed to account for the preference of Ce(IV) for mildly acidic conditions. The pK_a value of Ce(IV)-bound water is approximately −1.1 (Wulfsberg, 1987), which enables this metal ion center to generate hydrolytically active hydroxide nucleophiles even at low pH values. Secondly, the multinuclear Ce(IV) hydroxo species responsible for phosphodiester hydrolysis lose positive charge and Lewis acid strength as reaction pH is raised (Maldonado and Yatsimirsky, 2005). Among the lanthanide(III) ions tested, liposomes were cleaved only at pH 7.2, albeit in extremely low yields < 2%. Unlike cerium(IV), water molecules bound to Ln(III) ions have pK_a values that support phosphate ester bond hydrolysis under neutral to slightly alkaline conditions, e.g., ∼8.0 for Eu(III), ∼8.0 for Yb(III), and ∼8.5 for La(III) (Burgess, 1978; Wulfsberg, 1987). The hydrolytic superiority of cerium is likely to be related to its +4 oxidation state (Bracken et al., 1997). In addition to increasing the acidity of metal-bound water, the elevated charge density of Ce(IV) intensifies its Lewis acid strength.

The high cerium(IV) activity at lysosomal pH coupled with the ability to hydrolyze SM and PC phosphate ester bonds on the ceramide/diacylglycerol side of phosphate suggest that this metal ion center might serve as an acid sphingomyelinase or lysosomal phospholipase C mimic (**Figure 1I**). In order for such an enzyme mimic to be optimal, cleavage should occur at physiological temperature and should be greatly diminished in neutral environments. To further enhance and tune cerium(IV) chemistry, Williams et al. turned to the chelating ligand bis-tris propane (BTP; **Figure 1J**) (Williams et al., 2015). Upon the addition of BTP to optimized 37°C reactions, cerium(IV) hydrolyzed unactivated PC liposomes to release 5.7 times more inorganic phosphate at ∼pH 4.8 than at ∼pH 7.2, a major enhancement compared to the ∼2.1 fold increase that was observed in ligand free controls (20 h). In the presence of BTP, the yield of inorganic phosphate at pH 4.8 and 37°C was 67%, a value that is roughly equivalent to the percent of phospholipid molecules found on the metal-accessible exo surface of small liposomes (Entry 11 in **Table S1**). NMR studies indicated that the pH-dependent "on-off switch" of the BTP ligand is related to the pK_a values of its nitrogen donor atoms ($pK_{a1} = 6.8$, $pK_{a2} = 9.1$) (Maldonado and Yatsimirsky, 2005; Williams et al., 2015). At pH 4.8, near-complete donor atom protonation minimizes interactions between cerium(IV) and BTP. The hydrolytically active multinuclear Ce(IV) hydroxo species are unhindered and

free to promote hydrolysis through a mechanism in which Ce(IV) binds to negatively charged phosphate oxygen atoms in the lipid, activating phosphorous toward attack, while delivering a hydroxide nucleophile to an adjacent phosphodiester bond (**Figure 1K**) (Komiyama et al., 1999). At pH 7.2, nitrogen deprotonation enables BTP to bind to Ce(IV) and impede its ability to accelerate cleavage. The promising *in vitro* results pointing to cerium(IV) as a "lysosomal phospholipase mimic" are consistent with a small molecule approach to reversing the pathogenic lysosomal build-up of sphingomyelin that occurs in Niemann-Pick disease type A, a fatal lysosomal storage disease caused by mutations in the human ASM gene (Schuchman and Desnick, 2017).

In a related study, König and co-workers explored the effects of phosphatidylcholine liposomes on the interactions between the activated DNA model compound bis-4-nitrophenyl phosphate (BNPP) and Fe(III), Cu(II), Zn(II), Al(III), La(III), Ce(III), Eu(III), Tb(III), and Yb(III) (25°C and pH 7.4, 24 h; Entry 12 in **Table S1**; **Figure S4**) (Poznik et al., 2015). While the *d*- and *p*- block metal ions were less active, the five Ln(III) metal centers accelerated hydrolysis of the phosphodiester bonds of the external BNPP substrate. When unactivated PC liposomes were added to the reactions, the hydrolytic activity of only the lanthanide ions toward BNPP was markedly increased (∼11–19% final yield). The lanthanides were then shown to quench the fluorescence of membrane embedded carboxyfluorescein, leading the authors to propose a hydrolytic mechanism in which densely packed Ln(III) Lewis acid centers assembled at the lipid-water interface of the PC liposomes accelerate phosphodiester hydrolysis in a cooperative fashion. Dissimilar to Williams et al.'s data (Kassai et al., 2011; Williams et al., 2015), metal-assisted cleavage of unactivated bilayer phosphatidylcholine molecules was not reported.

CONCLUDING REMARKS

In this review, we have summarized and commented on key research studies in which metal ions and complexes were used to hydrolyze ester and phosphate ester lipid bonds. We found that the metal ion centers Al(III), Cu(II), and Zn(II) cleave neutral, unactivated ester bonds in acylglycerides and fatty acid esters, mainly at elevated temperatures (50–260°C). In contrast, the lanthanide/rare earth ions Ce(III), Eu(III), La(III), Lu(III), Tb(III), Tm(III), Yb(III), Y(III), and Ce(IV) work well at 25–37°C with lipids containing negatively charged phosphate ester bonds. These mild temperature conditions enable phospholipids in fully assembled liposomes to be cleaved. Among the lanthanides, Ln(III) ions were primarily used to hydrolyze *p*-nitrophenol activated phosphate ester lipid bonds in neutral to mildly alkaline pH environments (pH 7.0–8.5). In the case of phosphatidylinositol, the 2-hydroxyl group of inositol serves as an internal nucleophile, permitting Ln(III)-assisted hydrolysis of liposomes to proceed in the absence of a phosphate ester activating group. The lanthanide ion Ce(IV) favors mildly acidic conditions over near neutral pH,

and at 37°C is highly reactive toward the hydrolytic cleavage of unactivated phosphatidylcholine phosphate ester bonds. In addition to relating the mechanistic aspects of lipid hydrolysis, the research articles showcased in this review underscore the potential of metal ions and complexes to serve as hydrolytic agents in diverse applications ranging from biofuel production to therapeutics.

AUTHOR CONTRIBUTIONS

All authors listed have made a substantial, direct and intellectual contribution to the work, and approved it for publication.

FUNDING

SUPPLEMENTARY MATERIAL

The Supplementary Material for this article can be found online at: https://www.frontiersin.org/articles/10.3389/fchem.2019.00014/full#supplementary-material

REFERENCES

Almora-Barrios, N., Pogodin, S., Bellarosa, L., Garcia-Melchor, M., Revilla-Lopez, G., Garcia-Rates, M., et al. (2015). Structure, activity, and deactivation mechanisms in double metal cyanide catalysts for the production of polyols. *Chem. Cat. Chem.* 7, 928–935. doi: 10.1002/cctc.201402907

Appelqvist, H., Wäster, P., Kågedal, K., Öllinger, K. (2013). The lysosome: from waste bag to potential therapeutic target. *J. Mol. Cell Biol.* 5, 214–226. doi: 10.1093/jmcb/mjt022

Boyer, R. F., Wernette, M. E., Van Wylen, S., Faustman, E., and Titus, R. (1979). 2-Hydroxy acids as biochemical ligands. Copper(II)-facilitated hydrolysis of 2-hydroxy acid esters. *J. Inorg. Biochem.* 10, 205–213. doi: 10.1016/S0162-0134(00)80280-9

Bracken, K., Moss, R. A., and Ragunathan, K. G. (1997). Remarkably rapid cleavage of a model phosphodiester by complexed ceric ions in aqueous micellar solutions. *J. Am. Chem. Soc.* 119, 9323–9324. doi: 10.1021/ja971448b

Burgess, J. (1978). *Metal Ions in Solution*. New York, NY: Halstead Press.

Cepeda, S. S., Williams, D. E., and Grant, K. B. (2012). Evaluating metal ion salts as acid hydrolase mimics: metal-assisted hydrolysis of phospholipids at lysosomal pH. *Biometals* 25, 1207–1219. doi: 10.1007/s10534-012-9583-1

Cocco, L., Follo, M. Y., Manzoli, L., and Suh, P. G. (2015). Phosphoinositide-specific phospholipase C in health and disease. *J. Lipid Res.* 56, 1853–1860. doi: 10.1194/jlr.R057984

Coumans, A. E., and Hensen, E. J. M. (2017). A model compound (methyl oleate, oleic acid, triolein) study of triglycerides hydrodeoxygenation over alumina-supported NiMo sulfide. *Appl. Catal. B. Environ.* 201, 290–301. doi: 10.1016/j.apcatb.2016.08.036

Franklin, S. J. (2001). Lanthanide-mediated DNA hydrolysis. *Curr. Opin. Chem. Biol.* 5, 201–208. doi: 10.1016/S1367-5931(00)00191-5

Grant, K. B., and Kassai, M. (2006). Major advances in the hydrolysis of peptides and proteins by metal ions and complexes. *Curr. Org. Chem.* 10, 1035–1049. doi: 10.2174/138527206777435535

Hajjari, M., Tabatabaei, M., Aghbashlo, M., and Ghanavati, H. (2017). A review on the prospects of sustainable biodiesel production: A global scenario with an emphasis on waste-oil biodiesel utilization. *Renew. Sust. Energ. Rev.* 72, 445–464. doi: 10.1016/j.rser.2017.01.034

Hama, H. (2010). Fatty acid 2-hydroxylation in mammalian sphingolipid biology. *Biochim. Biophys. Acta.* 1801, 405–414. doi: 10.1016/j.bbalip.2009.12.004

Hauser, H., and Phillips, M. C. (1976). Conformation of the lecithin polar group in charged vesicles. *Nature* 261, 390–394. doi: 10.1038/261390a0

Jenkins, R. W., Canals, D., and Hannun, Y. A. (2009). Roles and regulation of secretory and lysosomal acid sphingomyelinase. *Cell Signal.* 21, 836–846. doi: 10.1016/j.cellsig.2009.01.026

Kassai, M., Teopipithaporn, R., and Grant, K. B. (2011). Hydrolysis of phosphatidylcholine by cerium(IV) releases significant amounts of choline and inorganic phosphate at lysosomal pH. *J. Inorg. Biochem.* 105, 215–223. doi: 10.1016/j.jinorgbio.2010.11.007

Kishimoto, Y., and Radin, N. S. (1963). Occurrence of 2-hydroxy fatty acids in animal tissues. *J. Lipid Res.* 4, 139–143.

Knothe, G. (2010). Biodiesel and renewable diesel: a comparison. *Prog. Energy Combust. Sci.* 36, 364–373. doi: 10.1016/j.pecs.2009.11.004

Komiyama, M., Takeda, N., and Shigekawa, H. (1999). Hydrolysis of DNA and RNA by lanthanide ions: mechanistic studies leading to new applications. *Chem. Commun.* 1443–1451. doi: 10.1039/a901621j

Li, Z., Jiang, H., Xie, W., Zhang, Z., Smrcka, A. V., and Wu, D. (2000). Roles of PLC-beta2 and -beta3 and PI3Kgamma in chemoattractant-mediated signal transduction. *Science* 287, 1046–1049. doi: 10.1126/science.287.5455.1046

Liu, H. X., Hu, J., Liu, X. T., Li, R. C., and Wang, K. (2001). Effects of lanthanide ions on hydrolysis of phosphatidylinositol in human erythrocyte membranes. *Chinese Sci. Bull.* 46, 401–403. doi: 10.1007/BF03183274

Maldonado, A. L., and Yatsimirsky, A. K. (2005). Kinetics of phosphodiester cleavage by differently generated cerium(IV) hydroxo species in neutral solutions. *Org. Biomol. Chem.* 3, 2859–2867. doi: 10.1039/b506170a

Mancin, F., Prins, L. J., Pengo, P., Pasquato, L., Tecilla, P., and Scrimin, P. (2016). Hydrolytic metallo-nanozymes: From micelles and vesicles to gold nanoparticles. *Molecules* 21:1014. doi: 10.3390/molecules21081014

Mancin, F., Scrimin, P., and Tecilla, P. (2012). Progress in artificial metallonucleases. *Chem. Commun.* 48, 5545–5559. doi: 10.1039/c2cc30952a

Matsumura, K., and Komiyama, M. (1994). Hydrolysis of phosphatidylinositol by rare-earth-metal ion as a phospholipase-C mimic. *J. Inorg. Biochem.* 55, 153–156. doi: 10.1016/0162-0134(94)85037-2

Matsuzawa, Y., and Hostetler, K. Y. (1980). Properties of phospholipase C isolated from rat liver lysosomes. *J. Biol. Chem.* 255, 646–652.

Moss, R. A., Park, B. D., Scrimin, P., and Ghirlanda, G. (1995). Lanthanide cleavage of phosphodiester liposomes. *Chem. Commun.* 1627–1628. doi: 10.1039/c39950001627

Ong, L. K., Nguyen, P. L. T., Soetaredjo, F. E., Ismadji, S., and Ju, Y. H. (2016). Direct reuse of Cu-laden wastewater for non-edible oil hydrolysis: basic mechanism of metal extraction and fatty acid production. *RSC Adv.* 6, 25359–25367. doi: 10.1039/C5RA23153A

Ong, L. K., Nguyen, P. L. T., Soetaredjo, F. E., Ismadji, S., and Ju, Y. H. (2017). Kinetic evaluation of simultaneous waste cooking oil hydrolysis and reactive liquid-liquid Cu extraction from synthetic Cu-containing wastewater: effect of various co-contaminants. *Sep. Purif. Technol.* 187, 184–192. doi: 10.1016/j.seppur.2017.06.049

Poznik, M., Maitra, U., and König, B. (2015). The interface makes a difference: lanthanide ion coated vesicles hydrolyze phosphodiesters. *Org. Biomol. Chem.* 13, 9789–9792. doi: 10.1039/C5OB01265A

Satyarthi, J. K., Srinivas, D., and Ratnasamy, P. (2011). Hydrolysis of vegetable oils and fats to fatty acids over solid acid catalysts. *Appl. Catal. A. Gen.* 391, 427–435. doi: 10.1016/j.apcata.2010.03.047

Schuchman, E. H., and Desnick, R. J. (2017). Types A and B Niemann-Pick disease. *Mol. Genet. Metab.* 120, 27–33. doi: 10.1016/j.ymgme.2016.12.008

Scrimin, P., Caruso, S., Paggiarin, N., and Tecilla, P. (2000). Ln(III)-catalyzed cleavage of phosphate-functionalized synthetic lipids: real time monitoring of vesicle decapsulation. *Langmuir* 16, 203–209. doi: 10.1021/la990804w

Scrimin, P., Tecilla, P., Moss, R. A., and Bracken, K. (1998). Control of permeation of lanthanide ions across phosphate-functionalized liposomal membranes. *J. Am. Chem. Soc.* 120, 1179–1185. doi: 10.1021/ja972041+

Wenk, M. R. (2010). Lipidomics: new tools and applications. *Cell* 143, 888–895. doi: 10.1016/j.cell.2010.11.033

Wezynfeld, N. E., Fraczyk, T., and Bal, W. (2016). Metal assisted peptide bond hydrolysis: chemistry, biotechnology and toxicological implications. *Coord. Chem. Rev.* 327, 166–187. doi: 10.1016/j.ccr.2016.02.009

Williams, D. E., Basnet, K., and Grant, K. B. (2015). Tuning cerium(IV)-assisted hydrolysis of phosphatidylcholine liposomes under mildly acidic and neutral conditions. *ChemBioChem* 16, 1474–1482. doi: 10.1002/cbic.201500041

Wischert, R., Florian, P., Coperet, C., Massiot, D., and Sautet, P. (2014). Visibility of Al surface sites of gamma-alumina: a combined computational and experimental point of view. *J. Phys. Chem. C* 118, 15292–15299. doi: 10.1021/jp503277m

Wulfsberg, G. (1987). *Principles of Descriptive Inorganic Chemistry*. Monterey, CA: Brooks/Cole Publishing Company.

Yu, L., Li, F. Z., Wu, J. Y., Xie, J. Q., and Li, S. (2016). Development of the aza-crown ether metal complexes as artificial hydrolase. *J. Inorg. Biochem.* 154, 89–102. doi: 10.1016/j.jinorgbio.2015.09.011

Mn-Mimochrome VI*a: An Artificial Metalloenzyme With Peroxygenase Activity

Linda Leone[1], Daniele D'Alonzo[1], Véronique Balland[2], Gerardo Zambrano[1], Marco Chino[1], Flavia Nastri[1], Ornella Maglio[1,3], Vincenzo Pavone[1] and Angela Lombardi[1]*

[1] Department of Chemical Sciences, University of Naples "Federico II", Naples, Italy, [2] Laboratoire d'Electrochimie Moléculaire, UMR 7591 CNRS, Université Paris Diderot, Sorbonne Paris Cité, Paris, France, [3] Institute of Biostructures and Bioimages, National Research Council, Naples, Italy

Manganese-porphyrins are important tools in catalysis, due to their capability to promote a wide variety of synthetically valuable transformations. Despite their great reactivity, the difficulties to control the reaction selectivity and to protect the catalyst from self-degradation hamper their practical application. Compared to small-molecule porphyrin complexes, metalloenzymes display remarkable features, because the reactivity of the metal center is finely modulated by a complex interplay of interactions within the protein matrix. In the effort to combine the catalytic potential of manganese porphyrins with the unique properties of biological catalysts, artificial metalloenzymes have been reported, mainly by incorporation of manganese-porphyrins into native protein scaffolds. Here we describe the spectroscopic and catalytic properties of Mn-Mimochrome VI*a (Mn-MC6*a), a mini-protein with a manganese deuteroporphyrin active site within a scaffold of two synthetic peptides covalently bound to the porphyrin. Mn-MC6*a is an efficient catalyst endowed with peroxygenase activity. The UV-vis absorption spectrum of Mn-MC6*a resembles that of Mn-reconstituted horseradish peroxidase (Mn-HRP), both in the resting and high-valent oxidized states. Remarkably, Mn-MC6*a shows a higher reactivity compared to Mn-HRP, because higher yields and chemoselectivity were observed in thioether oxidation. Experimental evidences also provided indications on the nature of the high-valent reactive intermediate and on the sulfoxidation mechanism.

Keywords: artificial metalloenzymes, biocatalysis, manganese porphyrins, oxidation catalysis, heme-protein models

INTRODUCTION

Nature mastered coordination chemistry in a fascinating manner, as proven by the remarkable features of metalloenzymes (Wolfenden and Snider, 2001; Valdez et al., 2014). To take full advantage of the rich chemistry of metal ions, in terms of spectroscopic, magnetic, and catalytic properties, proteins have evolved as complex macromolecular ligands. Indeed, the protein matrix exerts a fine control on the reactivity of metal ions, through a variety of interactions, ranging from coordinate and hydrogen bond, to hydrophobic and ionic interactions (Ragsdale, 2006; Maglio et al., 2012). This control allows proteins to benefit from the redox and Lewis-acid catalysis of metal ions. As in a mutual relationship, metal ions themselves can make the protein functional. Thanks to their preferred coordination geometry, metal ions may act as templates, binding various domains

of the protein together and bringing reactive groups in the correct relative orientation for activity (Maglio et al., 2012).

The strong interplay between metal cofactor and protein scaffold is finely exemplified by the functional versatility of heme-containing enzymes (Bowman and Bren, 2008; Poulos, 2014). Peroxidases, catalases and monooxygenases share, in their catalytic cycle, a similar high-valent iron–oxo intermediate, whose fate depends on the specific environment created by the surrounding protein matrix (Dolphin et al., 1971; Hersleth et al., 2006; Moody and Raven, 2018).
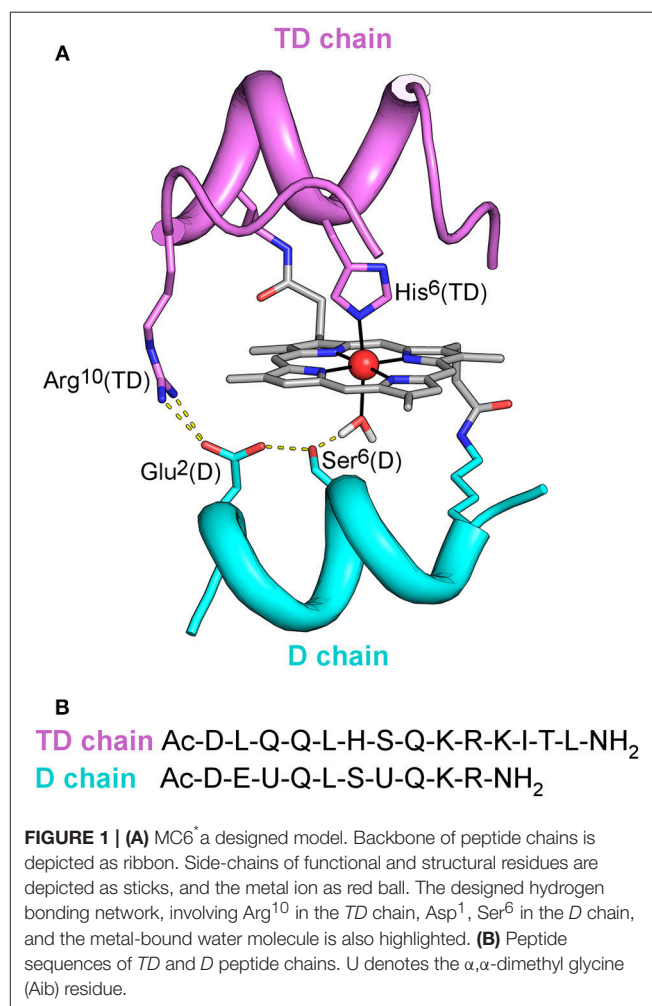
Studies on small-molecule mimics, based on synthetic metallo-porphyrinoid complexes, gave basic insights into the nature of the intermediates and into the reaction mechanisms of heme-enzymes (Groves, 2006; Karlin, 2010; Baglia et al., 2017). Modification of metallo-porphyrins with different chemical moieties, assembled to resemble and mimic the protein matrix, clearly highlighted the environment influence over metal cofactor reactivity (Nastri et al., 1998; Fujii, 2002). Nevertheless, with small-molecule mimics is very difficult to obtain the environment complexity offered by the protein matrix in natural systems.

In the last two decades, a variety of approaches have been exploited to cage metallo-porphyrins into protein scaffolds of different complexity for the development of artificial heme-enzymes (Nastri et al., 2013; Chino et al., 2018). By mimicking Nature's strategy, directed evolution allowed repurposing heme-enzymes toward abiotic reactions (Arnold, 2018). Heme-protein redesign, through scaffold engineering and/or cofactor replacement, afforded new enzymes with a variety of functionalities (Garner et al., 2011; Cai et al., 2013; Oohora et al., 2017). Further, de novo design approaches afforded the construction of artificial peroxidases with impressive enzymatic rate constants (Patel and Hecht, 2012; D'Souza et al., 2017; Watkins et al., 2017).

Using a structure-based approach and a miniaturization process (Lombardi et al., 2000), we developed a class of heme-protein models named Mimochromes (Nastri et al., 1998; Lombardi et al., 2001). Mimochromes consist of two small peptide chains covalently linked to the deuteroporphyrin through amide bonds between the heme-propionic groups and the ε-amino groups of lysine residues. The peptide chains are conceived to embrace the porphyrin in a helix-heme-helix sandwiched structure, thus reproducing the protein environment found in natural systems.

Starting from the prototype molecule (Mimochrome I, herein referred as MC1) (Nastri et al., 1997), a redesign approach allowed to optimize the scaffold (Lombardi et al., 2003; Di Costanzo et al., 2004). Subsequent rounds of design were aimed at engineering functionality in the optimized scaffold. The overall process afforded the catalytically active derivative Mimochrome VI (MC6), which mimics the asymmetry of natural proteins in both primary and secondary coordination spheres (Ranieri et al., 2010; Nastri et al., 2011). MC6 is made up of a tetradecapeptide (TD) bearing the His axial ligand, and a decapeptide (D) lacking coordinating residue, which allows to create a substrate binding pocket on the distal side of the heme. These structural features steered Fe^{III}-MC6 toward peroxidase catalysis.

The simplicity of the MC6 scaffold offered us the opportunity for structure/function relationship studies. The effects of second-shell interactions (Vitale et al., 2015) and of conformational constraints (Caserta et al., 2018) in tuning catalysis were systematically evaluated. Site-specific mutations in both peptide chains allowed to select MC6*a (**Figure 1**) as the best peroxidase catalyst among the mimochrome family. Fe^{III}-MC6*a exceeds the turnover frequency and the total turnover number (TON) of its best predecessor, displaying a 20-fold higher catalytic efficiency compared to that of natural horseradish peroxidase (HRP) in oxidation of 2,2′-azino-bis(3-ethylbenzothiazoline-6-sulphonic acid) (ABTS) (Caserta et al., 2018). Moreover, the cobalt derivative (Co-MC6*a) behaves as a very promising catalyst in hydrogen evolution reactions, as it was able to electrocatalytically reduce protons to hydrogen (H$_2$) in water at neutral pH under aerobic conditions, performing more than 230,000 turnovers (Firpo et al., 2018). Finally, we have also demonstrated that mimochromes can be successfully conjugated to gold nanoparticles (AuNPs) and/or immobilized onto electrode surfaces while preserving the redox properties and the peroxidase activity (Ranieri et al., 2010; Vitale et al., 2014; Zambrano et al., 2018).

FIGURE 1 | (A) MC6*a designed model. Backbone of peptide chains is depicted as ribbon. Side-chains of functional and structural residues are depicted as sticks, and the metal ion as red ball. The designed hydrogen bonding network, involving Arg^{10} in the TD chain, Asp^1, Ser^6 in the D chain, and the metal-bound water molecule is also highlighted. **(B)** Peptide sequences of TD and D peptide chains. U denotes the α,α-dimethyl glycine (Aib) residue.

The goal of the present work was to further evaluate the versatility of the MC6*a scaffold toward metal replacement, by swapping iron to manganese. Iron– and manganese–porphyrins have rich redox chemistry (Felton, 1978), as both metal ions have access to a wide range of oxidation and spin states. They also share a common metal-oxo species during catalysis, and the enhanced stability of Mn-oxo over the corresponding Fe-oxo species (Neu et al., 2015; Chino et al., 2018) has allowed to get deep insights into the nature of the active species and to shed light on their role in catalysis (Gelb et al., 1982; Nick et al., 2002). Further, the activation of Mn^{III} to the reactive Mn^{IV} or Mn^V species (Song et al., 2007; Neu et al., 2014) has been found to promote a variety of synthetically relevant reactions, ranging from the epoxidation (Srour et al., 2012) and sulfoxidation (Neu et al., 2014) up to the site-selective functionalization of unactivated C-H bonds (Martinez-Lorente et al., 1996; Costas, 2011; Liu et al., 2012; Liu and Groves, 2015).

Herein we report the synthesis and spectroscopic characterization of Mn-MC6*a, and of its high-valent Mn-oxo species. The ability of this species in promoting the oxy-functionalization of reducing substrates was also evaluated and compared with that of Fe-MC6*a. Both iron and manganese complexes showed peroxygenase activity, thus highlighting that MC6*a scaffold is able to host both metal-oxo species and tune their reactivity.

RESULTS AND DISCUSSION

Synthesis, Purification, and Analysis

The synthesis and purification of apo-MC6*a and Fe-MC6*a were carried out using previously described procedures (Caserta et al., 2018). The manganese ion insertion was successfully carried out by following a variation of literature methods (Caserta et al., 2018) using $Mn(OAc)_2$ as the metal source (Dolphin, 1978). LC-MS analysis confirmed manganese ion insertion into apo-MC6*a (**Figure S1**). Deconvolution analysis of the positive ESI-MS mass spectrum gave an experimental mass of 3489.2 ± 0.4 Da, in agreement with the theoretical value (3488.8 Da). Product identity was further confirmed by UV-vis absorption spectroscopy (**Figure 2**). The UV-vis spectrum of Mn-MC6*a in acid aqueous solution (H_2O 0.1% trifluoroacetic acid, TFA) shows a typical split Soret band (Boucher, 1968), with one component centered at 365 nm and a weaker component at 459 nm. The Q-band region is characterized by two bands at 542 nm (β) and 571 nm (α). Three additional weak absorption bands at 310, 390, 420 nm are also present. These spectral data are in good agreement with those reported for Mn-porphyrins, with a hexa-coordinated, high-spin Mn^{III} ion (Giovannetti et al., 2010). Mn-MC6*a stock solutions, analyzed for metal contents by atomic absorption spectroscopy, and properly diluted, enabled the calculation of a molar absorptivity of (7.86 ± 0.08) 10^4 M^{-1} cm^{-1} at 365 nm.

Spectroscopic and Electrochemical Characterization

UV-vis and circular dichroism (CD) spectroscopies were combined to gain information about the role of the 2,2,2-trifluoroethanol (TFE) and pH on the Mn^{III}-MC6*a structural
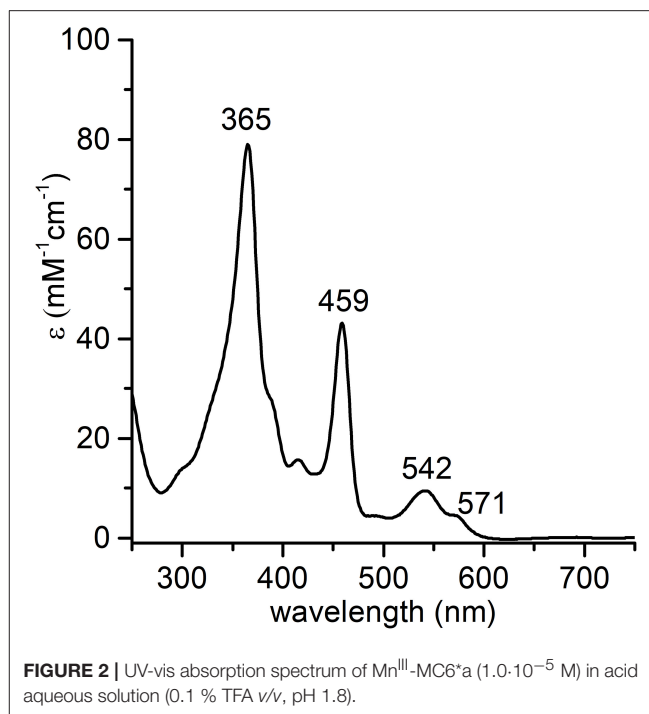

FIGURE 2 | UV-vis absorption spectrum of Mn^{III}-MC6*a ($1.0·10^{-5}$ M) in acid aqueous solution (0.1 % TFA v/v, pH 1.8).

and coordination properties. Electrochemical analysis was also performed to get further insight into the metal ion coordination states at different pHs.

Structural Properties of Mn^{III}-MC6*a by CD Spectroscopy

CD spectroscopy was used to analyze the structural properties of Mn^{III}-MC6*a. In particular, the role played by the helix-inducing solvent TFE on the structure was investigated (Hong et al., 1999; Vitale et al., 2015). To this end, far-UV CD spectra were acquired in 5 mM phosphate buffer solution at pH 6.5, at different TFE concentrations (in the range of 0–50% v/v) (**Figure 3**). Inspection of **Figure 3A** shows that in the absence of TFE the peptide chains are poorly structured, but reminiscent of an α-helix secondary structure (Whitmore and Wallace, 2008). **Figure 3B** shows the plot of θ_{222} as a function of TFE and **Table 1** reports far-UV region CD parameters at 0 and 40% TFE (v/v). Addition of TFE contributes to enhance the α-helical content, as assessed by: (i) the increase of the mean residue ellipticity at 222 nm (θ_{222}), (ii) the enhancement of the θ_{ratio} ($\theta_{222}/\theta_{min}$) that progressively approaches the unity, (iii) the shift of the lower minimum (λ_{min}) toward 207 nm, (iv) the λ_0 shift to higher wavelengths. Similarly to Fe^{III}-MC6*a (Caserta et al., 2018), the maximum α-helical content was reached at 40% TFE (v/v).

The induced Cotton effects in the Soret region were also examined to investigate the role of TFE on the stabilization of the global structure of the molecule. **Figure 3C** reports the CD spectra in the Soret region at 0 and 40% TFE (v/v). Two negative Cotton effects centered at 357 nm and 463 nm are observed in both CD spectra. In the absence of TFE, the most intense band at 357 nm appears very broad, while it is better resolved at 40% TFE (v/v) concentration. Moreover, the intensity
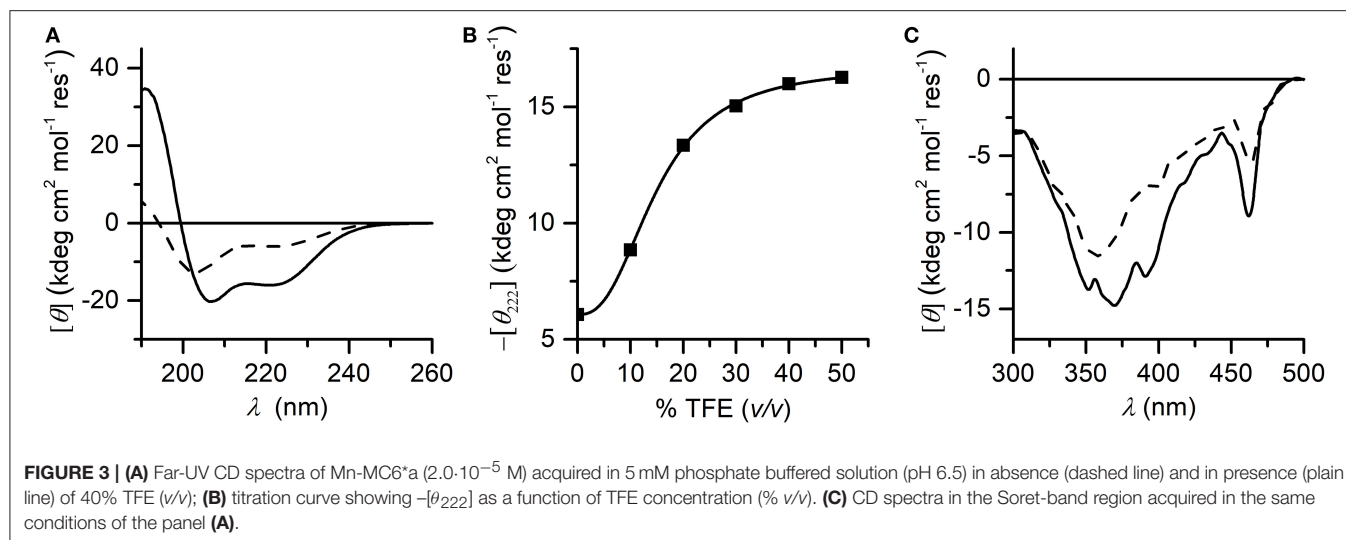
FIGURE 3 | (A) Far-UV CD spectra of Mn-MC6*a ($2.0 \cdot 10^{-5}$ M) acquired in 5 mM phosphate buffered solution (pH 6.5) in absence (dashed line) and in presence (plain line) of 40% TFE (*v/v*); **(B)** titration curve showing $-[\theta_{222}]$ as a function of TFE concentration (% *v/v*). **(C)** CD spectra in the Soret-band region acquired in the same conditions of the panel **(A)**.

TABLE 1 | Far-UV region CD parameters of Mn-MC6*a in phosphate buffer/TFE solution pH 6.5.

% TFE (*v/v*)	$[\theta_{222}]^a$	$[\theta_{min}]^{a,b}$ (λ, nm)	θ_{ratio}^c	λ_0^d (nm)
0	−6,072	−12,803 (203)	0.47	194
40	−16,266	−20,263 (207)	0.80	199

$^a[\theta]$ is expressed as mean residue ellipticity (deg cm² dmol⁻¹ res⁻¹); $^b[\theta_{min}]$ represents the $[\theta]$ value at the shorter wavelength minimum (reported in parentheses); $^c\theta_{ratio}$ is the ratio $[\theta_{222}]/[\theta_{min}]$; $^d\lambda_0$ represents the crossover wavelength.

of the Cotton effects for all bands increases upon TFE addition. The overall CD data indicate that both secondary and tertiary structures experience a TFE-dependent stabilization. As early reported for this class of compounds (Vitale et al., 2015; Caserta et al., 2018), the helical folding drives the peptide chains to interact with the porphyrin moiety, with consequent stabilization of the sandwiched structure. According to these data, all further spectroscopic and catalytic investigations were performed in aqueous solutions containing 40% (*v/v*) TFE.

Coordination Properties of Mn-MC6*a by UV-vis pH Titration

The coordination properties of Mn-MC6*a were investigated by a UV-vis pH titration, following the changes in the absorption spectrum over a wide pH range (2.0–11.0). The molar absorptivity at 365 nm (ε_{365}) was plotted as a function of $[H^+]$ and the experimental data points were fitted to an equation describing pH-dependent equilibria involving four species (Equation 8, Supporting Information).

The best fit gave three transitions with midpoints at pH 4.0 (pK_{a1}), 7.2 (pK_{a2}), and 9.8 (pK_{a3}) (**Figure 4A**). **Table 2** summarizes the absorption features of the four species participating to the equilibria, whose absorption spectra are reported in **Figure 4B**. At pH 2, the *bis*-aquo species was predominant (species **1**, **Figures 4C** and **D**), characterized by two

absorption bands at 365 and 458 nm in the Soret region (see **Table 2** and **Figure 4B**) (Giovannetti et al., 2010). A significant decrease in the absorbance, together with slight wavelength shifts of both bands, occurs as pH increases from 2.0 to 5.4. The component at 365 nm is blue-shifted while the other one is red-shifted. These spectral changes are reasonably attributed to the deprotonation of the His[9] side-chain ($pK_{a1} = 4.0$) to give a His-aquo coordination (species **2**) (Low et al., 1998). A further pH increase from 5.4 to 8.4 causes the spectrum to remain substantially unchanged, with a small increase of the Soret extinction coefficient. These spectroscopic features suggest the presence of a deprotonation equilibrium involving a second shell residue ($pK_{a2} = 7.2$), which does not perturb the first coordination environment and gives rise to species **3**. Upon pH increase from 8.4 to 11.0, substantial spectral changes occur both in the Soret band intensity and position. They may account for the deprotonation of the metal-bound water ligand ($pK_{a3} = 9.8$), leading to the alkaline form of Mn^III-MC6*a, with the His-hydroxy axial coordination (species **4**).

These assumptions are further supported by the electrochemical data recorded at the Mn-MC6*a complex at different pH values (in the range 5.5–13). The formal potential of the Mn^III/Mn^II determined by cyclic voltammetry was plotted as a function of pH (**Figure S2**). In the pH range 5.5–10, the formal potential shows no pH-dependence and the $E_{1/2}$ value for Mn^III/Mn^II is −0.31 V *vs.* NHE (Normal Hydrogen Electrode), which is attributed to the His-aquo axial coordination state. The lack of formal potential variation around pH 7 confirms that the acid-base equilibrium occurring around pH ∼7 does not alter the metal coordination state. Upon further pH increase to values higher than 10, a decrease of the formal potential was observed, which fully supports the hypothesis that deprotonation of the water ligand occurs, leading to increased stabilization of Mn^III vs. Mn^II in the His-hydroxy axial coordination state.

It is worth to note here that the $E_{1/2}$ value obtained for the His-aquo coordination state of Mn-MC6*a is slightly less negative than those reported for other Mn-porphyrin peptide conjugates
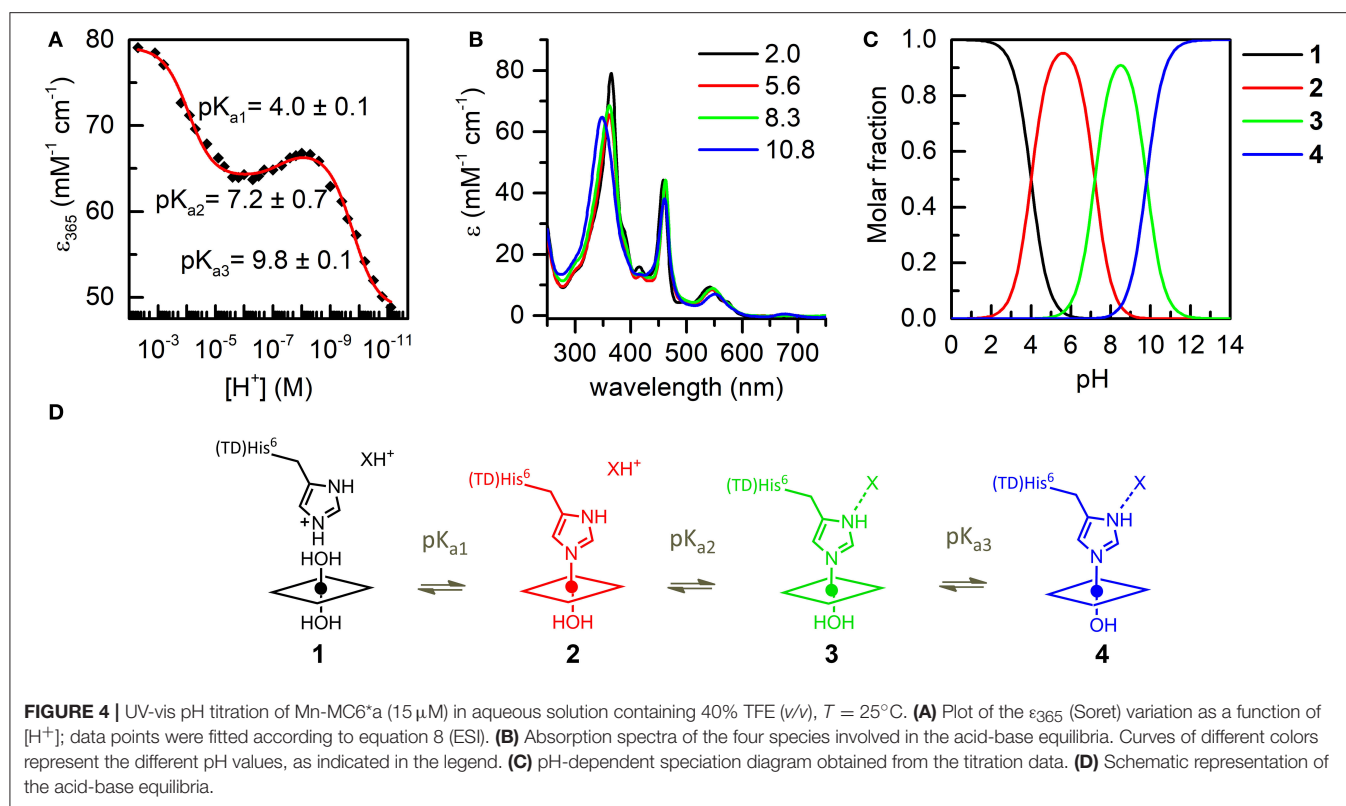
FIGURE 4 | UV-vis pH titration of Mn-MC6*a (15 μM) in aqueous solution containing 40% TFE (v/v), $T = 25°C$. **(A)** Plot of the ε_{365} (Soret) variation as a function of [H⁺]; data points were fitted according to equation 8 (ESI). **(B)** Absorption spectra of the four species involved in the acid-base equilibria. Curves of different colors represent the different pH values, as indicated in the legend. **(C)** pH-dependent speciation diagram obtained from the titration data. **(D)** Schematic representation of the acid-base equilibria.

TABLE 2 | UV-vis absorption maxima of Mn-MC6*a in H₂O/TFE solution (60/40 v/v) at different pH values.

pH	Species	Soret bands λ (nm)	Soret ε^a (mM^{-1} cm^{-1})	Q bands (β,α) λ(nm)
2.0	1	365, 458	79	542, 573
5.6	2	362, 462	64	547, 575 (sh)
8.3	3	362, 462	68	547, 575 (sh)
10.8	4	348, 460	65	552, 590 (sh)

^{a}Soret ε refers to the band at lower wavelength.

with similar coordination states, such as Mn-microperoxidase 8 (Mn-MP8, $E_{1/2} = -0.36$ V vs. NHE at pH 7.5) (Primus et al., 1999) and MnGGH ($E_{1/2} = -0.44$ V vs. NHE) (Ryabova and Nordlander, 2005). This indicates that the relative stability of oxidized vs. reduced state is decreased in the Mn-MC6*a complex. In parallel, the water molecule bound at the oxidized Mn^{III} metal ion is more acidic in the Mn-MC6*a complex (pK$_{a3}$ = 9.8) as compared with Mn-MP8 (pKa = 11.2) and MnGGH (pKa = 12). A similar effect was already reported in mutants of the H-NOX heme protein (Olea et al., 2010) and attributed to a lower electron density at the metal ion center. This in turn increases its Lewis acidity and thus the Bronsted acidity of the bound water molecule.

As widely reported in the literature (Tezcan et al., 1998; Reedy et al., 2008), heme exposure to solvent also allows to modulate the redox potential. In particular, a hydrophobic core, causing water

exclusion from the heme environment, determines an upshift in reduction potential. Thus, the observed shift on the $E_{1/2}$ value in Mn-MC6*a, with respect to Mn-MP8 and MnGGH, can be also attributed to a different environment around the His-aquo manganese porphyrin. Both Mn-MP8 and MnGGH lack a distal peptide chain, and therefore one side of the manganese porphyrin is fully exposed to the solvent. On the opposite, the presence of the distal chain in Mn-MC6*a creates a different environment, with a hydrophobic patch formed by the Aib methyl groups (Caserta et al., 2018). In such an environment, the reduced form of the redox center, as well as the His-hydroxy oxidized form, would be stabilized, thus causing a positive shift of the reduction potential and a downshift of the bound water pK$_a$ value with respect to Mn-MP8 and MnGGH. Finally, the hydrogen bond network within residues of the designed distal pocket (**Figure 1**) may also play a role in favoring water deprotonation.

Catalytic Studies

To ascertain the possible role of Mn-MC6*a in oxidation chemistry, the formation of high-valent Mn species was first investigated. Subsequently, the catalytic properties were explored in the sulfoxidation of phenyl thioethers, taken as model reaction, and compared with those of Fe-MC6*a.

Formation of High-Valent Mn Species

Spectroscopic studies upon treatment of Mn-MC6*a with oxidizing agents were first carried out. Addition of excess hydrogen peroxide (100 eq.) to a buffered solution (60 mM carbonate containing 40% TFE (v/v), pH 10) of the complex

(20 μM) led to a significant decrease in the intensity of the absorption bands at 358 and 461 nm, with the concurrent formation of a single Soret band at 393 nm. In the visible region, the intensity of the band at 547 nm decreased, while three new bands at 504, 530, and 612 nm appeared (**Figure 5A**). These spectral changes are consistent with the formation of the oxomanganyl [Mn^{IV}=O]$^{.+}$ radical cation. Indeed, a very similar absorption spectrum was observed, upon addition of hydrogen peroxide, for Mn-HRP (**Figure 5B**) (Khan et al., 1996) and Mn-MP8 (Primus et al., 2002) and was identified as the manganese analog of the "Compound I" of heme peroxidases (Dolphin et al., 1971; Hersleth et al., 2006). The observed spectroscopic profile excludes the formation of [Mn^{V}=O] even when stronger oxidizing agents were used (t-BuOOH, NaOCl, KHSO$_5$) (**Figure S3**). In order to rule out the possible involvement of hydroxyl radicals derived from photochemical decomposition of hydrogen peroxide (Weiss, 1952), the reaction was also carried out in the presence of D-mannitol (2.0 eq. with respect to H$_2$O$_2$), acting as radical scavenger (Desesso et al., 1994). The reaction outcome was not altered by the presence of the scavenger (data not shown), thus confirming the reactivity of Mn-MC6*a toward hydrogen peroxide. Stability and formation of [Mn^{IV}=O]$^{.+}$ depends on the equivalents of added peroxide. Mn^{III}-MC6*a was quantitatively converted into Compound I upon treatment with 100 eq. H$_2$O$_2$ and underwent complete bleaching within 20 min (**Figure S4A**). When lower peroxide concentrations were used, the observed yield of Mn-Compound I formation was lower, but it spontaneously returned to the resting state. Based on the Soret absorbance, the treatment of Mn^{III}-MC6*a with 10 eq. of H$_2$O$_2$ led to Mn-Compound I with a 76% yield, while catalyst restoring was around 55% (**Figure S4B**). Conversely, the reaction with an equimolar amount of H$_2$O$_2$ provided Mn-Compound I in 45%, and the restoring was almost quantitative (>90%) (**Figure S4C**). All these data demonstrate that MC6*a scaffold is able to host a [Mn^{IV}=O]$^{.+}$ species. This behavior distinguishes MC6*a from small-molecule Mn-porphyrins, which are typically able to provide both Mn^{IV}- and Mn^{V}-oxo intermediates (Huang and Groves, 2017). Notably, MC6*a is similar to manganese-reconstituted HRP in selectively forming the [Mn^{IV}=O]$^{.+}$ species, independently from the nature of the oxidizing agent (Khan et al., 1996, 1998; Nick et al., 2002). However, [HRP-Mn^{IV}=O]$^{.+}$ was characterized by a higher stability than [MC6*a-Mn^{IV}=O]$^{.+}$. Indeed, regardless of the equivalents of H$_2$O$_2$ added, [HRP-Mn^{IV}=O]$^{.+}$ is stable over hours, likely as the result of the the wide delocalization of the radical beyond the porphyrin ring (Khan et al., 1996).

The effect of pH on the rate of [MC6*a-Mn^{IV}=O]$^{.+}$ formation was also evaluated. The pH-dependent time-course of the reaction was monitored by following the variations in the absorbance at 393 nm upon addition of H$_2$O$_2$ (1.0 eq.) under different pH conditions (**Figure 6A**). The formation of Mn-Compound I was remarkably slow at pH values below 7.5 and a negligible amount of the high-valent species was observed. The initial reaction rate was significantly influenced by pH (**Figure 6B**), reaching the highest value at pH 10 (v_0 = 62.8 10^{-2} μM s^{-1}). At pH 11, a similar oxidation rate was observed
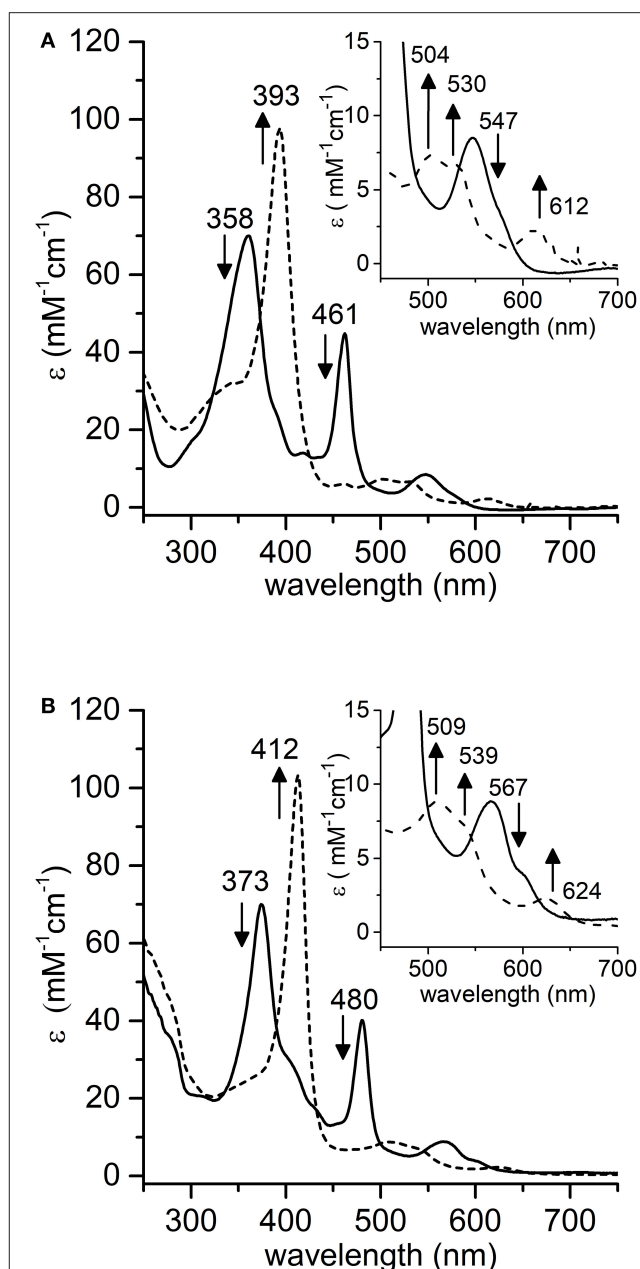

FIGURE 5 | Comparative UV-vis spectra of: **(A)** Mn-MC6*a (20 μM, 60 mM carbonate buffer pH 9.5 with 40% v/v TFE, T = 25°C) and **(B)** Mn-HRP (8.0 μM, 100 mM phosphate buffer pH 7.0, T = 25°C) before (plain lines) and after (dashed lines) addition of 100 eq. H$_2$O$_2$. Arrows indicate the direction of absorbance variations.

(v_0 = 57.2·10^{-2} μM s^{-1}), even though a subsequent decay of the [Mn^{IV}=O]$^{.+}$ species occurred. A conspicuous drop in reactivity was then found above pH 11 (pH 12, v_0 = 5.7·10^{-2} μM s^{-1}), which is attributed to decomposition of hydrogen peroxide in the alkaline medium and/or to Compound I instability (Ryabova and Nordlander, 2005). A similar behavior in Mn-Compound I formation was observed when a 10 eq. excess of H$_2$O$_2$ was used (data not shown).
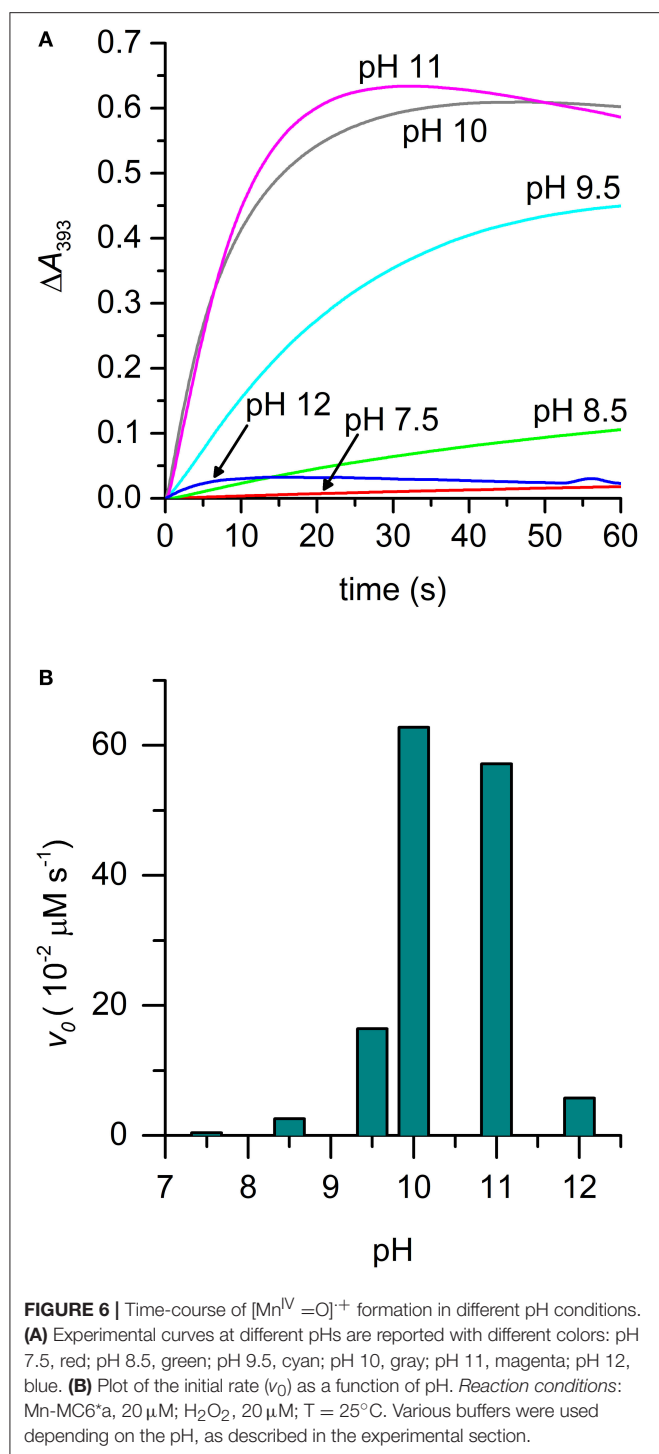
FIGURE 6 | Time-course of $[Mn^{IV}=O]^{.+}$ formation in different pH conditions. **(A)** Experimental curves at different pHs are reported with different colors: pH 7.5, red; pH 8.5, green; pH 9.5, cyan; pH 10, gray; pH 11, magenta; pH 12, blue. **(B)** Plot of the initial rate (v_0) as a function of pH. *Reaction conditions*: Mn-MC6*a, 20 μM; H_2O_2, 20 μM; T = 25°C. Various buffers were used depending on the pH, as described in the experimental section.

The alkaline pH value corresponding to the maximum reaction rate in Mn-Compound I formation is not unexpected. Indeed, as previously reported for manganese reconstituted heme-proteins and for model systems, manganese is less efficient than iron in lowering the pK_a value of H_2O_2. Thus, pH increase is required in order to assist H_2O_2 deprotonation, which is necessary for peroxide heterolytic cleavage and Compound I

formation (Khan et al., 1996; Primus et al., 2002; Yeh et al., 2002; Cai et al., 2013; Chino et al., 2018). Among Mn^{III} complexes, we evidenced that the pK_a of the distal axial ligand is downshifted as compared with the Mn-MP8 complex. This most likely explains that the maximum reactivity for Mn-MC6*a is observed at pH 10, two pH units below the value observed for Mn-MP8 (pH 11.9) (Yeh et al., 2002). Based on these pH values, it appears that Mn-MC6*a approaches the properties of Mn-HRP (maximum reactivity at physiological pH values) (Khan et al., 1996) better than Mn-MP8.
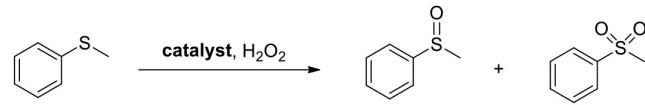
Sulfoxidation of Phenyl Thioethers

The ability of the high-valent $[Mn^{IV}=O]^{.+}$ species in catalyzing the oxy-functionalization of substrates was investigated. To this aim, the H_2O_2-mediated sulfoxidation of phenyl thioethers was chosen as model reaction and followed by GC-MS analysis (**Table 3**). First experiments were performed with thioanisole (100 eq.) as substrate, under the best conditions for Compound I formation (Mn-MC6*a:H_2O_2 = 1:100, pH 10.0, 40% *v/v* TFE). Complete conversion of the sulfide into the corresponding sulfoxide was achieved within 5 min by the addition of H_2O_2 (**Table 3**, entry 1). As formation of the high-valent $[Mn^{IV}=O]^{.+}$ was found to be strongly pH-dependent, the effect of pH on thioanisole sulfoxidation was also evaluated. **Figure 7A** reports the substrate conversion at various pHs, by monitoring the consumption of the substrate after 5 min of the reaction progress. A considerable increase in substrate conversion (up to 50-fold) was observed by raising the pH from 6.5 (2% conversion) to 10 (100% conversion). A further pH increase caused a small drop in the conversion (pH 11). Increasing the reaction time, almost complete substrate conversion was observed at any pH value (**Figure 7B**), although 7 h were required at pH 6.5. As unique exception, at pH 11 the reaction stopped at 74% yield, even after prolonged reaction times. However, further addition of peroxide (100 eq.) led to the complete conversion of the substrate within 5 min. This behavior excludes the lowering of the reaction yield by catalyst inactivation, while suggesting the occurrence of an alternative pathway, currently under investigation. Under optimized reaction conditions (Mn-MC6*a, 20 μM; thioanisole, 20 mM; H_2O_2, 20 mM, pH 10, 40% *v/v* TFE), the catalyst was able to perform 870 TONs in thioanisole oxidation.

Mn-MC6*a was also screened in the sulfoxidation of several phenyl sulfides, such as *p*-chlorothioanisole, *p*-nitrothioanisole, *p*-methoxythioanisole, cyclopropyl-phenyl sulfide. A similar reactivity was observed, regardless the presence of activating/deactivating groups by electronic or steric effects (**Table 4**). These results demonstrate that Mn-MC6*a is able to convert phenyl thioethers into the corresponding sulfoxides with high yields. The reactions were found to proceed with chemoselectivity between sulfoxide and sulfone products, as no traces of over-oxidized products (e.g., aryl sulfones) were detected. The only exception was found with *p*-chlorothioanisole, in which 13% of sulfone formation was observed (**Figures S5–S9**). Unfortunately, no detectable enantiomeric excess was observed.
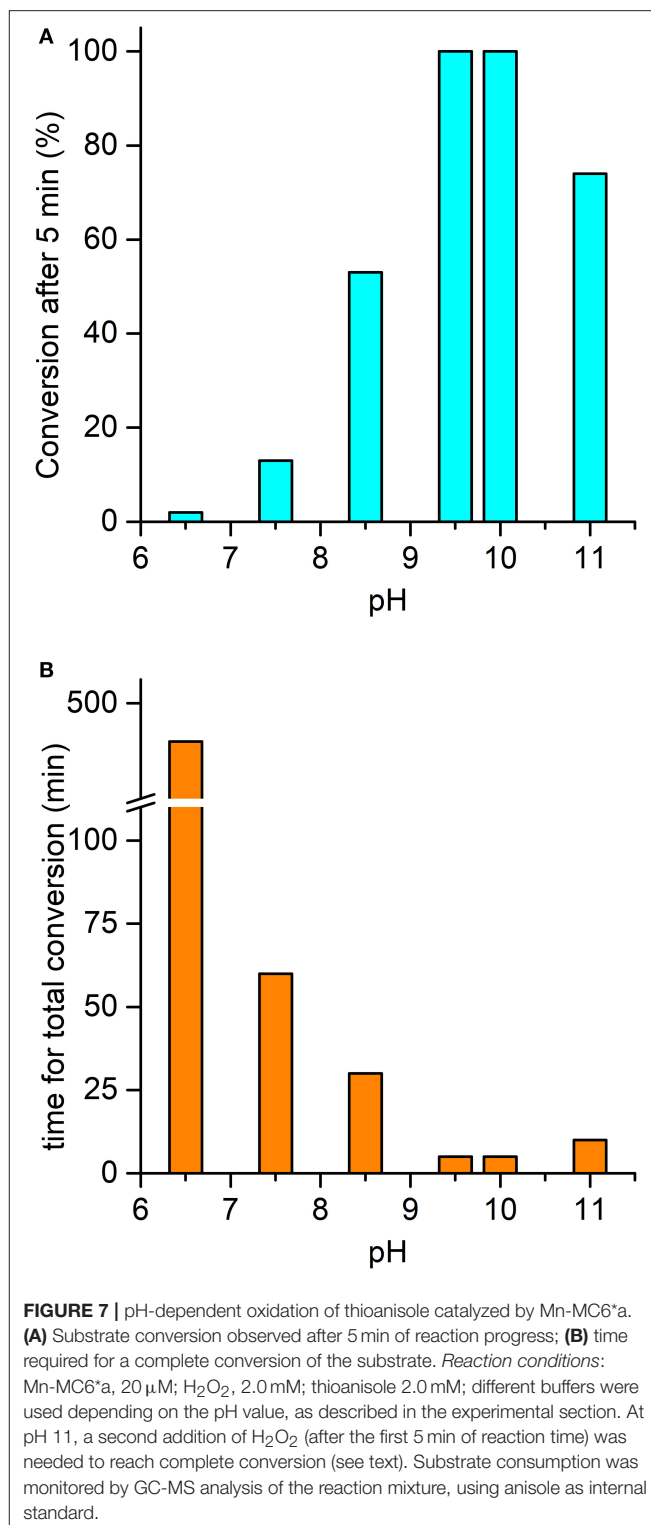
The pH-dependent profile of thioanisole sulfoxidation (**Figure 7A**) well correlates with the pH-dependent formation of

TABLE 3 | Enzyme-catalyzed H_2O_2-dependent oxidation of thioanisole.

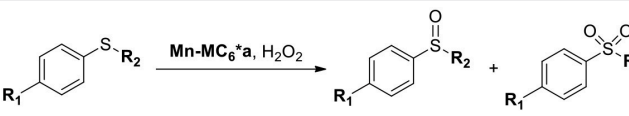| Entry	Catalyst	Catalyst:substrate: H_2O_2 (catalyst concentration)	Yield, % (time, min)	TON	Reference
1	Mn-MC6*a	1:100:100 (20 µM)	100 (5)	870[a]	This work
2	Fe-MC6*a	1:100:100 (20 µM)	97 (5)	1500[b]	This work
3	Mn-HRP	1:100:100 (9 µM)	4 (5)	4	This work
4	Fe-HRP	1:30:40 (330 µM)	95 (60)	28	Colonna et al., 1992
5	Cr-salophen-Mb(H64D/A71G)	1:100:100 (10 µM)	NA[c]	NA[c]	Ohashi et al., 2003
6	Mn-Cor-BSA	1:50:75 (200 µM)	83 (90)	150	Mahammed and Gross, 2005
7	Fe(TpCPP)-Xln10A	1:425:175 (20 µM)	85 (138)	145	Ricoux et al., 2009
8	Mn-salen-Mb(T39C/L72C)	1:40:40 (130 µM)	17 (10)	7[d]	Garner et al., 2011
9	Fe-TpSPP-NCS-3.24	1:500:500 (5 µM)	1.3 (120)	6.5[d]	Sansiaume-Dagousset et al., 2014
10	CoL-BSA	1:100:150 (2.7 µM)	98 (1,680)	98[d]	Tang et al., 2016

[a]TON was determined using a 1:1000:1000 catalyst:substrate:H_2O_2 ratio.

[b]TON was determined using a 1:2000:2000 catalyst:substrate:H_2O_2 ratio.

[c]Yield and TON not available from the reference. The reported reaction rate is 78 10^{-3} TON min^{-1}.

[d]TON was calculated based on the reported yield and catalyst:substrate ratio.

the high-valent $[Mn^{IV}=O]^{·+}$ species (**Figure 6B**). This finding strongly suggests a direct involvement of the Mn-oxo species in substrates oxy-functionalization. To shed light on the reaction mechanism, Mn-MC6*a catalyzed thioanisole oxidation was performed with ^{18}O-labeled hydrogen peroxide as the oxidant. GC-MS analysis revealed that the reaction with $H_2^{18}O_2$ produced sulfoxide with 96% ^{18}O-labeled oxygen (**Figure S6**). This result indicates a peroxygenase-like mechanism, with the oxygen incorporated into the sulfoxide deriving from $H_2^{18}O_2$ through an oxygen transfer mechanism from the Mn-oxo intermediate. The Mn-MC6*a-catalyzed oxidation of thioanisole was also monitored by UV-vis spectroscopy (**Figure 8**), in order to elucidate whether the reaction mechanism occurs *via* a direct oxygen transfer, or by a two-steps, single-electron transfer process, similarly to HRP (Goto et al., 1999). Addition of H_2O_2 (2 mM) to a buffered solution (pH 9.5) of the catalyst (20 µM) led to the formation of Compound I. Immediate addition of thioanisole (2 mM) to the reaction mixture led to the rapid disappearance of the bands related to Mn-Compound I and the concurrent return to the catalyst resting state. The presence of isosbestic points at 332, 373, 424, and 491 nm suggests a single-step conversion from $[Mn^{IV}=O]^{·+}$ to Mn^{III}. This observation

FIGURE 7 | pH-dependent oxidation of thioanisole catalyzed by Mn-MC6*a. **(A)** Substrate conversion observed after 5 min of reaction progress; **(B)** time required for a complete conversion of the substrate. *Reaction conditions*: Mn-MC6*a, 20 µM; H_2O_2, 2.0 mM; thioanisole 2.0 mM; different buffers were used depending on the pH value, as described in the experimental section. At pH 11, a second addition of H_2O_2 (after the first 5 min of reaction time) was needed to reach complete conversion (see text). Substrate consumption was monitored by GC-MS analysis of the reaction mixture, using anisole as internal standard.

indirectly excludes a reaction mechanism involving successive one-electron transfers. Conversely, these data are consistent with a direct oxygen transfer (Goto et al., 1999), involving the nucleophilic attack of the sulfide to Compound I. Further,

TABLE 4 | Mn-MC6*a-catalyzed oxidation of thioethers.

Entry	R_1	R_2	Conversion (%)[a]
1	H	Me	100
3	Cl	Me	87[b]
4	NO_2	Me	100
5	MeO	Me	100
6	H	C_3H_5	100

*Reaction conditions: Mn-MC6*a, 20 μM; sulfide, 2 mM; H_2O_2, 2 mM (1:100:100 catalyst:substrate:oxidant ratio), 60 mM carbonate buffer with 40% TFE (v/v). No traces of the corresponding sulfone were detected by GC-MS analysis, unless otherwise specified.*
[a]*Substrate consumption after 5 min of reaction progress.*
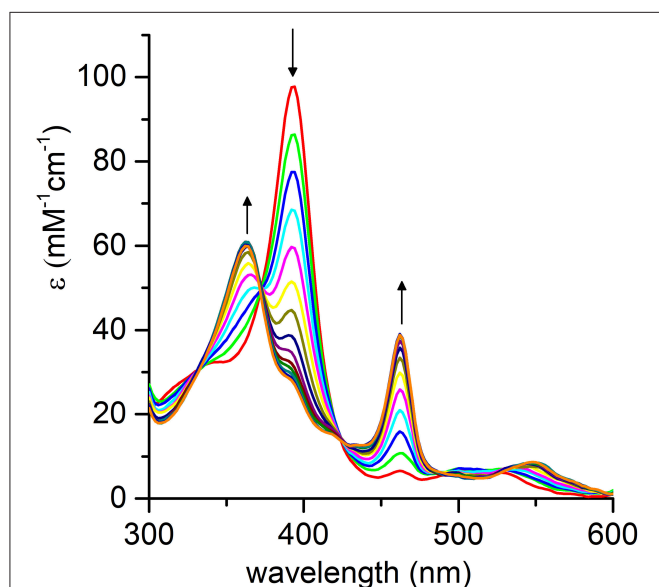[b]*A small amount (13%) of sulfone was detected.*

FIGURE 8 | Evolution of the UV-vis absorption spectrum of $[Mn^{IV}=O]^{·+}$ upon addition of thioanisole (100 eq.); arrows indicate the direction of absorbance variations. *Reaction conditions*: Mn-MC6*a, 20 μM; H_2O_2, 2.0 mM; thioanisole 2.0 mM; 60 mM carbonate buffer with 40% TFE (v/v), pH 9.5; T = 25°C.

the almost complete recovery of Mn^{III}-MC6*a (87%) revealed negligible catalyst degradation.

In order to evaluate the effect of metal ion in MC6*a peroxygenase activity, Fe^{III}-MC6*a was also screened toward thioanisole sulfoxidation. Under optimal conditions for Compound I formation (pH 6.5, 50% v/v TFE) (Caserta et al., 2018), Fe-MC6*a catalyzed the almost complete conversion of the substrate (97% conversion after 5 min by the addition of H_2O_2, **Table 3** entry 2) to the corresponding sulfoxide. A drop in the reactivity was observed at pH 9.5 (62% conversion after 5 min by the addition of H_2O_2). Similarly to Mn-MC6*a, no traces of over-oxidized products (e.g., aryl sulfones) were

detected. Further, experiments with ^{18}O-labeled hydrogen peroxide indicated the formation of the sulfoxide with 94% ^{18}O-labeled oxygen (data not shown). All these results strongly suggest catalysis by Fe^{III}-MC6*a through a peroxygenase-like mechanism, similarly to Mn^{III}-MC6*a. Under optimized reaction conditions (Fe-MC6*a, 20 μM; thioanisole, 100 mM; H_2O_2, 40 mM, pH 6.5, 50% v/v TFE), the catalyst was able to perform 1,500 TONs in thioanisole oxidation.

Reactivity toward thioanisole sulfoxidation as a function of pH clearly indicated different behaviors among the iron and manganese complexes. Indeed, complete conversion was observed at pH 9.5 for Mn-MC6*a, whereas conversion was lower (62%) at this pH when using Fe-MC6*a as catalyst. On the opposite, in the condition of maximum reactivity for the iron complex (pH 6.5, 97% conversion), Mn-MC6*a shows negligible activity (2% yield). This finding clearly reflects the different ability of iron and manganese in activating hydrogen peroxide (Chino et al., 2018). Nevertheless, it is important to outline that the MC6*a scaffold is able to drive the reactivity of the high-valent metal-oxo species toward peroxygenase catalysis at very different pH values, simply changing the metal ion.

CONCLUSION

This work was focused on the spectroscopic and functional characterization of Mn-MC6*a, an artificial metalloenzyme belonging to the mimochrome family. All the results demonstrate that MC6*a scaffold is able to accommodate manganese and tune its reactivity. In particular, spectroscopic characterization provided evidences for the formation, upon treatment of Mn^{III}-MC6*a with hydrogen peroxide, of the oxomanganyl $[Mn^{IV}=O]^{·+}$ radical cation. Notably, this species is able to catalyze peroxygenase reactions, through a direct oxygen-transfer pathway, with high conversion yields. A similar peroxygenase activity was also detected for Fe^{III}-MC6*a, previously demonstrated to be one of the most stable and efficient catalysts with peroxidase activity (Caserta et al., 2018).

Comparison of Fe-MC6*a and Mn-MC6*a with native and manganese-reconstituted HRPs revealed interesting features of our miniaturized protein scaffold. It is well known that HRP is evolved for the reduction of hydroperoxides because of its binding pocket, which is able to properly accommodate H_2O_2. Its high-valent iron-oxo intermediate (Compound I) usually catalyzes one– or two–electron oxidations of several substrates with high efficiency (Poulos, 2014). Native HRP has much lower peroxygenase activity, in which the two-electron reduction of Compound I is coupled to the transfer of the ferryl oxygen to a substrate. Only exception is the sulfoxidation of thioanisoles and related sulfur compounds (Colonna et al., 1992). However, mutations at the distal site are needed to enhance HRP peroxygenase activity, thus highlighting that inaccessibility of the ferryl oxygen suppresses direct interaction with substrates (Ozaki and Ortiz de Montellano, 1995; Savenkova et al., 1996, 1998). Further, oxidation of substrates by HRP through oxygen transfer is in competition with enzyme inactivation by spontaneous self-oxidation, at a rate dependent on the concentration of

oxidants and nature of the substrate (Colonna et al., 1992; Velde et al., 2001). Indeed, enhancement in the peroxygenase activity of peroxidases has been obtained by keeping the concentration of H_2O_2 at a low level (**Table 3** entry 4) (Colonna et al., 1992; Velde et al., 2001).

Manganese substitution in HRP causes a further decrease in its peroxygenase activity, because the high chemical stability of Mn-HRP Compound I (Nick et al., 2002) completely hinders its reactivity in oxygen-transfer reactions.

For a straightforward comparison with our systems, in this work we analyzed the reactivity of native HRP and Mn-HRP under our experimental conditions, i.e., catalyst/oxidant/substrate 1:100:100. Under these conditions, native HRP showed poor peroxygenase activity (10% conversion), probably because of catalyst inactivation by excess peroxide. Substitution of iron to manganese caused a further decrease in peroxygenase reactivity (4% conversion yield, **Table 3** entry 3). These data underline the power of our miniaturization approach in the construction of artificial metalloenzymes, affording a designed scaffold, MC6*a, able to host different metal ions. Indeed, swapping of iron to manganese leaves the catalytic activity almost unchanged. This behavior endows it with broad catalytic activity and versatility, being able to steer the active species toward peroxidative and/or peroxygenative catalysis. The finding that oxy-functionalization of thioanisole can be performed with similar yields at two very different pHs, simply changing iron to manganese (pH 6.5 and 9.5, respectively) can be important for applications with pH-sensitive substrates. Finally, it is worth noting that the activity of Fe– and Mn-MC6*a places them among the most active artificial biocatalysts available to date in the H_2O_2-mediated thioanisole oxidation (Ohashi et al., 2003; Mahammed and Gross, 2005; Ricoux et al., 2009; Garner et al., 2011; Sansiaume-Dagousset et al., 2014; Tang et al., 2016). In particular, a comparison of the catalytic performance in terms of TON between our catalysts and a variety of artificial metalloenzymes (**Table 3**) reveals that both Mn-MC6*a and Fe-MC6*a are robust catalysts, being able to perform 870 and 1,500 TONs, respectively. Further experiments are currently ongoing in order to shed light on the different robustness of the two catalysts.

In conclusion, the results herein reported demonstrate that MC6*a scaffold fills the middle-ground between native proteins and small-molecule catalysts. Despite its small structure, it holds enzyme-like structural features by tuning the reactivity of the metal center thanks to a properly designed distal site. It also embodies some typical features of metalloporphyrin catalysts, such as an easily accessible distal site for oxygen-transfer reactions (Neu et al., 2015). Future work will be devoted to exploring the catalytic versatility of Mn-MC6*a and Fe-MC6*a in promoting different reactions of synthetic and/or biotechnological interest.

MATERIALS AND METHODS

Mn^{II} acetate and glacial acetic acid was purchased from Sigma Aldrich. HPLC grade solvents were employed for chromatographic analyses and purifications (Romil). Solvents with higher degree of purity were used in the preparation of solutions for LC-MS, GC-MS, UV-Vis, and CD investigations (Ups grade, Romil). Phosphate and carbonate sodium salts (mono– and dibasic), for buffers preparation, thioanisole (analytical standard), hydrogen peroxide (H_2O_2) solution (30% w/w in water) and isotope labeled hydrogen peroxide ($H_2^{18}O_2$) solution (3% w/w in water) were supplied by Sigma Aldrich. 4-nitrothioanisole, 4-chlorothioanisole, 4-methoxythioanisole and cyclopropyl-phenyl-sulfide employed in catalytic assays were all provided (98% purity) by Alfa Aesar.

HPLC and LC-MS analysis were performed with a Shimadzu LC-10ADvp equipped with an SPDM10Avp diode-array detector. ESI-MS spectra were recorded on a Shimadzu LC-MS-2010EV system with ESI interface, Q-array-octapole-quadrupole mass analyzer and Shimadzu LC-MS solution Workstation software for data processing. Flash Chromatography was performed using a Biotage Isolera flash purification system, equipped with a diode-array detector.

Atomic absorption measurements were performed using a Shimadzu AA-7000 Series equipped with a graphite furnace atomizer. UV-vis analysis was performed on Cary Varian 50 Probe UV Spectrophotometer equipped with a thermostated cell holder and a magnetic stirrer. CD measurements were carried out on Jasco J-815 dichrograph, equipped with a thermostated cell holder (JASCO, Easton, MD, USA). GC-MS analyses were performed by a Shimadzu GCMS-QP2010 SE system equipped with an EI MS source and a quadrupole array as MS analyzer.

Synthesis and Purification of Mn-MC6*a

Apo-MC6*a was synthesized combining methods of solution and solid-phase peptide synthesis, as previously described by us (Caserta et al., 2018).

Manganese ion was inserted, according to the acetate method procedure (Dolphin, 1978), slightly modified by us. Mn^{II} acetate (10 eq.) was added to a solution of pure *apo*-MC6*a in 2/3 TFE/AcOH (v/v) ($C_{MC6*a} = 2.0 \cdot 10^{-4}$ M), and the reaction mixture was kept at 50°C for 24 h, refluxing under nitrogen atmosphere. The reaction was monitored by analytical reverse phase HPLC, using a C18 column (4.6 mm·150 mm; 5 μm), eluted with a linear gradient of acidic acetonitrile (0.1% TFA v/v) in acidic water (0.1% TFA v/v), from 10 to 50% over 30 min, at 1.0 mL·min^{-1} flow rate.

Once the reaction was completed, the solvent was removed under vacuum and the product was purified from the excess of manganese acetate by Reverse Phase-Flash Chromatography, on a SNAP KP-C18-HS 30 g column, using a gradient of acetonitrile in 0.1% aqueous TFA, 5% to 95% over 2 column volumes, at 25 mL·min^{-1} flow rate.

Determination of Molar Absorptivity of Mn-MC6*a

Molar absorptivity (ε) at 365 nm was determined for Mn-MC6*a using Atomic Absorption spectroscopy (AAS) and UV-vis spectroscopy. In detail, a stock solution of the catalyst ($\approx 2.0 \cdot 10^{-4}$ M) was prepared in H_2O 0.1% TFA (v/v) and its concentration was determined after mineralization using AAS.

Mineralization was carried out by treating aliquots (50 μL) of stock solution with HNO₃ (200 μL) at 95°C for 2 h. Then, the samples were diluted with H₂O 2% HNO₃ (*v/v*) to a final concentration of Mn^{III} ions of ≈2 ppb. Manganese concentration in the stock solution was determined by comparison with a calibration curve obtained using standards. Since metal:catalyst ratio is 1:1, the catalyst concentration was determined. Mn-MC6*a stock solution as determined via AAS was used to prepare different diluted samples, which were used to obtain the ε value at 365 nm by UV-Vis spectroscopy. The absorbance at 365 nm was plotted as a function of catalyst concentration (**Figure S10**). The experimental data were fitted to a Lambert-Beer's law, giving a $\varepsilon_{365} = (7.86 \pm 0.08) \cdot 10^4 \ M^{-1} \ cm^{-1}$.

CD Experiments

Solutions of Mn-MC6*a were prepared at $C = 2.0 \cdot 10^{-5}$ M in 5 mM phosphate buffer at pH 6.5, using various TFE percentages from 0 to 50% (*v/v*). Far-UV CD spectra were collected from 260 to 190 nm using cells of 0.1 cm path length; spectra in the Soret region were collected from 500 to 300 nm using cells of 1 cm path length. All spectra were recorded at 0.2 nm intervals with a 20 nm min^{-1} scan speed, at 2 nm bandwidth and at 16 s response. All measurements were performed at 25°C.

pH Titration Experiments

Solutions of Mn-MC6*a were prepared at $C = 1.5 \times 10^{-5}$ M, in a mixture of H₂O and TFE (60/40 *v/v*). Solutions of NaOH (1, 0.1, and 0.01 M) and TFA (0.1 and 1% *v/v* in water) were used to adjust the pH of the samples (dilution was < 1% and considered in the final data). The model employed for data fitting is reported in the Supporting Information (eqn. 1–8).

Electrochemistry Experiments

Cyclic voltammetry was performed in a small volume home-made cell by using an Autolab PGSTAT-12 potentiostat controlled by GPES-4 software. The cell was constituted by a small cylindrical vial surrounded by a septum perforated to allow positioning of the three electrodes as well as the argon tube. The working electrode was a glassy carbon electrode (CHInstruments Inc.), reference electrode was Ag/AgCl (WPI, Dri-ref, + 0.2 V vs. NHE at 25°C) and counter electrode was a platinum wire. The cell was filled with 0.35 mL of a 0.1 mM Mn-MC6*a solution, prepared from dilution of a 1 mM stock Mn-MC6*a solution in milliQ water (35 μL) into a mixture of the appropriate buffer (175 μL of a 250 mM stock solution) and TFE (140 μL). The working electrode was polished on 1 and 0.1 μm alumina and the solution degassed by argon bubbling prior measuring cyclic voltammograms at 10 mV·s^{-1} at room temperature. In the text, potentials are quoted *vs.* NHE.

Reaction of Mn^{III}-MC6*a With H₂O₂

Solutions of Mn-MC6*a ($C = 20$ μM) were prepared in 60 mM carbonate buffer containing 40% TFE (*v/v*) at pH 10. Reactions were initialized by addition of different amounts of hydrogen peroxide (1, 10, 100 eq.) from properly diluted stock solutions of H₂O₂ in water. Reaction progress was followed by continuously collecting UV-Vis spectra in the 250–750 nm region using a 9,600

nm/min scan speed. Catalyst recovery was estimated based on the Soret absorbance when no more changes were observed. Similar experiments were performed with a prepared sample of Mn-HRP. In these cases, 8.0 μM protein in 100 mM phosphate buffered solutions at pH 7 were employed.

In the pH-dependent experiments, reactions were initiated by addition of 1.0 eq. H₂O₂ to a buffered solution of the catalyst ($C = 20$ μM) containing 40% TFE (*v/v*). Different buffers were used depending on the pH: pH 6.5–8.5, phosphate buffer; pH 9.5–10 carbonate buffer. The pH of the solutions was adjusted with NaOH in the experiments at higher pH values. Reactions were monitored over 60 s by collecting the single-wavelength absorbance traces at 393 nm. The initial rate (v_0) was determined, for each pH value, as the slope of the reaction progress curve at $t = 0$ s.

All experiments were performed at $T = 25°C$, under magnetic stirring, using quartz cells of 1 cm path length.

Preparation of Mn-HRP

Mn-protoporphyrin IX, *apo*-HRP, and Mn-HRP were prepared according to literature procedures (Yonetani and Asakura, 1969). The insertion of Mn porphyrin into *apo*-peroxidase was assessed by UV-vis spectroscopy in comparison with literature data (Yonetani and Asakura, 1969; Khan et al., 1996). The homogeneity of the sample was ascertained by analytical Gel Filtration Chromatography (GFC), using a Yarra SEC-2000 column (7.8 mm·300 mm; 3 μm), with an isocratic flow of 0.05 M sodium phosphate 0.3 M NaCl pH 6.8 as mobile phase, at a flow rate of 0.35 mL min^{-1}. Fe-HRP was analyzed under the same experimental conditions for comparison (**Figure S11**). Molecular weight of the samples was determined based on a calibration curve obtained with standards (**Figure S12**). The GE Healthcare LMW Calibration kit, containing Conalbumin, Ovalbumin, Carbonic anhydrase and Ribonuclease A, all at a concentration of 1 mg/mL, was used for calibration. To prepare the calibration curve, K$_{av}$ of the proteins were calculated as follows:

$$K_{av} = \frac{V_e - V_0}{V_c - V_0}$$

where V_0 is column void volume, V_c is the geometric volume of column, V_e is the elution volume of the protein. A value of 48 kDa was found for the molecular weight of both Fe-HRP and Mn-HRP.

General Procedure for Sulfoxidation Reactions

Stock solutions of substrates (thioanisole, TA; *p*-chlorothioanisole, *p*CTA; *p*-nitrothioanisole, *p*NTA; *p*-methoxythioanisole, *p*MTA; cyclopropyl-phenyl sulfide, CPPS) were prepared dissolving a known amount of neat sulfide in TFE to a final concentration of 0.1 M.

All reactions were carried out at 20 μM catalyst concentration in 60 mM buffered solution with 40% TFE (*v/v*). Reactions with Mn-HRP and Fe-MC6*a as catalysts were performed in absence and in presence of 50% (*v/v*) TFE, respectively. Depending on the pH value, different buffers were used: pH 6.5–8.5,

phosphate buffer; pH 9.5–10.0, carbonate buffer. Reaction at pH 11 was performed in a 60 mM carbonate solution, whose pH was adjusted with NaOH. All reactions were carried out at room temperature and under magnetic stirring. All assays were performed at 1:100:100 catalyst:substrate:oxidant ratio. TON was determined using a 1:1,000:1,000 ratio and a 1:2,000:2,000 ratio for Mn- and Fe-MC6*a, respectively.

The catalyst was preloaded with substrate prior to addition of hydrogen peroxide. Reaction was then initialized by addition of hydrogen peroxide from a solution of 0.1 M H_2O_2 in water. For TA, reaction was carried out also using ^{18}O-labeled hydrogen peroxide to test the peroxygenase activity of Fe- and Mn-MC6*a. A solution of 90% ^{18}O-enriched H_2O_2, at 0.1 M concentration was used. Reaction progress was monitored by GC-MS, using anisole as internal standard. At different times, an aliquot of the reaction mixture (50 μL) was diluted with an equal volume of H_2O 0.1% TFA (v/v) and extracted with ethyl acetate (100 μL). Residual water was removed from the organic phase with anhydrous sodium sulfate. GC-MS analysis of the organic phase was performed using a Rxi-5Sil-MS Column with helium as carrier gas. A linear gradient from 80°C to 230°C with a rate of 18°C min^{-1} was used for thioanisole and pCTA; a linear gradient from 70° to 200°C with a rate of 15°C min^{-1} was used for CPPS; a linear gradient from 70° to 200°C with a rate of 18°C min^{-1}, and then from 200°C to 300°C with a rate of 40°C min^{-1} was used for pNTA and pMTA. MS analysis was performed in TIC (Total Ion Current) mode, exploring a range of m/z from 50 to 250 Th. The grade of conversion at different reaction times was determined based on substrate consumption, using the following equation:

$$Conversion\ (\%) = \frac{\left(\frac{A_{sub}}{A_{I.Std.}}\right)_0 - \left(\frac{A_{sub}}{A_{I.Std.}}\right)_x}{\left(\frac{A_{sub}}{A_{I.Std.}}\right)_0} \cdot 100$$

where A_{sub} and $A_{I.Std.}$ are the peak areas of substrate and internal standard, respectively, in the GC-MS TIC chromatogram. The subscript 0 indicates the trace acquired prior to addition of peroxide, while the subscript x is a specific time during the reaction course.

Control reactions in the absence of catalyst were also performed and gave no reaction progress.

AUTHOR CONTRIBUTIONS

LL and DD performed the spectroscopic and catalytic experiments. GZ synthesized and purified the molecule; VB performed the electrochemical measurements. MC, FN, and OM contributed to the design and discussion of the experiments. LL organized all the information in both main text and **Supplementary Material**. VP and AL analyzed results and provided critical feedback. AL and FN wrote the manuscript in consultation with the remaining authors.

FUNDING

ACKNOWLEDGMENTS

SUPPLEMENTARY MATERIAL

The Supplementary Material for this article can be found online at: https://www.frontiersin.org/articles/10.3389/fchem.2018.00590/full#supplementary-material

REFERENCES

Arnold, F. H. (2018). Directed evolution: bringing new chemistry to life. *Angew. Chem. Int. Ed.* 57, 4143–4148. doi: 10.1002/anie.201708408

Baglia, R. A., Zaragoza, J. P. T., and Goldberg, D. P. (2017). Biomimetic Reactivity of oxygen-derived manganese and iron porphyrinoid complexes. *Chem. Rev.* 117, 13320–13352. doi: 10.1021/acs.chemrev.7b00180

Boucher, L. J. (1968). Manganese porphyrin complexes. I. Synthesis and spectroscopy of manganese(III) protoporphyrin IX dimethyl ester halides. *J. Am. Chem. Soc.* 90, 6640–6645. doi: 10.1021/ja01026a014

Bowman, S. E. J., and Bren, K. L. (2008). The chemistry and biochemistry of heme c: functional bases for covalent attachment. *Nat. Prod. Rep.* 25, 1118–1130. doi: 10.1039/b717196j

Cai, Y. B., Li, X. H., Jing, J., and Zhang, J. L. (2013). Effect of distal histidines on hydrogen peroxide activation by manganese reconstituted myoglobin. *Metallomics* 5, 828–835. doi: 10.1039/c3mt20275e

Caserta, G., Chino, M., Firpo, V., Zambrano, G., Leone, L., D'Alonzo, D., et al. (2018). Enhancement of peroxidase activity in the artificial mimochrome VI catalysts through rational design. *Chembiochem* 19, 1823–1826. doi: 10.1002/cbic.201800200

Chino, M., Leone, L., Zambrano, G., Pirro, F., D'Alonzo, D., Firpo, V., et al. (2018). Oxidation catalysis by iron and manganese porphyrins within enzyme-like cages. *Biopolymers* 109:e23107. doi: 10.1002/bip.23107

Colonna, S., Gaggero, N., Carrea, G., and Pasta, P. (1992). Horseradish peroxidase catalysed sulfoxidation is enantioselective. *J. Chem. Soc. Chem. Commun.* 4, 357–358. doi: 10.1039/c39920000357

Costas, M. (2011). Selective C–H oxidation catalyzed by metalloporphyrins. *Coord. Chem. Rev.* 255, 2912–2932. doi: 10.1016/j.ccr.2011.06.026

Desesso, J. M., Scialli, A. R., and Goeringer, G. C. (1994). D-mannitol, a specific hydroxyl free radical scavenger, reduces the developmental toxicity of hydroxyurea in rabbits. *Teratology* 49, 248–259. doi: 10.1002/tera.1420490404

Di Costanzo, L., Geremia, S., Randaccio, L., Nastri, F., Maglio, O., Lombardi, A., et al. (2004). Miniaturized heme proteins: crystal structure of Co(III)-mimochrome IV. *J. Biol. Inorg. Chem.* 9, 1017–1027. doi: 10.1007/s00775-004-0600-x

Dolphin, D. (1978). *The Porphyrins, Volume I: Structure and Synthesis, 1st Edn.* New York, NY: Academic Press Inc.

Dolphin, D., Forman, A., Borg, D. C., Fajer, J., and Felton, R. H. (1971). Compounds I of catalase and horse radish peroxidase: π-cation radicals. *Proc. Natl. Acad. Sci. U.S.A.* 68, 614–618. doi: 10.1073/pnas.68.3.614

D'Souza, A., Wu, X., Yeow, E. K. L., and Bhattacharjya, S. (2017). Designed heme-cage β-sheet miniproteins. *Angew. Chem. Int. Ed. Engl.* 56, 5904–5908. doi: 10.1002/anie.201702472

Felton, R. H. (1978). "3–Primary redox reactions of metalloporphyrins," in *The Porphyrins*, ed D. Dolphin (New York, NY: Academic Press Inc), 53–125.

Firpo, V., Le, J. M., Pavone, V., Bren, K. L., and Lombardi, A. (2018). Hydrogen evolution from water catalyzed by cobalt-mimochrome VI*a, a synthetic mini-protein. *Chem. Sci.* doi: 10.1039/C8SC01948G

Fujii, H. (2002). Electronic structure and reactivity of high-valent oxo iron porphyrins. *Coord. Chem. Rev.* 226, 51–60. doi: 10.1016/S0010-8545(01)00441-6

Garner, D. K., Liang, L., Barrios, D. A., Zhang, J. L., and Lu, Y. (2011). Covalent anchor positions play an important role in tuning catalytic properties of a rationally designed MnSalen-containing metalloenzyme. *ACS Catal.* 1, 1083–1089. doi: 10.1021/cs200258e

Gelb, M. H., Toscano, W. A., and Sligar, S. G. (1982). Chemical mechanisms for cytochrome P-450 oxidation: spectral and catalytic properties of a manganese-substituted protein. *Proc. Natl. Acad. Sci. U.S.A.* 79, 5758–5762. doi: 10.1073/pnas.79.19.5758

Giovannetti, R., Alibabaei, L., and Pucciarelli, F. (2010). Spectral and kinetic investigation on oxidation and reduction of water soluble porphyrin–manganese(III) complex. *Inorg. Chim. Acta* 363, 1561–1567. doi: 10.1016/j.ica.2009.12.015

Goto, Y., Matsui, T., Ozaki, S., Watanabe, Y., and Fukuzumi, S. (1999). Mechanisms of sulfoxidation catalyzed by high-valent intermediates of heme enzymes: electron-transfer vs oxygen-transfer mechanism. *J. Am. Chem. Soc.* 121, 9497–9502. doi: 10.1021/ja9901359

Groves, J. T. (2006). High-valent iron in chemical and biological oxidations. *J. Inorg. Biochem.* 100, 434–447. doi: 10.1016/j.jinorgbio.2006.01.012

Hersleth, H. P., Ryde, U., Rydberg, P., Görbitz, C. H., and Andersson, K. K. (2006). Structures of the high-valent metal-ion haem–oxygen intermediates in peroxidases, oxygenases and catalases. *J. Inorg. Biochem.* 100, 460–476. doi: 10.1016/j.jinorgbio.2006.01.018

Hong, D. P., Hoshino, M., Kuboi, R., and Goto, Y. (1999). Clustering of fluorine-substituted alcohols as a factor responsible for their marked effects on proteins and peptides. *J. Am. Chem. Soc.* 121, 8427–8433. doi: 10.1021/ja990833t

Huang, X., and Groves, J. T. (2017). Oxygen activation and radical transformations in heme proteins and metalloporphyrins. *Chem. Rev.* 5, 2491–2553. doi: 10.1021/acs.chemrev.7b00373

Karlin, K. D. (2010). Bioinorganic chemistry: model offers intermediate insight. *Nature* 463, 168–169. doi: 10.1038/463168a

Khan, K. K., Mondal, M. S., and Mitra, S. (1996). Kinetic studies of the reaction of hydrogen peroxide with manganese-reconstituted horseradish peroxidase. *J. Chem. Soc. Dalton Trans.* 6, 1059–1062. doi: 10.1039/dt9960001059

Khan, K. K., Mondal, M. S., and Mitra, S. (1998). Kinetics and thermodynamics of the reaction of peroxides with manganese-reconstituted horseradish peroxidase: a stopped-flow transient kinetic investigation. *J. Chem. Soc., Dalton Trans.* 4, 533–536. doi: 10.1039/a707317h

Liu, W., and Groves, J. T. (2015). Manganese catalyzed C-H halogenation. *Acc. Chem. Res.* 48, 1727–1735. doi: 10.1021/acs.accounts.5b00062

Liu, W., Huang, X., Cheng, M. J., Nielsen, R. J., Goddard, W. A., and Groves, J. T. (2012). Oxidative aliphatic C-H fluorination with fluoride ion catalyzed by a manganese porphyrin. *Science* 337, 1322–1325. doi: 10.1126/science.1222327

Lombardi, A., Marasco, D., Maglio, O., Costanzo, L. D., Nastri, F., and Pavone, V. (2000). Miniaturized metalloproteins: application to iron–sulfur proteins. *Proc. Natl. Acad. Sci. U.S.A.* 97, 11922–11927. doi: 10.1073/pnas.97.22.11922

Lombardi, A., Nastri, F., Marasco, D., Maglio, O., Sanctis, G. D., Sinibaldi, F., et al. (2003). Design of a new mimochrome with unique topology. *Chem. Eur. J.* 9, 5643–5654. doi: 10.1002/chem.200304831

Lombardi, A., Nastri, F., and Pavone, V. (2001). Peptide-based heme-protein models. *Chem. Rev.* 101, 3165–3189. doi: 10.1021/cr000055j

Low, D. W., Abedin, S., Yang, G., Winkler, J. R., and Gray, H. B. (1998). Manganese microperoxidase-8. *Inorg. Chem.* 37, 1841–1843. doi: 10.1021/ic971166c

Maglio, O., Nastri, F., and Lombardi, A. (2012). "Structural and functional aspects of metal binding sites in natural and designed metalloproteins," in *Ionic Interactions in Natural and Synthetic Macromolecules*, eds A. Ciferri, A. Perico (Hoboken, NJ: Wiley-Blackwell; John Wiley & Sons, Inc.), 361–450.

Mahammed, A., and Gross, Z. (2005). Albumin-conjugated corrole metal complexes: extremely simple yet very efficient biomimetic oxidation systems. *J. Am. Chem. Soc.* 127, 2883–2887. doi: 10.1021/ja045372c

Martinez-Lorente, M. A., Battioni, P., Kleemiss, W., Bartoli, J. F., and Mansuy, D. (1996). Manganese porphyrins covalently bound to silica and montmorillonite K10 as efficient catalysts for alkene and alkane oxidation by hydrogen peroxide. *J. Mol. Catal. A* 113, 343–353. doi: 10.1016/S1381-1169(96)00109-4

Moody, P. C. E., and Raven, E. L. (2018). The nature and reactivity of ferryl heme in compounds I and II. *Acc. Chem. Res.* 51, 427–435. doi: 10.1021/acs.accounts.7b00463

Nastri, F., Bruni, R., Maglio, O., and Lombardi, A. (2013). "*De Novo* design of protein cages to accommodate metal cofactors," in *Coordination Chemistry in Protein Cages*, eds T. Ueno, Y. Watanabe (Hoboken, NJ: John Wiley & Sons, Inc; Wiley-Blackwell), 43–85.

Nastri, F., Lista, L., Ringhieri, P., Vitale, R., Faiella, M., Andreozzi, C., et al. (2011). A heme-peptide metalloenzyme mimetic with natural peroxidase-like activity. *Chem. Eur. J.* 17, 4444–4453. doi: 10.1002/chem.201003485

Nastri, F., Lombardi, A., D'Andrea, L. D., Sanseverino, M., Maglio, O., and Pavone, V. (1998). Miniaturized hemoproteins. *Biopolymers* 47, 5–22.

Nastri, F., Lombardi, A., Morelli, G., Maglio, O., D'Auria, G., Pedone, C., et al. (1997). Hemoprotein models based on a covalent helix–heme–helix sandwich: 1. design, synthesis, and characterization. *Chem. Eur. J.* 3, 340–349.

Neu, H. M., Baglia, R. A., and Goldberg, D. P. (2015). A balancing act: stability versus reactivity of Mn(O) complexes. *Acc. Chem. Res.* 48, 2754–2764. doi: 10.1021/acs.accounts.5b00273

Neu, H. M., Yang, T., Baglia, R. A., Yosca, T. H., Green, M. T., Quesne, M. G., et al. (2014). Oxygen-atom transfer reactivity of axially ligated Mn(V)-oxo complexes: evidence for enhanced electrophilic and nucleophilic pathways. *J. Am. Chem. Soc.* 136, 13845–13852. doi: 10.1021/ja507177h

Nick, R. J., Ray, G. B., Fish, K. M., Spiro, T. G., and Groves, J. T. (2002). Evidence for a weak Mn:O bond and a non-porphyrin radical in manganese-substituted horseradish peroxidase compound I. *J. Am. Chem. Soc.* 113, 1838–1840. doi: 10.1021/ja00005a062

Ohashi, M., Koshiyama, T., Ueno, T., Yanase, M., Fujii, H., and Watanabe, Y. (2003). Preparation of artificial metalloenzymes by insertion of chromium(III) schiff base complexes into apomyoglobin mutants. *Angew. Chem. Int. Ed.* 42, 1005–1008. doi: 10.1002/anie.200390256

Olea, C., Herzik, M. A., Kuriyan, J., and Marletta, M. A. (2010). Structural insights into the molecular mechanism of H-NOX activation. *Protein Sci.* 19, 881–887. doi: 10.1002/pro.357

Oohora, K., Meichin, H., Kihira, Y., Sugimoto, H., Shiro, Y., and Hayashi, T. (2017). Manganese(V) porphycene complex responsible for inert C–H bond hydroxylation in a myoglobin matrix. *J. Am. Chem. Soc.* 139, 18460–18463. doi: 10.1021/jacs.7b11288

Ozaki, S., and Ortiz de Montellano, P. R. (1995). Molecular engineering of horseradish peroxidase: thioether sulfoxidation and styrene epoxidation by Phe-41 leucine and threonine mutants. *J. Am. Chem. Soc.* 117, 7056–7064. doi: 10.1021/ja00132a003

Patel, S. C., and Hecht, M. H. (2012). Directed evolution of the peroxidase activity of a *de novo*-designed protein. *Protein Eng. Des. Sel.* 25, 445–452. doi: 10.1093/protein/gzs025

Poulos, T. L. (2014). Heme enzyme structure and function. *Chem. Rev.* 114, 3919–3962. doi: 10.1021/cr400415k

Primus, J. L., Boersma, M. G., Mandon, D., Boeren, S., Veeger, C., Weiss, R., et al. (1999). The effect of iron to manganese substitution on microperoxidase 8 catalysed peroxidase and cytochrome P450 type of catalysis. *J. Biol. Inorg. Chem.* 4, 274–283. doi: 10.1007/s007750050313

Primus, J. L., Grunenwald, S., Hagedoorn, P. L., Albrecht-Gary, A. M., Mandon, D., and Veeger, C. (2002). The nature of the intermediates in the reactions of Fe(III)- and Mn(III)-microperoxidase-8 with H_2O_2: a rapid kinetics study. *J. Am. Chem. Soc.* 124, 1214–1221. doi: 10.1021/ja016907u

Ragsdale, S. W. (2006). Metals and their scaffolds to promote difficult enzymatic reactions. *Chem. Rev.* 106, 3317–3337. doi: 10.1021/cr0503153

Ranieri, A., Monari, S., Sola, M., Borsari, M., Battistuzzi, G., Ringhieri, P., et al. (2010). Redox and electrocatalytic properties of mimochrome VI, a synthetic heme peptide adsorbed on gold. *Langmuir* 26, 17831–17835. doi: 10.1021/la103744x

Reedy, C. J., Elvekrog, M. M., and Gibney, B. R. (2008). Development of a heme protein structure–electrochemical function database. *Nucleic Acids Res.* 36, D307–D313. doi: 10.1093/nar/gkm814

Ricoux, R., Allard, M., Dubuc, R., Dupont, C., Maréchal, J. D., and Mahy, J. P. (2009). Selective oxidation of aromatic sulfide catalyzed by an artificial metalloenzyme: new activity of hemozymes. *Org. Biomol. Chem.* 7, 3208–3211. doi: 10.1039/b907534h

Ryabova, E. S., and Nordlander, E. (2005). Synthesis and reactivity studies of a manganese "microperoxidase" containing b-type heme. *Dalton Trans.* 7, 1228–1233. doi: 10.1039/b417331g

Sansiaume-Dagousset, E., Urvoas, A., Chelly, K., Ghattas, W., Maréchal, J. D., Mahy, J. P., et al. (2014). Neocarzinostatin-based hybrid biocatalysts for oxidation reactions. *Dalton Trans.* 43, 8344–8354. doi: 10.1039/C4DT00151F

Savenkova, M. I., Kuo, J. M., and Ortiz de Montellano, P. R. (1998). Improvement of peroxygenase activity by relocation of a catalytic histidine within the active site of horseradish peroxidase. *Biochemistry* 37, 10828–10836. doi: 10.1021/bi9725780

Savenkova, M. I., Newmyer, S. L., and Ortiz de Montellano, P. R. (1996). Rescue of His-42→Ala horseradish peroxidase by a Phe-41→His mutation engineering of a surrogate catalytic histidine. *J. Biol. Chem.* 271, 24598–24603. doi: 10.1074/jbc.271.40.24598

Song, W. J., Seo, M. S., George, S. D., Ohta, T., Song, R., Kang, M. J., et al. (2007). Synthesis, characterization, and reactivities of manganese(V)-oxo porphyrin complexes. *J. Am. Chem. Soc.* 129, 1268–1277. doi: 10.1021/ja066460v

Srour, H., Le Maux, P., and Simonneaux, G. (2012). Enantioselective manganese-porphyrin-catalyzed epoxidation and C-H hydroxylation with hydrogen peroxide in water/methanol solutions. *Inorg. Chem.* 51, 5850–5856. doi: 10.1021/ic300457z

Tang, J., Huang, F., Wei, Y., Bian, H., Zhang, W., and Liang, H. (2016). Bovine serum albumin–cobalt(II) Schiff base complex hybrid: an efficient artificial metalloenzyme for enantioselective sulfoxidation using hydrogen peroxide. *Dalton Trans.* 45, 8061–8072. doi: 10.1039/C5DT04507J

Tezcan, F. A., Winkler, J. R., and Gray, H. B. (1998). Effects of ligation and folding on reduction potentials of heme proteins. *J. Am. Chem. Soc.* 120, 13383–13388. doi: 10.1021/ja982536e

Valdez, C. E., Smith, Q. A., Nechay, M. R., and Alexandrova, A. N. (2014). Mysteries of metals in metalloenzymes. *Acc. Chem. Res.* 47, 3110–3117. doi: 10.1021/ar500227u

Velde, F., van Rantwijk, F., and Sheldon, R. A. (2001). Improving the catalytic performance of peroxidases in organic synthesis. *Trends Biotechnol.* 19, 73–80. doi: 10.1016/S0167-7799(00)01529-8

Vitale, R., Lista, L., Cerrone, C., Caserta, G., Chino, M., Maglio, O., et al. (2015). An artificial heme-enzyme with enhanced catalytic activity: evolution, functional screening and structural characterization. *Org. Biomol. Chem.* 13, 4859–4868. doi: 10.1039/C5OB00257E

Vitale, R., Lista, L., Lau-Truong, S., Tucker, R. T., Brett, M. J., Limoges, B., et al. (2014). Spectroelectrochemistry of Fe(III)- and Co(III)-mimochrome VI artificial enzymes immobilized on mesoporous ITO electrodes. *Chem. Commun.* 50, 1894–1896. doi: 10.1039/C3CC48489K

Watkins, D. W., Jenkins, J. M. X., Grayson, K. J., Wood, N., Steventon, J. W., Vay, K. K. L., et al. (2017). Construction and *in vivo* assembly of a catalytically proficient and hyperthermostable *de novo* enzyme. *Nat. Commun.* 8:358. doi: 10.1038/s41467-017-00541-4

Weiss, J. (1952). The decomposition of hydrogen peroxide by ionizing radiations and related problems. *Discuss. Faraday Soc.* 12, 161–169. doi: 10.1039/df9521200161

Whitmore, L., and Wallace, B. A. (2008). Protein secondary structure analyses from circular dichroism spectroscopy: methods and reference databases. *Biopolymers* 89, 392–400. doi: 10.1002/bip.20853

Wolfenden, R., and Snider, M. J. (2001). The depth of chemical time and the power of enzymes as catalysts. *Acc. Chem. Res.* 34, 938–945. doi: 10.1021/ar000058i

Yeh, H. C., Yu, C. H., Wang, J. S., Chen, S. T., Su, O. Y., and Lin, W. Y. (2002). Stopped-flow kinetic study of the peroxidase reactions of mangano-microperoxidase-8. *J. Biol. Inorg. Chem.* 7, 113–119. doi: 10.1007/s007750100271

Yonetani, T., and Asakura, T. (1969). Studies on cytochrome c peroxidase XV. comparison of manganese porphyrin-containing cytochrome c perxidase, horseradish peroxidase, and myoglobin. *J. Biol. Chem.* 244, 4580–4588.

Zambrano, G., Ruggiero, E., Malafronte, A., Chino, M., Maglio, O., Pavone, V., et al. (2018). Artificial heme enzymes for the construction of gold-based biomaterials. *Int. J. Mol. Sci.* 19:E2896. doi: 10.3390/ijms19102896

Di- and Tetrairon(III) μ-Oxido Complexes of an N3S-Donor Ligand: Catalyst Precursors for Alkene Oxidations

Biswanath Das[1], Afnan Al-Hunaiti[2†], Brenda N. Sánchez-Eguía[3], Erica Zeglio[1],
Serhiy Demeshko[4], Sebastian Dechert[4], Steffen Braunger[4], Matti Haukka[5], Timo Repo[2],
Ivan Castillo[3*] and Ebbe Nordlander[1*]

[1] Chemical Physics, Department of Chemistry, Lund University, Lund, Sweden, [2] Laboratory of Inorganic Chemistry,
Department of Chemistry, University of Helsinki, Helsinki, Finland, [3] Instituto de Química, Universidad Nacional Autónoma de
México, Mexico, Mexico, [4] Institute for Inorganic Chemistry, Georg-August-Universität Göttingen, Göttingen, Germany,
[5] Department of Chemistry, University of Jyväskylä, Jyväskylä, Finland

The new di- and tetranuclear Fe(III) μ-oxido complexes
$[Fe_4(\mu-O)_4(PTEBIA)_4](CF_3SO_3)_4(CH_3CN)_2]$ (**1a**), $[Fe_2(\mu-O)Cl_2(PTEBIA)_2](CF_3SO_3)_2$
(**1b**), and $[Fe_2(\mu-O)(HCOO)_2(PTEBIA)_2](ClO_4)_2$ (MeOH) (**2**) were prepared
from the sulfur-containing ligand (2-((2,4-dimethylphenyl)thio)-N,N-bis
((1-methyl-benzimidazol-2-yl)methyl)ethanamine (PTEBIA). The tetrairon complex
1a features four μ-oxido bridges, while in dinuclear **1b**, the sulfur moiety of the ligand
occupies one of the six coordination sites of each Fe(III) ion with a long Fe-S distance of
2.814(6) Å. In **2**, two Fe(III) centers are bridged by one oxido and two formate units, the
latter likely formed by methanol oxidation. Complexes **1a** and **1b** show broad sulfur-to-
iron charge transfer bands around 400–430 nm at room temperature, consistent with
mononuclear structures featuring Fe-S interactions. In contrast, acetonitrile solutions
of **2** display a sulfur-to-iron charge transfer band only at low temperature (228 K) upon
addition of H_2O_2/CH_3COOH, with an absorption maximum at 410 nm. Homogeneous
oxidative catalytic activity was observed for **1a** and **1b** using H_2O_2 as oxidant, but with
low product selectivity. High valent iron-oxo intermediates could not be detected by
UV-vis spectroscopy or ESI mass spectrometry. Rather, evidence suggest preferential
ligand oxidation, in line with the relatively low selectivity and catalytic activity observed in
the reactions.

Keywords: Fe-S interaction, oxidation, homogeneous catalysis, thioether, iron-oxo complex

INTRODUCTION

The interaction between iron and sulfur in metalloproteins and in biomimetic molecular systems
has attracted increased attention in recent years (Beinert et al., 1997; Ohnishi, 1998; Rao and
Holm, 2004; Ballmann et al., 2008a; Meyer, 2008; Lill, 2009). Among these, the majority of the
Fe/S structural motifs are dominated by clusters where the iron center is in distorted tetrahedral
environments (Beinert et al., 1997; Meyer, 2008); nonetheless, there are examples of molecular
systems where the Fe centers display diverse coordination geometries (Ballmann et al., 2008b; Fuchs
et al., 2010). In some typical molecular systems, the metal center has also been found to be involved

in secondary bonding interactions with ether-O and thioether-S units (Ballmann et al., 2008b). Although in all these examples sulfur, being a soft donor, displays preference for low valent Fe(II), there are molecular systems where the sulfur atom has been found to be bonded to high valent (III and IV) iron centers with distorted octahedral geometry (Harrop and Mascharak, 2004; McDonald et al., 2010; Widger et al., 2014). Overall, the Fe-S interaction in various molecular systems having iron in different formal oxidation states is an interesting field of research.

On the other hand, the selective and environmentally benign oxidation of hydrocarbons using affordable and efficient catalysts is another important area of modern synthetic chemistry. In this regard, bio-inspired iron chemistry has received increasing attention in recent decades due to the natural iron abundance in the earth crust, and the highly selective catalytic hydrocarbon oxidations of iron-containing oxygenases such as cytochrome P450 (Hasemann et al., 1995), soluble methane monooxygenase (sMMO) (Tinberg and Lippard, 2011), and Rieske dioxygenases (Wackett, 2002). Among the (catalytic) properties of these iron-based enzymes, the selective activation of C-H bonds under mild conditions is one of the most striking aspects. Many mono- and diiron complexes with various multidentate N-based ligands have been investigated in order to mimic the structures as well as functions of non-heme iron enzymes, and to potentially develop sophisticated oxidation catalysts (Costas et al., 2000, 2004; Sun et al., 2011; Lindhorst et al., 2015; Gamba et al., 2017). Such studies indicate that fine tuning of the coordination environment of the iron centers plays a crucial role in the catalytic activity, which includes O_2 binding, followed by electron-transfer from Fe to O_2 to afford either iron–superoxo (Fe^{III}-O_2^-), iron–peroxo (Fe^{III}-O_2^{2-}), or iron–oxo ($Fe^{IV/V}$ =O) species after initial O-O bond cleavage (Kim et al., 1997; Hazell et al., 2002; Rohde et al., 2003; Ye and Neese, 2011; De Visser et al., 2013; Wang et al., 2013a; Mitra et al., 2014; Nam, 2015).

A number of dinuclear Fe(III)-μ-oxido complexes relevant to the aforementioned enzymes from both structural and functional perspectives, have been studied as oxidation catalysts (Romakh et al., 2007; Visvaganesan et al., 2009; Wang et al., 2013a). Depending on the specific ligand environment, catalytic oxidation reactions using such dinuclear μ-oxido Fe(III) complexes can proceed via a radical intermediate or a high valent metal oxo species, or a combination of both, and the nature of these intermediates/active oxidants exerts a profound influence on the product distribution (Costas et al., 2000, 2004). The experimental evidence in all cases indicate that there is a strong influence of the ligand system on the catalytic activity, as well as the choice of oxidant (i.e., ultimate oxygen donor), which can also affect the product distribution (Costas et al., 2000, 2004). In spite of the extensive oxidative catalytic activity studies of these dinuclear Fe(III)-μ-oxido complexes, to the best of our knowledge there are very few well-characterized complexes that have been used as oxidation catalysts where sulfur occupies one of the coordination sites (McQuilken and Goldberg, 2012). The easily oxidizable nature of sulfur argues against its use in these types of systems (Widger et al., 2014), despite the fact that studying small molecular catalysts with

sulfur-containing ligands can be very useful in modeling key metal-sulfur interactions that play a significant role in non-heme enzymes. Studies on sulfur oxygenation in a number of biomimetic non-heme iron(III)-thiolate complexes indicate that a long Fe-S bond distance makes the sulfur unit susceptible to attack by O_2 in a reaction where iron maintains the +3 oxidation state (McQuilken and Goldberg, 2012). The active site of the non-heme iron enzyme cysteine dioxygenase (McCoy et al., 2006) is believed to pass through a Fe(III)-superoxo intermediate. DFT and QM/MM computational studies predict that the formation of the superoxo intermediate is followed by formation of an energetically favorable cyclic four-membered Fe-O-O-S ring structure that undergoes O-O bond cleavage to form a Fe(IV)(Oxo)-sulfinate analog. This metal oxo unit transfers the second oxygen atom to generate the cysteine-sulfinic acid product (Kumar et al., 2011; McQuilken and Goldberg, 2012).
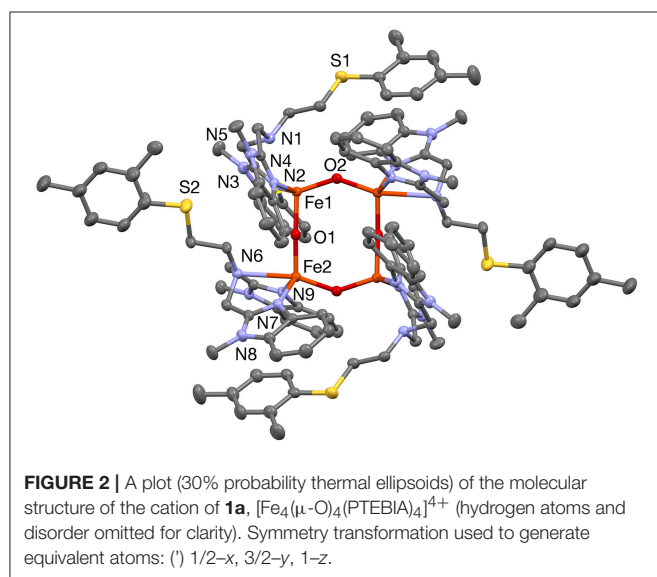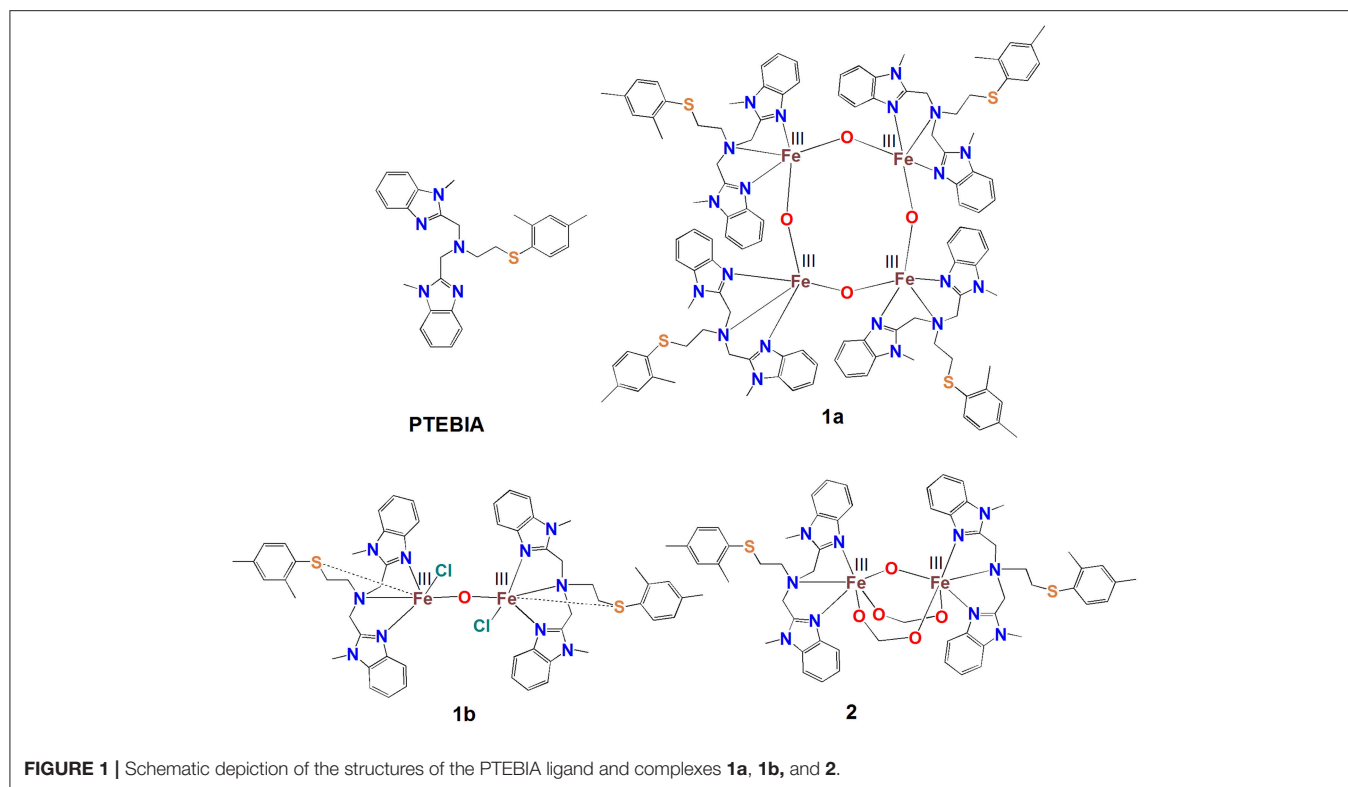
Goldberg and coworkers have reported Fe(II) complexes of interesting pentadentate ligand systems incorporating one sulfur donor in efforts to model the reactivity of the active site of cysteine dioxygenase. While a pentadentate ligand with one thiolate donor is oxidized to the corresponding sulfoxide upon reaction with dioxygen, an analogous thioether ligand permits formation of a non-heme Fe(IV)oxo species that can perform oxygen atom transfer (Widger et al., 2014). In this context, it is worth mentioning that one of the most realistic biomimetic model systems (both in terms of structure and reactivity) for cysteine dioxygenase, [$Tp^{Me,Ph}Fe^{II}CysOEt$] ($Tp^{Me,Ph}$ = hydridotris(3-phenyl-5-methylpyrazol-1-yl)borate), was reported by Limberg and coworkers (Sallmann et al., 2012), who used isotope ($^{16}O/^{18}O$) experiments to confirm that the treatment with dioxygen mainly leads to cysteine dioxygenase activity, i.e., deoxygenation of the bound cysteine ethyl ester.

Here, we describe new di- and tetranuclear Fe(III)-μ-oxido complexes with the thioether-containing PTEBIA ligand (Castillo et al., 2012), viz [$Fe_4(\mu$-O)$_4$(PTEBIA)$_4$](CF$_3$SO$_3$)$_4$(CH$_3$CN)$_2$] (**1a**), and [$Fe_2(\mu$-O)Cl$_2$(PTEBIA)$_2$](CF$_3$SO$_3$)$_2$ (**1b**) (**Figure 1**). The Fe-S interaction in these complexes and their efficiency as homogeneous oxidation catalyst precursors will be discussed. The UV-vis and mass spectrometric investigations of plausible active species in solution are also presented. In order to gain a better understanding of the spectroscopic features of the complexes, specifically regarding the Fe(III)-S interaction, we have also synthesized the dinuclear complex [$Fe_2(\mu$-O)(μ-HCOO)$_2$(PTEBIA)$_2$](ClO$_4$)$_2$(MeOH) (**2**) that features additional bridging formate ligands.

RESULTS AND DISCUSSION

Synthesis and Characterization of Complexes

The PTEBIA ligand was prepared following the procedure reported by Castillo and coworkers (Castillo et al., 2012). Addition of 1 equivalent of Fe(II)(OTf)$_2$ (OTf = triflate, CF$_3$SO$_3^-$) to a tetrahydrofuran solution of PTEBIA leads to an immediate change of the color of the ligand solution

FIGURE 1 | Schematic depiction of the structures of the PTEBIA ligand and complexes **1a**, **1b,** and **2**.

FIGURE 2 | A plot (30% probability thermal ellipsoids) of the molecular structure of the cation of **1a**, [Fe$_4$(μ-O)$_4$(PTEBIA)$_4$]$^{4+}$ (hydrogen atoms and disorder omitted for clarity). Symmetry transformation used to generate equivalent atoms: (') 1/2–*x*, 3/2–*y*, 1–*z*.

TABLE 1 | Selected bond lengths [Å] for **1a**.

Atoms	Bond lengths	Atoms	Bond lengths
Fe1–O2	1.780(3)	Fe2–N7	2.059(3)
Fe1–O1	1.798(3)	Fe2–N9	2.067(3)
Fe1–N2	2.076(3)	Fe1···Fe2'	3.3993(7)
Fe1–N4	2.081(3)	Fe1···Fe2	3.5646(9)
Fe2–O1	1.776(3)	Fe1···Fe1'	4.9297(8)
Fe2–O2'	1.811(3)	Fe2···Fe2'	4.9216(8)

Symmetry transformation used to generate equivalent atoms: (') 1/2–x, 3/2–y, 1–z.

have a distorted trigonal bipyramidal geometry, with N$_3$O$_2$ coordination environments. Selected bond lengths and bond angles for **1a** are listed in **Tables 1**, **2**, respectively. There are two types of Fe-O-Fe bond angles and four different Fe-O bond distances present in the cluster. The angles are 142.36(15)° for Fe1-O2-Fe2′ and 171.64(18)° for Fe1-O1-Fe2 (Symmetry transformation used to generate equivalent atoms: (') 1/2–*x*, 3/2–*y*, 1–*z*). The corresponding bond lengths are 1.780(3) Å for Fe1-O2 and 1.778(6) Å for Fe2-O2,' and 1.811(3) Å for Fe1-O1, and 1.776(3) Å for Fe2-O1. The sulfur donor sites are > 5.2 Å away from the nearest Fe(III) unit, and thus there is no plausible intramolecular Fe(III)-S interaction.

When PTEBIA contained a sub-stoichiometric amount of HCl from incomplete neutralization during the last synthetic step in the PTEBIA synthesis (as evidenced by the immediate precipitation of AgCl upon addition of AgNO$_3$ to a chloroform

to green. Refluxing of this green solution for 4 h, followed by crystallization by slow diffusion of diethylether into an acetonitrile solution of the product leads to yellow, needle shaped crystals of **1a** (**Figure 2**).

The solid-state structure of **1a** consists of a tetranuclear unit formed by four PTEBIA ligands, four bridging oxido ligands and four Fe(III) ions. To the best of our knowledge, this represents the first example of a tetrairon, tetra-oxido cluster with a sulfur-containing ligand. All the Fe(III) units

TABLE 2 | Selected bond angles [°] for **1a**.

Atoms	Bond angles	Atoms	Bond angles
O2–Fe1–O1	109.57(11)	O1–Fe2–N7	117.71(13)
O2–Fe1–N2	108.46(12)	O2'–Fe2–N7	97.80(12)
O1–Fe1–N2	98.24(12)	O1–Fe2–N9	114.80(13)
O2–Fe1–N4	113.86(13)	O2'–Fe2–N9	100.67(12)
O1–Fe1–N4	95.69(12)	N7–Fe2–N9	113.31(12)
N2–Fe1–N4	127.41(12)	Fe2–O1–Fe1	171.64(18)
O1–Fe2–O2'	109.46(11)	Fe1–O2–Fe2'	142.36(15)

Symmetry transformation used to generate equivalent atoms: (') 1/2–x, 3/2–y, 1–z.
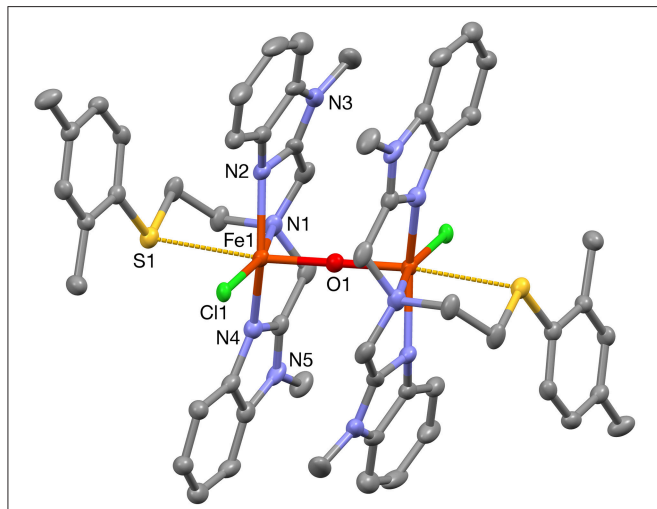

FIGURE 3 | A plot (30% probability thermal ellipsoids) of the molecular structure of the cation of **1b**, [Fe$_2$(μ-O)Cl$_2$(PTEBIA)$_2$]$^{2+}$ (hydrogen atoms omitted for clarity). Only one of the two crystallographically independent molecules is shown. Symmetry transformations used to generate equivalent atoms: (') 1–x, 1–y, 1–z.

TABLE 3 | Selected bond lengths [Å] for **1b**.

Atoms	Bond lengths	Atoms	Bond lengths
Fe1–O1	1.7910(7)	Fe2–O2	1.7905(7)
Fe1–N2	2.085(4)	Fe2–N14	2.094(4)
Fe1–N4	2.095(5)	Fe2–N12	2.099(4)
Fe1–Cl1	2.2925(12)	Fe2–N11	2.306(4)
Fe1–N1	2.298(4)	Fe2–Cl2	2.3131(12)
O1–Fe1'	1.7910(7)	O2–Fe2"	1.7904(7)
Fe1–S1	2.8364(17)	Fe2–S2	2.8147(16)
Fe1···Fe1'	3.5821(11)	Fe2···Fe2'	3.5809(11)

Symmetry transformations used to generate equivalent atoms: (') 1–x, 1–y, 1–z; (") 2–x, 1–y, –z.
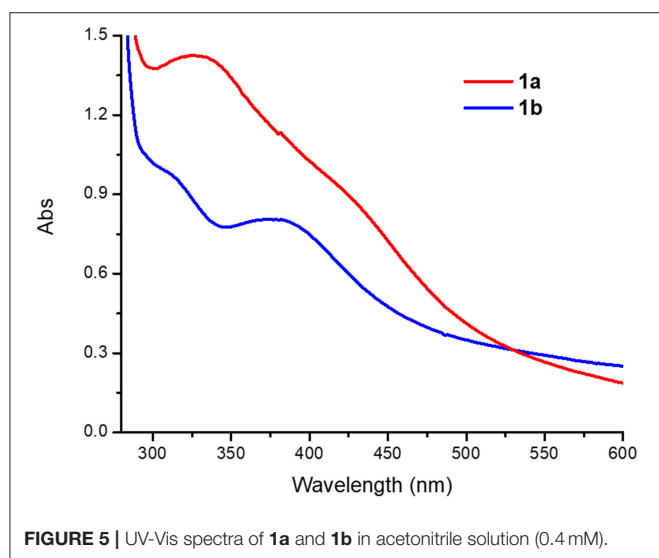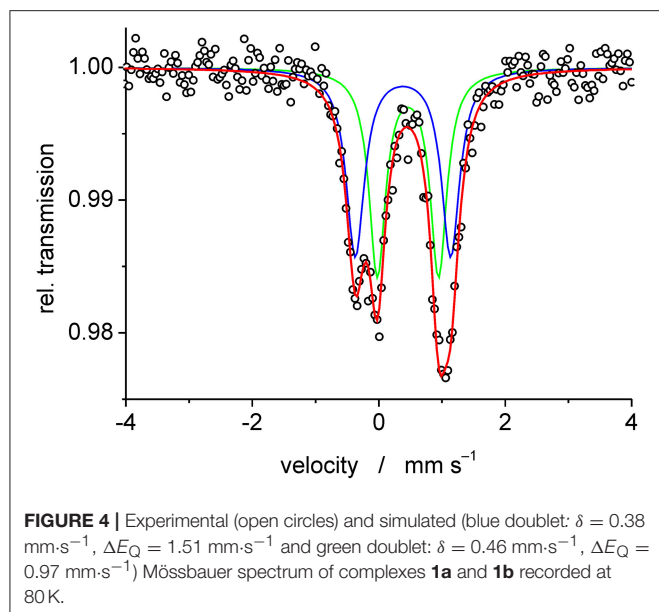
TABLE 4 | Selected bond angles [°] for **1b**.

Atoms	Bond angles	Atoms	Bond angles
O1–Fe1–N2	91.65(13)	O2–Fe2–N14	92.29(12)
O1–Fe1–N4	97.71(13)	O2–Fe2–N12	95.34(12)
N2–Fe1–N4	149.51(18)	N14–Fe2–N12	150.78(16)
O1–Fe1–Cl1	102.36(4)	O2–Fe2–N11	92.01(10)
N2–Fe1–Cl1	105.09(13)	N14–Fe2–N11	76.16(15)
N4–Fe1–Cl1	101.13(13)	N12–Fe2–N11	75.42(14)
O1–Fe1–N1	92.87(12)	O2–Fe2–Cl2	103.82(4)
N2–Fe1–N1	76.54(17)	N14–Fe2–Cl2	103.97(12)
N4–Fe1–N1	74.08(17)	N12–Fe2–Cl2	101.50(11)
Cl1–Fe1–N1	164.58(12)	N11–Fe2–Cl2	164.12(11)
Fe1–O1–Fe1'	180.00(4)	Fe2"–O2–Fe2	180.00(4)

Symmetry transformations used to generate equivalent atoms: (') 1–x, 1–y, 1–z; (") 2–x, 1–y, –z.

solution of PTEBIA•xHCl) (Castillo et al., 2012), formation of **1a** was accompanied by brown crystals of **1b**; the latter complex was also prepared independently from FeCl$_2$. Both complexes appear to be stable over a period of days in acetonitrile solution, but evaporation of the solvent results in oily products. Nonetheless, X-ray quality crystals of **1b** were isolated from cold acetonitrile solutions to acquire data at liquid N$_2$ temperature. The molecular structure of the cation in [Fe$_2$(μ-O)Cl$_2$(PTEBIA)$_2$](CF$_3$SO$_3$)$_2$ (**1b**) is shown in **Figure 3**, and selected bond lengths and bond angles are collated in **Tables 3, 4**, respectively. In the solid state, **1b** is a μ-oxido diiron(III) complex, with Fe(III) centers in a slightly distorted octahedral N$_3$SOCl coordination environment. The thioether moiety coordinates weakly with Fe(III)-S bond lengths of Fe-S bonds of 2.8364(17) and 2.8147(16) Å for the two crystallographically independent molecules found in the asymmetric unit (symmetry transformations used to generate equivalent atoms: (') 1–x, 1–y, 1–z; (") 2–x, 1–y, –z). This Fe-S distance is long in comparison to Fe-S distances reported by Widger et al. for mononuclear Fe(II) complexes (~2.3 Å) with the thioether containing ligand N3Py^{amide}SR (R = -(CH$_2$)$_2$CN) (Widger et al., 2014), but it is comparable to the long

Cu(I/II)-S(thioether) distance observed for coordination of methionine in plastocyanin (2.9 Å) (Sahoo and Ray, 2007). The Fe(III) centers are oxido-bridged and are 3.5821(11) and 3.5809(11)Å (two crystallographically independent molecules) apart from each other with an Fe-O-Fe angle of 180°, which is in accordance with similar dinuclear Fe(III)-μ-oxido complexes reported by McKenzie and coworkers (Vad et al., 2012) and Wang et al. (2003).

Mass spectrometric measurements of **1a** gave rise to two major peaks corresponding to the mononuclear complex, i.e. at 673.7 amu for [Fe(PTEBIA)(CF$_3$SO$_3$)]$^+$, and at 469.8 corresponding to protonated [HPTEBIA]$^+$ (**Figure S1**). A peak arising from **1b** was also observed at 559.7 amu, assigned to [Fe(PTEBIA)(Cl)]$^+$; no μ-oxido bridged species could be detected by either ESI or MALDI-TOF mass spectrometry. IR characterization revealed sharp resonances between 820 and 600 cm^{-1} assigned to asymmetric and symmetric Fe-O stretching modes of the Fe-O-Fe units in **1a** and **1b** (819, 749, 637 cm^{-1} in the former; 815, 780, 746, 633 cm^{-1} in the latter). Additional characterization of **1a** and **1b** was obtained by Mössbauer spectroscopy from 0.02 g of a batch of mixed crystals obtained from the reaction of Fe(OTf)$_2$ with PTEBIA, revealing the presence of two high spin Fe(III) centers with different coordination environments in a 1:1 ratio of **1a** and **1b** (**Figure 4**). Since more ionic coordination

FIGURE 6 | Molecular structure of [Fe$_2$(μ-O)(HCOO)$_2$(PTEBIA)$_2$] (**2**). Thermal ellipsoids are plotted at 30% probability; all hydrogen atoms and perchlorate anions have been omitted for the sake of clarity.

FIGURE 5 | UV-Vis spectra of **1a** and **1b** in acetonitrile solution (0.4 mM).

environments with higher coordination numbers result in higher isomer shifts (δ), the subspectrum with $\delta = 0.46$ mm·s^{-1} can be assigned to **1b**, whereas the subspectrum with $\delta = 0.38$ corresponds to **1a**.

Acetonitrile solutions of **1a** (0.4 mM) exhibit broad peaks with absorption maxima at 330 and 430 nm ($\varepsilon = 3,600$ and 2,280 M^{-1} cm^{-1}, respectively), while **1b** features slightly narrower peaks with absorption maxima at 320 and 390 nm ($\varepsilon = 2,400$ and 1,990 M^{-1} cm^{-1}, **Figure 5**). The peaks around 320–340 nm are in the so called "oxo dimer region" and are characteristic of Fe-O-Fe moieties, as has been observed for similar (μ-oxo)diiron(III) complexes (Reem et al., 1989; Kurtz, 1990; Do et al., 2012). The broad absorption bands around 390–430 nm can be assigned to weak sulfur to Fe(III) charge transfer bands (LMCT), similar to
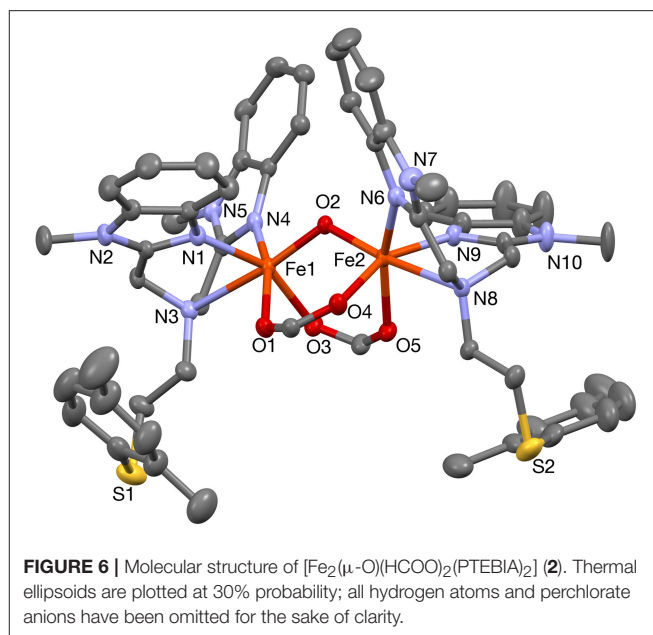
those observed in Cu(II) complexes with PTEBIA (Rodríguez Solano et al., 2011; Castillo et al., 2012).

Conversion of **1a** to **1b** was achieved in acetonitrile solution, as evidenced by UV-vis spectroscopy: addition of two equivalents of NBu$_4$Cl as a source of chloride to 0.4 mM solutions of **1a** resulted in spectra that are virtually identical to those of the chlorido-containing **1b**, see **Figure 5** and **Figure S2**.

To further probe the coordination mode of the PTEBIA ligand toward Fe(III) centers, equimolar amounts of Fe(II)(ClO$_4$)$_2$ and PTEBIA were heated to reflux in THF solution, followed by recrystallization from a methanolic solution by slow vapor diffusion of diethylether. Electrospray mass spectrometry on methanolic solutions of the green crystals obtained from the reaction show a major peak at 262.8 amu (see **Figure S3**), corresponding to the dicationic species [Fe(PTEBIA)]$^{2+}$. The solid-state structure reveals that the complex consists of another μ-oxido diiron(III) species ([Fe$_2$(μ-O)(HCOO)$_2$(PTEBIA)$_2$](ClO$_4$)$_2$(MeOH) (**2**), **Figure 6**), where both Fe(III) centers are in distorted octahedral environments with N$_3$O$_3$ donor sets. Selected bond distance and bond angles are collated in **Tables 5, 6**, respectively. The sulfur atoms are far apart from the Fe(III) centers (> 5.86 Å), ruling out any kind of direct interaction. The Fe(III) ions (Fe···Fe distance 3.121(9) Å) are coordinated by the N-donors of two PTEBIA ligands, as well as one bridging oxido and two formate ligands. The corresponding Fe-O-Fe angle is 121.046(1)°. The unexpected formate bridge is likely due to the aerobic oxidation of the methanol solvent in the presence of Fe(III) and PTEBIA, as has been observed by Que and co-workers in the related complex [Fe$_2$(μ-O)(μ-HCOO)(TPA)$_2$](ClO$_4$)$_3$ (TPA = tris(2-pyridylmethyl)amine) (Norman et al., 1998).

TABLE 5 | Selected bond lengths [Å] for **2**.

Atoms	Bond lengths	Atoms	Bond lengths
Fe1–O1	2.094(4)	Fe2–O2	1.795(4)
Fe1–O2	1.792(4)	Fe2–O4	2.051(3)
Fe1–O3	2.039(3)	Fe2–O5	2.074(4)
Fe1–N1	2.081(3)	Fe2–N6	2.104(5)
Fe1–N3	2.378(5)	Fe2–N8	2.376(5)
Fe1–N4	2.100(5)	Fe2–N9	2.080(3)
Fe1–S1	5.861(2)	Fe2–S2	5.874(2)
Fe1···Fe2	3.122(2)	O2–S2	7.531(3)

TABLE 6 | Selected bond angles [°] for **2**.

Atoms	Bond angles	Atoms	Bond angles
Fe2–Fe1–O1	74.0(1)	O1–Fe1–N1	81.7(1)
Fe2–Fe1–O2	29.5(1)	O1–Fe1–N3	90.6(1)
Fe2–Fe1–O3	80.5(1)	O1–Fe1–N4	163.5(1)
O1–Fe1–O2	97.7(1)	O2–Fe1–N1	103.0(1)
O1–Fe1–O3	86.1(1)	O2–Fe1–N3	171.3(1)
O2–Fe1–O3	99.5(1)	O2–Fe1–N4	98.6(1)
O2–Fe2–O4	98.3(1)	O3–Fe1–N1	155.6(2)
O2–Fe2–O5	97.8(1)	O3–Fe1–N3	83.7(1)
Fe2–Fe1–N1	115.7(1)	O3–Fe1–N4	88.9(1)
Fe2–Fe1–N3	158.6(1)	Fe1–Fe2–O2	29.4(1)
Fe2–Fe1–N4	120.6(1)	Fe1–Fe2–O4	80.1(1)

IR characterization of **2** shows characteristic asymmetric (ν_{asym}) and symmetric (ν_{sym}) C=O stretching bands as a broad peak at 1,614 cm^{-1} and two very sharp peaks for ν_{sym} at 1,490 and 1,453 cm^{-1}, consistent with the presence of two bridging formates (Deacon and Phillips, 1980; Kurtz, 1990; Das et al., 2014a,b, 2018). In addition, the presence of a very sharp band at 1,080 cm^{-1} confirms the presence of perchlorate anions; the bands at 744 and 620 cm^{-1} correspond to the asymmetric and symmetric stretching modes of the Fe-O-Fe units (Kurtz, 1990; Norman et al., 1990). Acetonitrile solutions of **2** (0.5 mM) exhibit an absorption maximum at 342 nm (ε = 4,400 M^{-1} cm^{-1}), characteristic of the Fe-O-Fe moiety (Kurtz, 1990; Norman et al., 1990; Do et al., 2012); unlike **1a** and **1b**, no lower energy bands were observed as the sulfur atom is not bound to the metal centers (**Figure 7**). Low temperature UV-vis experiments using a 1:1 (molar equivalent) of H$_2$O$_2$ (30 wt.% in H$_2$O) and CH$_3$COOH (> 99.7%) solution as oxidant and keeping overall complex:oxidant ratio at 1:2.5 reveal that the formate ligands of **2** may be protonated under these conditions, thus allowing the sulfur atom of PTEBIA to interact with the Fe(III) centers, as evidenced by the new absorption band at around 410 nm. This band is more prominent at low temperature (228 K) and appears only as a shoulder above 250 K (**Figure 7**) and was assigned to a S → Fe LMCT transition.
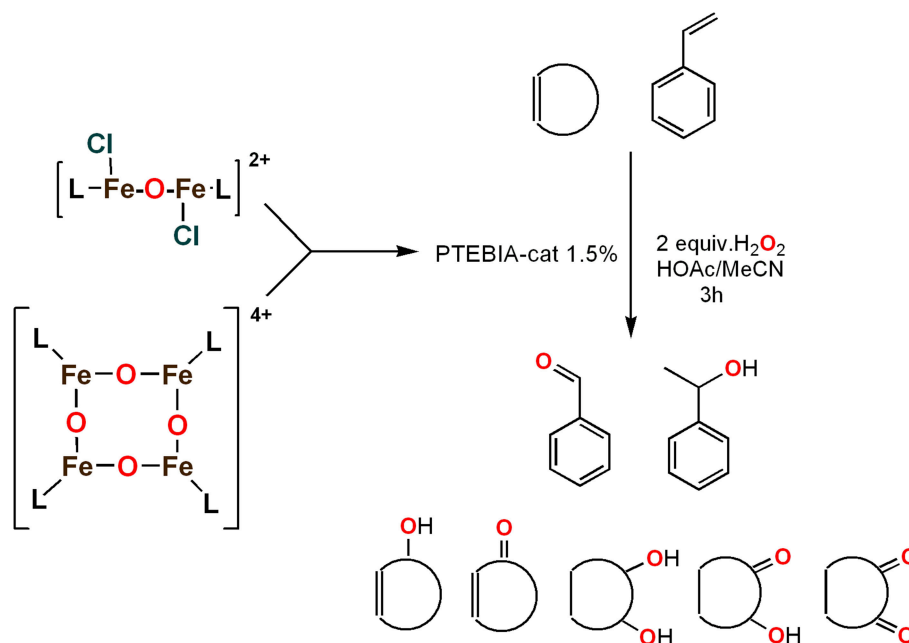
Oxidation Catalysis

Jacobsen et al. (White et al., 2001) have effected efficient epoxidation of terminal long-chain alkenes using an iron
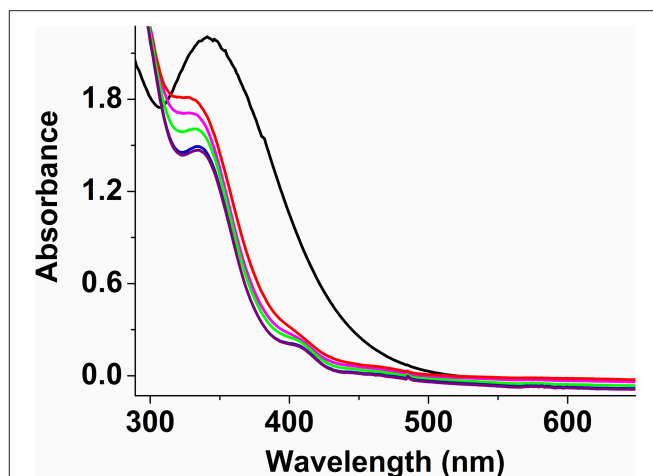
FIGURE 7 | UV-Vis spectra of complex **2** in acetonitrile solution at 298 K (black), and after addition of H$_2$O$_2$/acetic acid mixture (1:1) at 228 K (purple), 238 K (blue), 248 K (green), 258 K (pink), and 268 K (red).

complex based on the tetradentate N4-donor ligand mep (*N,N'*-dimethyl-*N,N'*-bis(2-pyridylmethyl)-ethane), H$_2$O$_2$ as oxidant and acetic acid as a promoter. These authors proposed that the active catalyst was the dinuclear ferric complex [Fe$_2$(μ-O)(μ-OAc)(mep)$_2$]$^+$. Later studies by Fujita and Que indicated that the catalyst was rather the mononuclear complex [Fe(II)(mep)(solv)$_2$]$^{2+}$ (solv=solvent (NCMe)) (Fujita and Que, 2004). Similarly, Stack and coworkers (Dubois et al., 2003) used an Fe(III)-O-Fe(III) complex with aqua and nitrogen donor ligands, [Fe$_2$(μ-O)(OH$_2$)$_2$(phen)$_2$]$^{4+}$ (phen=phenanthroline) as a catalyst/catalyst precursor for alkene epoxidation using peracetic acid as the oxidant. The combination of hydrogen peroxide with a suitable carboxylic acid (e.g., acetic acid) is believed to generate a peracid that in turn may generate a high valent metal oxo complex that functions as an active alkane/alkene oxidant (Fujita and Que, 2004), but it has also been suggested that the reaction of an Fe(II) complex with peracetic acid can lead to an Fe(III) κ^2-peracetate complex with subsequent dissociation of the peracetate ligand to form a ferryl acyl radical species, i.e., an (OAc$^.$)Fe(IV)=O species, that is an active oxidant (Wang et al., 2013b).

Palaniandavar and coworkers (Mayilmurugan et al., 2009) studied the use of Fe(III)$_2$(μ-O) complexes, containing pentadentate Fe(III) ions chelated by tetradentate N$_2$O$_2$ salen-based ligands, as catalysts/precatalysts for the oxidation of alkanes and arenes using the peracid *meta*-chloroperbenzoic acid (*m*-CPBA) as the ultimate oxidant. With few exceptions, the obtained yields and alcohol/ketone ratios were relatively low, suggesting a mixture of metal-based and radical oxidation reactions. We have previously investigated the ability of Fe(III)$_2$(μ-O) complexes with nitrogen and oxygen-based donor sets as active catalysts or precursors for the oxidation of alkanes and alkenes with hydrogen peroxide (Jarenmark et al., 2010; Das et al., 2015). A μ-oxo diiron(III) complex [{Fe(HIPCPMP)}$_2$(μ-O)(Piv)]ClO$_4$ (H$_2$IPCPMP = 2-{*N*-isopropyl-*N*-[(2-pyridyl)methyl]aminomethyl}-6-{*N*(carboxym

SCHEME 1 | Schematic depiction of the catalytic oxidation reactions effected by complexes **1a**/**1b**; *cf.* text and **Table 8**.

ethyl)-*N*-[(2-pyridyl)methyl] aminomethyl}-4-methylphenol; Piv = Pivalate) showed moderate activity in cyclohexane oxidation, using H_2O_2 as the oxidant, and evidence suggests that both metal-based and radical mechanisms were involved in the process (Jarenmark et al., 2010). A greater contribution of the metal-based mechanism was found when the tetranuclear Fe_2Li_2 complex $[Fe_2^{III}O(LiDPCPMPP)_2]$ [DPCPMPP = 3-[(3-{[bis(pyridin-2-ylmethyl)amino]methyl}-2-hydroxy-5-methylbenzyl)(pyridin-2-ylmethyl)amino]propanoate] was used as catalyst, based on the retention of configuration of the products observed in the oxidation of *cis*- or *trans*-1,2-dimethylcyclohexane (Das et al., 2015).

To assess the effect of the mixed N_3S donor set of PTEBIA on the activity and selectivity of iron complexes in the oxygenation of alkenes, we investigated the oxidation of styrene and a number of prototypical cyclic alkene substrates, viz. cyclohexene, 3-ethylcyclohexene, cyclooctene, under mild conditions (**Scheme 1**) using a bulk sample containing an approximate 1:1 mixture of **1a** and **1b** as catalyst precursor(s). The oxidation conditions were optimized by using cyclohexene as the model compound (**Table 7**). Based on the maximum reactivity and selectivity, acetonitrile was used as solvent with CH_3COOH as additive and H_2O_2 as oxidant. These optimized conditions were applied in all oxidation experiments involving the different substrates. Mass spectrometry (ESI-MS) indicated that mixtures of **1a** and **1b** convert to dimeric $[(Fe_2)(OAc)_2(\mu\text{-}O)(PTEBIA)_2(CF_3SO_3)]^+$ in acetonitrile solution, as evidenced by the peak detected at 1332.8 amu (**Figure S4**, **Supplementary Material**). Cyclohexene, cyclooctene and 3-ethylcyclohexene were oxidized in moderate conversions (29, 44, and 15%, **Table 8**) to the overoxidation products of the epoxides, namely diols and diketones. Although

TABLE 7 | Optimization conditions using cyclohexene as a model substrate; substrate:catalyst:oxidant:AcOH (100:1.5:200:80), solvent 3 ml, 3 h reaction time.

Entry	Temperature	Oxidant	Solvent	Conversion (%)
1	10°C	H_2O_2	MeCN	7[a]
2	35°C	H_2O_2	MeCN	29[b]
3	50°C	H_2O_2	MeCN	31[c]
4	35°C	H_2O_2	MeCN	29[b]
5	35°C	O_2	MeCN	2[a]
6	35°C	H_2O_2	H_2O	8
7	35°C	H_2O_2	MeOH	13
8*	35°C	H_2O_2	MeCN	20*
9**	35°C	H_2O_2	MeCN	3**

[a]*The main products are diol and 2-hexenol.*

[b]*the main products are 2-hexen-1-ol.*
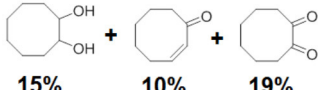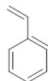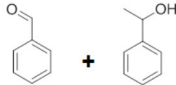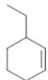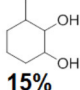
[c]*poor selectivity.*
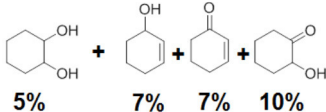
*No acetic acid.

**No catalyst.

styrene oxidation (63% yield) afforded benzylmethanol (by epoxide ring opening), the formation of benzaldehyde as the major product indicates that the main active species is likely a transient radical (single electron oxidation). In comparison to the previously reported μ-oxido di-iron(III) complexes with N and O-based ligands [e.g., 2,6-bis(*N*-methylbenzimidazol-2-yl)pyridine (Wang et al., 2003), DPCPMPP (Das et al., 2015)], the catalytic efficiency (% of product formation and TON) of **1a** and **1b** is comparatively low (Romakh et al., 2007; Das et al., 2015).

In addition to $[(Fe_2)(OAc)_2(\mu\text{-}O)(PTEBIA)_2(CF_3SO_3)]^+$ detected by ESI MS, the main peaks in the mass spectra, and their isotopic patterns are consistent with species formulated as

Entry	Substrate	Time	Products(Yield [%])	TON
1		3	5% 7% 7% 10%	19
2		8	15% 10% 19%	29
3		12	50% 13%	30
4		3	15%	10

Quantification by GC-MS experiments using 1,2-dichlorobenzene as internal standard. Time values are in hours.

monomeric [Fe(HPTEBIA)(OH)]⁺, [Fe(HPTEBIA)(O)(OH)]⁺, [Fe(PTEBIA)(O)(CH₃COO)]⁺, and the protonated form of the oxidized ligand [(HPTEBIA)(O)]⁺ (see **Figures S4–S6, Supplementary Material**), irrespective of whether **1a** and **1b** were analyzed separately or as a 1:1 mixture. This indicates that the active species present during turnover conditions appear to be identical regardless of the precursor. Preferential oxidation of the thioether moiety (generating the corresponding sulfoxide) over the metal center may be occurring, as reported by Goldberg and coworkers with the [Fe^{II}(N₃Py^{amide}SR)](BF₄)₂ system in the presence of 5 equivalents of mCPBA (McQuilken and Goldberg, 2012). No evidence of the formation of Fe(IV)=O species was observed in analogous experiments with mCPBA or PhIO as oxo-transfer reagents. From the catalytic oxidation results induced by H_2O_2 and CH_3COOH, we presume that catalysis with the current complex system does not involve heterolysis of the O-O bond to form a highly reactive Fe$^{(V)}$O species, which should result in higher product selectivity (Prat et al., 2013). Instead, it may proceed *via* homolysis to give transient [LFe$^{(IV)}$O] and hydroxyl radical (OH) intermediates, with participation of both species in the observed oxidations (Trettenhahn et al., 2006).

CONCLUSION

We have synthesized and characterized a new tetrairon tetraoxo cluster (**1a**) with a sulfur-containing ligand. In the UV-vis spectroscopic experiments, a prominent sulfur to iron charge transfer band (390–430 nm) was observed at room temperature for **1a** and the corresponding dinuclear Fe(III)-O-Fe(III) complex **1b**, whereas for the related dinuclear dicarboxylate-bridged Fe(III)-O-Fe(III) complex **2** it was only visible at low temperature (228 K) in the presence of H_2O_2/CH_3COOH (presumably after initial protonation/dissociation of the oxo and formate groups of **2**), and disappears at room temperature,

likely due to loss of the Fe-S bond and/or sulfoxidation of PTEBIA. The catalytic efficiency of the μ-oxido iron(III) complex mixture of **1a** and **1b** for the oxidation of alkenes has been investigated, revealing that they act as moderate oxidation catalyst(s)/catalyst precursor(s). The reaction appears to proceed partially through a metal-centered process in tandem with free-radical oxidation by reactive oxygen species. Low temperature UV-vis spectroscopy and mass spectrometry were employed to gain insight into possible reactive intermediates/active oxidation catalysts, revealing that both H_2O_2/CH_3COOH and PhIO preferably oxidize the thioether group of the ligand, in contrast with previous oxygenations with related copper-based PTEBIA systems, where the thioether functionality remains intact.

MATERIALS AND METHODS

The ligand PTEBIA was prepared following the procedure reported by Castillo et al. (2012). All reagents and solvents were of analytical or spectroscopic grade purchased from Sigma Aldrich, Fisher chemicals or VWR, and were used without further purification. Cyclohexene (≥ 99.0%) contained ∼0.01% of 2,6-di-*tert*-butyl-4-methylphenol as stabilizer and was used as received. *Caution!* Even though no problems were encountered in this work, caution should always be taken while using high concentrations of hydrogen peroxide (H_2O_2), as well as metal perchlorates.

Infrared spectra were recorded in the 4,000–400 cm^{-1} range on a Nicolet Avatar 360 FTIR spectrometer, as KBr pellets. Mass spectra were obtained on a JEOL JMS-SX-102A mass spectrometer at an accelerating voltage of 10 kV with a nitrobenzyl alcohol matrix and Xenon atoms at 6 keV (FAB⁺), a JEOL JMS-AX505HA spectrometer (Electron Ionization), or a Bruker Daltonics Esquire 6000 spectrometer with ion

trap (Electrospray). Elemental analyses were performed at the microanalytical facility of the Instituto de Química, UNAM, Mexico. Analytical achiral GC was performed on an Agilent 6850 GC with FID detector using an Agilent DB-WAX (30.0 m × 0.25 mm) column at mL/min He carrier gas flow. Chiral GC was performed on an Agilent 6850 GC with FID detector. The ^{1}H NMR spectra were recorded with a Varian Gemini 200 apparatus or a Varian Mercury 300 MHz spectrometer.

Substrate conversions in catalytic experiments were determined by GC-MS. The GC-MS analyses were performed with an Agilent 6890 N Network GC system equipped with a DB-1MS column (30 m × 0.25 mm) and an Agilent 5973 Network MS detector. Calibration curves were obtained from commercial products purchased from Aldrich or TCI when available or from pure isolated products obtained from a catalytic reaction using a FID-detector GC with a HP-INOWAX column (30 m × 0.25 mm) (1,2-dichlorobenzene used as an internal standard). The concentrations of each organic product were calibrated relative to that of an internal standard (1,2-dichlorobenzene) with a known concentration.

Syntheses

Synthesis of 1a

To 15 mL of a tetrahydrofuran solution of 0.13 g (0.26 mmol) of PTEBIA, 0.10 g (0.26 mmol) of Fe(II)(triflate)$_2$ were added and the solution was refluxed for 4 h under vigorous stirring. Immediately after the addition of Fe(II)(triflate)$_2$, the solution becomes turbid green, and on reflux it turns yellowish brown. The yellowish brown solution was filtered and the filtrate was collected in a 50 mL flask. Evaporation of the solvent under vacuum produces a tan oil. Overnight slow vapor diffusion of diethyl ether to a concentrated acetonitrile solution of the tan residue produces 0.12 g of 1a [Fe$_4$(μ-O)$_4$(PTEBIA)$_4$](CF$_3$SO$_3$)$_4$(CH$_3$CN)$_2$ as yellow microcrystals (65%). UV-vis (CH$_3$CN): λ_{max} = 335 nm (ε = 3,600 M^{-1} cm^{-1}), 430 nm ($\varepsilon \sim$ 2,280 M^{-1} cm^{-1}). ^{57}Fe Mössbauer (80 K) δ = 0.55 mm/s; ΔEQ = 1.15 mm/s; ESI-MS in acetonitrile solution calculated for [Fe(PTEBIA)(CF$_3$SO$_3$)]$^+$ (C$_{29}$H$_{31}$F$_3$FeN$_5$O$_3$S$_2$) (mononuclear species): 674.1; found 673.8. IR (KBr, cm^{-1}): 2953, 2924, 2856, 1767, 1722, 1539, 1501, 1456, 1365, 1250, 1226, 1160, 1028, 967, 913, 819, 749, 636, 574, 517, 432. Anal. Calcd for C$_{116}$H$_{124}$F$_{12}$Fe$_4$N$_{20}$O$_{16}$S$_4$: C, 50.44; H, 4.52; N, 10.14; S, 9.29; found: C, 50.19; H, 4.50; N, 9.88; S, 9.02.

Synthesis of 1b

The procedure is analogous to that for 1a, employing 33 mg (0.26 mmol) of FeCl$_2$. The brown solution was filtered and the filtrate was collected in a 50 mL flask. Evaporation of the solvent under vacuum produces a brown solid. Overnight slow vapor diffusion of diethyl ether to a concentrated acetonitrile solution of the brown solid affords 0.11 g of 1b [Fe$_2$(μ-O)Cl$_2$(PTEBIA)$_2$](CF$_3$SO$_3$)$_2$ as brown microcrystals [m.p. 195–197°C (dec)] (61%). UV-vis (CH$_3$CN): λ_{max} = 320 nm (ε = 2,400 M^{-1} cm^{-1}), 390 nm ($\varepsilon \sim$ 1,990 M^{-1} cm^{-1}). ^{57}Fe Mössbauer (80 K) δ = 0.28 mm/s; ΔEQ = 1.31 mm/s; ESI- MS in acetonitrile solution calculated for [Fe(PTEBIA)(Cl)]$^+$ (C$_{28}$H$_{31}$ClFeN$_5$S) (mononuclear species): 560.1; found 559.7. IR (KBr, cm^{-1}): 2935,

1736, 1597, 1491, 1452, 1426, 1378, 1256, 1223, 1151, 1100, 1054, 1029, 959, 932, 815, 780, 746, 700, 633, 572, 545, 516, 430. Anal. Calcd for C$_{58}$H$_{62}$Cl$_2$F$_6$Fe$_2$N$_{10}$O$_7$S$_4$: C, 48.51; H, 4.35; N, 9.75; S, 8.93; found: C, 48.32; H, 4.39; N, 9.00; S, 8.40.

Synthesis of 2

To a 20 mL tetrahydrofuran solution of 0.30 g (0.64 mmol) of PTEBIA, 0.16 g (0.64 mmol) of Fe(II)(ClO$_4$)$_2$ was added and the solution was refluxed for 3 h. The colorless solution of the ligand changes immediately to turbid green on addition of Fe(ClO$_4$)$_2$ and to yellowish green after 3 h of reflux. This yellowish green solution was filtered and the filtrate was dried under vacuum overnight in a 50 mL round bottom flask to get 0.64 g of 2 (74% yield). Slow vapor diffusion of diethyl ether for 4 days to the methanolic solution of 2 leads to needle-shaped yellowish green crystals of X-ray quality. UV-Vis (CH$_3$CN): λ_{max} = 335 nm (ε = 4,400 M^{-1} cm^{-1}). ESI-MS in acetonitrile solution calculated for [Fe(PTEBIA)]$^{2+}$ (C$_{28}$H$_{31}$FeN$_5$S)$^{2+}$ (mononuclear species): 262.6; found 262.8. IR (KBr, cm^{-1}): 3063, 3031, 2945, 2917, 1614, 1490, 1453, 1359, 1328, 1289, 1269, 1238, 1080, 928, 896, 865, 814, 795, 744, 695, 620, 545, 522, 489, 432. Anal. Calcd for 2: C, 51.38; H, 4.76; N, 10.33; S, 4.73; found: C, 50.99; H, 4.85; N, 10.45; S, 4.75.

Oxidation Experiments

Each catalytic experiment was performed at least twice and the reported conversion is the average value. A general procedure for the oxidation experiments is as follows: magnetic stirring bar, catalyst complex (18 μmol), 2 mL of CH$_3$CN, acetic acid (AcOH, 50 μL, 85 μmol), 230 μL of H$_2$O$_2$ (33% in water, 2.0 equivalents with respect to the substrate) and substrate (1 mmol) were placed in a Schlenk flask. The reaction mixture was stirred under argon at 35°C for the designated time. Sodium thiosulfate (ca. 400 mg, 2.5 mmol) was then added to the reaction mixture to quench further oxidation. 1,2-dicholorobenzene was added to the mixture followed by extraction with n-pentane and filtering through a silica gel column for analysis by GC-MS.

X-Ray Structure Determination

Crystal data and details of the data collections are given in **Table 9**. X-ray data for complexes 1a and 1b were collected on a STOE IPDS II diffractometer (graphite monochromated Mo-Kα radiation, λ = 0.71073 Å) by use of ω scans at −140°C. The structures were solved by direct methods (SHELXS-2014) and refined on F^2 using all reflections with SHELXL-2014 (Sheldrick, 2008). Non-hydrogen atoms were refined anisotropically. Hydrogen atoms were placed in calculated positions and assigned to an isotropic displacement parameter of 1.2 / 1.5 U_{eq}(C). In each compound one of the two CF$_3$SO$_3^-$ ions was found to be disordered [occupancy factors: 1a = 0.929(15)/0.071(15), 1b = 0.784(4)/0.216(4)]. SAME restraints and EADP constraints were used to model the respective disorders. In 1a one 2,4-dimethylphenyl moiety involving the carbon atoms C51(A/B/C) to C58(A/B/C) was found to be disordered about three positions A, B, and C along with acetonitrile (N21, C95, C96, belonging to B) and water (O31, belonging to C). After initial refinement the occupancy factors

TABLE 9 | Crystal data and refinement details for **1a**, **1b**, and **2**.

Compound	1a	1b	2
Empirical formula	$C_{126.40}H_{139.60}F_{12}Fe_4N_{25.20}O_{16.80}S_8$	$C_{58}H_{62}Cl_2F_6Fe_2N_{10}O_7S_4$	$C_{59}H_{68}Fe_2N_{10}O_{14}S_2Cl_2$
Formula weight	2988.50	1436.01	1387.95
Crystal size [mm^3]	$0.490 \times 0.130 \times 0.120$	$0.250 \times 0.190 \times 0.080$	$0.310 \times 0.120 \times 0.060$
Crystal system	monoclinic	triclinic	monoclinic
Space group	$C2/c$	$P-1$	$C2/c$
a [Å]	27.6133(7)	12.1859(7)	41.374(5)
b [Å]	23.9349(9)	14.7606(9)	19.4162(6)
c [Å]	25.3002(6)	19.5751(11)	29.330(4)
α [°]	90	76.965(5)	90.00
β [°]	116.592(2)	88.005(5)	145.75(3)
γ [°]	90	66.307(4)	90.00
V [Å^3]	14952.6(8)	3135.0(3)	13259(2)
Z	4	2	8
ρ [g/cm^3]	1.328	1.521	1.391
$F(000)$	6,195	1,480	5,776
μ [mm^{-1}]	0.573	0.759	0.650
T_{min} / T_{max}	0.6874 / 0.9120	0.8369 / 0.9385	0.8242/0.9625
θ-Range [°]	1.245–25.670	1.549–25.680	2.821–30.097
hkl-range	-33 -28, $\pm$ 29, -30 -29	± 14, ± 17, -23 -21	-53 $+30$, 0.25, 0.38
Measured refl.	56,783	34,525	11,746
Unique refl. [R_{int}]	14,101 [0.0808]	11,804 [0.0653]	15,192 [0.0384]
Observed refl. [$I > 2\sigma(I)$]	10,172	7,824	10,222
Data / restraints / param.	14,101 / 269 / 1,070	11,804 / 19 / 838	15,192/ 0/ 812
Goodness-of-fit (F^2)	1.045	1.037	1.099
$R1$, $wR2$ ($I > 2\sigma$ (I))	0.0654, 0.1632	0.0684, 0.1556	0.0625, 0.1795
$R1$, $wR2$ (all data)	0.0931, 0.1785	0.1108, 0.1748	0.0967, 0.1972
Resid. el. dens. [e/Å^3]	-0.492 / 0.755	-0.411 / 1.196	$-0.857/1.159$

were set to 0.5 for A, 0.1 for B and 0.4 for C. RIGU, FLAT, SADI [$d(1,3)_{C(ar)\cdots C(Me)}$] and DFIX ($d_{C(ar)-C(Me)}$ = 1.5 Å) restraints and EADP constraints were applied to model the disorder. The AFIX 66 instruction was applied for the carbon atoms of the ring. Furthermore, acetonitrile disordered about a 2-fold rotation axis and about two positions [occupancy factors: 0.277(7)/ 0.223(7)] was refined using RIGU restraints. Face-indexed absorption corrections were performed numerically with the program X-RED (Stoe & Cie and X-RED, 2005). The crystal of **2** was immersed in cryo-oil, mounted in a MiTeGen loop, and measured at a temperature of 170 K on a Rigaku Oxford Diffraction Supernova diffractometer using Mo Kα radiation. The *CrysAlisPro* (Rigaku Oxford Diffraction, 2013) software was used for cell refinement and data reduction. Empirical absorption correction based on equivalent reflections was [*CrysAlisPro* (Rigaku Oxford Diffraction, 2013)] was applied to the intensities before structure solutions. The structure was solved by charge flipping method using the *SUPERFLIP* (Palatinus and Chapuis, 2007) and the structure refinement was carried out using *SHELXL* (Sheldrick, 2015) program. The crystal of **2** contained solvent accessible voids but no satisfactory solvent model could be found. The contribution of the missing solvent to the calculated structure factors was taken into account by using the SQUEEZE routine of PLATON (Spek, 2009). The missing solvent was not taken into account

in the unit cell content. Hydrogen atoms were positioned geometrically and constrained to ride on their parent atoms, with C-H = 0.95–0.99 Å, O-H = 0.84 Å, and U_{iso} = 1.2–1.5 U_{eq} (parent atom). The highest peak is located 1.40 Å from atom S1 and the deepest hole is located 0.59 Å from atom S1.

Mössbauer Measurement

The Mössbauer spectrum was recorded at 80 K with a ^{57}Co source in a Rh matrix, using an alternating constant-acceleration Wissel Mössbauer spectrometer operated in the transmission mode and equipped with a Janis closed-cycle helium cryostat or with a Mössbauer-Spectromag cryostat. Isomer shifts (cf. caption, **Figure 3**) are given relative to iron metal at ambient temperature. Experimental data were simulated using the *Mfit* software (developed by E. Bill, Max-Planck Institute for Chemical Energy Conversion, Mülheim/Ruhr, Germany, 2008).

DATA AVAILABILITY

The raw data supporting the conclusions of this manuscript will be made available by the authors, without undue reservation, to any qualified researcher. Crystallographic data for the structures in this paper have been deposited with the Cambridge Crystallographic Data Center, CCDC, 12 Union

Road, Cambridge CB21EZ, UK. Copies of the data can be obtained free of charge on quoting the depository number CCDC 1874712 (**1a**), 1874713 (**1b**) or 1874714 (**2**) (Fax:+44-1223-336-033; E-Mail: deposit@ccdc.cam.ac.uk, http://www.ccdc.cam.ac.uk).

AUTHOR CONTRIBUTIONS

BD performed all complex syntheses, performed low temperature studies in collaboration with BS-E, participated in the oxidation experiments, and contributed to the writing of the manuscript. AA-H performed all oxidation experiments and contributed to the writing of the manuscript. BS-E and EZ synthesized the PTEBIA ligand. SebD performed all Mössbauer measurements and analysis of the Mössbauer data. SerD, SB, and MH collected X-ray data and solved the crystal structures. TR supervised the oxidation studies and analyzed the results in collaboration with AA-H and BD, and supplied funding for the work. IC led and designed the study, contributed to the writing of the manuscript and supplied funding for the work. EN led and designed the study, contributed to the writing of the manuscript and supplied funding for the work.

FUNDING

ACKNOWLEDGMENTS

SUPPLEMENTARY MATERIAL

The Supplementary Material for this article can be found online at: https://www.frontiersin.org/articles/10.3389/fchem.2019.00097/full#supplementary-material

REFERENCES

Ballmann, J., Albers, A., Demeshko, S., Dechert, S., Bill, E., Bothe, E., et al. (2008a). A synthetic analogue of rieske-type [2Fe-2S] clusters. *Angew. Chem. Int. Ed.* 47, 9537–9541. doi: 10.1002/anie.200803418

Ballmann, J., Dechert, S., Bill, E., Ryde, U., and Meyer, F. (2008b). Secondary bonding interactions in biomimetic [2Fe−2S] clusters. *Inorg. Chem.* 47, 1586–1596. doi: 10.1021/ic702095a

Beinert, H., Holm, R. H., and Münck, E. (1997). Iron-sulfur clusters: nature's modular, multipurpose structures. *Science* 277, 653–659.

Castillo, I., Ugalde-Saldívar, V. M., Rodríguez Solano, L. A., Sánchez Eguía, B. N., Zeglio, E., and Nordlander, E. (2012). Structural, spectroscopic, and electrochemical properties of tri- and tetradentate N₃ and N₃S copper complexes with mixed benzimidazole/thioether donors. *Dalton Trans.* 41, 9394–9404. doi: 10.1039/c2dt30756a

Costas, M., Chen, K., and Que, L. (2000). Biomimetic nonheme iron catalysts for alkane hydroxylation. *Coord. Chem. Rev.* 200–202, 517–544. doi: 10.1016/S0010-8545(00)00320-9

Costas, M., Mehn, M. P., Jensen, M. P., and Lawrence Que, J. (2004). Dioxygen activation at mononuclear nonheme iron active sites: enzymes, models, and intermediates. *Chem. Rev.* 104, 939–986. doi: 10.1021/cr020628n

Das, B., Al-Hunaiti, A., Haukka, M., Demeshko, S., Meyer, S., Shteinman, A. A., et al., Full list of authors (2015). Catalytic oxidation of alkanes and alkenes by H₂O₂ with a μ-oxido diiron(III) complex as catalyst/catalyst precursor. *Eur. J. Inorg. Chem.* 2015, 3590–3601. doi: 10.1002/ejic.201500576

Das, B., Daver, H., Pyrkosz-Bulska, M., Gumienna-Kontecka, E., Himo, F., and Nordlander, E. (2018). An unsymmetric ligand with a N₅O₂ donor set and its corresponding dizinc complex: a structural and functional phosphoesterase model. *Eur. J. Inorg. Chem.* 30, 4004–4013. doi: 10.1002/ejic.201701416

Das, B., Daver, H., Pyrkosz-Bulska, M., Persch, E., Barman, S. K., Mukherjee, R., et al. (2014a). A dinuclear zinc(II) complex of a new unsymmetric ligand with an N₅O₂ donor set: a structural and functional model for the active site of zinc phosphoesterases. *J. Inorg. Biochem.* 132, 6–17. doi: 10.1016/j.jinorgbio.2013.08.001

Das, B., Daver, H., Singh, A., Singh, R., Haukka, M., Demeshko, S., et al. (2014b). A heterobimetallic Fe III Mn II complex of an unsymmetrical dinucleating ligand: a structural and functional model complex for the active site of purple acid phosphatase of sweet potato. *Eur. J. Inorg. Chem.* 2014, 2204–2212. doi: 10.1002/ejic.201301375

De Visser, S. P., Rohde, J. U., Lee, Y. M., Cho, J., and Nam, W. (2013). Intrinsic properties and reactivities of mononuclear nonheme iron–oxygen

complexes bearing the tetramethylcyclam ligand. *Coord. Chem. Rev.* 257, 381–393. doi: 10.1016/j.ccr.2012.06.002

Deacon, G. B., and Phillips, R. J. (1980). Relationships between the carbon-oxygen stretching frequencies of carboxylato complexes and the type of carboxylate coordination. *Coord. Chem. Rev.* 33, 227–250. doi: 10.1016/S0010-8545(00)80455-5

Do, L. H., Xue, G., Que, L., and Lippard, S. J. (2012). Evaluating the identity and diiron core transformations of a (μ-Oxo)diiron(III) complex supported by electron-rich tris(pyridyl-2-methyl)amine ligands. *Inorg. Chem.* 51, 2393–2402. doi: 10.1021/ic202379b

Dubois, G., Murphy, A., and Stack, T. D. P. (2003). Simple iron catalyst for terminal alkene epoxidation. *Org. Lett.* 5, 2469–2472. doi: 10.1021/ol0347085

Fuchs, M. G., Dechert, S., Demeshko, S., Ryde, U., and Meyer, F. (2010). A five-coordinate [2Fe−2S] cluster. *Inorg. Chem.* 49, 5853–5858. doi: 10.1021/ic902559n

Fujita, M., and Que, L. (2004). *In situ* formation of peracetic acid in iron-catalyzed epoxidations by hydrogen peroxide in the presence of acetic acid. *Adv. Synth. Catal.* 346, 190–194. doi: 10.1002/adsc.200303204

Gamba, I., Codolà, Z., Lloret-Fillol, J., and Costas, M. (2017). Making and breaking of the OO bond at iron complexes. *Coord. Chem. Rev.* 334, 2–24. doi: 10.1016/j.ccr.2016.11.007

Harrop, T. C., and Mascharak, P. K. (2004). Fe(III) and Co(III) centers with carboxamido nitrogen and modified sulfur coordination: lessons learned from nitrile hydratase. *Acc. Chem. Res.* 37, 253–260. doi: 10.1021/ar0301532

Hasemann, C. A., Kurumbail, R. G., Boddupalli, S. S., Peterson, J. A., and Deisenhofer, J. (1995). Structure and function of cytochromes P450: a comparative analysis of three crystal structures. *Structure* 3, 41–62. doi: 10.1016/S0969-2126(01)00134-4

Hazell, A., McKenzie, C. J., Nielsen, L. P., Schindler, S., and Weitzer, M. (2002). Mononuclear non-heme iron(III) peroxide complexes: syntheses, characterisation, mass spectrometric and kinetic studies. *Dalton Trans.* 310–317. doi: 10.1039/b103844n

Jarenmark, M., Turitsyna, E. A., Haukka, M., Shteinman, A. A., and Nordlander, E. (2010). A monocarboxylate-bridged diiron(III) μ-oxido complex that catalyzes alkane oxidation by hydrogen peroxide. *N. J. Chem.* 34, 2118–2121. doi: 10.1039/c0nj00293c

Kim, C., Chen, K., Kim, J., and Que, L. (1997). Stereospecific alkane hydroxylation with H₂O₂ catalyzed by an iron(II)−tris(2-pyridylmethyl)amine complex. *J. Am. Chem. Soc.* 119, 5964–5965. doi: 10.1021/ja9642572

Kumar, D., Thiel, W., and de Visser, S. P. (2011). Theoretical study on the mechanism of the oxygen activation process in cysteine dioxygenase

enzymes. *J. Am. Chem. Soc.* 133, 3869–3882. doi: 10.1021/ja10 7514f

Kurtz, D. M. (1990). Oxo- and hydroxo-bridged diiron complexes: a chemical perspective on a biological unit. *Chem. Rev.* 90, 585–606. doi: 10.1021/cr00102a002

Lill, R. (2009). Function and biogenesis of iron–sulphur proteins. *Nature* 460, 831–838. doi: 10.1038/nature08301

Lindhorst, A. C., Haslinger, S., and Kühn, F. E. (2015). Molecular iron complexes as catalysts for selective C–H bond oxygenation reactions. *Chem. Commun.* 51, 17193–17212. doi: 10.1039/C5CC07146A

Mayilmurugan, R., Stoeckli-Evans, H., Suresh, E., and Palaniandavar, M. (2009). Chemoselective and biomimetic hydroxylation of hydrocarbons by non-heme μ-oxo-bridged diiron(iii) catalysts using m-CPBA as oxidant. *Dalton Trans.* 5101–5114. doi: 10.1039/b820771b

McCoy, J. G., Bailey, L. J., Bitto, E., Bingman, C. A., Aceti, D. J., Fox, B. G., et al. (2006). Structure and mechanism of mouse cysteine dioxygenase. *Proc. Natl. Acad. Sci. U.S.A.* 103, 3084–3089. doi: 10.1073/pnas.0509262103

McDonald, A. R., Bukowski, M. R., Farquhar, E. R., Jackson, T. A., Koehntop, K. D., Seo, M. S., et al. (2010). Sulfur versus iron oxidation in an iron–thiolate model complex. *J. Am. Chem. Soc.* 132, 17118–17129. doi: 10.1021/ja1045428

McQuilken, A. C., and Goldberg, D. P. (2012). Sulfur oxygenation in biomimetic non-heme iron–thiolate complexes. *Dalton Trans.* 41, 10883–10899. doi: 10.1039/c2dt30806a

Meyer, J. (2008). Iron–sulfur protein folds, iron–sulfur chemistry, and evolution. *J. Biol. Inorg. Chem.* 13, 157–170. doi: 10.1007/s00775-007-0318-7

Mitra, M., Lloret-Fillol, J., Haukka, M., Costas, M., and Nordlander, E. (2014). Evidence that steric factors modulate reactivity of tautomeric iron–oxo species in stereospecific alkane C–H hydroxylation. *Chem. Commun.* 50, 1408–1410. doi: 10.1039/C3CC47830K

Nam, W. (2015). Synthetic mononuclear nonheme iron–oxygen intermediates. *Acc. Chem. Res.* 48, 2415–2423. doi: 10.1021/acs.accounts.5b00218

Norman, R. E., Leising, R. A., Yan, S., and Que, L. (1998). Unexpected assembly of a (μ-oxo)(μ-formato)diiron(III) complex from an aerobic methanolic solution of Fe(III) and the TPA ligand. *Inorg. Chim. Acta* 273, 393–396. doi: 10.1016/S0020-1693(97)06058-1

Norman, R. E., Yan, S., Que, L., Backes, G., Ling, J., Sanders-Loehr, J., et al. (1990). (μ.-Oxo)(μ.-carboxylato)diiron(III) complexes with distinct iron sites. Consequences of the inequivalence and its relevance to dinuclear iron-oxo proteins. *J. Am. Chem. Soc.* 112, 1554–1562. doi: 10.1021/ja00160a039

Ohnishi, T. (1998). Iron–sulfur clusters/semiquinones in Complex I. *Biochim. Biophys. Acta Bioenerg.* 1364, 186–206. doi: 10.1016/S0005-2728(98)00027-9

Palatinus, L., and Chapuis, G. (2007). *SUPERFLIP* – a computer program for the solution of crystal structures by charge flipping in arbitrary dimensions. *J. Appl. Crystallogr.* 40, 786–790. doi: 10.1107/S0021889807029238

Prat, I., Company, A., Postils, V., Ribas, X., Que, L., Luis, J. M., et al. (2013). The mechanism of stereospecific C–H oxidation by Fe(Pytacn) complexes: bioinspired non-heme iron catalysts containing cis-labile exchangeable sites. *Chem. A Eur. J.* 19, 6724–6738. doi: 10.1002/chem.201300110

Rao, P. V., and Holm, R. H. (2004). Synthetic analogues of the active sites of iron–sulfur proteins. *Chem. Rev.* 104, 527–560. doi: 10.1021/cr020615+

Reem, R. C., McCormick, J. M., Richardson, D. E., Devlin, F. J., Stephens, P. J., Musselman, R. L., et al. (1989). Spectroscopic studies of the coupled binuclear ferric active site in methemerythrins and oxyhemerythrin: the electronic structure of each iron center and the iron-oxo and iron-peroxide bonds. *J. Am. Chem. Soc.* 111, 4688–4704. doi: 10.1021/ja00195a024

Rigaku Oxford Diffraction (2013). *CrysAlisPro, Agilent Technologies Inc.* Yarnton: Oxfordshire.

Rodríguez Solano, L. A., Aguíñiga, I., López Ortiz, M., Tiburcio, R., Luviano, A., Regla, I., et al. (2011). Bis(2-methylbenzimidazolyl)amine-derived copper complexes and their antineoplastic activity. *Eur. J. Inorg. Chem.* 2011, 3454–3460. doi: 10.1002/ejic.201100301

Rohde, J. U., In, J. H., Lim, M. H., Brennessel, W. W., Bukowski, M. R., Stubna, A., et al. (2003). Crystallographic and spectroscopic characterization of a nonheme Fe(IV)-O complex. *Science* 299, 1037–1039. doi: 10.1126/science.299.5609.1037

Romakh, V. B., Therrien, B., Georg, S.-F., and Shul'pin, G. B. (2007). Dinuclear manganese complexes containing chiral 1,4,7-triazacyclononane-derived ligands and their catalytic potential for the oxidation of olefins, alkanes, and alcohols. *Inorg. Chem.* 46, 1315–1331. doi: 10.1021/ic061950+

Sahoo, S. C., and Ray, M. (2007). Ferrocene substitution in amino acids strengthens the axial binding in Cu(II) complexes and separates the hydrophobic and hydrophilic region in the crystals. *Dalton Trans.* 5148–5155. doi: 10.1039/b709662c

Sallmann, M., Siewert, I., Fohlmeister, L., Limberg, C., and Knispel, C. (2012). A Trispyrazolylborato iron cysteinato complex as a functional model for the cysteine dioxygenase. *Angew. Chemie Int. Ed.* 51, 2234–2237. doi: 10.1002/anie.201107345

Sheldrick, G. M. (2008). A short history of *SHELX*. *Acta Crystallogr. Sect. A* 64, 112–122. doi: 10.1107/S0108767307043930

Sheldrick, G. M. (2015). Crystal structure refinement with *SHELXL*. *Acta Crystallogr. Sect. C* 71, 3–8. doi: 10.1107/S2053229614024218

Spek, A. L. (2009). Structure validation in chemical crystallography. *Acta Crystallogr. Sect. D* 65, 148–155. doi: 10.1107/S090744490804362X

Stoe & Cie and X-RED (2005). *Program for Data Reduction and Absorption Correction.* Darmstadt: Stoe & Cie GmbH.

Sun, C. L., Li, B. J., and Shi, Z. J. (2011). Direct C–H transformation via iron catalysis. *Chem. Rev.* 111, 1293–1314. doi: 10.1021/cr100198w

Tinberg, C. E., and Lippard, S. J. (2011). Dioxygen activation in soluble methane monooxygenase. *Acc. Chem. Res.* 44, 280–288. doi: 10.1021/ar1001473

Trettenhahn, G., Nagl, M., Neuwirth, N., Arion, V. B., Jary, W., Pöchlauer, P., et al. (2006). A hexanuclear iron(III) carboxylate with an [Fe$_6$(μ_3-O)$_3$(μ_2-OH)]$^{11+}$ core as an efficient catalyst for cycloalkane oxidation. *Angew. Chemie Int. Ed.* 45, 2794–2798. doi: 10.1002/anie.200504406

Vad, M. S., Lennartson, A., Nielsen, A., Harmer, J., McGrady, J. E., Frandsen, C., et al. (2012). An aqueous non-heme Fe(IV)oxo complex with a basic group in the second coordination sphere. *Chem. Commun.* 48, 10880–10882. doi: 10.1039/c2cc35746a

Visvaganesan, K., Suresh, E., and Palaniandavar, M. (2009). Highly selective hydroxylation of alkanes catalyzed by (μ-oxo)bis(μ-carboxylato)-bridged diiron(III) complexes: involvement of mononuclear iron(III) species in catalysis. *Dalton Trans.* 3814–3823. doi: 10.1039/b901508f

Wackett, L. P. (2002). Mechanism and applications of Rieske non-heme iron dioxygenases. *Enzyme Microb. Technol.* 31, 577–587. doi: 10.1016/S0141-0229(02)00129-1

Wang, D., Ray, K., Collins, M. J., Farquhar, E. R., Frisch, J. R., Gómez, L., et al. (2013a). Nonheme oxoiron(IV) complexes of pentadentate N5 ligands: spectroscopy, electrochemistry, and oxidative reactivity. *Chem. Sci.* 4, 282–291. doi: 10.1039/C2SC21318D

Wang, X., Wang, S., Li, L., Sundberg, E. B., and Gacho, G. P. (2003). Synthesis, structure, and catalytic activity of mononuclear iron and (μ-oxo)diiron complexes with the ligand 2,6-bis(n-methylbenzimidazol-2-yl)pyridine. *Inorg. Chem.* 42, 7799–7808. doi: 10.1021/ic0259437

Wang, Y., Janardanan, D., Usharani, D., Han, K., Que, L., and Shaik, S. (2013b). Nonheme iron oxidant formed in the presence of H$_2$O$_2$ and acetic acid is the cyclic ferric peracetate complex, not a perferryloxo complex. *ACS Catal.* 3, 1334–1341. doi: 10.1021/cs400134g

White, M. C., Doyle, A. G., and Jacobsen, E. N. (2001). A synthetically useful, self-assembling MMO mimic system for catalytic alkene epoxidation with aqueous H$_2$O$_2$. *J. Am. Chem. Soc.* 123, 7194–7195. doi: 10.1021/ja015884g

Widger, L. R., Davies, C. G., Yang, T., Siegler, M. A., Troeppner, O., Jameson, G. N. L., et al. (2014). Dramatically accelerated selective oxygen-atom transfer by a nonheme iron(IV)-oxo complex: tuning of the first and second coordination spheres. *J. Am. Chem. Soc.* 136, 2699–2702. doi: 10.1021/ja410240c

Ye, S., and Neese, F. (2011). Nonheme oxo-iron(IV) intermediates form an oxyl radical upon approaching the C-H bond activation transition state. *Proc. Natl. Acad. Sci. U.S.A.* 108, 1228–1233. doi: 10.1073/pnas.1008411108

A New Mixed-Valence Mn(II)Mn(III) Compound With Catalase and Superoxide Dismutase Activities

Rafael O. Costa[1], Sarah S. Ferreira[2], Crystiane A. Pereira[1], Jeffrey R. Harmer[3], Christopher J. Noble[3], Gerhard Schenk[4], Roberto W. A. Franco[5], Jackson A. L. C. Resende[6], Peter Comba[7,8], Asha E. Roberts[7,8], Christiane Fernandes[1]* and Adolfo Horn Jr.[1]*

[1] Laboratório de Ciências Químicas, Universidade Estadual do Norte Fluminense Darcy Ribeiro, Campos dos Goytacazes, Brazil, [2] Instituto Federal Fluminense, Campos dos Goytacazes, Brazil, [3] Centre for Advanced Imaging, University of Queensland, Brisbane, QLD, Australia, [4] School of Chemistry and Molecular Biosciences, University of Queensland, Brisbane, QLD, Australia, [5] Laboratório de Ciências Físicas, Universidade Estadual do Norte Fluminense Darcy Ribeiro, Campos dos Goytacazes, Brazil, [6] Instituto de Ciências Exatas e da Terra, Campus Universitário do Araguaia, Universidade Federal do Mato Grosso, Barra do Garças, Brazil, [7] Anorganisch-Chemisches Institut, Universität Heidelberg, Heidelberg, Germany, [8] Interdisziplinäres Zentrum für Wissenschaftliches Rechnen, Heidelberg, Germany

The synthesis, X-ray molecular structure, physico-chemical characterization and dual antioxidant activity (catalase and superoxide dismutase) of a new polymeric mixed valence Mn(III)Mn(II) complex, containing the ligand $H_2BPClNOL$ (N-(2-hydroxybenzyl)-N-(2-pyridylmethyl)[(3-chloro)(2-hydroxy)] propylamine) is described. The monomeric unit is composed of a dinuclear Mn(II)Mn(III) moiety, [Mn(III)(μ-HBPClNOL)(μ-BPClNOL)Mn(II)(Cl)](ClO_4)·$2H_2O$, **1**, in which the Mn ions are connected by two different bridging groups provided by two molecules of the ligand $H_2BPClNOL$, a phenoxide and an alkoxide group. In the solid state, this mixed valence dinuclear unit is connected to its neighbors through chloro bridges. Magnetic measurements indicated the presence of ferromagnetic [$J = +0.076(13)$ cm^{-1}] and antiferromagnetic [$J = -5.224(13)$ cm^{-1}] interactions. The compound promotes $O_2^{\bullet-}$ dismutation in aqueous solution (IC$_{50}$ = 0.370 μmol dm^{-3}, k_{cat} = 3.6x10^6 M^{-1} s^{-1}). EPR studies revealed that a high-valent Mn(III)-O-Mn(IV) species is involved in the superoxide dismutation catalytic cycle. Complex **1** shows catalase activity only in the presence of a base, e.g., piperazine or triethylamine. Kinetic studies were carried out in the presence of piperazine and employing two different methods, resulting in k_{cat} values of 0.58 ± 0.03 s^{-1} (detection of O_2 production employing a Clark electrode) and 2.59 ± 0.12 s^{-1} (H_2O_2 consumption recorded via UV-Vis). EPR and ESI-(+)-MS studies indicate that piperazine induces the oxidation of **1**, resulting in the formation of the catalytically active Mn(III)-O-Mn(IV) species.

Keywords: catalase, superoxide dismutase, tripodal ligand, mix-valent manganese, polymeric manganese, reaction mechanism

INTRODUCTION

The best described and studied forms of reactive oxygen species (ROS) are the superoxide anion ($O_2^{\bullet-}$) and hydrogen peroxide (H_2O_2), which can produce the extremely reactive hydroxyl radical ($HO^{\bullet}$). Although performing key roles in biochemical processes such as the cell signaling, gene expression, and immune response, these oxidants also induce damage on cellular constituents, causing DNA, protein and lipid oxidation (Hancock et al., 2001; Halliwell, 2006; Morano et al., 2012). The uncontrolled generation of ROS has been related to many pathologies, including neurodegenerative disorders (Alzheimer's disease, amyotrophic lateral sclerosis, etc.) and is also thought to have an important action in the aging progression (Lane, 2003; McCord and Edeas, 2005; Valko et al., 2007).

Complex organisms such as human beings are able to co-exist with free radicals and have established pathways to employ such ROS as oxidation/reduction switches, in a process known as redox signaling (Allen and Tresini, 2000; Lane, 2003). Hence, a certain level of oxidation performed by free radicals is required in biosystems, but increased oxidative levels may result in damages to the normal functioning of biological systems, resulting in pathophysiological conditions.

As a protection stratagem to counter the deleterious properties of ROS, aerobic organisms have developed antioxidant metalloenzymes, e.g., glutathione peroxidase (GPx), catalases (CATs), and superoxide dismutases (SODs) (Costa and Moradas-Ferreira, 2001; Valko et al., 2007). Whereas GPx and CATs act on H_2O_2, SODs induce superoxide dismutation. GPx contains selenium in the active site (Lu and Holmgren, 2009) while CATs possess an iron(III) heme prostetic cofactor or a dinuclear manganese active site (Bravo et al., 1999; Antonyuk et al., 2000). In SODs, iron, manganese, copper/zinc or nickel have been reported at the active site (Tainer et al., 1982; Ludwig et al., 1991; Kerfeld et al., 2003; Barondeau et al., 2004). SOD is assumed to be the main mediator to control the damaging effects of the superoxide anion *in vivo*. However, several practical restrictions (large size, low cell permeability, short circulating half-life, antigenicity, high manufacturing costs) have restricted the usage of SODs as a possible clinical treatment (McCord and Edeas, 2005).

An alternative to the use of antioxidant metalloenzymes to decrease the level of ROS is the development of synthetic compounds which may mimic the activity of such enzymes (Mahammed and Gross, 2011). Several biomimetics that can decompose ROS produced during oxidative stress (e.g., using metal ion ligands such as salen, porphyrins, corroles, or non-aromatic macrocycles) have already been reported (Doctrow et al., 2002; Day, 2007; Eckshtain et al., 2009; Batinić-Haberle et al., 2010; Kupershmidt et al., 2010; Tovmasyan et al., 2015; Weekley et al., 2017; Signorella et al., 2018).

Previously, we have described the synthesis of a tripodal tetradentade ligand HPClNOL = 1-(bispyridin-2-ylmethyl-amino)-3-chloropropan-2-ol (Horn et al., 2005a) and studied its coordination behavior with manganese(II) salts (**Figure 1**) (Lessa et al., 2007; Ribeiro et al., 2015). Their antioxidant properties have been also evaluated as a model for SOD and/or CAT enzymes (Lessa et al., 2009; Ribeiro et al., 2015). In an attempt to develop new and more active compounds with SOD/CAT activities, we employed a similar tripodal tetradentate ligand, i.e., H$_2$BPClNOL = N-(2-hydroxybenzyl)-N-(2-pyridylmethyl)[(3-chloro)(2-hydroxy)] propylamine (**Figure 1**) (Horn et al., 2000), for the synthesis of a related manganese compound. Here, we present the properties of the new and rare polymeric mixed valence Mn(II)Mn(III) complex and the evaluation of its kinetic properties and mechanism of action with respect to its SOD and CAT mimetic activities.

EXPERIMENTAL SECTION

Materials and Methods

All chemicals and reagents were purchased from Sigma-Aldrich and used as such. UV-Vis, EPR, and MS investigations were carried out employing spectroscopic, HPLC or MS quality solvents. Dimethylsulfoxide (DMSO) was distilled over drying agents under an inert atmosphere, prior to EPR studies. It was stored over drying agents under inert atmosphere and transferred by syringe.

Physical Chemical Characterization

Infrared spectra were recorded on a Shimadzu FT-IR 8300 spectrophotometer. The solid sample was prepared in a KBr pellet and the spectrum were recorded over the frequency range of 400–4,000 cm^{-1}. UV-Vis spectra for the ligand and for the Mn complex were recorded in CH$_3$CN on a UV-Vis Varian Cary 50 Bio spectrophotometer. The electrical conductivity of a 1×10^{-3} mol dm^{-3} CH$_3$CN solution of **1** was measured with a Biocristal conductometer. Melting points were measured on a Microquimica MQAPF-301 apparatus. The purity of the complex was determined by combustion elemental analyses conducted with a Thermo Scientific FLASH 2000 CHNS/O analyzer. Full scan mass spectra were obtained on a MicroTOF LC Bruker Daltonics spectrometer equipped with an electrospray source operating in positive ion mode. Samples were dissolved in a CH$_3$CN/H$_2$O (50/50) solution and were injected in the apparatus by direct infusion. Theoretical isotopic patterns were calculated using the software ESI Compass 1.3 for micrOTOF, DataAnalysis version 4.0 SP 1 from Bruker Daltonik GmbH. EPR spectra were recorded on a Bruker Elexsys E500 EPR spectrometer equipped with a Bruker ER036TM Teslameter and frequency counter for calibration of the magnetic field and microwave frequency, respectively. Low temperature (140 K) at the sample position employed a nitrogen flow-through system in conjunction with a liquid nitrogen Eurotherm ER4131vt temperature controller. Computer simulation of the dimanganese EPR spectra employed Molecular Sophe28 in conjunction with Octave29 to optimize the spin Hamiltonian parameters. The magnetic data were collected using an MPMS-XL 5T (Quantum Design) SQUID magnetometer. Sample preparation involved pressing the powder into PTFE tape to prevent field-induced reorientation. Data were corrected for diamagnetic contributions from the sample using Pascal's constants, and from the sample holder. Effective magnetic moments were calculated using the relationship $\mu_{\text{eff}} = 2.828(\chi_M T)^{1/2}$.
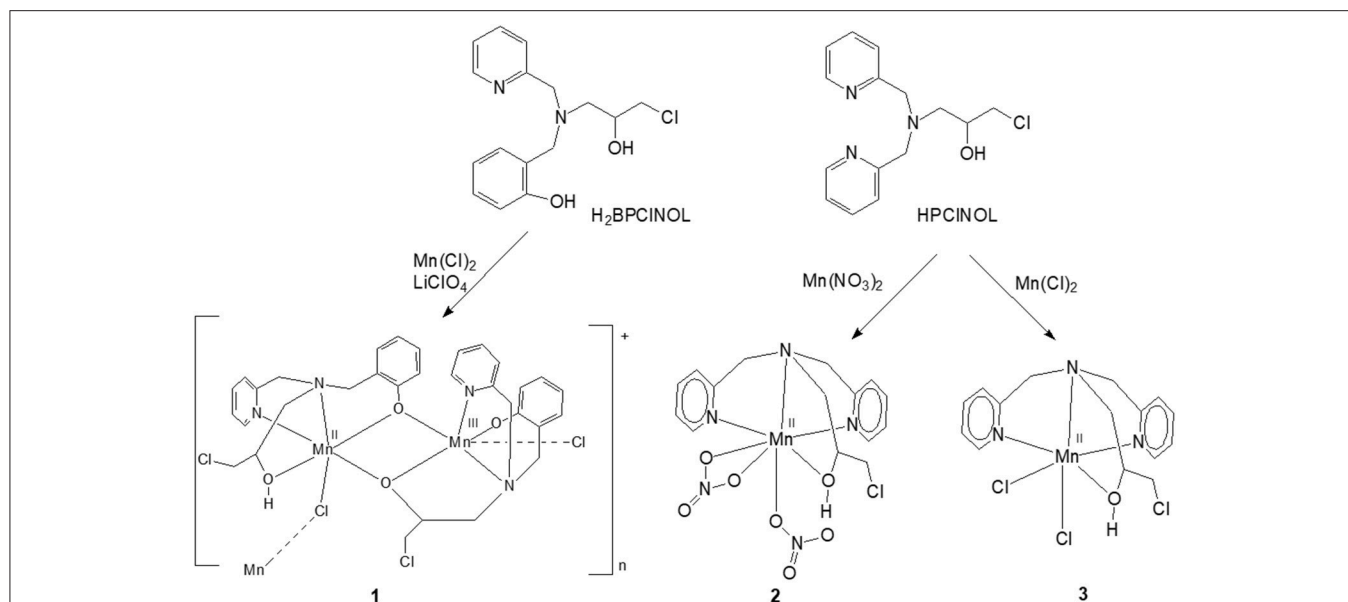
FIGURE 1 | Scheme of synthesis of **1** and the related manganese complexes **2** and **3** described previously by our group; both have SOD/CAT activities. Only the monomeric unit of the cation **1** is shown (Lessa et al., 2007, 2009; Ribeiro et al., 2015).

Ligand and Complex Syntheses

The ligand $H_2BPClNOL$ was synthesized by a reaction between the secondary amine N-(2-hydroxybenzyl)-N-(pyridin-2-ylmethyl)amine (HBPA) and epichlorohydrin, as reported previously (Horn et al., 2000). The complex $([(HBPClNOL)Mn(II)Mn(III)(BPClNOL)(Cl)](ClO_4)\cdot 2H_2O)_n$, **1** (**Figure 1**), was prepared in a reaction between $H_2BPClNOL$ (1.0 mmol, 0.31 g), dissolved in 10 cm^3 of propan-2-ol and a solution containing $MnCl_2\cdot 4H_2O$ (1.0 mmol, 0.20 g) and $LiClO_4$ (1 mmol, 0.11 g), by refluxing over 1 h. After allowing the brown solution to stand for a few days, a crystalline brown solid was filtered off, washed with ethyl ether and dried under vacuum. After removing the crystals, the slow evaporation of the solvent resulted in the formation of an unidentified oily material. Yield: 0.20 g (22%). m.p. 243°C. IR (cm^{-1}): ν(OH), 3422–3483 (s); ν(CH), 3,067 and 3,030 (s); ν(CH$_2$), 2,969(s); ν(CH$_2$), 2,924 (s); (C=C and C=N), 1,601 (s), 1,574 (s), 1,478 (s) and 1,456 (s); ν(ClO$_4^-$), 1,121 and 1,020 (s); γ (CH), 758 (s) and 775 (s). Anal. calcd for $[(HBPClNOL)Mn(II)Mn(III)(BPClNOL)(Cl)](ClO_4)2H_2O$ ($C_{32}H_{39}Cl_4Mn_2N_4O_{10}$, MW = 891.37 g mol^{-1}): C, 43.12; H, 4.41; N, 6.29. Found: C, 42.77; H, 4.01; N, 5.92%. Ω = 123 μS cm^{-1} (1:1 electrolyte, CH_3CN).

X-Ray Crystallography

The single crystal X-ray diffraction data of complex **1** were collected at 150(2)K on a Bruker D8 Venture diffractometer equipped with Photon 100 CMOS detector and using MoKα radiation (0.71073 Å) from an INCOATEC micro-focus source. Final lattice parameter values and integrated intensities were obtained using SAINT software (SAINT, 2015), and a multi-scan absorption correction was applied with SADABS (Krause et al.,

2015). The structure was solved by direct methods using intrinsic phasing implemented in SHELXT (Sheldrick, 2015). The model was refined applying the full-matrix least-squares method using SHELXL (Sheldrick, 2015). All non-hydrogen atoms were refined with anisotropic displacement parameters. Hydrogen atoms were placed at calculated positions and refined using a riding model.

Catalase-Like Activity

Catalase activity was measured by employing two different methods: (i) the decrease of H_2O_2 concentration was followed by UV-Vis spectroscopy at 240 nm (Beers and Sizer, 1952), and (ii) the rate of O_2 production was measured employing a Clark-type electrode from Hansatech Instruments, model Oxygraph+.

The concentration of the H_2O_2 was previously determined by iodide/thiosulfate titration according to the literature (Ribeiro et al., 2009). All the reactions between complex **1** and H_2O_2 were performed in buffered and unbuffered solutions, as well as in the presence of piperazine. For the studies in unbuffered water solutions, 0.2 cm^3 of an aqueous solution of complex **1** (2.5×10^{-4} mol dm^{-3}) was added to a cuvette, followed by the addition of a certain amount (dependent on the required concentration) of water and H_2O_2 to reach a final volume of 2.2 cm^3. Subsequently, the decrease in the absorption of the band attributed to H_2O_2 was monitored in a 1 cm path length cell. A similar study was performed using a buffered system (phosphate buffer, 0.05 mol dm^{-3}, pH 7.8). For the study with piperazine, 0.2 cm^3 of an aqueous solution of complex **1** (2.5×10^{-4} mol dm^{-3}) was added to a cuvette, followed by the addition of 0.1 cm^3 of an aqueous solution of piperazine (0.1 mol dm^{-3}) and appropriate amounts of water and H_2O_2 to reach a final volume of 2.2 cm^3. In this solution, the final concentration of **1** was 2.27×10^{-5} mol dm^{-3}, while that of the piperazine was 4.54×10^{-3} mol dm^{-3},

with a resulting pH of 9.73. The experiments were always carried out at 25°C. The consumption of H_2O_2 was again monitored spectrophotometrically as described above. These measurements were performed in triplicates and the kinetic parameters (i.e., K_M, k_{cat}, k_{cat}/K_M) were determined from a fit of the data to the Michaelis-Menten equation. Using the Clark electrode, the O_2 production was followed for 120 s, but the rate of the reaction was measured during the first 50 s. The concentrations of **1** and piperazine were the same as described for the UV-Vis experiments.

The reaction was also investigated by EPR. A fresh solution of **1** was prepared in CH_3CN (1.10^{-3} mol dm^{-3}). From this solution 0.200 cm^3 was placed in an EPR tube, which was then frozen at 140 K and the EPR spectrum recorded. The tube was then allowed to thaw at room temperature ($\sim$15 min). To this solution, in the EPR tube, 50 mm^3 of an aqueous solution of piperazine (0.1 mol dm^{-3}) was added. The solution was frozen again and the EPR spectrum recorded. Subsequently, the sample was allowed to thaw again ($\sim$15 min), and 50 mm^3 of an aqueous solution of H_2O_2 (0.1 mol dm^{-3}) was added. After freezing, another EPR spectrum was recorded. This study was repeated in duplicates.

All these experiments were carried out using crystalline samples that contains a mixture of two diastereomers (see x-ray section for more details).

SOD-Like Activity

The SOD activity of complex **1** was assessed employing the nitroblue tetrazolium (NBT) method, using xanthine/xanthine oxidase as a source of the superoxide anion, as described previously (Ribeiro et al., 2015). The kinetic studies were carried out in phosphate buffer (pH = 7.8). Stock solutions of xanthine (4.5×10^{-4} mol dm^{-3}), NBT (5.6×10^{-5} mol dm^{-3}) and xanthine oxidase (0.2 U cm^{-3}), all purchased from Sigma-Aldrich, were prepared using phosphate buffer. In a control (blank) experiment the stock solutions of xanthine (1 cm^3) and NBT (1 cm^3) were mixed with phosphate buffer (0.4 cm^3), and, at the end, xanthine oxidase (0.20 cm^3) was added to the cuvette. To evaluate the SOD activity of **1**, different concentrations of the complex were added to the cuvette: 9.62×10^{-8}, 1.92×10^{-7}, 3.85×10^{-7}, 5.77×10^{-7}, and 7.69×10^{-7} mol dm^{-3}.

The obtained IC_{50} was transformed to k_{cat} employing the equation proposed by McCord and Fridovich, $k_{cat} = k_{NBT}$ x $[NBT]/IC_{50}$, where $K_{NBT} = 5.94$ x 10^4 M^{-1} s^{-1} (Grau et al., 2014; Ledesma et al., 2015).

The SOD like activity of **1** was also studied by EPR. A solution containing superoxide anion radical was generated in DMSO using the procedure described previously (Valentine et al., 1984). Briefly, 7 mg of KO_2 was stirred in 1 cm^3 of dried DMSO, for 2 h, resulting in a pale yellow solution (0.1 mol dm^{-3}). A fresh solution of **1** was prepared in dried DMSO (1.6×10^{-3} mol dm^{-3}), resulting in a brown solution. The KO_2 solution (0.200 cm^3) was placed in an EPR tube and the solution frozen and the spectrum recorded. The tube was removed from the cavity and allowed to sit at room temperature until a pale yellow solution was obtained again. Then, 200 μL of the solution of complex **1** was added to the former, resulting in a color change from

pale yellow to reddish brown. The solution was frozen and the spectrum recorded. To follow the changes in the intensity of the superoxide EPR signal, the tube was removed from the cavity and allowed to thaw at room temperature; this was repeated until no more changes in the intensity of the spectrum were observed. This study was repeated in duplicate. As a control, a similar reaction was carried out using a $MnCl_2 \cdot 4H_2O$ solution (1.6×10^{-3} mol dm^{-3}).

All these experiments were carried out using crystalline samples that contain a mixture of two diastereomers (see x-ray section for more details).

RESULTS AND DISCUSSION

Syntheses

The ligand $H_2BPClNOL$ is a tripodal ligand with a N_2O_2 donor atom set and is able to form mono- and dinuclear complexes with different metal ions, including iron, nickel, copper and zinc (see below for more details about these complexes). Here, we report the first manganese complex obtained with this ligand. The reaction between $H_2BPClNOL$ and $MnCl_2 \cdot 4H_2O$ resulted in a

TABLE 1 | Crystal data and structure refinement details for complex **1**.

Empirical formula	$[Mn_2(C_{16}H_{17}ClN_2O_2)(C_{16}H_{18}ClN_2O_2)Cl]ClO_4 \cdot 1.67(H_2O)$
Formula weight	891.35
Temperature/K	150.15
Crystal system	Monoclinic
Space group	$P2_1/n$
a/Å	14.2991(15)
b/Å	12.4755(12)
c/Å	21.676(2)
α/°	90
β/°	103.558(5)
γ/°	90
Volume/Å^3	3759.0(7)
Z	4
ρ_{calc}g/cm^3	1.575
μ/mm^{-1}	1.016
F(000)	1828.0
Crystal size/mm^3	0.29 × 0.137 × 0.115
Radiation	MoKα (λ = 0.71073)
2Θ range for data collection/°	4.388 to 50.7
Index ranges	$-17 \leq h \leq 16, -14 \leq k \leq 15, -17 \leq l \leq 26$
Reflections collected	24450
Independent reflections	6847 [R_{int} = 0.0958, R_{sigma} = 0.1010]
Data/restraints/parameters	6847/19/498
Goodness-of-fit on F^2	1.023
Final R indexes [I $\geq 2\sigma$ (I)]	R_1 = 0.0753, wR_2 = 0.1747
Final R indexes [all data]	R_1 = 0.1271, wR_2 = 0.2087
Largest diff. peak/hole / e Å^{-3}	0.99/-1.11

new compound that was isolated in the form of brownish crystals suitable for X-ray diffraction. The X-ray data have revealed (see below) the presence of an unusual, one dimensional mixed-valence Mn(II)Mn(III) chain. The elemental analysis agrees with the X-ray data, indicating high purity of the prepared compound. This complex is stable in air, in the solid state and in CH_3CN solution. Its solution shows a brownish color, suggesting the presence of manganese in oxidation state higher than +2. This indicates that $H_2BPClNOL$ shows a different behavior when compared with HPClNOL, which forms mononuclear Mn(II) complexes (**Figure 1**).

X-Ray Molecular Structure

The molecular structure of **1** was solved by X-ray diffraction and the crystallographic data are presented in **Tables 1** and **2**. The data reveal the formation of a chain (**Figure 2**), where each subunit contains a heterovalent dimanganese (II/III) core, two molecules of the ligand and one chloro ligand, resulting in the composition [Mn(II)Mn(III)(HBPClNOL)(BPClNOL)Cl]$^+$, where HBPClNOL and BPClNOL stand for the mono- and dianionic form of $H_2BPClNOL$, respectively. The monomers are connected through chloro bridges, which are asymmetrically bound to the manganese centers [Mn1-Cl1 = 2.4908 (17), Mn2-Cl1$_i$ = 2.6162(18) Å]. As shown in **Figure 1**, the ligand $H_2BPClNOL$ has two oxygen (phenol and alcohol) and two nitrogen (pyridine and tertiary amine) atoms as coordinating groups; interesting is the fact that the two molecules of the

ligand coordinate differently to the metal centers, mainly with respect to their phenol and alcohol groups (see **Figure 1**). For a better explanation of the molecular structure of complex **1**, we label the two molecules of the ligand present in this complex as A and B in the X-ray structure representation (**Figure 2**). Ligand A (monoanion) shows a tetradentate coordination mode in which the phenol is acting as a bridging group [Mn1-O1A= 2.249(4) and Mn2-O1A= 1.934(4) Å] and the alcohol group is protonated and acts as a terminal ligand [Mn1-O2A= 2.201(5) Å]. On the other hand, in ligand B (dianion), the alcohol is deprotonated and acting as a bridging group [Mn2-O2B = 1.899(4), Mn1-O2B = 2.129(4)Å], while the phenol group is deprotonated as well but coordinating as a non-bridging ligand only to Mn2 [Mn2-O1B = 1.892(5) Å]. Furthermore, the carbon atom of the alcohol group is chiral and two isomers are present in the compound. In ligand A, the R isomer is observed, while the S isomer is seen in ligand B. It is important to note that compound **1** crystallizes in the centrosymmetric space group P2$_1$/n. Due to the relation of symmetry associated with this space group, the crystal also shows molecules in which the isomers are opposite to those observed in the molecule shown in **Figure 2**. Molecules showing two chiral centers can form four diastereomers, which can be identified as RR, SS, RS, and SR. The x-ray data revealed that only two of them were formed, the RS and SR. Although the RR and SS were foreseen, they were not present in the crystals evaluated by x-ray analyses, even when the crystals were obtained from different syntheses. It is possible that the RR and SS diatereomers did not crystallize togheter with the RS and SR species, since they can result in compounds with different solubility, or that the dinuclear species are not formed due to steric hindrance. This can be one reason to explain the low yield observed in the synthesis. We hope to address this behavior in a future work.

The averaged bond lengths around the two metal ions are 2.27 and 2.11 Å for the Mn1 and Mn2 ions, respectively. Based on (i) the bond distances, (ii) the fact that the Mn(III) ion has a smaller ionic radius than Mn(II) (Gelasco et al., 1997; Singh et al., 2015), (iii) the asymmetric coordination of the bridging chloride, and (iv) the fact that the dianionic form of $H_2BPClNOL$ is a harder Lewis base than the monoanionic one, it is plausible to assume that Mn1 and Mn2 are in the +2 and +3 oxidation states, respectively. Furthermore, the Mn1-Cl1 bond lengths are similar to those observed in other complexes containing Mn(II)-Cl bonds (2.425–2.472 Å) (Reddig et al., 2004). The Mn···Mn distance is 3.1593(14) Å, which is significantly shorter than the distances observed for a series of dinuclear Mn(II) complexes containing derivatives of the ligand 2-{[bis(pyridin-2-ylmethyl)amino]-methyl}phenol [3.392(8) to 3.493(2) Å] (Reddig et al., 2004). Furthermore, for a family of complexes containing the ligand 1,3-bis(salicylideneamino)-2-propanol, with which dinuclear Mn(II)Mn(II), Mn(II)Mn(III), Mn(III)Mn(III) and Mn(III)Mn(IV) complexes with di-µ-alkoxide bridges were generated, the Mn···Mn distance is in the range between 3.25 and 3.33 Å (Gelasco et al., 1997).

TABLE 2 | Selected bonds distances (Å) and angles (deg) for complex **1**.

Mn1—O1A	2.249(4)	Mn2—O1B	1.892(5)
Mn1—O2A	2.201(5)	Mn2—O2B	1.899(4)
Mn1—N1A	2.240(5)	Mn2—N1B	2.263(5)
Mn1—N2A	2.314(5)	Mn2—N2B	2.073(5)
Mn1—O2B	2.129(4)	Mn2—O1A	1.934(4)
Mn1—Cl1	2.4908(17)	Mn2—Cl1$^{(i)}$	2.6162(18)
Mn1—Mn2	3.1593(14)		
O2B—Mn1—O2A	95.50(17)	O1B—Mn2—O2B	172.81(17)
O2B—Mn1—N1A	153.49(19)	O1B—Mn2—O1A	103.45(18)
O2A—Mn1—N1A	111.01(19)	O2B—Mn2—O1A	82.53(17)
O2B—Mn1—O1A	70.50(14)	O1B—Mn2—N2B	93.3(2)
O2A—Mn1—O1A	148.14(17)	O2B—Mn2—N2B	81.9(2)
N1A—Mn1—O1A	86.07(17)	O1A—Mn2—N2B	158.3(2)
O2B—Mn1—N2A	112.75(18)	O1B—Mn2—N1B	87.18(19)
O2A—Mn1—N2A	75.43(18)	O2B—Mn2—N1B	97.12(19)
N1A—Mn1—N2A	75.44(19)	O1A—Mn2—N1B	87.82(18)
O1A—Mn1—N2A	83.74(18)	N2B—Mn2—N1B	79.22(19)
O2B—Mn1—Cl1	88.78(12)	O1B—Mn2—Cl1$^{(i)}$	87.15(14)
O2A—Mn1—Cl1	85.96(13)	O2B—Mn2—Cl1$^{(i)}$	88.45(14)
N1A—Mn1—Cl1	93.05(15)	O1A—Mn2—Cl1$^{(i)}$	94.21(14)
O1A—Mn1—Cl1	120.95(13)	N2B—Mn2—Cl1$^{(i)}$	100.39(15)
N2A—Mn1—Cl1	152.45(15)	N1B—Mn2—Cl1$^{(i)}$	174.28(15)
Mn1—O1A—Mn2	97.84(2)	Mn1—O2B—Mn2	103.21(2)

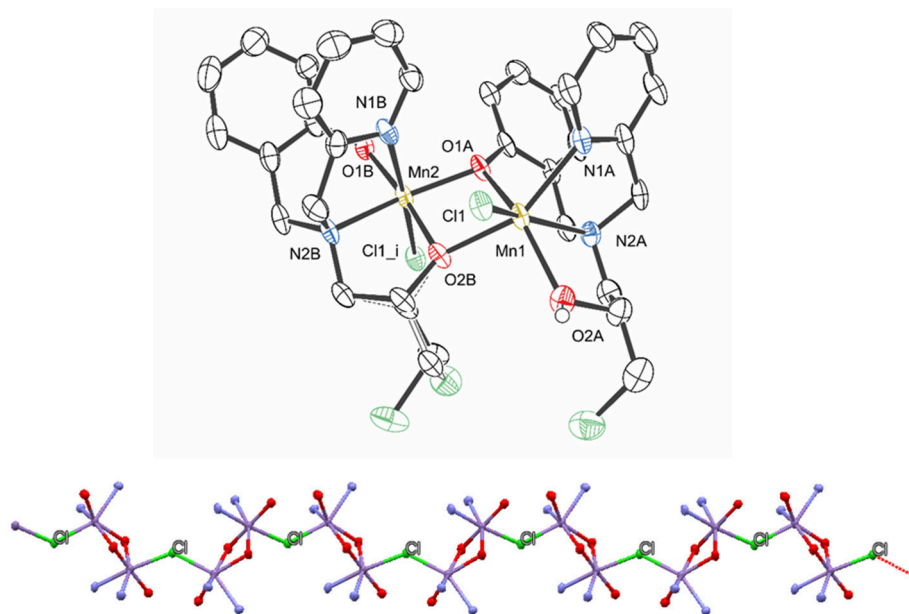*Symmetry codes : (i) −x+3/2, y−1/2, −z+1/2; (ii) −x+3/2, y+1/2, −z+1/2*

FIGURE 2 | Structure representation of compound **1** (hydrogen atoms, perchlorate anion, and water of crystallyzation were omitted for clarity) **(Top)** and view of the polymeric chain **(Bottom)**, highlighting the chloro bridges that connect the monomers (only the atoms coordinated to the manganese centers are shown for clarity). The ellipsoids are drawn at 50% probability.

Several structures containing $H_2BPClNOL$ and other metal ions have been described in the literature. This ligand forms a dinuclear complex with Cu(II), containing di-chloro bridges. However, mononuclear Cu(II), Zn(II), and Fe(III) complexes have also been observed (Fernandes et al., 2010; Gomes et al., 2017). Interestingly, in the presence of Ni(II), a dinuclear species containing two phenoxide bridges was formed (Horn et al., 2006a), while the structures of three diiron(III) complexes demonstrate the presence of alkoxide bridges (Horn et al., 2005b, 2006b). In contrast, the mixed valence +2/+3 dinuclear Mn species described here has mixed bridging groups (alkoxide and phenoxide moieties). It appears that the oxidation state of the metal ions is a determining factor for the identity of the bridging groups [i.e., oxidation state-dependent isomerism (Mitić et al., 2003)]. Thus, the homovalent +3/+3 (iron complexes) and +2/+2 (nickel complex) systems have dialkoxide and diphenoxide bridges, respectively, while the heterovalent +2/+3 systems have an alkoxide and a phenoxide bridge.

Infrared, UV-VIS, ESI-(+)-MS, and EPR Characterization

The IR spectrum of the Mn(III)Mn(II) complex **1** was recorded and compared with that of its free ligand $H_2BPClNOL$ in the region between 4,000 and 400 cm^{-1}. For $H_2BPClNOL$, characteristic bands of the aromatic group are observed at 1,595, 1,558, 1,475, and 1,433 cm^{-1}, assigned to ν C=N and ν C=C. For complex **1**, the corresponding bands are observed at 1,601, 1,574, 1,478, and 1,456 cm^{-1}. $H_2BPClNOL$ also shows an intense band at 1,289 cm^{-1} that is attributed to ν C-O of the phenol group; the corresponding feature is observed at 1,275 cm^{-1} in complex **1**.

Furthermore, **1** has two intense bands at 1,121 and 1,080 cm^{-1}, which are associated with the perchlorate anion. These bands are absent in the spectrum of the ligand.

The electronic spectrum in acetonitrile of complex **1** is dominated by intense bands in the UV range: 238 nm ($\varepsilon = 1.8 \times 10^4$ dm^3 mol^{-1} cm^{-1}), 262 nm ($\varepsilon = 1.5 \times 10^4$ dm^3 mol^{-1} cm^{-1}), 316 nm ($\varepsilon = 4.7 \times 10^4$ dm^3 mol^{-1} cm^{-1}) and 364 nm ($\varepsilon = 3.3 \times 10^4$ dm^3 mol^{-1} cm^{-1}). In the Vis range, a shoulder is observed at 459 nm (3.0×10^3 dm^3 mol^{-1} cm^{-1}). While the UV bands are attributed to $\pi \rightarrow \pi^*$ intraligand transitions, the lower energy transition is assigned to a phenolate $\rightarrow$ Mn^{III} LMCT transition (Karsten et al., 2002; Singh et al., 2015).

The analysis of a solution containing complex **1** by ESI-(+)-MS indicated the presence of peaks with m/z of 201, 307, 359, 377, 419, 665, 718, 735, 754, and 763. The peaks at m/z 307 and 201 are ascribed to the protonated form of the ligand and to its fragment, respectively. The peak at m/z 665 is ascribed to a mononuclear cation containing two molecules of $H_2BPClNOL$ (herewith referred to as H_2L): $[Mn(III)(HL)_2]^+$. The peaks with m/z 718, 735, 754 and 763 are ascribed to $[Mn(III)Mn(II)(L)_2]^+$, $[Mn_2(III)(L)_2(OH)]^+$, $[Mn(III)Mn(II)(HL)(L)(Cl)]^+$, $[Mn_2(III)(L)_2(CN)(H_2O)]^+$, respectively. These proposed assignments are based on the comparison of the simulated and experimental isotopic pattern and on the MS/MS data for each peak (see **Figures ESI1–9** in Supplementary Material). MS/MS data indicate that the cations with m/z 763, 754, and 735 yield the cation with m/z 718, which corresponds to a dinuclear Mn(III)Mn(II) arrangement, in agreement with the data obtained from x-ray diffraction. It should be pointed out that the species with m/z 718 and the one with m/z 754 both agree with the presence of mixed valence Mn

centers. In particular, the species associated with *m/z* 754 is in perfect agreement with the molecular structure observed for the monomeric unit, as revealed by x-ray diffraction. A proposal for the structure of the main signals observed in the ESI-(+)-MS study is presented as suplementary information.

Due to the novelty of the mixed-valent, mixed-bridged and polymeric structure of **1** in the solid state, the effect of CH_3CN, DMSO, and H_2O on the molecular arrangement was investigated by EPR at 1.8 K (**Figure ESI10**) and 140 K (**Figure 3**) in order to probe if solvents promote structural changes. While the spectra recorded in H_2O and DMSO are similar, they differ significantly from the spectrum in CH_3CN, indicating that the solvent has a considerable effect on the structure of the compound.

In the solid state, compound **1** shows only one broad band around g = 2 (see **Figure ESI10**), but when measured in a CH_3CN solution a six-line signal at g ∼2, which is characteristic of Mn(II) ions, and a broad band at g ∼7 are observed, indicating a significant change in the magnetic behavior of the system after solubilization. Broad resonances at low field have been previously described for coupled Mn(II)Mn(III) systems, and were interpreted in terms of the presence of ferro- or antiferromagnetically coupled Mn(II)Mn(III) cores. A feature of this low field signal is that for an antiferromagnetically coupled system, the signal disappears when the temperature decreases (Smith et al., 2009). On the other hand, in ferromagnetically-coupled Mn(II)Mn(III) dimers, the signal grows at low temperatures (Gelasco et al., 1997). We have observed that the signal around g ∼7 increases upon lowering the temperature from 140 K to 1.8 K (**Figure ESI11**), which indicates that complex **1** contains a ferromagnetically-coupled Mn(II)Mn(III) dimer. This interpretation was further confirmed by magnetic measurements (see below). In addition, in Mn(II)Mn(III) systems with antiferromagnetic coupling, multiline features with as many as 36 lines can be observed around g = 2 due to the population of the S = ½ state of the dinuclear manganese

system (Smith et al., 2009; Sano et al., 2013; Jung and Rentschler, 2015; Magherusan et al., 2018). In contrast, for ferromagnetically-coupled Mn(II)Mn(III) complexes published EPR data vary, including compounds that only show a signal at low field (g >5), or only a signal at high field (g ∼ 2), or a combination of both features (Schake et al., 1991; Gelasco et al., 1997; Rane et al., 2000). Thus, the spectral features of compound **1** are in agreement with other ferromagnetically-coupled Mn(II)Mn(III) systems, and the difference between the spectra in the solid state and in the CH_3CN solution is ascribed to the dissociation of the polymeric structure in solution, leaving the dinuclear antiferromagnetically-coupled Mn(II)Mn(III) system.

In DMSO (and H_2O) the EPR spectrum features six sharp lines (due to a ^{55}Mn hyperfine intetraction, I =5/2), typical of an isolated Mn(II) species and very similar to those obtained for the mononuclear complex [Mn(II)(HPClNOL)(NO₃)₂], **2** (**Figure 1**) (Lessa et al., 2009). HPClNOL is similar to H₂BPClNOL, the ligand employed in this study, but has two pyridine groups instead of one pyridine and one phenol group (**Figure 1**). The same behavior was observed in aqueous solution. This observation suggests that the dinuclear structure of the monomer is not stable in DMSO and water and, therefore, only the six-line signal typical of isolated Mn(II) centers was observed (Lessa et al., 2009). In contrast, in acetonitrile, the dimeric structure is stable, resulting in a decrease in resolution and intensity of the features associated with the Mn(II) center.

Magnetism

The magnetic susceptibility of complex **1** was measured over the temperature range 2–300 K at 0.05 T. The experimental data are presented as a $\chi_M T$ vs. T plot (**Figure 4**) of the $Mn^{II}Mn^{III}$ dinuclear unit.

The room temperature value of 7.20 cm³ mol^{-1} K (μ = 7.59 BM) is slightly lower than the theoretical value for two non-interacting spin systems of 7.38 cm³ mol^{-1} K (μ = 7.68 BM g = 2, S_A = 5/2, S_B = 2). The susceptibility steadily decreases with decreasing temperature, indicating antiferromagnetic interactions between the two metal centers. The low temperature value of 1.32 cm³ mol^{-1} K (μ = 3.25 BM) is higher than the low temperature limit ($\chi_M T$ = 0.38 cm³ mol^{-1} K, μ = 1.73 BM g = 2, S = 1/2) of an antiferromagnetically coupled system of this kind. In a simple dinuclear complex, this would indicate the presence of mononuclear impurities, however, the X-ray crystal structure indicates that the dinuclear $Mn^{II}(\mu$-$OR)_2Mn^{III}$ units are bridged by a chloride ion to form a one dimesion chain. The compound thus has a chain structure with alternating S = 2: S = 5/2 spin carriers and $(\mu$-OR$)_2$: μ-Cl interaction pathways. For this reason, attempts to fit the data for a single coupling constant were unsatisfactory, and we considered the Heisenberg chain Hamiltonian instead. The spin Hamiltonian in zero field is:

$$\mathbf{H} = -J \sum_i \mathbf{S}_{B_i}[(1+\alpha)\,\mathbf{S}_{A_i} + (1-\alpha)\,\mathbf{S}_{A_{i+1}}]$$

The derivation of the function for an alternating ferromagnetic chain compound was described by Pei (Pei et al., 1988), where
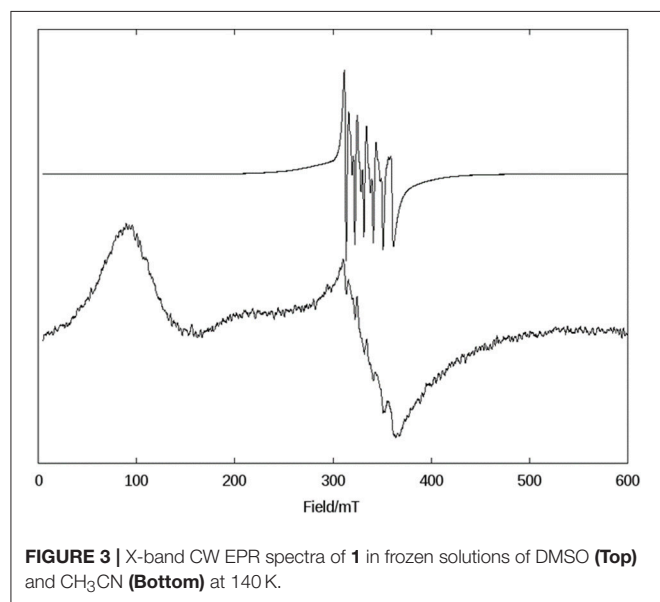

FIGURE 3 | X-band CW EPR spectra of **1** in frozen solutions of DMSO **(Top)** and CH_3CN **(Bottom)** at 140 K.
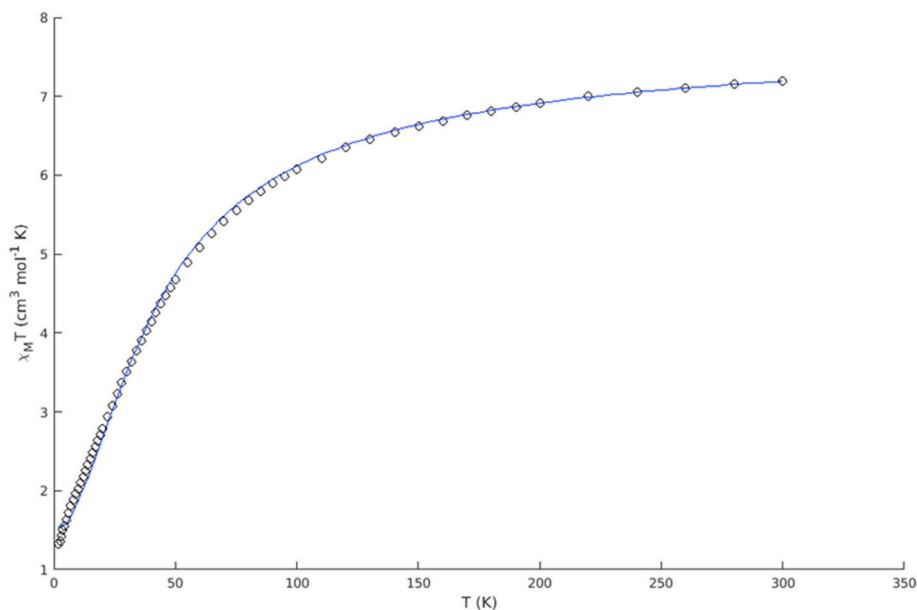
FIGURE 4 | Experimental $\chi_M T$ vs. T plot of complex **1** (open circles) and best fit (blue solid line).

$\chi_M T$ is defined as:

$$\chi_M T = \frac{N\beta^2}{3k} \frac{g^2 [s(s+1)(1-P)+2QR]+2gG(Q+R)+G^2(1+P)}{1-P}$$

with

$$G = g_A[S_A(S_A+1)]^{1/2} \quad g = g_B \quad s = S_B \quad x = J/kT$$

$$P = \frac{A_1}{A_0}$$

$$Q = \frac{x[(1+\alpha)B_0+(1-\alpha)B_1]}{A_0}$$

$$R = \frac{x[(1-\alpha)B_0+(1+\alpha)B_1]}{A_0}$$

$$A_0 = \frac{2\pi}{\Lambda^2} \sum_{\sigma=-s}^{s} \sum_{\varepsilon=\pm} \frac{\varepsilon \exp(\sigma\lambda_\varepsilon)}{\sigma^2}(\sigma\lambda_\varepsilon - 1)$$

$$A_1 = \frac{\pi}{\Lambda^2} \sum_{\sigma=-s}^{s} \sum_{\varepsilon=\pm} \frac{\varepsilon \exp(\sigma\lambda_\varepsilon)}{\sigma^4}[\sigma^3\lambda_\varepsilon^3 - 3\sigma^2\lambda_\varepsilon^2$$
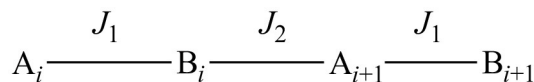$$+ (6-\sigma^2\lambda^2)\sigma\lambda_\varepsilon + \sigma^2\lambda^2 - 6]$$

$$B_0 = \frac{2\pi}{\Lambda^2} \sum_{\sigma=-s}^{s} \sum_{\varepsilon=\pm} \varepsilon \exp(\sigma\lambda_\varepsilon)$$

$$B_1 = \frac{\pi}{\Lambda^2} \sum_{\sigma=-s}^{s} \sum_{\varepsilon=\pm} \frac{\varepsilon \exp(\sigma\lambda_\varepsilon)}{\sigma^2}[\sigma^2\lambda_\varepsilon^2 - 2\sigma\lambda_\varepsilon + 2 - \sigma^2\lambda^2]$$

$$\lambda_+ = -2x \quad \lambda_- = \alpha \ \lambda_+ \quad \lambda^2 = 2x^2(1+\alpha^2) \quad \Lambda^2 = x^2(1+\alpha^2)$$

with $g_A = g_B = 2.05$, $S_A = 5/2$ and $S_B = 2$. The data were fit for α and J, where J is defined as:

$$J = J_{AB}[S_A(S_A+1)]^{1/2}$$

SCHEME 1 | A representation of the exchange coupling constants (J_1 and J_2) of an alternating ferrimagnetic chain complex; A and B represent the two different spin carriers.

The two different coupling pathways (J_1 and J_2) are represented in **Scheme 1** and the coupling constants are then given by:

$$J_1 = J_{AB}(1+\alpha) \qquad J_2 = J_{AB}(1-\alpha)$$

The best fit gave $\alpha = 1.029(2)$ and $J = -7.614(40)$ cm^{-1}, resulting in two exchange coupling constants of $J_1 = -5.224(13)$ and $J_2 = +0.076(13)$ cm^{-1}. The antiferromagnetic coupling (J_1) is ascribed to the interaction via the chloro bridge, where the more linear M-Cl-M angle of 129.34° is expected to facilitate antiferromagnetic interactions (Orchard, 2003). This conclusion is in agreement with other similar chloro bridged complexes (Fu et al., 1996; Gibson et al., 2003; Coates et al., 2010; Hirotsu et al., 2012; Zou et al., 2012).

The very weak ferromagnetic coupling (J_2) is attributed to exchange via the di-OR bridge. The Mn-OR-Mn angles were found to be 97.84° and 103.21°, with a Mn-O-O-Mn torsion angle of 156.56°, which is consistent with ferromagnetic exchange (Gelasco et al., 1997; Wittick et al., 2004; Naiya et al., 2012; Hänninen et al., 2013). Similar structural features have also been observed in a set of di- and trinuclear mixed valence manganese complexes (Hänninen et al., 2013). The ferromagnetic coupling constants of the dinuclear complexes were found in the range

of $+2.15(6)$ to $+7.9(7)$ cm^{-1}, whereas a much smaller coupling constant of $+0.04(7)$ cm^{-1} was observed in the case of one of the trinuclear complexes. The smaller value of J was attributed to a shift of the central Mn^{II} ion out of the plane of the bridging oxygens, reducing the ferromagnetic contribution to the coupling between the dxy and dx^2-y^2 orbitals. This distortion is not observed in the present case, and the small ferromagnetic coupling likely stems from the slightly elongated Mn-OR bond lengths of complex **1** (1.897–2.250 Å, average 2.052 Å) when compared to the reported dinuclear complexes (1.889–1.934 Å, average 1.912 Å).

The confirmation of the presence of ferromagnetic coupling involving the Mn(II)-(μ-OR)$_2$-Mn(III) explains the behavior of the signal seen at $g \sim 7$ in the EPR spectrum, which does not disappear when the temperature drops from 140 to 1.8 K.

Superoxide Dismutase (SOD) Activity

The SOD-like activity of complex **1** was studied employing the NBT assay in aqueous buffered solution (pH 7.8). NBT is a compound that undergoes reduction in the presence of superoxide anions, resulting in a purple species that may be monitored at 560 nm. The superoxide anions are generated at a constant rate by the xanthine/xanthine oxidase system (O'Connor et al., 2012). In this assay, the capability of the compound of interest (i.e., **1**) to prevent NBT reduction is evaluated. Thus, the concentration of the compound that inhibits 50% of NBT reduction corresponds to the IC$_{50}$. As a control we determined that the pure ligand was not active. Relevant results are summarized in **Table 3**, together with corresponding data for other compounds, including the native SOD enzymes. The kinetic parameters (IC$_{50}$ and k_{cat}) related to the SOD-like activity of complex **1** are similar to those of complex **3** reported by us previously (see **Table 3**), and are in the same range observed for other manganese compounds.

Attempts to evaluate the interaction between an aqueous solution of **1** and the superoxide anion produced by the xanthine/xanthine oxidase system by EPR, as published previously (dojindo.com)[1], were unsuccessful. Therefore, although the SOD activity of **1** was measured in a buffered aqueous solution, we carried out an EPR investigation of the reaction in DMSO. In this context it is important to highlight that the EPR spectrum of **1** in water and in DMSO are identical, revealing the presence of mononuclear species.

A DMSO solution of KO$_2$ shows an anisotropic EPR spectrum ($g_{//} = 2.11$ and $g_{\perp} = 2.01$) characteristic of O$_2^{\bullet-}$ (**Figure 5A**) (Valentine et al., 1977). In dry DMSO the spectrum for complex **1** displays a six-line pattern, typical of isolated Mn(II) species as discussed above (**Figures 3, 5B**). **Figure 5C** shows the spectrum recorded immediately after the interaction between the superoxide anion and complex **1**. In this case, a 16-line feature is observed, which was previously ascribed to a Mn(III)Mn(IV) dimer containing an oxo bridge (Dubois et al., 2008; Jiang et al., 2009; Mitić et al., 2009). The simulation of this 16-line spectrum is shown in **Figure ESI12**, and is in excellent agreement with the

[1]https://www.dojindo.com/Shared/Protocol/SpinTrapApplication.pdf Retrieved: 09/11/2017.

TABLE 3 | Kinetic parameters of reported manganese superoxide dismutase mimetics containing tripodal amine ligands and the natural enzyme.

Compound	SOD Activity		References
	IC$_{50}$ (μM)	10^6 k_{cat} (M^{-1}s^{-1})	
1[a]	0.370 ± 0.012	3.4	This work
3 [a]	0.34 ± 0.02	3.7	Ribeiro et al., 2015
[Mn(II)(TMIMA)$_2$]$^{2+}$[b]	1.6 ± 0.1	3.6	Durot et al., 2005
[Mn(II)(BMPG)(H$_2$O)]$^{+}$[b]	1.2 ± 0.5	4.8	Durot et al., 2005
[Mn(BIG)(H$_2$O)$_2$]$^{+}$[b]	3.7 ± 0.6	1.5	Durot et al., 2005
[Mn(IPG)(MeOH)]$^{+}$[b]	3.0 ± 0.6	1.9	Durot et al., 2005
[Mn(PBMPA)Cl(H$_2$O)]$^{a/b}$	2.67 ± 0.37	4.9	Pap et al., 2012
CuZn-SOD[a]	0.03	n.d	Weser et al., 1981
CuZn-SOD[c]	0.0026	n.d	Suksrichavalit et al., 2008
Human MnSOD[d]	–	800	Ramilo et al., 1999
T. thermophiles[e]	–	0.002	Bull et al., 1991

[a]*study carried out with xanthine/xanthine oxidase-mediated reduction of NBT;* [b]*study carried out with xanthine/xanthine oxidase-mediated reduction of cytochrome c;* [c]*study carried out with xanthine/xanthine oxidase SOD assay kit-WST;* [d]*pulse radiolysis;. [e]KO$_2$. HPClNOL, 1-[bis(pyridin-2-ylmethyl)amino]-3-chloropropan-2-ol; TMIMA, tris[(1-methyl-2-imidazolyl)methyl]amine; BMPG, N,N-bis[(6-methyl-2-pyridyl)methyl]-glycinate; BIG, N,N-bis[(1-methyl-2-imidazolyl)methyl]glycinate; IPG, N-[(1-methyl-2-imidazolyl)methyl]-N-(2-pyridylmethyl)glycinate; PBMPA, N-propanoate-N,N-bis-(2-pyridylmethyl)amine.*

experimental data. The simulation was performed employing the expression (Lessa et al., 2009):

$$H = \beta B \cdot g \cdot S + \sum_{j=1}^{2} S \cdot A_{Mn} \cdot I_{Mn} - g_n \beta_n B \cdot I_{Mn}$$

with the following g and A(Mn) matrices: $g_x = 2.0014$, $g_y = 2.0030$, $g_z = 1.9865$, $A[Mn(III)]_{1x} = 136.3 \times 10^{-4}$ cm^{-1}, $A[Mn(III)]_{1y} = 155.5 \times 10^{-4}$ cm^{-1}, $A[Mn(III)]_{1z} = 103.4 \times 10^{-4}$ cm^{-1}, $A[Mn(IV)]_{2x} = 75.3 \times 10^{-4}$ cm^{-1}, $A[Mn(IV)]_{2y} = 68.6 \times 10^{-4}$ cm^{-1}, $A[Mn(IV)]_{2z} = 77.4 \times 10^{-4}$ cm^{-1}. These spin Hamiltonian parameters are similar to those for other Mn(III)-(μ-O)-Mn(IV) species reported previously [Mn(III): $S = 2$, Mn(IV): $S = 3/2$, ground state $S = 1/2$; (Horner et al., 1999)].

As a control, we performed a reaction between a KO$_2$ solution (DMSO) and Mn(Cl)$_2$·4H$_2$O. In this case, a different behavior was observed when compared to **1**. The signal associated with Mn(II) disappeared, suggesting that it underwent oxidation. Furthermore, the signal of the superoxide radical remained visible, indicating that MnCl$_2$ did not promote the disproportionation of all superoxide molecules present in solution. On the other hand, compound **1** extinguished the EPR signal associated with the superoxide radical (see **Figure ESI13**).

Thus, using EPR spectroscopy we could demonstrate that in DMSO, compound **1** can decompose the superoxide anion, whose reaction pathway involves the formation of a dimanganese high-valent Mn(III)-oxo-Mn(IV) species, which is stable for at least 1 h (**Figure 5D**).

Catalase (CAT) Activity

Bacterial catalases from organisms such as *Lactobacillus plantarum, Thermus thermophiles,* or *Thermoleophilum album* (Whittaker, 2012) possess a dinuclear manganese cluster in their active sites. However, we also demonstrated that the mononuclear compounds **2** and **3** (**Figure 1**) have catalase activity (Lessa et al., 2009; Ribeiro et al., 2015). Since **1** in the solid state and in acetonitrile contains a dimanganese center, but forms a mononuclear complex in DMSO and H_2O, it is plausible to assume that it may show CAT activity as well. We thus investigated the H_2O_2 disproportionation promoted by **1** under three different conditions. Firstly, the reaction was investigated in distilled water, but no activity was observed. Secondly, the reaction was performed in a buffered solution (phosphate buffer, 0.05 mol dm^{-3}, pH 7.8), but again, no activity was observed. This behavior differs significantly from that observed for compounds **2** and **3**, which show CAT activity
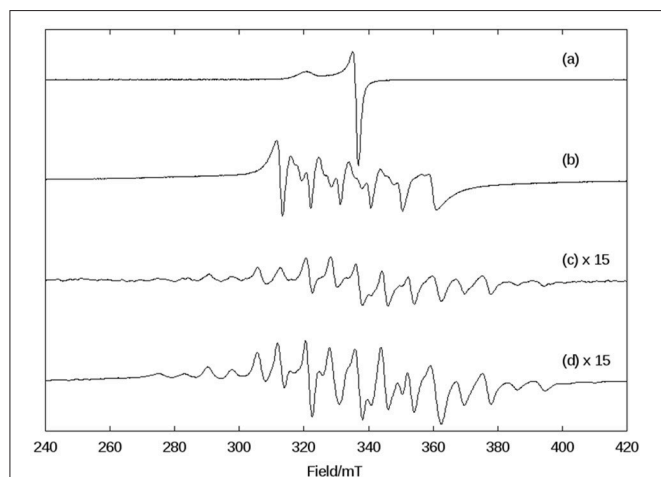
in pure water as well as buffered solutions (Lessa et al., 2009; Ribeiro et al., 2015). Thirdly, the assay was carried out with piperazine (0.1 mol dm^{-3}, pH = 9.73) in an aqueous solution and bubbles were produced immediately after the addition of H_2O_2. Therefore, kinetic measurements were conducted in the presence of piperazine. The time course of O_2 production at 25 °C in the presence of piperazine and at different concentrations of H_2O_2 is illustrated in **Figure 6**. The data were analyzed by a fit to the Michaelis-Menten equation. A similar study was performed by measuring the consumption of H_2O_2 by UV-Vis (see **Figure ESI14**). Relevant parameters are summarized in **Table 4**, together with corresponding data for other manganese compounds for comparison.

The data presented in **Table 4** reveal that the kinetic rates obtained for **1** are lower when O_2 production is measured than when the consumption of H_2O_2 is recorded. This observation suggests that in the UV-Vis experiment, the change in the reading at 240 nm related to the H_2O_2 molecule may be influenced by changes in the absorption of **1** at this wavelength. Therefore, the UV-Vis method may not be suitable to evaluate the decomposition rate of H_2O_2 when in the presence of molecules that show intense absorption in a comparable wavelength range. Hence, we consider the kinetic parameters obtained with the Clark electrode as more reliable.

The kinetic data show that **1** is less active than other dinuclear manganese complexes containing tripodal ligands (tpa, bpia, L_1-L_5). This may be explained by the presence of piperazine, which can compete with H_2O_2 by the manganese coordination site. Furthermore, the presence of water has been considered as an inhibitor, too, as exemplified by the compound $[Mn_2^{II}(tpa)_2(\mu$-$Cl)_2]^{2+}$, whose k_{cat} decreased around 50 times when the reaction was perfomed in CH_3CN/H_2O instead of anhydrous CH_3CN. Thus, **1** shows a k_{cat} comparable to that of $[Mn_2^{II}(tpa)_2(\mu$-$Cl)_2]^{2+}$.

In an attempt to gain insight into the role of piperazine in the catalytic process, we investigated the interactions between complex **1** and piperazine with different techniques. In **Figure 7** the electronic spectrum of **1** dissolved in water is shown as a function of an increasing amount of piperazine. Piperazine
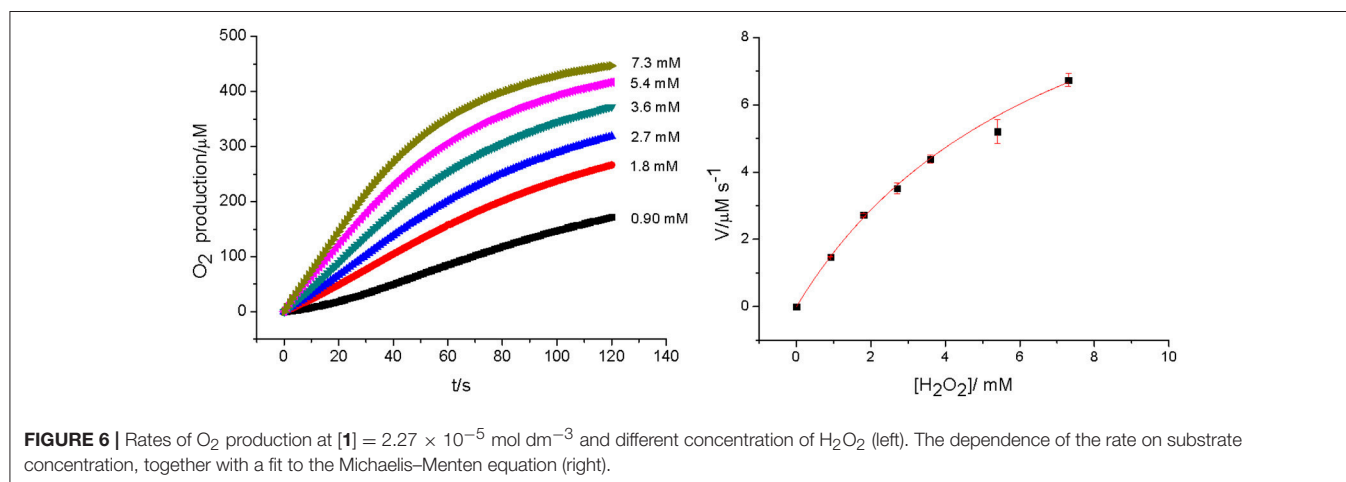

FIGURE 5 | X-band CW EPR spectra in DMSO at 140 K of **(A)** superoxide (KO_2), **(B)** complex **1** in dry DMSO, **(C)** the complex **1** immediately after the reaction with superoxide, and **(D)** the complex **1**, 1 h after the reaction with superoxide.

FIGURE 6 | Rates of O_2 production at [**1**] = 2.27×10^{-5} mol dm^{-3} and different concentration of H_2O_2 (left). The dependence of the rate on substrate concentration, together with a fit to the Michaelis–Menten equation (right).

TABLE 4 | Kinetic parameters of reported manganese catalase mimetics containing tripodal amine ligands and the natural enzyme.

Compound	k_{cat} (s^{-1})	K_M (mM)	k_{cat}/K_m (M^{-1} s^{-1})	Solvent system	References
1[a]	2.59 ± 0.12	11.7 ± 1.1	221.3	H$_2$O + piperazine	This work
1[b]	0.58 ± 0.03	7.23 ± 0.48	80.2	H$_2$O + piperazine	This work
[Mn$^{II}_2$(tpa)$_2$(μ-Cl)$_2$]$^{2+}$	107	3.1	34,516	CH$_3$CN	Shin et al., 2010
[Mn$^{II}_2$(tpa)$_2$(μ-Cl)$_2$]$^{2+}$	1.97	1.47	1,340	CH$_3$CN + H$_2$O	Shin et al., 2010
[Mn^{II}(bpia)(μ-OAc)]$^{2+}_2$	1,100	31.5	34,000	CONHCH$_3$	Triller et al., 2002
[Mn$_2$(L$_1$-L$_5$)$_2$Cl$_2$]	87.8–283	18–54.3	2,750–7,800	H$_2$O/MeOH	Reddig et al., 2004
CAT(*T. thermophilus*)	2.6 × 10^5	83	3.1 × 10^6		Shank et al., 1994

[a]*Evaluated by UV-Vis spectroscopy by following H$_2$O$_2$ consumption.*
[b]*Measured by electrochemical O$_2$ detection.*
Tpa, (tris(2-pycolyl)amine); bpia, bis-(picolyl)(N-methylimidazol-2-yl)amine); L1-L$_5$, derivatives of 2-{[bis(pyridin-2-ylmethyl)amino]methyl}phenol.

alone does not have any electronic transitions above 300 nm. However, two new distinct transitions were observed when this reagent was added to a solution containing complex **1**. The first transition (shoulder) at 459 nm, associated with a LMCT in complex **1** (*vide supra*), gained intensity and was red-shifted to ~500 nm. The increase in the intensity of this phenolate → Mn(III) LMCT as a function of piperazine concentration suggests that Mn(II) is undergoing oxidation. A second relevant band appears as a shoulder around 390 nm and is ascribed to an oxo Mn(III)/(IV) transition (Lessa et al., 2009). The driving force for the oxidative process may be linked to either the direct coordination of piperazine to the manganese ion or the deprotonation of the coordinating alcohol group from the ligand (which is protonated as seen in the molecular structure solved by x-ray diffraction). The spectral changes observed in **Figure 7** also reveal the existence of two consecutive reactions. The band at 500 nm increases faster than the shoulder around 390 nm, supporting the hypothesis that the first step involves the oxidation induced by piperazine, resulting in an intermediate that reacts with O$_2$. The final species contains a Mn(III)-oxo-Mn(IV) core, as evidenced by ESI-MS and EPR results (see below).

The interaction between piperazine and complex **1** was also investigated using ESI-(+)-MS spectrometry. **Figure 8** shows the spectra of the pure compound (A) and in the presence of piperazine (B).

The peak assignment of **1** was discussed above. In the presence of piperazine the base peak is still at *m/z* 307. However, some new species appear, including those at *m/z* 390, 445 (see **Figures ESI15–16**) and 734. Of particular relevance is the peak at *m/z* 734, which is absent in the spectrum of **1**. The calculated and experimental isotopic patterns for this peak are shown in **Figure 9**. The best simulation (position and intensity) was obtained by assuming the presence of two overlapping species: [(BPClNOL)Mn(III)-(μ-O)-Mn(IV)(BPClNOL)]$^+$ with *m/z* 734 and [Mn$_2$(III)(L)$_2$(OH)]$^+$ with *m/z* 735. The last signal was also observed in the mass spectrum of **1** (see above) while the signal at *m/z* 734 is a new species formed in the reaction between **1** and piperazine. Thus, in agreement with the UV-Vis spectral data (**Figure 7**), mass spectrometry supports a mechanism whereby
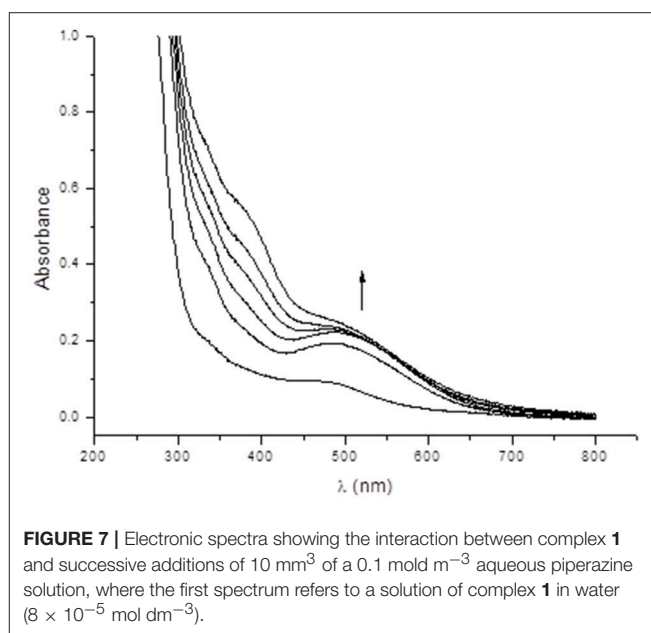

FIGURE 7 | Electronic spectra showing the interaction between complex **1** and successive additions of 10 mm^3 of a 0.1 mold m^{-3} aqueous piperazine solution, where the first spectrum refers to a solution of complex **1** in water (8 × 10^{-5} mol dm^{-3}).

piperazine induces the oxidation of **1** to a high-valent Mn(III)-(μ-O)-Mn(IV) species with *m/z* 734.

The complex formed upon mixing **1**, piperazine and H$_2$O$_2$ was also probed by EPR spectroscopy. As discussed above, when **1** is exposed to H$_2$O$_2$ no oxygen production is observed. Not surprisingly, thus, the EPR spectrum of **1** in CH$_3$CN and in the presence of H$_2$O$_2$ is virtually identical to that of the complex alone (i.e., **Figure 3,** bottom). However, when piperazine is added to **1,** an immediate change occurs that is consistent with the formation of a species containing a Mn(III)-(μ-O)-Mn(IV) center (**Figure 10A**); the relevant EPR spectrum has a 16-line feature that is typical of mixed-valent Mn(III)Mn(IV)-μ-oxo-bridged species (Horner et al., 1999; Dubois et al., 2008; Jiang et al., 2009; Mitić et al., 2009) supporting the data observed by UV-Vis and ESI-MS. The experimental spectrum could be simulated (see ESI, **Figure ESI17**) using the same equation and parameters employed in the simulation of the spectrum
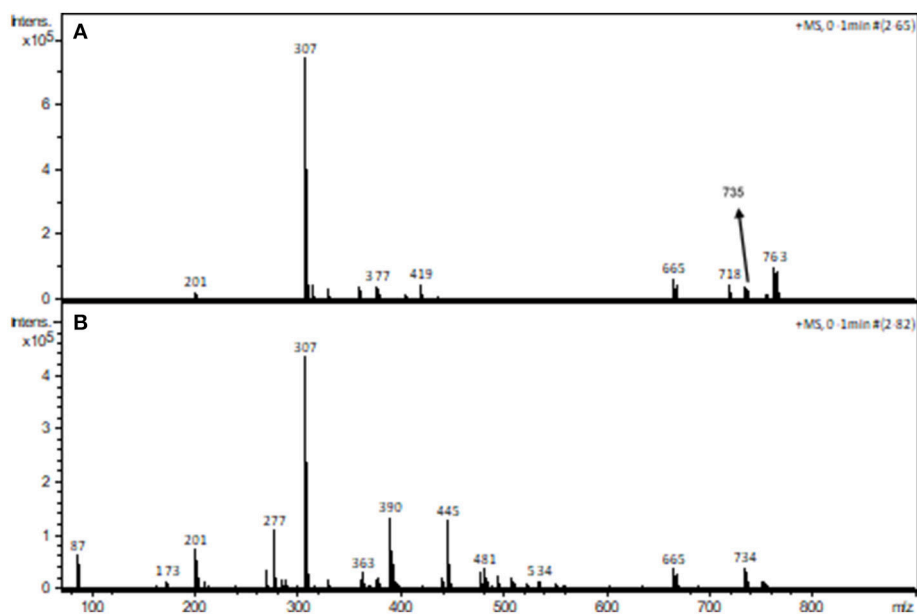
FIGURE 8 | ESI-(+)-MS spectra of complex **1** in the absence **(A)** and in the presence **(B)** of piperazine in CH_3CN/H_2O.
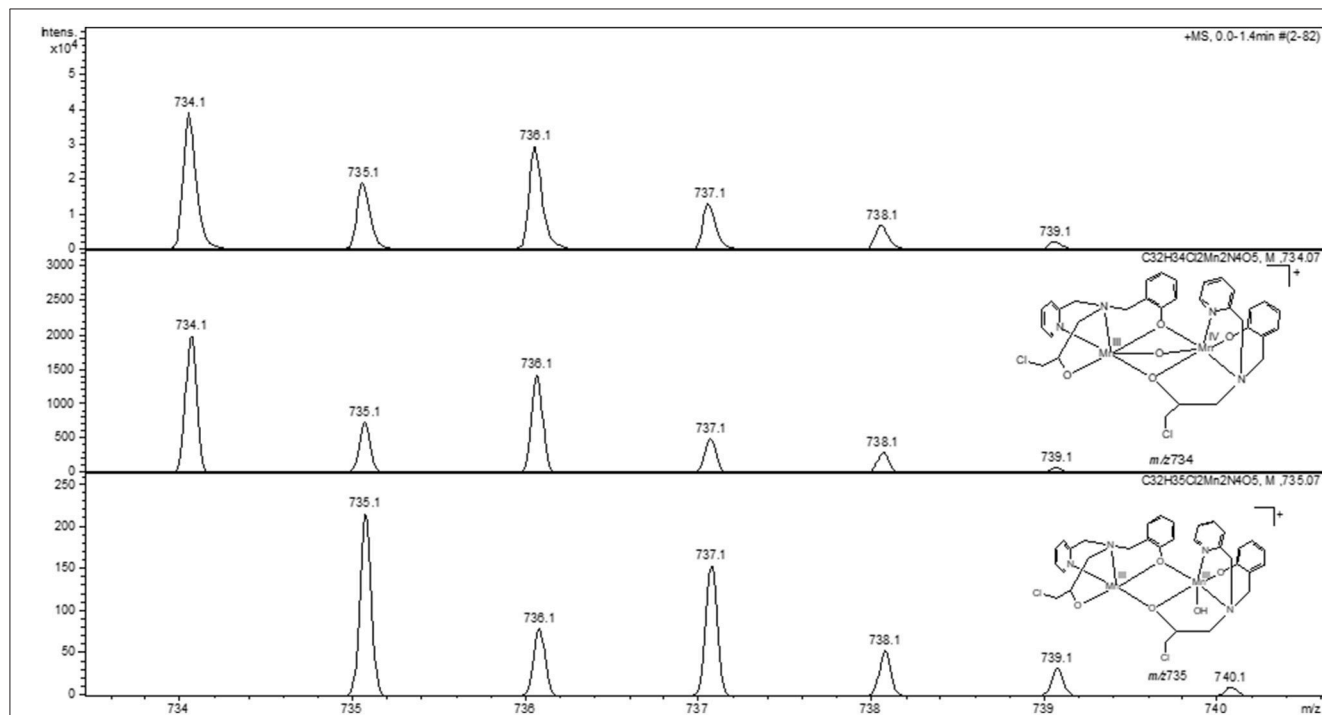

FIGURE 9 | Experimental **(Top)** and calculated **(Middle, Bottom)** isotopic patterns for the ion at m/z 734. Proposed structures for the species are also shown.

obtained for the reaction between **1** and superoxide (**Figures 5**, **ESI12**).

Upon the addition of H_2O_2 the spectrum of Mn(III)-(μ-O)-Mn(IV) changes with the loss of some resonances (**Figure 10B**). Now, at least 10 lines are observed, which suggests the formation

of a new chemical species. We tentatively assign this new intermediate as a Mn(II)Mn(III) species, since this compound type has been described as presenting a 12 line spectrum (Larson et al., 1992; Gelasco et al., 1997; Mitić et al., 2009; Smith et al., 2009).
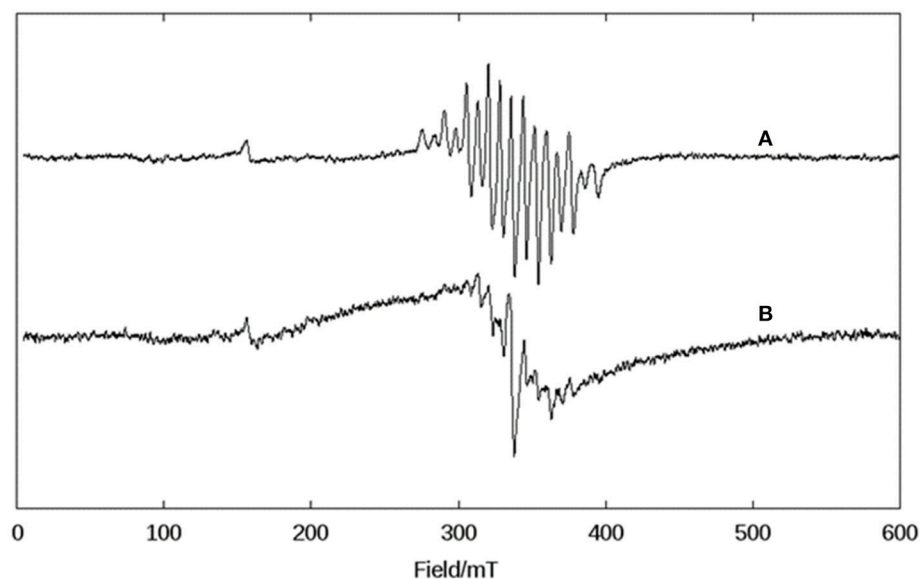
FIGURE 10 | X-band CW EPR spectra of **1** in CH_3CN at 140 K. **(A)** After the addition of piperazine and **(B)** after the addition of H_2O_2 to a solution containing the complex and piperazine.
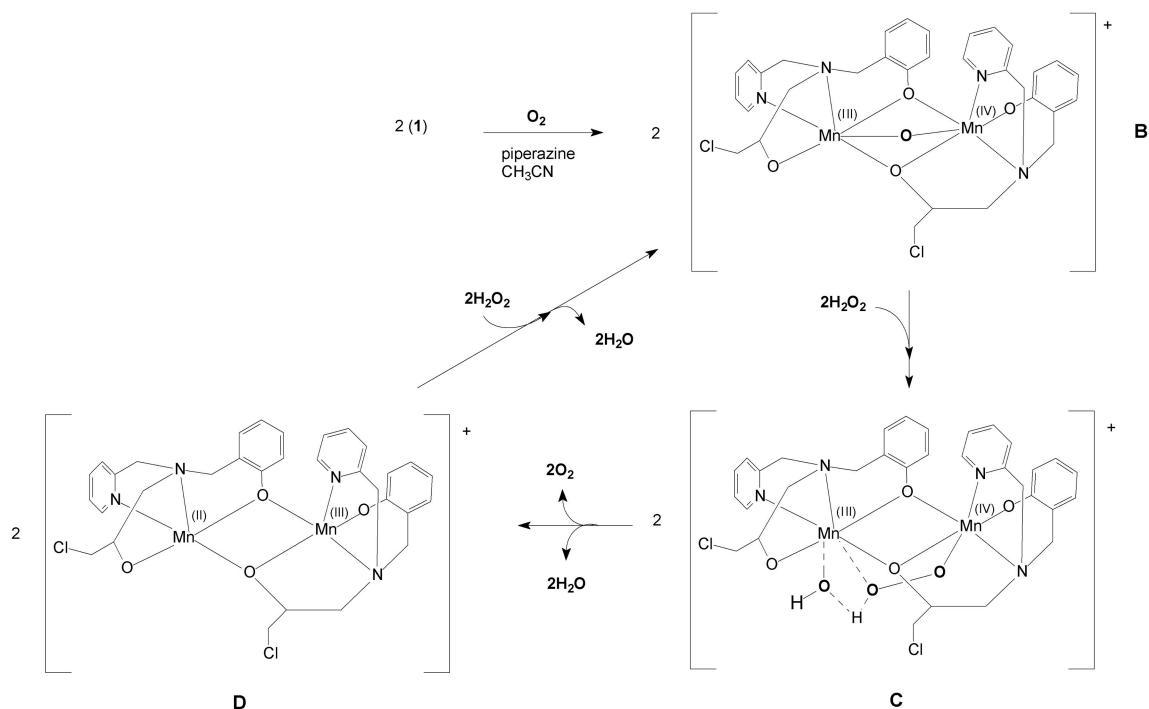

FIGURE 11 | Mechanistic proposal for the H_2O_2 disproportionation reaction promoted by complex **1** based on EPR, ESI-(+)-MS and kinetic data.

Previously, we have reported an investigation of the CAT activity of complex **2** (**Figure 1**). Similar to complex **1**, a Mn(III)-Mn(IV) intermediate was observed by EPR (Lessa et al., 2009). In the present study the Mn(III)Mn(IV) compound is formed after the interaction of a mixed-valent Mn(II)Mn(III) species with piperazine under aerobic conditions.
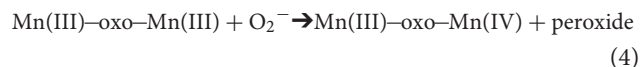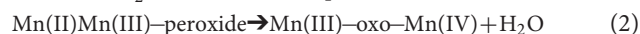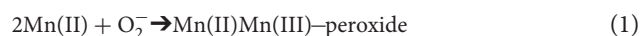
In contrast, for **2** the formation of a Mn(III)Mn(IV) species was shown to be due to the reaction between a homo-valent Mn(II) complex and H_2O_2. Another difference is that for **1**, only one μ-oxo bridge is proposed to be present, while for **2,** two μ-oxo bridges connect the metal ions.

It has been shown that the presence of a base (e.g., imidazole, trimethylamine) increases the CAT activity of synthetic compounds and it has been proposed that this increase is associated with the deprotonation of the H_2O_2 molecule (Devereux et al., 2002; Grau et al., 2014; Kose et al., 2015). While piperazine is a base it is also a chelator, and hence it could promote CAT reactivity using either property. However, our combined data strongly support the interpretation that piperazine induces changes in the oxidation state and in the coordination environment of the manganese centers in complex **1**. A plausible pathway is by promoting the deprotonation of the alcohol function, which changes the Lewis acidity of the Mn(II), leading to its oxidation in the presence of O_2 to generate the Mn(III)-oxo-Mn(IV) species. In order to substantiate this hypothesis, we performed a test reaction between **1** and H_2O_2, but using triethylamine instead of piperazine (see ESI **Figure ESI18**). The result revealed a similar catalase activity, suggesting that both piperazine and triethylamine act as a base. EPR studies of the interaction between **1** and triethylamine reveleal the formation of a Mn(III)-oxo-Mn(IV) unit, since a 16-line EPR spectrum was observed (**Figure ESI19**), confirming that both bases (piperazine, triethylamine) induce the formation of the same intermediate.

Mechanistic Proposals

The evaluation of the IC_{50} has shown that **1** is able to prevent NBT reduction in the presence of superoxide anions (**Table 3**). Furthermore, we have demonstrated that **1** interacts directly with this ROS in DMSO, promoting its decomposition, as seen by the disappearance of the superoxide radical signal (**Figure 5**). As a consequence of the reaction, the characteristic 6-line EPR spectrum from a Mn(II) complex was transformed into a 16-line one, which is typical of a Mn(III)Mn(IV)-coupled species containing a μ-oxo bridge (Larson et al., 1992; Gelasco et al., 1997; Lessa et al., 2009; Mitić et al., 2009; Smith et al., 2009). Additionally, the EPR spectra of **1** in water and in DMSO are equivalent, indicating that the dinuclear structure is broken in solution, generating Mn(II) and Mn(III) species. Therefore, it is plausible to assume that the chemical species present in the water solution employed in the catalytic study is similar to the one present in the DMSO solution employed for the superoxide dismutation study monitored via EPR. Thus, we propose that in the initial step of the reaction the superoxide anion reacts with two mononuclear Mn(II) species (observed by EPR), resulting in a peroxo complex (Equation 1) containing a Mn(II)Mn(III) center, which subsequently is further oxidized to a high-valent Mn(III)Mn(IV) species (Equation 2). The two electrons involved in this process are necessary to reduce the peroxide species to water, leading to the formation of a μ-oxo bridge which was detected by EPR (Equation 2). These two steps are similar to those proposed for the compounds $[Mn(BIG)(H_2O)_2]^+$ and [Mn(IPG)(MeOH)] (Policar et al., 2001). The reaction of this high-valent species with another superoxide generates molecular oxygen with the concomitant formation of a Mn(III)-oxo-Mn(III) species (Equation 3). This homo-valent species may be re-oxidized by the reaction with another superoxide molecule, forming H_2O_2 and the high-valent Mn(III)Mn(IV) species in the process (Equation 4), which then enters the reaction again at the

step described by Equation (3).

$$2Mn(II) + O_2^- \rightarrow Mn(II)Mn(III)\text{–peroxide} \tag{1}$$

$$Mn(II)Mn(III)\text{–peroxide} \rightarrow Mn(III)\text{–oxo–}Mn(IV) + H_2O \tag{2}$$

$$Mn(III)\text{–oxo–}Mn(IV) + O_2^- \rightarrow Mn(III)\text{–oxo–}Mn(III) + O_2 \tag{3}$$

$$Mn(III)\text{–oxo–}Mn(III) + O_2^- \rightarrow Mn(III)\text{–oxo–}Mn(IV) + \text{peroxide} \tag{4}$$

Commonly SOD mimetics are already in the active form to promote the reduction of superoxide to peroxide and molecular oxygen. For example, Mn-porphyrins and Mn-salen compounds show SOD like activity in which the oxidation state changes between III/II (Shin et al., 2010; Signorella et al., 2018). For such systems the catalytic process usually involves a step for the oxidation of superoxide, thus forming molecular oxygen, and another step for the reduction of superoxide, resulting in the formation of hydrogen peroxide (ping-pong mechanism). On the other hand, complexes containing tripodal amine ligands sometimes need to be activated to promote the disproportionation of ROS (Lessa et al., 2009; Signorella et al., 2018) as observed for the compounds $[Mn(BIG)(H_2O)_2]^+$ and [Mn(IPG)(MeOH)] (Policar et al., 2001), which, after reacting with superoxide, are transformed into the dinuclear species Mn^{III}-$(\mu$-$O)_2$-Mn^{IV}. The same behavior was described for the mononuclear compounds $[Mn^{II}(N4py)(OTf)](OTf)$ (Leto et al., 2013).

A proposed model for the CAT mechanism employed by **1** is shown in **Figure 11**. When **1** is placed in contact with piperazine, an oxidation process occurs, transforming the system to Mn(III)-(μ-O)-Mn(IV). Thus, we propose that **1** is transformed to B, the mixed-valent μ-oxo bridged species that was observed by UV-Vis, ESI-MS and EPR. The next step (B➔C in **Figure 11**) occurs after the addition of H_2O_2. The formation of a new Mn(III)Mn(IV) complex is proposed, in which a hydroperoxide molecule displaces the μ-oxo group. This interpretation would explain why the 16-line EPR feature disappears in the presence of H_2O_2 (**Figure 10**). In this unstable arrangement, the peroxide molecule may transfer two electrons to the binuclear Mn(III)Mn(IV) cluster, resulting in the release of molecular oxygen and water and the generation of a Mn(II)Mn(III) center (D in **Figure 11**). Further reaction with H_2O_2 results in the formation of the Mn(III)-oxo-Mn(IV) species again (B in **Figure 11**) and release of H_2O.

The proposed mechanism for the CAT activity presented by **1** is significantly different from that proposed for **2**. **1** needs to be transformed into the active species by piperazine, forming a Mn(III)-(μ-O)-Mn(IV). In contrast, **2** reacts directly with H_2O_2 and a Mn(III)-(μ-O)$_2$-Mn(IV) intermediate is formed.

CONCLUSIONS

In this study we have reported the synthesis and characterization of an unusual mixed-valent manganese compound which forms a polymeric linear chain in the solid state. It consists of

Mn(II)Mn(III) subunits, in which the manganese ions are connected by a phenoxide and an alkoxide bridge (**Figures 1, 2**). The subunits are linked via chloro bridges. In the solid state, **1** shows two distinct magnetic interactions. An antiferromagnetic one $[J = -5.224(13) \text{ cm}^{-1}]$ is observed between the monomers (through chloro bridges) and a ferromagnetic coupling $[J = +0.076(13) \text{ cm}^{-1}]$ is observed in the monomeric unit (via the alkoxide/phenoxide bridges). The latter interaction supports the attribution that the signal observed in the EPR spectrum at g around 7 is a result of a ferromagnetic coupled Mn(III)Mn(II) system, and therefore, that the compound remains as a dinuclear center in CH_3CN. In contrast, EPR spectroscopy has revealed that in DMSO and H_2O solutions the dinuclear structure is broken, leading to monomeric Mn(II) and Mn(III) units (**Figure 3**). Importantly, in aqueous environment, the compound has dual antioxidant activity, i.e., it acts both as a catalase and as superoxide dismutase. For the reaction with superoxide, a Mn(III)-(μ-O)-Mn(IV) species was identified as intermediate by EPR. With respect to the catalase activity, we found that the resting Mn(II)Mn(III) species is active only in presence of a base such as piperazine or trimethylamine. It was shown that piperazine promotes the formation of an active Mn(III)-(μ-O)-Mn(IV). An intermediate of the reaction of this Mn(III)-(μ-O)-Mn(IV) species with H_2O_2 could also be detected by EPR, suggesting that the formation of a Mn(II)Mn(III) species that promote the CAT activity of **1**, involves a $Mn^{II}Mn^{III}/Mn^{III}Mn^{IV}$ redox couple.

AUTHOR'S NOTE

AUTHOR CONTRIBUTIONS

RC, SF, and CP carried out the syntheses, the characterization of the compounds and the kinetics experiments. JH, CN, and RF carried out the EPR experiments, and the simulations of the data. JR performed the x-ray experiments and the data treatment. PC and AR were responsible for the magnetism measurements and data interpretation. GS contributed in the analyses and discussion of kinetic data. CF and AH conceived and planned the experiments, supervised the progress of this work, and took the lead in writing the manuscript. All authors discussed the results and contributed to the final manuscript.

FUNDING

ACKNOWLEDGMENTS

SUPPLEMENTARY MATERIAL

The Supplementary Material for this article can be found online at: https://www.frontiersin.org/articles/10.3389/fchem. 2018.00491/full#supplementary-material

REFERENCES

Allen, R. G., and Tresini, M. (2000). Oxidative stress and gene regulation. *Free Radic. Biol. Med.* 28, 463–499. doi: 10.1016/S0891-5849(99)00242-7

Antonyuk, S. V., Melik-Adamyan, V. R., Popov, A. N., Lamzin, V. S., Hempstead, P. D., Harrison, P. M., et al. (2000). Three-dimensional structure of the enzyme dimanganese catalase from *Thermus thermophilus* at 1 Å resolution. *Crystallogr. Rep.* 45, 105–116. doi: 10.1134/1.171145

Barondeau, D. P., Kassmann, C. J., Bruns, C. K., Tainer, J. A., and Getzoff, E. D. (2004). Nickel superoxide dismutase structure and mechanism. *Biochemistry* 43, 8038–8047. doi: 10.1021/bi0496081

Batinić-Haberle, I., Rebouças, J. S., and Spasojević, I. (2010). Superoxide dismutase mimics: chemistry, pharmacology, and therapeutic potential. *Antioxid. Redox Signal.* 13, 877–918. doi: 10.1089/ars.2009.2876

Beers, R. F Jr., and Sizer, I. W. (1952). A spectrophotometric method for measuring the breakdown of hydrogen peroxide by catalase. *J. Biol. Chem.* 195, 133–140.

Bravo, J., Mate, M. J., Schneider, T., Switala, J., Wilson, K., Loewen, P. C., et al. (1999). Structure of catalase HPII from *Escherichia coli* at 1.9 Å resolution. *PROTEINS: Struct. Funct. Genet.* 34, 155–166. doi: 10.1002/(SICI)1097-0134(19990201)34:2

Bull, C., Niederhoffer, E. C., Yoshida, T., and Fee, J. A. (1991). Kinetic studies of superoxide dismutases: properties of the manganese-containing protein from *Thermus thermophilus*. *J. Am. Chem. Soc.* 113, 4069–4076. doi: 10.1021/ja00011a003

Coates, C. M., Fiedler, S. R., McCullough, T. L., Albrecht-Schmitt, T. E., Shores, M. P., and Goldsmith, C. R. (2010). Synthesis and characterization of an asymmetric, linear, trinuclear manganese(II) complex. *Inorg. Chem.* 49, 1481–1486. doi: 10.1021/ic901758s

Costa, V., and Moradas-Ferreira, P. (2001). Oxidative stress and signal transduction in Saccharomyces cerevisiae: insights into ageing, apoptosis and diseases. *Mol. Aspects Med.* 22, 217–246. doi: 10.1016/S0098-2997(01)00012-7

Day, B. J. (2007). Catalase and glutathione peroxidase mimics. *Biochem. Pharmacol.* 77, 285–296. doi: 10.1016/j.bcp.2008.09.029

Devereux, M., McCann, M., Leon, V., McKee, V., and Ball, R. J. (2002). Synthesis and catalytic activity of manganese(II) complexes of heterocyclic carboxylic acids: X-ray crystal structures of [Mn(pyr)$_2$]n, [Mn(dipic)(bipy)$_2$]·4.5H$_2$O and [Mn(chedam)(bipy)]·H$_2$O (pyr=2-pyrazinecarboxylic acid; dipic=pyridine-2,6-dicarboxylic acid; chedam=chelidamic acid(4-hydroxypyridine-2,6-dicarboxylic acid); bipy=2,2-bipyridine). *Polyhedron* 21, 1063–1071. doi: 10.1016/S0277-5387(02)00842-2

Doctrow, S. R., Huffman, K., Marcus, C. B., Tocco, G., Malfroy, E., Adinolfi, C. A., et al. (2002). Salen-manganese complexes as catalytic scavengers of hydrogen peroxide and cytoprotective agents: structure-activity relationship studies. *J. Med. Chem.* 45, 4549–4558. doi: 10.1021/jm020207y

Dubois, L., Pécaut, J., Charlot, M. F., Baffert, C., Collomb, M. N., Deronzier, A., et al. (2008). Carboxylate ligands drastically enhance the rates of oxo exchange and hydrogen peroxide disproportionation by oxo manganese compounds of potential biological significance. *Chem. Eur. J.* 14, 3013–3025. doi: 10.1002/chem.200701253

Durot, S., Policar, C., Cisnetti, F., Lambert, F., Renault, J. P., Pelosi, G., et al. (2005). Series of Mn complexes based on *N*-centered ligands and superoxide – reactivity in an anhydrous medium and SOD-like activity in an aqueous medium correlated to Mn^{II}/Mn^{III} redox potentials. *Eur. J. Inorg. Chem.* 3513–3523. doi: 10.1002/ejic.200400835

Eckshtain, M., Zilbermann, I., Mahammed, A., Saltsman, I., Okun, Z., Maimon, E., et al. (2009). Superoxide dismutase activity of corrole metal complexes. *Dalton Trans.* 14, 7879–7882. doi: 10.1039/b911278b

Fernandes, C., Horn, A. Jr., Vieira-da-Motta, O., de Assis, V. M., Rocha, M. R., Mathias L da, S., et al. (2010). Synthesis, characterization and antibacterial activity of FeIII, CoII, CuII and ZnII complexes probed by transmission electron microscopy. *J. Inorg. Biochem.* 104, 1214–1223. doi: 10.1016/j.jinorgbio.2010.07.011

Fu, Y., Li, Q., Zhou, Z., Dai, W., Wang, D., Mak, T. C. W., et al. (1996). The first example of a bis-monohelical complex: the crystal and molecular structure of [Mn$_2$(dmqpy)$_2$(H$_2$O)$_2$(μ-Cl)][ClO$_4$]$_3$·4H$_2$O (dmqpy = 6,6-dimethyl-2,2′ : 6′, 2″ : 6″,2‴ : 6-quinquepyridine). *Chem. Commun.* 1549–1550. doi: 10.1039/CC9960001549

Gelasco, A., Kirk, M. L., Kampf, J. W., and Pecoraro, V. L. (1997). The [Mn(2)(2-OHsalpn)(2)](2-,-,0,+) system: synthesis, structure, spectroscopy, and magnetism of the first structurally characterized dinuclear manganese series containing four distinct oxidation states. *Inorg. Chem.* 36, 1829–1837. doi: 10.1021/ic970140i

Gibson, V. C., McTavish, S., Redshaw, C., Solan, G. A., White, A. J. P., and Williams, D. J. (2003). From monomeric to polymeric manganese complexes bearing bis(imino)pyridine and related ligands. *Dalton Trans.* 221–226. doi: 10.1039/b207384f

Gomes, C. A., Lube, L. M., Fernandes, C., Franco, R. W. A., Resende, J. A. L. C., Horn, A., et al. (2017). A new system for cyclohexane functionalization employing iron(III) catalysts and trichloroisocyanuric acid. *New J. Chem.* 41, 11498–11502. doi: 10.1039/C7NJ01164D

Grau, M., Rigodanza, F., White, A. J., Sorarù, A., Carraro, M., Bonchio, M., et al. (2014). Ligand tuning of single-site manganese-based catalytic antioxidants with dual superoxide dismutase and catalase activity. *Chem. Commun.* 50, 4607–4609. doi: 10.1039/C4CC00758A

Halliwell, B. (2006). Reactive species and antioxidants. Redox biology is a fundamental theme of aerobic life. *Plant Physiol.* 141, 312–322. doi: 10.1104/pp.106.077073

Hancock, J. T., Desikan, R., and Neill, S. J. (2001). Role of reactive oxygen species in cell signaling pathways. *Biochem. Soc. Trans.* 29, 345–350. doi: 10.1042/bst0290345

Hänninen, M. M., Välivaara, J., Mota, A. J., Colacio, E., Lloret, F., and Sillanpää, R. (2013). Ferromagnetic dinuclear mixed-valence Mn(II)/Mn(III) complexes: building blocks for the higher nuclearity complexes. structure, magnetic properties, and density functional theory calculations. *Inorg. Chem.* 52, 2228–2241. doi: 10.1021/ic302731z

Hirotsu, M., Shimizu, Y., Kuwamura, N., Tanaka, R., Kinoshita, I., Takada, R., et al. (2012). Anion-controlled assembly of four manganese ions: structural, magnetic, and electrochemical properties of tetramanganese complexes stabilized by xanthene-bridged Schiff base ligands. *Inorg. Chem.* 51, 766–768. doi: 10.1021/ic202287k

Horn, A., Fernandes, C., Bortoluzzi, A. J., Vugman, N. V., and Herbst, M. H. (2005a). Coordination chemistry of the new ligand 1-(bis-pyridin-2-ylmethyl-amino)-3-chloropropan-2-ol (HPClNOL) with copper(II). X-ray crystal structure, spectroscopic and electrochemical properties of the complex [Cu(HPClNOL)(CH 3CN)](ClO4)2. *J. Mol. Struct.* 749, 96–102. doi: 10.1016/j.molstruc.2005.03.045

Horn, A., Fim, L., Bortoluzzi, A. J., Szpoganicz, B., and Fernandes, C. (2006a). Solid state and solution characterization of a new dinuclear nickel (II) complex: the search for synthetic models for urease. *J. Mol. Struct.* 797, 154–164. doi: 10.1016/j.molstruc.2006.03.043

Horn, A., Neves, A., Vencato, I., Drago, V., Zucco, C., Werner, R., et al. (2000). A new dinucleating N,O donor ligand (H$_2$BPClNOL) and the structural and magnetic properties of two diiron complexes with the di-μ-Alkoxo Motif. *J. Braz. Chem. Soc.* 11, 7–10. doi: 10.1590/S0103-50532000000100002

Horn, A., Vencato, I., Bortoluzzi, A. J., Drago, V., Novak, M. A., and Neves, A. (2006b). Synthesis, molecular structure and spectroscopic, electrochemical and magnetic properties of a new dinuclear iron complex containing μ-sulfate-di-μ-alkoxo bridges. Evaluating the influence of the sulfate bridge on the physicochemical properties of the di-μ-alkoxo-diiron unit. *J. Braz. Chem. Soc.* 17, 1584–1593. doi: 10.1590/S0103-50532006000800015

Horn, A., Vencato, I., Bortoluzzi, A. J., Hörner, R., Silva, R. A. N., Szpoganicz, B., et al. (2005b). Synthesis, crystal structure and properties of dinuclear iron(III) complexes containing terminally coordinated phenolate/H$_2$O/OH$^-$ groups as models for purple acid phosphatases: efficient hydrolytic DNA cleavage. *Inorg. Chim. Acta* 358, 339–351. doi: 10.1016/j.ica.2004.09.021

Horner, O., Anxolabéhère-Mallart, E., Charlot, M. F., Tchertanov, L., Guilhem, J., Mattioli, T. A., et al. (1999). A new manganese dinuclear complex with phenolate ligands and a single unsupported oxo bridge. Storage of two positive charges within less than 500 mV. relevance to photosynthesis. *Inorg. Chem.* 38, 1222–1232. doi: 10.1021/ic980832m

Jiang, X., Liu, H., Zheng, B., and Zhang, J. (2009). Coordination modes of bridge carboxylates in dinuclear manganese compounds determine their catalase-like activities. *Dalton Trans.* 8714–8723. doi: 10.1039/b907687e

Jung, M., and Rentschler, E. (2015). Magnetic and spectroscopic study on a new asymmetric mixed-valence Mn2(II,III) coordination compound. *Z. Anorg. Allg. chem.* 641, 2277–2281. doi: 10.1002/zaac.201500551

Karsten, P., Neves, A., Bortoluzzi, A. J., Strähle, J., and Maichle-Mössmer, C. (2002). Synthesis, structure and catalase-like activity of a new dinuclear mixed valence Mn^{II}Mn^{III} complex containing an unsymmetric N$_5$O$_2$ donor ligand. *Inorg. Chem. Commun.* 5, 434–438. doi: 10.1016/S1387-7003(02)00435-5

Kerfeld, C. A., Yoshida, S., Tran, K. T., Yeates, T. O., Cascio, D., Bottin, H., et al. (2003). The 1.6 Å resolution structure of Fe-superoxide dismutase from the thermophilic cyanobacterium *Thermosynechococcus elongatus*. *J. Biol. Inorg. Chem.* 8, 707–714. doi: 10.1007/s00775-003-0469-0

Kose, M., Goring, P., Lucas, P., and Mckee, V. (2015). Mono-, di- and tri-nuclear manganese(II) complexes derived from a quinquedentate ligand: Superoxide dismutase and catalase mimetic studies. *Inorg. Chim. Acta* 435, 232–238. doi: 10.1016/j.ica.2015.07.010

Krause, L., Herbst-Irmer, R., Sheldrick, G. M., and Stalke, D. (2015). Comparison of silver and molybdenum microfocus X-ray sources for single-crystal structure determination. *J. Appl. Crystallogr.* 48, 3–10. doi: 10.1107/S1600576714022985

Kupershmidt, L., Okun, Z., Amit, T., Mandel, S., Saltsman, I., Mahammed, A., et al. (2010). Metallocorroles as cytoprotective agents against oxidative and nitrative stress in cellular models of neurodegeneration. *J. Neurochem.* 113, 363–373. doi: 10.1111/j.1471-4159.2010.06619.x

Lane, N. (2003). A unifying view of ageing and disease: the double-agent theory. *J. Theor. Biol.* 225, 531–540. doi: 10.1016/S0022-5193(03)00304-7

Larson, E., Haddy, A., Kirk, M. L., Sands, R. H., Hatfield, W. E., and Pecoraro, V. L. (1992). Asymmetric mixed-valent complex {[Mn(2-OH-3,5-Cl$_2$-SALPN)]$_2$(THF)}ClO$_4$ shows a temperature-dependent interconversion between g = 2 multiline and low-field EPR signals. *J. Am. Chem. Soc.* 114, 6263–6265. doi: 10.1021/ja00041a065

Ledesma, G. N., Eury, H., Anxolabéhère-Mallart, E., Hureau, C., and Signorella, S. R. (2015). A new mononuclear manganese(III) complex of an unsymmetrical hexadentate N3O3 ligand exhibiting superoxide dismutase and catalase-like activity: synthesis, characterization, properties and kinetics studies. *J. Inorg. Biochem.* 146, 69–76. doi: 10.1016/j.jinorgbio.2015.02.012

Lessa, J. A., Horn, A., Bull, E. S., Rocha, M. R., Benassi, M., Catharino, R. R., et al. (2009). Catalase vs peroxidase activity of a manganese(II) compound: identification of a Mn(III)-(μ-O)₂-Mn(IV) reaction intermediate by electrospray ionization mass spectrometry and electron paramagnetic resonance spectroscopy. *Inorg. Chem.* 48, 4569–4579. doi: 10.1021/ic801969c

Lessa, J. A., Horn, A., Pinheiro, C. B., Farah, L. L., Eberlin, M. N., Benassi, M., et al. (2007). Synthesis, solid-state and in-solution structures of a new seven coordinated manganese(II) complex via X-ray diffraction and electrospray ionization mass spectrometry. *Inorg. Chem. Commun.* 10, 863–866. doi: 10.1016/j.inoche.2007.04.001

Leto, D. F., Chattopadhyay, S., Day, V. W., and Jackson, T. A. (2013). Reaction landscape of a pentadentate N5-ligated Mn(II) complex with O₂·⁻ and H₂O₂ includes conversion of a peroxomanganese(III) adduct to a bis(μ-oxo)dimanganese(III,IV) species. *Dalton Trans.* 42, 13014–13025. doi: 10.1039/c3dt51277k

Lu, J., and Holmgren, A. (2009). Selenoproteins. *J. Biol. Chem.* 284, 723–727. doi: 10.1074/jbc.R800045200

Ludwig, M. L., Metzger, A. L., and Pattridge, K. A. (1991). Stallings WC manganese superoxide dismutase from *Thermus thermophilus*. A structural model refined at 1.8 A resolution. *J. Mol. Biol.* 219, 335–358. doi: 10.1016/0022-2836(91)90569-R

Magherusan, A. M., Zhou, A., Farquhar, E. R., García-Melchor, M., Twamley, B., Que, L. Jr., et al. (2018). Mimicking class I b Mn2-ribonucleotide reductase: a MnII2 complex and its reaction with superoxide. *Angew. Chem. Int. Ed. Engl.* 57, 918–922. doi: 10.1002/anie.201709806

Mahammed, A., and Gross, Z. (2011). The importance of developing metal complexes with pronounced catalase-like activity. *Catal. Sci. Technol.* 1, 535–540. doi: 10.1039/c1cy00063b

McCord, J. M., and Edeas, M. A. (2005). SOD, oxidative stress and human pathologies: a brief history and a future vision. *Biomed. Pharmacother.* 59, 139–142. doi: 10.1016/j.biopha.2005.03.005

Mitić, N., Noble, C. J., Gahan, L. R., Hanson, G. R., and Schenk, G. (2009). Metal-ion mutagenesis: conversion of a purple acid phosphatase from sweet potato to a neutral phosphatase with the formation of an unprecedented catalytically competent Mn(II)Mn(II) active site. *J. Am. Chem. Soc.* 131, 8173–8179. doi: 10.1021/ja900797u

Mitić, N., Saleh, L., Schenk, G., Bollinger, J. M. Jr., and Solomon, E. I. (2003). Rapid-freeze-quench magnetic circular dichroism of intermediate X in ribonucleotide reductase: new structural insight. *J. Am. Chem. Soc.* 125, 11200–11201. doi: 10.1021/ja036556e

Morano, K. A., Grant, C. M., and Moye-Rowley, W. S. (2012). The response to heat shock and oxidative stress in *Saccharomyces cerevisiae*. *Genetics* 190, 1157–1195. doi: 10.1534/genetics.111.128033

Naiya, S., Biswas, S., Drew, M. G., Gómez-García, C. J., and Ghosh, A. (2012). A ferromagnetic methoxido-bridged Mn(III) dimer and a spin-canted metamagnetic μ(1,3)-azido-bridged chain. *Inorg. Chem.* 51, 5332–5341. doi: 10.1021/ic300274n

O'Connor, M., Kellett, A., McCann, M., Rosair, G., McNamara, M., Howe, O., et al. (2012). Copper(II) complexes of salicylic acid combining superoxide dismutase mimetic properties with DNA binding and cleaving capabilities display promising chemotherapeutic potential with fast acting *in vitro* cytotoxicity against cisplatin sensitive and resistant cancer cell lines. *J. Med. Chem.* 55, 1957–1968. doi: 10.1021/jm201041d

Orchard, A. F. (2003). *Magnetochemistry.* New York, NY: Oxford University Press Inc.

Pap, J. S., Kripli, B., Bors, I., Bogáth, D., Giorgi, M., Kaizer, J., et al. (2012). Transition metal complexes bearing flexible N3 or N3O donor ligands: Reactivity toward superoxide radical anion and hydrogen peroxide. *J. Inorg. Biochem.* 117, 60–70. doi: 10.1016/j.jinorgbio.2012.08.012

Pei, Y., Kahn, O., Sletten, J., Renard, J. P., Georges, R., Gianduzzo, J. C., et al. (1988). Structure and magnetism of the first alternating bimetallic chain compound MnCu(obp)(H₂O)₃.cntdot.H₂O [obp = oxamidobis(propionato)]. *Inorg. Chem.* 27, 47–53. doi: 10.1021/ic00274a011

Policar, C., Durot, S., Lambert, F., Cesario, M., Ramiandrasoa, F., and Morgenstern-Badarau, I. (2001). New MnII complexes with an N/O coordination sphere from tripodal N-centered ligands – characterization from solid state to solution and reaction with superoxide in non-aqueous and aqueous media. *Eur. J. Inorg. Chem.* 1807–1818. doi: 10.1002/1099-0682(200107)2001:7

Ramilo, C. A., Leveque, V., Guan, Y., Lepocki, J. R., Tainer, J. A., Nick, H. S., et al. (1999). Interrupting the hydrogen bond network at the active site of human manganese superoxide dismutase. *J. Biol. Chem.* 274, 27711–27740. doi: 10.1074/jbc.274.39.27711

Rane, S. Y., Khan, E. M., Thube, D. R., Padhye, S. B., Date, S. K., and Bakare, P. P. (2000). A ferro- and antiferro-magnetically coupled binuclear manganese (II,III) complex of an orthofunctionalised para-naphthoquinone: Synthesis and characterization by thermogravimetric, thermochromic, cyclic voltammetric, magnetic and EPR studies. *Ind. J. Chem.* 39, 1117–1123.

Reddig, N., Pursche, D., Kloskowski, M., Slinn, C., Baldeau, S. M., and Rompel, A. (2004). Tuning the catalase activity of dinuclear manganese complexes by utilizing different substituted tripodal ligands. *Eur. J. Inorg. Chem.* 4, 879–887. doi: 10.1002/ejic.200300157

Ribeiro, J. P., Segundo, M. A., Reis, S., and Lima, J. L. (2009). Spectrophotometric FIA methods for determination of hydrogen peroxide: application to evaluation of scavenging capacity. *Talanta* 79, 1169–1176. doi: 10.1016/j.talanta.2009.02.039

Ribeiro, T. P., Fernandes, C., Melo, K. V., Ferreira, S. S., Lessa, J. A., Franco, R. W., et al. (2015). Iron, copper, and manganese complexes with *in vitro* superoxide dismutase and/or catalase activities that keep Saccharomyces cerevisiae cells alive under severe oxidative stress. *Free Radic. Biol. Med.* 80, 67–76. doi: 10.1016/j.freeradbiomed.2014.12.005

SAINT (2015). *Bruker APEX3 and SAINT*. Madison, WI: Bruker AXS Inc.

Sano, Y., Weitz, A. C., Ziller, J. W., Hendrich, M. P., and Borovik, A. S. (2013). Unsymmetrical bimetallic complexes with MII–(μ-OH)–MIII cores (MIIMIII = FeIIFeIII, MnIIFeIII, MnIIMnIII): structural, magnetic, and redox properties. *Inorg. Chem.* 52, 10229–10231. doi: 10.1021/ic401561k

Schake, A. R., Schmitt, E. A., Conti, A. J., Streib, W. E., Huffman, J. C., Hendrickson, D. N., et al. (1991). Preparation and properties of mononuclear and ferromagnetically coupled dinuclear manganese complexes with 2, 2′biphenoxide. *Inorg. Chem.* 30, 3192–3199. doi: 10.1021/ic00016a017

Shank, M., Barynin, V., and Dismukes, G. C. (1994). Protein coordination to manganese determines the high catalytic rate of dimanganese catalases. Comparison to functional catalase mimics. *Biochemistry* 33, 15433–15436. doi: 10.1021/bi00255a025

Sheldrick, G. M. (2015). Crystal structure refinement with SHELXL. *Acta Crystallograph. Sect. C* 71, 3–8. doi: 10.1107/S2053229614024218

Shin, B. K., Kim, M., and Han, J. (2010). Hydrogen peroxide disproportionation by the [TPA₂Mn₂(μ-Cl)₂]²⁺ complex. *Polyhedron* 29, 2560–2568. doi: 10.1016/j.poly.2010.05.029

Signorella, S., Palopoli, C., and Ledesma, G. (2018). Rationally designed mimics of antioxidant manganoenzymes: role of structural features in the quest for catalysts with catalase and superoxide dismutase activity. *Coord. Chem. Rev.* 365, 75–102. doi: 10.1016/j.ccr.2018.03.005

Singh, R., Haukka, M., McKenzie, C. J., and Nordlander, E. (2015). High turnover catalase activity of a mixed-valence MnIIMnIII complex with terminal carboxylate donors. *Eur. J. Inorg. Chem.* 21, 3485–3492. doi: 10.1002/ejic.201500468

Smith, S. J., Riley, M. J., Noble, C. J., Hanson, G. R., Stranger, R., Jayaratne, V., et al. (2009). Structural and catalytic characterization of a heterovalent Mn(II)Mn(III) complex that mimics purple acid phosphatases. *Inorg. Chem.* 48, 10036–10048. doi: 10.1021/ic9005086

Suksrichavalit, T., Prachayasittikul, S., Piacham, T., Isarankura-Na-Ayudhya, C., Nantasenamat, C., and Prachayasittikul, V. (2008). Copper complexes of nicotinic-aromatic carboxylic acids as superoxide dismutase mimetics. *Molecules* 13, 3040–3056. doi: 10.3390/molecules13123040

Tainer, J. A., Getzoff, E. D., Beem, K. M., Richardson, J. S., and Richardson, D. C. (1982). Determination and analysis of the 2 A-structure of copper, zinc superoxide dismutase. *J. Mol. Biol.* 160, 181–217. doi: 10.1016/0022-2836(82)90174-7

Tovmasyan, A., Maia, C. G., Weitner, T., Carballal, S., Sampaio, R. S., Lieb, D., et al. (2015). A comprehensive evaluation of catalase-like activity of different classes of redox-active therapeutics. *Free Radic. Biol. Med.* 86, 308–321. doi: 10.1016/j.freeradbiomed.2015.05.018

Triller, M. U., Hsieh, W-Y, Pecoraro, V. L., Rompel, A., and Krebs, B. (2002). Preparation of highly efficient manganese catalase mimics. *Inorg. Chem.* 41, 5544–5554. doi: 10.1021/ic025897a

Valentine, J. S., Miksztal, A. R., and Sawyer, D. T. (1984). Methods for the study of superoxide chemistry in nonaqueous solutions. *Methods Enzymol.* 105, 71–81. doi: 10.1016/S0076-6879(84)05010-2

Valentine, J. S., Tatsuno, Y., and Nappa, M. (1977). Superoxotetraphenylporphinatozinc(1-). *J. Am. Chem. Soc.* 99, 3522–3523.

Valko, M., Leibfritz, D., Moncol, J., Cronin, M. T., Mazur, M., and Telser, J. (2007). Free radicals and antioxidants in normal physiological functions and human disease. *Int. J. Biochem. Cell Biol.* 39, 44–84. doi: 10.1016/j.biocel.2006.07.001

Weekley, C. M., Kenkel, I., Lippert, R., Wei, S., Lieb, D., Cranwell, T., et al. (2017). Cellular fates of manganese(II) pentaazamacrocyclic superoxide dismutase (SOD) mimetics: fluorescently labeled MnSOD mimetics, X-ray absorption spectroscopy, and X-ray fluorescence microscopy studies. *Inorg. Chem.* 56, 6076–6093. doi: 10.1021/acs.inorgchem.6b03073

Weser, U., Schubotz, L. M., and Lengfelder, E. (1981). Imidazole-bridged copper complexes as Cu_2Zn_2- superoxide dismutase models. *J. Molec. Catal.* 13, 249–261. doi: 10.1016/0304-5102(81)85025-0

Whittaker, J. W. (2012). Non-heme manganese catalase - the 'other' catalase. *Arch. Biochem. Biophys.* 525, 111–120. doi: 10.1016/j.abb.2011.12.008

Wittick, L. M., Murray, K. S., Moubaraki, B., Batten, S. R., Spiccia, L., and Berry, K. J. (2004). Synthesis, structure and magnetism of new single molecule magnets composed of $Mn_2^{II}Mn_2^{III}$ alkoxo-carboxylate bridged clusters capped by triethanolamine ligands. *Dalton Trans.* 1003–1011. doi: 10.1039/b312672b

Zou, L. F., Zhao, L., Guo, Y. N., Tang, J., Wang, Q. L., and Li, Y. H. (2012). N1,N5-Bis(3-ethoxysalicylidene)-di-imino-3-azapentane-based Mn^{3+}, Co^{3+} and Cu^{2+} complexes: Synthesis, coordination behavior and magnetic properties. *Inorg. Chim. Acta* 382, 65–71. doi: 10.1016/j.ica.2011. 10.019

An Asymmetrically Substituted Aliphatic Bis-Dithiolene Mono-Oxido Molybdenum(IV) Complex With Ester and Alcohol Functions as Structural and Functional Active Site Model of Molybdoenzymes

Mohsen Ahmadi[1], Christian Fischer[1], Ashta C. Ghosh[2] and Carola Schulzke[1]*

[1] Institut für Biochemie, Universität Greifswald, Greifswald, Germany, [2] Departement de Chimie Moléculaire, Université Grenoble Alpes, UMR CNRS 5250, Grenoble, France

A Mo^{IV} mono-oxido bis-dithiolene complex, $[MoO(mohdt)_2]^{2-}$ (mohdt = 1-methoxy-1-oxo-4-hydroxy-but-2-ene-2,3-bis-thiolate) was synthesized as a structural and functional model for molybdenum oxidoreductase enzymes of the DMSO reductase family. It was comprehensively characterized by *inter alia* various spectroscopic methods and employed as an oxygen atom transfer (OAT) catalyst. The ligand precursor of mohdt was readily prepared by a three-step synthesis starting from dimethyl-but-2-ynedioate. Crystallographic and ^{13}C-NMR data support the rationale that by asymmetric substitution the electronic structure of the ene-dithio moiety can be fine-tuned. The $Mo^{IV}O$ bis-dithiolene complex was obtained by *in situ* reaction of the de-protected ligand with the metal precursor complex *trans*-$[MoO_2(CN)_4]^{4-}$. The catalytic oxygen atom transfer mediated by the complex was investigated by the model OAT reaction from DMSO to triphenylphosphine with the substrate transformation being monitored by ^{31}P NMR spectroscopy. $[MoO(mohdt)_2]^{2-}$ was found to be catalytically active reaching 93% conversion, albeit with a rather low reaction rate (reaction time 56 h). The observed overall catalytic activity is comparable to those of related complexes with aromatic dithiolene ligands despite the novel ligand being aliphatic in nature and originally perceived to perform more swiftly. The respective results are rationalized with respect to a potential intermolecular interaction between the hydroxyl and ester functions together with the electron-withdrawing functional groups of the dithiolene ligands of the molybdenum mono-oxido complex and equilibrium between the active monomeric $Mo^{IV}O$ and $Mo^{VI}O_2$ and the unreactive dimeric $Mo_2^{V}O_3$ species.

Keywords: artificial molybdenum active site, aliphatic dithiolene, oxygen atom transfer, Moco model, Mo^{IV} oxo complex

INTRODUCTION

Molybdenum dependent enzymes are essential contributors to the life of nearly every known organism on earth being it an ancient archaeon, a plant or a mammal which includes the modern human being (Mendel, 2007; Edwards et al., 2015). To date, four such molybdenum dependent enzymes have been discovered to be part of the human organism, which are sulfite oxidase (SO), xanthine dehydrogenase (XDH), aldehyde oxidase (AO), and mARC (Garner and Bristow, 1985; Hille, 2013; Hille et al., 2014; Schulzke and Ghosh, 2014). Defects in the maturation of the molybdenum cofactors (**Figure 1**), which can occur at different stages of the respective multistep biosynthesis, cause diseases (e.g., isolated sulfite oxidase deficiency: iSOD) due to the non-functioning of the molybdenum enzymes. This has consequences such as brain damage, motor retardation, convulsions etc. beginning right after birth and typically leading to infancy or early childhood death (Reiss, 2000). The extreme instability of the molybdenum cofactor prevents it from being biotechnologically produced and applied as treatment. Understanding exactly what makes Moco unstable and what makes it catalytically active is therefore of great interest for those aiming at developing an artificial cofactor which might be used as a respective drug in the future. This constitutes the motivation for our group and specifically for the study discussed in the following as one of many approaches. A moiety including molybdenum and one or two dithiolene ligands (representing molybdopterin—MPT; see **Figure 1**) is one of the most common motives in molybdenum cofactor bio-inorganic chemistry (Rajagopalan, 1997; Schulzke and Samuel, 2011).

During the last 20 years, various bis-dithiolene mono-oxido molybdenum complexes have been developed and investigated (Donahue et al., 1998; Lim and Holm, 2001; Enemark et al., 2004; Döring et al., 2010; Schulzke, 2016; Ghosh et al., 2017). Such model compounds have helped understanding the roles of the dithiolene type ligands in the active sites of the DMSOR family enzymes, e.g., how they affect the electron and atom transfer reactivity during catalysis. Still, a comprehensive

understanding of the roles of the different substituents is yet to be accomplished. During the catalytic reactions of these enzymes, molybdenum cycles between the oxidation states Mo^{IV} (d^2) and Mo^{VI} (d^0) constituting the fully reduced and fully oxidized active species. The oxidation state Mo^V (d^1) is part of the regeneration of the active site by two proton coupled electron transfer steps (PCET). Dithiolenes are *non-innocent* ligands which can affect the electronic structure of their molybdenum (and tungsten) complexes by providing the central metal with electron density shifted from a sulfur p-orbital bearing a lone pair to an empty metal d-orbital by respective orbital overlap or even by full ligand to metal charge transfer (LMCT) (Kirk et al., 2004; Sugimoto et al., 2009). Although the role of molybdenum in the DMSOR enzymes for the catalysis of the oxygen atom transfer reactions (OAT) is quite well-understood, the role of the molybdopterin ligand (MPT) remains to be comprehensively deciphered. The synthesis of MPT or any artificial close relative of it represents a major chemical challenge and the respective attempts are still ongoing in a small number of research groups, although some significant advances have already been reported (Bradshaw et al., 1998, 2001a; Sugimoto et al., 2005; Williams et al., 2012, 2015; Basu and Burgmayer, 2015; Gisewhite et al., 2018). Holm and coworkers have not only developed OAT model reactions relevant for the molybdenum enzymes' interconversion but have also extensively reviewed them already in the 1980's (Berg and Holm, 1985; Holm, 1987). In many model reactivity studies dimethyl sulfoxide (DMSO) was employed for the oxidation of $Mo^{IV}O$ complexes, which is a natural substrate of DMSO reductase, and organic phosphines (PR_3, as easy to handle *non*-natural co-substrates) were used for the reduction of $Mo^{VI}O_2$, **Scheme 1**.

Both, $[Mo^{IV}O(dt)_2]$ as well as $[Mo^{VI}O_2(dt)_2]$ complexes (dt = dithiolene ligand) employing distinct dithiolenes were reported by us before and shown to be active catalysts for
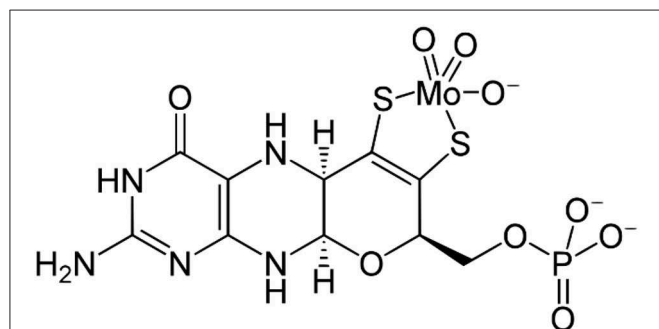
FIGURE 1 | The chemical structure of the "free" biosynthesized molybdenum cofactor (Moco) prior to insertion into the apoproteins including the tricyclic molybdopterin ligand (MPT). Note: for XO and AO one oxido ligand will be replaced by a sulfido ligand before the active site is formed; in SO a cysteine binds molybdenum in the active site pocket.
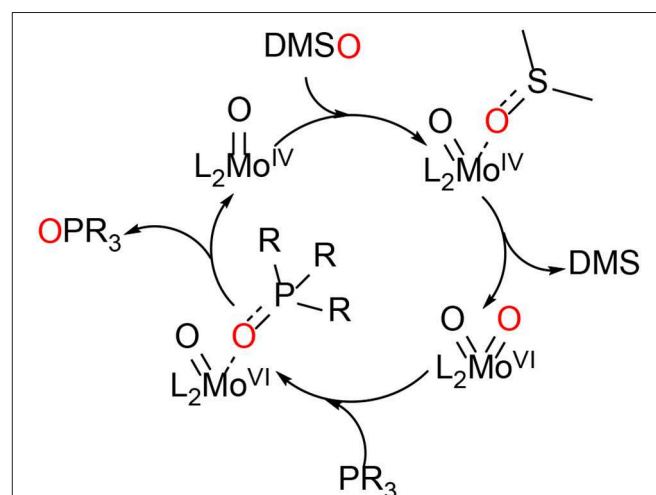
SCHEME 1 | The model OAT reaction between DMSO and a phosphine catalyzed by a molybdenum bis-dithiolene complex (L = ene-dithiolate ligand; R = alkyl or aryl).

the OAT reaction with varied capabilities (Ghosh et al., 2017). What became apparent from many studies from others as well as our own, was the detrimental influence of aromatic dithiolenes on the catalytic performance, in particular of those in which the ene of the dithiolene is actually part of the aromatic moiety, e.g., in benzenedithiolate (Fischer and Fischer, 2017). Aliphatic dithiolene ligands, in contrast, have proven to be much more instable species and consequently also much better catalysts due to the higher activity. Introduced here are now a new aliphatic dithiolene ligand and its $Mo^{IV}O$ bis-dithiolene complex. Both were characterized comprehensively as were all ligand precursors. The IR and UV-vis spectroscopic data of the complex were compared to known data of related compounds and the complex' ability to catalyze OAT reactions was investigated. The observed surprisingly poor performance is discussed referring to (i) the presence of specific substituents (ester and alcohol groups), (ii) crystallographic and spectroscopic data revealing *inter alia* information about bond lengths and strengths, (iii) substrate formation monitoring, and (iv) probable intermolecular interactions.

EXPERIMENTAL

Synthetic Procedures

All reactions and manipulations were carried out using standard Schlenk and glove box techniques under an atmosphere of high purity nitrogen (Schlenk) or argon (glove box). All solvents were dried, distilled and either degassed or purged with dinitrogen or argon prior to use. Ethylene trithiocarbonate (Kim et al., 2008) and the molybdenum precursor $K_3Na[MoO_2(CN)_4]\cdot 6H_2O$ (Smit et al., 1993) were synthesized according to previously reported procedures.

Dimethyl 2-Thio-1,3-Dithiole-4,5-Dicarboxylate (1)

In a modification of a literature procedure (Easton and Leaver, 1965) dimethyl but-2-ynedioate (18.3 mmol, 2.25 mL) and ethylene trithiocarbonate (18.3 mmol, 2.52 g) were heated to reflux for 10 h under N_2 in anhydrous toluene. The solution was left to cool to r.t. and filtered. The remaining solution was kept at $-20°C$ and adding *n*-hexane to the solution led to precipitation of yellowish crystalline compound 1. Yield: 3.8 g, 85%. ^{1}H NMR (CDCl$_3$, 300 MHz): δ (ppm): 3.90 (s, 6H, CH$_3$). ^{13}C NMR (CDCl$_3$, 75 MHz): δ (ppm): 207.2 (C=S), 157.9 (C=O), 138.1 (C=C), 53.85 (CH$_3$). FT–IR bands (KBr pallet, cm^{-1}): 3446 (br), 2954 (s), 2918 (w), 1745 (s), 1720 (s), 1552 (s), 1257 (br), 1101 (s), 1087 (m), 1060 (s), 1008(s), 993(s), 921(s), 837 (w), 777(w), 761(w), 744(w), 698(w), 511 (m). APCI-MS (EI): m/z calculated for C$_7$H$_6$O$_4$S$_3$: 249.94; Found: 250.71 [M+H$^+$]. Elemental analysis for C$_7$H$_6$O$_4$S$_3$: calc. (%): C, 33.59; H, 2.42; S, 38.43. Found: C, 34.65; H, 2.46; S, 37.38.

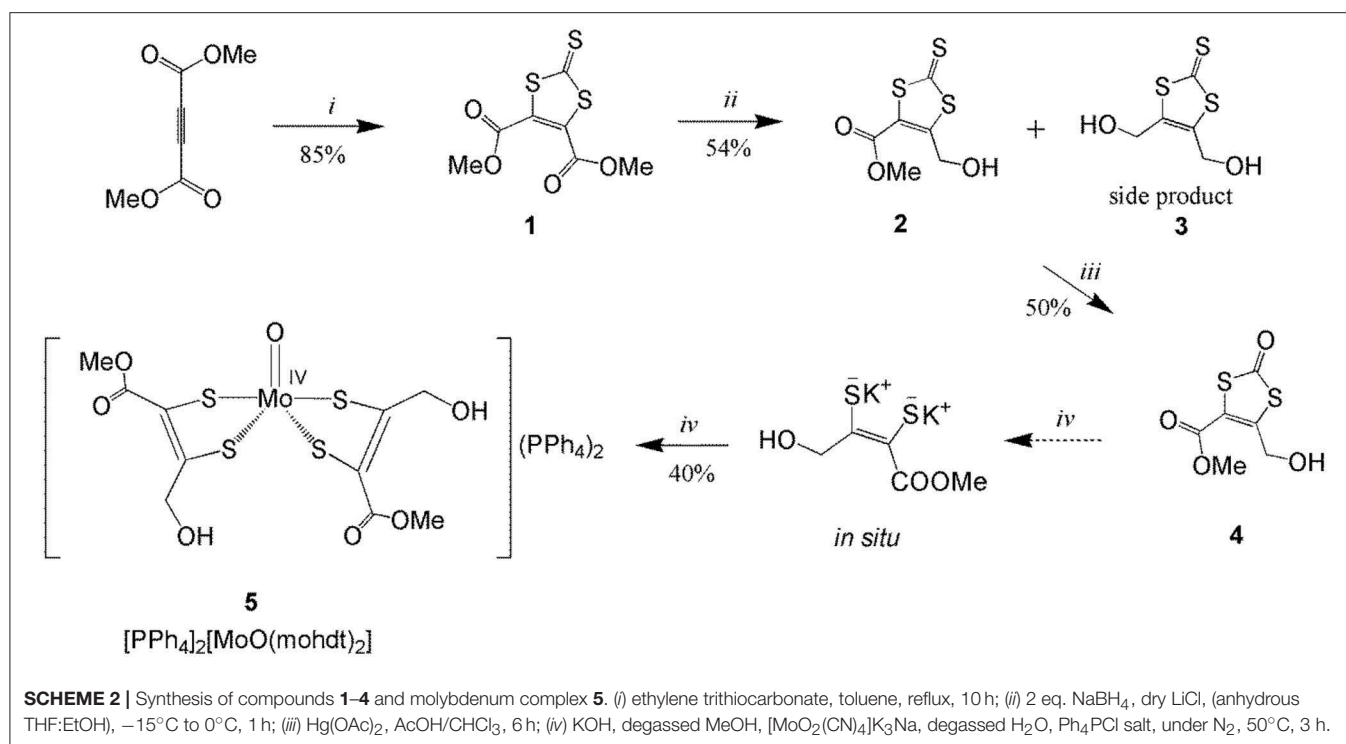### Methyl 5-(Hydroxymethyl)-2-Thioxo-1,3-Dithio-4-Carboxylate (2)

To a well-stirred solution of 1 (3.62 g, 14.5 mmol) and dry LiCl (1.22 g, 29 mmol) in anhydrous THF (40 mL) and EtOH (15 mL) at -15 to $-10°C$ powdered sodium borohydride (NaBH$_4$,

1.15 g, 30.5 mmol) was slowly added in small portions over a duration of 20 min. An exothermic reaction took place and the temperature was kept under $-10°C$ at all times and for further 30 min. Then H$_2$O (150 mL, 0°C) was added followed by concentrated aqueous HCl (4 N, carefully and portion-wise) until the evolution of H$_2$ gas ceased. The mixture was extracted with EtOAc (3× 100 mL), and the extract was dried over Na$_2$SO$_4$. Evaporation of the solvent gave a yellow oily residue which was re-dissolved in CH$_2$Cl$_2$/EtOAc (2:1, 25 mL) and purified by column chromatography. The first yellow fraction contained trace amounts of the starting material and the second fraction contained the mono-alcohol. The second fraction was concentrated *in vacuo* to give brownish-yellow crystalline compound 2 (see **Scheme 2**). Yield: 1.6 g, 54%. ^{1}H NMR (CDCl$_3$, 300 MHz): δ (ppm): 4,94 (s, 2H, CH$_2$), 3.88 (s, 3H, CH$_3$). ^{13}C NMR (CDCl$_3$, 75 MHz): δ (ppm): 210.7 (C=S), 163.6 (C=O), 158.6 (CO–C=C), 124.82 (CH$_2$–C=C), 60.5 (CH$_2$), 52.9 (CH$_3$). FT–IR bands (KBr pallet, cm^{-1}): 3446 (br), 3012 (w), 2951 (s), 2924 (w), 2017 (br), 1994 (br), 1745 (s), 1718 (m), 1627 (m), 1618 (m), 1550 (m), 1435 (s), 1261 (br), 1070 (s), 758 (s), 599 (w), 514 (w), 460 (m). APCI-MS (EI): m/z calculated for C$_6$H$_6$O$_3$S$_3$: 221.95; Found: 222.8 [M+H$^+$]. Elemental analysis for C$_8$H$_{10}$O$_4$S$_3$ (1/2 × EtOAc as co-crystallized lattice solvent) calc. (%): C, 36.07; H, 3.71; S, 36.11. Found: C, 36.31; H, 3.32; S, 36.16. The side product (4,5-bis(hydroxymethyl)-1,3-ene-dithio-2-thione (3, di-alcohol) was collected from the third fraction by column chromatography as yellow needle shaped microcrystalline solid (see **Scheme 2**). ^{1}H NMR (CD$_3$OD, 300 MHz): δ (ppm): 4.52 (s, 2H, CH$_2$). ^{13}C NMR (CD$_3$OD, 75 MHz): δ (ppm): 214.4 (C=S), 143.5 (C=C), 57.8 (CH$_2$). FT–IR bands (KBr pallet, cm^{-1}): 3421 (br), 2953 (s), 1982 (br), 1718 (br), 1436 (m), 1361 (w), 1327 (w), 1247 (m), 1201 (m), 1180 (m), 1074 (m), 1053 (s), 1035 (m), 991 (s), 635 (m), 518 (m). APCI-MS (EI): m/z calculated for C$_5$H$_6$O$_2$S$_3$: 193.95; Found: 194.80 [M+H$^+$].

4-Methyl-Carboxylate-5-Hydroxymethyl-1,3-ene-Dithio-2-One (4, mohdtC=O)

Four equivalents of mercury acetate, Hg(OAc)$_2$ (7 g, 21.8 mmol) were added to a stirred solution of 2 (1 g, 5 mmol) in 100 mL AcOH/CHCl$_3$ (2:1) for 6 h. The reaction was followed by TLC (silica, DCM). The resulting pale green mixture was filtered through a Celite pad to remove the mercury salts (mainly HgS). The resulting solution was washed first with water and then with aqueous NaHCO$_3$ and dried over Na$_2$SO$_4$. The final light yellowish powder was collected after short silica column chromatography (DCM/EtOAc; 3:1). Yield: 0.5 g, 50%. ^{1}H NMR (CDCl$_3$, 300 MHz): δ (ppm): 4.93 (s, 2H, CH$_2$), 3.86 (s, 3H, CH$_3$). ^{13}C NMR (CDCl$_3$, 75 MHz): δ (ppm) = 188.7 (C=O$_{oxo}$), 160.2 (C=O$_{COOMe}$), 151.6 (CO–C=C), 117.6 (CH$_2$–C=C), 60.1 (CH$_2$), 53.1 (CH$_3$). FT–IR bands (KBr pallet, cm^{-1}): 3483 (br), 2956 (w), 1701(s), 1654 (s), 1618 (m), 1544 (m), 1435 (s), 1352 (m), 1286 (br), 1220 (m), 1068 (m), 1029 (w), 970 (w), 952 (w), 894 (w), 813 (w), 759 (w), 607 (w), 470 (w). APCI-MS (EI): m/z calculated for C$_6$H$_6$O$_4$S$_2$: 205.97; Found: 206.80 [M+H$^+$]. Elemental analysis for C$_6$H$_6$O$_4$S$_2$: calc. (%): C, 34.94; H, 2.93; S, 31.09. Found: C, 35.01; H, 2.95; S, 30.52. Electronic absorption

SCHEME 2 | Synthesis of compounds **1–4** and molybdenum complex **5**. (*i*) ethylene trithiocarbonate, toluene, reflux, 10 h; (*ii*) 2 eq. NaBH$_4$, dry LiCl, (anhydrous THF:EtOH), −15°C to 0°C, 1 h; (*iii*) Hg(OAc)$_2$, AcOH/CHCl$_3$, 6 h; (*iv*) KOH, degassed MeOH, [MoO$_2$(CN)$_4$]K$_3$Na, degassed H$_2$O, Ph$_4$PCl salt, under N$_2$, 50°C, 3 h.

spectral data in CH$_3$CN (λ_{max}, nm (ε/M^{-1} cm^{-1})): 211 (2682), 285 (br, 2340).

[Ph$_4$P]$_2$[MoO(mohdt)$_2$] (5)

The ligand precursor **4** (0.12 g, 0.6 mmol) was added to a Schlenk flask containing 16 mL of 0.1 M KOH solution in anhydrous methanol under N$_2$ atmosphere and stirred for 2 h. The solution turned light yellow and to this a blue solution of K$_3$Na[MoO$_2$(CN)$_4$]·6H$_2$O (0.15 g, 0.3 mmol) dissolved in 8 mL degassed water was added by cannula under N$_2$. The reaction mixture was stirred at 50°C for 3 h. Then 0.21 g of tetraphenylphosphine chloride, Ph$_4$PCl dissolved in 8 mL degassed water was added to the reaction mixture. The final red solution was concentrated in vacuum to dryness. It was then dissolved in 40 ml of CH$_3$CN and the residue was filtered off. The organic solution was transferred to another Schlenk flask and anhydrous diethyl ether was added slowly. The brownish-red precipitate was collected and dried under reduced pressure. Yield: 0.3 g, 40%. ^{1}H NMR (CD$_3$CN, 300 MHz): δ (ppm): 7.80-8.93 (m, 4H, Ph$_4$P$^+$), 7.51-7.75 (m, 16H, Ph$_4$P$^+$), 4.57 (s, 4H, CH$_2$), 3.66 (s, 3H, CH$_3$). ^{13}C NMR (CD$_3$CN, 75 MHz): δ (ppm): 165.2 (CO), 152.8 (CO–$\underline{C}$=C), 136.35, 135.7, 135.5, 131.3, 131.2, 119.4 (CH$_2$–$\underline{C}$=C), 63.7 (CH$_2$), 54.7 (CH$_3$). FT–IR bands (KBr pallet, cm^{-1}): 3431 (br), 3055 (w), 3022 (w), 2924 (s), 1718 (br), 1585 (m), 1541(s), 1483 (s), 1436 (s), 1330 (br), 1228 (s), 1188 (w), 1165, 1109 (s), 1026 (w), 997 (s), 977 (s), 925 (s), 885 (s), 758 (s), 723 (s), 688 (s), 615 (w), 526 (s), 459 (w). MALDI-TOF-MS (Negative ion linear mode using 2,5-dihydroxybenzoic acid, DHB as matrix): m/z calculated for C$_{10}$H$_{12}$MoO$_7$S$_4$: 469.85, Found: 469.26. Elemental analysis for C$_{58}$H$_{54}$MoO$_7$P$_2$S$_4$: calc.

(%): C, 60.62; H, 4.74; S, 11.16. Found: C, 60.70; H, 4.37; S, 11.10. Electronic absorption data in CH$_3$CN (λ_{max}, nm (ε = M^{-1} cm^{-1})): 225 (10653), 256 (sh, 2563), 265 (2758), 277 (2340), 323 (1023).

Physical Measurements

NMR measurements were recorded on a Bruker Avance II-300 MHz instrument. All samples were dissolved in deuterated solvents and chemical shifts (δ) are given in parts per million (ppm) using solvent signals as reference (CDCl$_3$ ^{1}H: δ = 7.24 ppm; ^{13}C: δ = 77.0 ppm; CD$_3$OD ^{1}H: δ = 3.31, 4.87 ppm; ^{13}C: δ = 49.15 ppm, CD$_3$CN ^{1}H: δ = 1.94 ppm; ^{13}C: δ = 1.3 ppm) related to external tetramethylsilane (δ = 0 ppm). Spectra were obtained at 25°C unless otherwise noted. Coupling constants (*J*) are reported in Hertz (Hz) and splitting patterns are designated as s (singlet), d (doublet), t (triplet), q (quartet), quint (quintet), sext (sextet), m (multiplet), dd (doublet of doublet). Infrared spectra were recorded as KBr disks in the range 4000–400 cm^{-1} on a PerkinElmer Fourier-Transform Infrared (FT–IR) spectrophotometer. The assignment of the bands was done with subjective appreciation: w, weak; m, medium; s, strong; vs, very strong; br, broad. UV/Vis spectra were recorded on a Shimadzu UV-3600 spectrophotometer. Elemental analyses (C, H, N and S) were carried out with an Elementar Vario Micro Cube elemental analyzer. Mass spectra of organic molecules (APCI) were recorded with the high performance compact mass spectrometer Advion Expression CMS. Resolution: 0.5–0.7 m/z units (FWHM) at 1,000 m/z units sec^{-1} over the entire acquisition range. For compound **5** the mass spectra were measured on a Bruker microflex matrix assisted

laser desorption/ionization (MALDI-TOF) spectrometer and the Advion Expression CMS spectrometer.

Electrochemical measurements were carried out with an AUTOLAB PGSTAT12 potentiostat/galvanostat using a glassy carbon working electrode with a reaction surface of 1 mm^2 in acetonitrile solution with 0.1 M of $[nBu_4N][PF_6]$ as supporting electrolyte. A platinum knob electrode (together with internal referencing vs. ferrocene/ferrocenium; F_c/F_c^+) was used as reference electrode and a platinum rod electrode as auxiliary electrode. All measurements were controlled with the NOVA software and carried out inside a glove box under argon atmosphere.

X-Ray Crystallography

Suitable single crystals of compounds **1**, **2**, **3**, and **4** were mounted on a thin glass fiber coated with paraffin oil. X-ray single-crystal structural data were collected at low temperature (170 K) using a STOE-IPDS II diffractometer equipped with a normal-focus, 2.4 kW, sealed-tube X-ray source with graphite-mono-chromated MoK$_\alpha$ radiation (λ = 0.71073 Å). The program XArea was used for integration of diffraction profiles; numerical absorption correction was made with the programs X-shape and X-red32; all from STOE$^©$. The structure was solved by SIR92 (A. Altomare et al., 1993) or SHELXL-2013 (Sheldrick, 2008) and refined by full-matrix least-squares methods using SHELXL-2013 or SHELXL-2016 (Sheldrick, 2008, 2015). The non-hydrogen atoms were refined anisotropically. The oxygen bound alcohol hydrogen atoms in **2**, **3** and **4** were refined freely. All other hydrogen atoms were refined isotropically on calculated positions using a riding model with their U_{iso} values constrained to 1.5U_{eq} of their pivot atoms for methyl and hydroxyl groups and to 1.2U_{eq} for all other C-H bonds. All calculations were carried out using SHELXL-2013/16 and the WinGX system, Ver2014.01 (Farrugia, 2012). Crystallographic data were deposited with the Cambridge Crystallographic Data Centre, CCDC, 12 Union Road, Cambridge CB21EZ, UK. These data can be obtained free of charge on quoting the depository numbers CCDC (**1**) 1858446, (**2**) 1858448, (**3**) 1858449, and (**4**) 1858447 by FAX (+44-1223-336-033), email (deposit@ccdc.cam.ac.uk) or their web interface (at http://www.ccdc.cam.ac.uk). Crystal and refinement data are summarized in **Table 1**. Details of crystal structural data are tabulated in the electronic supporting information (**Tables S1–S18**).

RESULTS AND DISCUSION

Syntheses

The synthetic route to dithiolene ligand precursors **1–4** along with the complexation reaction are displayed in **Scheme 2**. The ligand mohdt is readily obtained by a three-step procedure starting from dimethyl but-2-ynedioate. Trithiocarbonate **1** was synthetized by reaction of the symmetrical alkyne with ethylene trithiocarbonate in anhydrous toluene under reflux conditions in a modified literature procedure (Easton and Leaver, 1965). Compound **1** was then reduced by little more than two equivalents of sodium borohydride (NaBH$_4$) in the presence of LiCl and dry THF/EtOH similar to procedures applied

TABLE 1 | Crystal and refinement data for **1**, **2**, **3**, and **4** at 170 K.

	1	2	3	4
Formula	$C_7H_6O_4S_3$	$C_5H_6O_2S_3$	$C_6H_6O_3S_3$	$C_6H_6O_4S_2$
Mw	250.30	194.28	222.29	206.23
Crystal system	Monoclinic	Monoclinic	Monoclinic	Monoclinic
Space group	$P2_1/c$	$P2_1/c$	$P2_1/c$	$P2_1/n$
a [Å]	13.209(3)	9.6501(19)	12.653(3)	3.8936(8)
b [Å]	9.4789(19)	11.081(2)	4.5334(9)	9.1518(18)
c [Å]	8.1022(16)	14.588(3)	15.650(3)	22.568(5)
β [°]	102.27(3)	97.81(3)	94.58(3)	93.07(3)
d$_{calc}$ [mg/m^3]	1.677	1.670	1.650	1.706
Z	4	8	4	4
V [Å^3]	991.3(4)	1545.5(5)	894.8(3)	803.0(3)
μ [mm^{-1}]	0.730	0.891	0.790	0.631
reflns collected/unique	10584/2666	9074/3238	9059/2421	7550/2142
reflns/R$_{int}$	0.0882	0.0759	0.0674	0.0488
R$_1^a$ (wR$_2^b$) (I>2σ(I))	0.0405 (0.0771)	0.0357 (0.0589)	0.0635 (0.1628)	0.0336 (0.0730)
GOF [F^2]	0.988	0.894	0.966	1.034
residual density [Å^{-3}]	0.262/−0.372	0.294/−0.352	0.536/−0.475	0.320/−0.371

$^a R_1 = \sum ||F_o|-|F_c||/\sum |F_o|$.
$^b R_w = [\sum \{w(F_o^2 - F_c^2)^2\}/\sum \{w(F_o^2)^2\}]^{1/2}$.

previously (Jeppesen et al., 1999; Bellanger et al., 2012) but in distinct stoichiometry as a different, asymmetric compound was targeted here. The reduced unsymmetrical trithiocarbonate **2** was collected as major compound after column chromatography. Also a small amount of symmetrically substituted compound **3** (which was the target in the two reports cited above) as side product could be isolated and identified suggesting that the stoichiometric amount of NaBH$_4$ needs to be controlled very carefully in this reduction reaction.

An often applied procedure for the synthesis of oxo-dithiocarbonate compounds is oxidizing the thione moiety in trithiocarbonate backbones with mercury acetate in the presence of acetic acid utilizing mercury's thiophilicity (Nguyen et al., 2010). Compound **2** was oxidized accordingly and then purified by column chromatography yielding the final dithiolene precursor **4**, mohdtC=O (see **Scheme 2**).

A detailed comparison of infrared, ^{1}H and ^{13}C NMR spectroscopic data of the trithiocarbonates (**1**, **2**, and **3**) and the dithiocarbonate **4** reveals some interesting aspects of the C=S, C=O and C=C functional groups. The C=S signals in the ^{13}C NMR spectra of **1**, **2** and **3** were observed at δ 207.2, 210.8, and 214.4 ppm, respectively, which differs as expected from the C=O signal of **4** at δ 188.7 ppm (see **Supplementary Material**). The differences in the ^{13}C NMR spectra for the C=C bonds in **1** (138.1 ppm; ester only), **2** (158.6 and 124.8 ppm; mixed) and **3** (143.5 ppm, hydroxyl only) are predominantly due to the presence (or absence) of the electron-donating and -withdrawing

ester and hydroxyl functions, respectively. Most notably, in the unsymmetrically substituted **2** the comparable downfield and upfield shifts are more pronounced than in the symmetric compounds indicating a considerable push-pull effect induced by the asymmetry (see also the discussion in the structural characterization part below). Changing the C=S (**2**) to a C=O (**4**) function results in an upfield shift by ca. 7 ppm for both carbon atoms of the C=C moiety (151.6 and 117.6 ppm, mixed). The ^{1}H NMR spectrum of **4** in CDCl$_3$ displays two singlets at δ = 3.86 and 4.93 ppm, assigned to the methyl and methylene protons, respectively, which is almost identical to the values obtained for **2**. This indicates that an exchange of C=O for C=S has no effect on these protons. Compared to the symmetric species the methylene protons are shifted downfield by ca. 0.4 ppm and the methyl protons are shifted upfield by an average of 0.03 ppm. The C=S stretching frequencies in the IR spectra for **1**, **2**, and **3** were observed at 1067, 1070, and 1053 cm^{-1} (Liu et al., 2010), respectively, while the C=O$_{oxo}$ frequency in **4** is found at 1,654 cm^{-1} in accordance with the generally stronger bond between C and O (see **Supplementary Material**).

Complex **5** was synthesized according to a modified method already reported in the literature (Bradshaw et al., 2001b). The elemental analysis, the infrared, electronic absorption and NMR spectroscopic data, and the MALDI-TOF mass spectrometric data of **5** unambiguously support the formation of the mono-oxido Mo^{IV} center coordinated by two {S$_2$C$_2$(CO$_2$Me)(CH$_2$OH)}$^{2-}$ ligands. A comparison with known data of a closely related compound from the literature (Coucouvanis et al., 1991) and the similarity of the respective analyses further validates the proposed chemical structure of the complex. The molecular ion peak of **5** was detected at m/z 469.3 by MALDI-TOF-MS in the negative ion linear mode using 2,5-dihydroxy benzoic acid (DHB, 10 mg/mL in acetonitrile/water mixture (1/1, v/v) containing 0.1% TFA) (see **Supplementary Material**). The molecular ion peak of complex **5** was also detected by ESI-MS (-) analysis with a fitting isotopic pattern at m/z 460.2 to 469.1. The tetraphenylphosphonium counter cations (PPh$_4^+$) were observed at m/z 339.0 in the positive ESI-MS mode (see **Supplementary Material**).

The ^{13}C-NMR signals for the C=C bond in **4** are slightly shifted to the downfield/deshielded/higher frequency region in complex **5**, which is a characteristic difference between a free dithiolene ligand precursor and the de-protected ene-dithiolate ligand coordinated to a Mo^{IV}O center. The π-delocalization within the dithiolene and the charge donation to the metal can be assessed considering the frequency of the C=C stretching mode in the FT-IR spectrum typically found in a range of 1,400–1,600 cm^{-1} as the C=C bond weakens with increased donation to the metal (Garton et al., 1997). A tentative assignment of the band at 1,541 cm^{-1} to this vibration, which is only marginally shifted from 1,544 cm^{-1}, supports the presence of the ene-dithiolate rather than reduction of the metal with concomitant oxidation of the ligand to a radical species (partial thione character). The M=O stretching frequency of **5** at 925 cm^{-1} exhibits a substantial shift from the Mo precursor 728 cm^{-1} (**Figure 2**) (Ghosh et al., 2017). This is comparable to reported related Mo^{IV}O complexes such as [MoO{S$_2$C$_2$(COOMe)$_2$}$_2$]$^{2-}$
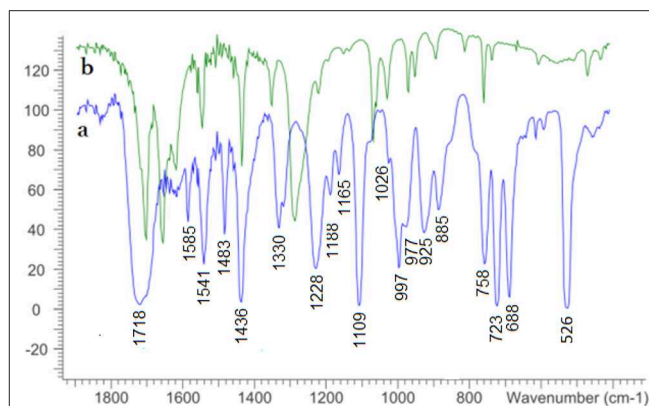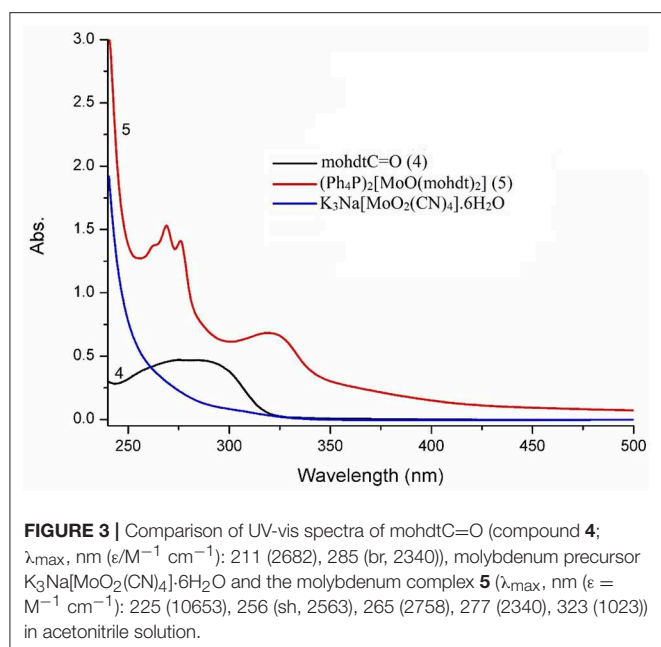

FIGURE 2 | Solid state FT-IR spectra of complex **5** (a, bottom) and ligand precursor **4** (b, top) measured as KBr pellets.

(Coucouvanis et al., 1991), [MoO{S$_2$C$_2$(CN)$_2$}$_2$]$^{2-}$ (Donahue et al., 1998) and [MoO{S$_2$C$_2$(CONH$_2$)$_2$}$_2$]$^{2-}$ (Oku et al., 1997). The IR spectrum of mohdtC=O (**4**) further shows two sharp bands at 1,710 cm^{-1}, at 1,654 cm^{-1} and one medium signal at 1,618 cm^{-1} belonging to (C=O)$_{ester}$ and (C=O)$_{oxo}$ dithiolene stretching frequencies, respectively. The (C=O)$_{ester}$ vibration is shifted to higher frequency in complex **5** (ν(C=O)$_{ester}$: 1,718 cm^{-1}) and (C=O)$_{oxo}$ has disappeared after complexation as expected (see **Figure 2**). Further C–O and C–S frequencies are difficult to identify/assign as they are masked by the dominating C–H stretching bands of the Ph$_4$P$^+$ counter-cation in the region 688–758 cm^{-1} (Tchouka et al., 2011).

Electronic spectra of the molybdenum precursor, ligand precursor **4** and the resulting Mo^{IV}O complex (**5**) were recorded in CH$_3$CN solution (**Figure 3**). The UV-vis spectra display absorption bands in the region 256–323 nm, characteristic of ligand to metal charge transfer (LMCT) and of intra-ligand charge transfer as also strongly suggested by comparison with the spectrum of the protected ligand. The two broad bands of rather similar shape for the ligand (ca. 250–310 nm) and complex **5** at λ$_{max}$ 323 nm (ε = 1,023 M^{-1} cm^{-1}) are most likely due to the same transition albeit shifted as would be expected after coordination. The corresponding bands and extinction coefficients of molybdenum complexes bearing two different dithiolene ligands, representing another type of non-symmetry, such as (Et$_4$N)$_2$[Mo^{IV}O(S$_2$C$_2$(CO$_2$Me)$_2$)(bdtCl$_2$)] (λ$_{max}$ 531 nm; ε = 340 M^{-1} cm^{-1}) (Sugimoto et al., 2009) and (Ph$_4$P)$_2$[Mo^{IV}O(edt)(mnt)] (λ$_{max}$ 433 nm; ε = 1,110 M^{-1} cm^{-1}) (Donahue et al., 1998) are comparable to those of complex **5** reported here. The intensities (extinction coefficients) of the reported bands are well in accordance, while the observed band energy for complex 5 is higher (band at lower wavelength). In the complex we therefore tentatively assign the band at 323 nm to an LLCT transition. The single very broad absorption signal belonging to the dithiolene ligand precursor **4** is narrowed and exhibits a bathochromic shift in complex **5** indicative of a significant change in the electronic structure with more distinct LLCT transitions at

FIGURE 3 | Comparison of UV-vis spectra of mohdtC=O (compound 4; λ_{max}, nm (ε/M^{-1} cm^{-1}): 211 (2682), 285 (br, 2340)), molybdenum precursor K$_3$Na[MoO$_2$(CN)$_4$]·6H$_2$O and the molybdenum complex 5 (λ_{max}, nm (ε = M^{-1} cm^{-1}): 225 (10653), 256 (sh, 2563), 265 (2758), 277 (2340), 323 (1023)) in acetonitrile solution.
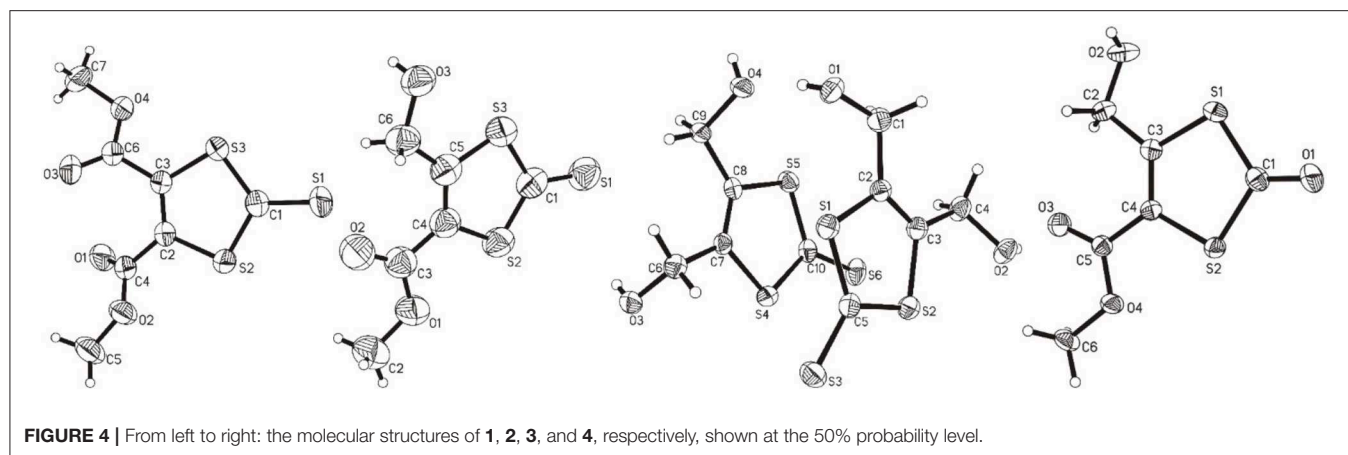
slightly lower energy, as expected upon loss of the protecting C=O function (potentially engaged in resonance structures), coordination to a metal center and formation of new mixed metal-ligand molecular orbitals. Similar observations were made previously with a series of moderately related strictly aliphatic complexes (cyclohexane, pyrane, and thiopyrane derived ligands) with signals in the region 260–476 nm (Sugimoto et al., 2005). Coucouvanis and co-workers reported UV-vis data of the complex (Et$_4$N)$_2$[MoO(S$_2$C$_2$COOMe)$_2$], which can be considered the closest relative of the new complex at λ_{max}: 360, 460(sh) and 550 nm (Coucouvanis et al., 1991) albeit without extinction coefficients. Replacing the strongly electron withdrawing ester function by the ethyl alcohol substituent apparently shifts the transitions to higher energy; possibly also due to increasing ligand field strength when more electron density can be pushed toward the central metal. The recorded values for 5 are further comparable to related (Et$_4$N)$_2$[MoO(S$_2$C$_2$(COPh)$_2$)$_2$] with phenyl-keto substituents (λ_{max}: 310 (sh), 338 (sh), 400 nm), the bands of which fall in between those of complex 5 and the Coucouvanis complex (Ansari et al., 1987).

The observed shift in the UV-vis data from the Cocouvanis complex (all ester) to complex 5 (mixed; ester and alcohol) corresponds also to the electrochemical properties of both. The cyclic voltammogram of 5 (see Figure S26) exhibits a reversible redox process for the Mo^{IV}↔Mo^V transition ([MoO(mohdt)$_2$]$^{2-}$/[MoO(mohdt)$_2$]$^-$) at −0.62 V vs. [Fc]/[Fc]$^+$ which constitutes a decrease in potential compared to the all ester complex at −0.074 V vs. [Fc]/[Fc]$^+$ (value given in the report: −0.03 V vs. SCE) (Coucouvanis et al., 1991); i.e., the electron pushing alcohol substituent facilitates oxidation of the complex whereas the complex with two electron withdrawing ester substituents is more easily reduced.

Structural Characterization

The molecular structures of 1, 2, 3, and 4 are shown in Figure 4 and the selected comparable bond distances and angles are listed in Table 2. All ligands were (re-)crystallized by the slow diffusion method. The structure of 1 was published previously in a databank without any accompanying discussion (Neil Bricklebank et al., 2003). In the X-ray structure of compound 3 two independent molecules are present in the unit cell, which differ slightly with respect to the angles of the -CH$_2$-OH substituents to the ene moiety (rmsd 0.305; max. distance 0.5464 Å). All three ene-trithiocarbonate compounds (1–3) crystallized in the monoclinic $P2_1/c$ space group whereas compound 4 (ene-dithiocarbonate) crystallized in the monoclinic $P2_1/n$ space group. A description of a crystal structure of 3 in a different space group ($C2/c$) and with only one molecule in the asymmetric unit is available in Acta Cryst (Pløger et al., 2006). The ene-trithiocarbonate rings are structurally all similar and exhibit C=S, C–S and C=C distances in ranges of 1.632(4)−1.659(3), 1.718(3)−1.748(3) and 1.339(4)−1.347(4) Å, respectively.

However, the ene carbon atoms' C–S bond distances in the four ligand precursor molecules upon close inspection are rather noteworthy. The intention of utilizing distinct substituents and an asymmetrically substituted dithiolene ligand for the complex synthesis was to fine-tune the electronic properties of the ligand (and consequently of the complex) hypothesizing that with a push-pull-effect the ligand's non-innocence (i.e., its ability to donate electron density/electrons to the metal center) should be raised. While one half of the ene-dithiolate moiety has a stronger preference for donating electron density toward the metal center than the other, then such donation should be facilitated compared to a system in which both substituents compete for the exact same effect and having the exact same properties. The resonance of such system, however, is expected to be decreased, translating into lower stability which is typically concomitant to higher reactivity (secondary effect; see Figure S27). That such primary effect was indeed realized at least in the ligand precursors is strongly supported by the distances between the ene-carbon atoms and the sulfur atoms as well as by the ^{13}C-NMR data as already discussed above (Figure 5). The two (or four in case of 3 with the two independent molecules in the asymmetric unit) ene-C-S bond distances in the symmetric molecules of 1 and 3 are much more similar to each other than to those in the unsymmetric molecules of 2 and 4. Most notably, the C-S bond lengths involving the ester substituted ene carbon are significantly longer in 2 and 4 than in the case of 1 (ester only) and those involving the alcohol substituted ene carbon atoms are much shorter than in the case of 3 (alcohol only). The unsymmetric substitution apparently increases the C-S single bond character of the ester side of the ene-dithio moiety and the C-S double bond character of the alcohol side. The latter will facilitate electron density donation toward the coordinated metal upon complex formation from this side of the molecule, as there is apparently already more density available in the respective bonds compared to the ester sides of the molecules. These metrical observations coincide with ^{13}C-NMR data of the ene functional group discussed above. In fact, the chemical shifts of the symmetric molecules (1 and 3) are even closer to each other

FIGURE 4 | From left to right: the molecular structures of **1**, **2**, **3**, and **4**, respectively, shown at the 50% probability level.

TABLE 2 | Selected bond lengths [Å] and angles [°] for **1**, **2**, **3**, and **4**.

	1	2	3	3	4
			Trithiocarbonate mole 1	Trithiocarbonate mole 2	
LENGTHS					
C=S/O	1.636(3)	1.632(4)	1.659(3)	1.641(3)	1.204(2)
C–S (A)	1.727(3)	1.718(4)	1.718(3)	1.728(3)	1.776(2)
C–S (B)	1.732(3)	1.740(4)	1.659(3)	1.728(3)	1.760(2)
C=C	1.345(4)	1.346(5)	1.339(4)	1.347(4)	1.349(3)
ANGLES					
S=C–S (A)	122.50(18)	124.3(2)	123.85(17)	123.1(2)	123.17(16)
S=C–S (B)	124.59(18)	122.9(2)	122.78(19)	124.71(19)	123.79(16)
S–C–S	112.90(16)	112.8(2)	113.36(17)	112.18(16)	113.03(11)
C=C–S (A)	116.3(2)	115.9(3)	116.4(2)	115.7(2)	116.75(15)
C=C–S (B)	116.5(2)	116.5(3)	116.2(2)	116.0(2)	118.10(15)

than they are to the shifts of either of the ene carbon atoms in the unsymmetric molecules. This means, that exchanging just one of two substituents results in a stronger modulation of the electronic structure compared to replacing both substituents.
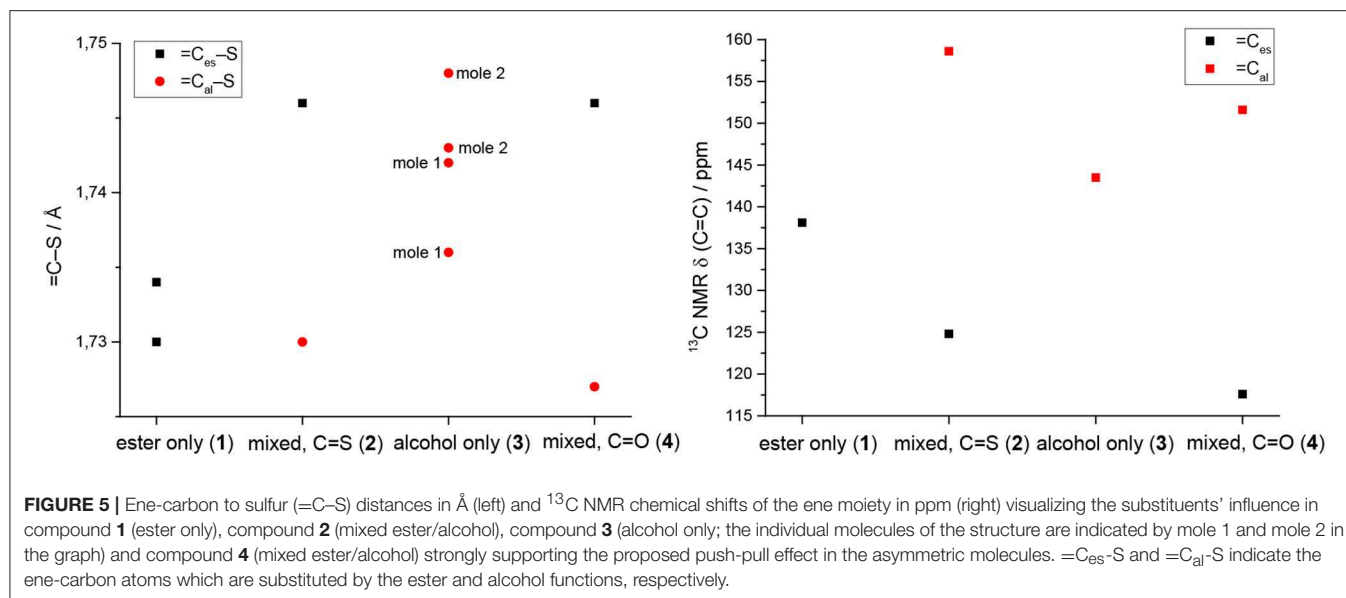
With respect to the influence of the protecting group, the C=O oxo distance in **4** is 1.204(2) Å, which is necessarily shorter than the C=S distances in ene-trithiocarbonates due to the smaller size of oxygen atoms compared to sulfur. The other bond distances of the ene-dithiocarbonate moiety are slightly longer than the observed ranges for the ene-tritiocarbonates (OC–S: 1.760/1.776 Å; C=C 1.349 Å) (see **Table 2**). This indicates somehow stronger donation of electron density toward the C=O functional group of the ene-dithiocarbonate than to the respective C=S of the ene-trithiocarbonates.

Figure 6 shows projections of the crystal packing in the structures of **1**, **2**, **3**, and **4** along the *a* or *b* axes. The hydrogen bonding/short contacts present in all structures are depicted in blue. Only for **1** all ene-trithiocarbonate moieties are coplanar within the crystal lattice whereas for the other three compounds the planar parts of the molecular structures are arranged in angles up to nearly perpendicular (87.63°; **3**) to each other. X-ray suitable single crystals of complex **5** remained

elusive, unfortunately, despite considerable and repeated efforts of recrystallization.

OAT Catalysis

The OAT activity of Mo^{IV}O bis-dithiolene complex **5** was investigated with the model oxygen atom transfer reaction between DMSO and PPh$_3$ (see **Scheme 3**; based on Ref. Berg and Holm, 1985). The reaction progress was monitored by ^{31}P-NMR spectroscopy. The reaction typically proceeds *via* oxygen atom transfer from DMSO to the Mo^{IV}O moiety resulting in dimethyl sulfide and a Mo^{VI}O$_2$ species which then oxidizes the acceptor substrate PPh$_3$ yielding OPPh$_3$ and concurrently completing the catalytic cycle (Lorber et al., 1997; Tucci et al., 1998). In this mechanism, the phosphorous atom of the alkyl-phosphines is performing a nucleophilic attack on one of the two oxido ligands on the Mo^{VI} center by donation into the empty Mo=O π* orbital generating the phosphine oxide intermediate, while a free electron pair of the oxygen atom is simultaneously attacking the P–C σ* orbital (Holm, 1987; Smith et al., 2000). I.e., an electron pair on phosphorous establishes an initial single bond with oxygen and for the respective P=O double bond a lone pair on oxygen is used. At the same time one electron pair of

FIGURE 5 | Ene-carbon to sulfur (=C–S) distances in Å (left) and ^{13}C NMR chemical shifts of the ene moiety in ppm (right) visualizing the substituents' influence in compound **1** (ester only), compound **2** (mixed ester/alcohol), compound **3** (alcohol only; the individual molecules of the structure are indicated by mole 1 and mole 2 in the graph) and compound **4** (mixed ester/alcohol) strongly supporting the proposed push-pull effect in the asymmetric molecules. =C$_{es}$-S and =C$_{al}$-S indicate the ene-carbon atoms which are substituted by the ester and alcohol functions, respectively.

the Mo=O double bond becomes the new second lone pair on oxygen and the other electron pair of the former metal oxygen double bond remains entirely at the metal center (severing the bond between Mo and O), so that the two-electron reduction of the metal/oxidation of phosphorous proceeds smoothly together with the transfer of oxygen from metal to substrate.

DMSO is used as oxygen donor source and simultaneously employed as solvent and substrate with consequentially very high excess to the catalyst. PPh$_3$ was chosen as expedient model substrate for its high solubility in organic solvents and its suitable affinity toward oxygen. A 3 mM catalyst loading was employed together with 3 eq. of PPh$_3$ and 0.5 mL of deoxygenated DMSO in an airtight NMR tube at room temperature. ^{31}P-NMR spectroscopy is the most convenient method to monitor the reaction progress since substrate (PPh$_3$) and product (PPh$_3$O) demonstrate well-separated resonance signals (PPh$_3$: s, −5.8 ppm and PPh$_3$O: s, 26.6 ppm in DMSO-d_6). Reaction monitoring by NMR started immediately after preparation of the reaction mixture under N$_2$ atmosphere. The concentration of PPh$_3$ (at −5.8 ppm) decreased gradually with the reaction time and at the end of the reaction PPh$_3$O was the dominating species (**Figure 7**).

As the central metal is involved in a two electron redox-process, electron density buffering by a non-innocent ligand is considered beneficial for such reactions. The aim of this study was to optimize this electron density buffering by the asymmetric ligand substitution and a respective push-pull effect (present in the ligand precursor as evidenced by structural and spectroscopic data). A one-sided preference for electron donation induced by the introduction of one electron donating alcohol substituent was supposed to better support the involved redox processes and increase the complex' reactivity. However, the reaction proceeds very slowly with the maximum conversion (93%) of applied PPh$_3$ (9 mM) reached after ∼2.5 days with a not entirely steady progress under the applied reaction conditions (rather hot summer days, cooler nights, no temperature control;

see **Figure S22**). We therefore abstained from trying to extract specific kinetic parameters for this transformation.

The disappointingly low reaction velocity can be attributed not entirely to the low activity of **5** but also to the comparably mild oxidizing substrate. Although well-established by the Holm group, the DMSO/PPh$_3$ system has its disadvantages with respect to the known very slow conversion of Mo^{IV} to Mo^{VI} with DMSO. When adding Me$_3$NO as a stronger oxidizing agent to a freshly prepared solution of **5** and PPh$_3$ in DMSO-d6 we observed 36.52% conversion overnight (within 15 h), which constitutes a slight acceleration in comparison but still not the anticipated rapid catalytic process.

The most frequently investigated molybdenum centers in oxidoreductase model chemistry are Mo^{IV}O and Mo^{VI}O$_2$ species which are comparable to the native co-factors regarding the oxidation states and they bear transferable oxido ligands (McMaster et al., 2004b). These complexes, however, in particular when mixed in a reaction medium while circling through catalysis, can also form dimeric or oligomeric assemblies transforming terminal oxido ligands into μ-oxido functions, e.g., dimeric and chemically inert Mo$_2^V$O$_3$ moieties, which are catalytically inactive (McMaster et al., 2004a; Mitra and Sarkar, 2013; Hille et al., 2016). Confirming their chemical structures, a number of X-ray diffraction studies of such dimeric species are reported in the literature (Tatsumisago et al., 1982; Ratnani et al., 1990; Sellmann et al., 1992; Thompson et al., 1993; Awwal et al., 2007; Pal et al., 2007; Mitra and Sarkar, 2013) albeit not with bis-dithiolene molybdenum centers. In fact Subramanian et al. have stated that the reduction of Mo^{VI}O$_2$L$_2$ species necessarily leads to μ-oxo-bridged dimers (Subramanian et al., 1984). The formation of such species constitutes a general problem associated with catalytic/kinetic investigations of OAT, although in the best cases monomeric Mo^{IV}O plus Mo^{VI}O species and dimeric Mo$_2^V$O$_3$ are in equilibrium with considerable amounts left of the former pair so that catalytic activity can still persist (Holm, 1987, 1990).
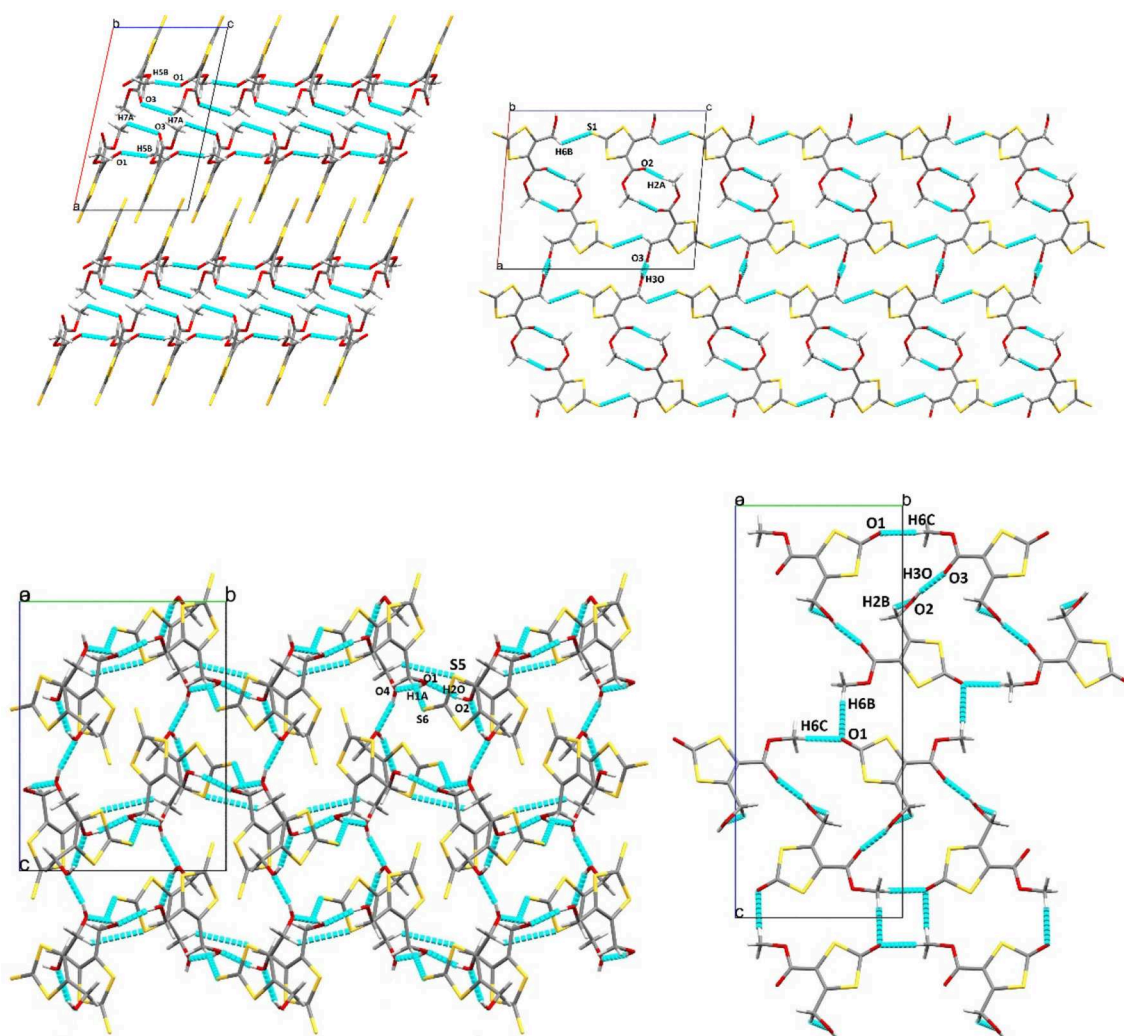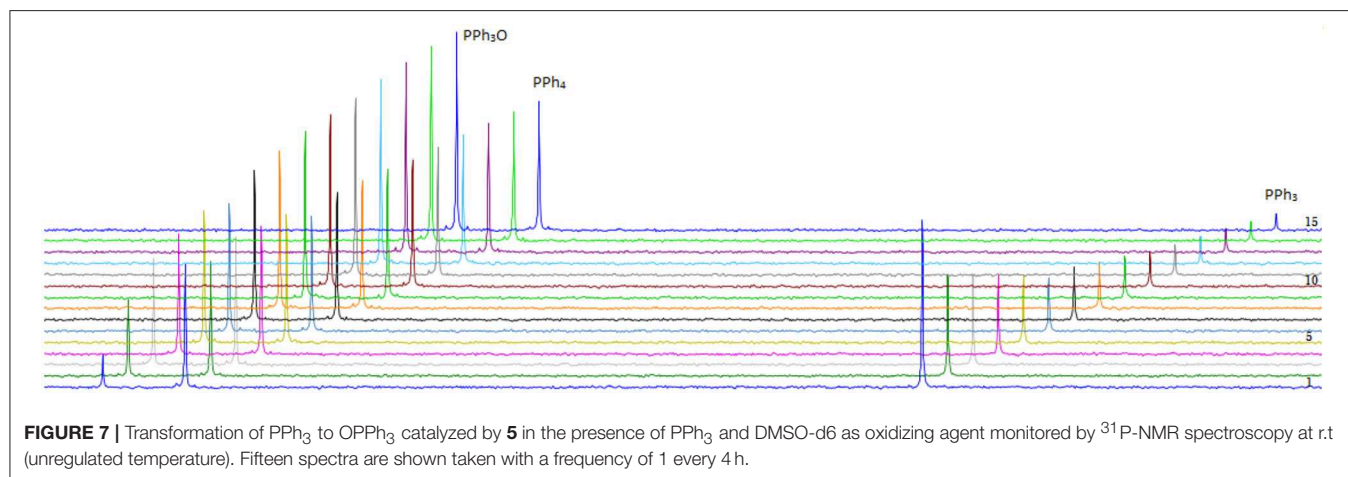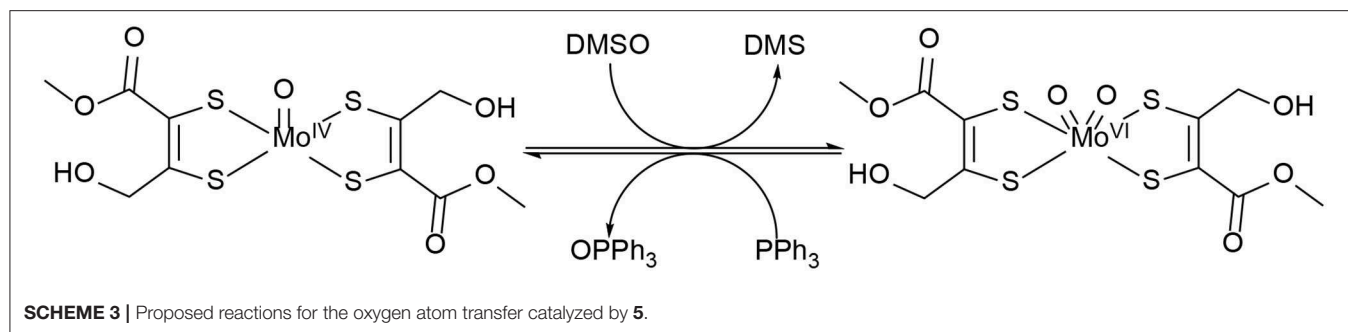
FIGURE 6 | Crystal packing projection views along the *b* axis of **1** (top left), and **2** (top right), and along the *a* axis of **3** (bottom left) and **4** (bottom right). Selected hydrogen bonding/short contacts (Å): (**1**): C(5)–H(5B)···O(1): 2.522, C(7)–H(7A) ···O(3): 2.708, C(4)–O(3): 3.001; (**2**): O(3)–H(3O)···O(3): 1.89(6), C(2)–H(2A)···O(2): 2.59, S(1)–H(6B): 2.960; (**3**): O(1)–H(1O)···O(4): 1.95(4), CO(2)–H(2O)···O(1): 1.90(4), O(3)–H(3O)···O(2): 2.10(4), O(4)–H(4O)···O(3): 1.89(4), H(1A)–S(6): 2.946, S(5)–H(9B): 2.979; (**4**): O(1)–H(6C): 2.503, O(2)–H(2B): 2.441, O(3)–H(3O): 1.999, O(1)–H(6B): 2.594.

In order to verify whether the slowness of the OAT reaction was indeed due to dimer formation, a solution of 3 mM complex **5** in the presence of oxidizing agent trimethylaminoxid (TMAO) in acetonitrile was prepared and monitored by UV-Vis spectroscopy under anaerobic condition. It was observed that after the initial formation of the transient $Mo^{VI}O_2$ species (here very broad signal at λ_{max}: 540 nm), it swiftly decomposed again while the signal for the catalytically inert $Mo_2^VO_3$ species (typical signal at λ_{max}: 375 nm) (Villata et al., 2000; Sugimoto et al., 2003; Pal et al., 2007) exhibited a steady rise (see **Figure S22**). The change in the UV-vis with the progress of the reaction exhibits clean isosbestic points indicating the simultaneous presence of only two (not three) species. This can be explained by the fact that the transient di-oxo species is of particularly low concentration, hence, nearly invisible in the UV-vis as the dimer formation is essentially instant as soon as the di-oxo species is available.

The typical dimerization is particularly problematic for those systems with bis-dithiolene co-ligands bearing aliphatic backbones without steric or electronic protection. When aromatic dithiolene ligands are used (and this refers to both, an aromatic substituent on the ene- moiety as well as the ene moiety being part of an aromatic ring as in benzene-dithiolate) molybdenum dithiolene complexes are typically much more stable and, hence, much less reactive than those with aliphatic dithiolene systems (Fischer and Fischer, 2017). Dithiolene ligands bearing electron withdrawing groups as substituents typically exhibit weak Mo–S bonds. This does promote the Mo=O bond and concomitantly stabilizes the monomeric species by electronic tuning but it also decreases the catalytic

SCHEME 3 | Proposed reactions for the oxygen atom transfer catalyzed by **5**.

FIGURE 7 | Transformation of PPh$_3$ to OPPh$_3$ catalyzed by **5** in the presence of PPh$_3$ and DMSO-d6 as oxidizing agent monitored by ^{31}P-NMR spectroscopy at r.t (unregulated temperature). Fifteen spectra are shown taken with a frequency of 1 every 4 h.

activity (Hille et al., 2016). In contrast, dithiolene ligands with electron donating groups push electron density toward the metal center and by that decrease the Lewis acidity of molybdenum. It was shown previously that the Mo=O bond is weakened in dithiolene complexes with aliphatic backbones in particular with electron donating substituents (Hille et al., 2016). Taking all this into consideration we attribute the slowness of the catalyzed OAT reaction observed for complex **5** predominantly to the formation of the dimeric and chemically inert Mo$_2^V$O$_3$ species as the aliphatic substituents on the used dithiolene ligand have mixed electron donating and electron withdrawing character, intended to fine tune the electronic structure of the complex and balance stability and reactivity. The dimerization may benefit from the presence of ester and hydroxyl functions on the dithiolene which constitute excellent functionalities for hydrogen bonding, which potentially results in close proximity of the catalytic centers even in solution. Previously, the presence of hydrogen bonding potential, in particular for intramolecular hydrogen bonding was perceived to be beneficial for catalysis (Oku et al., 1997; Okamura et al., 2016a,b). However, in this case it appears to be rather detrimental. The respective potential interactions between two complexes might facilitate formation of the catalytically inactive dimer by intermolecular hydrogen bonds (see **Figure S23** for a proposed interaction). An accelerated dimer formation would slow down the catalytic OAT reaction significantly by inactivation of the present catalyst species and in addition by preventing the catalytically active species to diffuse

freely into the solution. The observed actual reactivity, in fact, is more comparable to a system with aromatic backbone, e.g., to one previously reported by our group ((Bu$_4$N)$_2$[Mo^{IV}O(ntdt)$_2$] and (Ph$_4$P)$_2$[Mo^{VI}O$_2$(ntdt)$_2$]; ntdt = 2-naphthyl-1,4-dithiolate) (Ghosh et al., 2017) than to other aliphatic systems. Although the strategy of combining electron pushing and electron withdrawing substituents generally appears to achieve the anticipated fine-tuning of the electronic structure (evident at least for the ligand precursor) it did not translate into the targeted increase in reactivity. Apparently, further consideration needs to go into the exact nature of the utilized substituents. For respective next generation compounds the ability to engage in hydrogen bonding should be assessed from the very beginning.

CONCLUSIONS

The aliphatic dithiolene ligand, 1-methoxy-1-oxo-4-hydroxy-but-2-ene-2,3-bis-thiolate (mohdt) and its Mo bis-dithiolene complex were synthetized and comprehensively characterized. The unsymmetrically substituted dithiolene ligand is subject to a push-pull effect modulating its electronic structure. A comparison of structural-metrical and ^{13}C-NMR data of four related ligand precursor compounds reveals that substituent effects are indeed much more pronounced in unsymmetric than in symmetric molecules. ^{13}C-NMR data in particular turned out to be rather sensitive to such effects and should be

considered a valuable tool for respective assessments. Since the synthesized complex can be considered a structural model for the molybdopterin bearing DMSO reductases with respect to the immediate coordination sphere, it was also tested for its catalytic oxygen atom transfer ability in DMSO by mixing the catalyst with PPh$_3$ at room temperature. The molybdenum complex catalyzes the OAT reaction from DMSO to PPh$_3$ up to a 93% conversion within 56 h. In contrast to the expectations based on the evidenced push-pull effect, the catalytic performance of complex **5** is unexpectedly slow most likely due to the formation of dimeric Mo^V species after initial oxidative transformation of Mo^{IV}O to Mo^{VI}O$_2$ species. This is possibly supported by hydrogen bonding effects of the ligands' substituents and certainly not hindered by any steric bulk.

AUTHOR CONTRIBUTIONS

MA: syntheses, experiments, and drafting the manuscript. AG: syntheses, experiments, and supporting manuscript drafting. CF: scientific support of the project, catalysis, and kinetic evaluation. CS: study design, in charge of overall direction, managing the project, and finalizing the report.

ACKNOWLEDGMENTS

SUPPLEMENTARY MATERIAL

The Supplementary Material for this article can be found online at: https://www.frontiersin.org/articles/10.3389/fchem. 2019.00486/full#supplementary-material

REFERENCES

Altomare, A., Cascarano, G., Giacovazzo, C., Guagliardi, A., Burla, M. C., Polidori, G., et al. (1993). *SIR*92—a program for automatic solution of crystal structures by direct methods. *J. Appl. Crystallogr.* 26:343.

Ansari, M. A., Chandrasekaran, J., and Sarkar, S. (1987). Synthesis and characterization of a mononuclear molybdenum(IV) oxo complex (Et$_4$N)$_2$[MoO(S$_2$C$_2$(COPh)$_2$)$_2$]. *Inorg. Chim. Acta* 133, 133–136. doi: 10.1016/s0020-1693(00)84384-4

Awwal, L., Drake, J. E., Hursthouse, M. B., Kumar, R., Light, M. E., Ratnani, R., et al. (2007). Synthesis and characterization of binuclear oxomolybdenum(V) and dioxomolybdenum(VI) O,O′-ditolyl dithiophosphate complexes: crystal structures of Mo$_2$O$_3$[S$_2$P(OC$_6$H$_4$Me-o)$_2$]$_4$, Mo$_2$O$_3$[S$_2$P(OC$_6$H$_4$Me-m)$_2$]$_4$ and MoO$_2$[S$_2$P(OC$_6$H$_4$Me-p)$_2$]$_2$. *Polyhedron* 26, 3973–3979. doi: 10.1016/j.poly.2007.04.034

Basu, P., and Burgmayer, S. J. (2015). Recent developments in the study of molybdoenzyme models. *J. Biol. Inorg. Chem.* 20, 373–383. doi: 10.1007/s00775-014-1228-0

Bellanger, H., Darmanin, T., Taffin de Givenchy, E., and Guittard, F. (2012). Superhydrophobic hollow spheres by electrodeposition of fluorinated poly(3,4-ethylenedithiopyrrole). *RSC Adv.* 2, 10899–10906. doi: 10.1039/C2RA21665E

Berg, J. M., and Holm, R. H. (1985). Model for the active site of oxo-transfer molybdoenzymes: synthesis, structure, and properties. *J. Am. Chem. Soc.* 107, 917–925. doi: 10.1021/ja00290a029

Bradshaw, B., Collison, D., Garner, C. D., and Joule, J. A. (2001a). Stable pyrano[2,3-*b*]quinoxalines and pyrano[2,3-*g*]pteridines related to molybdopterin. *Chem. Commun.* 1, 123–124. doi: 10.1039/B008544H

Bradshaw, B., Dinsmore, A., Collison, D., Garner, C. D., and Joule, J. A. (2001b). The synthesis of pyrano[2,3-b]quinoxalines related to molybdopterin. *J. Chem. Soc.* 24, 3232–3238. doi: 10.1039/b108576j

Bradshaw, B., Dinsmore, A., Garner, C. D., and Joule, J. A. (1998). Synthesis of a cobalt complex of a pyrano[2,3-b]quinoxaline-3,4-dithiolate related to molybdopterin. *Chem. Commun.* 3, 417–418. doi: 10.1039/a708366a

Coucouvanis, D., Hadjikyriacou, A., Toupadakis, A., Koo, S. M., Ileperuma, O., Draganjac, M., et al. (1991). Studies of the reactivity of binary thio- and tertiary oxothiomolybdates toward electrophiles. Reactions with dicarbomethoxyacetylene and the synthesis and structures of the [Et$_4$N$_2$[MoO(L)$_2$], anti-[Et$_4$N]$_2$[Mo$_2$O$_2$S$_2$(L)$_2$]], syn-[Ph$_4$P]$_2$[Mo$_2$O$_2$S$_2$(L)$_2$].cntdot.2DMF, Ph$_4$P]$_2$[Mo(L)$_3$]DMF.cntdot.C$_6$H$_6$, and [Ph$_4$P]$_2$[Mo$_2$S$_2$(L)$_4$]2CH$_2$Cl$_2$ complexes (L = 1,2-dicarbomethoxy-1,2-ethylenedithiolate). *Inorg. Chem.* 30, 754–767. doi: 10.1021/ic00004a028

Donahue, J. P., Goldsmith, C. R., Nadiminti, U., and Holm, R. H. (1998). Synthesis, structures, and reactivity of bis(dithiolene)molybdenum(IV,VI) complexes related to the active sites of molybdoenzymes. *J. Am. Chem. Soc.* 120, 12869–12881. doi: 10.1021/ja982914f

Döring, A., Schulzke, C., and Zhang, Q. (2010). Synthesis, characterization and structural analysis of isostructural dinuclear molybdenum and tungsten oxo-bis-mu-sulfido-benzenedithiolene complexes. *Inorg. Chim. Acta* 363, 4140–4144. doi: 10.1016/j.ica.2010.05.036

Easton, D. B. J., and Leaver, D. (1965). 1,3-Dipolar reactivity of 1,2-dithiole-3-thiones and 1,3-dithiolan-2-thiones. *Chem. Commun.* 22, 585–586. doi: 10.1039/C19650000585

Edwards, M., Roeper, J., Allgood, C., Chin, R., Santamaria, J., Wong, F., et al. (2015). Investigation of molybdenum cofactor deficiency due to MOCS$_2$ deficiency in a newborn baby. *Meta Gene* 3, 43–49. doi: 10.1016/j.mgene.2014.12.003

Enemark, J. H., Cooney, J. J., Wang, J. J., and Holm, R. H. (2004). Synthetic analogues and reaction systems relevant to the molybdenum and tungsten oxotransferases. *Chem. Rev.* 104, 1175–1200. doi: 10.1021/cr020609d

Farrugia, L. (2012). WinGX and ORTEP for windows: an update. *J. Appl. Crystallogr.* 45, 849–854. doi: 10.1107/S0021889812029111

Fischer, C., and Fischer, L. (2017). Molybdenum and tungsten enzymes: bioinorganic chemistry. *R. Soc. Chem.* 20, 94–129. doi: 10.1039/9781782628828-00094

Garner, C. D., and Bristow, S. (1985). "Molybdenum enzymes," in *Metal Ions in Biology, Vol. 7*, ed T. G. Spiro (New York, NY: John Wiley and Sons, Inc.), 343.

Garton, S. D., Hilton, J., Oku, H., Crouse, B. R., Rajagopalan, K. V., and Johnson, M. K. (1997). Active site structures and catalytic mechanism of rhodobacter sphaeroides dimethyl sulfoxide reductase as revealed by resonance Raman spectroscopy. *J. Am. Chem. Soc.* 119, 12906–12916. doi: 10.1021/ja972109l

Ghosh, A. C., Samuel, P. P., and Schulzke, C. (2017). Synthesis, characterization and oxygen atom transfer reactivity of a pair of Mo(iv)O- and Mo(vi)O$_2$-enedithiolate complexes—a look at both ends of the catalytic transformation. *Dalton Trans.* 46, 7523–7533. doi: 10.1039/C7DT01470H

Gisewhite, D. R., Yang, J., Williams, B. R., Esmail, A., Stein, B., Kirk, M. L., et al. (2018). Implications of pyran cyclization and pterin conformation on oxidized forms of the molybdenum cofactor. *J. Am. Chem. Soc.* 140, 12808–12818. doi: 10.1021/jacs.8b05777

Hille, R. (2013). The molybdenum oxotransferases and related enzymes. *Dalton Trans.* 42, 3029–3042. doi: 10.1039/c2dt32376a

Hille, R., Hall, J., and Basu, P. (2014). The mononuclear molybdenum enzymes. *Chem. Rev.* 114, 3963–4038. doi: 10.1021/cr400443z

Hille, R., Schulzke, C., and Kirk, M. L. (2016). *Molybdenum and Tungsten Enzymes: Bioinorganic Chemistry*, eds R. Hille, C. Schulzke, and M. L. Kirk. Cambridge, UK: The Royal Society of Chemistry.

Holm, R. H. (1987). Metal-centered oxygen atom transfer reactions. *Chem. Rev.* 87, 1401–1449. doi: 10.1021/cr00082a005

Holm, R. H. (1990). The biologically relevant oxygen atom transfer chemistry of molybdenum—from synthetic analog systems to enzymes. *Coordinat. Chem. Rev.* 100, 183–221. doi: 10.1016/0010-8545(90)85010-P

Jeppesen, J. O., Takimiya, K., Thorup, N., and Becher, J. (1999). A novel tetrathiafulvalene building block. *Synthesis* 5, 803–810.

Kim, H. S., Nguyen, D. Q., Cheong, M., Kim, H., Lee, H., Ko, N. H., et al. (2008). One-pot synthesis of ethylene trithiocarbonate from ethylene carbonate. *Appl. Catalysis A General* 337, 168–172. doi: 10.1016/j.apcata.2007.12.012

Kirk, M. L., McNaughton, R. L., and Helton, M. E. (2004). "The electronic structure and spectroscopy of metallo-dithiolene complexes," In *Dithiolene Chemistry, Vol. 52*, ed E. I. Stiefel (New York, NY: John Wiley and Sons, Inc.), 111–212.

Lim, B. S., and Holm, R. H. (2001). Bis(dithiolene)molybdenum analogues relevant to the DMSO reductase enzyme family: synthesis, structures, and oxygen atom transfer reactions and kinetics. *J. Am. Chem. Soc.* 123, 1920–1930. doi: 10.1021/ja003546u

Liu, B., Wu, B., Xu, J., Wu, Z., Zhao, Y., Zheng, X., et al. (2010). Resonance Raman intensity analysisof the excited-state photochemical dynamicsof dimethyl 1,3-dithiole-2-thione-4,5-dicarboxylate in the A-band absorption. *J. Raman Spectroscopy* 41, 1185–1193. doi: 10.1002/jrs.2580

Lorber, C., Rosaria Plutino, M., I., Elding, L., and Nordlander, E. (1997). Kinetics of oxygen-atom transfer reactions involving molybdenum dithiolene complexes. *J. Chem. Soc. Dalton Trans.* 21, 3997–4004.

McMaster, J., Tunney, J. M., and Garner, C. D. (2004a). "Chemical analogues of the catalytic centers of molybdenum and tungsten dithiolene-containing enzymes," in *Dithiolene Chemistry*, ed E. I. Stiefel (New York, NY: John Wiley and Sons, Inc.), 539–583.

McMaster, J., Tunney, J. M., and Garner, C. D. (2004b). "Chemical analogues of the catalytic centers of molybdenum and tungsten ditholene-containing enzymes," in *Dithiolene Chemistry, Vol. 52*, ed E. I. Stiefel (New York, NY: John Wiley and Sons, Inc.), 539–584.

Mendel, R. R. (2007). Biology of the molybdenum cofactor. *J. Exp. Bot.* 58, 2289–2296. doi: 10.1093/jxb/erm024

Mitra, J., and Sarkar, S. (2013). Oxo–Mo(IV)(dithiolene)thiolato complexes: analogue of reduced sulfite oxidase. *Inorg. Chem.* 52, 3032–3042. doi: 10.1021/ic302485c

Neil Bricklebank, S. J. C., and Michael, B., Hursthouse. (2003). *Crystal Structure Report Archive*. U.S. National Library of Medicine National Center for Biotechnology Information, Bethesda, MD, United States. doi: 10.5258/ecrystals/902

Nguyen, Tle A., Demir-Cakan, R., Devic, T., Morcrette, M., Ahnfeldt, T., Auban-Senzier, P., et al. (2010). 3-D coordination polymers based on the tetrathiafulvalenetetracarboxylate (TTF-TC) derivative: synthesis, characterization, and oxidation issues. *Inorg. Chem.* 49, 7135–7143. doi: 10.1021/ic100950n

Okamura, T., Omi, Y., Hirano, Y., and Onitsuka, K. (2016a). Comparative studies on the contribution of NH⋯S hydrogen bonds in tungsten and molybdenum benzenedithiolate complexes. *Dalton Trans.* 45, 15651–15659. doi: 10.1039/C6DT02250B

Okamura, T.-A., Yamada, T., Hasenaka, Y., Yamashita, S., and Onitsuka, K. (2016b). Unexpected reaction promoted by NH+⋯O=Mo hydrogen bonds in nonpolar solvents. *Eur. J. Inorg. Chem.* 2016, 2952–2961. doi: 10.1002/ejic.201600081

Oku, H., Ueyama, N., and Nakamura, A. (1997). Association of oxo–molybdenum dithiolene complexes with a multiamide additive and its influence on the ease of O-atom transfer. *Inorg. Chem.* 36, 1504–1516. doi: 10.1021/ic951277g

Pal, K., Maiti, R., Chaudhury, P. K., and Sarkar, S. (2007). Synthesis, structure and reactions of a series of 1,2-dicyanoethylenedithiolate coordinated dimeric Mo(V) complexes. *Inorg. Chim. Acta* 360, 2721–2733. doi: 10.1016/j.ica.2007.01.018

Pløger, J. M., Petersen, B. M., Bond, A. D., and Jeppesen, J. O. (2006). 4,5-Bis(hydroxymethyl)-1,3-dithiole-2-thione. *Acta Crystallogr.* E62, o2066–o2068. doi: 10.1107/S1600536806014140

Rajagopalan, K. V. (1997). The molybdenum cofactors—perspective from crystal structure. *J. Biol. Inorg. Chem.* 2, 786–789. doi: 10.1007/pl00010648

Ratnani, R., Bohra, R., Srivastava, G., and Mehrotra, R. C. (1990). Crystal and molecular structure of µ-oxobis[bis(dipropyl dithiophosphato) oxomolybdenum(V)]. *J. Crystallogr. Spectroscopic Res.* 20, 541–544. doi: 10.1007/bf01221894

Reiss, J. (2000). Genetics of molybdenum cofactor deficiency. *Hum. Genet.* 106, 157–163. doi: 10.1007/s004390051023

Schulzke, C. (2016). "An overview of the synthetic strategies, reaction mechanisms and kinetics of model compounds relevant to molybdenum- and tungsten-containing enzymes," in *Molybdenum and Tungsten Enzymes: Bioinorganic Chemistry, Vol. 6*, eds R. Hille, C. Schulzke, and M. L. Kirk (Cambridge: Royal Soc Chemistry), 1–7.

Schulzke, C., and Ghosh, A. C. (2014). "Molybdenum and tungsten oxidoreductase models," in *Bioinspired Catalysis*, eds W. Weigand and P. Schollhammer (Weinheim: Wiley-VCH Verlag GmbH and Co. KGaA), 349–382.

Schulzke, C., and Samuel, P. P. (2011). *Molybdenum and Tungsten Cofactor Model Chemistry*. New York, NY: Nova Science Publishers Inc.

Sellmann, D., Grasser, F., Knoch, F., and Moll, M. (1992). Übergangsmetallkomplexe mit Schwefelliganden, LXXX. Synthese, Struktur, Oxotransfer- und redoxgekoppelte Kondensationsreaktionen von Molybdän-Oxo-Komplexen mit dem sterisch anspruchsvollen vierzähnigen Thioether-Thiolat-Liganden 'buS4'2⁻ ('buS4'2- = 1,2-Bis(2-mercapto-3,5-di-t-butylphenylthio)ethan(2⁻)). *Z. Naturforschung B* 47:61. doi: 10.1515/znb-1992-0114

Sheldrick, G. (2015). SHELXT—Integrated space-group and crystal-structure determination. *Acta Crystallogr.* 71, 3–8. doi: 10.1107/S2053273314026370

Sheldrick, G. M. (2008). A short history of SHELX. *Acta Cryst. A* 64, 112–122. doi: 10.1107/S0108767307043930

Smit, J. P., Purcell, W., Roodt, A., and Leipoldt, J. G. (1993). Kinetics of the substitution reaction between aquaoxotetracyanomolybdate(IV) and cyanide/hydrogen cyanide. *Polyhedron* 12, 2271–2277. doi: 10.1016/S0277-5387(00)88267-4

Smith, P. D., Millar, A. J., Young, C. G., Ghosh, A., and Basu, P. (2000). Detection, isolation, and characterization of intermediates in oxygen atom transfer reactions in molybdoenzyme model systems. *J. Am. Chem. Soc.* 122, 9298–9299. doi: 10.1021/ja0008362

Subramanian, P., Kaul, B., and Spence, J. T. (1984). Modelling the molybdenum centers of the molybdenum hydroxylases. *J. Mol. Catal.* 23, 163–177. doi: 10.1016/0304-5102(84)80004-8

Sugimoto, H., Harihara, M., Shiro, M., Sugimoto, K., Tanaka, K., Miyake, H., et al. (2005). Dioxo-molybdenum(VI) and mono-oxo-molybdenum(IV) complexes supported by new aliphatic dithiolene ligands: new models with weakened MoO bond characters for the arsenite oxidase active site. *Inorg. Chem.* 44, 6386–6392. doi: 10.1021/ic050234p

Sugimoto, H., Siren, K., Tsukube, H., and Tanaka, K. (2003). Mono-dithiolene molybdenum(IV) complexes of cis-1,2-dicyano-1,2-ethylenedithiolate (mnt²⁻): new models for molybdenum enzymes. *Eur. J. Inorg. Chem.* 2003, 2633–2638. doi: 10.1002/ejic.200200638

Sugimoto, H., Tatemoto, S., Suyama, K., Miyake, H., Itoh, S., Dong, C., et al. (2009). Dioxomolybdenum(VI) complexes with Ene-1,2-dithiolate ligands: synthesis, spectroscopy, and oxygen atom transfer reactivity. *Inorg. Chem.* 48, 10581–10590. doi: 10.1021/ic901112s

Tatsumisago, M., Matsubayashi, G. E., Tanaka, T., Nishigaki, S., and Nakatsu, K. (1982). Synthesis, spectroscopy, and X-ray crystallographic analysis of (η3-dithiobenzoato-SCS')oxo(trithioperoxybenzoato-S,S'S'')molybdenum(IV) and µ-oxo-bis[bis(dithiobenzoato-SS')oxomolybdenum(V)]. *J. Chem. Soc. Dalton Trans.* 1982, 121–127. doi: 10.1039/DT9820000121

Tchouka, H., Meetsma, A., Molnár, G., Rechignat, L., and Browne, W. R. (2011). Solution and single crystal spectroscopic characterization of (PPh₄)₂[Fe(CN)₅(imidazole)]·2H₂O. *J. Mol. Struct.* 999, 39–48. doi: 10.1016/j.molstruc.2011.05.027

Thompson, R. L., Lee, S., Geib, S. J., and Cooper, N. J. (1993). Intramolecular bridge/terminal oxo exchange within oxomolybdenum $[Mo_2^VO_3]^{4+}$ complexes containing linear oxo bridges. *Inorg. Chem.* 32, 6067–6075. doi: 10.1021/ic00078a026

Tucci, G. C., Donahue, J. P., and Holm, R. H. (1998). Comparative kinetics of oxo transfer to substrate mediated by bis(dithiolene)dioxomolybdenum and -tungsten complexes. *Inorg. Chem.* 37, 1602–1608. doi: 10.1021/Ic971426q

Villata, L. S. A., Féliz, M. R., and Capparelli, A. L. (2000). Photochemical and catalytic properties of dimeric species of molybdenum(V). *Coordinat. Chem. Rev.* 196, 65–84. doi: 10.1016/S0010-8545(99)00186-1

Williams, B. R., Fu, Y., Yap, G. P., and Burgmayer, S. J. (2012). Structure and reversible pyran formation in molybdenum pyranopterin dithiolene models of the molybdenum cofactor. *J. Am. Chem. Soc.* 134, 19584–19587. doi: 10.1021/ja310018e

Williams, B. R., Gisewhite, D., Kalinsky, A., Esmail, A., and Burgmayer, S. J. (2015). Solvent-dependent pyranopterin cyclization in molybdenum cofactor model complexes. *Inorg. Chem.* 54, 8214–8222. doi: 10.1021/acs.inorgchem.5b00532

Conflict of Interest Statement: The authors declare that the research was conducted in the absence of any commercial or financial relationships that could be construed as a potential conflict of interest.

Reaction Mechanism and Substrate Specificity of *Iso*-orotate Decarboxylase: A Combined Theoretical and Experimental Study

Xiang Sheng[1], Katharina Plasch[2], Stefan E. Payer[2], Claudia Ertl[2], Gerhard Hofer[3], Walter Keller[3], Simone Braeuer[4], Walter Goessler[4], Silvia M. Glueck[2,5], Fahmi Himo[1]* and Kurt Faber[2]*

[1] Department of Organic Chemistry, Arrhenius Laboratory, Stockholm University, Stockholm, Sweden, [2] Institute of Chemistry, Organic & Bioorganic Chemistry, University of Graz, Graz, Austria, [3] Institute of Molecular Biosciences, University of Graz, Graz, Austria, [4] Institute of Chemistry, Analytical Chemistry, University of Graz, Graz, Austria, [5] Austrian Centre of Industrial Biotechnology (ACIB GmbH), Graz, Austria

The C-C bond cleavage catalyzed by metal-dependent *iso*-orotate decarboxylase (IDCase) from the thymidine salvage pathway is of interest for the elucidation of a (hypothetical) DNA demethylation pathway. IDCase appears also as a promising candidate for the synthetic regioselective carboxylation of *N*-heteroaromatics. Herein, we report a joint experimental-theoretical study to gain insights into the metal identity, reaction mechanism, and substrate specificity of IDCase. In contrast to previous assumptions, the enzyme is demonstrated by ICPMS/MS measurements to contain a catalytically relevant Mn^{2+} rather than Zn^{2+}. Quantum chemical calculations revealed that decarboxylation of the natural substrate (5-carboxyuracil) proceeds *via* a (reverse) electrophilic aromatic substitution with formation of CO_2. The occurrence of previously proposed tetrahedral carboxylate intermediates with concomitant formation of HCO_3^- could be ruled out on the basis of prohibitively high energy barriers. In contrast to related *o*-benzoic acid decarboxylases, such as γ-resorcylate decarboxylase and 5-carboxyvanillate decarboxylase, which exhibit a relaxed substrate tolerance for phenolic acids, IDCase shows high substrate fidelity. Structural and energy comparisons suggest that this is caused by a unique hydrogen bonding of the heterocyclic natural substrate (5-carboxyuracil) to the surrounding residues. Analysis of calculated energies also shows that the reverse carboxylation of uracil is impeded by a strongly disfavored uphill reaction.

Keywords: computational chemistry, biocatalysis, *iso*-orotate decarboxylase, reaction mechanism, substrate specificity, metal identity

INTRODUCTION

Iso-orotate decarboxylase (IDCase), an enzyme involved in the thymidine salvage pathway, catalyzes the non-oxidative decarboxylation of *iso*-orotate (5-carboxyuracil; 5caU; **1a**) to uracil (U; **1b**) (Smiley et al., 2005; Leal et al., 2007) (**Scheme 1A**). The latter can be directly converted to uridine monophosphate (UMP) by uracil phosphoribosyltransferase (UPRTase) in most organisms

SCHEME 1 | Decarboxylation of (hetero)aromatics catalyzed by **(A)** *iso*-orotate decarboxylase (IDCase), **(B)** γ-resorcylate decarboxylase (γ-RSD), and **(C)** 5-carboxyvanillate decarboxylase (LigW).

FIGURE 1 | Metal-ligand distance (red bars) for IDCase (PDB 4HK7) with **(A)** Zn^{2+} and **(B)** Mn^{2+} in the active site compared with database likelihoods (CSD); **(C)** ICPMS/MS analysis of metal ions (Mn^{2+} and Zn^{2+}) in IDCase (sulfur determination for quantitative analysis of protein).

(Smiley et al., 2005). In the genomes of *Neurospora crassa* and *Aspergillus nidulans*, the IDCase gene is downstream from a gene encoding a dioxygenase termed thymine-7-hydroxylase, which oxidizes the methyl group of 5-methyluracil (thymin) to a carboxylate, thereby providing the substrate for IDCase (Smiley et al., 2005) and completing the pathway.

The enzyme is inactive on the regio-isomer orotic acid (6-carboxyuracil) and the reverse carboxylation of uracil (Palmatier et al., 1970), but decarboxylates 5-carboxy-2-thiouracil (Smiley et al., 1999) and 5-carboxycytosine (5caC) (Xu et al., 2013). The conversion of 5caC to cytosine (C) via decarboxylation (Schiesser et al., 2012) is suggested as the C-C cleaving step in a hypothetical DNA demethylation pathway mediated by Tet proteins (He et al., 2011; Ito et al., 2011), although such a "DNA decarboxylase" has not yet been identified. Hence, detailed knowledge of the structure and reaction mechanism of IDCase would provide valuable information on the identification of this putative DNA decarboxylase.

A number of crystal structures of IDCase from *Cordyceps militaris* and *Metarhizium anisopliae* have been obtained (Xu et al., 2013), and structural and sequence analysis showed that IDCase belongs to the amidohydrolase superfamily (Xu et al., 2013). A metal ion, identified as zinc, was observed to be coordinated by one aspartate and three histidine residues and the substrate is supposed to be directly bound to the metal by both the hydroxyl and the carboxylate group (Xu et al., 2013). The K_m and k_{cat} values were determined to be 22.4 ±
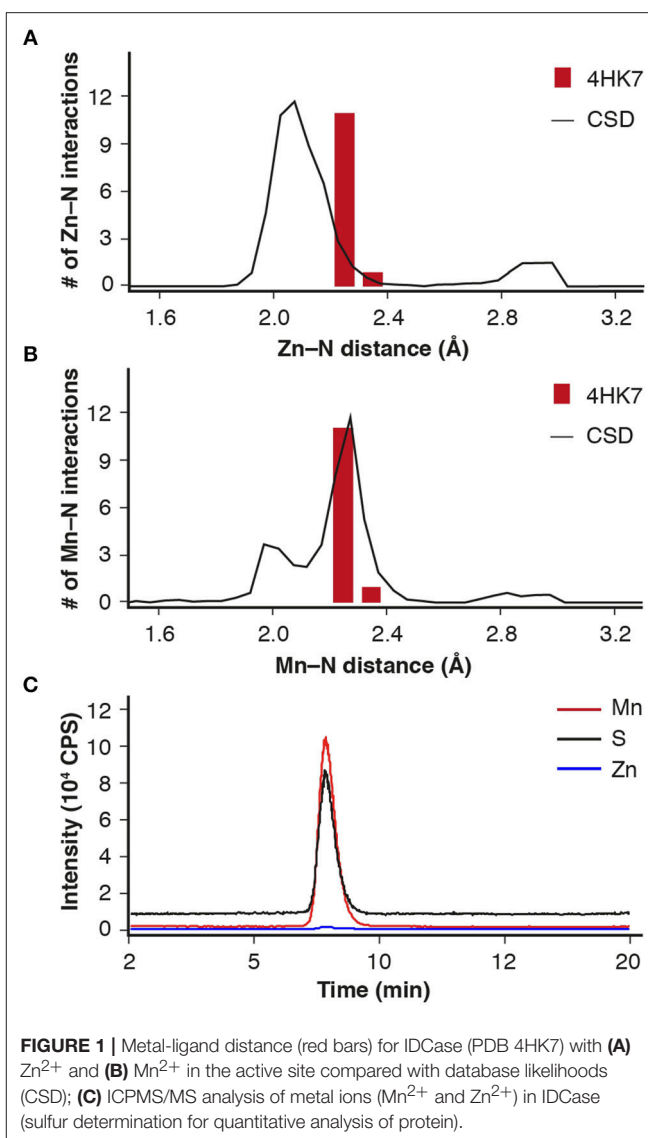
1.3 µM and 4.17 ± 0.09 min^{-1} for the IDCase from *C. militaris*, and 18.6 ± 1.9 µM and 2.02 ± 0.08 min^{-1} for IDCase from *M. anisopliae*, respectively (Xu et al., 2013). As a member of cog2159 of the amidohydrolase superfamily (Seibert and Raushel, 2005), IDCase shows structural and substrate similarities with other enzymes from the same family (**Scheme 1**), such as γ-resorcylate decarboxylase (also called 2,6-dihydroxybenzoic acid decarboxylase, 2,6-DHBD) from *Rhizobium* sp. (γ-RSD_Rs) (Wuensch et al., 2012; Sheng et al., 2018) and 5-carboxyvanillate decarboxylases from *Sphingomonas paucimobilis* (LigW_Sp) and from *Novosphingobium aromaticivorans* (LigW_Na) (Peng et al., 2002, 2005; Vladimirova et al., 2016; Sheng et al., 2017).

Interestingly, from a synthetic standpoint, *ortho*-benzoic acid decarboxylases (*o*-BDCs), such as 2,6-DHBD, have been shown to possess a remarkably broad substrate range for the reverse regioselective carboxylation of phenolic compounds to produce aromatic carboxylic acids used as pharmaceuticals

as well as building blocks for organic synthesis (Ishii et al., 2004; Yoshida et al., 2004; Matsui et al., 2006; Iwasaki et al., 2007; Ienaga et al., 2013; Wuensch et al., 2014). This

constitutes a biological alternative to the (chemical) Kolbe–Schmitt carboxylation process, which requires high pressure and temperature (Lindsey and Jeskey, 1957). Aiming to extend this
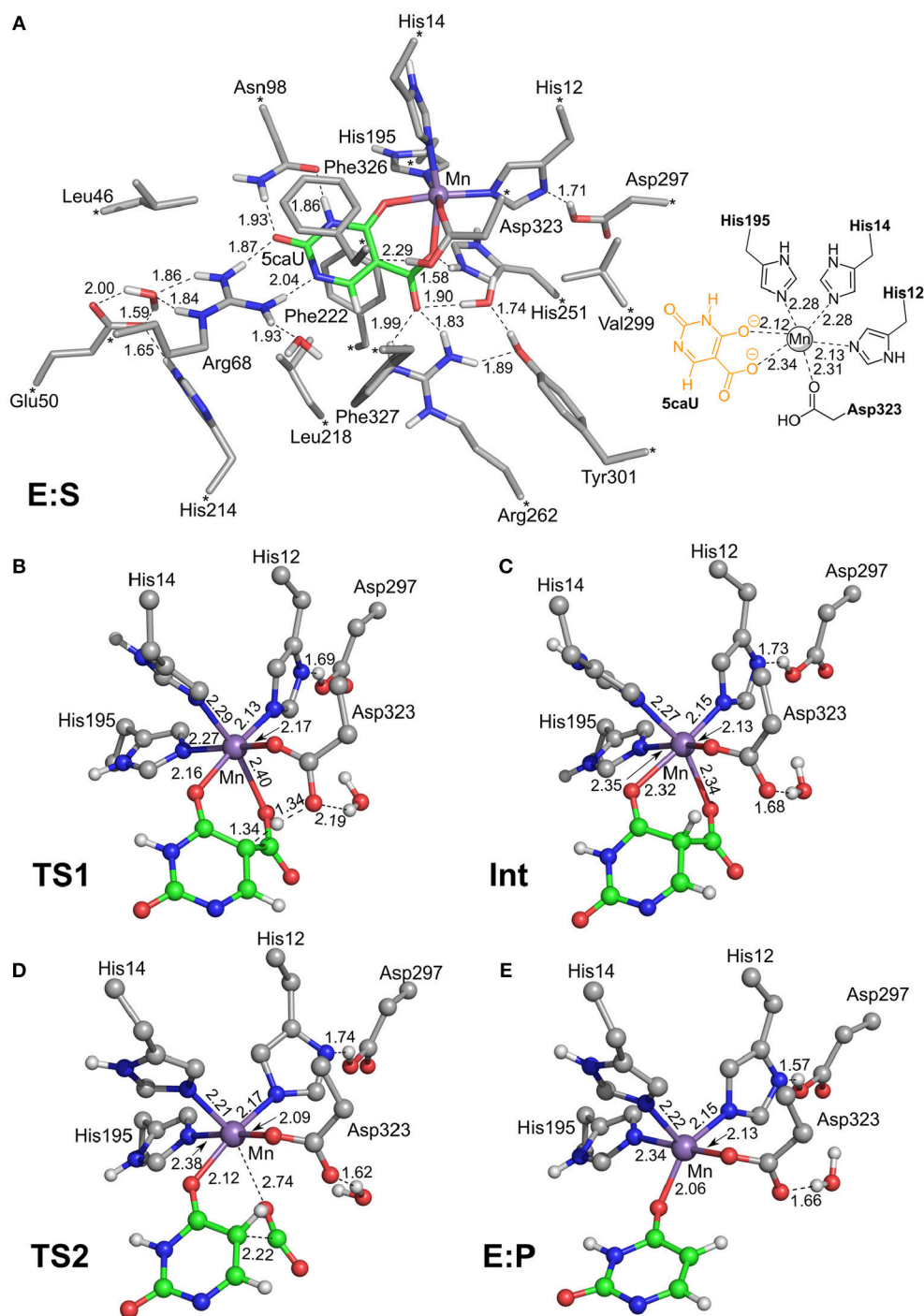
FIGURE 2 | Optimized structures of intermediates and transition states along the reaction pathway proposed for IDCase. **(A)** The enzyme-substrate complex **E:S**, **(B)** the TS for the protonation step, **(C)** the intermediate after the protonation step, **(D)** the TS for the C-C bond cleavage step, and **(E)** the enzyme-product complex **E:P**. For clarity, only polar hydrogen atoms and hydrogens on the substrate are shown, and the full model is only shown for **E:S**. The atoms fixed during geometry optimization are marked with asterisks in **E:S** and selected distances are given in Å.

method to the regioselective carboxylation of N-heteroaromatics, IDCase appeared as promising candidate.

In the present study, the metal dependence of IDCase is unambiguously established by means of ICPMS/MS experiments, followed by a detailed quantum chemical investigation to elucidate its reaction mechanism. Aiming at using IDCase in the reverse carboxylation reaction, the natural substrate and a range of synthetic analogs (such as structurally related pyrimidine and phenol derivatives) were examined. Sequence alignment of IDCase with related metal-dependent decarboxylases is performed and their active sites are compared. Finally, an energy analysis of different substrate binding modes is conducted.

RESULTS AND DISCUSSION

Metal-Dependence

All structures of IDCase showed a metal at the active site, which was assumed to be Zn^{2+} based on fluorescence spectroscopy (PDB 4LAK and 4HJW) (Xu et al., 2013). In the substrate (iso-orotate)-bound IDCase structure (Asp323Asn mutant, PDB 4LAM), the metal is coordinated to C4-hydroxyl group of the pyrimidine ring and one oxygen of the carboxylate group and H-bonded to four amino acid residues (His12, His14, His195, and Asp323Asn).

Analysis of the metal-ligand distance of the (putative) Zn^{2+} in the crystal structure of IDCase (PDB 4HK7) (Zheng et al., 2014, 2017) showed that the metal–nitrogen bonds are too long for Zn^{2+}, but fit nicely to a larger metal, such as Mn^{2+}, which is frequently found in mechanistically related o-BDCs and LigWs (Sheng et al., 2017, 2018) (Figures 1A,B). In order to solve this discrepancy, ICPMS/MS measurements coupled to size exclusion chromatography were performed, which unambiguously proved the presence of Mn^{2+} (Figure 1C, red line) instead of Zn^{2+} (blue line) in the Escherichia coli expressed enzyme from C. militaris.

Reaction Mechanism

To investigate the reaction mechanism of IDCase, quantum chemical calculations were performed on the basis of the crystal structure of the Asp323Asn mutant from C. militaris in complex with the substrate (PDB 4LAM) (Xu et al., 2013). A large active site model consisting of 310 atoms was designed by modifying the mutated Asn323 back to the native Asp residue (Figure 2). Since the metal was identified above as in fact being Mn^{2+}, the

zinc ion previously proposed in the crystal structure is replaced by manganese. The computational methods and the details of the active site model are given in the **Supplementary Material**.

We envisioned that the reaction of IDCase could follow a similar mechanism as the one suggested for γ-RSD (Sheng et al., 2018) and LigW (Sheng et al., 2017), because all of them belong to cog2159 of the amidohydrolase superfamily (Seibert and Raushel, 2005). As shown in **Scheme 2**, the reaction would thus start with a proton transfer from Asp323 to the C5 atom of substrate, followed by C-C bond cleavage to generate CO_2 and uracil. Overall, this sequence of events would bear a strong resemblance to those involved in the (reverse) electrophilic aromatic substitution. Indeed, this mechanistic scenario turned out to have feasible energy barriers (black line in **Figure 3**). The calculated barrier for the overall reaction, 20.7 kcal/mol, is in quite good agreement with the experimental value, which is ca 19 kcal/mol as converted from the experimental k_{cat} for IDCase from C. militaris (4.17 min^{-1}) (Xu et al., 2013).

In the enzyme-substrate complex (**E:S** in **Figure 2A**), the substrate adopts a similar binding mode as in γ-RSD in complex with 2-nitroresorcinol (PDB 4QRO) (Sheng et al., 2018) and also LigW complexed with 2-nitrovanillate (PDB 4QRN) (Vladimirova et al., 2016). The barrier for the proton transfer from Asp323 to the C5 atom is calculated to be 14.1 kcal/mol, and the resulting intermediate (**Int**) is 9.2 kcal/mol higher in energy than **E:S** (**Figure 3**). At the transition state (**TS1**), the lengths of the breaking Asp323 O-H bond and the forming

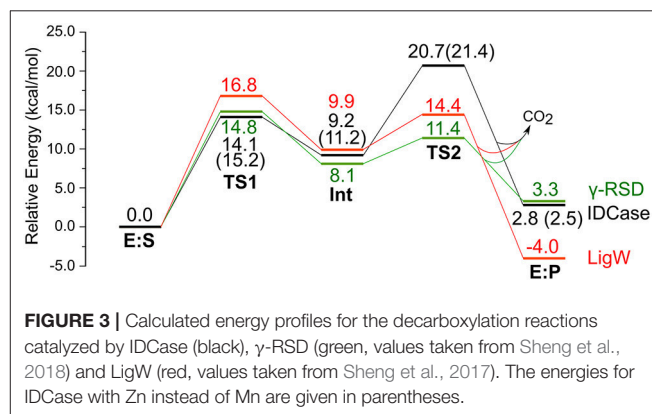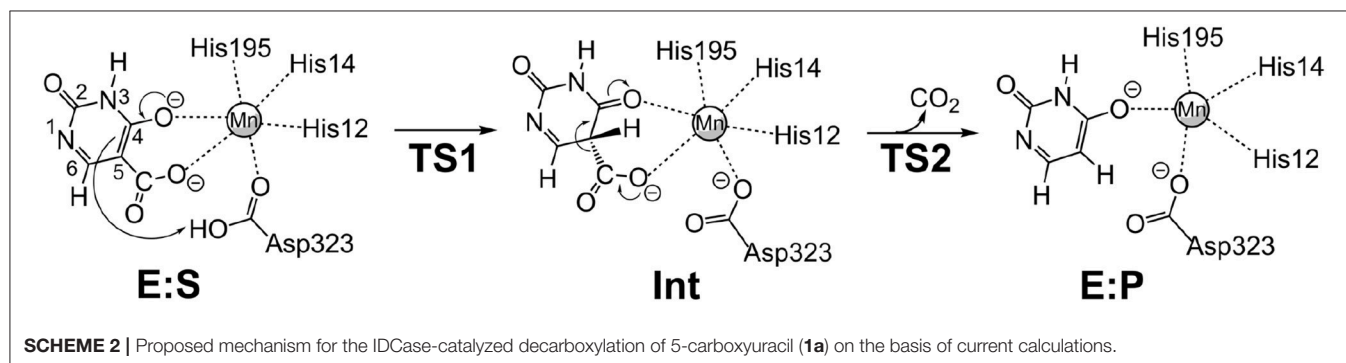**FIGURE 3 |** Calculated energy profiles for the decarboxylation reactions catalyzed by IDCase (black), γ-RSD (green, values taken from Sheng et al., 2018) and LigW (red, values taken from Sheng et al., 2017). The energies for IDCase with Zn instead of Mn are given in parentheses.

SCHEME 2 | Proposed mechanism for the IDCase-catalyzed decarboxylation of 5-carboxyuracil (**1a**) on the basis of current calculations.

C5-H bond are both 1.34 Å (**Figure 2B**). The subsequent C-C bond cleavage is calculated to be the rate-limiting step with a barrier of 11.5 kcal/mol relative to **Int**, i.e., 20.7 kcal/mol higher than **E:S** (**Figure 3**). At **TS2**, the length of the breaking C-C bond is 2.22 Å (**Figure 2D**). The enzyme-product complex (**E:P**, **Figure 2E**) is 2.8 kcal/mol higher than **E:S** (**Figure 3**), including the contribution of entropy gain from the release of CO_2.

Comparison of the calculated energy profile of the IDCase mechanism with those of LigW and γ-RSD (**Figure 3**) reveals some interesting features. The first step, the protonation of the substrate carbon, has very similar barriers for the three enzymes (14–17 kcal/mol), but for the subsequent C-C bond cleavage, IDCase is calculated to have a significantly higher barrier than the other two enzymes (20.7 kcal/mol for IDCase vs. 14.4 and 11.4 kcal/mol for LigW and γ-RSD, respectively). This matches the trends observed experimentally for the rate constants for these enzymes.

As discussed above, IDCase was originally suggested to be a zinc-dependent enzyme (Xu et al., 2013). Based on this, two possible mechanisms were proposed previously, both of which lead to the formation of HCO_3^- and uracil as products (Xu et al., 2013). One mechanism involves a tetrahedral carboxylated Asp/Glu (mixed anhydride) intermediate formed by nucleophilic attack of Asp323 onto the substrate's carboxylate group, while the other one involves a hydrated carboxylate intermediate. We have examined these possibilities assuming Zn as the metal ion, but both of them turned out to be associated with prohibitively high energies and can thus be ruled out (see **Supplementary Material** for detailed discussion).

On the other hand, we also tested the mechanism shown in **Scheme 2** with Zn instead of Mn, and the obtained barrier was only 0.7 kcal/mol higher than that with Mn (**Figure 3**). The optimized structures are given in the **Supplementary Material**. This result shows that also Zn can serve as the metal ion in IDCase, which is in stark contrast to the case of γ-RSD for which previous calculations showed that the Mn-enzyme is active while the Zn-enzyme is associated with very high energy barriers (Sheng et al., 2018).

Substrate Specificity

In order to explore the utility of IDCase for biocatalytic purposes, its substrate tolerance was elucidated using a range of heterocyclic and homocyclic analogs of the natural substrate [5-carboxyuracil (**1a**)] in the decarboxylation and reverse carboxylation direction, respectively (**Figure 4**). The activity of IDCase overexpressed in *E. coli* was verified under standard conditions in aqueous buffer pH 7.5 at 30°C by decarboxylation of 5-carboxyuracil (**1a**), which showed nearly full conversion within 24 h.

The reverse carboxylation of uracil (**1b**) using the standard carboxylation procedure in presence of 3 M bicarbonate (Wuensch et al., 2012) did not show any product formation, corroborating observations of Palmatier et al. (1970). In addition, pyrimidine derivatives (**2–5**), which are electronically and sterically closely related to uracil (**1b**), were investigated to explore IDCase for the carboxylation of heterocyclic compounds (**Figure 4**). None of them reacted.

As alternative CO_2 source to bicarbonate, gaseous carbon dioxide under pressure (∼30–40 bar) was recently successfully employed for the carboxylation of resorcinol (1,3-dihydroxybenzene) with conversion of up to 68% by *o*-benzoic acid decarboxylases (Plasch et al., 2018). Attempts to carboxylate uracil (**1b**) by IDCase using pressurized CO_2 (30 bar) were unsuccessful.

Since the decarboxylation catalyzed by IDCase is calculated to follow a similar mechanism compared to those of γ-RSD and LigW (Sheng et al., 2017, 2018), and γ-RSD exhibited a broad substrate scope for phenols and phenolic carboxylic acids in the carboxylation and decarboxylation direction, respectively (Ishii et al., 2004; Yoshida et al., 2004; Matsui et al., 2006; Iwasaki et al., 2007; Ienaga et al., 2013; Wuensch et al., 2014), we tested whether IDCase could promote the decarboxylation of *o*-hydroxybenzoic acids **6a–11a**, however, without success. Furthermore, we expected that the enhanced electron-density of (*iso*-cyclic) phenols (**6b–11b**) compared to (heterocyclic) uracil (**1b**) might augment electrophilic aromatic substitution thereby allowing the reverse carboxylation reaction. Again, carboxylation of **6b–11b** failed. For reason of comparison, we performed a
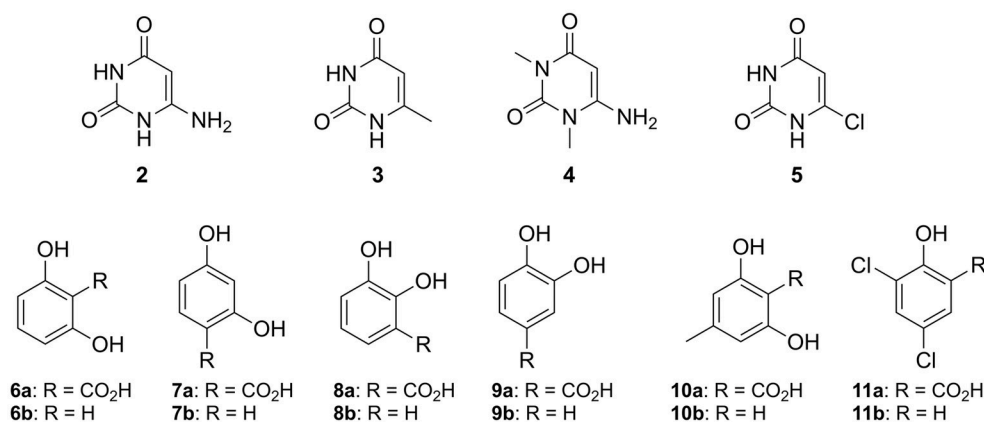

FIGURE 4 | Non-natural substrates for activity screening of IDCase: Pyrimidine derivatives (**2–5**) for carboxylation and phenolic carboxylic acids (**6a–11a**) and phenols (**6b−11b**) for decarboxylation and carboxylation, respectively.

microwave-assisted Kolbe-Schmitt carboxylation (Stark et al., 2009) in a carbonate-based ionic liquid using the natural substrate **1b**. No product formation was detected proving that this reaction is not feasible.

In view of the structural and mechanistic similarity of IDCase with *o*-BDCs, such as γ-RSD, which show a broad substrate tolerance with up to >97% conversion toward the thermodynamically disfavored carboxylation direction (Wuensch et al., 2014; Sato et al., 2015; Plasch et al., 2017), the lack of reactivity of IDCase was puzzling. In order to explain the high substrate specificity of IDCase for 5-carboxyuracil (**1a**) and its inability to catalyze the reverse carboxylation, we inspected its active site and its mode of action in more detail.
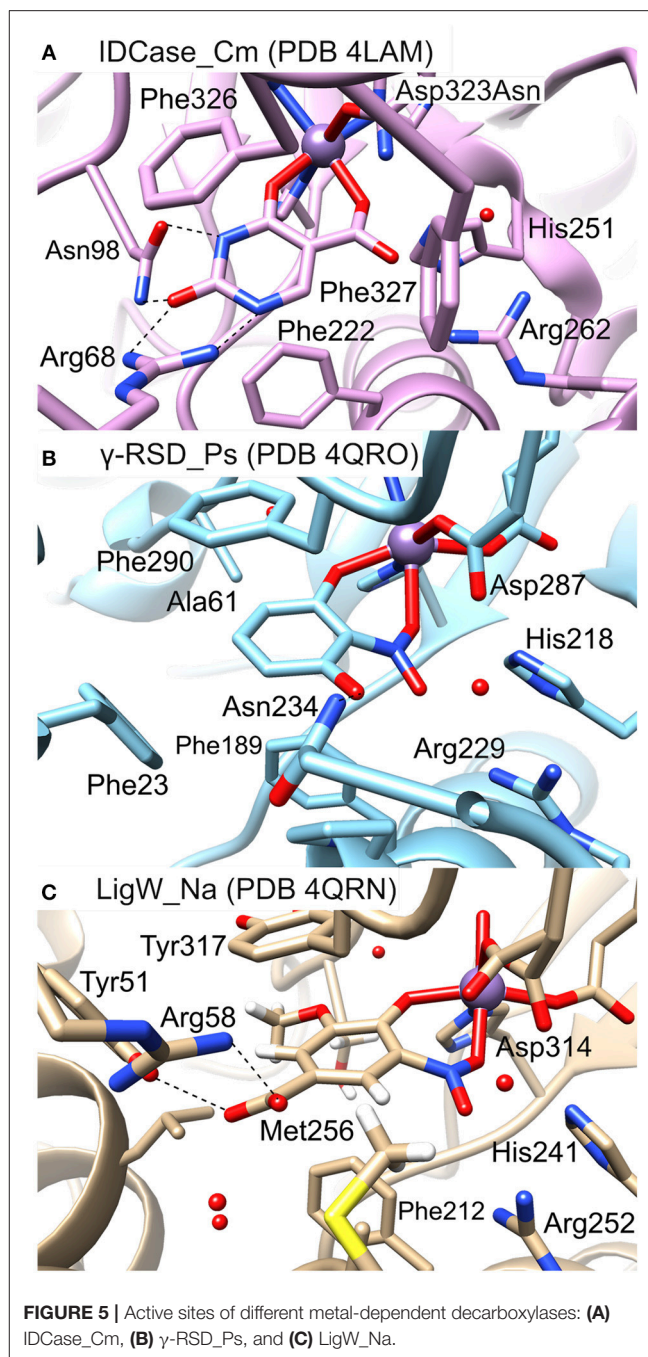
Sequence Alignment and Active Site Comparison

Sequence alignment of IDCase was performed with γ-RSDs (γ-RSD_Ps 27% and γ-RSD_Rs 29% identity) and LigWs (LigW_Sp 26% and LigW_Na 25% identity) by means of a fixed Arg-residue (see **Supplementary Material**). Despite the low sequence similarities of <30%, striking structural similarities concerning the requirement for a divalent metal together with several conserved catalytically relevant amino acid residues in the active sites are apparent.

In **Figure 5** the active sites of IDCase_Cm, γ-RSD_Ps and LigW_Na are compared. The residues forming hydrogen bonds with the carboxylate group of 5caU in IDCase (His251, Arg262, and Asp323) are well conserved in γ-RSD (His218, Arg229, and Asp287, respectively) and LigW (His241, Arg252, and Asp314, respectively).

Three phenylalanine residues (Phe222, Phe326, and Phe327) interact with the aromatic ring of 5caU in IDCase. Two of the positions are occupied by aromatic residues in γ-RSD (Phe189 and Phe290) and LigW (Phe212 and Tyr317), while the third is either replaced by a polar residue in γ-RSD (Asn234) or replaced by Met256 in LigW. The Asn234 residue in γ-RSD assists in the substrate binding by forming a hydrogen bond with the hydroxyl group of γ-resorcylate, while the methyl group of Met256 forms a hydrophobic interaction with the aromatic proton of the 5-carboxyvanillate substrate in LigW.

Further comparison of the structures reveals important roles of the Arg68 and Asn98 residues in the substrate binding and specificity of IDCase. Namely, Arg68 forms hydrogen bonds with both N1 and the C2 carbonyl group of the substrate, while Asn98 forms hydrogen bonds with N3-H and the carbonyl group (**Figure 5A**). This advantageous hydrogen-bonding network between the aromatic ring of the substrate and the active site residues is missing in the case of non-natural substrates, which results in lower binding affinities for these compounds. In LigW and γ-RSD, the Arg68 and Asn98 positions are either empty or occupied by different residues. In LigW, the Tyr51 and Arg58 residues form hydrogen bonds with the C1 carboxylate group rather than the aromatic ring (**Figure 5C**), while in γ-RSD only Phe23 provides interaction with the aromatic ring of γ-resorcylate (**Figure 5B**). This analysis provides thus a basis to understand how the active sites of these enzymes are adapted to

FIGURE 5 | Active sites of different metal-dependent decarboxylases: **(A)** IDCase_Cm, **(B)** γ-RSD_Ps, and **(C)** LigW_Na.

bind their respective natural substrates, which might explain the observed inability of IDCase to process non-natural substrates. Accordingly, it is conceivable that suitable mutations of the Arg68 and Asn98 residues could help to expand the substrate scope of IDCase.

Energetic Considerations

To shed more light on the reasons for the high substrate specificity of IDCase, it is instructive to consider the different binding modes of the natural substrate and compare them to inactive non-natural substrates. In the previous study on the
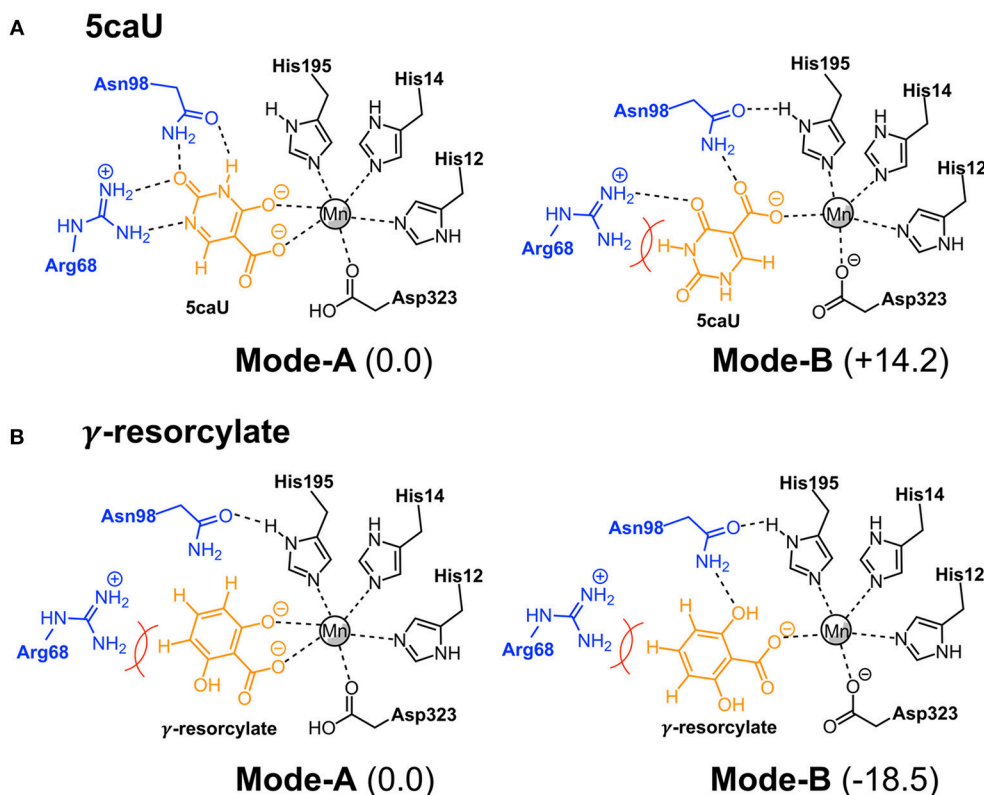
FIGURE 6 | Binding modes of 5caU **(A)** and γ-resorcylate **(B)** in IDCase. Relative energies for each substrate are given in kcal/mol.

reaction mechanism of γ-RSD it was found that the substrate, in addition to the productive binding mode in which it binds to the metal with both the hydroxyl and the carboxylate groups (here called **Mode-A**), it can also bind in an unproductive mode only through the coordination of one oxygen atom of the carboxylate group (called **Mode-B**) (Sheng et al., 2018). Inspired by this, we wondered whether the non-natural substrates would bind to IDCase unproductively, which could explain their lack of reactivity and hence the high substrate specificity observed for this enzyme.

To examine this idea, we compared the energies of the two different binding modes for both the natural substrate 5caU (**1a**) and γ-resorcylate (**6a**) as a representative case of the non-natural substrates. Accordingly, the substrates were placed in the active site manually, and the structures were optimized and the energies evaluated.

For 5caU, **Mode-A** is indeed much more favorable than **Mode-B**, with a calculated energy difference of 14.2 kcal/mol (**Figure 6A**). This is due to the fact that the hydrogen bonding network to the surrounding residues in **Mode-B** is not as optimal as in **Mode-A**. In particular, the hydrogen bonds to Arg68 are broken, which leads to substrate repulsion. Interestingly, in the case of γ-resorcylate the energy trend is reversed and **Mode-B** is now calculated to be 18.5 kcal/mol lower than **Mode-A** (**Figure 6B**). Here, Asn98 plays an important role in forming

favorable hydrogen bonds to the γ-resorcylate in **Mode-B** but not in **Mode-A**. As discussed above, it was previously shown that **Mode-B**, despite its lower energy, is in fact an unproductive binding mode in the reaction of γ-RSD (Sheng et al., 2018). The situation should be similar for IDCase, which could rationalize the lack of decarboxylation activity when using γ-resorcylate and other phenolic carboxylic acids with this enzyme.

Furthermore, to gain insight into the lack of the reverse carboxylation activity of IDCase (see above), it is helpful to compare the obtained energy profile for this enzyme with those of γ-RSD and LigW. As shown in **Figure 3**, IDCase is calculated to have a higher barrier for the overall reaction than γ-RSD and LigW (20.7 kcal/mol for IDCase vs. 16.8 and 14.8 kcal/mol for LigW and γ-RSD, respectively). It is interesting to combine these findings about the barriers with the overall driving forces calculated for the three net reactions catalyzed by these enzymes (corresponding to the reactions of **Scheme 1**)[1]. The calculations show that the decarboxylation reaction of IDCase (**Scheme 1A**) is 11.3 and 7.5 kcal/mol more exergonic than those of γ-RSD (**Scheme 1B**) and LigW (**Scheme 1C**), respectively. This means that the barrier for the reverse carboxylation is much less

---

[1]It is important to emphasize that the driving force corresponds to the net reaction catalyzed by the enzyme and should not to be confused with the energy difference between the enzyme-substrate and enzyme-product complexes.

favorable for IDCase compared to LigW and γ-RSD, which could explain the lack of such activity for IDCase.

CONCLUSIONS

Combined theoretical and experimental techniques have been employed in the present study to determine the metal identity, investigate the reaction mechanism and elucidate the substrate specificity of IDCase. ICPMS/MS measurements demonstrated the IDCase from *C. militaris* contains a catalytically relevant Mn^{2+} ion rather than the previously assumed Zn^{2+} ion. Detailed analysis of the mechanism of action by quantum chemical methods revealed that decarboxylation of the natural substrate (5-carboxyuracil) proceeds via a (reverse) electrophilic aromatic substitution with formation of CO_2, similar to that of γ-RDC and LigW, while previous proposals (yielding HCO_3^-) could be ruled out on the basis of prohibitively high energy barriers. Comparison of the crystal structure of IDCase_Cm with the structures of the related γ-RSD_Ps and LigW_Na, and an energy analysis of different substrate binding modes, suggested that the reason for the unexpected high substrate fidelity of IDCase is due to a specific substrate binding via a hydrogen-bonding network involving the N-H and C=O moieties in its natural substrate 5-carboxyuracil. In contrast to related decarboxylases acting on benzoic acids, possessing a broad substrate tolerance, the (reverse) carboxylation of uracil by IDCase is not feasible, and it is argued to be due to an enhanced energy demand of this uphill reaction.

AUTHOR CONTRIBUTIONS

XS performed the quantum chemical calculations. KP, SP, CE, GH, and SB performed the experimental work. WK, WG, SG, FH, and KF supervised the work. All authors contributed to the analysis of the results and to the writing of the paper.

ACKNOWLEDGMENTS

SUPPLEMENTARY MATERIAL

The Supplementary Material for this article can be found online at: https://www.frontiersin.org/articles/10.3389/fchem.2018.00608/full#supplementary-material

Data sheet 1 | General experimental procedures, preparation of substrates and analytical procedures, HPLC analysis, ICP-MS measurements, structural biology, sequence alignment, computational methods, additional computational results and Cartesian coordinates of optimized structures.

REFERENCES

He, Y., F., Li, B. Z., Li, Z., Liu, P., Wang, Y., Tang, Q., et al., (2011). Tet-mediated formation of 5-carboxylcytosine and its excision by TDG in mammalian DNA. *Science* 333, 1303–1307. doi: 10.1126/science.1210944

Ienaga, S., Kosaka, S., Honda, Y., Ishii, Y., and Kirimura, K. (2013). p-Aminosalicylic acid production by enzymatic Kolbe–Schmitt reaction using salicylic acid decarboxylases improved through site-directed mutagenesis. *Bull. Chem. Soc. Jpn.* 86, 628–634. doi: 10.1246/bcsj.20130006

Ishii, Y., Narimatsu, Y., Iwasaki, Y., Arai, N., Kino, K., and Kirimura, K. (2004). Reversible and nonoxidative gamma-resorcylic acid decarboxylase: characterization and gene cloning of a novel enzyme catalyzing carboxylation of resorcinol, 1,3-dihydroxybenzene, from Rhizobium radiobacter. *Biochem. Biophys. Res. Commun.* 324, 611–620. doi: 10.1016/j.bbrc.2004.09.091

Ito, S., Shen, L., Dai, Q., Wu, S. C., Collins, L. B., Swenberg, J. A., et al. (2011). Tet proteins can convert 5-methylcytosine to 5-formylcytosine and 5-carboxylcytosine. *Science* 333, 1300–1303. doi: 10.1126/science.1210597

Iwasaki, Y., Kino, K., Nishide, H., and Kirimura, K. (2007). Regioselective and enzymatic production of γ-resorcylic acid from resorcinol using recombinant *Escherichia coli* cells expressing a novel decarboxylase gene. *Biotechnol. Lett.* 29, 819–822. doi: 10.1007/s10529-007-9309-6

Leal, J., Squina, F. M., Martinez-Rossi, N. M., and Rossi, A. (2007). The transcription of the gene for iso-orotate decarboxylase (IDCase), an enzyme of the thymidine salvage pathway, is downregulated in the pregc mutant strain of *Neurospora crassa* grown under phosphate starvation. *Can. J. Microbiol.* 53, 1011–1015. doi: 10.1139/W07-064

Lindsey, A. S., Jeskey, H. (1957). The Kolbe-Schmitt reaction. *Chem. Rev.* 57, 583–620.

Matsui, T., Yoshida, T., Yoshimura, T., and Nagasawa, T. (2006). Regioselective carboxylation of 1,3-dihydroxybenzene by 2,6-dihydroxybenzoate

decarboxylase of *Pandoraea* sp. 12B-2. *Appl. Microbiol. Biotechnol.* 73, 95–102. doi: 10.1007/s00253-006-0437-z

Palmatier, R. D., McCroskey, R. P., and Abbott, M. T. (1970). The enzymatic conversion of uracil 5-carboxylic acid to uracil and carbon dioxide. *J. Biol. Chem.* 245, 6706–6710.

Peng, X., Masai, E., Kasai, D., Miyauchi, K., Katayama, Y., and Fukuda, M. (2005). A second 5-carboxyvanillate decarboxylase gene, ligW2, is important for lignin-related biphenyl catabolism in *Sphingomonas paucimobilis* SYK-6. *Appl. Environ. Microbiol.* 71, 5014–5021. doi: 10.1128/AEM.71.9.5014-5021.2005

Peng, X., Masai, E., Kitayama, H., Harada, K., Katayama, Y., and Fukuda, M. (2002). Characterization of the 5-carboxyvanillate decarboxylase gene and its role in lignin-related biphenyl catabolism in *Sphingomonas paucimobilis* SYK-6. *Appl. Environ. Microbiol.* 68, 4407–4415. doi: 10.1128/AEM.68.9.4407-4415.2002

Plasch, K., Hofer, G., Keller, W., Hay, S., Heyes, D. J., Dennig, A., et al., (2018). Pressurized CO2 as carboxylating agent for the biocatalytic ortho-carboxylation of resorcinol. *Green Chem.* 20, 1754–1759. doi: 10.1039/C8GC00008E

Plasch, K., Resch, V., Hitce, J., Popłonski, J., Faber, K., and Glueck, S. M. (2017). Regioselective enzymatic carboxylation of bioactive (poly)phenols. *Adv. Synth. Catal.* 359, 959–965. doi: 10.1002/adsc.201601046

Sato, M., Sakurai, N., Suzuki, H., Shibata, D., and Kino, K. (2015). Enzymatic carboxylation of hydroxystilbenes by the γ-resorcylic acid decarboxylase from Rhizobium radiobacter WU- under reverse reaction conditions. *J. Mol. Catal. B* 122, 348–352. doi: 10.1016/j.molcatb.2015.10.006

Schiesser, S., Hackner, B., Pfaffeneder, T., Müller, M., Hagemeier, C., Truss, M., et al. (2012). Mechanism and stem-cell activity of 5-carboxycytosine decarboxylation determined by isotope tracing. *Angew. Chem. Int. Ed.* 51, 6516–6520. doi: 10.1002/anie.201202583

Seibert, C. M., and Raushel, F. M. (2005). Structural and catalytic diversity within the amidohydrolase superfamily. *Biochemistry* 44, 6383–6391. doi: 10.1021/bi047326v

Sheng, X., Patskovsky, Y., Vladimirova, A., Bonanno, J. B., Almo, S. C., Himo, F., et al. (2018). Mechanism and structure of γ-resorcylate decarboxylase. *Biochemistry* 57, 3167–3175. doi: 10.1021/acs.biochem.7b01213

Sheng, X., Zhu, W., Huddleston, J., Xiang, D. F., Raushel, F. M., Richards, N. G. J., and Himo, F. A. (2017). Combined experimental-theoretical study of the LigW-catalyzed decarboxylation of 5-carboxyvanillate in the metabolic pathway for lignin degradation. *ACS Catal.* 7, 4968–4974. doi: 10.1021/acscatal.7b01166

Smiley, J. A., Angelot, J. M., Cannon, R. C., Marshall, E. M., and Asch, D. K. (1999). Radioactivity-based and spectrophotometric assays for isoorotate decarboxylase: identification of the thymidine salvage pathway in lower eukaryotes. *Anal. Biochem.* 266, 85–92. doi: 10.1006/abio.1998.2935

Smiley, J. A., Kundracik, M., Landfried, D. A., Barnes, V. R. Sr, and Axhemi, A. A. (2005). Genes of the thymidine salvage pathway: thymine-7-hydroxylase from a Rhodotorula glutinis cDNA library and iso-orotate decarboxylase from *Neurospora crassa*. *Biochim. Biophys. Acta* 1723, 256–264. doi: 10.1016/j.bbagen.2005.02.001

Stark, A., Huebschmann, S., Sellin, M., Kralisch, D., Trotzki, R., and Ondruschka, B. (2009). Microwave-assisted Kolbe-Schmitt synthesis using ionic liquids or Dimcarb as reactive solvent. *Chem. Eng. Technol.* 32, 1730–1738. doi: 10.1002/ceat.200900331

Vladimirova, A., Patskovsky, Y., Fedorov, A. A., Bonnano, J. B., Fedorov, E. V., Toro, R., et al. (2016). Substrate distortion and the catalytic reaction mechanism of 5-carboxyvanillate decarboxylase. *J. Am. Chem. Soc.* 138, 826–836. doi: 10.1021/jacs.5b08251

Wuensch, C., Glueck, S. M., Gross, J., Koszelewski, D., Schober, M., and Faber, K. (2012). Regioselective enzymatic carboxylation of phenols and hydroxystyrene derivatives. *Org. Lett.* 14, 1974–1977. doi: 10.1021/ol300385k

Wuensch, C., Gross, J., Steinkellner, G., Lyskowski, A., Gruber, K., Glueck, S. M., et al. (2014). Regioselective ortho-carboxylation of phenols catalyzed by benzoic acid decarboxylases: a biocatalytic equivalent to the Kolbe–Schmitt reaction. *RSC Adv.* 4, 9673–9679. doi: 10.1039/c3ra47719c

Xu, S., Li, W., Zhu, J., Wang, R., Li, Z., Xu, G.-L., et al. (2013). Crystal structures of isoorotate decarboxylases reveal a novel catalytic mechanism of 5-carboxyl-uracil decarboxylation and shed light on the search for DNA decarboxylase. *Cell Res.* 23, 1296–1309. doi: 10.1038/cr.2013.107

Yoshida, T., Hayakawa, Y., Matsui, T., and Nagasawa, T. (2004). Purification and characterization of 2,6-dihydroxybenzoate decarboxylase reversibly catalyzing nonoxidative decarboxylation. *Arch. Microbiol.* 181, 391–397. doi: 10.1007/s00203-004-0668-2

Zheng, H., Chordia, M. D., Cooper, D. R., Chruszcz, M., Müller, P., Sheldrick, G. M., and Minor, W. (2014). Validation of metal-binding sites in macromolecular structures with the CheckMyMetal web server. *Nat. Protoc.* 9, 156–170. doi: 10.1038/nprot.2013.172

Zheng, H., Cooper, D. R., Porebski, P. J., Shabalin, I. G., Handing, K. B., Minor, W. (2017). CheckMyMetal: a macromolecular metal-binding validation tool. *Acta Crystallogr. Sect. D: Struct. Biol.* 73, 223–233. doi: 10.1107/S2059798317001061

Nanomaterials Exhibiting Enzyme-Like Properties (Nanozymes): Current Advances and Future Perspectives

Sanjay Singh*

Division of Biological and Life Sciences, School of Arts and Sciences, Ahmedabad University, Ahmedabad, India

Biological enzymes are macromolecular catalysts that catalyze the biochemical reactions of the natural systems. Although each enzyme performs a particular function, however, holds several drawbacks, which limits its utilization in broad-spectrum applications. Natural enzymes require strict physiological conditions for performing catalytic functions. Their limited stability in harsh environmental conditions, the high cost of synthesis, isolation, and purification are some of the significant drawbacks. Therefore, as an alternative to natural enzymes, recently several strategies have been developed including the synthesis of molecules, complexes, and nanoparticles mimicking their intrinsic catalytic properties. Nanoparticles exhibiting the properties of an enzyme are termed as "nanozymes." Nanozymes offer several advantages over natural enzymes, therefore, a rapid expansion of the development of artificial biocatalysts. These advantages include simple methods of synthesis, low cost, high stability, robust catalytic performance, and smooth surface modification of nanomaterials. In this context, nanozymes are tremendously being explored to establish a wide range of applications in biosensing, immunoassays, disease diagnosis and therapy, theranostics, cell/tissue growth, protection from oxidative stress, and removal of pollutants. Considering the importance of nanozymes, this article has been designed to comprehensively discuss the different enzyme-like properties, such as peroxidase, catalase, superoxide dismutase, and oxidase, exhibited by various nanoparticles.

Keywords: nanozymes, peroxidase, oxidase, superoxide dismutase, metalloenzymes

INTRODUCTION

Recent expansions in the area of nanotechnology have led to an exponential growth in development of nanomaterials exhibiting natural enzyme-like activities (Nanozymes), possessing several advantageous merits (Wei and Wang, 2013). Natural enzymes require strict physiological conditions for performing catalytic functions. Their limited stability in harsh environmental conditions, the high cost of synthesis, isolation, and purification are some of the significant drawbacks. Unlike natural enzymes, nanozymes offer unflinching biocatalytic activity even in the extreme conditions of pH, temperatures and resistance to the digestion from proteases. Therefore, it was imperative to develop efficient alternatives for artificial enzymes. Thus, in recent years, researchers have focused on utilizing the catalytic powers of chemical molecules, such as

cyclodextrins, metal-complexes, porphyrins, polymeric, and supramolecules, as alternatives to natural enzymes (Jeon et al., 1998; Raynal et al., 2014). However, the catalytic efficiency and biocompatibility were some of the harboring concerns with these molecules.

In this pursuit, the discovery of iron-oxide-based artificial peroxidase enzyme was reported by Gao et al. (2007). It was the first report to show that, similar to natural horseradish peroxidase enzyme, the inorganic nanoparticles could also exhibit the oxidation of typical peroxidase substrates and could be used for antibody-based identification, separation, and detection of analytes of interest. Subsequently, several nanomaterials (metallic, metal oxides, and carbon-based nanoparticles) were investigated for possessing intrinsic biological enzyme-like catalytic activities, predominantly, catalytic activities similar to peroxidase, oxidase, catalase, and superoxide dismutase enzymes (Karakoti et al., 2010; Pirmohamed et al., 2010; Singh, 2016; Karim et al., 2018; Zhang et al., 2018; Zhao et al., 2018). This rapid expansion in nanozyme research was possible due to the several advantages inorganic nanoparticles possess over natural enzymes, such as simple methods of synthesis, low cost, high stability, robust catalytic performance, and smooth surface modification. Therefore, nanozymes are being widely explored to establish a wide range of applications in biosensing, immunoassays, disease diagnosis and therapy, theranostics, cell/tissue growth and proliferation, protection from oxidative stress, and removal of pollutants (Xie et al., 2012; Lin et al., 2014; Zhou et al., 2017). Broadly, the nanozymes that have been discovered so far can be divided into two categories, antioxidants and pro-oxidants, considering their functions as either scavenging the free radicals or generating free radicals during the catalytic reaction, respectively.

ANTIOXIDANT NANOZYMES

In the biological system, antioxidants are required to protect the cells/tissues from damage imposed by the excess of free radicals, generated during the normal biochemical reactions of the body. The human body has a well-established endogenous antioxidant system, which is mostly orchestrated by free radical scavenging enzymes such as catalase, superoxide dismutase (SOD), glutathione peroxidase, glutathione reductase, peroxiredoxins, etc. Among inorganic antioxidants, cerium oxide nanoparticles (CeNPs) are reported by Self and colleagues to exhibit scavenging of superoxide radicals and degradation of hydrogen peroxide under *in vitro*, *in vivo*, and other animal models (Korsvik et al., 2007; Heckert et al., 2008a; Karakoti et al., 2009).

The below section will comprehensively cover the overview of nanoparticles reported to exhibit antioxidant enzyme-like activities.
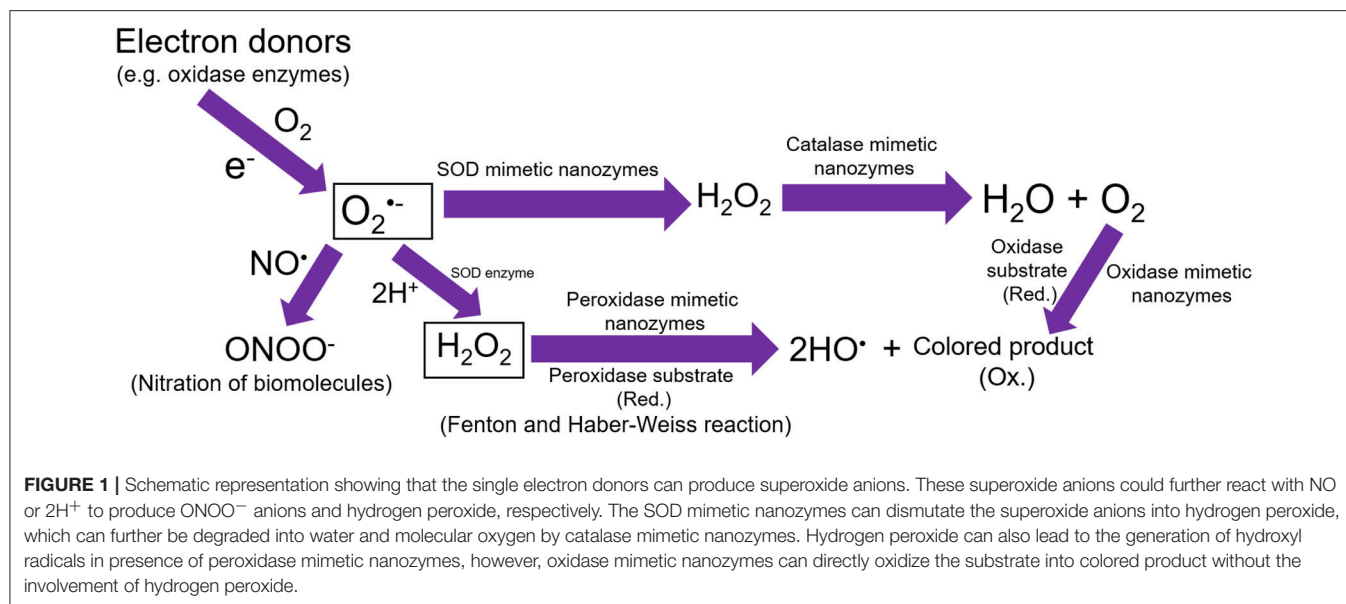
Superoxide Dismutase Mimetic Nanoparticles

SOD enzyme is one of the unique antioxidant enzymes, and not many nanoparticle types have been developed to exhibit the superoxide anions scavenging activity, except CeNPs. Therefore,

this subsection will mainly focus on the CeNPs and their SOD enzyme-like activities. Our research group has also done comprehensive research on the mechanism of protection of mammalian cells stressed with high superoxide radicals (SOD mimetic activity) and hydrogen peroxide (catalase mimetic activity) (Singh et al., 2016; Patel et al., 2018; Rather et al., 2018). Mechanistically, it has reported with substantial evidence that the high Ce^{+3}/Ce^{+4} ratio of surface "Ce" atoms from CeNPs exhibit SOD mimetic activity, whereas, the lower ratio of Ce^{+3}/Ce^{+4} leads to the catalase mimetic activity (Dhall and Self, 2018) (**Figure 1**). Since the natural SOD enzyme plays a vital protective role in the scavenging of superoxide anions, however, its short-term stability and the high cost of synthesis creates an opportunity to develop an efficient alternative. In one such effort, manganese-containing biscyclohexylpyridine complex (M40403), was synthesized, which exhibited SOD enzyme-like activities but only to a certain extent (Muscoli et al., 2003). Inspired by this discovery, Seal and Self groups first reported the use of CeNPs as an alternative to SOD enzyme with better catalytic efficiency (Heckert et al., 2008a; Karakoti et al., 2009, 2010). Through kinetics, authors also state that CeNPs (3–5 nm) showed better SOD mimetic activity than native CuZn SOD (rate constant: 3.6×10^9 M^{-1} s^{-1} and 1.1×10^5 M^{-1} s^{-1}, respectively) (Korsvik et al., 2007). When comparing the catalytic efficiency of single CeNP with the most recently calculated rate constant of CuZn SOD (~ 1.3–2.8×10^{-9} $M^{-1}s^{-1}$) for their SOD activity, the former showed better scavenging of superoxide radicals than the authentic enzyme itself. The superoxide anion scavenging ability of the CeNPs has also been confirmed by electron paramagnetic resonance (EPR) measurements, and the possible dismutation of superoxide radicals by CeNPs could be catalyzed as follows.

$$O_2^{\bullet -} + Ce^{+4} \rightarrow O_2 + Ce^{+3}$$

$$O_2^{\bullet -} + Ce^{+3} + 2H^+ \rightarrow H_2O_2 + Ce^{+4}$$
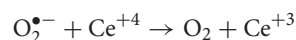
It has also been reported that CeNPs show an auto-regeneration process, whereby nanoparticles regenerate the Ce^{+3} oxidation state atoms from oxidized Ce^{+4} atoms (during the superoxide radical dismutation process), within a few days, which further makes CeNPs ready to neutralize another superoxide radical. Although some initial studies have reported that CeNPs could also scavenge hydroxyl radicals, however, any conclusive data was not shown as their EPR data suggest that CeNPs does not neutralize hydroxyl radicals (Heckert et al., 2008b; Zou et al., 2018). Our group has found that CeNPs have a high affinity for superoxide radicals and therefore eliminate them efficiently. In one of our recent studies, we explored the antioxidant and concomitant anti genotoxic nature of CeNPs toward the oxidative insult generated by buthionine sulfoximine (BSO) in human keratinocytes (HaCaT cells) (Singh et al., 2016). It is reported that BSO inhibits the synthesis of the γ-glutamylcysteinesynthetase enzyme, which leads to the depletion of glutathione (GSH), thus

FIGURE 1 | Schematic representation showing that the single electron donors can produce superoxide anions. These superoxide anions could further react with NO or $2H^+$ to produce $ONOO^-$ anions and hydrogen peroxide, respectively. The SOD mimetic nanozymes can dismutate the superoxide anions into hydrogen peroxide, which can further be degraded into water and molecular oxygen by catalase mimetic nanozymes. Hydrogen peroxide can also lead to the generation of hydroxyl radicals in presence of peroxidase mimetic nanozymes, however, oxidase mimetic nanozymes can directly oxidize the substrate into colored product without the involvement of hydrogen peroxide.

negatively modulates the cellular redox potential. Our results suggested that CeNPs can protect HaCaT cells from BSO-induced oxidative damage when cells were pre-incubated with CeNPs. We estimated the cell survival and intracellular levels of ROS, release of lactate dehydrogenase enzyme (due to membrane damage), and nuclear fragmentation.

Further, the study of the expression of antioxidant genes and proteins, [thioredoxin reductase (TrxR) and peroxiredoxin 6 (Prx6)] showed that, due to pretreatment of CeNPs, there was limited need for the induction of these antioxidant genes and concomitant enzymes involved in the defense against oxidative stress. Although CeNPs are the most studied and well-established nanozyme exhibiting SOD enzyme-like activity, Platinum nanoparticles (PtNPs) encapsulated in apo-ferritin have also been shown to exhibit SOD enzyme-like activities (Jawaid et al., 2014; Liu et al., 2014). PtNPs retain their SOD mimetic activity in cell culture models; however, the overall efficiency was reported to be significantly lower than CeNPs (on the weight basis). Growing evidence reports several applications of CeNPs toward the protection of cell culture and animal models from free radicals, and concurrently argues for the antioxidant role of CeNPs. However, many of these reports do not confirm the type of activity (either SOD or catalase) of CeNPs, which could be due to the poor characterization. Dugan and co-workers (Ali et al., 2004, 2008) have shown that fullerenes (C60) and their derivatives can also exhibit the SOD enzyme-like activities. Using EPR studies, they found that fullerenes could also scavenge the superoxide anions as well as hydroxyl radicals with almost the same efficiency. Exposure of these fullerenes to *in vitro* cultured cortical neurons imparted protection against the toxic effects induced by N-methyl D-aspartate. Fullerenes protected the Ab-peptide by the scavenging of the superoxide radicals thus the neurotoxicity was also significantly reduced. Authors later reported a tris-malonic acid derivative of the fullerene molecule that has lower efficiency than natural SOD enzyme,

with a comparable rate constant of $[k_{(fullerene)}]$ of 2×10^6 mol^{-1} s^{-1}], about 100-fold slower than the SOD enzyme (Ali et al., 2004).

Catalase Mimetic Nanoparticles

Biological catalase enzyme catalyzes the decomposition of the excess of cellular hydrogen peroxide into water and molecular oxygen. Generally, the dismutation of superoxide radicals by SOD enzyme leads to the generation of hydrogen peroxide. Owing to the significant role of hydrogen peroxide toward either biological signaling or production of extremely reactive hydroxyl radicals, it is a stable and less reactive species in the cytoplasm. It is well-established that hydrogen peroxide undergoes "Fenton reaction" in the presence of any transition metal ions and forms hydroxyl radicals, which are detrimental to biological molecules [(Heckert et al., 2008b; Leifeld et al., 2018)]. Therefore, it is essential that the excess of cytoplasmic hydrogen peroxides must be converted to water and molecular oxygen using catalase enzyme. However, in the absence of functional catalase enzyme, the excess of hydrogen peroxides could give rise to several diseases, such as acatalasemia, diabetes, and vitiligo. Therefore, an alternative to biological catalase is imperative, and researchers have developed several types of nanoparticles exhibiting catalase enzyme-like activities including cerium oxide, iron oxides, gold nanoparticles (AuNPs), and Cobalt oxide nanoparticles (Mu et al., 2014; Wang et al., 2016; Zhang et al., 2017; Bhagat et al., 2018; Vallabani and Singh, 2018). Among several types of nanomaterials reported, CeNPs (high $Ce^{+4}/{+3}$ ratio), and iron oxide nanoparticles have been studied in detail. Recently, we have investigated the alteration in catalase mimetic activity of CeNPs when suspended in biologically relevant buffers, and our results show that unlike SOD mimetic CeNPs (high $Ce^{+3}/{+4}$ oxidation state), catalase mimetic CeNPs (high $Ce^{+4}/{+3}$ oxidation state) are robust and do not compromise their catalytic activity (Singh and Singh, 2015).

The degradation of hydrogen peroxide by CeNPs can be represented as follows:

$$2H_2O_2 + Ce^{+4} \rightarrow 2H_2 + 2O_2 + Ce^{+3}$$
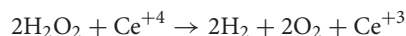
Our recent study suggests that catalase mimetic CeNPs can protect hepatic cells from cytotoxicity and genetic damage induced from the elevated concentrations of hydrogen peroxide in the absence of functional cellular catalase enzyme. Human hepatic cells were exposed with 3-aminotriazole (3-AT) to artificially inhibit the function of cellular catalase enzyme, which resulted in the high level of hydrogen peroxide accumulation. Results reveal that CeNPs can protect hepatic cells from 3-AT mediated early apoptosis and DNA damage (Singh and Singh, 2019). The genomics and proteomics studies revealed that CeNPs did not elicit the natural antioxidant defense system of the hepatic cells even in the absence of functional catalase enzyme, which suggested that the cellular protection was solely due to the hydrogen peroxide degradation by catalase mimetic CeNPs. This finding demonstrates the reinforcement of CeNPs as pharmacological agents for the treatment of diseases related to nonfunctional biological catalase enzyme in the mammalian cells.

Additionally, there are few hydrolytic nanozymes reported to hydrolyze the toxic biological agents such as neurotoxic organophosphates. In an attempt, Khulbe et al. (2018) showed the development of Zr-incorporated CeO_2 nanocatalyst for efficient hydrolysis of nerve agents such as methyl paraoxon to less toxic monoesters. It was a first report showing a nanozymes catalyzing a two-step hydrolysis reaction with a faster catalytic rate ($t_{1/2}$ value of 1.2 and 3.5 min for methyl paraoxon and methyl parathion hydrolysis, respectively) than the single-step hydrolysis reaction reported earlier by others. Thiol passivated AuNPs have also been found to exhibit hydrolytic enzyme-like activities by following the hydrolytic cleavage of phosphate diester bonds from DNA. Cleavage of plasmid DNA by AuNPs resulted in the conversion of the compact supercoiled conformation of the plasmid (form I) to the relaxed circular (form II), due to a cut in one of the two strands leading to a remarkable change in mobility of the nicked plasmid during electrophoresis (Mancin et al., 2016).

Iron oxide nanoparticles are also reported to exhibit catalase enzyme-like activities, however, strong supporting literature has not been developed so far. Chen et al. have recently reported that iron oxide nanoparticles show a pH (7.4) dependent nanozymatic activity (Chen et al., 2012), however, at acidic pH peroxidase enzyme-like activity was reported. Using EPR studies, authors confirmed that hydroxyl radical formation occurs at acidic pH but not at neutral pH, suggesting that at acidic conditions iron oxide nanoparticles show "Fenton-like chemistry." This observation was further supported by their cellular toxicity studies, where iron oxides entrapped in acidic lysosomes undergo hydroxyl radical formation and thus induce cell death, however, iron oxide nanoparticles dispersed in cytoplasm did not cause any harm to cells. The latter effect could be due to the catalase-like activity of iron oxide nanoparticles in neutral pH cytoplasm.

Although there have been several such studies with a variety of nanoparticles showing biological catalase enzyme-like activities, however, limited to the *in vitro* studies. Further validation into higher order *in vivo* experimental models is imperative in order to explore the potentials of antioxidant nanoparticles. Further, detailed elucidation of the mechanism of antioxidant activity of nanozymes in biological systems would assist their broad applications in biomedicine.
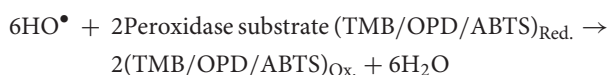
PRO—OXIDANT NANOZYMES

The term "pro-oxidant nanozymes" refers to the action of nanozymes which induces oxidative stress by producing free radicals in mammalian cells or inhibiting their antioxidant system. Common drugs such as analgesic paracetamol and anticancerous methotrexate are known to generate free radicals and therefore considered as pro-oxidants. Similarly, transition metals such as Iron and Copper etc. are also reported to undergo Fenton reaction and Haber-Weiss reaction, and subsequently produce excessive free radicals (Rahal et al., 2014). Therefore, nanozymes catalyzing the reactions (such as peroxidase and oxidase), which involves the generation of free radicals, can also be regarded as pro-oxidant nanozymes.

Peroxidase Mimetic Nanoparticles

Natural peroxidases consist of a large family, and they predominantly utilize hydrogen peroxide to oxidize peroxidase substrates. Peroxidase enzymes are of considerable importance because they act as detoxifying agents for free radicals (e.g., glutathione peroxidase) and also facilitate the defense against invading pathogens (e.g., myeloperoxidase) (Strzepa et al., 2017). Further, HRP is well known for their applications in bioanalytical and clinical chemistry, for the conversion of colorless substrate into colored product leading to the detection of analytes. We and others have recently shown that specific nanomaterials can exhibit peroxidase enzyme like catalytic activities. A schematic representation of peroxidase activity exhibited by nanozymes has been shown in **Figure 1**. Although iron oxides are predominantly reported to have excellent peroxidase enzyme-like activity, other nanomaterials have also received considerable attention. The very first report by Gao et al. showed that different sizes of iron oxide nanoparticles (30, 50, and 300 nm) could oxidize the colorless TMB into a blue colored product in the presence of hydrogen peroxide at acidic pH (Gao et al., 2007). However, the smaller sized particles could exhibit higher peroxidase-like activity than corresponding bigger sized ones. Authors compared the peroxidase activity of iron oxide nanoparticles with natural HRP enzyme and found that in both cases it was dependent on the reaction temperature and pH. However, unlike HRP, the nanoparticles remain stable and retain their catalytic activity after the incubation at a broader range temperature [4–90°C and pH (1–12)]. The kinetic analysis revealed that the substrate affinity (Km) value of iron oxide nanoparticles with hydrogen peroxide was higher than HRP (154 and 3.7 mM, respectively), suggesting that a higher concentration of hydrogen peroxide is needed to obtain the maximum activity for iron oxide nanoparticles.

Further, the Km value of iron oxide nanoparticles with TMB was about four times lesser than HRP (0.098 and 0.43 mM, respectively), suggesting that nanoparticles have a higher affinity for the substrate (TMB) than HRP, therefore, at the same molar concentrations, nanoparticles showed 40 times higher activity than HRP. Soon after this work, several reports have been published on the peroxidase activity and related sensing and detection applications of iron oxide and other nanoparticles. Among them, Wei and Wang developed a unique sensing platform for the detection of hydrogen peroxide and glucose using iron oxide nanoparticles as a peroxidase mimic (Wei and Wang, 2008). The results of these studies stimulated rapid expansion in the use of iron oxide nanoparticles as an alternative of peroxidase enzyme and researchers across the world use them for different applications. Among iron oxide nanoparticle types, magnetite nanoparticles have grabbed most attention and thus been studied extensively. There are several more types of iron-based nanomaterials which are reported to exhibit peroxidase-like activity. Among them, Fe-S nanosheets were prepared by a micelle-assisted strategy and their peroxidase activity was studied. It was argued that due to the large surface area of nanosheets, the peroxidase activity was found to be better than that of corresponding spherical nanoparticles of Fe-S (Dai et al., 2009). Similarly, Fe-S nanoneedles are also shown to have better peroxidase activity than spherical Fe-S nanoparticles (Dutta et al., 2012).

Additionally, FeTe nanorods demonstrated better peroxidase activity than spherical iron oxide nanoparticles. Thus, these studies suggest that the shape and size of nanoparticles significantly governs the peroxidase activity of nanozymes. Other nanomaterials such as nanostructured layered double hydroxide (LDH) and CuS superstructures are also reported to exhibit excellent peroxidase-like activity, which has been translated into constructing electrochemical and colorimetric sensors (He et al., 2012; Zhang et al., 2012). The peroxidase mimetic activity exhibited by nanozymes could be catalyzed by following two steps:

$$3H_2O_{2+} \text{ Peroxidase mimetic nanozymes} \rightarrow 6HO^\bullet$$

$$6HO^\bullet + 2\text{Peroxidase substrate (TMB/OPD/ABTS)}_{Red.} \rightarrow 2(\text{TMB/OPD/ABTS})_{Ox.} + 6H_2O$$

All of the studies reporting intrinsic peroxidase-like activity of iron oxide nanoparticles have shown that acidic pH (pH 4.0) is one of the fundamental requirements driving the oxidation of peroxidase substrates (TMB, OPD, ABTS), which finally results in corresponding colorimetric product formation used in the detection of a variety of analytes. Therefore, the detection sensitivity is significantly dependent on the ability of oxidation of peroxidase substrate by iron oxide nanoparticles in the presence of hydrogen peroxide. The limited sensitivity and pH condition constraint is a major limitation with the sensing of biomolecules at physiological pH. In this context, we have recently developed a strategy which can avoid the fundamental limitation of acidic pH of peroxidase reaction and shift the optimum pH for peroxidase activity of iron oxide nanoparticles at physiological pH by using ATP (Vallabani et al., 2017). We found that in the presence of ATP, iron oxide nanoparticles exhibit strong peroxidase activity at physiological pH. It was clear that ATP facilitates the single electron transfer reaction, through complexation with iron oxide nanoparticles, which leads to the generation of hydroxyl radicals responsible for enhanced peroxidase activity at physiological pH. Iron oxide nanoparticles showed higher affinity to TMB (Km = 0.37 mM) at pH 7.4 than at pH 4.0 (Km = 0.43 mM). Nanoparticles also showed higher affinity to hydrogen peroxide (Km = 54.6 mM) than HRP (Km = 3.7 mM), whereas higher reaction velocity (4.83 times) than HRP. We also utilized this strategy to develop a single step detection of glucose with a detection limit of 50 µM. This method was further extended to monitor glucose levels in human blood serum within 5 min at pH 7.4. AuNPs are also reported to exhibit peroxidase-like activity, which has been used for the detection of several biomolecules. Our research group has shown that the peroxidase-like activity of AuNPs (30 nm) can be improved by at least three-fold in the presence of ATP (Shah et al., 2015). Mechanistically, we found that negatively charged ATP facilitates to stabilize positively charged, oxidized TMB through a simple electrostatic interaction. A similar observation has also reported with the use of ionic liquids, which are high viscosity liquids, to improve the thermal stability of oxidized products but completely inhibit the enzyme-like activity of nanoparticle (Lin et al., 2013). Therefore, ATP can be used for selectively boosting the peroxidase-like activity of nanomaterials, which can subsequently be translated into the sensitive detection of analytes. V_2O_5 nanowires are also reported to exhibit intrinsic peroxidase activity, following the similar catalytic reactions as described above. André et al. (2011) have recently reported V_2O_5 nanowires showing an exceptional peroxidase reaction with a turnover frequency (k_{cat}) of 2.5×10^3 s^{-1}. The reported Km values of the nanowires for the oxidation of ABTS and hydrogen peroxide was found to be 0.4 and 2.9 µM, respectively at pH 4.0. These values are significantly smaller than the reported kinetic values of HRP reported earlier. Another report by Natalio et al. shows that the peroxidase activity of V_2O_5 nanozymes could be used for a potential alternative to conventional anti-biofouling agents to avoid marine biofouling (Natalio et al., 2012). Several other types of bimetallic and composite nanomaterials are reported to show excellent peroxidase enzyme-like activity, thus illustrate the growing interest and efforts for developing novel nanozymes to efficiently catalyze the biological reactions.

Oxidase Mimetic Nanoparticles

The reactions catalyzed by oxidase enzyme involve oxidation of the substrate by molecular oxygen, which is converted into water or hydrogen peroxide. Unlike the peroxidase reaction, oxidase enzymes do not require hydrogen peroxide, instead they produce H_2O_2 and in some cases superoxide radicals. Due to the *in situ* generation of hydrogen peroxide and superoxide radicals, oxidase enzyme and nanozymes imitating this oxidase activity can efficiently oxidize the colorless substrates into corresponding

color products, which makes them ideal agents for detection of biological or chemical molecules. Recently several nanomaterials are reported to exhibit oxidase enzyme-like activities (Luo et al., 2010; Cao and Wang, 2011; Fan et al., 2011; He et al., 2011; Wan et al., 2012; Shah et al., 2018). A schematic representation of oxidase activity exhibited by nanozymes has been shown in **Figure 1**.

It is well documented that the properties of nanoparticles can be tuned by altering their methods of synthesis, surface modification, size, shape, and even composition. Researchers have utilized these strategies to develop materials with different properties and activities, including the nanozymatic activities. In this context, based on the variation in $Ce^{+3/+4}$ ratio, CeNPs are reported to show SOD, and catalase-like activities (discussed above), however, coated with dextran showed oxidase mimicking properties (Asati et al., 2009, 2011). Authors have shown that oxidase mimicking CeNPs could oxidize several colorimetric substrates (ABTS, TMB, and DOPA) under acidic pH in the absence of hydrogen peroxide. The oxidase activity of CeNPs was reported to be dependent on pH, size and dextran coating thickness. The reaction kinetics of CeNPs was compared with HRP and a faster rate constant for the nanozyme was observed ($1-7 \times 10^{-7}$ $M^{-1}s^{-1}$ of CeNPs than 1×10^{-8} $M^{-1}s^{-1}$ of HRP). Later, Perez and co-workers utilized the oxidase activity of CeNPs for the development of an assay, for the detection of lung tumor cells. Authors conjugated CeNPs with poly (acrylic acid) (PAA) and subsequently functionalized by folic acid. This conjugate was specifically able to recognize lung tumor cells (A549 cell culture model), which selectively express the elevated levels of folate receptors.

In addition to CeNPs, few other nanoparticles have recently been studied for oxidase-like properties. Among them Fe_2O_3 nanowires were reported to exhibit oxidase enzyme-like activity, and a glucose sensor was developed by fabricating an array of Fe_2O_3 nanowires. This system showed a linear range of glucose detection (0.015–8 mM) with a limit of detection of 6 mM (Cao and Wang, 2011). We have also reported the synthesis of Fe-Pt alloy nanoparticles using non-ionic surfactant polyoxyethylene cholesteryl ether. These alloy NPs exhibited a robust oxidase enzyme-like activity with about 10-folds of the reaction velocity compared to the other oxidase mimicking nanoparticles reported. Analysis of kinetic parameters (Km and Vmax) of Fe-Pt alloy nanoparticles revealed that the Km value for the affinity between the substrate (TMB) and Fe-Pt alloy NPs is 0.03 mM, suggesting that the affinity with the substrate is lower than the other compared Pt-based bi-metallic nanoparticles. However, the reaction velocity (Vmax) was found at 1.42×10^{-5} mM/s, ten-folds higher than the most Pt-based catalytic nanoparticles (8.3×10^{-6} and 0.26×10^{-5} for Au-Pt and Pd-Pt alloy nanoparticles, respectively) (He et al., 2011; Zhang et al., 2011).

A biocompatibility study revealed that these NPs are nontoxic to human liver cells (up to 150 μM), suggesting that they hold strong potential to be used for multiple biomedical applications (Karakoti et al., 2010). Another report showed that MnO_2 nanowires could also show oxidase enzyme-like activity. These nanowires were further conjugated with antibodies and
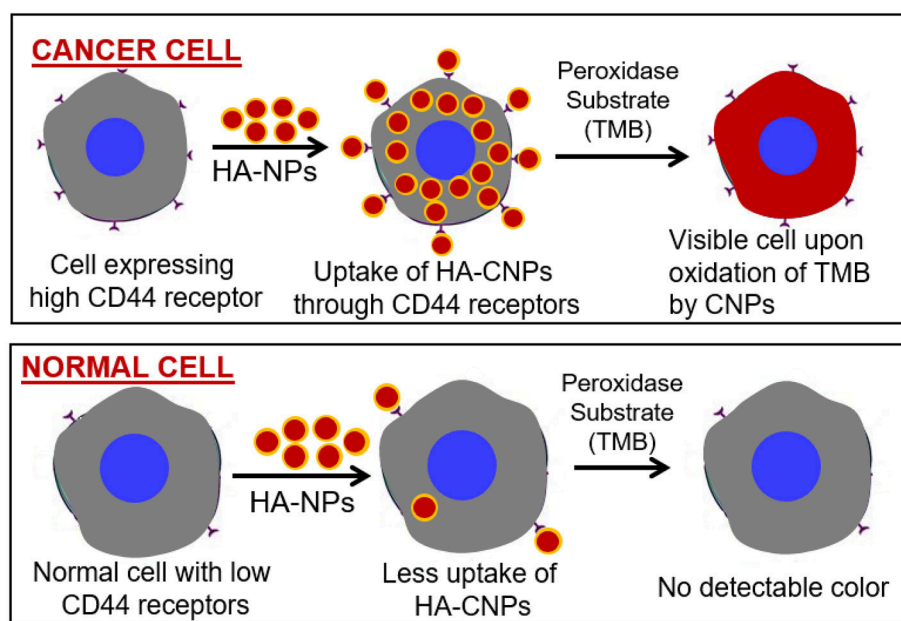

FIGURE 2 | Peroxidase enzyme mimetic nanozymes can differentiate between cancer and normal cells. Peroxidase mimetic cerium oxide nanoparticles (CNPs) coated with HA can bind with the CD44 receptors expresses selectively on cancer cells. During peroxidase reaction these nanoparticles could convert the peroxidase substrate into colored product leading to the identification of cancer cells. Due to the low expression of CD44 receptors on normal cells, peroxidase mimetic nanoparticles would not be attached with cells and thus exhibit no peroxidase reaction.

utilized for development of an immunoassay of sulfate-reducing bacteria. A MnO_2 incorporated immunoassay platform showed better pathogen detection performance than HRP-based ELISA, although both methods showed good sensitivity and high selectivity toward bacteria (Wan et al., 2012).

Rossi and co-workers reported the oxidase enzyme-like activity in citrate-capped AuNPs by catalyzing the aerobic oxidation of glucose with dissolved oxygen, in a similar reaction catalyzed by an oxidase enzyme (Comotti et al., 2004; Beltrame et al., 2006). This report was surprising as other metallic nanoparticles, such as Ag, Cu, Pt, and Pd, did not show any significant oxidase-like activity. However, authors reported the Eley-Rideal mechanism of catalysis, which supports the hypothesis of glucose being adsorbed on the AuNPs surface followed by reaction with molecular oxygen. This reaction produces gluconic acid and hydrogen peroxide by following the typical Michaelis–Menten reaction kinetics. Through kinetic parameter analysis authors reported that native enzyme was ∼55 times more active than the AuNPs-based nanozyme. Later, Fan et al. (2011) developed an innovative microRNA sensing technology utilizing the oxidase mimicking activity of AuNPs. Considering the different affinities of AuNPs for ssDNA and dsDNA, and the coupling of the system with HRP, the colorimetric or chemiluminescent signals were generated, which could offer the detection of single-base-pair mismatch differentiation (Luo et al., 2010; Zheng et al., 2011).

SUMMARY AND FUTURE PROSPECTS

Although it is well established that nanozymes possess several distinct advantages over natural enzymes as well as other reported artificial enzymes, they still face several limitations. These issues need to be addressed to utilize their biomedical potential to the fullest. Nanozymes hold all the physicochemical and optoelectronic properties of nanomaterials including size, shape, and composition-dependent unique properties. The interesting plasmonic properties of noble metal nanoparticles and superparamagnetic properties of iron oxide and other magnetic nanoparticles could be developed into an efficient theranostic system. Recent developments in the novel and easy surface modification strategies of nanoparticles could be used for surface decoration of nanozymes with targeting ligands for identification of the cells/tissues of interest. Efforts have been made to develop such multifunctional nanozymes; however, such materials frequently lose the catalytic effect upon surface modification. It is of prime importance to investigate the possible alteration of nanozymes activity upon dispersing them into biologically relevant buffers. With SOD mimetic CeNPs, we have observed that nanoparticles lose their SOD-like activity when dispersed in phosphate buffer (pH 7.4) (Singh et al., 2011). Mechanistically, it was found that "Ce" has a very high affinity for phosphate anions, producing cerium phosphate, which does not show SOD mimetic activity.

Similarly, the catalytic activity of other nanozymes must also be investigated when dispersed in relevant buffers, to achieve any biological application. Therefore, strategies which could produce nanozymes coated with desired biomolecules without

any significant drop in catalytic activity could be developed for sensing applications. For example, peroxidase activity mimicking nanoparticles, coated with hyaluronic acid (HA), could be used to identify the CD44 overexpressing cancer cells by merely performing a peroxidase reaction (**Figure 2**).

The catalytic efficiency of most nanozymes is still poorer than natural enzymes and other organic catalysts. Therefore, in the near future, efforts must be devoted toward developing high-performance nanozymes. Some progress has already been made in this direction. We and others have identified few molecules which can efficiently boost the catalytic activity of nanozymes (Simos et al., 2012; Wang et al., 2017; Shah and Singh, 2018). Wang et al. (2017) have shown that the peroxidase-like activity of porous $LaNiO_3$ nanocubes was improved by inducing its +3 oxidation state in $LaNiO_3$ perovskite. The peroxidase-like activity of porous $LaNiO_3$ perovskite with Ni^{+3} was ∼58-folds, which was ∼22-folds higher than that of NiO with Ni^{+2} and Ni nanoparticles with Ni^0.

Biological enzymes are highly selective to their targets; however, nanozymes show limited selectivity toward their substrates. For example, most of the nanozymes showing peroxidase-like activity are reported to be used for glucose detection. The activity seen is mainly due to the glucose oxidase enzyme, rather than peroxidase active nanozymes. Therefore, efforts must be devoted to developing nanozymes of high selectivity toward the given substrates. Interestingly, Dhall et al. (2017) have shown that tungstate and molybdate can inhibit the phosphatase activity without altering the oxidative state of CeNPs, however, this did not affect the catalase activity of nanoparticles. These observations suggest that nanozymes do have specific reaction hot-spots on their surface which undergo catalytic reactions. Therefore, it might be possible to inhibit one of the catalytic activities from the nanozymes exhibiting multiple enzyme-like properties. There are metabolic processes orchestrated by multienzyme complexes, which offer several advantages over individual enzyme-catalyzed reactions. However, a functional nanozyme with multiple enzyme-like activities is still limited. Therefore, synthesis of such multifunctional nanozymes would be the hot topic of study in this area. We have reported the synthesis of a multifunctional enzyme consisting of Gold (core)-CeO_2 (shell) nanoparticles (Au/CeO_2 CSNPs) exhibiting peroxidase, catalase, and superoxide dismutase enzyme-like activities. The nanozyme activities could be tuned simply by varying the reaction pH.

Further, the kinetic parameters of peroxidase reaction shown by nanozyme were comparable to natural HRP enzyme. Additionally, the functional assemblies of several individual nanozymes together would also open new paradigms for development of nanozymes with synergistic catalytic activity of different components (Wilner et al., 2009). More of these developments would open new directions for the development of single platform sensors and theranostics, which could be applicable in multiple biosensing and biomedical applications. Most of the nanozymes are reported to exhibit their catalytic activity by redox activity by surface atoms. However, the catalytic activity may be further improved by manipulating the core of the nanozymes by doping with some rare-earth elements. Such

strategies would add more redox "hot-spots" for catalytic activity and thus enhance the activity of nanozymes.

Unlike natural enzymes, the size and composition of most nanozymes are not uniform, with the exception of fullerene-based nanozymes. Further, batch-to-batch variation in size and shape of nanoparticles/nanozymes, and thus alterations in physicochemical properties, requires increased focus on improving the synthesis protocol in order to produce the monodispersed nanozymes with atomically precise structures. The rational design of an atomically precise nanozyme for a specific activity could be achieved by advanced computation-assisted technology. So far there are only limited types of enzymatic activities (SOD, peroxidase, catalase, and oxidase) which can be performed by nanozymes; therefore, nanozyme research needs to broaden more to cover other types of enzyme activities. Such efforts will help realize the clinical potential of nanozymes in nanomedicines, biotechnology, and other related areas.

Above all, the safety concerns of nanomaterials are currently receiving considerable attention due to their possible effects on human health and environment (Mahmoudi et al., 2011; Horie et al., 2012). "Safe-by-design" approach for nanomaterial/nanozyme synthesis could be utilized to develop biocompatible materials. Additionally, the coating of biocompatible polymers such as polyethylene glycol and dextran over the nanoparticles surface has been reported to impart biocompatibility. For example, dextran-coated iron oxide nanoparticles (Resovist) have been approved by the US Food and Drug Administration for clinical use. Therefore, more such nanozymes must be developed as a biocompatible catalyst for biomedical applications.

CONCLUSION

The comprehensive summary of this review suggests that nanozymes are an emerging technology having the enormous potential of biomedical applications. Although the current literature of nanozymes has mostly covered the mimicking of four types of biological enzymes (SOD, catalase, oxidase, and peroxidase), nanozymes with other enzyme-like activities need to be synthesized. Antioxidant nanozymes have been shown to protect mammalian cells from the oxidative stress; however, pro-oxidant nanozymes are explored to use them in biosensing, and other immunoassays. Although most of the current nanozyme literature is about the in-vitro catalytic activity, and immunoassay applications, however, few reports about their interaction at nano-bio interface. These studies are motivating but still leave many questions unanswered, which encourages further research. Detailed characterization of nanozymes upon administration in vivo conditions would shed light about the formation of protein corona and the interaction with cationic and anionic molecules dispersed in living organisms. Undoubtedly, in the coming years, research on nanozymes will continue to expand at the interface of nanomedicines, animal biotechnology, enzymology, and materials science.

AUTHOR CONTRIBUTIONS

The author confirms being the sole contributor of this work and has approved it for publication.

ACKNOWLEDGMENTS

REFERENCES

Ali, S. S., Hardt, J. I., and Dugan, L. L. (2008). SOD activity of carboxyfullerenes predicts their neuroprotective efficacy: a structure-activity study. *Nanomedicine* 4, 283–294. doi: 10.1016/j.nano.2008.05.003

Ali, S. S., Hardt, J. I., Quick, K. L., Kim-Han, J. S., Erlanger, B. F., Huang, T. T., et al. (2004). A biologically effective fullerene (C60) derivative with superoxide dismutase mimetic properties. *Free Radic. Biol. Med.* 37, 1191–1202. doi: 10.1016/j.freeradbiomed.2004. 07.002

André, R., Natálio, F., Humanes, M., Leppin, J., Heinze, K., Wever, R., et al. (2011). V2O5 nanowires with an intrinsic peroxidase-like activity. *Adv. Funct. Mater.* 21, 501–509. doi: 10.1002/adfm.201 001302

Asati, A., Kaittanis, C., Santra, S., and Perez, J. M. (2011). pH-tunable oxidase-like activity of cerium oxide nanoparticles achieving sensitive fluorigenic detection of cancer biomarkers at neutral pH. *Anal. Chem.* 83, 2547–2553. doi: 10.1021/ac102826k

Asati, A., Santra, S., Kaittanis, C., Nath, S., and Perez, J. M. (2009). Oxidase-like activity of polymer-coated cerium oxide nanoparticles. *Angew. Chem. Int. Ed. Engl.* 48, 2308–2312. doi: 10.1002/anie.200805279

Beltrame, P., Comotti, M., Della Pina, C., and Rossi, M. (2006). Aerobic oxidation of glucose: II. Catalysis by colloidal gold. *Appl. Catalysis A Gen.* 297, 1–7. doi: 10.1016/j.apcata.2005.08.029

Bhagat, S., Srikanth Vallabani, N. V., Shutthanandan, V., Bowden, M., Karakoti, A. S., and Singh, S. (2018). Gold core/ceria shell-based redox active nanozyme mimicking the biological multienzyme complex phenomenon. *J. Colloid. Interface Sci.* 513, 831–842. doi: 10.1016/j.jcis.2017.11.064

Cao, X., and Wang, N. (2011). A novel non-enzymatic glucose sensor modified with Fe2O3 nanowire arrays. *Analyst* 136, 4241–4246. doi: 10.1039/c1an15367f

Chen, Z., Yin, J. J., Zhou, Y. T., Zhang, Y., Song, L., Song, M., et al. (2012). Dual enzyme-like activities of iron oxide nanoparticles and their implication for diminishing cytotoxicity. *ACS Nano* 6, 4001–4012. doi: 10.1021/nn300291r

Comotti, M., Della Pina, C., Matarrese, R., and Rossi, M. (2004). The catalytic activity of "naked" gold particles. *Angew. Chem. Int. Ed. Engl.* 43, 5812–5815. doi: 10.1002/anie.200460446

Dai, Z., Liu, S., Bao, J., and Ju, H. (2009). Nanostructured FeS as a mimic peroxidase for biocatalysis and biosensing. *Chemistry* 15, 4321–4326. doi: 10.1002/chem.200802158

Dhall, A., Burns, A., Dowding, J., Das, S., Seal, S., and Self, W. (2017). Characterizing the phosphatase mimetic activity of cerium oxide nanoparticles and distinguishing its active site from that for catalase

mimetic activity using anionic inhibitors. *Environ. Sci. Nano.* 4, 1742–1749. doi: 10.1039/C7EN00394C

Dhall, A., and Self, W. (2018). Cerium oxide nanoparticles: a brief review of their synthesis methods and biomedical applications. *Antioxidants* 7:E97. doi: 10.3390/antiox7080097

Dutta, A. K., Maji, S. K., Srivastava, D. N., Mondal, A., Biswas, P., Paul, P., et al. (2012). Synthesis of FeS and FeSe nanoparticles from a single source precursor: a study of their photocatalytic activity, peroxidase-like behavior, and electrochemical sensing of H2O2. *ACS Appl. Mater. Interfaces* 4, 1919–1927. doi: 10.1021/am300408r

Fan, J., Yin, J. J., Ning, B., Wu, X., Hu, Y., Ferrari, M., et al. (2011). Direct evidence for catalase and peroxidase activities of ferritin-platinum nanoparticles. *Biomaterials* 32, 1611–1618. doi: 10.1016/j.biomaterials.2010.11.004

Gao, L., Zhuang, J., Nie, L., Zhang, J., Zhang, Y., Gu, N., et al. (2007). Intrinsic peroxidase-like activity of ferromagnetic nanoparticles. *Nat. Nanotechnol.* 2, 577–583. doi: 10.1038/nnano.2007.260

He, W., Jia, H., Li, X., Lei, Y., Li, J., Zhao, H., et al. (2012). Understanding the formation of CuS concave superstructures with peroxidase-like activity. *Nanoscale* 4, 3501–3506. doi: 10.1039/c2nr30310h

He, W., Liu, Y., Yuan, J., Yin, J. J., Wu, X., Hu, X., et al. (2011). Au@Pt nanostructures as oxidase and peroxidase mimetics for use in immunoassays. *Biomaterials* 32, 1139–1147. doi: 10.1016/j.biomaterials.2010.09.040

Heckert, E. G., Karakoti, A. S., Seal, S., and Self, W. T. (2008a). The role of cerium redox state in the SOD mimetic activity of nanoceria. *Biomaterials* 29, 2705–2709. doi: 10.1016/j.biomaterials.2008.03.014

Heckert, E. G., Seal, S., and Self, W. T. (2008b). Fenton-like reaction catalyzed by the rare earth inner transition metal cerium. *Environ. Sci. Technol.* 42, 5014–5019. doi: 10.1021/es8001508

Horie, M., Kato, H., Fujita, K., Endoh, S., and Iwahashi, H. (2012). *In vitro* evaluation of cellular response induced by manufactured nanoparticles. *Chem. Res. Toxicol.* 25, 605–619. doi: 10.1021/tx200470e

Jawaid, P., Rehman, Mu., Yoshihisa, Y., Li, P., Zhao, Q., Hassan, M. A., et al. (2014). Effects of SOD/catalase mimetic platinum nanoparticles on radiation-induced apoptosis in human lymphoma U937 cells. *Apoptosis* 19, 1006–1016. doi: 10.1007/s10495-014-0972-5

Jeon, W. B., Bae, K. H., and Byun, S. M. (1998). Dimeric beta-cyclodextrin-based supramolecular ligands and their copper(II) complexes as metalloenzyme models. *J. Inorg. Biochem.* 71, 163–169. doi: 10.1016/S0162-0134(98)10049-1

Karakoti, A., Singh, S., Dowding, J. M., Seal, S., and Self, W. T. (2010). Redox-active radical scavenging nanomaterials. *Chem. Soc. Rev.* 39, 4422–4432. doi: 10.1039/b919677n

Karakoti, A. S., Singh, S., Kumar, A., Malinska, M., Kuchibhatla, S. V., Wozniak, K., et al. (2009). PEGylated nanoceria as radical scavenger with tunable redox chemistry. *J. Am. Chem. Soc.* 131, 14144–14145. doi: 10.1021/ja9051087

Karim, M. N., Anderson, S. R., Singh, S., Ramanathan, R., and Bansal, V. (2018). Nanostructured silver fabric as a free-standing NanoZyme for colorimetric detection of glucose in urine. *Biosens. Bioelectron.* 110, 8–15. doi: 10.1016/j.bios.2018.03.025

Khulbe, K., Roy, P., Radhakrishnan, A., and Mugesh, G. (2018). An unusual two-step hydrolysis of nerve agents by a nanozyme. *ChemCatChem* 10, 4826–4831. doi: 10.1002/cctc.201801220

Korsvik, C., Patil, S., Seal, S., and Self, W. T. (2007). Superoxide dism Korsvik utase mimetic properties exhibited by vacancy engineered ceria nanoparticles. *Chem. Commun.* 10, 1056–1058. doi: 10.1039/b615134e

Leifeld, V.,Dos Santos, P. T. M., Zelinski, D. W., and Igarashi-Mafra, L. (2018). Ferrous ions reused as catalysts in Fenton-like reactions for remediation of agro-food industrial wastewater. *J. Environ. Manage.* 222, 284–292. doi: 10.1016/j.jenvman.2018.05.087

Lin, Y., Ren, J., and Qu, X. (2014). Catalytically active nanomaterials: a promising candidate for artificial enzymes. *Acc. Chem. Res.* 47, 1097–1105. doi: 10.1021/ar400250z

Lin, Y., Zhao, A., Tao, Y., Ren, J., and Qu, X. (2013). Ionic liquid as an efficient modulator on artificial enzyme system: toward the realization of high-temperature catalytic reactions. *J. Am. Chem. Soc.* 135, 4207–4210. doi: 10.1021/ja400280f

Liu, Y., Wu, H., Li, M., Yin, J. J., and Nie, Z. (2014). pH dependent catalytic activities of platinum nanoparticles with respect to the decomposition of

hydrogen peroxide and scavenging of superoxide and singlet oxygen. *Nanoscale* 6, 11904–11910. doi: 10.1039/C4NR03848G

Luo, W., Zhu, C., Su, S., Li, D., He, Y., Huang, Q., et al. (2010). Self-catalyzed, self-limiting growth of glucose oxidase-mimicking gold nanoparticles. *ACS Nano* 4, 7451–7458. doi: 10.1021/nn102592h

Mahmoudi, M., Azadmanesh, K., Shokrgozar, M. A., Journeay, W. S., and Laurent, S. (2011). Effect of nanoparticles on the cell life cycle. *Chem. Rev.* 111, 3407–3432. doi: 10.1021/cr1003166

Mancin, F., Prins, L. J., Pengo, P., Pasquato, L., Tecilla, P., and Scrimin, P. (2016). Hydrolytic metallo-nanozymes: from micelles and vesicles to gold nanoparticles. *Molecules* 21:E1014. doi: 10.3390/molecules21081014

Mu, J., Zhang, L., Zhao, M., and Wang, Y. (2014). Catalase mimic property of Co3O4 nanomaterials with different morphology and its application as a calcium sensor. *ACS Appl. Mater. Interfaces* 6, 7090–7098. doi: 10.1021/am406033q

Muscoli, C., Cuzzocrea, S., Riley, D. P., Zweier, J. L., Thiemermann, C., Wang, Z. Q., et al. (2003). On the selectivity of superoxide dismutase mimetics and its importance in pharmacological studies. *Br. J. Pharmacol.* 140, 445–460. doi: 10.1038/sj.bjp.0705430

Natalio, F., André, R., Hartog, A. F., Stoll, B., Jochum, K. P., Wever, R., et al. (2012). Vanadium pentoxide nanoparticles mimic vanadium haloperoxidases and thwart biofilm formation. *Nat. Nanotechnol.* 7, 530–535. doi: 10.1038/nnano.2012.91

Patel, P., Kansara, K., Singh, R., Shukla, R. K., Singh, S., Dhawan, A., et al. (2018). Cellular internalization and antioxidant activity of cerium oxide nanoparticles in human monocytic leukemia cells. *Int. J. Nanomed.* 13, 39–41. doi: 10.2147/IJN.S124996

Pirmohamed, T., Dowding, J. M., Singh, S., Wasserman, B., Heckert, E., Karakoti, A. S., et al. (2010). Nanoceria exhibit redox state-dependent catalase mimetic activity. *Chem. Commun.* 46, 2736–2738. doi: 10.1039/b922024k

Rahal, A., Kumar, A., Singh, V., Yadav, B., Tiwari, R., Chakraborty, S., et al. (2014). Oxidative stress, prooxidants, and antioxidants: the interplay. *Biomed. Res. Int.* 2014:761264. doi: 10.1155/2014/761264

Rather, H. A., Thakore, R., Singh, R., Jhala, D., Singh, S., and Vasita, R. (2018). Antioxidative study of Cerium Oxide nanoparticle functionalised PCL-Gelatin electrospun fibers for wound healing application. *Bioact. Mater.* 3, 201–211. doi: 10.1016/j.bioactmat.2017.09.006

Raynal, M., Ballester, P., Vidal-Ferran, A., and van Leeuwen, P. W. (2014). Supramolecular catalysis. Part 2: artificial enzyme mimics. *Chem. Soc. Rev.* 43, 1734–1787. doi: 10.1039/C3CS60037H

Shah, J., Purohit, R., Singh, R., Karakoti, A. S., and Singh, S. (2015). ATP-enhanced peroxidase-like activity of gold nanoparticles. *J. Colloid Interface Sci.* 456, 100–107. doi: 10.1016/j.jcis.2015.06.015

Shah, J., and Singh, S. (2018). Unveiling the role of ATP in amplification of intrinsic peroxidase-like activity of gold nanoparticles. *3 Biotech* 8:67. doi: 10.1007/s13205-017-1082-1

Shah, K., Bhagat, S., Varade, D., and Singh, S. (2018). Novel synthesis of polyoxyethylene cholesteryl ether coated Fe-Pt nanoalloys: a multifunctional and cytocompatible bimetallic alloy exhibiting intrinsic chemical catalysis and biological enzyme-like activities. *Colloids Surf. A Physicochem. Eng. Aspects* 553, 50–57. doi: 10.1016/j.colsurfa.2018.05.034

Simos, Y. V., Verginadis, I. I., Toliopoulos, I. K., Velalopoulou, A. P., Karagounis, I. V., Karkabounas, S. C., et al. (2012). Effects of catechin and epicatechin on superoxide dismutase and glutathione peroxidase activity, *in vivo*. *Redox Rep.* 17, 181–186. doi: 10.1179/1351000212Y.0000000020

Singh, R., Karakoti, A. S., Self, W. T., Seal, S., and Singh, S. (2016). Redox-sensitive cerium oxide nanoparticles protect human keratinocytes from oxidative stress induced by glutathione depletion. *Langmuir* 32, 12202–12211. doi: 10.1021/acs.langmuir.6b03022

Singh, R., and Singh, S. (2015). Role of phosphate on stability and catalase mimetic activity of cerium oxide nanoparticles. *Colloids Surf. B Biointerfaces* 132, 78–84. doi: 10.1016/j.colsurfb.2015.05.005

Singh, R., and Singh, S. (2019). Redox-dependent catalase mimetic cerium oxide-based nanozyme protect human hepatic cells from 3-AT induced acatalasemia. *Colloids Surf. B Biointerfaces* 175, 625–635. doi: 10.1016/j.colsurfb.2018.12.042

Singh, S. (2016). Cerium oxide based nanozymes: redox phenomenon at biointerfaces. *Biointerphases* 11:04B202. doi: 10.1116/1.4966535

Singh, S., Dosani, T., Karakoti, A. S., Kumar, A., Seal, S., and Self, W. T. (2011). A phosphate-dependent shift in redox state of cerium oxide nanoparticles and its effects on catalytic properties. *Biomaterials* 32, 6745–6753. doi: 10.1016/j.biomaterials.2011.05.073

Strzepa, A., Pritchard, K. A., and Dittel, B. N. (2017). Myeloperoxidase: a new player in autoimmunity. *Cell. Immunol.* 317, 1–8. doi: 10.1016/j.cellimm.2017.05.002

Vallabani, N. V. S., Karakoti, A. S., and Singh, S. (2017). ATP-mediated intrinsic peroxidase-like activity of Fe3O4-based nanozyme: one step detection of blood glucose at physiological pH. *Colloids Surf. B Biointerfaces* 153, 52–60. doi: 10.1016/j.colsurfb.2017.02.004

Vallabani, N. V. S., and Singh, S. (2018). Recent advances and future prospects of iron oxide nanoparticles in biomedicine and diagnostics. *3 Biotech* 8:279. doi: 10.1007/s13205-018-1286-z

Wan, Y., Qi, P., Zhang, D., Wu, J., and Wang, Y. (2012). Manganese oxide nanowire-mediated enzyme-linked immunosorbent assay. *Biosens. Bioelectron.* 33, 69–74. doi: 10.1016/j.bios.2011.12.033

Wang, X., Cao, W., Qin, L., Lin, T., Chen, W., Lin, S., et al. (2017). Boosting the peroxidase-like activity of nanostructured nickel by inducing Its 3+ oxidation state in LaNiO3 perovskite and its application for biomedical assays. *Theranostics* 7, 2277–2286. doi: 10.7150/thno.19257

Wang, X., Yang, Q., Cao, Y., Hao, H., Zhou, J., and Hao, J. (2016). Metallosurfactant ionogels in imidazolium and protic ionic liquids as precursors to synthesize nanoceria as catalase mimetics for the catalytic decomposition of H2 O2. *Chemistry* 22, 17857–17865. doi: 10.1002/chem.201603743

Wei, H., and Wang, E. (2008). Fe3O4 magnetic nanoparticles as peroxidase mimetics and their applications in H2O2 and glucose detection. *Anal. Chem.* 80, 2250–2254. doi: 10.1021/ac702203f

Wei, H., and Wang, E. (2013). Nanomaterials with enzyme-like characteristics (nanozymes): next-generation artificial enzymes. *Chem. Soc. Rev.* 42, 6060–6093. doi: 10.1039/c3cs35486e

Wilner, O. I., Weizmann, Y., Gill, R., Lioubashevski, O., Freeman, R., and Willner, I. (2009). Enzyme cascades activated on topologically programmed DNA scaffolds. *Nat. Nanotechnol.* 4, 249–254. doi: 10.1038/nnano.2009.50

Xie, X., Xu, W., and Liu, X. (2012). Improving colorimetric assays through protein enzyme-assisted gold nanoparticle amplification. *Acc. Chem. Res.* 45, 1511–1520. doi: 10.1021/ar300044j

Zhang, H., Liang, X., Han, L., and Li, F. (2018). "Non-Naked" gold with glucose oxidase-like activity: a nanozyme for tandem catalysis. *Small* 14:e1803256. doi: 10.1002/smll.201803256

Zhang, K., Hu, X., Liu, J., Yin, J. J., Hou, S., Wen, T., et al. (2011). Formation of PdPt alloy nanodots on gold nanorods: tuning oxidase-like activities via composition. *Langmuir* 27, 2796–2803. doi: 10.1021/la104566e

Zhang, W., Dong, J., Wu, Y., Cao, P., Song, L., Ma, M., et al. (2017). Shape-dependent enzyme-like activity of Co3O4 nanoparticles and their conjugation with his-tagged EGFR single-domain antibody. *Colloids Surf. B Biointerfaces* 154, 55–62. doi: 10.1016/j.colsurfb.2017.02.034

Zhang, Y., Tian, J., Liu, S., Wang, L., Qin, X., Lu, W., et al. (2012). Novel application of CoFe layered double hydroxide nanoplates for colorimetric detection of H(2)O(2) and glucose. *Analyst* 137, 1325–1328. doi: 10.1039/c2an00035k

Zhao, M., Tao, Y., Huang, W., and He, Y. (2018).Reversible pH switchable oxidase-like activities of MnO2 nanosheets for a visual molecular majority logic gate. *Phys. Chem. Chem. Phys.* 20, 28644–28648. doi: 10.1039/C8CP05660A

Zheng, X., Liu, Q., Jing, C., Li, Y., Li, D., Luo, W., et al. (2011). Catalytic gold nanoparticles for nanoplasmonic detection of DNA hybridization. *Angew. Chem. Int. Ed. Engl.* 50, 11994–11998. doi: 10.1002/anie.201105121

Zhou, Y., Liu, B., Yang, R., and Liu, J. (2017). Filling in the gaps between nanozymes and enzymes: challenges and opportunities. *Bioconjug. Chem.* 28, 2903–2909. doi: 10.1021/acs.bioconjchem.7b00673

Zou, S., Zhu, X., Zhang, L., Guo, F., Zhang, M., Tan, Y., et al. (2018). Biomineralization-inspired synthesis of cerium-doped carbonaceous nanoparticles for highly hydroxyl radical scavenging activity. *Nanoscale Res. Lett.* 13:76. doi: 10.1186/s11671-017-2427-8

Advantages of publishing in Frontiers

OPEN ACCESS
Articles are free to read for greatest visibility and readership

FAST PUBLICATION
Around 90 days from submission to decision

HIGH QUALITY PEER-REVIEW
Rigorous, collaborative, and constructive peer-review

TRANSPARENT PEER-REVIEW
Editors and reviewers acknowledged by name on published articles

Frontiers
Avenue du Tribunal-Fédéral 34
1005 Lausanne | Switzerland

Visit us: www.frontiersin.org
Contact us: info@frontiersin.org | +41 21 510 17 00

REPRODUCIBILITY OF RESEARCH
Support open data and methods to enhance research reproducibility

DIGITAL PUBLISHING
Articles designed for optimal readership across devices

FOLLOW US
@frontiersin

IMPACT METRICS
Advanced article metrics track visibility across digital media

EXTENSIVE PROMOTION
Marketing and promotion of impactful research

LOOP RESEARCH NETWORK
Our network increases your article's readership